ure; and, by virtue of the equilibrium $C_{(graphite)} + 2H_2 = CH_4$, a CH_4–H_2 mixture of known p_{CH_4} and p_{H_2} has a unique activity of carbon at any temperature. Consequently, CO–CO_2 and CH_4–H_2 mixtures can be used as gas phases of fixed activity of carbon for use in the establishment of heterogeneous equilibria between a gas phase and a condensed phase. Similarly, CO–CO_2 and H_2–H_2O mixtures can be used as gas phases of fixed oxygen pressure and H_2–H_2S mixtures can be used as gas phases of fixed sulfur pressure. The activities of carbon in liquid and solid iron have been determined by equilibrating iron with CO–CO_2 and CH_4–H_2 mixtures and measuring the equilibrium carbon content of the metal phase, and the activities of oxygen and sulfur in liquid iron have been determined by equilibrating iron with H_2O–H_2 and H_2S–H_2 mixtures, respectively. In more simple gas–metal equilibria the activities of hydrogen and nitrogen in iron have been determined by measuring the solubilities of the gases as functions of gas pressure. Activities in the system Fe–Fe_2O_3 have been determined by experimental observation of the variation of the composition of small samples of condensed phases with temperature and oxygen pressure imposed by an equilibrating gas phase. The variation, with composition, of the activity of Fe in the system is determined by Gibbs–Duhem integration of the corresponding measured variation of the equilibrium partial pressure of oxygen. The oxygen content of liquid iron in equilibrium with pure liquid iron oxide at 1600°C is 0.23 wt%. If the oxide of a less noble metal than iron is dissolved in the liquid iron oxide, the activity of iron oxide, and hence the equilibrium oxygen content of the liquid iron are decreased. If the latter is x wt%, the activity of FeO, relative to pure Fe-saturated iron oxide as the standard state, in the oxide solution is $x/0.23$. This technique has been used to determine the activity of FeO in CaO–FeO and CaO–FeO–SiO_2 melts saturated with liquid iron.

One step more complex is the establishment of equilibrium between a gas phase and two condensed phases. The equilibrium between manganese, manganous oxide and a CO–CO_2 mixture, expressed as $Mn + CO_2 = MnO + CO$ requires:

$$K = \frac{p_{CO} a_{MnO}}{p_{CO_2} a_{Mn}}. \tag{84}$$

Thus, at a given temperature, the equilibrium between pure Mn (at unit activity) and Mn-saturated pure MnO (at unit activity) occurs at a unique value of the ratio p_{CO}/p_{CO_2} given by eq. (84). If a metal more noble than Mn is embedded in an excess of MnO and subjected to a lower p_{CO}/p_{CO_2} ratio, manganese is transferred from the MnO to the metal phase until the activity of Mn required by eq. (84) and the imposed p_{CO}/p_{CO_2} is established. The manganese content of the alloy corresponding to the imposed activity is determined by chemical analysis. The other component of the alloy must be sufficiently more noble than Mn that formation and solution of its oxide in the MnO phase is negligible. The activity of Mn in Mn–Pt alloys has been determined in this manner. Having determined this relationship, the activity of MnO in oxide melts containing oxides more stable than MnO can be determined by equilibrating a small sample of Pt with an excess of oxide melt and a CO–CO_2 gas mixture. Again, as Mn is distributed between the Pt–Mn alloy and the oxide melt in accordance with eq. (84) and the imposed

References: p. 469.

p_{CO}/p_{CO_2}, chemical analysis of the equilibrated Pt–Mn alloy yields a_{Mn} and hence, from eq. (84), the value of a_{MnO} in the oxide melt. In this application the other oxide component must be of a metal which is sufficiently less noble than Mn that the extent of its solution in the Pt Mn phase is negligible. This technique has been used to determine the activity of MnO in systems such as $MnO–SiO_2$, $MnO–TiO_2$, $MnO–Al_2O_3$, $MnO–B_2O_3$ and $MnO–CaO–SiO_2$.

Other examples of determination of activities by establishing equilibrium between a binary alloy, a nonmetallic phase of known composition and a gas phase include:

$$\begin{aligned}
&\text{Fe(in Fe–Ni alloys)} + H_2O = FeO + H_2;\\
&2\text{Cr(in Cr–Ni alloys)} + 3H_2O = Cr_2O_3 + 3H_2;\\
&3\text{Mn(in Mn–Cu alloys)} + CH_4 = Mn_3C + 2H_2;\\
&2\text{Cu(in Cu–Au alloys)} + H_2S = Cu_2S + H_2;\\
&3\text{Si(in Si–Ag alloys)} + N_2\ (\text{in } N_2–H_2 \text{ mixtures}) = Si_3N_4.
\end{aligned} \tag{85}$$

Again, in this application, the "inert" metal must be sufficiently more noble than the primary component metal that its occurrence in the equilibrium nonmetallic phase is negligible. Corrections are required in systems where the nonmetallic phase is not a line compound. Thus, for example, in eq. (85), the activity of FeO is that in the wustite equilibrated with the imposed partial pressure of oxygen, relative to Fe-saturated wustite as the standard state. Equation (85) has also been used to determine the activity of FeO in $FeO–SiO_2$ melts by establishing the equilibrium $Fe + H_2O = FeO$ (in $FeO–SiO_2$ melts) $+ H_2$.

If the difference between the nobilities of the metals is small enough that an oxide solution is produced in equilibrium with the binary alloy phase a different approach is taken. For example, if a small specimen of an Fe–Mn alloy is equilibrated with an excess of an FeO–MnO solid solution, the exchange equilibrium $Fe + MnO = Mn + FeO$ is established, wherein $K = a_{Mn}a_{FeO}/a_{Fe}a_{MnO}$. From chemical analysis of the equilibrated Fe–Mn alloy and knowledge of the activities in the system Fe Mn, the ratio $\gamma_{FeO}/\gamma_{MnO}$ in the equilibrating oxide solution is obtained as:

$$\frac{\gamma_{FeO}}{\gamma_{MnO}} = K\frac{a_{Fe}X_{MnO}}{a_{Mn}X_{FeO}},$$

and Gibbs–Duhem integration of the variation of this ratio with composition in the oxide solution according to eq. (81) yields the individual activity coefficients, and hence activities, of the components of the oxide solution. This technique has been used to determine activities in the systems $Fe_2SiO_4–Co_2SiO_4$ and $Fe_2SiO_4–Mn_2SiO_4$.

Activities have been determined by establishing equilibrium among three condensed phases and a gas phase. As an example, the activity of SiO_2 in $CaO–MgO–Al_2O_3–SiO_2$ melts has been determined by establishing the equilibrium

$$SiO_2 + 2C = Si + 2CO \tag{86}$$

in systems comprising a silicate melt, solid graphite, liquid iron and CO gas at 1 atm pressure, and by establishing the equilibrium

$$SiO_2 + 2SiC = 3Si + 2CO \tag{87}$$

in systems comprising a silicate melt, solid SiC, liquid iron and CO gas at 1 atm pressure. The activity of SiO_2 is obtained from chemical analysis of the equilibrated liquid phases, knowledge of the equilibrium constants for the reactions given by eqs. (86) and (87) and knowledge of the activity of Si in Fe–Si–C melts. Gibbs–Duhem integration of the results yielded activities in the systems $CaO–SiO_2$, $CaO–Al_2O_3$, $MgO–SiO_2$, $CaO–Al_2O_3–SiO_2$, $MgO–CaO–SiO_2$ and $MgO–Al_2O_3–SiO_2$.

10.3. Electrochemical measurement of activity

The EMF of a reversible galvanic cell, ε, is related to the free energy change, ΔG, for the cell reaction as $\Delta G = -z F \varepsilon$ where F is Faraday's constant and z is the number of Faradays required for the cell reaction. Thus, in a concentration cell of the type

pure metal A | ionic conductor containing metal A ions of valence z_A | alloy A–B,

the cell reaction is A(pure) $\rightarrow$ A(in the A–B alloy) for which $\Delta G = RT \ln a_A$ (in the A B alloy). Thus the activity of A in the alloy is obtained as $\ln a_A = -(z_A F \varepsilon / RT)$. The determination of activity by measurement of the EMF of an electrochemical cell requires that the electrolyte be a purely ionic conductor and that the valency z_A be defined. A further requirement is that the extent of the exchange reaction at the cathode–electrolyte interface between B in the alloy and A in the electrolyte be negligible. If this condition is not met, the measured EMF contains a contribution of unknown magnitude arising from the transfer of electrolyte between regions of different composition. In practice the extent of the exchange reaction is rendered negligible by ensuring that B is significantly more noble than A. Molten chlorides are purely ionic conductors and hence these melts are popular as liquid electrolytes. The concentrations of low valent cations in the electrolyte are minimized by dissolving the chlorides in mixtures of alkali chlorides.

The activity of Al in Al–Ag melts in the range 700–800°C has been obtained from measurement of the EMFs of cells of the type

$$Al_{(l)} \,|\, Al^{3+}(\text{in KCl–NaCl}) \,|\, Al–Ag_{(l)}.$$

Similarly the activities of Cd in Cd–Pb, Cd–Bi, Cd–Sb and Cd–Sn alloys, and the activities of Cu in Cu–Au melts and Ag in Ag–Au melts have been determined from concentration cells with liquid chloride electrolytes.

The cell

$$Mg_{(l)} \,|\, MgCl_{2(l)} \,|\, Cl_{2(g,1\ atm)}$$

is a formation cell in which the cell reaction is $Mg + Cl_2 = MgCl_2$. With pure liquid Mg, pure liquid $MgCl_2$ and Cl_2 at 1 atm pressure, the free energy change is the standard free energy change, ΔG^0, and the EMF is the standard EMF, $\varepsilon^0 = -\Delta G^0 / 2F$. Alloying the anode with a more noble metal such as Al alters the free energy change for the cell reaction to $\Delta G = \Delta G^0 - RT \ln a_{Mg}$ (in the alloy) and hence the cell EMF to

$$\varepsilon = \varepsilon^0 + \frac{RT}{2F} \ln a_{Mg} \text{ (in the alloy)}. \tag{88}$$

References: p. 469.

Equation (88) has been used to determine the activities of Mg in Mg–Al melts from EMF measurements in the range 700–880°C.

Similarly, the formation cell

$$Pb_{(l)} | PbO_{(l)} | O_{2(g,1\ atm)}$$

has a standard EMF of $\varepsilon^0 = -\Delta G^0/2F$. Alloying the PbO electrolyte with the oxide of a less noble metal, such as SiO_2, changes the cell EMF to:

$$\varepsilon = \varepsilon^0 - \frac{RT}{2F} \ln a_{PbO} \text{ (in PbO–SiO}_2\text{)},$$

and this has been used as the basis for electrochemical determination of the activities in the system PbO–SiO_2 in the range 850–1050°C.

Within wide ranges of temperature and oxygen pressure, ZrO_2 and ThO_2 in the fluorite structure, stabilized by solid solution with CaO and Y_2O_3, respectively, exhibit unusually high conductivities and transport numbers for O^{2-} of essentially unity. Consequently CaO–ZrO_2 and Y_2O_3–ThO_2 have been used as solid electrolytes in oxygen concentration cells of the type

$$Pt,\ O_{2(g,\text{ at pressure } P_1)} | CaO\text{–}ZrO_2 | O_{2(g,\text{ at pressure } P_2)},\ Pt,$$

in which the cell reaction is $O_{2(g,\text{at pressure } P1)} \rightarrow O_{2(g,\text{at pressure } P2)}$ and the cell EMF is $\varepsilon = -\Delta G/4F = -(RT/4F) \ln P_2/P_1$. The oxygen pressure at the electrodes can be fixed by using equilibrated metal–metal–oxide couples, e.g., with Fe–FeO and Ni–NiO the cell becomes

$$Fe,\ FeO | CaO\text{–}ZrO_2 | Ni,\ NiO,$$

with a cell reaction of NiO + Fe = FeO + Ni. With the electrodes Fe–FeO and (Fe–Ni)–FeO, the cell reaction is $Fe_{(pure)} \rightarrow Fe_{(\text{in the Fe–Ni alloy})}$ and the cell EMF is

$$\varepsilon = -\frac{RT}{2F} \ln a_{Fe} \text{ (in the alloy)}. \tag{89}$$

This method is similar to that discussed in connection with eq. (85). In the chemical equilibration technique the oxygen pressure is imposed, and the Fe–Ni alloy in equilibrium with FeO and the imposed oxygen pressure is produced in the experimental apparatus. In the EMF technique the oxygen pressure in equilibrium with a given Fe–Ni alloy and FeO is measured. Equation (89) has been used as the basis for electrochemical determination of the activities in a large number of solid and liquid binary alloy systems, the majority of which contained Fe, Co, Ni or Cu as the less noble metal. The activity of Si in Fe–Si alloys at 1550°C and 1600°C has been determined with electrodes of Cr, Cr_2O_3 and SiO_2, Fe–Si and activities in the systems Ta–W and Ta–Mo have been determined with a Y_2O_3–ThO_2 electrolyte and Ta, Ta_2O_5 and Ta–X, Ta_2O_5 electrodes. The activities of SnO in SnO–SiO_2 melts and PbO in PbO–SiO_2 melts have been determined from cells of the type M, MO|CaO–ZrO_2|M, MO–SiO_2.

Other solid electrolytes which have been used include β-alumina and soft soda glass for measurement of the activity of sodium in alloys, and glasses containing K^+ and Ag^+

for study of K and Ag alloys, respectively. It can be expected that, as new solid state electrolytes are developed for possible use in fuel cells, they will be applied to the determination of activities by EMF measurements.

Bibliography

ALCOCK, C. B., Principles of Pyrometallurgy (Academic Press, London, 1976).

BELTON, G. R., Langmuir Adsorption, the Gibbs Adsorption Isotherm and Interfacial Kinetics in Liquid Metal Systems, Metallurg. Trans. **B7** (1976) 35.

BELTON, G. R., and R. J. FRUEHAN, The Determination of Activities by Mass-Spectrometry – Some Additional Methods, Metallurg. Trans. **2** (1971) 291.

CALLEN, H. B., Thermodynamics (Wiley, New York, 1960).

CHANDRASEKHARAIAH, M. S., O. M. SREEDHARAN and E. CHATTOPADHYAY, Thermodynamic Studies of Alloys and Intermetallic Compounds, in: Solid Electrolytes and Their Applications, ed. E. C. Subbarao (Plenum, New York, 1980).

ELLINGHAM, H. J. T., Reducibility of Oxides and Sulfides in Metallurgical Processes, J. Soc. Chem. Ind. **63** (1944) 125.

ELLIOTT, J. F., Physical Chemistry of Liquid Metal Solutions, in: Metallurgical Treatises, eds. J. F. Elliott and J. Tien (The Metallurgical Society of AIME, Warrendale, PA, 1981).

ELLIOTT, J. F., M. GLEISER and V. RAMAKRISHNA, Thermochemistry for Steelmaking (Addison Wesley, Reading, MA, 1963).

FAST, J. D., Entropy (McGraw Hill, New York, 1962).

GASKELL, D. R., Introduction to Metallurgical Thermodynamics, 2nd Ed. (McGraw–Hill, New York, 1981).

GOKCEN, N. A., Thermodynamics (Techscience, Hawthorne, CA, 1977).

HULTGREN, R., P. D. DESAI, D. T. HAWKINS, M. GLEISER and K. K. KELLEY, Selected Values of the Thermodynamic Properties of Binary Alloys (American Society for Metals, Metals Park, OH, 1973).

KUBASCHEWSKI, O., C. B. ALCOCK and P. J. SPENCER, Materials Thermochemistry, 6th Ed. (Pergamon Press, New York, 1993).

LEWIS, G. N., and M. RANDALL, Thermodynamics, 2nd Ed., revised by K. S. Spitzer and L. Brewer (McGraw–Hill, New York, 1961).

LUPIS, C. H. P., Chemical Thermodynamics of Materials (North–Holland, Amsterdam, 1983).

MOORE, J. J., Chemical Metallurgy, 2nd Ed. (Butterworths, London, 1990).

ROSENQUIST, T., Principles of Extractive Metallurgy (McGraw–Hill, New York, 1974).

STEINER, A., and K. L. KOMAREK, Thermodynamic Activities in Solid Ni–Al Alloys, Trans. Metallurg. Soc. AIME **230** (1964) 786.

SWALIN, R. A., Thermodynamics of Solids, 2nd Ed. (Wiley, New York, 1972).

TURKDOGAN, E. T., Physical Chemistry of High Temperature Technology (Academic, New York, 1980).

WAGNER, C., Thermodynamics of Alloys (Addison–Wesley, Reading, MA, 1952).

CHAPTER 6

PHASE DIAGRAMS

ARTHUR D. PELTON

Département de Génie Métallurgique
Ecole Polytechnique, Case Postale 6079, Station "Centre Ville"
Montréal, Québec H3C 3A7, Canada

R. W. Cahn and P. Haasen†, eds.
Physical Metallurgy; fourth, revised and enhanced edition

1. Introduction

The study of phase equilibria and phase transformations is central to nearly all branches of metallurgy and materials science. Although departures from equilibrium will occur in any real system, a knowledge of the equilibrium state under a given set of conditions is the starting point for the understanding of most processes.

A phase diagram is a graphical representation of the loci of thermodynamic variables when equilibrium among the phases of a system is established under a given set of conditions. The phase diagrams most familiar to the metallurgist are those for which temperature and composition are the axes. These are discussed in §§ 2 and 3 for binary (two-component) and ternary (three-component) systems, and in § 4 for multicomponent systems. However, the effect of other variables such as total pressure and chemical potential of the components (e.g., the partial pressure of oxygen) may often be of interest. In § 6, different types of phase diagrams are discussed along with the general rules governing their construction.

Throughout the chapter, the thermodynamic origin of phase diagrams is stressed. With the advent of modern computer techniques, the relationship between phase diagrams and the thermodynamic properties of the system has become of increasing practical importance. As discussed in § 2.10, a quantitative coupling of the two is now possible. Furthermore, as discussed in § 5, the computer-assisted thermodynamic approach often permits good estimates of unknown multicomponent phase diagrams to be made, and can often significantly reduce the experimental effort required to measure the phase diagram of a system.

2. Binary phase diagrams

The temperature composition (T–X) phase diagram of the Bi–Sb system is shown in fig. 1 (HULTGREN *et al.* [1963]). The abscissa is the composition, expressed as *mole fraction* of Sb, X_{Sb}. Note that $X_{Sb} = 1 - X_{Bi}$. Phase diagrams are also often drawn with the composition axis expressed as weight percent.

At all compositions and temperatures in the area above the line labelled *liquidus*, single-phase liquid alloys will be observed, while at all compositions and temperatures

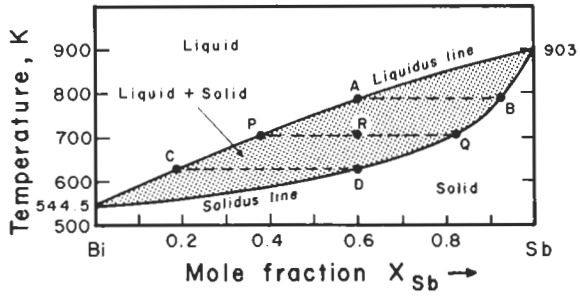

Fig. 1. Phase diagram of the Bi–Sb system (after HULTGREN *et al.* [1963]).

below the line labelled *solidus*, alloys exist as single-phase solid solutions. An alloy sample at equilibrium at a temperature and overall composition between these two curves will consist of a mixture of solid and liquid phases, the compositions of which are given by the liquidus and solidus compositions at that temperature. For example, a Bi–Sb sample of overall composition $X_{Sb} = 0.60$ at $T = 700$ K (at point R in fig. 1) will consist, at equilibrium, of a mixture of liquid alloy of composition $X_{Sb} = 0.37$ (point P) and solid alloy of composition $X_{Sb} = 0.82$ (point Q). The line PQ is called a *tie-line* or *conode*. As the overall composition is varied at 700 K between points P and Q, the compositions of the liquid and solid phases remain fixed at P and Q, and only the relative proportions of the two phases change. From a simple mass balance, one can derive the *lever rule* for binary systems: (moles of liquid)/(moles of solid) = RQ/PR. Hence, at 700 K a sample of Bi–Sb alloy with overall composition $X_{Sb} = 0.60$ consists of liquid and solid phases in the molar ratio $(0.82 - 0.60)/(0.60 - 0.37) = 0.96$. Were the composition axis expressed as weight percent, then the lever rule would give the weight ratio of the two phases.

Suppose that a liquid Bi–Sb alloy with composition $X_{Sb} = 0.60$ is cooled very slowly from an initial temperature of 900 K. When the temperature has decreased to the liquidus temperature of 780 K (point A) the first solid appears, with a composition at point B ($X_{Sb} = 0.93$). As the temperature is decreased further, solid continues to precipitate with the compositions of the two phases at any temperature being given by the liquidus and solidus compositions at that temperature and with their relative proportions being given by the lever rule. Solidification is complete at 630 K, the last liquid to solidify having composition $X_{Sb} = 0.18$ (point C).

The process just described is known as equilibrium cooling. At any temperature during equilibrium cooling the solid phase has a uniform (homogeneous) composition. In the preceding example, the composition of the solid phase during cooling varies along the line BQD. Hence, in order for the solid particles to have a uniform composition at any temperature, diffusion of Sb from the center to the surface of the growing particles must occur. Since solid state diffusion is a relatively slow process, equilibrium cooling conditions are only approached if the temperature is decreased very slowly. If a Bi–Sb alloy of composition $X_{Sb} = 0.60$ is cooled very rapidly from the liquid, concentration gradients will be observed in the solid grains, with the concentration of Sb decreasing towards the surface from a maximum of $X_{Sb} = 0.93$ (point B) at the center. Furthermore, in this case solidification will not be complete at 630 K since at 630 K the average concentration of Sb in the solid particles will now be greater than $X_{Sb} = 0.60$. These considerations are discussed more fully in ch. 9.

At $X_{Sb} = 0$ and $X_{Sb} = 1$ in fig. 1 the liquidus and solidus curves meet at the equilibrium melting points, or *temperatures of fusion*, of Bi and Sb, which are: $T^0_{f(Bi)} = 544.5$ K, $T^0_{f(Sb)} = 903$ K.

The phase diagram is influenced by the total pressure, P. Unless otherwise stated, T–X diagrams for alloy systems are usually presented for $P = \text{const.} = 1$ atm. However, for equilibria involving only solid and liquid phases, the phase boundaries are typically shifted only by the order of a few hundredths of a degree per bar change in P (see ch. 5, § 3). Hence, the effect of pressure upon the phase diagram is generally negligible

References: p. 531.

unless the pressure is of the order of hundreds of atmospheres. On the other hand, if gaseous phases are involved then the effect of pressure is very important (§ 2.12).

2.1. The thermodynamic origin of phase diagrams

In this section we shall consider first of all the thermodynamic origin of simple "lens-shaped" phase diagrams in binary systems with complete liquid and solid miscibility.

An example of such a diagram was given in fig. 1. Another example is the Ge–Si phase diagram in the lowest panel of fig. 2 (HANSEN [1958]). In the upper three panels of fig. 2 are shown, to scale, the molar Gibbs energies of the solid and liquid phases, g^s and g^l, at three temperatures. As illustrated in the top panel, g^s varies with composition

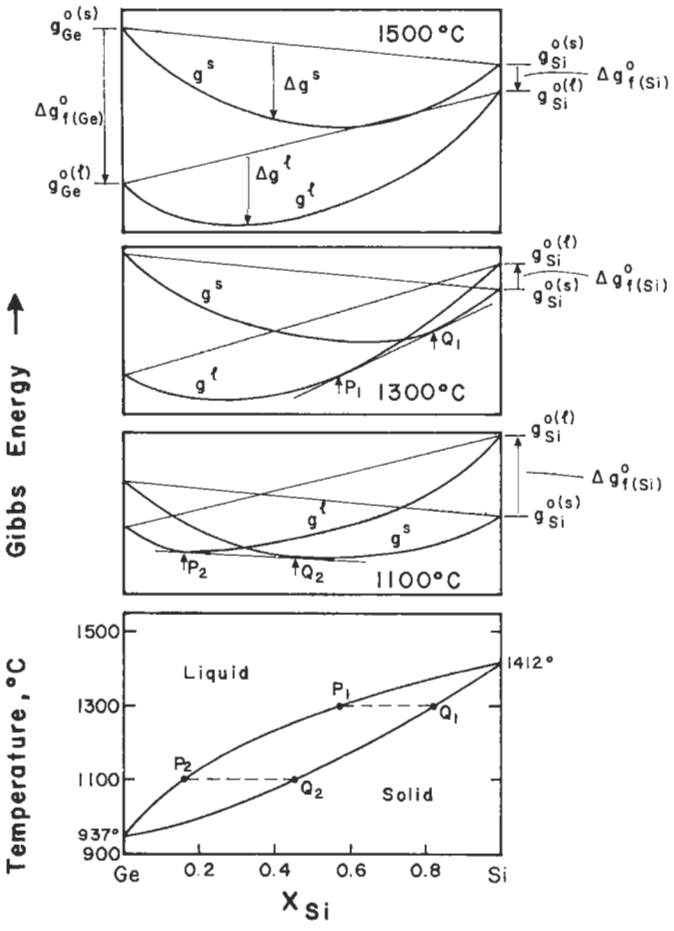

Fig. 2. Ge–Si phase diagram (after HANSEN [1958]) and Gibbs energy-composition curves at three temperatures, illustrating the common tangent construction.

between the standard molar Gibbs energies of pure solid Ge and of pure solid Si, $g_{Ge}^{0(s)}$ and $g_{Si}^{0(s)}$, while g^l varies between the standard molar Gibbs energies of the pure liquid components $g_{Ge}^{0(l)}$ and $g_{Si}^{0(l)}$. The molar *Gibbs energies of mixing* of the solid and liquid phases, Δg^s and Δg^l, are negative and are equal to the difference between the Gibbs energy of the solution and a simple weighted average of the Gibbs energies of the pure unmixed components in each phase.

The difference between $g_{Si}^{0(l)}$ and $g_{Si}^{0(s)}$ is equal to the standard molar Gibbs energy of fusion (melting) of pure Si, $\Delta g_{f(Si)}^0 = (g_{Si}^{0(l)} - g_{Si}^{0(s)})$. Similarly for Ge, $\Delta g_{f(Ge)}^0 = (g_{Ge}^{0(l)} - g_{Ge}^{0(s)})$. The Gibbs energy of fusion of a pure component may be written as:

$$\Delta g_f^0 = \Delta h_f^0 - T\Delta s_f^0, \tag{1}$$

where Δh_f^0 and Δs_f^0 are the standard molar enthalpy and entropy of fusion. Since, to a first approximation, Δh_f^0 and Δs_f^0 are independent of T, Δg_f^0 is approximately a linear function of T. If $T > T_f^0$, then Δg_f^0 is negative. If $T < T_f^0$, then Δg_f^0 is positive. Hence, as seen in fig. 2, as T decreases, the g^s curve descends relative to g^l. At 1500°C, $g^l < g^s$ at all compositions. Therefore, by the principle that a system always seeks the state of minimum Gibbs energy at constant T and P, the liquid phase is stable at all compositions at 1500°C. At 1300°C, the curves of g^s and g^l cross. The line P_1Q_1, which is the *common tangent* to the two curves, divides the composition range into three sections. For compositions between pure Ge and P_1, a single-phase liquid is the state of minimum Gibbs energy. For compositions between Q_1 and pure Si, a single-phase solid solution is the stable state. Between P_1 and Q_1, total Gibbs energies lying on the tangent line P_1Q_1 may be realized if the system adopts a state consisting of two phases with compositions at P_1 and Q_1 and with relative proportions given by the lever rule. Since the tangent line P_1Q_1 lies below both g^s and g^l, this two-phase state is more stable than either phase alone. Furthermore, no other line joining any point on g^l to any point on g^s lies below the line P_1Q_1. Hence, this line represents the true equilibrium state of the system, and the compositions P_1 and Q_1 are the liquidus and solidus compositions at 1300°C.

It may be shown that the common tangency condition also results in equal *activities* of each component in the two phases at equilibrium. That is, equality of activities and minimization of total Gibbs energy are equivalent criteria for equilibrium between phases.

As T is decreased to 1100°C, the points of common tangency are displaced to higher concentrations of Ge. For $T < 937$°C, $g^s < g^l$ at all compositions.

It should be noted that absolute values of Gibbs energies cannot be defined. Hence, the relative positions of $g_{Ge}^{0(l)}$ and $g_{Si}^{0(l)}$ in fig. 2 are completely arbitrary. However, this is immaterial for the preceding discussion, since displacing both $g_{Si}^{0(l)}$ and $g_{Si}^{0(s)}$ by the same arbitrary amount relative to $g_{Ge}^{0(l)}$ and $g_{Ge}^{0(s)}$ will not alter the compositions of the points of common tangency.

It should also be noted that in the present discussion of equilibrium phase diagrams we are assuming that the physical dimensions of the single-phase regions in the system are sufficiently large that surface (interfacial) energy contributions to the Gibbs energy can be neglected. For very fine grain sizes in the sub-micron range however, surface energy effects can noticeably influence the phase boundaries.

References: p. 531.

The shape of the two-phase (solid + liquid) "lens" on the phase diagram is determined by the Gibbs energies of fusion, Δg_f^0 of the components and by the mixing terms, Δg^s and Δg^l. In order to observe how the shape is influenced by varying Δg_f^0, let us consider a hypothetical system A–B in which Δg^s and Δg^l are ideal Raoultian (§ 2.2). Let $T_{f(A)}^0 = 800$ K and $T_{f(B)}^0 = 1200$ K. Furthermore, assume that the entropies of fusion of A and B are equal and temperature-independent. The enthalpies of fusion are then given from eq. (1) by the expression $\Delta h_f^0 = T_f^0 \Delta s_f^0$ since $\Delta g_f^0 = 0$ when $T = T_f^0$. Calculated phase diagrams for $\Delta s_f^0 = 3$, 10 and 30 J/mol K are shown in fig. 3. A value of $\Delta s_f^0 \approx 0$ is typical of most metals (*Richard's rule*). However, when the components are ionic compounds such as ionic oxides, halides, etc., then Δs_f^0 can be significantly larger since there are several atoms per formula unit. Hence, two-phase "lenses" in binary ionic salt or oxide phase diagrams tend to be "fatter" than those encountered in alloy systems. If we are considering vapour–liquid equilibria rather than solid–liquid equilibria, then the shape is determined by the entropy of vaporization, Δs_V^0 (§ 2.12). Since $\Delta s_V^0 \approx 10 \Delta s_f^0$, two-phase (liquid + vapour) lenses tend to be very wide.

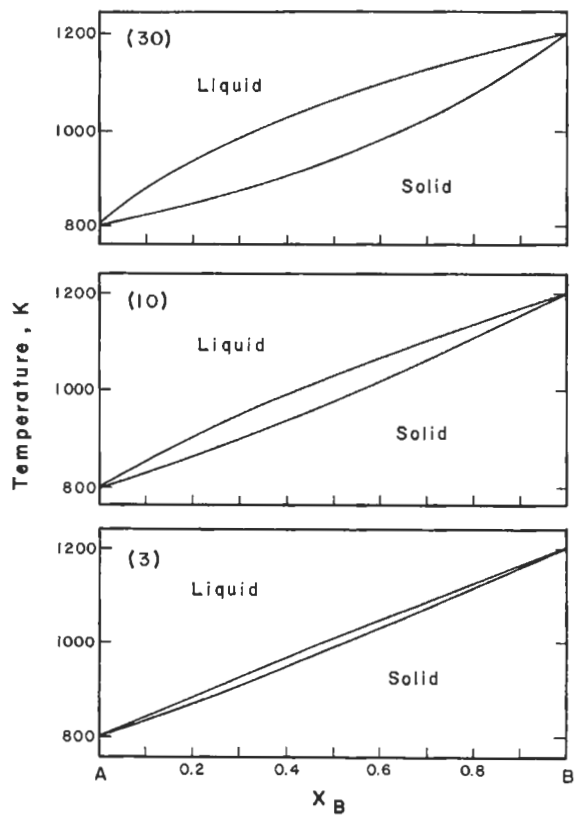

Fig. 3. Phase diagrams for a system A–B with ideal solid and liquid solutions with $T^o_{f(A)} = 800$ K and $T^o_{f(B)} = 1200$ K, calculated for entropies of fusion $\Delta s^o_{f(A)} = \Delta s^o_{f(B)} = 3$, 10 and 30 J/mol K.

2.2. Minima and maxima in two-phase regions

As discussed in ch. 6, § 6, the Gibbs energies of mixing, Δg^s and Δg^l, may each be expressed as the sum of an ideal (Raoultian) term which is purely entropic and which is given by the Boltzmann equation for a random substitutional solution of A and B particles, and an *excess* term, g^E.

$$\Delta g = RT(X_A \ln X_A + X_B \ln X_B) + g^E, \tag{2}$$

where X_A and X_B are the mole fractions of the components. An *ideal* or *Raoultian* solution is defined as one in which $g^E = 0$. Both the solid and liquid phases in the Ge–Si system (fig. 2) are approximately ideal. With two ideal solutions, a "lens-shaped" two-phase region always results. However, in most alloy systems, even approximately ideal behaviour is the exception rather than the rule.

If $g^E > 0$ then the system is said to exhibit positive deviations from ideality. If $g^E < 0$, then we speak of negative deviations.

Curves of g^s and g^l for a hypothetical system A–B are shown schematically in fig. 4 at a constant temperature below the melting points of pure A and B such that the solid state is the stable state for both pure components. However, in this system $g^{E(l)} < g^{E(s)}$ so that g^s presents a flatter curve than does g^l and there exists a central composition region in which $g^l < g^s$. Hence, there are two common tangent lines, P_1Q_1 and P_2Q_2. Such a situation gives rise to a phase diagram with a minimum in the two-phase region as observed in the Au–Cu system shown in fig. 5 (HULTGREN *et al.* [1963]). At a composition and temperature corresponding to the minimum point, liquid and solid of the same composition exist in equilibrium.

A two-phase region with a minimum point as in fig. 5 may be thought of as a two-phase "lens" which has been "pushed down" by virtue of the fact that the liquid is relatively more stable than the solid. Thermodynamically, this relative stability is expressed as $g^{E(l)} < g^{E(s)}$.

Conversely, if $g^{E(l)} > g^{E(s)}$ to a sufficient extent, then a two-phase region with a maximum will result. In alloy systems, such maxima are nearly always associated with the existence of an intermetallic phase, as will be discussed in § 2.8.

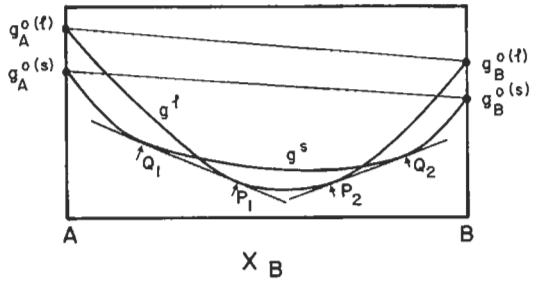

Fig. 4. Isothermal Gibbs-energy-composition curves for solid and liquid phases in a system A–B in which $g^{E(l)} < g^{E(s)}$. A phase diagram of the type in fig. 5 results.

References: p. 531.

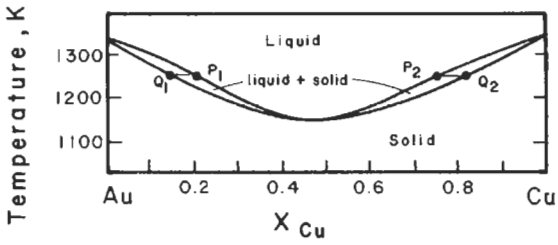

Fig. 5. Phase diagram of the Au–Cu system (after HULTGREN *et al.* [1963]).

2.3. Miscibility gaps

If $g^E > 0$ for a solution, then the solution is thermodynamically less stable than an ideal solution. In an alloy system this can result from a large difference in atomic diameter of the components, which will lead to a (positive) lattice strain energy, or from differences in valence, or from other factors.

In the Au–Ni system, g^E is positive in the solid phase. In the top panel of fig. 6 is plotted $g^{E(s)}$ at 1200 K (HULTGREN *et al.* [1963]) as well as the ideal Gibbs energy of mixing, Δg^{ideal}, also at 1200 K. The sum of these two terms is the Gibbs energy of mixing $\Delta g^s = \Delta g^{ideal} + g^{E(s)}$, which is plotted at 1200 K as well as at other temperatures in the central panel of fig. 6. Now,

$$\Delta g^{ideal} = RT\left(X_{Au} \ln X_{Au} + X_{Ni} \ln X_{Ni}\right)$$

is always negative and varies directly with T, whereas g^E varies less rapidly with temperature. As a result, the sum, $\Delta g^s = \Delta g^{ideal} + g^E$, becomes less negative as T decreases. However, the limiting slopes to the Δg^{ideal} curve at $X_{Au} = 1$ and $X_{Ni} = 1$ are both infinite

$$\left(\lim_{X_{Au}\to 1} d\left(\Delta g^{ideal}\right)/dX_{Au} = \lim_{X_{Ni}\to 1} d\left(\Delta g^{ideal}\right)/dX_{Ni} = \infty\right),$$

whereas the limiting slopes of g^E are always finite (Henry's Law). Hence, Δg^s will always be negative as $X_{Au} \to 1$ and $X_{Ni} \to 1$ no matter how low the temperature. As a result, below a certain temperature the curves of Δg^s will exhibit two negative "humps". Common tangent lines P_1Q_1, P_2Q_2, P_3Q_3 to the two humps define the ends of tie-lines of a two-phase solid–solid *miscibility gap* in the Au–Ni phase diagram which is shown in the lower panel in fig. 6 (HULTGREN *et al.* [1963]). The peak of the gap occurs at the *critical* or *consolute* temperature and composition, T_c and X_c.

When $g^{E(s)}$ is positive for the solid phase in a system it is usually also the case that $g^{E(l)} < g^{E(s)}$, since the unfavourable factors (such as a difference in atomic dimensions) which are causing $g^{E(s)}$ to be positive will have less of an influence upon $g^{E(l)}$ in the liquid phase owing to the greater flexibility of the liquid structure to accommodate different atomic sizes, valencies, etc. Hence, a solid–solid miscibility gap is often associated with a minimum in the two-phase (solid + liquid) region as in the Au–Ni system.

Below the critical temperature the curve of Δg^s exhibits two inflection points

indicated by the letter "s" in fig. 6. These are known as the *spinodal points*. On the phase diagram their locus traces out the *spinodal curve* as illustrated in fig. 6. The spinodal

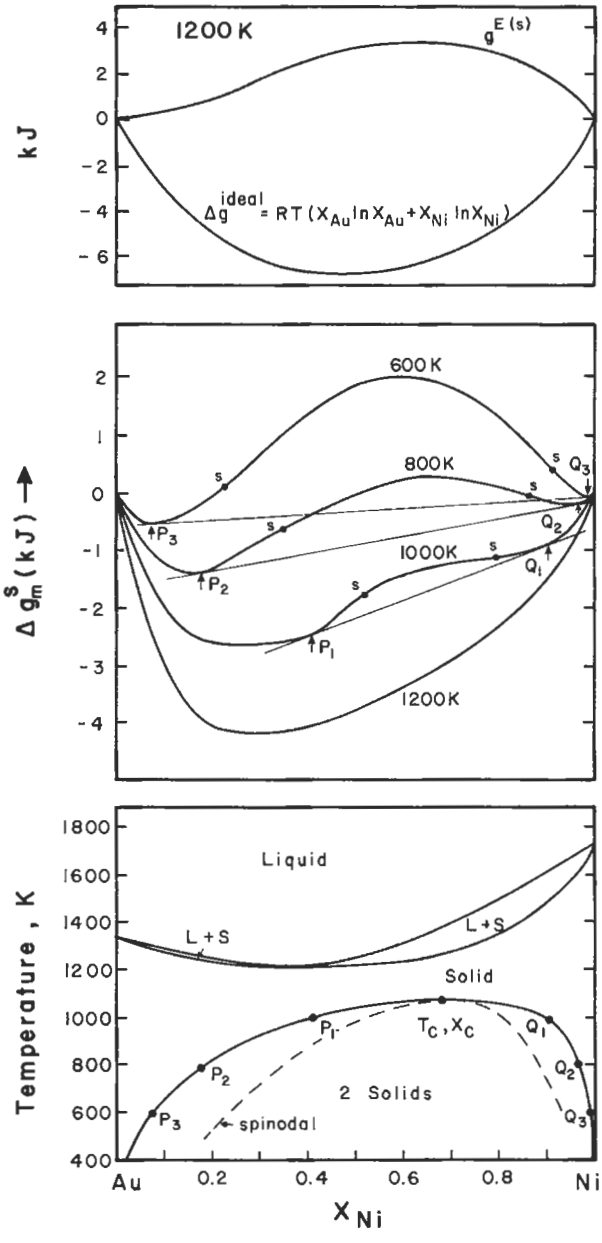

Fig. 6. Phase diagram and Gibbs energy curves of solid solutions for the Au–Ni system (after HULTGREN *et al.* [1963]). Letters "s" indicate spinodal points.

References: p. 531.

curve is not part of the equilibrium phase diagram, but it is important in the kinetics of phase separation as discussed in ch. § 15.

2.4. Simple eutectic systems

The more positive g^E in a system is, the higher is T_c and the wider is the miscibility gap at any temperature. Suppose that $g^{E(s)}$ is sufficiently positive that T_c is higher than the minimum in the (solid + liquid) region. The result will be a phase diagram such as that of the Ag–Cu system shown in fig. 7 (HULTGREN *et al.* [1963]).

In the upper panel of fig. 7 are shown the Gibbs energy curves at 1100 K. The two common tangents define two two-phase regions. As the temperature is decreased below 1100 K, the g^s curve descends relative to g^l, and the two points of tangency, P_1 and P_2, approach each other until, at $T = 1052$ K, P_1 and P_2 become coincident at the composition E. That is, at $T = 1052$ K there is just one common tangent line contacting the two portions of the g^s curve at compositions A and B and contacting the g^l curve at E. This temperature is known as the *eutectic temperature*, T_E, and the composition E is the *eutectic composition*. For temperatures below T_E, g^l lies completely above the common

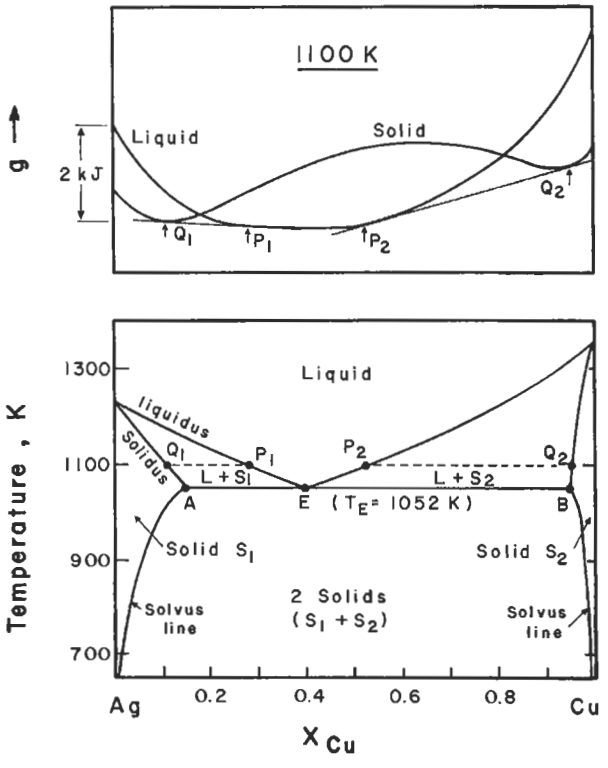

Fig. 7. Phase diagram and Gibbs energy curves at 1100 K of the Ag–Cu system (after HULTGREN *et al.* [1963]). Solid Ag and Cu are both fcc.

tangent to the two portions of the g^s curve and so, for $T < T_E$ a solid–solid miscibility gap is observed. The phase boundaries of this two-phase region are called the *solvus* lines. The word eutectic is from the Greek for "to melt well" since an alloy has the lowest melting point at the eutectic composition E.

This description of the thermodynamic origin of simple eutectic phase diagrams is strictly correct only if the pure solid components A and B have the same crystal structure (see § 2.6).

Suppose a Ag–Cu alloy of composition $X_{Cu} = 0.28$ (composition P_1) is cooled from the liquid state very slowly under equilibrium conditions. At 1100 K the first solid appears with composition Q_1. As T decreases further, solidification continues with the liquid composition following the liquidus curve from P_1 to E and the composition of the solid phase following the solidus curve from Q_1 to A. The relative proportions of the two phases at any T are given by the lever rule. At a temperature $T = (T_E + \delta)$ just above T_E, two phases are observed: a solid of composition A and a liquid of composition E. At a temperature $T = (T_E - \delta)$ just below T_E, two solids with compositions A and B are observed. Therefore, at T_E, during cooling, the following *binary eutectic reaction* occurs:

$$\text{liquid} \rightarrow \text{solid}_1 + \text{solid}_2. \tag{3}$$

Under equilibrium conditions the temperature will remain constant at $T = T_E$ until all the liquid has solidified, and during the reaction the compositions of the three phases will remain fixed at A, B and E. For this reason the eutectic reaction is called an *invariant* reaction.

The morphologies of two-phase grains resulting from the co-precipitation of two solids during eutectic reactions are discussed in detail in ch. 8.

2.5. Binary phase diagrams with no intermediate phases

2.5.1. Thermodynamic origin illustrated by simple regular solution theory

Many years ago VAN LAAR [1908] showed that the thermodynamic origin of a great many of the observed features of binary phase diagrams can be illustrated at least qualitatively by simple regular solution theory. As discussed in ch. 5, § 6.2, a *regular* solution is one in which:

$$g^E = \Omega X_A X_B, \tag{4}$$

where Ω is a parameter independent of temperature and composition.

In fig. 8 are shown several phase diagrams calculated for a hypothetical system A–B containing a solid and a liquid phase with melting points of $T^0_{f(A)} = 800$ K and $T^0_{f(B)} = 1200$ K and with entropies of fusion of both A and B set to 10 J/mol K, which is a typical value for metals. The solid and liquid phases are both regular with $g^{E(s)} = \Omega^s X_A X_B$ and $g^{E(l)} = \Omega^l X_A X_B$. The parameters Ω^s and Ω^l have been varied systematically to generate the various panels of fig. 8.

In panel (n) both phases are ideal. Panels (l–r) exhibit minima or maxima depending upon the sign and magnitude of $(g^{E(l)} - g^{E(s)})$, as has been discussed in § 2.2. In panel (h) the liquid is ideal but positive deviations in the solid give rise to a solid–solid miscibility gap as

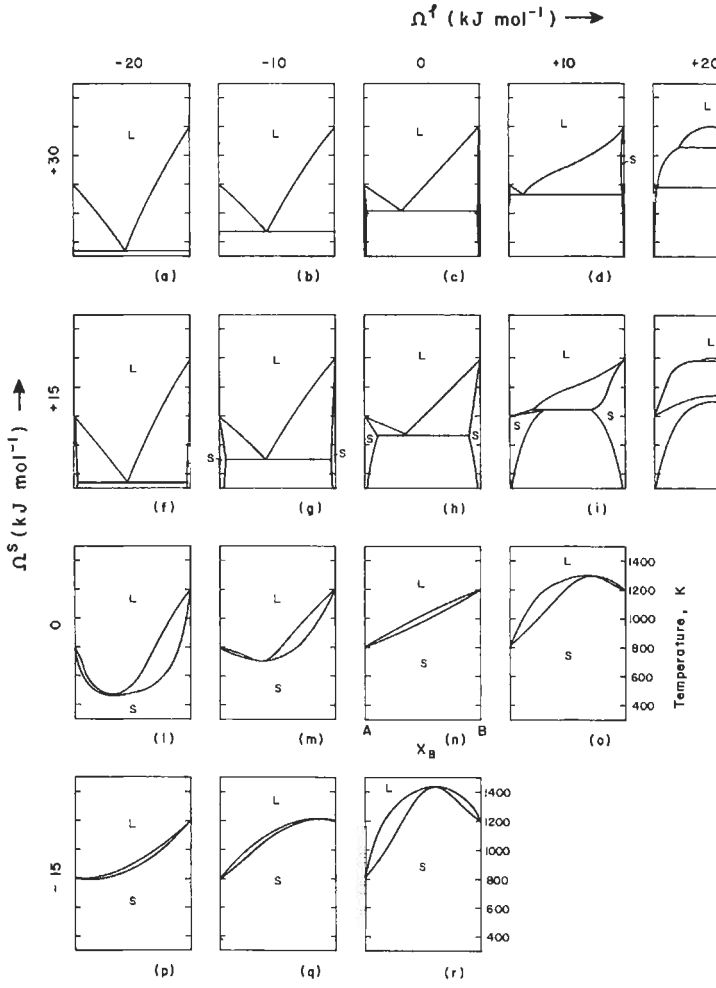

Fig. 8. Topological changes in the phase diagram for a system A–B with regular solid and liquid phases, brought about by systematic changes in the regular solution parameters Ω^s and Ω^l. Melting points of pure A and B are 800 K and 1200 K. Entropies of fusion of both A and B are 10.0 J/mol K. (PELTON and THOMPSON [1975].)

discussed above in § 2.4. On passing from panel (h) to panel (c), an increase in $g^{E(s)}$ results in a widening of the miscibility gap so that the solubilities of A in solid B and of B in solid A decrease. Panels (a–c) illustrate that negative deviations in the liquid cause a relative stabilization of the liquid with resultant lowering of the eutectic temperature.

Eutectic phase diagrams are often drawn with the maximum solid solubility occurring at the eutectic temperature (as in fig. 7). However fig. 8d, in which the maximum solubility of A in the B-rich solid solution occurs at approximately $T = 950$ K, illustrates that this need not be the case even for simple regular solutions.

2.5.2. Liquid–liquid immiscibility - monotectics

In fig. 8e, positive deviations in the liquid have given rise to a *liquid–liquid miscibility gap*. An example of a real system with such a phase diagram is the Cu–Pb system shown in fig. 9 (HULTGREN *et al.* [1963]). If a Cu–Pb alloy with $X_{Pb} = 0.10$ is cooled slowly from the liquid state, solid Cu begins to appear at 1260 K. Upon further cooling the liquid composition follows the liquidus curve to point A at $T = 1227$ K. The following invariant *monotectic reaction* then occurs:

$$\text{liquid}_A \rightarrow \text{liquid}_B + \text{Cu}_{(\text{solid})}, \tag{5}$$

where liquid_A and liquid_B are liquids with compositions at points A and B. The temperature remains constant at the monotectic temperature and the compositions of all phases remain fixed until liquid_A is completely consumed. Cooling then continues with precipitation of copper with the liquid composition following the liquidus line from B to the eutectic E.

Returning to fig. 8, we see that in panel (d) the positive deviations in the liquid are not large enough to produce immiscibility but they do result in a flattening of the liquidus which is often described as a "tendency to immiscibility". An example of such a flattened (or "S-shaped") liquidus resulting from a positive $g^{E(l)}$ is shown later for the Cd–Pb system in fig. 12.

2.5.3. Peritectics

The invariant which appears in fig. 8i is known as a *peritectic*. The Au–Fe system shown in fig. 10 (HULTGREN *et al.* [1963]) exhibits a peritectic PQR at 1441 K as well as another at about 1710 K. The Gibbs energy curves, g^l and g^{fcc}, of the liquid and solid face-centred cubic phases are shown schematically at the peritectic temperature of $T_p = 1441$ K in the upper panel of fig. 10. One common tangent line PQR to g^l and to the two portions of g^{fcc} can be drawn.

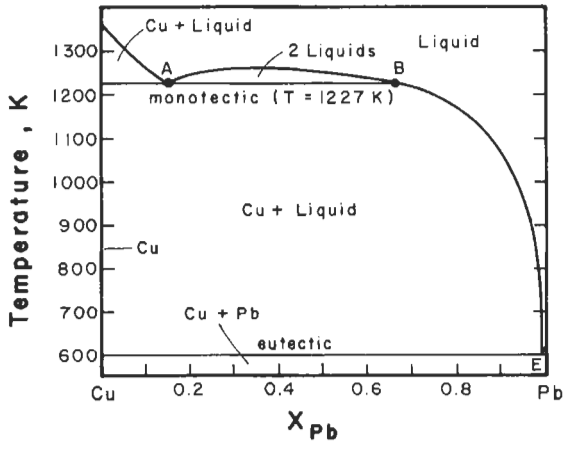

Fig. 9. The Cu–Pb phase diagram (after HULTGREN *et al.* [1963]).

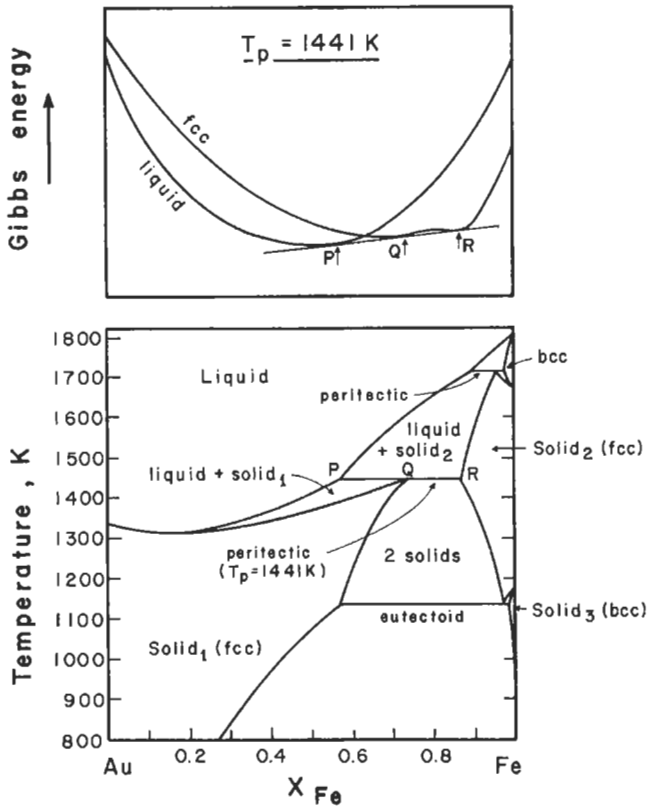

Fig. 10. Phase diagram and Gibbs energy curves at the peritectic temperature of 1441 K for the Au–Fe system (after HULTGREN *et al.* [1963]).

Suppose that a Au–Fe alloy of composition $X_{Fe} = 0.65$ is cooled very slowly from the liquid state. At a temperature $(T_p + \delta)$ just above 1441 K, a liquid phase of composition P and an fcc phase of composition R are observed at equilibrium. At a temperature $(T_p - \delta)$ just below 1441 K, the two phases at equilibrium are liquid and solid with compositions P and Q respectively. The following invariant *binary peritectic reaction* thus occurs upon cooling:

$$\text{liquid} + \text{solid}_2 \rightarrow \text{solid}_1. \tag{6}$$

This reaction occurs isothermally with all three phases at fixed compositions (at points P, Q and R). In the case of an alloy with overall composition between P and Q, the reaction occurs isothermally until all solid_2 is consumed. In the case of an alloy with overall composition between Q and R, it is the liquid which will first be completely consumed.

A peritectic reaction between a liquid and solid_2 occurs on the surface of the particles

of solid$_2$ which can rapidly become coated with solid$_1$. By preventing contact between liquid and solid$_2$, this coating may greatly retard further reaction to such an extent that equilibrium conditions can only be achieved by extremely slow cooling.

2.5.4. Syntectics

The invariant in fig. 8k in which a solid decomposes upon heating into two liquids is known as a *syntectic*. It is rarely observed in alloy systems. Examples are found in the K–Pb and K–Zn systems (HANSEN [1958]). A phase diagram similar to fig. 8j, although without the tiny miscibility gap, is exhibited by the Au–Pt system (HANSEN [1958]).

2.6. Limited mutual solid solubility

In § 2.4 the region of two solids in the Ag–Cu phase diagram of fig. 7 was described as a miscibility gap in the solid phase. That is, only one g^s curve was drawn. If, somehow, the appearance of the liquid phase could be suppressed, then the two solvus lines in fig. 7, when projected upwards, would meet at a critical point (as in the Au–Ni system in fig. 6) above which one continuous solid solution would exist at all compositions.

Such a description is justifiable only if the pure solid components have the same crystal structure. This is the case for Ag–Cu since solid Ag and Cu are both fcc. The same assumption was made in our treatment of the peritectic Au–Fe system (fig. 10) in which the region of two solids was treated as a miscibility gap. Again in this case this description is permissible since Au and Fe are both fcc in this temperature range.

However, consider the simple eutectic system A–B in fig. 11 in which pure solid A and B are hcp (hexagonal close-packed) and fcc respectively. In this case, if the formation of the liquid phase could be suppressed the two solvus lines could not project upward to meet at a critical point, since this would imply that above this critical temperature a continuous series of solid solutions varying smoothly from hcp to fcc could exist. Such a situation is prohibited by symmetry conditions. That is, one continuous curve for g^s cannot be drawn. Each solid phase must have its own separate Gibbs energy curve, as shown schematically in the upper panels of fig. 11. In this figure, $g_A^{0(fcc)}$ is the *standard molar Gibbs energy of pure fcc A* and $g_B^{0(hcp)}$ is the standard molar Gibbs energy of pure hcp B. Such quantities may be defined in a number of different and non-equivalent ways as will be discussed below.

A real system with a phase diagram similar to fig. 11 is the Cd–Pb system shown in fig. 12 (ASHTAKALA *et al.* [1981]). Gibbs energy curves at a temperature below the eutectic are shown schematically in the upper panel. Let us derive an expression for g^{fcc} under the assumption that the Pb-rich fcc solid solution is a *Henrian solution*. As discussed in ch. 5, § 6.2, when a solution is sufficiently dilute in one component, Henrian behaviour may be assumed. That is, the activity of the solvent is ideal ($a_{solvent} = X_{solvent}$; $\gamma^0_{solvent} = 1$), while for the solute, $a_{solute} = \gamma^0_{solute} X_{solute}$, where the *Henrian activity coefficient*, γ_{solute}, is independent of composition. At $T_E = 247.8°C$ in fig. 12, Cd in the Pb-rich fcc solution at $X_{Pb} = 0.940$ exists in equilibrium with virtually pure solid hcp Cd. Thus, in the fcc solution, $a_{Cd} \approx 1.0$ with respect to pure solid hcp Cd as standard state. Hence, $\gamma^0_{Cd} = a_{Cd}/X_{Cd} = 1.0/0.060 = 16.67$ at 247.8°C. We can now express g^{fcc} as:

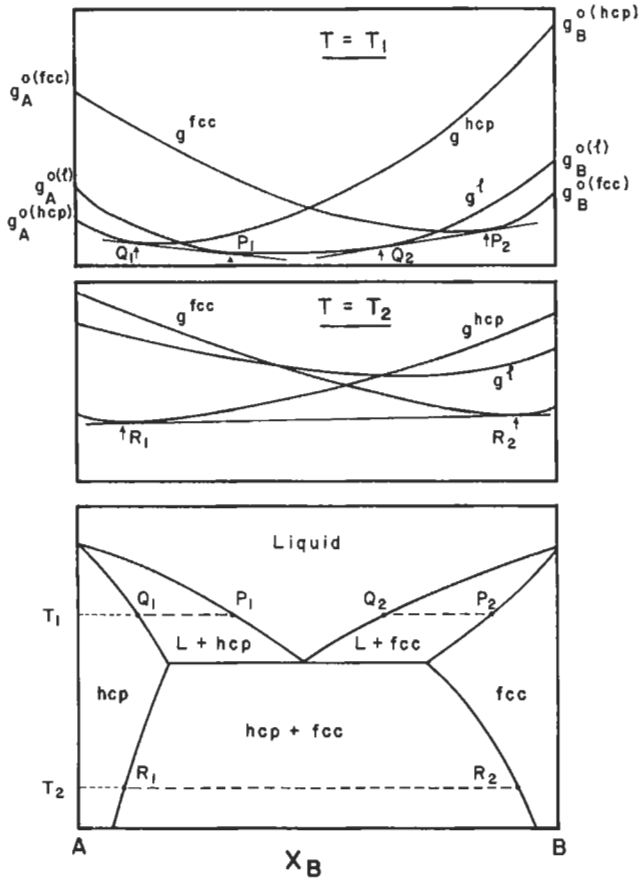

Fig. 11. Phase diagram and Gibbs energy curves at two temperatures for a simple eutectic system A–B in which pure solid A and B have different crystal structures.

$$\begin{aligned} g^{\text{fcc}} &= \left(X_{\text{Cd}} g_{\text{Cd}}^{0(\text{hcp})} + X_{\text{Pb}} g_{\text{Pb}}^{0(\text{fcc})}\right) + RT\left(X_{\text{Cd}} \ln a_{\text{Cd}} + X_{\text{Pb}} \ln a_{\text{Pb}}\right) \\ &= \left(X_{\text{Cd}} g_{\text{Cd}}^{0(\text{hcp})} + X_{\text{Pb}} g_{\text{Pb}}^{0(\text{fcc})}\right) + RT\left(X_{\text{Cd}} \ln(\gamma_{\text{Cd}}^{0} X_{\text{Cd}}) + X_{\text{Pb}} \ln X_{\text{Pb}}\right) \end{aligned} \tag{7}$$

However, since γ_{Cd}^{0} is independent of composition we can combine terms as follows:

$$\begin{aligned} g^{\text{fcc}} &= \left[X_{\text{Cd}}\left(g_{\text{Cd}}^{0(\text{hcp})} + RT \ln \gamma_{\text{Cd}}^{0}\right) + X_{\text{Pb}} g_{\text{Pb}}^{0(\text{fcc})}\right] \\ &\quad + RT\left(X_{\text{Cd}} \ln X_{\text{Cd}} + X_{\text{Pb}} \ln X_{\text{Pb}}\right). \end{aligned} \tag{8}$$

Let us now define:

$$g_{\text{Cd}}^{0(\text{fcc})} = \left(g_{\text{Cd}}^{0(\text{hcp})} + RT \ln \gamma_{\text{Cd}}^{0}\right).$$

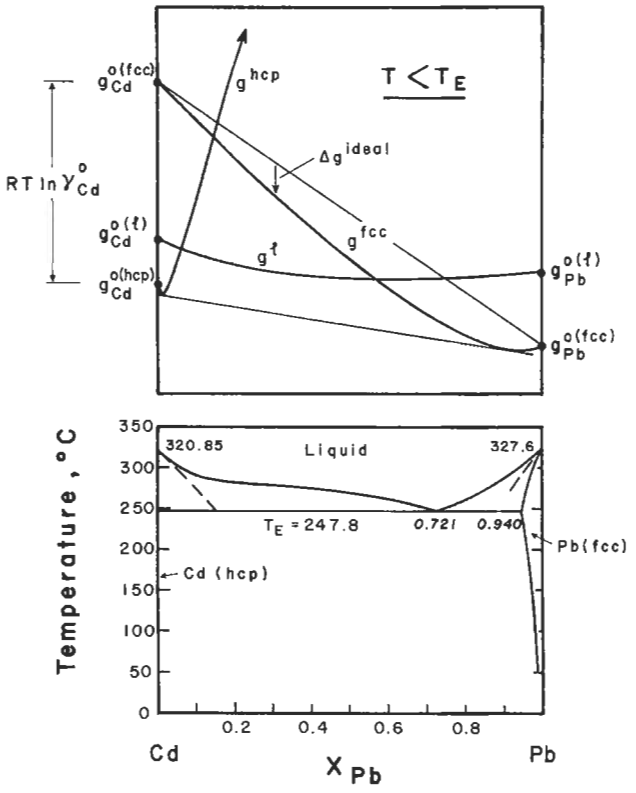

Fig. 12. Phase diagram of the Cd–Pb system (after ASHTAKALA *et al.* [1981]) and Gibbs energy curves (schematic) at a temperature below the eutectic. Dashed lines indicate limiting liquidus slopes calculated for zero solid solubility.

From eq. (8) it can be seen that relative to $g_{Cd}^{0(fcc)}$ defined in this way and to $g_{Pb}^{0(fcc)}$ the fcc solution is ideal. This is illustrated in fig. 12.

At 247.8°C in Cd–Pb, $(g_{Cd}^{0(fcc)} - g_{Cd}^{0(hcp)}) = RT \ln \gamma_{Cd}^{0} = R(247.8 + 273.15) \ln 16.67 = 12.19$ kJ/mol. As a first approximation we could take this value to be independent of T, or as a second approximation we could evaluate γ_{Cd}^{0} at other temperatures along the solidus and express $(g_{Cd}^{0(fcc)} - g_{Cd}^{0(hcp)})$ as, say, a linear function of T.

Although the above treatment has the advantage of numerical simplicity, it suffers from the difficulty that the numerical value of $(g_{Cd}^{0(fcc)} - g_{Cd}^{0(hcp)})$ is solvent–dependent and will be different for, say, solutions of Cd in fcc Cu and Cd in fcc Pb. For purposes of predicting binary phase diagrams from first principles or for estimating ternary phase diagrams from binary phase diagrams (§ 5.5) it would be desirable if $g_{Cd}^{0(fcc)}$ could be defined to be system-independent so as to be truly the "standard molar Gibbs energy of metastable fcc Cd". A great deal of effort has been expended by the international CALPHAD group under the impetus of Kaufman (KAUFMAN and BERNSTEIN [1970]) and

co-workers to compile tables of *lattice stabilities* for metals in the fcc, hcp, bcc, and liquid states (that is, to obtain a set of relative values of $g^{0(fcc)}$, $g^{0(hcp)}$, $g^{0(bcc)}$ and $g^{0(l)}$ for every metal). In some cases, these can be calculated by extrapolating thermodynamic data from regions of T and P where the phases are stable. In other cases, lattice stabilities can be estimated partly from theoretical calculations and partly from the analysis of a large number of binary phase diagrams followed by a judicious choice of the "best" values which most closely fit the greatest number of systems. Tabulations of lattice stabilities are now available for many metals (DINSDALE [1991]).

2.7. Calculation of limiting slopes of phase boundaries

In fig. 12 we see that the solubility of Pb in solid Cd is very small. The actual solubility at T_E is about 0.14 mol% (HANSEN [1958]). In thermodynamic terms this means that g^{hcp} increases very rapidly as Pb is added to solid Cd (see fig. 12), or that the Henrian activity coefficient γ^0_{Pb} is very large. The fact that the solubility of Cd in solid Pb is much greater than that of Pb in solid Cd can be understood in terms of the Hume–Rothery rule (ch. 4) that solubilities are greater when the solute atoms are smaller than the solvent atoms, since the lattice strain energy will be less and hence g will rise less rapidly upon addition of solute.

As discussed later in § 7, it is usually more difficult experimentally to determine a solidus than it is to measure liquidus temperatures. However, if the liquidus has been measured in the limit as $X_{solvent} \rightarrow 1$, then the limiting slope of the solidus can be calculated. Let component B be the solvent in a system A–B. The partial Gibbs energies of B along the liquidus and solidus are equal ($g^l_B - g^s_B = 0$). Hence:

$$\left(g^l_B - g^{0(l)}_B\right) - \left(g^s_B - g^{0(s)}_B\right) = -\left(g^{(0)l}_B - g^{0(s)}_B\right). \tag{9}$$

But: $(g^l_B - g^{0(l)}_B) \equiv RT \ln a^l_B$ and $(g^s_B - g^{0(s)}_B) \equiv RT \ln a^s_B$, where a^s_B and a^s_B are activities of B on the liquidus and solidus with respect to the pure liquid and pure solid standard states respectively. Hence, eq. (9) may be written as:

$$RT \ln a^l_B - RT \ln a^s_B = -\Delta g^0_{f(B)}. \tag{10}$$

In the limit $X_B \rightarrow 1$, Raoult's Law holds for both phases. That is, $a^l_B \rightarrow X^l_B$ and $a^s_B \rightarrow X^s_B$. Hence, in the limit, eq. (10) may be written as:

$$RT \ln X^l_B / X^s_B = -\Delta g^0_{f(B)}. \tag{11}$$

Furthermore, in the limit, $T \rightarrow T^0_{f(B)}$ and from eq. (1) $\Delta g^0_{f(B)} \rightarrow \Delta h^0_{f(B)}(1 - T/T^0_{f(B)})$. Finally, $\lim_{X_B \rightarrow 1}(\ln X_B) = (X_B - 1)$. Substituting these limiting values into eq. (11) we obtain:

$$\lim_{X_B \rightarrow 1}\left(dX^l_B/dT - dX^s_B/dT\right) = \Delta h^0_{f(B)}/R\left(T^0_{f(B)}\right)^2. \tag{12}$$

If the limiting slope of the liquidus, $\lim_{X_B \rightarrow 1}(dX^l_B/dT)$, is known, then the limiting slope of the solidus can be calculated via eq. (12) if the enthalpy of fusion is known.

For the Cd–Pb system, limiting liquidus slopes were calculated for both components

from eq. (12) under the assumption that there is no solid solubility (that is, that $dX_B^s/dT = 0$). These are shown as the dashed lines on fig. 12. In Cd-rich solutions, agreement with the measured limiting liquidus slope is very good, but in Pb-rich solutions the poor agreement indicates the existence of appreciable solid solubility as has been confirmed by direct measurement.

2.8. Intermediate phases

The phase diagram of the Ag–Mg system (HULTGREN *et al.* [1963]) is shown in fig. 13. An *intermetallic phase*, β', is seen centered approximately about the composition

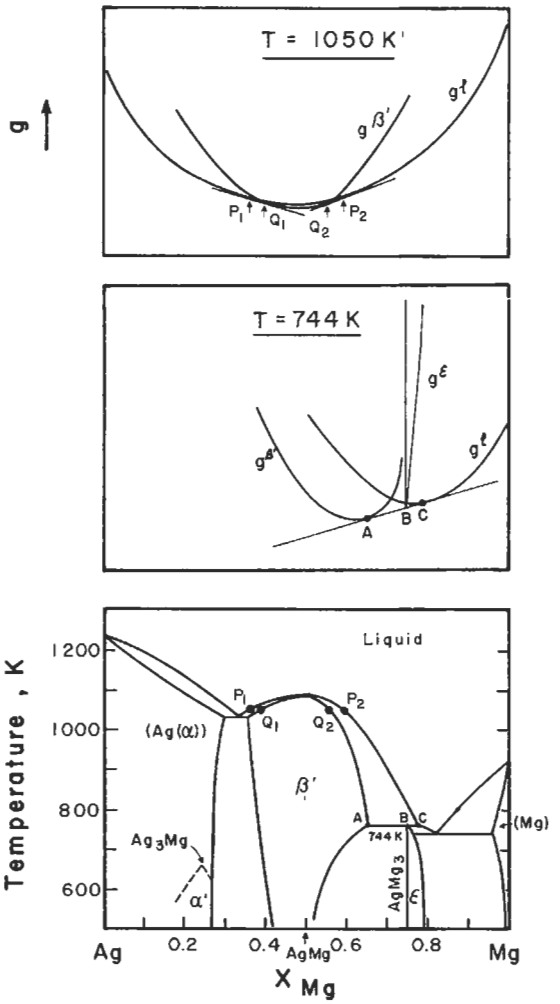

Fig. 13. Ag–Mg phase diagram (after HULTGREN *et al.* [1963]) and Gibbs energy curves (schematic) at 744 K and 1050 K.

References: p. 531.

$X_{Mg} = 0.5$. The Gibbs energy curve for such an intermetallic phase has the form shown schematically in the upper panel of fig. 13. $g^{\beta'}$ rises quite rapidly on either side of its minimum which occurs near $X_{Mg} = 0.5$. As a result, the β' phase appears on the phase diagram only over a limited composition range. This form of the curve $g^{\beta'}$ results from the fact that when $X_{Ag} \approx X_{Mg}$ a particularly stable crystal structure exists in which Ag and Mg atoms preferentially occupy different sites. The two common tangents P_1Q_1 and P_2Q_2 give rise to a maximum in the two-phase (β' + liquid) region in the phase diagram. (Although the maximum is observed very near $X_{Mg} = 0.5$, there is no thermodynamic reason for the maximum to occur exactly at this composition.)

The Na–Bi phase diagram is shown in fig. 14 (HANSEN [1958]). Gibbs energy curves at 700°C are shown schematically in the upper panel. $g(Na_{3/4}Bi_{1/4})$ rises extremely rapidly on either side of its minimum which occurs at $X_{Na} = 3/4$, $X_{Bi} = 1/4$. (We write $g(Na_{3/4}Bi_{1/4})$ rather than $g(Na_3Bi)$ in order to normalize to a basis of one mole of metal atoms.) As a result, the points of tangency Q_1 and Q_2 of the common tangents P_1Q_1 and P_2Q_2 are nearly (but not exactly) coincident. Hence, the composition range over which single-phase Na_3Bi exists (sometimes called the *range of stoichiometry* or *homogeneity*

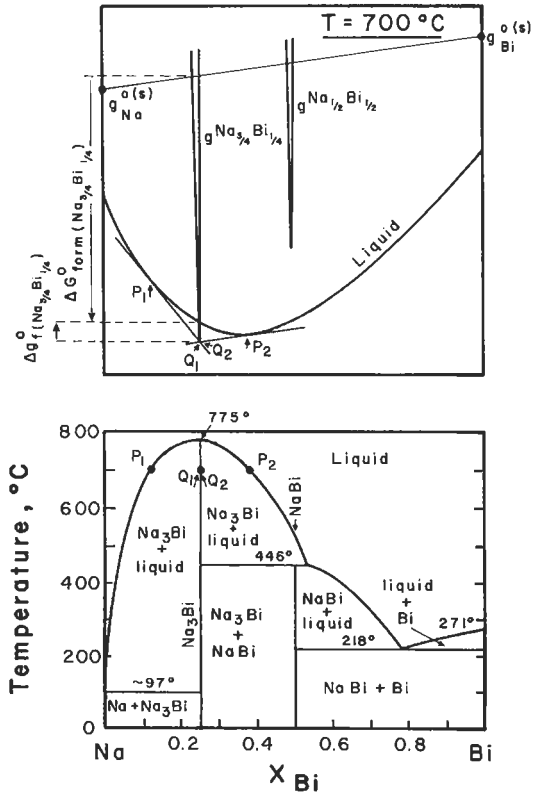

Fig. 14. Na–Bi phase diagram (after HANSEN [1958]) and schematic Gibbs energy curves at 700°C.

range of Na_3Bi) is very narrow (but never zero). The two regions labelled (Na_3Bi + liquid) in fig. 14 are the two sides of a two-phase region which passes through a maximum just like the (β' + liquid) regions in fig. 13. Because the Na_3Bi single-phase region is so narrow we refer to Na_3Bi as an *intermetallic compound*. In the case of Na_3Bi, any slight deviation from the stoichiometric composition causes a very large increase in Gibbs energy. Owing to the large difference in electronegativities of Na and Bi, Na_3Bi could be considered to be a semi-ionic compound. Deviations from stoichiometry would require the substitution of Na on Bi sites or vice versa which would be energetically very unfavourable.

If stoichiometric Na_3Bi is heated, it will melt isothermally at 775°C to form a liquid of the same composition. That is, the melting behaviour of Na_3Bi is similar to that of a pure element. Such intermetallic compounds are called *congruently melting* or simply *congruent compounds*. The β' phase in fig. 13 might also be called a congruent intermetallic compound AgMg (or $AgMg_{1\pm\delta}$). It is debatable, however, whether a phase with such a wide range of composition should really be called a "compound".

It should be noted with regard to the congruent melting of Na_3Bi in fig. 14 that the limiting slopes dT/dX of the two liquidus curves at the congruent melting point (775°C) are both zero, since we are really dealing with a maximum in a two-phase region and not with the melting of an element.

Another intermetallic phase, the ε phase, is also observed in the Ag–Mg system, fig 13. This phase has a narrow range of stoichiometry around the composition $AgMg_3$. This phase is associated with a *peritectic* invariant ABC at 744 K. The Gibbs energy curves are shown schematically at the peritectic temperature in the central panel of fig. 13. One common tangent line can be drawn to g^l, $g^{\beta'}$, and g^{ε}.

Suppose that a liquid alloy of composition $X_{Mg} = 0.7$ is cooled very slowly from the liquid state. At a temperature just above 744 K a liquid phase of composition C and a β' phase of composition A are observed at equilibrium. At a temperature just below 744 K, the two phases at equilibrium are β' of composition A and ε of composition B. The following *invariant peritectic reaction* thus occurs upon cooling (cf. § 2.5.3):

$$\text{liquid} + \beta'(\text{solid}) \rightarrow \varepsilon(\text{solid}). \tag{13}$$

This reaction occurs isothermally at 744 K with all three phases at fixed compositions (at points A, B and C). For an alloy with overall composition between points A and B the reaction proceeds until all the liquid has been consumed. In the case of an alloy with overall composition between B and C, the β' phase will be the first to be completely consumed.

The $AgMg_3(\varepsilon)$ compound is said to *melt incongruently*. If solid $AgMg_3$ is heated, it will melt isothermally at 744 K, by the reverse of the above peritectic reaction (14), to form a liquid of composition C and another solid phase, β', of composition A.

Another example of an *incongruent compound* is the compound NaBi in fig. 14. This compound has a very narrow range of stoichiometry. When heated, it melts incongruently (or peritectically) at the peritectic temperature of 446°C to form another solid, Na_3Bi, and a liquid of composition $X_{Bi} \approx 0.53$.

An incongruent compound is always associated with a peritectic. (The word peritectic comes from the Greek for (loosely) "to melt in an indirect way".) However, the converse

is not necessarily true. A peritectic is not always associated with an intermediate phase. See, for example, fig. 10.

For purposes of phase diagram computations involving very stoichiometric compounds such as Na_3Bi, we may, to a good approximation, consider the Gibbs energy curve, $g(Na_{3/4}Bi_{1/4})$, to have zero width. Then all we need is the numerical value of $g(Na_{3/4}Bi_{1/4})$ at the minimum. This value is usually expressed in terms of the *Gibbs energy of fusion of the compound*, $\Delta g^0_{f(Na_{3/4}Bi_{1/4})}$, or in terms of the "*Gibbs energy of formation*", $\Delta g^0_{form(Na_{3/4}Bi_{1/4})}$, of the compound from solid Na and Bi according to the reaction $\frac{3}{4}Na_{(s)} + \frac{1}{4}Bi_{(s)} = Na_{3/4}Bi_{1/4(s)}$. Both these quantities are interpreted graphically in fig. 14.

2.9. Topology of binary phase diagrams

In ch. 5, § 8.2 the *Gibbs phase rule* was derived.:

$$F = C - P + 2, \tag{14}$$

where C is the number of components, P the number of phases in equilibrium, and F the number of degrees of freedom or variance. That is, F is the number of parameters which can and must be specified in order to completely specify the state of the system. In the present context, the thermodynamic parameters are temperature, total pressure, and the compositions of the phases at equilibrium. Since binary temperature–composition phase diagrams are plotted at constant pressure, usually 1 bar, one degree of freedom is already used up. In a binary system, $C = 2$. Hence, for binary isobaric T–X diagrams the phase rule reduces to:

$$F = 3 - P. \tag{15}$$

Binary T–X diagrams contain single-phase areas and two-phase areas. In the single-phase areas, $F = 3 - 1 = 2$. That is, temperature and composition can be varied independently. These regions are thus called *bivariant*. In two-phase regions, $F = 3 - 2 = 1$. If, say, T is chosen, then the compositions of both phases are fixed by the ends of the tie-lines. Two-phase regions are thus termed *univariant*. Note that the overall composition can be varied within a two-phase region at constant T, but the overall composition is not a variable in the sense of the phase rule. Rather, it is the compositions of the individual phases at equilibrium that are the variables to be considered in counting the number of degrees of freedom.

When three phases are at equilibrium in a binary system at constant pressure, $F = 3 - 3 = 0$. Hence, the compositions of all three phases as well as T are fixed. There are two general types of three-phase *invariants* in binary phase diagrams. These are the *eutectic-type* and *peritectic-type* invariants as illustrated in fig. 15. Let the three phases concerned be called α, β and γ, with β as the central phase as shown in fig. 15. α, β and γ can be solid, liquid or gaseous phases. At the eutectic-type invariant, the following invariant reaction occurs isothermally as the system is cooled:

$$\beta \rightarrow \alpha + \gamma, \tag{16}$$

whereas, at the peritectic-type invariant the invariant reaction upon cooling is:

$$\alpha + \gamma \rightarrow \beta \tag{17}$$

Some examples of eutectic-type invariants are: (i) *eutectics* (fig. 7) in which $\alpha = \text{solid}_1$, $\beta = \text{liquid}$, $\gamma = \text{solid}_2$. The eutectic reaction is $l \rightarrow s_1 + s_2$; (ii) *monotectics* (fig. 9) in which $\alpha = \text{liquid}_1$, $\beta = \text{liquid}_2$, $\gamma = \text{solid}$. The monotectic reaction is $l_2 \rightarrow l_1 + s$; (iii) *eutectoids* (fig. 10) in which $\alpha = \text{solid}_1$, $\beta = \text{solid}_2$, $\gamma = \text{solid}_3$. The eutectoid reaction is $s_2 \rightarrow s_1 + s_3$; (iv) *catatectics* in which $\alpha = \text{liquid}$, $\beta = \text{solid}_1$, $\gamma = \text{solid}_2$. The catatectic reaction is $s_1 \rightarrow l + s_2$.

Some examples of peritectic type invariants are: (i) *peritectics* (fig. 10) in which $\alpha = \text{liquid}$, $\beta = \text{solid}_1$, $\gamma = \text{solid}_2$. The peritectic reaction is $l + s_2 \rightarrow s_1$; (ii) *syntectics* (fig. 8k) in which $\alpha = \text{liquid}_1$, $\beta = \text{solid}$, $\gamma = \text{liquid}_2$. The syntectic reaction is $l_1 + l_2 \rightarrow s$; (iii) *peritectoids* in which $\alpha = \text{solid}_1$, $\beta = \text{solid}_2$, $\gamma = \text{solid}_3$. The peritectoid reaction is $s_1 + s_3 \rightarrow s_2$.

An important rule of construction which applies to invariants in binary phase diagrams is illustrated in fig. 15. This *extension rule* states that at an invariant the extension of a boundary of a two-phase region must pass into the adjacent two-phase region and not into the single-phase region. Examples of both correct and incorrect constructions are given in fig. 15. To understand why the "incorrect extension" shown is not correct, consider that the $(\alpha + \gamma)$ phase boundary line indicates the composition of the γ-phase in equilibrium with the α-phase as determined by the common tangent to the

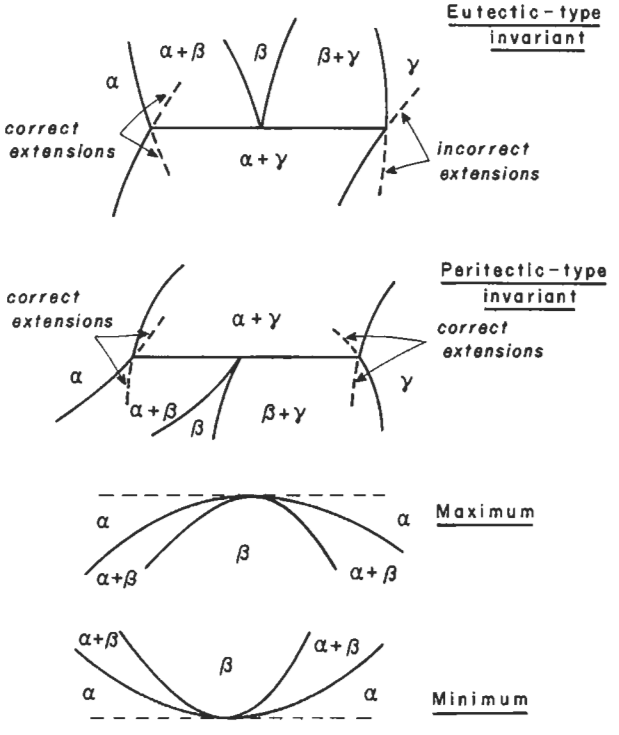

Fig. 15. Some topological units of construction of binary phase diagrams illustrating rules of construction.

References: p. 531.

Gibbs energy curves. Since there is no reason for the Gibbs energy curves or their derivatives to change discontinuously at the invariant temperature, the extension of the $(\alpha + \gamma)$ phase boundary also represents the composition of the γ-phase in equilibrium with the α-phase. Hence, for this line to extend into a region labelled as single-phase γ is incorrect.

Two-phase regions in binary phase diagrams can terminate: (i) on the pure component axes (at $X_A = 1$ or $X_B = 1$) at a transformation point of pure A or B; (ii) at a critical point of a miscibility gap; (iii) at an invariant. Two-phase regions can also exhibit maxima or minima. In this case, both phase boundaries must pass through their maximum or minimum at the same point as shown in fig. 15.

All the *topological units* of construction of binary phase diagrams have now been discussed. The phase diagram of a binary alloy system will usually exhibit several of these units. As an example, the Fe–Mo phase diagram (KUBASCHEWSKI [1982]) is shown in fig. 16. The invariants in this system are: peritectics at 1540, 1488, and 1450°C; eutectoids at 1235 and 1200°C; peritectoids at 1370 and 950°C. The two-phase (liquid $+\gamma$) region passes through a minimum at $X_{Mo} = 0.2$.

Between 910°C and 1390°C is a two-phase $(\alpha + \gamma)$ γ-*loop*. Pure Fe adopts the fcc γ structure between these two temperatures but exists as the bcc α phase at higher and lower temperatures. Mo however, is more soluble in the bcc than in the fcc structure. That is, $g_{Mo}^{0(bcc\text{-}Fe)} < g_{Mo}^{0(fcc\text{-}Fe)}$ as discussed in § 2.6. Therefore, small additions of Mo stabilize the bcc structure.

2.9.1. Order-disorder transformations

In fig. 13 for the Ag–Mg system, a transformation from an α' to an α phase is shown occurring at approximately 390 K at the composition Ag_3Mg. This is an *order–disorder*

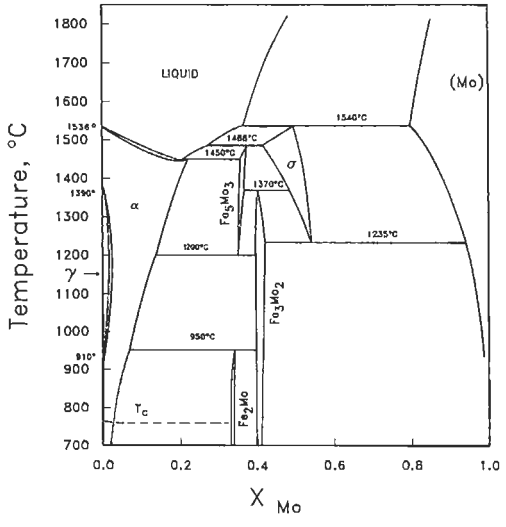

Fig. 16. Fe–Mo phase diagram (KUBASCHEWSKI [1982]).

transformation. Below the transformation temperature, *long-range ordering* (superlattice formation) is observed. An *order parameter* may be defined which decreases to zero at the transformation temperature. This type of phase transformation is not necessarily a first-order transformation like those considered so far in this chapter. Unlike transformations which involve atomic displacements over distances large compared with atomic dimensions, order–disorder transformations, at least at the stoichiometric composition (Ag_3Mg is this example), occur by atomic rearrangement over distances of the order of atomic dimensions. The slope of the curve of Gibbs energy versus T is not necessarily discontinuous at the transformation temperature. For a detailed discussion see ch. 4, § 4.1.1, INDEN [1982], and PITSCH and INDEN [1991].

A type of order–disorder transformation of importance in ferrous metallurgy is the magnetic transformation. Below its *Curie temperature* of 769°C, Fe is ferromagnetic. Above this temperature it is not. The transformation involves a change in ordering of the magnetic domains and is not first-order. Additions of alloying elements will change the temperature of transformation. Magnetic transformations are treated in ch. 29. See also MIODOWNIK [1982], INDEN [1982] and HILLERT and JARL [1978].

2.10. Application of thermodynamics to phase diagram analysis

In recent years, the development of solution models, numerical methods and computer software has permitted a quantitative application of thermodynamics to phase diagram analysis. Computer programs are available which permit phase diagrams to be generated from equations for the Gibbs energies of the phases. Other programs have been written to perform simultaneous critical evaluations of available phase diagram measurements and of available thermodynamic data (calorimetric data, measurements of activities, etc.) with a view to obtaining optimized equations for the Gibbs energies of each phase which best represent all the data. These equations are consistent with thermodynamic principles and with theories of solution behaviour.

The phase diagram can be calculated from these optimized thermodynamic equations, and so one set of self-consistent equations describes all the thermodynamic properties and the phase diagram. This technique of analysis greatly reduces the amount of experimental data needed to characterize a system fully. All data can be tested for internal consistency. The data can be interpolated and extrapolated more accurately, and metastable phase boundaries can be calculated. All the thermodynamic properties and the phase diagram can be represented and stored by means of a small set of coefficients.

Finally and most importantly, it is often possible to estimate the thermodynamic properties and phase diagrams of ternary and higher-order systems from the assessed parameters for their binary sub-systems as will be discussed in § 5. The analysis of binary systems is thus the first and most important step in the development of databases for multicomponent systems.

The computer coupling of thermodynamics and phase diagrams is a growing field of much current research interest. The international Calphad Journal, published by Pergamon Press, and an annual international meeting, the Calphad Conference, are now devoted to this subject.

References: p. 531.

2.10.1. Polynomial representation of excess properties

Empirical equations are required to express the excess thermodynamic properties of the solution phases as functions of composition and temperature. For many simple binary substitutional solutions, a good representation is obtained by expanding the molar excess enthalpy and entropy as polynomials in the mole fractions X_A and X_B of the components:

$$h^E = X_A X_B(h_0 + h_1(X_B - X_A) + h_2(X_B - X_A)^2 + h_3(X_B - X_A)^3 + \ldots) \tag{18}$$

$$s^E = X_A X_B(s_0 + s_1(X_B - X_A) + s_2(X_B - X_A)^2 + s_3(X_B - X_A)^3 + \ldots) \tag{19}$$

where the h_i and s_i are empirical coefficients. As many coefficients are used as are required to represent the data in a given system. For most systems it is a good approximation to assume that the coefficients h_i and s_i are independent of temperature.

If the series are truncated after the first term, then:

$$g^E = h^E - Ts^E = X_A X_B(h_0 - Ts_0) \tag{20}$$

This is the same as eq. (4) for a regular solution. Hence, the polynomial representation can be considered to be an extension of regular solution theory. When the expansions are written in terms of the composition variable $(X_B - X_A)$ as in eqs. (18) and (19) they are said to be in *Redlich–Kister* form. Other equivalent polynomial expansions such as orthogonal Legendre series have been discussed by PELTON and BALE [1986].

Differentiation of eqs. (18) and (19) yields the following expansions for the partial excess properties:

$$h_A^E = X_B^2 \sum_{i=0} h_i \left[(X_B - X_A)^i - 2iX_A(X_B - X_A)^{i-1} \right] \tag{21}$$

$$h_B^E = X_A^2 \sum_{i=0} h_i \left[(X_B - X_A)^i + 2iX_B(X_B - X_A)^{i-1} \right] \tag{22}$$

$$s_A^E = X_B^2 \sum_{i=0} s_i \left[(X_B - X_A)^i - 2iX_A(X_B - X_A)^{i-1} \right] \tag{23}$$

$$s_B^E = X_A^2 \sum_{i=0} s_i \left[(X_B - X_A)^i + 2iX_B(X_B - X_A)^{i-1} \right] \tag{24}$$

2.10.2. Least-squares optimization

Eqs. (18), (19) and (21) to (24) are linear in terms of the coefficients. Through the use of these equations, all integral and partial excess properties (g^E, h^E, s^E, g_i^E, h_i^E, s_i^E) can be expressed by linear equations in terms of the one set of coefficients $\{h_i, s_i\}$. It is thus possible to include all available experimental data for a binary phase in one simultaneous linear least-squares optimization as discussed by BALE and PELTON [1983],

LUKAS *et al.* [1977] and DÖRNER *et al.* [1980], and specialized software for such optimizations is available.

The technique of coupled thermodynamic/phase diagram analysis is best illustrated by an example. The phase diagram of the Cd–Na system with points measured by several authors is shown in fig. 17. From electromotive force measurements on alloy concentration cells, several authors have measured the activity coefficient of Na in liquid alloys. These data are shown in fig. 18 at 400°C. From the temperature dependence of $g^{E}_{Na} = RT \ln \gamma_{Na}$, the partial enthalpy of Na in the liquid was obtained via the Gibbs–Helmholtz equation. The results are shown in fig. 19. Also, h^{E} of the liquid has been measured (KLEINSTUBER [1961]) by direct calorimetry.

Along the Cd-liquidus in fig. 17 the partial Gibbs energy of Cd in the liquid is equal to that of essentially pure solid Cd with which it is in equilibrium:

$$g^{l}_{Cd} = g^{o(s)}_{Cd} \tag{25}$$

Hence,

$$g^{l}_{Cd} - g^{o(l)}_{Cd} = g^{o(s)}_{Cd} - g^{o(l)}_{Cd} \tag{26}$$

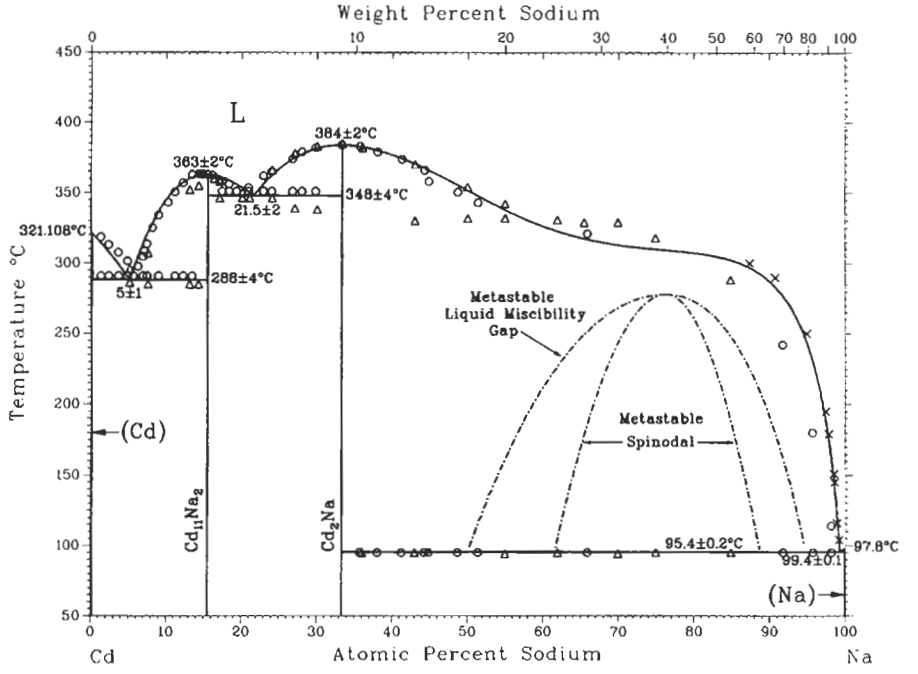

Fig. 17. Cd–Na phase diagram calculated from optimized thermodynamic parameters (Reprinted from PELTON [1988]).

o KURNAKOW and KUSNETZOV [1907]

Δ MATHEWSON [1906]

× WEEKS and DAVIES [1964]

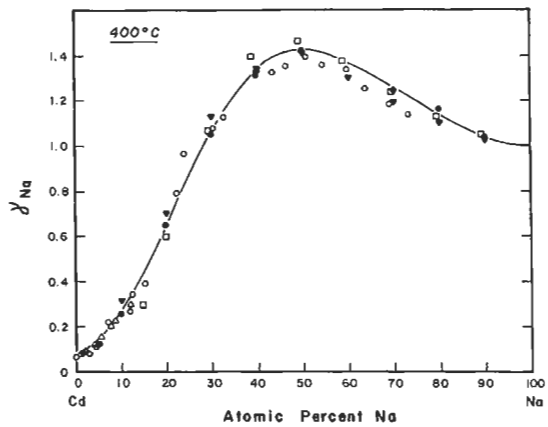

Fig. 18. Sodium activity coefficient in liquid Cd–Na alloys at 400°C. Line is calculated from optimized thermodynamic parameters (Reprinted from PELTON [1988]).
□ HAUFFE [1940]
● LANTRATOV and MIKHAILOVA [1971]
Δ MAIOROVA *et al.* [1976]
∇ ALABYSHEV and MORACHEVSKII [1957]
○ BARTLETT *et al.* [1970]

$$RT \ln X^{1}_{Cd} + g^{E(l)}_{Cd} = -\Delta g^{o}_{f(Cd)} \tag{27}$$

Therefore, from the experimental liquidus composition X^{1}_{Cd}, and from a knowledge of the Gibbs energy of fusion, $g^{E(l)}_{Cd}$ at the measured liquidus points can be calculated from eq. (27).

Similar equations relating the liquidus compositions along the $Cd_{11}Na_2$- and Cd_2Na-liquidus lines to the partial excess Gibbs energies of the liquid and to the Gibbs energies of fusion of $Cd_{11}Na_2$ and Cd_2Na can be written based upon the graphical construction shown in fig. 14.

The thermodynamic data for g^{E}_{Na}, h^{E}_{Na} and h^{E} as well as the measured liquidus points and the Gibbs energies of fusion of the compounds were optimized simultaneously by a least-squares technique to obtain the following optimized expressions (PELTON [1988]):

$$h^{E(l)} = X_{Cd}X_{Na}\left(-12508 + 20316\left(X_{Na} - X_{Cd}\right) - 8714\left(X_{Na} - X_{Cd}\right)^2\right) \text{J/mol} \tag{28}$$

$$s^{E(l)} = X_{Cd}X_{na}\left(-15.452 + 15.186\left(X_{Na} - X_{Cd}\right) - 10.062\left(X_{Na} - X_{Cd}\right)^2 - 1.122\left(X_{Na} - X_{Cd}\right)^3\right) \text{ J/mol K} \tag{29}$$

$$\Delta G^{o}_{f\left(\frac{1}{13}Cd_{11}Na_2\right)} = 6816 - 10.724\ T \quad \text{J/g-atom} \tag{30}$$

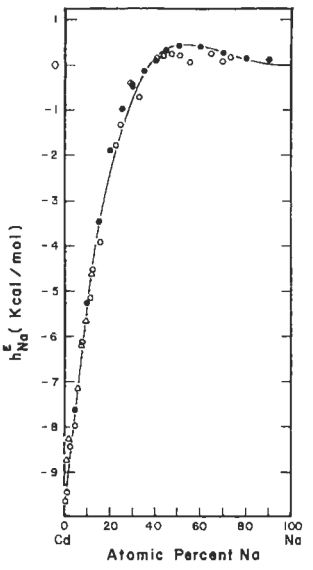

Fig. 19. Partial excess exthalpy of sodium in liquid Cd–Na alloys. Line is calculated from optimized thermodynamic parameters (Reprinted from PELTON [1988]).
● LANTRATOV and MIKHAILOVA [1971]
Δ MAIOROVA *et al.* [1976]
○ BARTLETT *et al.* [1970]

$$\Delta G^o_{f\left(\frac{1}{3}Cd_2Na\right)} = 8368 - 12.737\ T \quad \text{J/g-atom} \tag{31}$$

$$\Delta G^o_{f(Cd)} = 6201 - 10.4344\ T \quad \text{J/g - atom} \tag{32}$$

$$\Delta G^o_{f(Na)} = 2598 - 7.0035\ T \quad \text{J/g-atom} \tag{33}$$

The Gibbs energies of fusion of Cd and Na were taken from CHASE [1983] and were not changed in the optimization. The optimized enthalpies of fusion of 6816 and 8368 J/g-atom for the two compounds in eqs. (30, 31) were modified from the values of 6987 and 7878 J/g-atom measured by ROOS [1916]. These changes are within the experimental error limits. Eq. (28) reproduces the calorimetric data within 200 J/mol^{-1}. Eqs. (22, 24) can be used to calculate h^E_{Na} and γ^E_{Na}. The calculated curves are compared to the measured points in figs. 18 and 19. The phase diagram shown in fig. 17 was calculated from eqs. (28) to (33). Complete details of the analysis of the Cd–Na system are given by PELTON [1988].

It can thus be seen how one simple set of equations can simultaneously and self-consistently describe all the thermodynamic properties and the phase diagram of a binary system. The exact optimization procedure will vary from system to system depending on the type and accuracy of the available data, the number of phases present, the extent of

solid solubility, etc. A large number of optimizations have been published in the Calphad Journal since 1977.

2.10.3. Calculation of metastable phase boundaries

In the Cd–Na system just discussed, the liquid exhibits positive deviations from ideal mixing. That is, $g^{E(l)} > 0$. This fact is reflected in the very flat liquidus in fig. 17 as was discussed in § 2.5.2.

By simply not including any solid phases in the calculation, the metastable liquid miscibility gap as well as the spinodal curve (§ 2.3) can be calculated as shown in fig. 17. These curves are of importance in the formation of metallic glasses by rapid quenching (see ch. 19, § 2.1).

Other metastable phase boundaries, such as the extension of a liquidus curve below a eutectic, can also be calculated thermodynamically simply by excluding one or more phases during the computations.

2.11. Solution models

Polynomial expansions, as in eqs (18, 19), give an adequate representation of the excess mixing properties for simple substitutional solutions in which deviations from regular solution behaviour are not too large. In other cases, more sophisticated models are required.

The Gibbs energy of a regular solution is given by combining eqs. (2) and (4). The ideal mixing term in eq. (2) is a consequence of the assumption that A and B atoms form a random substitutional solution. The parameter Ω in eq (4) can be interpreted as resulting from the fact that the energy of A–B bonds in the solution is different from that of A–A and B–B bonds. Suppose that A–B bonds are energetically favourable. The solution is thereby stabilized, $\Omega < 0$ and $g^E < 0$. However, the distribution will then no longer be random because A and B atoms will tend to favour each other as nearest neighbours, and so the ideal mixing term, $RT(X_A \ln X_A + X_B \ln X_B)$ in eq. (2) is no longer correct. For relatively small deviations from ideality, the random mixing approximation is often acceptable. However, for larger deviations, the non-randomness becomes important. In such cases, a simple polynomial expansion for g^E as in eqs. (18, 19) is insufficient.

The regular solution model can be extended to account for this non-randomness through the *quasichemical model for short-range ordering* developed by GUGGENHEIM [1935] and FOWLER and GUGGENHEIM [1939]. Many liquid alloy solutions exhibit short-range ordering. The ordering is strongest when one component is relatively electropositive (on the left side of the periodic table) and the other is relatively electronegative. Liquid alloys such as Alk–Au (HENSEL [1979]), Alk–Pb (SABOUNGI *et al.* [1985]) and Alk–Bi (PETRIC *et al.* [1988]), where Alk = (Na, K, Rb, Cs) exhibit strong short-range ordering, as do liquid semiconductor solutions such as Ga–As and In–Sb. The quasichemical model has been recently adapted to permit thermodynamic/phase diagram optimizations of such systems (PELTON and BLANDER [1984, 1986, 1988]).

Short-range ordering in liquid alloys has also been modeled by treating such solutions as substitutional solutions of A atoms, B atoms and A_mB_n "complexes". See for example, LÜCK *et al.* [1989]. For most alloy systems, however, such *association models* are not physically realistic.

For an *interstitial solution* the ideal Gibbs energy of mixing is that of a random distribution of the solute atoms over the interstitial sites. For example, in an interstitial solution of C in γ-Fe, X_C moles of C atoms are distributed over X_{Fe} octahedral sites. The molar Gibbs energy of mixing is thus:

$$\begin{aligned}\Delta g &= RT\left(\frac{X_{Fe}}{X_{Fe}+X_C}\right)\left(\frac{X_C}{X_{Fe}}\ln\frac{X_C}{X_{Fe}}+\frac{(X_{Fe}-X_C)}{X_{Fe}}\ln\frac{(X_{Fe}-X_C)}{X_{Fe}}\right)\\ &= RT\left(X_C\ln\frac{X_C}{1-2X_C}+X_{Fe}\ln\left(1-\frac{X_C}{X_{Fe}}\right)\right)+g^E\end{aligned} \tag{34}$$

The ideal activities are thus:

$$a_C^{ideal} = X_C/(1-2X_C) \tag{35}$$

$$a_{Fe}^{ideal} = (1-X_C/X_{Fe}) \tag{36}$$

When modeling an interstitial solution, one should employ these expressions.

A multicomponent interstitial solution such as M_1–M_2–C–N, where M_1 and M_2 are metals, can be considered to consist of two sublattices: a metallic sublattice on which M_1 and M_2 are distributed, and an interstitial sublattice on which C, N (and vacant sites) are distributed. General sublattice models, of which such solutions are a special case, have been discussed by HILLERT *et al.* [1985]. An example of application to the Fe–Cr–V–C system is given in § 5.

Examples of *non-stoichiometric compound phases* were shown in figs 13 and 16. When these exhibit a relatively narrow range of stoichiometry, as is the case for $AgMg_3$ in fig. 14, the phase is conveniently described as a dilute solution of defects in the stoichiometric compound. For example, consider a compound $A_{1-y}B_y$. The lattice sites normally occupied by A atoms we shall call "A sites", and those normally occupied by B atoms are "B sites". The dissolution of excess B in the compound can occur by the formation of *defects*. Example of such defects are (i) B atoms occupying A sites; (ii) vacant A sites; (iii) B atoms occupying interstitial sites; etc. Generally, one type of defect will predominate in any given system when B is in excess, and this is called the majority defect for solutions with excess B. When excess A is added to $A_{1-y}B_y$, then another majority defect predominates. It should, of course, be noted that certain compounds, such as FeO, or Nb_3Al near room temperature, do not even contain the stoichiometric composition within their range of single-phase stoichiometry.

Despite the large number of defect types which can occur, a quite general thermodynamic model can be proposed. Let X_1 be the mole fraction of the majority defects which occur when A is in excess. This is the mole fraction of these defects on the sublattice (or interstitial lattice) which they occupy. Similarly, X_2 is the mole fraction of

the majority defects which occur when B is in excess. Let g_1 and g_2 be the energies required to form one mole of each type of defect in the limit when X_1 and X_2 are very small. Assume that the concentrations X_1 and X_2 are small enough that interactions between defects are negligible (Henry's Law) and that the number of lattice sites does not change appreciably from that in the defect-free compound. Assume further that the defects are randomly distributed. The molar Gibbs energy of the solution relative to the hypothetical defect-free compound is then:

$$g = \frac{RT}{\beta_1}\left(X_1 \ln X_1 + (1 - X_1)\ln(1 - X_1)\right) + \frac{RT}{\beta_2}\left(X_2 \ln X_2 + (1 - X_2)\ln(1 - X_2)\right) + \frac{1}{\beta_1} g_1 X_1 + \frac{1}{\beta_2} g_2 X_2 \tag{37}$$

where $1/\beta_1$ and $1/\beta_2$ are the numbers of moles of lattice sites available to each type of defect. For a given deviation from the stoichiometric composition represented by $A_{1-y-\delta}B_{y+\delta}$:

$$\delta = \frac{X_2}{\beta_2} - \frac{X_1}{\beta_1} \tag{38}$$

and by minimizing g with respect to X_1 and X_2 it can be shown that:

$$\left(\frac{X_1}{1 - X_1}\right)^{\frac{1}{\beta_1}} \left(\frac{X_2}{1 - X_2}\right)^{\frac{1}{\beta 2}} = \exp\left(\frac{-\left(\frac{g_1}{\beta_1} + \frac{g_2}{\beta_2}\right)}{RT}\right) \tag{39}$$

If values of the energy parameters g_1 and g_2 are given, eqs. (38, 39) can be solved for any δ to give X_1 and X_2 which can then be substituted back into eq. (37) to give g. When g_1 and g_2 are very large, g rises very steeply on either side of its minimum, and the range of stoichiometry is very narrow as for the case of the compounds in fig. 14. In the case of the compound $AgMg_3$ in fig. 13, $g_1 > g_2$. That is, it is easier to form defects by adding excess Mg than by adding excess Ag. Hence, the Gibbs energy curve rises more steeply on the Ag side, and as a result, Mg is more soluble in $AgMg_3$ than is Ag.

Defects are discussed in chs. 9, 18 and 20. For an example of an application of the defect model to phase diagram calculations, see PELTON [1991]. For a treatment of defect models as examples of general sublattice models, see HILLERT *et al.* [1985].

2.12. Binary phase diagrams involving a gaseous phase

The effect of total pressure, P, upon the Gibbs energy change for the transformation of one mole of pure component A from the α- to the β-phase is given by:

$$\Delta g_A^{\alpha\to\beta} = \Delta g_A^{0(\alpha\to\beta)} + \int_{P=1}^{P} \left(v_A^{\beta} - v_A^{\alpha}\right) dP, \tag{40}$$

where $\Delta g_A^{0(\alpha-\beta)}$ is the standard (i.e. at $P = 1$ atm) molar Gibbs energy of transformation and where v_A^α and v_B^α are the molar volumes of the phases. For solids and liquids, molar volumes are sufficiently small that the final term in eq. (40) is negligible unless P is very large. If a gaseous phase is involved, however, this is no longer the case. If gaseous A is ideal and monatomic, and since $v_A^g = RT/P >> v_A^l$, the molar Gibbs energy of vaporization is given by:

$$\Delta g_A^v = \Delta g_A^{0(v)} + RT \ln P . \tag{41}$$

where $\Delta g_A^{0(v)}$ is the standard Gibbs energy of vaporization (when P = 1 atm) which is given by:

$$\Delta g_A^{0(v)} = \Delta h_A^{0(v)} - T\Delta s_A^{0(v)} \tag{42}$$

For example, the enthalpy of vaporization of Zn is $\Delta h_{Zn}^{0(v)} = 115300$ J/mol at its normal boiling point of 1180 K (BARIN *et al.* [1977]). Assuming that $\Delta h^{0(v)}$ is independent of T, we calculate that $\Delta s_{Zn}^{0(v)} = 115300/1180 = 97.71$ J/mol K. Hence, Δg_{Zn}^v at any T and P is given by:

$$\Delta g_{Zn}^v = (115300 - 97.71T) + RT \ln P \tag{43}$$

A similar expression can be derived for the other component, Mg.

Curves of g^l and g^v at a constant T and P are shown in the upper panel of fig. 20. The common tangent construction generates the equilibrium vapour and liquid compositions. A temperature–composition phase diagram, at constant pressure, can then be generated as the curve for g^v descends relative to g^l as the temperature is raised. Alternatively, the isothermal pressure–composition diagram shown in the lower panel of fig. 20 is generated as the curve for g^v descends relative to g^l as the pressure is lowered. The diagram at 1250 K in fig. 20 was calculated under the assumption of ideal liquid and vapour mixing ($g^{E(l)} = g^{E(v)} = 0$).

3. *Ternary phase diagrams*

In this section, an introduction to ternary phase diagrams will be given. A complete discussion of the subject is beyond the scope of this chapter. For more detailed treatments see PRINCE [1966], WEST [1965] or BERGERON and RISBUD [1984].

3.1. The ternary composition triangle

In a ternary system with components A–B–C the sum of the mole fractions is unity. $(X_A + X_B + X_C) = 1$. Hence, there are two independent composition variables. A representation of composition, symmetrical with respect to all three components may be obtained with the equilateral "composition triangle" as shown in fig. 21. Compositions at the corners of the triangle correspond to the pure components. Along the edges of the triangle are found compositions corresponding to the three binary subsystems A–B, B–C and C–A. Lines of constant mole fraction X_A are parallel to the B–C edge, while lines of

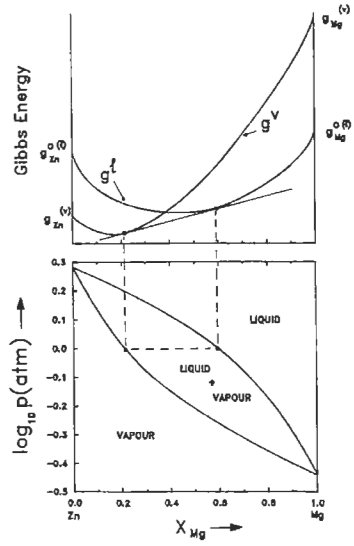

Fig. 20. Pressure-composition phase diagram of the Zn–Mg system at 1250 K calculated for ideal vapour and liquid solutions. Upper panel illustrates common tangent construction at a constant pressure and temperature.

constant X_B and X_C are parallel to the C–A and A–B edges respectively. For example at point **a** in fig. 21, $X_A = 0$, $X_B = 0.7$ and $X_C = 0.3$. At point **b**, $X_A = 0.3$, $X_B = 0.2$ and $X_C = 0.5$.

Similar equilateral composition triangles can also be drawn with coordinates in terms of weight% of the three components.

3.2. Ternary space model

A ternary temperature–composition "phase diagram" at constant total pressure may be plotted as a three-dimensional "space model" within a right triangular prism with the equilateral composition triangle as base and temperature as vertical axis. Such a space model for a simple eutectic ternary system A–B–C is illustrated in fig. 22. On the three vertical faces of the prism we find the phase diagrams of the three binary subsystems, A–B, B–C and C–A which, in this example, are all simple eutectic binary systems. The binary eutectic points are at $\mathbf{e}_1$, $\mathbf{e}_2$ and $\mathbf{e}_3$. Within the prism we see three *liquidus surfaces* descending from the melting points of pure A, B and C. Compositions on these surfaces correspond to compositions of liquid in equilibrium with A-, B- and C-rich solid phases.

In a ternary system at constant pressure, the Gibbs phase rule, eq. (14), becomes:

$$F = 4 - P. \tag{44}$$

When the liquid and one solid phase are in equilibrium, $P = 2$. Hence, $F = 2$, and the system is bivariant. A ternary liquidus is thus a two-dimensional surface. We may choose two variables, say T and one composition coordinate of the liquid, but then the other liquid composition coordinate and the composition of the solid are fixed.

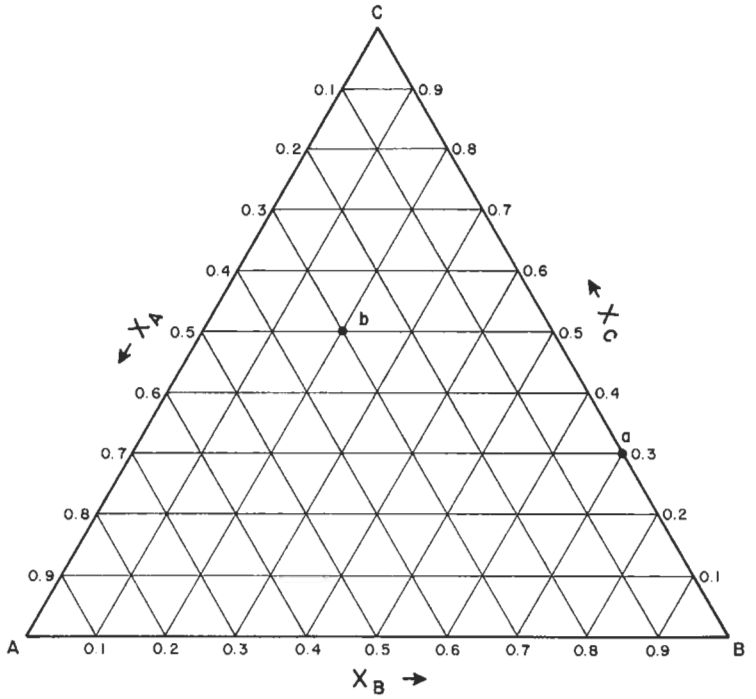

Fig. 21. The equilateral ternary composition triangle.

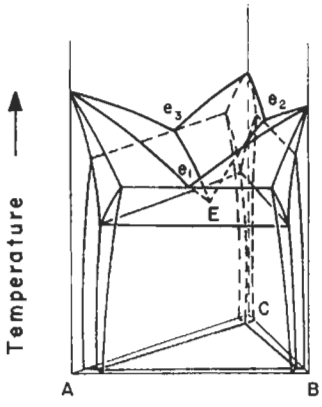

Fig. 22. Perspective view of ternary space model of a simple eutectic ternary system. $\mathbf{e}_1$, $\mathbf{e}_2$, $\mathbf{e}_3$ are the binary eutectics and **E** is the ternary eutectic. The base of the prism is the equilateral composition triangle.

References: p. 531.

The A- and B-liquidus surfaces in fig. 22 intersect along the line $\mathbf{e}_1$E. Liquids with 0compositions along this line are therefore in equilibrium with A-rich and B-rich solid phases simultaneously. That is, $P=3$ and so $F=1$. Such "valleys" are thus called *univariant lines*. The three univariant lines meet at the *ternary eutectic point* E at which $P=4$ and $F=0$. This is an invariant point since the temperature and the compositions of all four phases in equilibrium are fixed.

3.3. Polythermal projections of liquidus surfaces

A two-dimensional representation of the ternary liquidus surface may be obtained as an orthogonal projection upon the base composition triangle. Such a *polythermal projection* of the liquidus of the Bi–Sn–Cd system (BRAY *et al.* [1961–62]) is shown in fig. 23. This is a simple eutectic ternary system with a space model like that shown in fig. 22. The constant temperature lines on fig. 23 are called *liquidus isotherms*. The univariant valleys are shown as the heavier lines. By convention, the large arrows indicate the directions of decreasing temperature along these lines.

Let us consider the sequence of events which occur during the equilibrium cooling from the liquid of an alloy of overall composition **a** in fig. 23 ($X_{Bi}=0.05$, $X_{Sn}=0.45$, $X_{Cd}=0.50$). Point **a** lies within the *field of primary crystallization* of Cd. That is, it lies within the composition region in fig. 23 in which Cd-rich solid will be the first solid to precipitate upon cooling. As the liquid alloy is cooled, the Cd-liquidus surface is reached at $T \approx 465$ K (slightly below the 473 K isotherm). A solid Cd-rich phase begins to precipitate at this temperature. Now, in this particular system, Bi and Sn are nearly insoluble in solid Cd, so that the solid phase is virtually pure Cd (note that this fact cannot be deduced from fig. 23 alone). Therefore, as solidification proceeds, the liquid becomes depleted in Cd, but the ratio X_{Sn}/X_{Bi} in the liquid remains constant. Hence, the composition path followed by the liquid (its *crystallization path*) is a straight line passing through point **a** and projecting to the Cd-corner of the triangle. This crystallization path is shown on fig. 23 as the line **ab**.

In the general case in which a solid solution rather than a pure component or stoichiometric compound is precipitating, the crystallization path will not be a straight line. However, for equilibrium cooling, a straight line joining a point on the crystallization path at any T to the overall composition point **a** will extend through the composition, on the solidus surface, of the solid phase in equilibrium with the liquid at that temperature.

When the composition of the liquid has reached point **b** in fig. 23 at $T \approx 435$ K, the relative proportions of the solid Cd and liquid phases at equilibrium are given by the *lever rule* applied to the *tie-line* **dab**: (moles of liquid)/(moles of Cd) = **da**/**ab**, where **da** and **ab** are the lengths of the line segments. Upon further cooling the liquid composition follows the univariant valley from **b** to E while Cd and Sn-rich solids co-precipitate as a binary eutectic mixture. When the liquidus composition attains the ternary eutectic composition E at $T \approx 380$ K the invariant *ternary eutectic reaction* occurs:

$$\text{liquid} \rightarrow s_1 + s_2 + s_3, \tag{45}$$

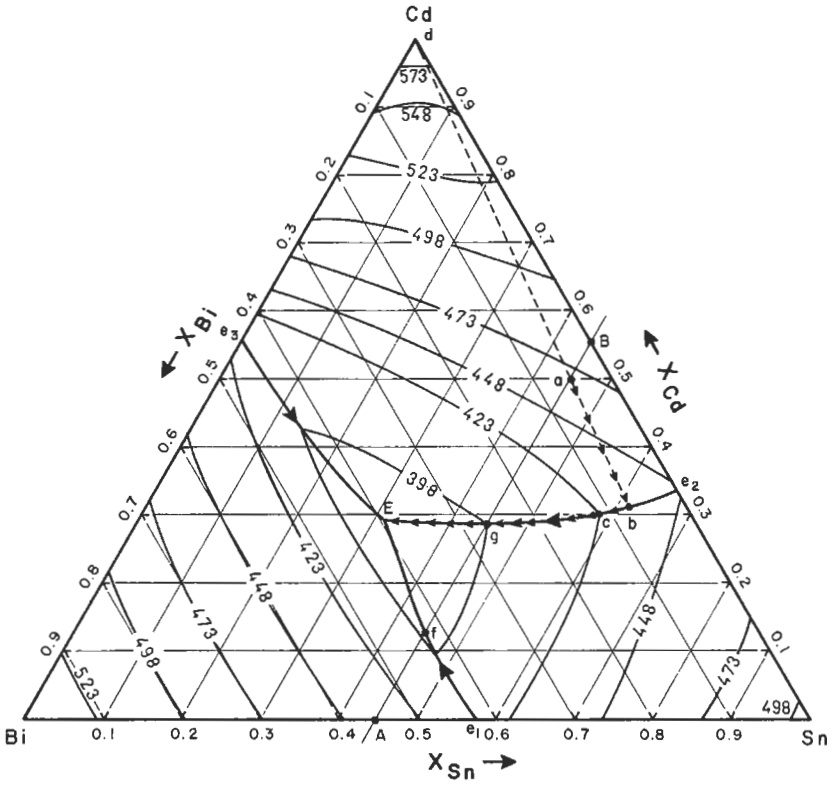

Fig. 23. Projection of the liquidus surface of the Bi–Sn–Cd system (after BRAY *et al.* [1961–62]). Small arrows show crystallization path of an alloy of overall composition at point **a**.

where s_1, s_2 and s_3 are the three solid phases and where the compositions of all four phases as well as T remain fixed until all liquid is solidified.

In order to illustrate several of the features of polythermal projections of liquidus surfaces, a projection of the liquidus of a hypothetical system A–B–C is shown in fig. 24. For the sake of simplicity, isotherms are not shown, but only the univariant lines with arrows to show the directions of decreasing temperature. The binary subsystems A–B and C–A are simple eutectic systems, while the binary subsystem B–C contains one congruent binary phase, ε and one incongruent binary phase, δ, as shown in the insert in fig. 24. The letters **e** and **p** indicate binary eutectic and peritectic points. The ε and δ phases are called *binary compounds* since they have compositions within a binary subsystem. Two *ternary compounds*, η and ζ, with compositions within the ternary triangle as indicated in fig. 24, are also found in this system. All compounds as well as pure solid A, B and C (the "α, β and γ" phases) are assumed to be stoichiometric (i.e. there is no solid solubility). The fields of primary crystallization of all the solids are indicated in parentheses in fig. 24. The composition of the ε phase lies within its field,

References: p. 531.

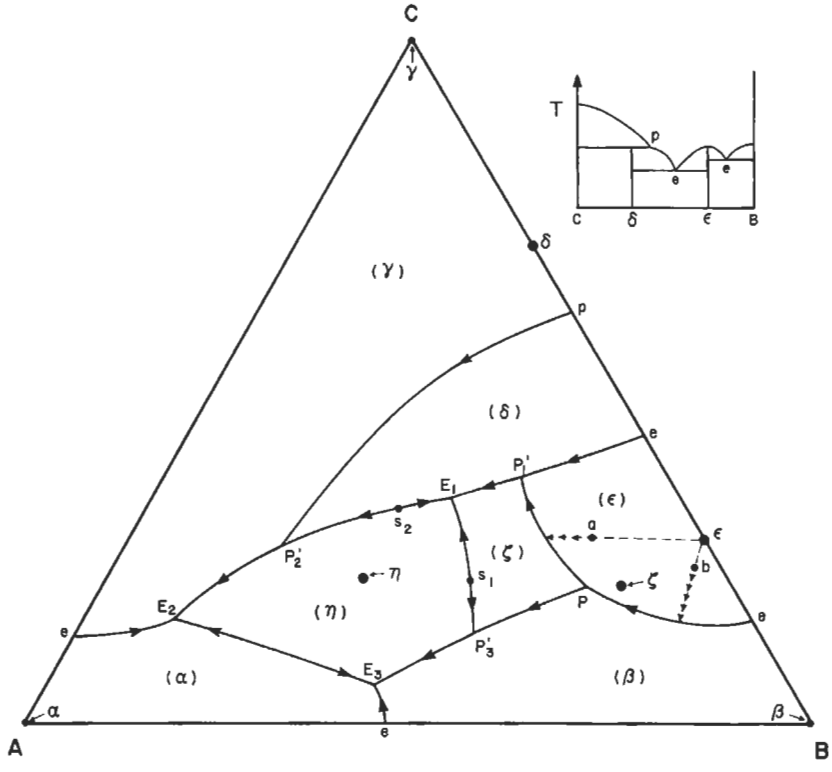

Fig. 24. Projection of the liquidus surface of a system A–B–C. The binary subsystems A–B and C–A are simple eutectic systems. The binary phase diagram B–C is shown in the insert. All solid phases are assumed pure stoichiometric components or compounds. Small arrows show crystallization paths of alloys of compositions at points **a** and **b**.

since ε is a congruent compound, while the composition of the δ phase lies outside of its field since δ is incongruent. Similarly for the ternary compounds, η is a congruently melting compound while ζ is incongruent. For the congruent compound η, the highest temperature on the η-liquidus occurs at the composition of η.

The univariant lines meet at a number of *ternary eutectics* E_i (three arrows converging), a *ternary peritectic* P (one arrow entering, two arrows leaving the point), and several *ternary quasi-peritectics* P'_i (two arrows entering, one arrow leaving). Two *saddle points* **s** are also shown. These are points of maximum T along the univariant line but of minimum T on the liquidus surface along a section joining the compositions of the two solids. For example, $\mathbf{s}_1$ is at a maximum along the univariant $E_1P'_3$, but is a minimum point on the liquidus along the straight line $\zeta\mathbf{s}_1\eta$.

Let us consider the events occurring during the cooling from the liquid of an alloy of overall composition **a** in fig. 24. The primary crystallization product will be the ε phase. Since this is a pure stoichiometric solid the crystallization path of the liquid will be along

a straight line passing through **a** and extending to the composition of ε as shown on the figure.

Solidification of ε continues until the liquid attains a composition on the univariant valley. Then the liquid composition follows the valley towards the point P_1' in co-existence with ε and ζ. At point P_1' the invariant *ternary quasi-peritectic reaction* occurs isothermally:

$$\text{liquid} + \varepsilon \rightarrow \delta + \zeta. \tag{46}$$

Since there are two reactants in a quasi-peritectic reaction, there are two possible outcomes: (i) The liquid is completely consumed before the ε-phase; in this case, solidification will be complete at the point P_1'. (ii) ε is completely consumed before the liquid; in this case, solidification will continue with decreasing T along the univariant line $P_1'E_1$ with co-precipitation of δ and ζ until, at E, the liquid will solidify eutectically (liquid $\rightarrow \delta + \zeta + \eta$). To determine whether condition (i) or (ii) occurs, we use the mass balance criterion that, for three-phase equilibrium, the overall composition must always lie within the *tie-triangle* formed by the compositions of the three phases. Now, the triangle joining the compositions of δ, ε, and ζ does not contain the point **a**, but the triangle joining the compositions of δ, ζ, and liquid at P_1' does contain the point **a**. Hence, case (ii) occurs.

An alloy of overall composition **b** in fig. 24 solidifies with ε as primary crystallization product until the liquid composition contacts the univariant line. Thereafter, co-precipitation of ε and β occurs with the liquid composition following the univariant valley until the liquid reaches the peritectic composition P. The invariant *ternary peritectic reaction* then occurs isothermally:

$$\text{liquid} + \varepsilon + \beta \rightarrow \zeta. \tag{47}$$

Since there are three reactants, there are three possible outcomes: (i) Liquid is consumed before either ε or β and solidification terminates at P. (ii) ε is consumed first; solidification then continues along the path PP_3'. (iii) β is consumed first and solidification continues along the path PP_1'. Which outcome occurs depends on whether the overall composition **b** lies within the tie-triangle (i) $\varepsilon\beta\zeta$, (ii) $\beta\zeta$P or (iii) $\varepsilon\zeta$P. In the example shown, case (i) will occur.

3.4. Ternary isothermal sections

Isothermal projections of the liquidus surface do not give information on the compositions of the solid phases at equilibrium. However, this information can be presented at any one temperature on an *isothermal section* such as that shown for the Bi–Sn–Cd system at 423 K in fig. 25. This phase diagram is a constant temperature slice through the space model of fig. 22.

The liquidus lines bordering the one-phase liquid region of fig. 25 are identical to the 423 K isotherms of the projection in fig. 23. Point **c** in fig. 25 is point **c** on the univariant line in fig. 23. An alloy with overall composition in the one-phase liquid region of fig. 25 at 423 K will consist of a single liquid phase. If the overall composition lies within one of the two-phase regions, then the compositions of the two phases are given

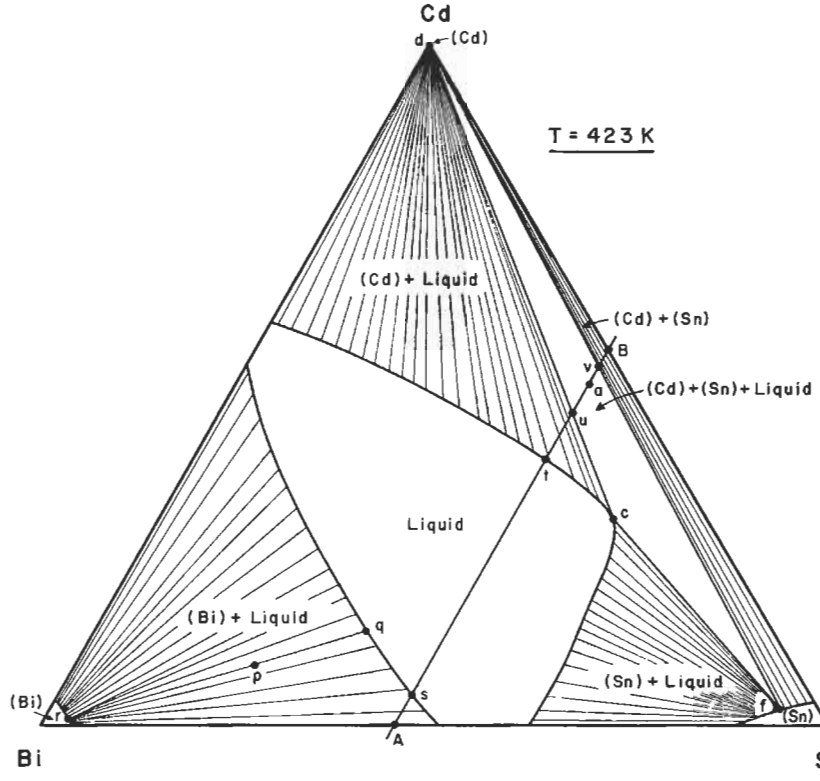

Fig. 25. Isothermal section of Bi–Sn–Cd system at 423 K (after BRAY *et al.* [1961–62]). Extents of solid solubility in Bi and Sn have been exaggerated for clarity of presentation.

by the ends of the *tie-line* containing the overall composition. For example, a sample with overall composition **p** in fig. 25 will consist of a liquid of composition **q** on the liquidus and a solid Bi-rich alloy of composition **r** on the solidus. The relative proportions of the two phases are given by the lever rule: (moles of liquid)/(moles of solid) = **pr**/**pq**, where **pr** and **pq** are the lengths of the line segments.

In the case of solid Cd, the solid phase is nearly pure Cd, so all tie-lines of the (Cd + liquid) region converge nearly to the corner of the triangle. In the case of Bi- and Sn-rich solids, some solid solubility is observed. (The actual extent of this solubility is somewhat exaggerated in fig. 25 for the sake of clarity of presentation.) Alloys with overall compositions rich enough in Bi or Sn to lie within the single-phase (Sn) or (Bi) regions of fig. 25 will consist, at 423 K, of single-phase solid solutions. Alloys with overall compositions at 423 K in the two-phase (Cd + Sn) region will consist of two solid phases.

Alloys with overall compositions within the three-phase triangle **dcf** will, at 423 K, consist of three phases: Cd- and Sn-rich solids with compositions at **d** and **f**, and liquid

of composition **c**. To understand this better, consider an alloy of composition **a** in fig. 25, which is the same composition as the point **a** in fig. 23. In § 3.3 we saw that when a alloy of this composition is cooled, the liquid follows the path **ab** on fig. 23 with primary precipitation of Cd and then follows the univariant line with co-precipitation of Cd and Sn so that at 423 K the liquid will be at the composition point **c**, and two solid phases are in equilibrium with the liquid.

3.4.1. Topology of ternary isothermal sections

At constant temperature the Gibbs energy of each phase in a ternary system is represented as a function of composition by a surface plotted in a right triangular prism with Gibbs energy as vertical axis and the composition triangle as base. Just as the compositions of phases at equilibrium in binary systems are determined by the points of contact of a common tangent line to their isothermal Gibbs energy curves, so the compositions of phases at equilibrium in a ternary system are given by the points of contact of a common tangent plane to their isothermal Gibbs energy surfaces. A common tangent plane can contact two Gibbs energy surfaces at an infinite number of pairs of points. thereby generating an infinite number of tie-lines within a two-phase area on an isothermal section. A common tangent plane to three Gibbs energy surfaces contacts each surface at a unique point, thereby generating a three-phase tie-triangle.

Hence, the principal topological units of construction of an isothermal ternary phase diagram are three-phase ($\alpha + \beta + \gamma$) tie-triangles as in fig. 26 with their accompanying two-phase and single-phase areas. Each corner of the tie-triangle contacts a single-phase region, and from each edge of the triangle there extends a two-phase region. The edge of the triangle is a limiting tie-line of the two-phase region.

For overall compositions within the tie-triangle, the compositions of the three phases at equilibrium are fixed at the corners of the triangle. The relative proportions of the three phases are given by the *lever rule* of tie-triangles which can be derived from mass balance considerations. At an overall composition **q** in fig. 26, for example, the relative proportion of the γ-phase is given by projecting a straight line from the γ-corner of the triangle (point **c**) through the overall composition **q** to the opposite side of the triangle, point **p**. Then: (moles of γ)/(total moles) = **qp/cp** if compositions are expressed in mole fractions, or (weight of γ)/(total weight) = **qp/cp** if compositions are in weight percent.

Isothermal ternary phase diagrams are generally composed of a number of these topological units. An example for the Al–Zn–Mg system at 25°C is shown in fig. 27 (KÖSTER and DULLENKOPF [1936]). The β, γ, δ, θ, η and ζ phases are binary intermetallic compounds with small (~1%) ranges of stoichiometry which can dissolve a limited amount (~1–6%) of the third component. The τ phase is a ternary phase with a single-phase region existing over a fairly extensive oval-shaped central composition range. Examination of fig. 27 shows that it consists of the topological units of fig. 26.

An extension rule, a case of *Schreinemakers's rule* (SCHREINEMAKERS [1915]) for ternary tie-triangles is illustrated in fig. 26. At each corner, the extension of the boundaries of the single-phase regions, indicated by the dashed lines, must either both project into the triangle as at point **a**, or must both project outside the triangle as at point **b**, and furthermore the angle between these extensions must be less than 180°. For a proof, see LIPSON and WILSON [1940].

References: p. 531.

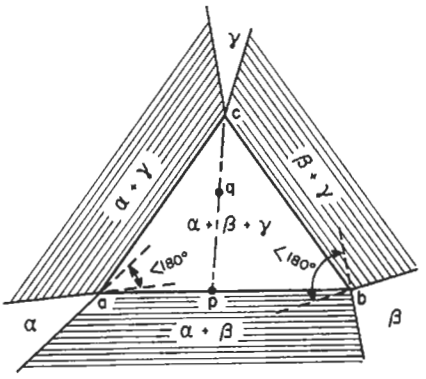

Fig. 26. A tie-triangle in a ternary isothermal section illustrating the lever rule and the extension rule.

Many published phase diagrams violate this rule. For example, it is violated in fig. 27 at the δ-corner of the $(\varepsilon + \delta + \tau)$ tie-triangle.

Another important rule of construction, whose derivation is evident, is that within any two-phase region tie-lines must never cross each other.

3.5. Ternary isopleths (constant composition sections)

A vertical *isopleth*, or constant composition section through the space model of the Bi–Sn–Cd system is shown in fig. 28. The section follows the line **AB** in fig. 23.

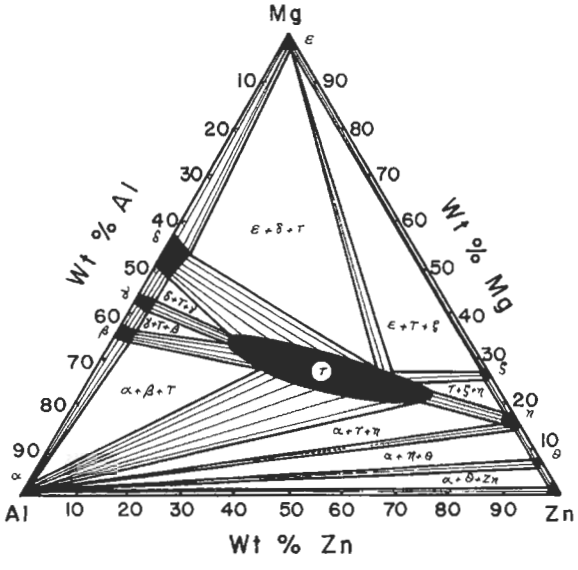

Fig. 27. Ternary isothermal section of the Al–Zn–Mg system at 25°C (after KÖSTER and DULLENKOPF [1936]).

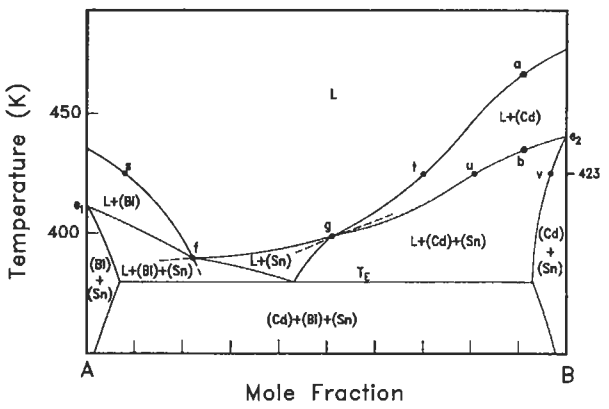

Fig. 28. Isopleth (constant composition section) of the Bi–Sn–Cd system following the line **AB** of fig. 23.

The phase fields on fig. 28 indicate which phases are present when an alloy with an overall composition on the line **AB** is equilibrated at any temperature. For example, consider the cooling from the liquid state, of an alloy of composition **a** which is on the line **AB** (see fig. 23). At T ≈ 465 K, precipitation of the solid (Cd) phase begins at point **a** in fig. 28. At T ≈ 435 K (point **b** in figs. 23 and 28) the solid (Sn) phase begins to appear. Finally, at the eutectic temperature T_E, the ternary eutectic reaction occurs, leaving solid (Cd) + (Bi) + (Sn) at lower temperatures. The intersection of the isopleth with the univariant lines on fig. 23 occurs at points **f** and **g** which are also indicated in fig. 28. The intersection of this isopleth with the isothermal section at 423 K is shown in fig. 25. The points **s**, **t**, **u** and **v** of fig. 25 are also shown on fig. 28.

It is important to note that on an isopleth, the tie-lines do not, in general, lie in the plane of the diagram. Therefore, the diagram gives information only on which phases are present, not on their compositions. The boundary lines on an isopleth do not in general indicate the phase compositions, but only the temperature at which a phase appears or disappears for a given overall composition. The lever rule cannot be applied on an isopleth.

Certain topological rules apply to isopleths. As a phase boundary line is crossed, one and only one phase either appears or disappears. This *Law of Adjoining Phase Regions* (PALATNIK and LANDAU [1964]) is illustrated by fig. 28. The only apparent exception occurs for the horizontal invariant line at T_E. However, if we consider this line to be a degenerate infinitely narrow four-phase region (L + (Cd) + (Bi) + (Sn)), then the law is also obeyed here.

Three or four boundary lines meet at intersection points. At an intersection point, *Schreinemakers' rule* applies (SCHREINEMAKERS [1915]). This rule states that the boundaries of the phase field with the smallest number of phases, when extrapolated, must either both fall within the phase field with the greatest number of phases (as at point **f** in fig. 28) or else both fall outside this region (as at point **g** in fig. 28).

Apparent exceptions to these rules (such as, for example, five boundaries meeting at an intersection point) can occur if the section passes exactly through a node (such as a ternary eutectic point) of the space model. However, these apparent exceptions are really only limiting cases. See PRINCE [1963] or PRINCE [1966].

References: p. 531.

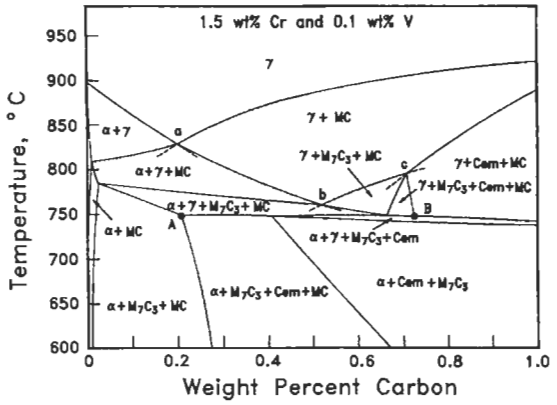

Fig. 29. Section of the Fe–Cr–V–C system at 1.5 wt.% Cr and 0.1 wt.% V (LEE and LEE [1992]).

4. *Multicomponent phase diagrams*

Only a brief outline of multicomponent phase diagrams can be presented here. For more detailed treatments see PALATNIK and LANDAU [1964], PRINCE [1963], PRINCE [1966] and HILLERT [1985].

For alloy systems of four or more components, two-dimensional sections are usually plotted with one or more compositional variables held constant. Hence, these sections are similar to the ternary isopleths discussed in § 3.5. In certain cases, sections at constant chemical potential of one or more components (for example, at constant oxygen partial pressure) can be useful. These are discussed in § 6.

Two sections of the Fe–Cr–V–C system (LEE and LEE [1992]) are shown in figs. 29, 30. The diagram in fig. 29 is a T-composition section at constant Cr and V content, while fig. 30 is a section at constant T = 850°C and constant C content of 0.3 wt.%. The

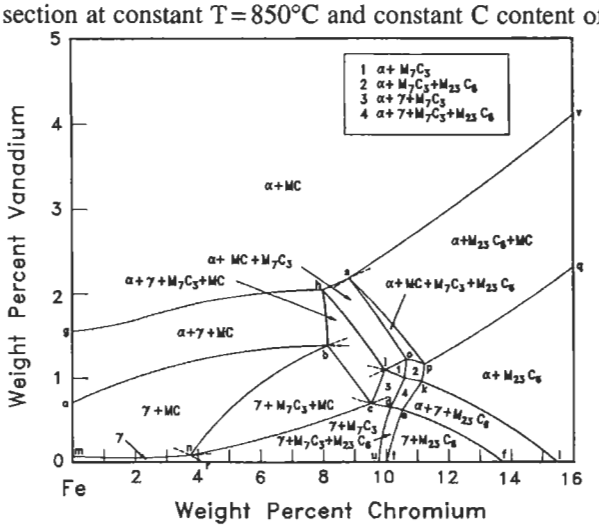

Fig. 30. Section of the Fe–Cr–V–C system at 850°C and 0.3 wt.% C (LEE and LEE [1992]).

interpretation and topological rules of construction of these sections are the same as those for ternary isopleths as discussed in § 3.5. In fact, the same rules apply to a two-dimensional constant–composition section for a system of any number of components. The phase fields on the diagram indicate the phases present at equilibrium for an overall composition lying on the section. Tie-lines do not, in general, lie in the plane of the diagram so the diagram does not give information on the compositions or amounts of the phases present. As a phase boundary is crossed, one and only one phase appears or disappears (Law of Adjoining Phase Regions). If temperature is an axis, as in fig. 29, then horizontal invariants like the line AB in fig. 29 can appear. These can be considered as degenerate infinitely narrow phase fields of (C + 1) phases, where C is the number of components (for isobaric diagrams). For example in fig. 29, on the line AB, five phases are present. Three or four phase boundaries meet at intersection points at which *Schreinemakers' rule* applies. This rule was given in § 3.5. It is illustrated by the extrapolations in fig. 29 at points **a**, **b** and **c** and in fig. 30 at points **b**, **c**, **n**, **i** and **s**. The applicability of Schreinemakers' rule to systems of any number of components was noted by HILLERT [1985], although no formal proof has been presented.

4.1. Zero phase fraction lines

An interesting and useful method of constructing multicomponent phase diagrams through the use of *zero phase fraction (ZPF)* lines has recently been proposed (GUPTA *et al.* [1986]). A ZPF line divides a two-dimensional phase diagram into two regions. On one side of the line a phase occurs, while on the other side it does not. For example, in fig. 30 the ZPF line for the α phase is the line **abcdef**. The ZPF line for the γ phase is **ghijkl**. For the MC phase the ZPF line is **mnciopq**. The ZPF line for M_7C_3 is **rnbhspket**, and for $M_{23}C_6$ it is **udjosv**. These five ZPF lines yield the entire two-dimensional phase diagram. The usefulness of this methodology for estimating phase diagrams for multicomponent systems from experimental data was discussed by GUPTA *et al.* [1986]. The method also holds promise for the thermodynamic calculation of phase diagrams (§ 5).

4.2. Nomenclature for invariant reactions

As discussed in § 2.9, in a binary isobaric temperature–composition phase diagram there are two possible types of invariant reactions: "eutectic type" invariant reactions ($\beta \rightarrow \alpha + \gamma$), and "peritectic type" invariant reactions ($\alpha + \gamma \rightarrow \beta$). In a ternary system, there are "eutectic type" ($\alpha \rightarrow \beta + \gamma + \delta$), "peritectic type" ($\alpha + \beta + \gamma \rightarrow \delta$) and "quasi-peritectic type" ($\alpha + \beta \rightarrow \gamma + \delta$) invariants (§ 3.3). In a system of C components, the number of types of invariant reaction is equal to C. A reaction with one reactant, such as $\alpha \rightarrow \beta + \gamma + \delta + \varepsilon$ is clearly a "eutectic type" invariant reaction but in general there is no standard terminology. These reactions are conveniently described according to the numbers of reactants and products (in the direction which occurs upon cooling). Hence, the reaction $\alpha + \beta \rightarrow \gamma + \delta + \varepsilon$ is a $2 \rightarrow 3$ reaction; the reaction $\alpha \rightarrow \beta + \gamma + \delta$ is a $1 \rightarrow 3$ reaction; and so on. The ternary peritectic type $3 \rightarrow 1$ reaction ($\alpha + \beta + \gamma \rightarrow \delta$) is an invariant reaction in a ternary system, a univariant reaction in a quaternary system, a bivariant reaction in a quinary system, etc.

References: p. 531.

5. *Thermodynamic calculation of ternary and multicomponent phase diagrams*

Among 70 metallic elements are formed $70!/3!67! = 54740$ ternary systems and 916895 quaternary systems. In view of the amount of work involved in measuring even one isothermal section of a relatively simple ternary phase diagram, it is very important to have means of estimating ternary and higher-order phase diagrams. The most fruitful approach to such predictions is via thermodynamic methods. In recent years, large advances have been made in this area by the international Calphad group. Many key papers have been published in the Calphad Journal.

As a first step in the thermodynamic approach to calculating a ternary phase diagram one critically analyzes the experimental phase diagrams and thermodynamic data for the three binary subsystems of the ternary system in order to obtain a set of mathematical expressions for the Gibbs energies of the binary phases as was discussed in § 2.10 and § 2.11. Next, equations based on solution models are used to estimate the Gibbs energies of the ternary phases from the Gibbs energies of the binary phases. The ternary phase diagram is then calculated from these estimated ternary Gibbs energies by means of common tangent plane or total Gibbs energy minimization algorithms.

For a phase for which the excess Gibbs energies in the binary systems have been expressed by polynomial expansions (§ 2.10.1) a satisfactory estimation of the Gibbs energy of the ternary phase can often be obtained with the following equation proposed by KOHLER [1960]:

$$g^{E} = (1 - X_A)^2 g^{E}_{B/C} + (1 - X_B)^2 g^{E}_{C/A} + (1 - X_C)^2 g^{E}_{A/B} \tag{48}$$

In this equation, g^E is the excess molar Gibbs energy at a composition point in the ternary phase and $g^E_{B/C}$, $g^E_{C/A}$ and $g^E_{A/B}$ are the excess Gibbs energies in the three binary subsystems at the same molar ratios X_B/X_C, X_C/X_A and X_A/X_B as at the ternary point. If the ternary solution as well as the three binary solutions are all regular then eq. (48) is exact. In the general case, a physical interpretation of eq. (48) is that the contribution to g^E from, say, pair interactions between A and B particles is constant at a constant ratio X_A/X_B apart from the dilutive effect of the C particles which is accounted for by the term $(1 - X_C)^2$ taken from regular solution theory. Other very similar equations, all based upon extension of regular solution theory, are also regularly used. These all give quite similar results. For a discussion see SPENCER and BARIN [1979] or HILLERT [1980].

For more complex solutions involving structural ordering or more than one sublattice, appropriate solution models for representing the binary properties have been discussed in § 2.11. In such cases, eq. (48) or similar equations should not be used for estimating the ternary excess Gibbs energies. Rather, equations consistent with the appropriate solution model should be used. For the quasichemical model, these have been discussed by PELTON and BLANDER [1986]. For the sublattice model, see HILLERT *et al.* [1985].

As an example of the calculation of a ternary phase diagram, the experimental isothermal section at 923 K of the Cr–Ni–Fe phase diagram is compared in fig. 31 with the diagram calculated solely from optimized binary thermodynamic properties (CHART

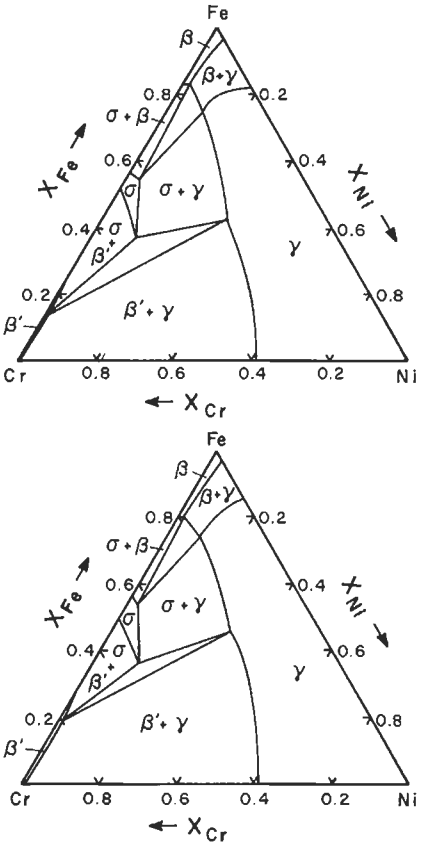

Fig. 31. Isothermal section at 923 K of the Cr–Ni–Fe phase diagram from CHART *et al.* [1979]. Lower diagram is experimental; upper diagram is calculated from binary data.

et al. [1979]). Such estimated phase diagrams are often quite acceptable for many purposes. However, the agreement between the experimental and calculated diagrams can usually be greatly improved by the inclusion of one or more "ternary terms" with adjustable coefficients in the equations for g^E. For example, the ternary term $aX_AX_BX_C$, which is zero in all three binary subsystem could be added to eq. (48) and the value of the parameter a which gives the best optimized fit to measured ternary phase diagram points could be determined. This, of course, requires that ternary measurements be made, but only a very few experimental points will usually suffice rather than the large number of measurements required for a fully experimental determination. In this way, the coupling of the thermodynamic approach with a few well chosen experimental measurements can greatly reduce the experimental effort involved in determining multicomponent phase diagrams.

An example of a coupled thermodynamic/phase diagram evaluation and calculation for a multicomponent system is the work of LEE and LEE [1992] on the Fe–Cr–V–C

system. The diagrams in figs 29, 30 were calculated thermodynamically by these authors. For the solid alloy and carbide phases, interstitial sublattice models were used. For the liquid phase, a substitutional model was employed. All available phase diagram and thermodynamic data for the binary and ternary subsystems, as well as for the quaternary system, were simultaneously optimized in order to obtain the best sets of binary and ternary parameters of the model equations for g^E for each phase as well as optimized equations for the standard Gibbs energies of the compounds. In this way, all the diverse data sets were smoothed and made consistent with each other and with thermodynamic principles. Any desired type of two-dimensional phase diagram section for the quaternary system can be calculated from the database of model parameters.

6. *Phase diagrams with potentials as axes*

So far we have considered mainly isobaric temperature–composition phase diagrams. However, there are many other kinds of phase diagrams of metallurgical interest with pressure, chemical potentials, volume, etc. as axes. These can be classified into geometrical types according to their topological rules of construction.

For instance, binary isothermal P–X diagrams as in fig. 20 are members of the same type as binary isobaric T–X diagrams since they are both formed from the same topological units of construction. Other useful phase diagrams of this same geometrical type are isothermal chemical potential–composition diagrams for ternary systems. An example is shown in the lowest panel of fig. 32 (PELTON and THOMPSON [1975]) for the Co–Ni–O system at T = 1600 K (and at a constant total hydrostatic pressure of 1 atm). Here the logarithm of the equilibrium partial pressure of O_2 is plotted versus the metal ratio $\xi = n_{Ni}/(n_{CO} + n_{Ni})$, where n_i = number of moles of i. There are two phases in this system under these conditions, a solid alloy solution stable at lower p_{O_2}, and a solid solution of CoO and NiO stable at higher p_{O_2}. For instance, point **a** gives p_{O_2} for the equilibrium between pure Co and pure CoO at 1600 K. Between the two single-phase regions is a two-phase (alloy + oxide) region. At any overall composition on the tie-line **cd** between points **c** and **d**, two phases will be observed, an alloy of composition **d** and an oxide of composition **c**. The lever rule applies just as for binary T–X diagrams.

The usual isothermal section of the ternary Co–Ni–O system at 1600 K is shown in the top panel of fig. 32. There are two single-phase regions with a two-phase region between them. The single-phase areas are very narrow since oxygen is only very slightly soluble in the solid alloy and since CoO and NiO are very stoichiometric oxides. In the central panel of fig. 32 this same diagram is shown but with the composition triangle "opened out" by putting the oxygen corner at infinity. This can be done if the vertical axis becomes $\eta = n_O/(n_{Co} + n_{Ni})$ with the horizontal axis as $\xi = n_{Ni}/(n_{Co} + n_{Ni})$. These are known as *Jänecke coordinates*. It can be seen in fig. 32 that each tie-line, **ef**, of the isothermal section corresponds to a tie-line, **cd** of the log diagram. This underscores the fact that every tie-line of a ternary isothermal section corresponds to a constant chemical potential of each of the components.

Another example of a log diagram is shown for the Fe–Cr–O system at 1573

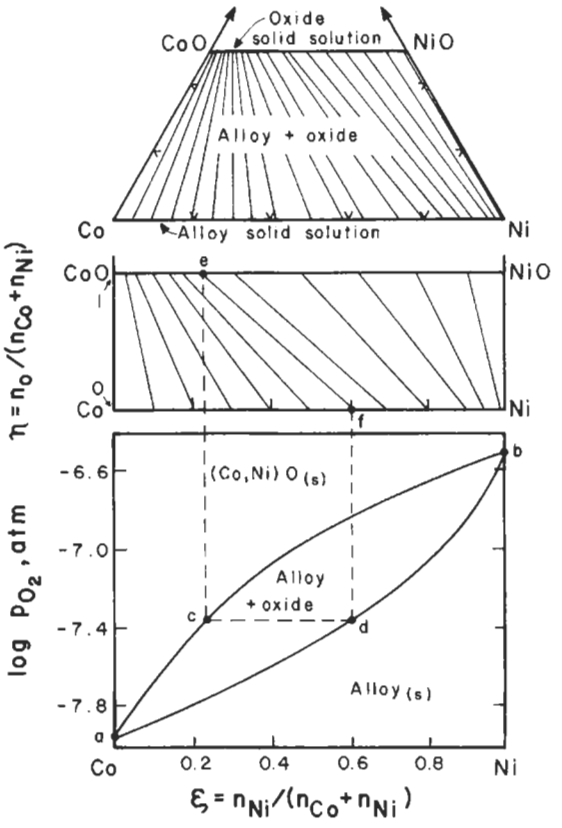

Fig. 32. Corresponding type-2 and type-3 phase diagrams for the Co–Ni–O system at 1600 K (from PELTON and THOMPSON [1975]).

K in the lower panel of fig. 33 (PELTON and SCHMALZRIED [1973]). The corresponding ternary isothermal section in Jänecke coordinates is shown in the upper panel. Each of the invariant three-phase tie-triangles in the isothermal section corresponds to an invariant line in the log p_{O_2}-ξ diagram. For example, the (spinel + (Fe, Cr)O + alloy) triangle with corners at points **a**, **b** and **c** corresponds to the "eutectic-like" invariant with the same phase compositions **a**, **b** and **c** at log $p_{O_2} \approx -10.7$. We can see that within a three-phase tie-triangle, p_{O_2} is constant.

An example of yet another kind of phase diagram of this same geometrical type is shown in fig. 34. For the quaternary Fe–Cr–O–SO_2 system at T = 1273 K and at constant $p_{SO_2} = 10^{-7}$ atm, fig. 34 is a plot of log p_{O_2} versus the molar metal ratio ξ (PELTON [1991]). Since log p_{O_2} varies as $-1/2$ log p_{S_2} when p_{SO_2} and T are constant, fig. 34 is also a plot of log p_{S_2} versus ξ.

It can be seen that the diagrams discussed above are of the same geometrical type as binary T–X diagrams since they are all composed of the same topological units of

References: p. 531.

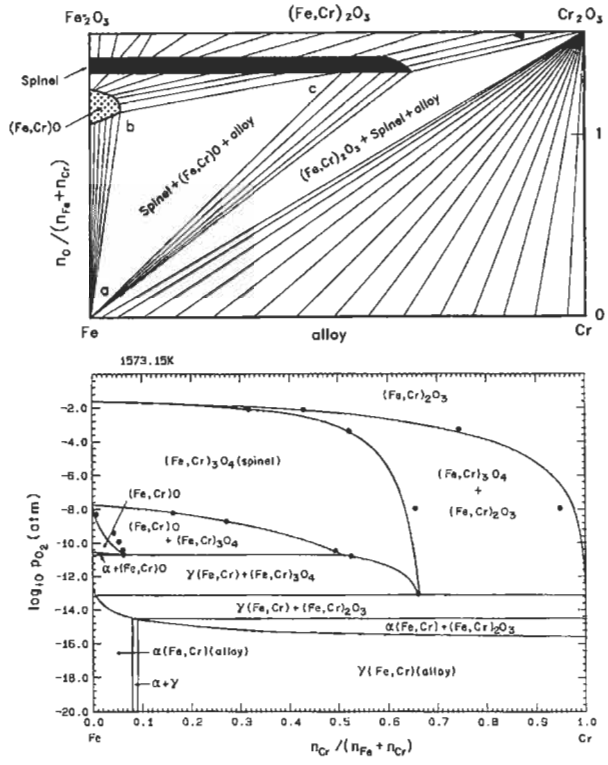

Fig. 33. Corresponding type-2 and type-3 phase diagrams for the Fe–Cr–O system at 1573 K (PELTON and SCHMALZRIED [1973]). Experimental points from KATSURA and MUAN [1964].

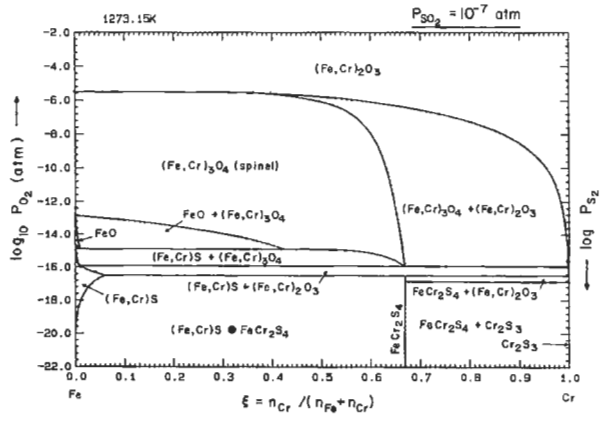

Fig. 34. Calculated type-2 phase diagram of log p_{O_2} versus molar metal ratio at T = 1273 K and $p_{SO_2} = 10^{-7}$ atm for the Fe–Cr–O–SO_2 system (PELTON [1991]).

construction as in fig. 15. Their interpretation is thus immediately clear to anyone familiar with binary T–X diagrams. Chemical potential–composition diagrams (figs. 32–34) are useful in the study of high temperature oxidation of alloys, metallurgical roasting processes, etc.

The log p_{O_2}-ξ diagrams in figs. 33, 34 were calculated by the same algorithm which produced the binary phase diagram of fig. 17. This algorithm operates by computing common tangent lines to the Gibbs energy–composition curves of the phases. The diagrams in figs. 33, 34 were calculated from optimized mathematical expressions for the Gibbs energy curves of all the phases. With these same optimized equations, $\log p_{O_2}$-ξ diagrams at other temperatures can be calculated, as can T–ξ diagrams at constant p_{O_2} which are also of the same geometrical type. For details see PELTON *et al.* [1979].

Another important geometrical type of phase diagram is exemplified by P–T phase diagrams for one-component systems as shown for H_2O in fig. 35. In such diagrams, which are discussed in ch. 5, § 3, bivariant single-phase regions are indicated by areas, univariant two-phase regions by lines, and invariant three-phase regions by *triple points.* An important rule of construction is the *extension rule* which is illustrated by the dashed lines in fig. 35. At a triple point, the extension of any two-phase line must pass into the single-phase region of the third phase.

Another kind of phase diagram of the same geometrical type is shown in fig. 36. For the Fe–S–O system at T = 800 K, the axes of the diagram are the equilibrium partial pressures of S_2 and O_2. Single-phase areas indicate which pure compounds of Fe are stable under the given conditions. Two-phase regions are lines. Three phases can co-exist only at triple points. The extension rule given above applies at all triple points. Such *stability diagrams* or *predominance diagrams* are useful in the study of oxidation, corrosion, roasting, etc. They have been treated in ch. 5, § 6.2 and have been discussed by KELLOGG and BASU [1960], INGRAHAM and KELLOGG [1963], PELTON and THOMPSON [1975], BALE *et al.* [1986] and BALE [1990]. They lend themselves to rapid computer calculation by Gibbs energy minimization from thermodynamic data stored in computerized data banks (BALE *et al.* [1986], BALE [1990]). Their usefulness is by no means restricted to metal–sulphur–oxygen systems or to systems of three components.

As another example of this same geometrical type of diagram, a plot of $RT \ln p_{O_2}$

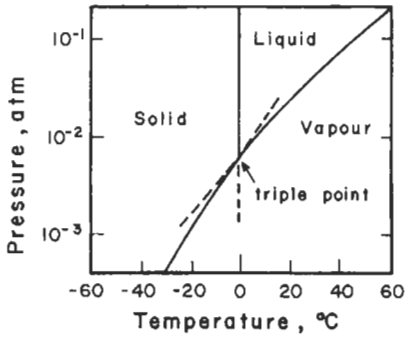

Fig. 35. Type-1 *P–T* phase diagram of H_2O.

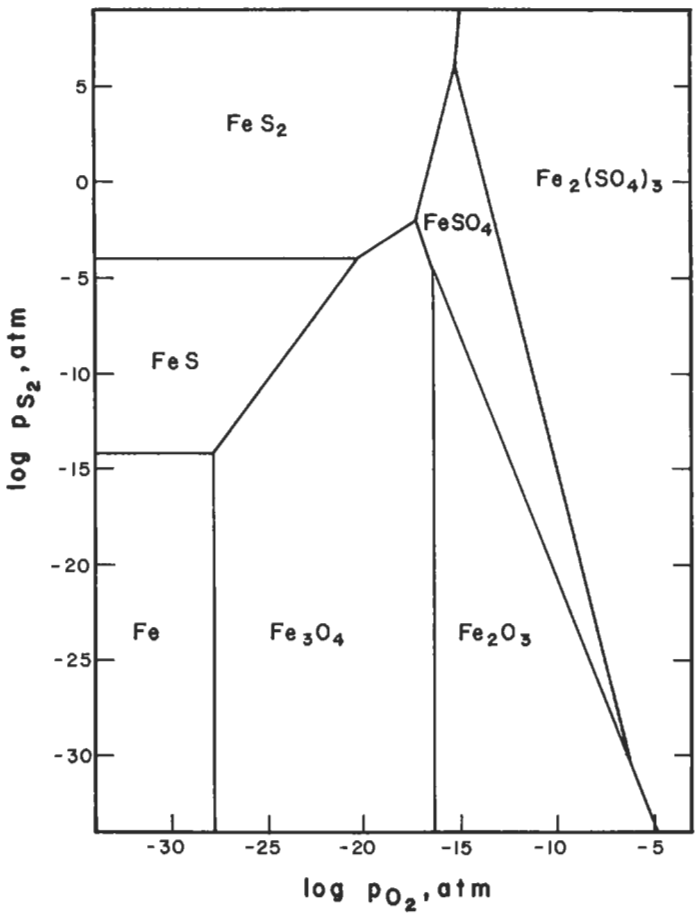

Fig. 36. Type-1 predominance diagram for Fe–S–O at 800 K.

versus T for the Fe–O system is shown in fig. 37b. Again, one-, two-, and three-phase regions are indicated by areas, lines and triple points respectively. In fig. 37a is the binary T-composition phase diagram for the Fe–O system. The correspondence between figs 37a and 37b is evident. Each two-phase line of fig. 37b "opens up" to a two-phase region of fig. 37a. Each tie-line of a two-phase region in fig. 37a can thus be seen to correspond to a constant p_{O_2}. Triple points in fig. 37b become horizontal invariant lines in fig. 37a.

Yet another type of phase diagram is shown in fig. 38. This is an isothermal section at constant molar metal ratio $n_{Cr}/(n_{Fe}+n_{Cr})=0.21$ for the Fe–Cr–S–O system. This diagram was calculated thermodynamically from model parameters (LAPLANTE [1993]). The axes are the equilibrium sulfur and oxygen partial pressures. Three or four boundary lines can meet at an intersection point. Some of the boundary lines on fig. 38 separate a two-phase region ($\alpha+\beta$)

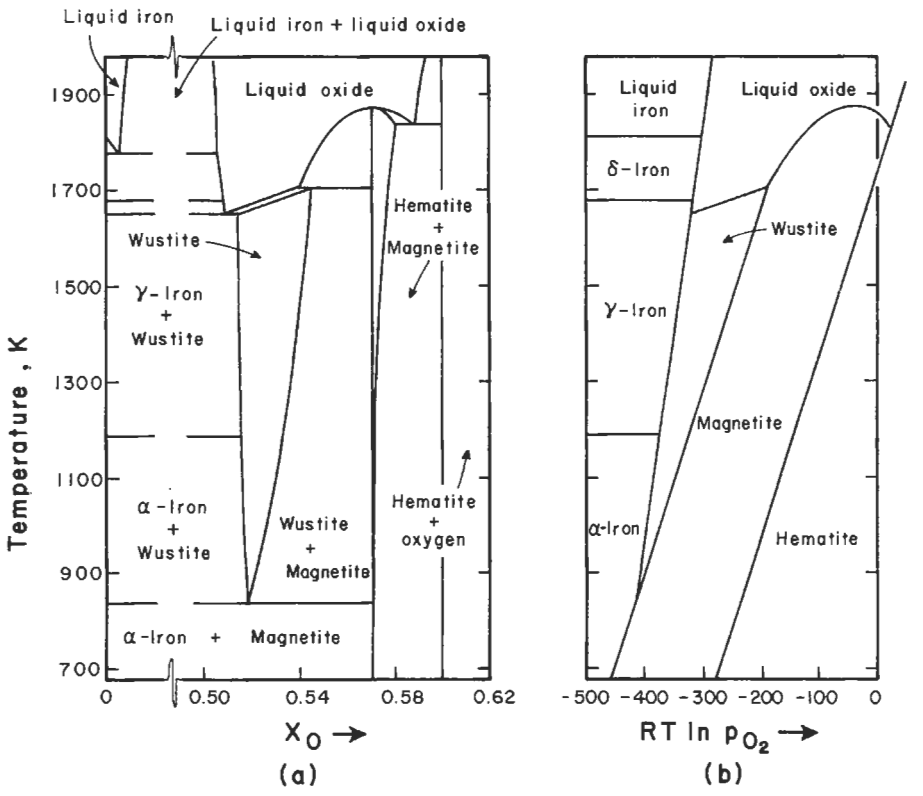

Fig. 37. Corresponding type-1 and type-2 phase diagrams for the Fe–O system (after MUAN and OSBORN [1965]).

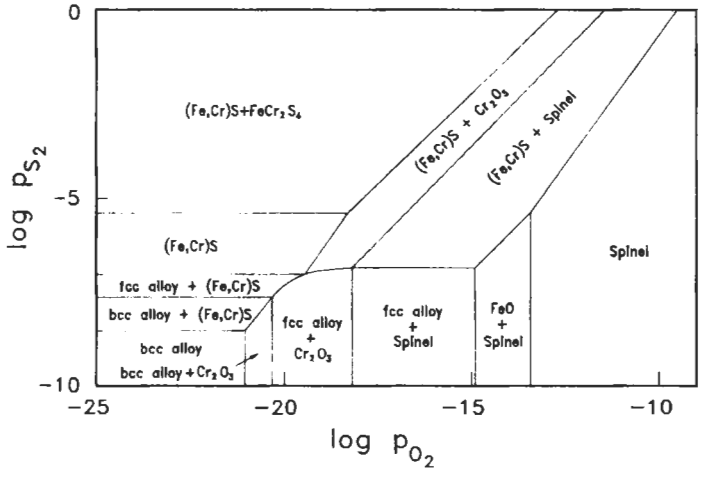

Fig. 38. Phase diagram of log p_{S_2} versus log p_{O_2} at 1273 K and constant molar metal ratio $n_{Cr}/(n_{Fe}+n_{Cr})=0.21$ in the Fe–Cr–S–O system (LAPLANTE [1993]).

References: p. 531.

from another two-phase region ($\alpha + \gamma$). These lines thus represent the conditions for three-phase ($\alpha + \beta + \gamma$) equilibrium. The Law of Adjoining Phase Regions (§ 3.5) applies to fig. 38 if these 3-phase lines are considered as degenerate infinitely narrow phase fields.

6.1. Classification of phase diagrams

In a system of C components we can define (C+2) *thermodynamic potentials*, ϕ_i. These are T, P, μ_1, μ_2, ..., μ_c (where μ_j is the chemical potential of component j). For each potential ϕ_i we can define a "*corresponding*" *extensive variable* q_i. For the potentials T, P and μ_j the corresponding extensive variables are S, V and n_j (entropy, volume and moles of component j). When two phases, α and β, are in equilibrium, $\phi_i^\alpha = \phi_i^\beta$ for all i.

If we choose any three potentials, designated ϕ_1, ϕ_2 and ϕ_3, and if we hold ϕ_4, ϕ_5, ..., ϕ_{c+2} constant, then a plot of ϕ_1 versus ϕ_2 will have the geometry of figs. 35, 36. Such diagrams were termed *type-1 phase diagrams* by PELTON and SCHMALZRIED [1973]. A general type-1 diagram is shown in fig. 39b. On a type-1 diagram the lines give the conditions for two-phase equilibrium, and the triple points are three-phase points.

If we now replace the ϕ_2 axis of the type-1 diagram by the ratio q_2/q_3 (or equivalently, by $q_2/(q_2+q_3)$), then we obtain a "*corresponding*" *type-2 phase diagram* as illustrated in fig. 39a. A corresponding type-2 diagram is also obtained by replacing ϕ_1 by q_1/q_3 as in fig. 39d. Two-phase lines in the type-1 diagram become two-phase regions with tie-lines in the corresponding type-2 diagrams. Triple points become invariant lines.

Consider the binary Fe–O system in fig. 37. Let $\phi_1 = T$, $\phi_2 = \mu_O$, $\phi_3 = \mu_{Fe}$, $\phi_4 = P$. Fig.

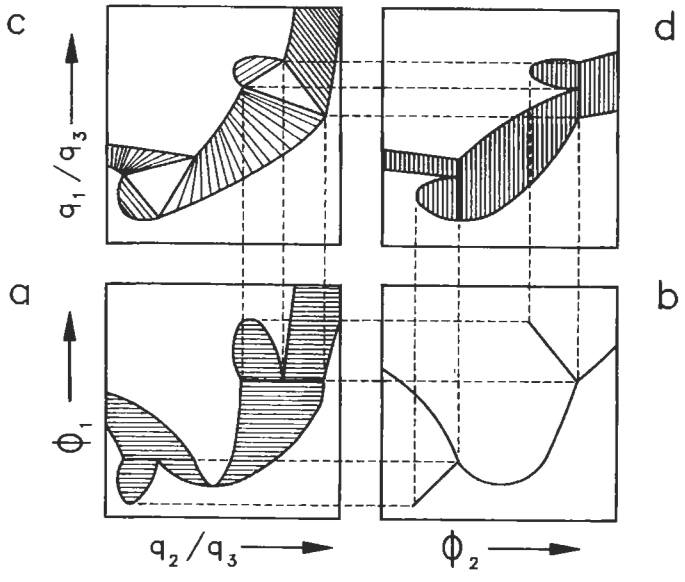

Fig. 39. Schematic representation of the three types of phase diagrams illustrating the general topology of (a) ϕ_1 *vs.* q_2/q_3, (b) ϕ_1 *vs.* ϕ_2, (c) q_1/q_3 *vs.* q_2/q_3, and (d) ϕ_2 *vs.* q_1/q_3, plots. (ϕ_4, ϕ_5, ... are kept constant).

37b is a type-1 diagram of ϕ_1 versus ϕ_2 with ϕ_4 constant. Fig. 37a is the corresponding type-2 diagram obtained by replacing ϕ_2 by the ratio $q_2/(q_2+q_3)=n_O/(n_O+n_{Fe})$.

Figs 20, 32 (lower panel), 33 (lower panel) and 34 are also type-2 diagrams. Type-2 diagrams are exemplified by binary isobaric T-composition diagrams. Consider the Fe–Cr–O system in fig. 33. Let $\phi_1=\mu_O$, $\phi_2=\mu_{Cr}$, $\phi_3=\mu_{Fe}$, $\phi_4=T$, $\phi_5=P$. the lower panel in fig. 33 is a type-2 diagram of ϕ_1 versus $q_2/(q_2+q_3)$ at constant ϕ_4 and ϕ_5. In the Fe–Cr–O–SO_2 system in fig. 34 there is one more component and therefore, one more potential, $\phi_6=\phi_{SO_2}$. By also holding this potential constant, we obtain the type-2 diagram of fig. 34.

If, as well as replacing ϕ_2 in a type-1 diagram by q_2/q_3, we also replace ϕ_1 by q_1/q_3, then a *corresponding type-3 phase diagram* results as shown in fig. 39c. In this diagram, triple points have become tie-triangles. Type-3 diagrams are exemplified by isothermal isobaric sections of ternary systems as in figs. 25, 27 and 31. The upper panel of fig. 33 shows the type-3 diagram corresponding to the type-2 diagram in the lower panel. The potential $\phi_1=\mu_O$ has been replaced by $q_1/(q_2+q_3)=n_O/(n_{Fe}+n_{Cr})$. This gives the type-3 diagram in Jänecke coordinates. This is usually transformed to the more usual Gibbs triangle representation as illustrated in fig. 32.

For a more detailed discussion of this classification scheme, see PELTON and SCHMALZRIED [1973] and PELTON and THOMPSON [1975].

Type-1, -2, and -3 phase diagrams are all sections at constant potentials (ϕ_4, ϕ_5, ... ϕ_{c+2}). Hence, all tie-lines lie in the plane of the diagram. When sections are taken at constant composition, then different geometries result. Fig. 38 is an example of a constant composition section in which both axes are potentials. Figs 28 and 29 are constant composition sections in which one axis is a potential, T, while the other axis is a composition variable. In fig. 30, both axes are composition variables. The geometrical rules of construction of these diagrams have already been discussed (§ 3.5, § 4). The difference among them is that fig. 30 contains no degenerate phase fields, while in fig. 38 lines can be degenerate phase fields, and in figs. 28 and 29 only horizontal lines can be degenerate phase fields.

For more detailed discussions of the classification of phase diagrams, including projections and diagrams with more than two dimensions, see PALATNIK and LANDAU [1964], PRINCE [1963] and HILLERT [1985].

As a final note on the topology of phase diagrams, the construction of multicomponent constant–composition sections by means of zero phase fraction (ZPF) lines was discussed in § 4.1 and illustrated by fig. 30. It should be noted that this method applies to any two-dimensional phase diagram section and can be used to construct any phase diagram in the present article (with the exception of the projections in figs. 23, 24 and 27). When one or both axes are potentials, then parts of the ZPF lines for two phases may be coincident.

7. *Experimental techniques of measuring phase diagrams*

It is beyond the scope of the present article to give a complete discussion of experimental techniques. Only a brief survey of the major techniques will be presented

with a view to providing the reader with some insight into the difficulties involved. More detailed discussions are given by RAYNOR [1970], MACCHESNEY and ROSENBERG [1970], BUCKLEY [1970], and HUME–ROTHERY *et al.* [1952].

As has been discussed in § 5, modern techniques of computer coupling of thermodynamics and phase diagrams can significantly reduce the amount of experimental effort required to characterize a phase diagram completely, particularly in the case of multicomponent systems.

7.1. Thermal analysis

Liquidus temperatures are commonly determined by the measurement of *cooling curves*. Consider the binary alloy A–B of composition 1 in fig. 40. A sample of liquid alloy, of the order of 50 g, is held in a crucible in a furnace. The furnace temperature is then decreased slowly at a uniform rate, usually not exceeding 1°C per minute, while the temperature of the alloy is measured by a calibrated recording thermocouple. A graph of sample temperature versus time (the *cooling curve*) is shown in fig. 41a. At the liquidus temperature (point **a** in fig. 40), solidification commences with the evolution of heat. This causes a decrease in the cooling rate of the specimen with, ideally, a resultant abrupt change of slope of the curve as shown in fig. 41a. When solidification is complete at the solidus composition (point **b** in fig. 40), heat evolution ceases and, ideally, another change of slope of the cooling curve is observed. From the "idealized" cooling curve of fig. 41a, one can then read the liquidus and solidus temperatures. For an alloy of composition 2, the idealized cooling curve is shown in fig. 41b. There is a change of

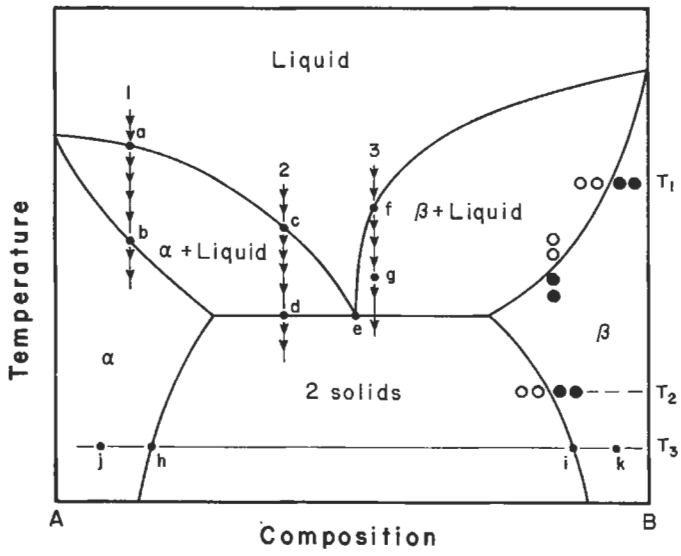

Fig. 40. Binary phase diagram to illustrate some experimental techniques; solid circles: single-phase alloy, open circles: two-phase alloy.

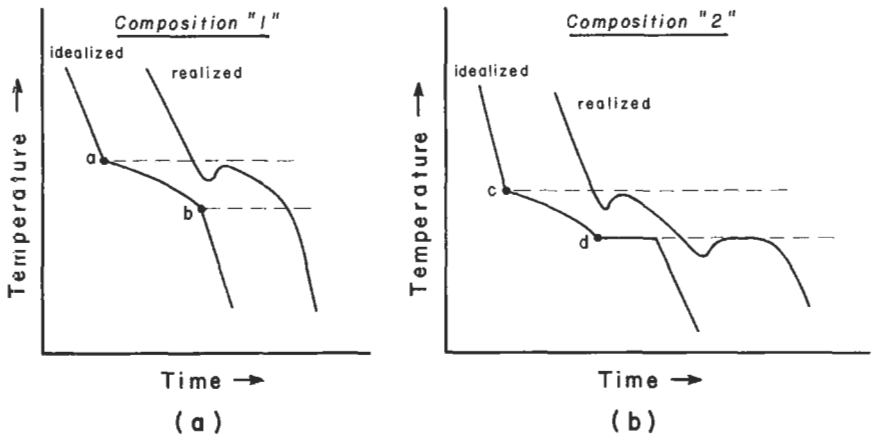

Fig. 42. Cooling curves for alloys of compositions 1 and 2 of fig. 40.

slope at the liquidus, and a plateau at the eutectic temperature since, ideally, the sample temperature remains constant until the invariant eutectic solidification reaction is complete.

In a real experiment, however, cooling curves of the type labelled "realized" in fig. 41 are usually obtained. Some degree of undercooling (or *supercooling*) is almost always observed. The sample must be cooled below the transformation temperature before nucleation of the new phase occurs. The temperature then rises again. However, at a liquidus the temperature will never rise all the way back up to the liquidus, so that some extrapolation technique must be used to estimate the liquidus temperature. At a eutectic, the equilibrium eutectic temperature may be regained by the sample after supercooling provided that the quantity of material solidifying eutectically is large enough to yield a sufficient evolution of heat. Supercooling may be minimized by stirring or by constantly jolting the sample to induce nucleation.

It is important that temperature gradients within the sample be eliminated by stirring and by the use of a furnace with a good constant temperature zone. Otherwise, part of the sample will start to solidify before the rest and the cooling curve will show a rounded rather than an abrupt change of slope.

At compositions where the liquidus is steep, such as the composition 3 in fig. 40, the rate of heat evolution is small. That is, on descending from the liquidus at point **f** to a point **g** an appreciable distance below the liquidus, only a small amount of heat is evolved since, as can be seen from the lever rule, only a small amount of solid is precipitated. Hence, it is more difficult to determine the exact temperature of the change in slope of the cooling curve, and the technique of thermal analysis is less precise. For very steep liquidus lines, a method of segregation and sampling or quenching may be preferable, as will be discussed below.

For liquidus temperatures below about 1000°C, absolute accuracies of the order of ± 1°C can be obtained by cooling curve methods under optimal conditions. For temperat-

ures of the order of 100°C or lower, accuracies of ±0.25°C may be obtained.

In principle, solidus temperatures can be determined by the method of cooling curves as shown for the idealized curve in fig. 41a. In certain very favourable cases, with very slow cooling rates, this may be possible. However, in most cases a curve such as the "realized" curve of fig. 41a will be observed, in which determination of the solidus temperature is extremely imprecise. The reasons for this are, firstly, that the solid phase will contain concentration gradients so that solidification will not be complete at the equilibrium solidus temperature; secondly, that the precipitated solid phase will insulate the thermocouple from the sample thereby reducing sensitivity; and thirdly, that by the time the solidus temperature is approached the sample temperature will have lagged well behind the furnace temperature so that the cooling rate will start to accelerate rapidly. For these reasons, solidus temperatures are better measured by *heating curves* which are, in most respects, analogous to cooling curves. An important precaution here is to ensure, by means of a long anneal, that the solid sample is homogeneous before commencing the experiment. In general, it is more difficult to measure solidus temperatures with accuracy than it is to measure liquidus temperatures.

In principle, a peritectic invariant can also be evidenced by a plateau on a cooling curve. However, as discussed in § 2.5.3, peritectic reactions are frequently greatly retarded kinetically so that only a weak short thermal arrest may actually be observed.

In general, the precision of thermal analysis experiments may be increased by the use of Differential Thermal Analysis (DTA) in which two thermocouples, connected in opposition, are placed, respectively, in the sample and in a standard specimen which undergoes no phase transformation in the temperature range of study. The danger in DTA experiments is that, because of the large surface to volume ratio of the small samples used, specimen temperatures often do not increase sufficiently after supercooling.

7.2. Sampling techniques and quenching techniques

As discussed above, thermal analysis may be inaccurate for determining the position of a steep liquidus. In such a case, a segregation and sampling technique may prove best. Suppose an alloy of overall composition and temperature in the (liquid + solid) region at point **g** in fig. 40 is held at temperature until equilibrium is established. A specimen of the liquid phase is then obtained, perhaps by suction in a ceramic tube. Chemical analysis will then give the composition of the liquidus at this temperature. A similar technique might be used to measure the compositions of the boundaries of a liquid–liquid miscibility gap. Clearly these methods depend for accuracy on a clean separation of the phases and on the prevention of oxidation and of volatilization losses while the sampling device is inserted into the container.

The principle of *quenching techniques* for solidus determinations is illustrated at temperature T_1 in fig. 40. Samples at each of the four overall compositions shown at T_1 are held at temperature long enough for equilibrium to be attained. They are then quenched rapidly. When examined microscopically, samples from the two-phase zone will exhibit regions of rapidly quenched liquid which can be distinguished from the solid grains. In this way the solidus composition can be bracketed. Alternatively, one could

quench samples of the same composition annealed at different temperatures, thereby bracketing the solidus temperature as is also illustrated in fig. 40.

Because of the slowness of solid state reactions, thermal analysis is rarely a useful technique for locating phase boundaries involving two solid phases. However, in such cases annealing and quenching followed by microscopic observation to determine whether one or two phases are present can often be used to bracket the phase boundary as illustrated for the solvus line in fig. 40 at T_2.

Another method of determining phase boundaries in the solid state involves the annealing of a sample in a two-phase (solid_1 + solid_2) region followed by quenching and subsequent quantitative analysis by any of several techniques to determine the compositions of the two phases present. The relevant techniques of quantitative metallography are discussed in ch. 10, § 7, where several examples are quoted of the use of such techniques to determine solid solubility limits.

In all techniques involving quenching, it is essential that the quench be as rapid as possible so as to avoid any diffusion, segregation or reaction during cooling.

7.3. Other techniques

Suppose that one wishes to determine the compositions (points **h** and **i**) of the phase boundaries at T_3 in fig. 40. Samples at a number of compositions at T_3 between points **j** and **k** are annealed and quenched. The lattice spacings of the α and β phases are then measured by X-ray techniques. The lattice spacings, when plotted versus composition, vary continuously in the single-phase regions, but remain constant in the two-phase region. Extrapolation of the single-phase and two-phase portions of the lattice spacing versus composition curve to their point of intersection then gives the composition of the phase boundary. If too much decomposition occurs upon quenching, then high-temperature X-ray techniques may be required to perform the measurements at temperature.

A technique which is similar in principle consists in measuring the electrical conductivity of specimens at various compositions at T_3 along the line between points **j** and **k**. Again, sharp breaks in the plot of conductivity versus composition are noted at the phase boundaries. This technique is often quite rapid, and can be carried out at elevated temperatures without the necessity of quenching.

In the interdiffusion technique, polished pellets of compositions **j** and **k** are clamped together and annealed at T_3. Following quenching, a composition versus distance scan is performed across the specimen by, say, microprobe analysis. A sharp discontinuity in the curve is observed at the interface, the compositions at either side being the phase boundary compositions **h** and **i**. This technique can also often be used to indicate the presence and compositions of one or more intermediate phases in one single experiment (see for example, SCHMALZRIED [1974]).

A great many other techniques of phase diagram measurement exist, such as dilatometric (HUME–ROTHERY *et al.* [1952], SINHA *et al.* [1967]), hardness (BARREAU and CIZERON [1979]), and magnetic measurements (ch. 29, § 6, also SUCKSMITH [1939]). The complete determination of an alloy phase diagram usually requires a combination of several techniques (e.g., a combination of dilatometry and magnetic measurements (SERVANT *et al.* [1973])).

References: p. 531.

8. *Bibliography*

8.1. Compilations of phase diagrams

The classic compilation in the field of binary alloy phase diagrams is that of HANSEN [1958]. This work was continued by ELLIOTT [1965] and SHUNK [1969]. These compilations contain critical commentaries. A non-critical compilation of binary alloy phase diagrams was prepared by MOFFAT [1978-1992]. HULTGREN *et al.* [1973] have critically evaluated the phase diagrams and thermodynamic properties of several binary alloy systems. An extensive non-critical compilation of binary and ternary phase diagrams of metallic systems has been edited by AGEEV [1959–1978]. An index to all compilations of binary alloy phase diagrams up to 1979 was prepared by MOFFAT [1979]. A critical compilation of binary phase diagrams involving Fe has been published by ORTRUD KUBASCHEWSKI [1982].

Ternary alloy phase diagrams were compiled by AGEEV [1959–1978] and by GUERTLER *et al.* [1969]. A bibliography of ternary and multicomponent metallic phase diagrams for the period 1955–1973 was published by PRINCE [1978]. VCH publishers (NY) are producing a series of volumes of compilations of ternary alloy phase diagrams known as "Ternary Alloys". Eight volumes, in alphabetical order, have already appeared.

Since 1979, the American Society for Metals in collaboration with the National Institute of Science and Technology and with national organizations in several countries, has undertaken a project whose goal is a complete critical evaluation of all binary and ternary alloy phase diagrams. All available literature on phase equilibria, crystal structures, and often on thermodynamic properties is cited and critically evaluated in great detail by "category editors" who are each responsible for a group of systems. Evaluations of important systems usually run to several pages. The evaluations are peer reviewed and the majority are published in the *Journal of Phase Equilibria*, (formerly the *Bulletin of Alloy Phase Diagrams*) (ASM International, Materials Park, Ohio). More than 2500 binary evaluations have been completed. Condensed versions of approximately 2800 evaluations have been published in three volumes (MASSALSKI *et al.* [1990]). When a "category" of evaluations (e.g. all binary phase diagrams with Cu) is completed, a monograph is published as part of the ASM Monograph Series.

An extensive bibliography of binary and multicomponent phase diagrams of all types of systems (metallic, ceramic, aqueous, organic, etc.) has been compiled by WISNIAK [1981]. A bibliographical database known as THERMDOC on thermodynamic properties and phase diagrams of systems of interest to materials scientists, with monthly updates, is available through Thermodata (Domaine Universitaire, Saint-Martin d'Hères, France).

8.2. Texts and review articles

A large number of texts and review articles covering all aspects of the theory, measurement and applications of phase diagrams are available. Only a selected few are listed here. A classical discussion of phase diagrams in metallurgy was given by RHINES [1956]. A definitive text on the theory of phase diagrams is that of PALATNIK and LAUDAU [1964]. Treatments of the geometry of multicomponent phase diagrams are

given by PRINCE [1963], PRINCE [1966] and HULTGREN [1985]. Good discussions of the interpretation of binary and ternary diagrams are given by WEST [1965] and BERGERON and RISBUD [1984]. A series of five volumes edited by ALPER [1970–1978] discusses many aspects of the theory, interpretation, measurement and applications of phase diagrams in materials science.

9. *Acknowledgements*

Thanks are due to Mr. Jacques Desrochers for the task of preparing the drawings and to Mrs. Johanne Gaulin for her help with the manuscript.

References

AGEEV, N. V., ed., 1959–1978, Phase Diagrams of Metallic Systems, vol. 1–22 (Academy of Sciences of USSR, Moscow).

ALABYSHEV, A. F. and A. G. MORACHEVSKII, 1957, Z. Neorg. Khim. **2**, 669.

ALPER, A. M., ed., 1970–1978, Phase Diagrams – Materials Science and Technology, vol. 1–5 (Academic, New York).

ASHTAKALA, S., C. W. BALE and A. D. PELTON, 1981, Bull. Alloy Phase Diagrams **2**, 83.

BALE, C. W., 1990, Canad. Metall. Quart. **29**, 263.

BALE, C. W., and A. D. PELTON, 1983, Metallurg. Trans., **14B**, 77.

BALE, C. W., A. D. PELTON and W. T. THOMPSON, 1986, Canad. Metall. Quart. **25**, 107.

BARIN, I., O. KNACKE and O. KUBASCHEWSKI, 1977, Thermochemical Properties of Inorganic Substances (Springer–Verlag, Berlin).

BARREAU, O., and G. CIZERON, 1979, Mém. Sci. Rev. Mét. **76**, 729.

BARTLETT, H. E., A. J. NEETHLING and P. CROWTHER, 1970, J. Chem. Thermo. **2**, 523.

BERGERON, C. J. and S. H. RISBUD, 1984, Introduction to Phase Equilibria in Ceramics (Amer. Ceramic Soc., Columbus, Ohio).

BRAY, H. J., F. D. BELL and S. J. HARRIS, 1961–62, J. Inst. Metals **90**, 24.

BUCKLEY, R. A., 1970, in: Techniques of Metals Research, ed. R. A. Rapp (Interscience, New York) vol. IV, part I.

CHART, T., F. PUTLAND and A. DINSDALE, 1979, in: Proc. Calphad VIII Conference, Stockholm, 1979, eds. B. Uhrenius and M. Hillert (Royal Institute of Technology, Stockholm) p. 183.

CHASE, M. W., 1983, Bull. Alloy Phase Diag. **4**, 124.

DINSDALE, A. T., 1991, Calphad J. **15**, 317.

DÖRNER, P., E.-Th. HENIG, H. KRIEG, H. L. LUCAS and G. PETZOW, 1980, Calphad J. **4**, 241.

ELLIOTT, R. P., 1965, Constitution of Binary Alloys, First Supplement (McGraw–Hill, New York).

FOWLER, R. H. and E. A. GUGGENHEIM, 1939, Statistical Thermodynamics, pp 350–366 (Cambridge Univ. Press, Cambridge, U.K.).

GUERTLER, W., M. GUERTLER and E. ANASTASIADIAS, 1969, A Compendium of Constitutional Ternary Diagrams of Metallic Systems, WADC Technical Report 58–615 (Parts I, II, III) U.S. Dept. of Commerce, Springfield, VA).

GUGGENHEIM, E. A., 1935, Proc. Roy. Soc. **A148**, 304.

GUPTA, H., J. E. MORRAL and H. NOWOTNY, 1986, Scripta Metall. **20**, 889.

HANSEN, M., 1958, Constitution of Binary Alloys, 2nd Ed. (McGraw–Hill, New York; 1st Ed.: Springer, Berlin, 1936).

HAUFFE, K., 1940, Z. Elektrochem. **46**, 348.

HENSEL, F., 1979, Adv. Phys. **28**, 555.

HILLERT, M., 1980, Calphad J. **4**, 1.
HILLERT, M., 1985, Int. Metall. Rev. **30**, 45.
HILLERT, M., and M. JARL, 1978, Calphad J. **2**, 227.
HILLERT, M., B. JANSSON, B. SUNDMAN and J. AGREN, 1985, Metall. Trans. **16A**, 261.
HULTGREN, R., R.L. ORR, P.D. ANDERSON and K.K. KELLY, 1963, Selected Values of Thermodynamic Properties of Metals and Alloys (Wiley, New York).
HULTGREN, R., P.D. DESAI, D.T. HAWKINS, M. GLEISER, K.K. KELLY and D.D. WAGMAN, 1973, Selected Values of the Thermodynamic Properties of the Elements and Binary Alloys, vol. 1, 2 (ASM, Metals Park, OH).
HUME–ROTHERY, W., J.W. CHRISTIAN and W.B. PEARSON, 1952, Metallurgical Equilibrium Diagrams (Inst. of Physics, London).
INDEN, G, 1982, Bull. Alloy Phase Diagrams **2**, 412.
INGRAHAM, T.R. and H.H. KELLOGG, 1963, TMS-AIME **227**, 1419.
KATSURA, T. and A. MUAN, 1964, TMS-AIME **230**, 77.
KAUFMAN, L., and H. BERNSTEIN, 1970, Computer Calculation of Phase Diagrams (Academic, New York).
KELLOGG, H.H. and S.K. BASU, 1960, TMS–AIME **218**, 70.
KLEINSTUBER, T., 1961, Ph.D. Thesis, Univ. Munich, Germany.
KOHLER, F., 1960, Monatsh. Chemie **91**, 738.
KÖSTER, W., and W. DULLENKOPF, 1936, Z. Metallk. **28**, 309.
KUBASCHEWSKI, O., 1982, Iron Binary Phase Diagrams (Springer–Verlag, NY).
KURNAKOV, N.S. and A.N. KUSNETZOW, 1907, Z. Anorg. Chem. **52**, 173.
LANTRATOV, M.F. and A.G. MIKHAILOVA, 1971, Zh. Prikl. Khimii **44**, 1778.
LAPLANTE, S., 1993, Final year project, Ecole Polytechnique, Montreal.
LEE, B.J. and D.N. LEE, 1992, J. Phase Equilib. **13**, 349.
LEVIN, E.M., C.R. ROBBINS, H.F. MCMURDIE, R.S. ROTH, T. NEGAS, L.P. COOK, J.R. DENNIS, M.A. CLEVINGER and D. MCKENNA, 1964–1992, Phase Diagrams for Ceramists (and Supplements) (Am. Ceramic Soc., Columbus, Ohio).
LIPSON, H. and A.J.C. WILSON, 1940, J. Iron Steel Inst. **142**, 122.
LÜCK, R., U. GERLING and B. PREDEL, 1989, Z. Metallkunde **80**, 270.
LUKAS, H.L., E.-Th. HENIG and B. ZIMMERMANN, 1977, Calphad J. **1**, 225.
MACCHESNEY, J.B., and P.E. ROSENBERG, 1970, in: Phase Diagrams – Materials Science and Technology, ed. A.M. Alper (Academic, New York) vol. 1, ch. 3.
MAIOROVA, E.A., A.G. MORACHEVSKII and S.G. KOVALENKO, 1976, Elektrochimiya **12**, 313.
MASSALSKI, T.B., P.R. SUBRAMANIAN, H. OKAMOTO and L. KACPRZAK, 1990, Binary Alloy Phase Diagrams, 2nd ed., vol. 1, 2 and 3 (ASM International, Materials Park, Ohio).
MATHEWSON, C.H., 1906, Z. Anorg. Chem. **50**, 180.
MIODOWNIK, A.P., 1982, Bull. Alloy Phase Diagrams **2**, 406.
MOFFATT, W.G., 1979, The Index to Binary Phase Collections (General Electric, Schenectady, NY).
MOFFATT, W.G., 1978–1992, Handbook of Binary Phase Diagrams (and Supplements) (Genium Publishing Corp., Schenectady, NY).
MUAN, A., and F. OSBORN, 1965, Phase Equilibria Among Oxides in Steelmaking (AddisonWesley, Reading, MA).
PALATNIK, L.S. and A.I. LANDAU, 1964, Phase Equilibria in Multicomponent Systems (Holt, Rinehart and Winston, NY).
PELTON, A.D., 1988, Bull. Alloy Phase Diag. **9**, 41.
PELTON, A.D., 1991, Thermodynamics and Phase Diagrams of Materials, in: Materials Science and Technology, Vol. 5, Eds. R.W. Cahn, P. Haasen and E.J. Kramer (VCH, NY).
PELTON, A.D. and C.W. BALE, 1986, Metall. Trans. **17A**, 1057.
PELTON, A.D. and M. BLANDER, 1984, Proc. AIME Symp. on Molten Salts and Slags, 281 (The Metall. Soc., AIME, Warrendale, PA).
PELTON, A.D. and M. BLANDER, 1986, Metall. Trans. **17B**, 805.
PELTON, A.D. and M BLANDER, 1988, Calphad J. **12**, 97.
PELTON, A.D. and H. SCHMALZRIED, 1973, Metallurg. Trans. **4**, 1395.

PELTON, A. D., and W. T. THOMPSON, 1975, Prog. Solid State Chem. **10**, Part 3, 119.
PELTON, A. D., H. SCHMALZRIED and J. STICHER, 1979, J. Phys. Chem. Solids **40**, 1103.
PETRIC, A., A. D. PELTON and M.-L. SABOUNGI, 1988, J. Electrochem. Soc. **135**, 2754.
PITSCH, W. and G. INDEN, 1991, Atomic Ordering, in: Materials Science and Technology, Vol. 5, Eds. R. W. Cahn, P. Haasen and E. J. Kramer (VCH, NY).
PRINCE, A., 1963, Metall. Rev. **8**, 213.
PRINCE, A., 1966, Alloy Phase Equilibria (Elsevier, Amsterdam).
PRINCE, A., 1978, Multicomponent Alloy Constitution Bibliography 1955–73 (The Metals Society, London).
RAYNOR, G. V., 1970, Phase Diagrams and Their Determination, in: Physical Metallurgy, 2nd Ed., Ed. R. W. Cahn (North–Holland, Amsterdam) ch. 7.
RHINES, F. N., 1956, Phase Diagrams in Metallurgy (McGraw–Hill, New York).
ROOS, G. D., 1916, Z. Anorg. Chem. **94**, 329.
SABOUNGI, M.-L., S. J. HERRON and R. KUMAR, 1985, Ber. Bunsenges, Phys. Chem. **89**, 375.
SCHMALZRIED, H., 1974, Solid State Reactions (Academic, New York), ch. 7.
SCHREINEMAKERS, F. A. H., 1915, Proc. K. Akad. Wetenschappen, Amsterdam (Section of Sciences) **18**, 116.
SERVANT, C., O. CIZERON and P. LACOMBE, 1973, J. Iron Steel Inst. **211**, 75.
SHUNK, F. A., 1969, Constitution of Binary Alloys, Second Supplement (McGraw–Hill, New York).
SINHA, A. K., R. A. BUCKLEY and W. HUME–ROTHERY, 1967, J. Iron Steel Inst. (London) **205**, 191.
SPENCER, P. J., and I. BARIN, 1979, Mater. Eng. Appl., Sci and Tech. Press, Reigate, U.K. **1**, 167.
SUCKSMITH, W., 1939, Proc. Roy. Soc. [A] **170**, 551
VAN LAAR, J. J., 1908, Z. Phys. Chem. **63**, 216; **64**, 257.
WEEKS, J. R. and H. A. DAVIES, 1964, AEC Report, Conf. 660712–1, BNL–10372.
WEST, D. R. F., 1965, Ternary Equilibrium Diagrams (McMillan, New York).
WISNIAK, J., 1981, Phase Diagrams: A Literature Source Book, vol. 1 and 2 (Elsevier, NY).

CHAPTER 7

DIFFUSION IN METALS AND ALLOYS

J. L BOCQUET, G. BREBEC, Y. LIMOGE

Centre d'Etudes de Saclay
Département d'Etudes du Comportement des Matériaux
Section de Recherches de Métallurgie Physique
91191 Gif sur Yvette, Cedex, France

R. W. Cahn and P. Haasen†, eds.
Physical Metallurgy; fourth, revised and enhanced edition

1. Macroscopic and microscopic theories of diffusion

In this section we will present the macroscopic and microscopic theories of diffusion. The former provides a description of the observed phenomena (which are fluxes), starting from the formalism associated with the thermodynamics of irreversible processes; one then obtains a formal expression of these fluxes as a function of thermodynamic forces and of parameters which are called the *phenomenological coefficients*. In the latter approach the fluxes are calculated by starting from atomic mechanisms. The parameters used in this case are the jump frequencies; they have a clear physical meaning, as opposed to the phenomenological coefficients which are only coefficients of proportionality. This step encompasses two parts: on the one hand the random walk modelling which starts with atomic jump frequencies and builds the macroscopic diffusion coefficient, and on the other hand the jump theory which defines the jump frequencies themselves from the very properties of the system and its defects. For both formalisms, however, a knowledge of the underlying atomic mechanisms is required in order to describe the diffusion phenomena properly. Thus we begin with a short review of the possible mechanisms. Finally we present briefly the modern simulation tools, the use of which is steadily increasing in diffusion studies.

1.1. The mechanisms of diffusion

In crystalline solids, the atoms occupy well defined equilibrium positions (regardless of thermal vibrations); they move by jumping successively from an equilibrium site to another. The different possible mechanisms for dense structures are schematized in fig. 1.

1.1.1. Exchange mechanisms

In the *direct exchange mechanism* (fig. 1–1) two neighbouring atoms exchange their positions. This mechanism is unlikely for dense structures, for it would involve large distortions and would then entail too large activation energies.

In the *cyclic exchange mechanism* as proposed by ZENER [1951], N atoms exchange themselves simultaneously (in fig. 1–2, $N = 4$); the energy involved is much lower than in the direct exchange, but this mechanism remains unlikely, because of the constraint imposed by a collective motion.

At the present time there are no experimental supports for any such mechanisms in crystallized metals and alloys. In metallic liquids cooperative motions are more likely operating.

1.1.2. Mechanisms involving point defects

In thermal equilibrium a crystal always contains point defects. The best known are vacancies, divacancies and interstitials. The presence of these defects in the crystals will allow the atoms to move without too large lattice distortions. The properties of these point defects are described in ch. 18.

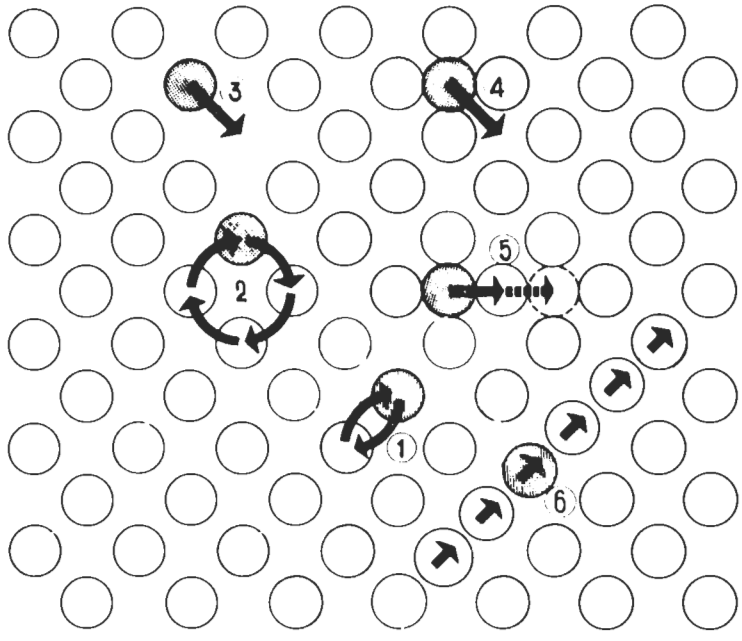

Fig. 1. Mechanisms of diffusion in crystals, after ADDA and PHILIBERT [1966]: (1) direct exchange, (2) cyclic exchange, (3) vacancy, (4) interstitial, (5) interstitialcy, (6) crowdion.

1.1.2.1. Interstitial mechanisms. In the *interstitial mechanism* (fig. 1–4) the atoms move from interstitial site to interstitial site. Usually small interstitial atoms, like hydrogen or carbon in metals, diffuse through the lattice by this mechanism.

The *interstitialcy* is somewhat more complex; as sketched in fig. 1–5, the atoms move from interstitial to substitutional site and vice versa. At higher temperatures, this mechanism contributes to silver diffusion in the silver halides. In metals and alloys with a dense structure the interstitial formation energy is so large that the concentration of these defects is completely negligible at thermal equilibrium. The situation is quite different when the material is out of equilibrium (for instance when it is plastically deformed or irradiated); under these conditions one can create *Frenkel pairs*, namely an equal number of vacancies and interstitials, which will both contribute to the diffusion. In metals and alloys the self-interstitial atom is not centered on the interstitial site: it has a dumbbell split configuration around a stable position. It is generally recognized that the self-interstitial is split along a <100> direction in fcc and along a <110> in bcc materials (SCHILLING [1978]; ch. 18, § 3.3.2.2). The case of the mixed dumbbell (one solute + one solvent) is not so simple (see for example LAM *et al.* [1983]). The elementary jumps for these split interstitials are shown in fig. 2. At low temperatures, under irradiation, the interstitial would have a *crowdion* configuration (SEEGER [1976]; fig. 1–6); at a higher temperature this crowdion would convert into a split interstitial.

References: p. 651.

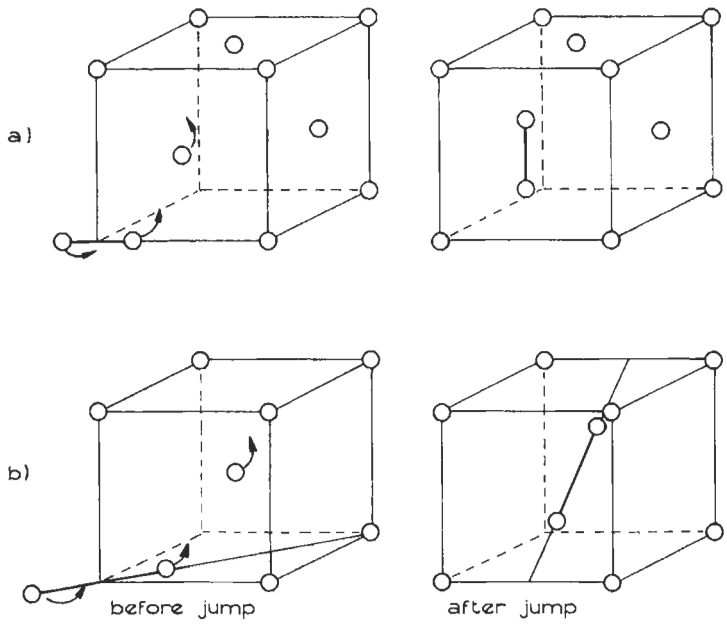

Fig. 2. Elementary jumps of the split interstitials (a) in fcc metals and (b) in bcc metals.

1.1.2.2. Vacancy mechanisms. In metals and alloys, near the melting point, the vacancy concentration is about 10^{-3} to 10^{-4} site fraction. These vacancies allow the atoms to move rather easily, and this mechanism is operating in most cases, with jumps to nearest neighbour sites (NN), or also to next nearest neighbour ones (NNN) in bcc crystals.

Besides monovacancies there are *vacancy aggregates*: divancancies, trivacancies, etc., which can contribute to the diffusion (ch. 18, § 2.2.2.1). The ratio divacancies/ monovacancies generally increases with temperature, so that the divacancy contribution to the diffusion also increases. We will see that numerous anomalies observed at high temperature (leading to curvature of the Arrhenius plot) are attributed to the divancancies. In dilute alloys there is often a binding energy between solutes and vacancies, and the resulting solute–vacancy pairs (complexes) also contribute to the diffusion. The *relaxation mechanism* which is a variant of the vacancy mechanism was proposed by NACHTRIEB and HANDLER [1954]. The underlying idea is that a large relaxation around a vacancy distorts its surroundings to such an extent that a liquid-like diffusion mechanism can take place; this idea has now been abandoned.

Molecular dynamics calculations by DA FANO and JACUCCI [1977] have shown that at high temperatures, when the atom jump frequency becomes large, a dynamical correlation between successive jumps can occur so that a vacancy can move more than one jump distance; these *vacancy double jumps* are an alternative explanation for the observed curvature of the Arrhenius plot.

1.1.2.3. Mixed mechanisms. For some systems it has been necessary to devise more complex mechanisms in order to account for abnormally fast diffusion. The dissociative

model by FRANK and TURNBULL [1956] was the first attempt at explanation. It assumed that the fast diffusing solute dissolves both substitutionally and interstitially; the mass transport is then due to a mixed vacancy and interstitial mechanism. MILLER [1969] has improved this mechanism by introducing the idea of vacancy-interstitial pairs. For more details see § 4.3.2.

1.1.2.4. Short-lived Frenkel pairs. Numerical simulations have revealed that, at least in non compact phases at high temperatures, short-lived Frenkel pairs can form *homogeneously* and give rise to closed rings of replacement of various sizes (4 atoms and above). At the end of the sequence the pair recombines (DOAN and ADDA [1987]).

1.1.3. Mechanisms involving extended defects

Linear defects (dislocations) and planar defects (surfaces, interfaces, grain boundaries, etc.) are disordered regions in which the atomic migration is easier than in the bulk. These preferential paths of diffusion are called *short-circuits*. The diffusion mechanisms are not yet well known but it is a topic where one is expecting rapid theoretical advances owing to the increasing power of computers. For more details see § 7.

1.2. The macroscopic theory of diffusion

1.2.1. Generalities

Diffusion is an irreversible phenomenon; its description requires the use of the proper formalism, namely *thermodynamics of irreversible processes* (TIP).

We refer the reader, for a detailed discussion of the subject, to specialized books and articles (PRIGOGINE [1947], HOWARD and LIDIARD [1964], MÜNSTER [1966], DE GROOT and MAZUR [1969]).

For measuring a flux, it is necessary to define a frame of reference; for the crystallized solid there are two preferred reference frames: the *laboratory reference frame* is bound to the ends of the sample which are assumed to be not affected by diffusion (we will neglect the sample size variation) whereas the *lattice reference frame* is rigidly bound to the atomic planes. It is possible to mark this lattice reference frame with inert markers such as very thin refractory wires, oxide particles, scratches on the surface etc.. These inert markers neither contribute nor alter the diffusion but "follow" the motion of the neighbouring atomic planes. Hereafter we will denote fluxes measured with respect to the laboratory frame by J^0 and fluxes measured with respect to the lattice frame by J.

The vacancy mechanism most commonly operates in metals and alloys; we will present the TIP formalism with this assumption. We assume further that the medium is isotropic; no chemical reactions take place; no viscous phenomena and no size variations occur; and, last, that mechanical equilibrium is achieved. We will restrict the discussion to the case of a binary alloy since only these alloys have been widely studied theoretically and experimentally.

1.2.2. Binary alloys and the vacancy mechanism

In a binary alloy there are three species: A, B and vacancies V; there will then be three fluxes, J_A, J_B and J_V in the lattice reference frame or J_A^0, J_B^0 and J_V^0 in the

laboratory frame. For a sample subjected to concentration gradients, ∇n_i, a temperature gradient, ∇T, and an electric field, E, it has been shown (BREBEC [1978]) that:

$$J_A = -D_A \nabla n_A + \left(L_{AA} Z_A^* + L_{AB} Z_B^*\right) eE - \left(L_{AA} Q_A^* + L_{AB} Q_B^*\right) \frac{\nabla T}{T} \tag{1}$$

$$J_B = -D_B \nabla n_B + \left(L_{BA} Z_A^* + L_{BB} Z_B^*\right) eE - \left(L_{BA} Q_A^* + L_{BB} Q_B^*\right) \frac{\nabla T}{T} \tag{2}$$

$$J_V = -\left(J_A + J_B\right) \tag{3}$$

$$v = \frac{J_V}{n} = -\frac{J_A + J_B}{n} \tag{4}$$

$$J_A^O = J_A + n_A v \text{ and } J_B^O = J_B + n_B v \tag{5}$$

We have omitted the vector notation for simplicity but we must keep in mind that J_i, ∇n_i, ∇T, E and v are vectors. Symbols are defined in what follows.

D_A and D_B are the *intrinsic diffusion coefficients*; they are given by:

$$D_A = kT\varphi\left(\frac{L_{AA}}{n_A} - \frac{L_{AB}}{n_B}\right), \qquad D_B = kT\varphi\left(\frac{L_{BB}}{n_B} - \frac{L_{BA}}{n_A}\right) \tag{6}$$

where k is the Boltzmann constant and L_{AA}, L_{AB}, L_{BA} and L_{BB} are the *phenomenological coefficients* which depend on the intensive quantities such as temperature, concentration, etc.; further they verify the *Onsager reciprocity relation* $L_{ij} = L_{ji}$, (here $L_{AB} = L_{BA}$); φ is the *thermodynamic factor* of the A-B solution; it is given by:

$$\varphi = 1 + \frac{\partial \log \gamma_A}{\partial \log C_A} = 1 + \frac{\partial \log \gamma_B}{\partial \log C_B} \tag{7}$$

where γ_A and γ_B are the thermodynamic activity coefficients. n_A, n_B and n_V are the numbers of A and B atoms and vacancies per unit volume, respectively.

The number of sites per unit volume is equal to:

$$n = n_A + n_B + n_V$$

We now define the *atomic fractions*, taking into account the three species:

$$N_A = \frac{n_A}{n}, \; N_B = \frac{n_B}{n} \text{ and } N_V = \frac{n_V}{n}$$

or, taking into account only the A and B atoms:

$$C_A = \frac{n_A}{n_A + n_B} \text{ and } C_B = \frac{n_B}{n_A + n_B}$$

Since n_V is always small ($n_V \ll n_A + n_B$), the two definitions are practically equivalent.

Z_A^* and Z_B^* are the *effective valences* for A and B and e the absolute value of the charge of an electron. If the material is an insulator or an ionic conductor, these effective valences are equal to the ionic valences z_A and z_B. In a metallic alloy for which the electrical conductivity is due to the electronic carriers there is a momentum transfer from these carriers (electrons or holes) to the A and B atoms. This is equivalent to a force which has to be added to the electrostatic force; as a consequence an effective valence can be defined (see § 6).

Q_A^* and Q_B^* are energies per mole and are related to the *heats of transport* q_A^* and q_B^*. Physically these heats of transport define the *heat flux*, J_q associated with the matter fluxes J_A and J_B when there is no thermal gradient. Actually it can be shown that:

$$J_q = q_A^* J_A + q_B^* J_B + \alpha \frac{\nabla T}{T} \tag{8}$$

which implies:

$$J_q = q_A^* J_A + q_B^* J_B \text{ when } \nabla T = 0$$

In metals and alloys the assumption is often made that the vacancies are in thermal equilibrium everywhere in the sample; this implies that the vacancy sources and sinks (dislocations, grains boundaries, etc.) are effective enough to fulfil this assumption. When this equilibrium condition is well obeyed we have:

$$Q_A^* = q_A^* - \Delta H_{FV} \text{ and } Q_B^* = q_B^* - \Delta H_{FV}$$

ΔH_{FV} is the *vacancy formation enthalpy* in the alloy.

When the requirement of local equilibrium is not met, no simple relation holds between Q_i^*'s and q_i^*'s.

Finally, v is the lattice velocity measured with respect to the laboratory frame. The physical reason for the lattice displacements is related to the fact that vacancies are not conservative species (they can be created or destroyed at certain lattice sites). In fig. 3 we have sketched the process responsible for the inert marker displacement; we see, in this simple example, that the lattice moves to the right because the vacancies created on the left are eliminated on the right.

We notice from equations (1)–(5) that the fluxes measured in the laboratory frame equal to:

$$J_A^O = C_B J_A - C_A J_B, \qquad J_B^O = -\left(C_B J_A - C_A J_B\right)$$

so that $J_A^O + J_B^O = 0$

1.2.3. Some special cases

1.2.3.1. Chemical diffusion. In the absence of electric fields and thermal gradients, eqs. (1)–(5) become:

$$J_A = -D_A \nabla n_A, \qquad J_B = -D_B \nabla n_B, \qquad v = \left(D_A - D_B\right)\nabla N_A \tag{9}$$

References: p. 651.

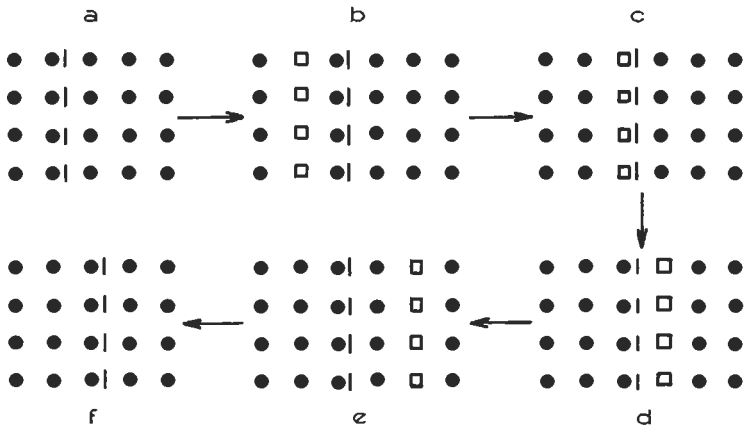

Fig. 3. Schematic representation of the displacement of inert markers (solid circles: atoms; squares: vacancies; dashes: inert markers: (a) initial state; (b) creation of a plane of vacancies; (c, d, e) displacement of the vacancy plane towards the right; (f) elimination of the vacancies. Comparison between (a) and (f) shows that the inert markers are displaced to the right.

In the laboratory frame we have:

$$J_A^O = -J_B^O = \tilde{D}\nabla n_A \tag{10}$$

where:

$$\tilde{D} = N_B D_A + N_A D_B \tag{11}$$

$\tilde{D}$ is the *chemical diffusion coefficient.*

We see that, for binary alloys, the fluxes have the form of *Fick's first law*:

$$J_i = -D_i \nabla n_i$$

In the lattice frame there are two independent fluxes and thus two intrinsic coefficients, whereas in the laboratory frame there is only one flux and one chemical diffusion coefficient.

1.2.3.2. Dilute systems. For dilute alloys n_B (or C_B) $\rightarrow 0$ and $\varphi \rightarrow 1$; on the other hand it can be shown (§ 4.1.2.1) that L_{BB}/n_B tends to a finite value, whereas L_{BA}/n_A, which is of the order of n_B, tends towards zero. So:

$$D_{B,n_B \rightarrow 0} = kT \frac{L_{BB}}{n_B} = D_{B^*} \tag{12}$$

This coefficient is the *solute diffusion coefficient at infinite dilution.* It will be denoted by D_{B^*} to distinguish it from D_B and to recall that diffusion is generally studied with radioactive isotopes which are used at great dilution; then we will also replace n_B by n_{B^*}. D_A does not become as simple as D_B because the cross-term L_{AB}/n_B does not tend to zero with n_B (§ 4.1.2.1).

For these dilute systems the flux of solute is equal to:

$$J_{B^*} = -D_{B^*}\nabla n_{B^*} + \frac{n_{B^*}D_{B^*}}{kT} Z_B^{**} eE - \frac{n_{B^*}D_{B^*}}{kT^2} Q_B^{**}\nabla T \tag{13}$$

where:

$$Z_B^{**} = Z_B^* + \frac{L_{AB}}{L_{BB}} Z_A^* \text{ (the apparent effective valence)}$$

$$Q_B^{**} = Q_B^* + \frac{L_{AB}}{L_{BB}} Q_A^* \text{ (the apparent heat of transport)}$$

Because $Z_{B^*}^* = Z_B^*$ and $q_{B^*}^* = q_B^*$(same chemical species) we have dropped the asterisk on B in Z_B^*, Z_B^{**}, Q_B^* and Q_B^{**}.

Equation (13) has the generalized form of Fick's first Law:

$$J_i = -D_i\nabla n_i + < v >_i n_i$$

When B atoms are isotopes A* of the element A, eq. (13) becomes:

$$J_{A^*} = -D_{A^*}\nabla n_{A^*} + \frac{n_{A^*}D_{A^*}}{kT} Z_A^{**} eE - \frac{n_{A^*}D_{A^*}}{kT^2} Q_A^{**} \tag{14}$$

It can be shown, (HOWARD and LIDIARD [1964]), that:

$$\frac{1}{f_0} = 1 + \frac{L_{A^*A}}{L_{A^*A^*}} \tag{15}$$

The apparent valency and heat of transport are therefore given by:

$$Z_A^{**} = \frac{Z_A^*}{f_0} \text{ and } Q_A^{**} = \frac{Q_A^*}{f_0}$$

where f_0 is the *correlation factor for self-diffusion*; its presence stems from the non-ramdom character of the tracer atom displacements by a vacancy mechanism. D_{A^*} is the *self-diffusion coefficient*, given by:

$$D_{A^*} = kT\frac{L_{A^*A^*}}{n_{A^*}} \tag{16}$$

1.2.4. The various diffusion coefficients

Diffusion coefficients have the dimension Length^2 Time^{-1}. In the international system of units they are expressed in m^2s^{-1}. The CGS system (cm^2s^{-1}) is still widely used. We will show now which experimental situations correspond to these various coefficients.

The *chemical diffusion coefficient* $\tilde{D}$ describe the interdiffusion of A and B (fig. 4a); it can be measured from the curve C_A (or C_B) versus x; in general it depends on the concentration.

The *intrinsic coefficients* D_A and D_B correspond to a similar experiment; but to obtain them it is necessary to determine $\tilde{D}$ and v [see eqs. (9) and (11)]. v is obtained from the displacement of inert markers (see *Kirkendall effect*, § 5.3.1.1). These coefficients depend also on the concentration.

The *solute diffusion coefficient at infinite dilution* D_{B^*} corresponds to the experimental situation shown in fig. 4b. A thin layer of B* atoms has been deposited on the A surface so that $C_{B^*} \sim 0$ and B* diffuses in pure A.

The *self-diffusion coefficient* D_{A^*} corresponds to a similar situation when B* is replaced by A*.

Two other diffusion coefficients are defined as shown in fig. 4c; they are the *self-diffusion coefficients in an homogeneous alloy* AB which are denoted by $D^{AB}_{B^*}$. The B* (or A*) concentration is always negligible so that the alloy composition is not modified by the diffusing species. These coefficients depend on the concentration. An alternative notation often used for dilute alloys is:

$$D_{A^*}(C_B) \equiv D^{AB}_{A^*},\ D_{B^*}(C_B) \equiv D^{AB}_{B^*}$$

where C_B is the concentration of B.

The macroscopic description presented above cannot account for the A* and B* diffusion into AB alloys; it would be necessary to derive the flux equations for four species A, A*, B, B* (plus vacancies); this is beyond the scope of this review and we refer the reader to HOWARD and LIDIARD [1964] for more details. Thus it is possible to show that the self-diffusion coefficients in the alloy and the intrinsic diffusion coefficients are related by:

$$D_A = D^{AB}_{A^*}\varphi r_A \quad D_B = D^{Ab}_{B^*}\varphi r_B \tag{17}$$

where φ is the thermodynamic factor and r_A and r_B are terms which will be made explicit in § 5.1.2. These relations, (17), were first established by DARKEN [1948] in a

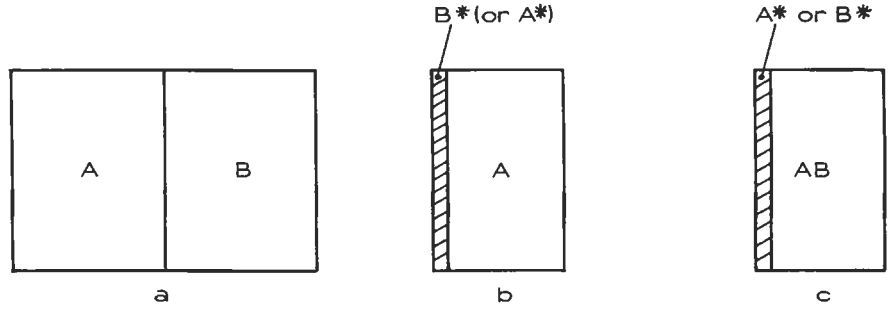

Fig. 4. Different types of diffusion experiments: (a) chemical diffusion → $\tilde{D}$; (b) self or solute diffusion in pure metals → D_{A^*} or D_{B^*}; (c) self-diffusion in homogeneous alloys → $D^{AB}_{A^*}$ or $D^{AB}_{B^*}$

simplified form for the case when $r_A = r_B = 1$.

1.2.5. Fick's second Law

We have seen that the fluxes in a binary alloy have the form:

$$J_i = -D_i \nabla n_i \quad \text{or} \quad J_i = -D_i \nabla n_i + n_i < v >_i$$

By using the *conservation equation*:

$$\frac{\partial n_i}{\partial t} = -\mathrm{div} J_i$$

we obtain *Fick's second Law*; this partial differential equation can be solved for given initial and boundary conditions. D_i and $<v>_i$ can then be obtained from a comparison between the experimental and the calculated concentration curve C(x).

When D_i and $<v>_i$ are constant and the diffusion is along the x direction Fick's second Law has the form:

$$\frac{\partial n_i}{\partial t} = D_i \frac{\partial^2 n_i}{\partial x^2} \tag{18}$$

or

$$\frac{\partial n_i}{\partial t} = D_i \frac{\partial^2 n_i}{\partial x^2} - < v >_i \frac{\partial n_i}{\partial x} \tag{19}$$

The geometry which is most commonly used for measuring D_i is a thin layer deposited onto a "semi-infinite sample" (see fig. 4b and 4c); in this case the solution of eq. (18) has the well-known form:

$$n_i(x,t) = \frac{Q}{\sqrt{\pi D_i t}} \exp\left(-\frac{x^2}{4 D_i t}\right) \tag{20}$$

where Q is the quantity of the diffusing species deposited per unit surface, so that D_i is obtained from the slope of the straight line: log n_i versus x^2.

In the presence of an electric field, the equation to be solved is eq. (19); very often the geometry used is a thin layer sandwiched between two semi-infinite samples. The solution is then:

$$n_i(x,t) = \frac{Q}{2\sqrt{\pi D_i t}} \exp\left[-\frac{(x - < v >_i t)^2}{4 D_i t}\right] \tag{21}$$

$<v>_i$ is obtained from the displacement of the maximum of the curve $n_i(x)$ with respect to the origin (defined by the welding interface).

For chemical diffusion (see fig. 4a), $\tilde{D}$ is not constant, we have then to solve:

$$\frac{\partial n_i}{\partial t} = \frac{\partial}{\partial x}\left(\tilde{D}_i \frac{\partial n_i}{\partial x}\right) \tag{22}$$

References: p. 651.

MATANO [1933] has shown that, when $\tilde{D}_i$ depends on x through n_i:

$$\tilde{D}_i(n_i) = -\frac{1}{2t}\frac{\int_0^{n_i} x \, d \, n_i}{(dn_i/dx)} \tag{23}$$

the x origin must be chosen so that:

$$\int_0^{n_{i,\max}} x \, d \, n_i = 0 \tag{24}$$

This origin defines the *Matano plane*. In fig. 5 the different terms of eqs. (23) and (24) are illustrated.

Numerous solutions of the diffusion equation can be found in CRANK [1956] and CARSLAW and JAEGER [1959]. We will see that in some cases Fick's first law is not valid; the first restriction is related to the discontinuous nature of crystals (lattice effect) and will be discussed in § 1.3.5. The second restriction is met in chemical diffusion (spinodal decomposition: CAHN [1967]; ch. 15, § 3.1). In both cases the discrepancy with Fick's law becomes noticeable only for harmonics of concentration with short wavelengths.

1.3. The random walk theory of diffusion

The aim of the random walk theory is to describe the observed macroscopic effects from the atomic jumps which are the elementary processes in diffusion.

1.3.1. Einstein relation and flux expression

For a *random walk motion*, EINSTEIN [1905] has shown that the diffusion coefficient of species i along the x direction is given by:

$$D_i = \frac{\overline{X^2}}{2\tau} \tag{25}$$

where $\overline{X^2}$ is the mean square displacement along the x direction for the duration τ. If X_k is the displacement of the k^{th} atom along the x direction during τ, we have:

$$\overline{X^2} = \frac{1}{N}\sum_{k=1}^{N} X_k^2 \tag{26}$$

where N is the number of diffusing atoms of species i.

In many cases the motion is not random but the expression (25) still holds provided that $\tau \to 0$.

According to LE CLAIRE [1958] and MANNING [1968], the flux J_i measured with respect to the lattice reference frame is equal to:

$$J_i = < v >_i \, n_i - D_i \frac{\partial n_i}{\partial x} - n_i \frac{\partial D_i}{\partial x} \tag{27}$$

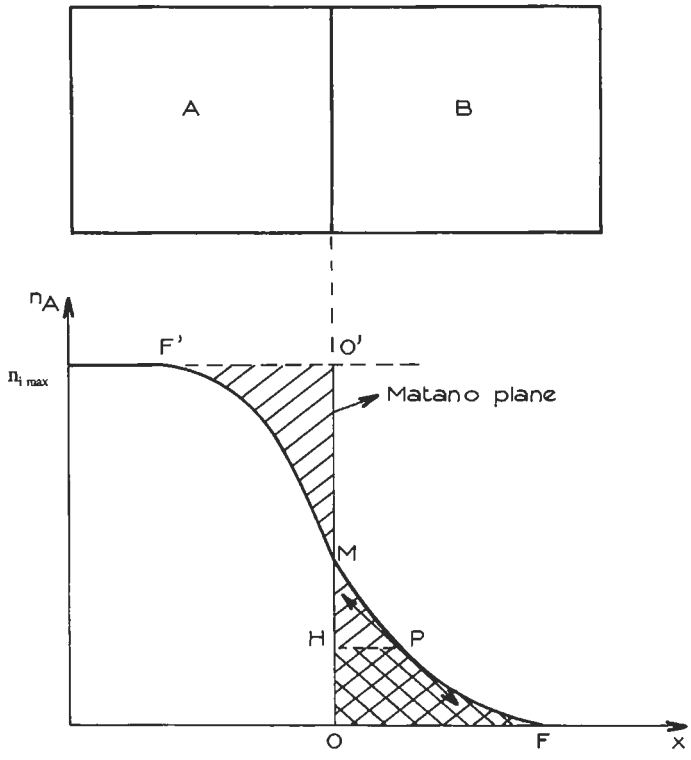

Fig. 5. Matano method for the calculation of $\tilde{D}$. The Matano plane is defined by the equality of the two areas F'O'M and FOM (hatched surfaces). $\int_0^{n_i} x\, dn_i$ is equal to the area HPFO (doubly hatched surface), dn_i/dx is the slope of the tangent to the concentration curve at P.

where:

$$< v >_i = \lim_{\tau \to 0} \frac{\overline{X}}{\tau} \tag{28}$$

D_i is given by eq. (25) when $\tau \to 0$, $\overline{X^2}$ is the mean displacement during τ for species i.

These relations, (25), (27) and (28), are valid for anisotropic media but to save space we have omitted the more precise notation D_{ix}, $<v>_{ix}$ etc...

1.3.2. Calculation of $\overline{X}$ and $\overline{X^2}$ in terms of jump frequencies

It is easy to show that:

$$\overline{X} = \sum_{i=1}^{n} \overline{x_i} \tag{29}$$

$$\overline{X^2} = \sum_{i=1}^{n} \overline{x_i^2} + 2 \sum_{1=1}^{n-1} \sum_{j=i+1}^{n} \overline{x_i x_j} \tag{30}$$

where x_i is the i th displacement along x and n is the mean number of atomic jumps during τ. The overbar denotes an average over a large number of atoms.

1.3.2.1. Expression for $\overline{X^2}$. For a truly random walk motion the last term in eq. (30), $P = 2 \sum\sum \overline{x_i x_j}$, *vanishes*. When $\overline{X}$ differs from zero (chemical diffusion, electro and thermal diffusion, etc.) this term P is also different from zero but is has been shown that the $\overline{X}$ contribution to P is of the order to τ^2 whereas the $\sum \overline{x_i^2}$ term, eq. (30), is of the order of τ; as a consequence the $\overline{X}$ contribution to P is negligible when $\tau \to 0$.

But even if $\overline{X} = 0$, the P term is not necessarily equal to zero, owing to the mechanism of diffusion. We will see later that for most diffusion mechanisms the successive atomic jumps are not independent of each other, and *that the motion is not a truly random walk*. This can be easily understood for the vacancy mechanism: the vacancy concentration is so low ($\sim 10^{-4}$ to the melting point) that two consecutive atomic jumps are likely due to the same vacancy and it is obvious that after one jump an atom has a greater than random probability of making a reverse jump; there is *correlation*. This correlation between the directions of two successive jumps initiated by the same vacancy reduces the efficiency of the walk with respect to a truly random walk. Correlation occurs for all defect-assisted diffusion mechanisms except for the purely interstitial and exchange mechanisms; it is related to the low concentration of point defects (vacancies, divacancies, interstitials, etc.) and decreases when this concentration increases (WOLF [1980]).

How to take this effect into account will be reported in § 1.3.4. *To summarize, we can always calculate $\overline{X^2}$ by assuming $\overline{X} = 0$, because when $\tau \to 0$, $\overline{X^2}$* does not depend on $\overline{X}$.

For a truly random walk motion, $P = 0$ and we have:

$$\overline{X^2} = \tau \sum_{k=1}^{z} \Gamma_k x_k^2 \tag{31}$$

where z is the number of jump directions, Γ_k the mean atomic jump frequency for the k direction and x_k the displacement along x for a k-jump. Hence:

$$D_{random} = \tfrac{1}{2} \sum_{k=1}^{z} \Gamma_k x_k^2. \tag{32}$$

For cubic lattices all the frequencies Γ_k are equal, and:

$$D_{random} = \frac{\Gamma l^2}{6} \tag{33}$$

where $\Gamma = \sum_k \Gamma_k$ is the total jump frequency and l is the jump distance ($\frac{1}{2} a\sqrt{2}$ for fcc, $\frac{1}{2} a\sqrt{3}$ for bcc).

1.3.2.2. Expression for $\overline{\overline{X}}$. With the same notation as for $\overline{X^2}$ we have:

$$\overline{\overline{X}} = \tau \sum_{k=1}^{z} \Gamma_k x_k = < v > \tau \tag{34}$$

For the case where $\overline{X}$ is not zero, the potential energy of the atoms versus their position is schematized in fig. 6 (for simplicity we have shown regular energy barriers which correspond to a mean displacement $\overline{X}$ independent of x). The shape of this energy diagram is due to a force F_i acting on the atoms such that (see fig. 6):

$$\Delta W = \frac{F_i x_j}{2}$$

The atom jumps are easier towards the right than towards the left (in fig. 6) and if $\Delta W \ll kT$ we have for thermally activated jumps:

$$\Gamma(\rightarrow) = \Gamma_0\left(1 + \frac{F_i x_j}{2kT}\right) \quad \Gamma(\leftarrow) = \Gamma_0\left(1 - \frac{F_i x_j}{2kT}\right) \tag{35}$$

where Γ_0 is the jump frequency when $F_i = 0$; $\rightarrow$ denotes jumps towards the right and $\leftarrow$ jumps towards the left.

We then obtain, with eqs. (34) and (35):

$$< v >_i = \frac{\overline{X}}{\tau} = \frac{F_i D_i}{kT} \tag{36}$$

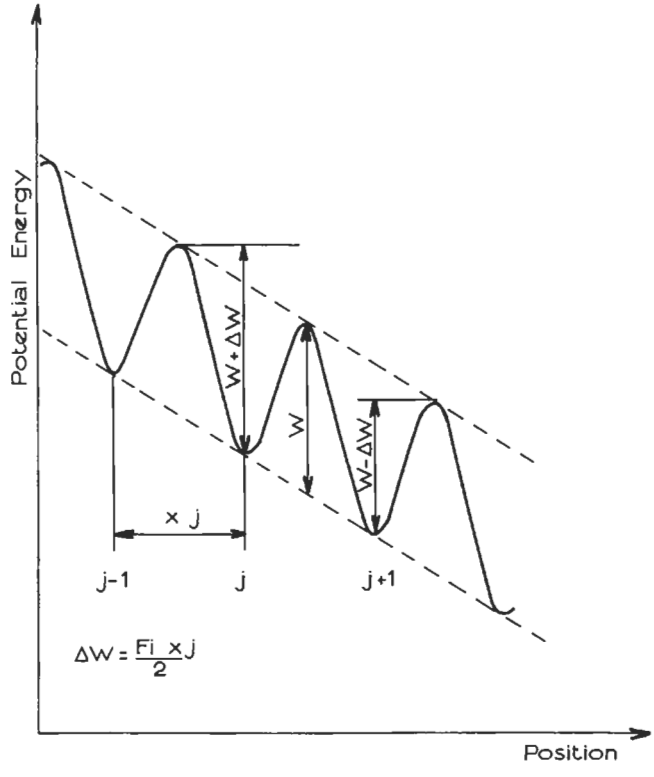

Fig. 6. Schematic representation of the potential energy diagram of the atoms when a constant force is present.

References: p. 651.

This expression is the *Nernst–Einstein relation.*

F_i has the following forms, according to the nature of the field acting on the atoms:

$$F_i = Z_i^* eE \text{ for an electric field,}$$

$$= -\frac{Q_{i\alpha}^*}{T}\frac{dT}{dx} \text{ for a thermal gradient,}$$

$$= -k\frac{\partial \log \gamma_i}{\partial x} \text{ for a concentration gradient,} \tag{37}$$

where Z_i^* is the effective valence, $Q_{i\alpha}^* = q_{i\alpha}^* - h_{fv\alpha}$, $q_{i\alpha}^*$ is the heat of transport for an α-type jump of the species i, $h_{fv\alpha}$ is the vacancy formation enthalpy on a site from which an α-type jump is possible, γ_i is the coefficient of activity of species i in the alloy at the position x; this last term can be evaluated from a thermodynamical study of the alloy; we will see in § 6 how it is possible to measure and calculate Z^* and Q^*. We observe that with the microscopic approach there are as many heats of transport as there are different types of jumps, whereas with the macroscopic approach the number of the heats of transport is equal to the number of species.

The expression for $\overline{X}$, eq. (36), is not complete because the diffusion mechanism can give rise to an additional term; in order to go further it is thus necessary to adopt a particular model for diffusion. We will consider the case of a binary alloy and a vacancy mechanism.

1.3.3. Binary alloys and vacancy mechanism

In the case of a vacancy mechanism there is a coupling between A and B fluxes through the vacancy flux. This coupling, known as the *vacancy flow effect*, contributes to $\langle v \rangle_i$ in addition to the force F_i. The calculation of this term is rather tedious and for more details we refer the reader to MANNING [1968]. Two cases have to be considered, depending on whether it is a dilute or a concentrated alloy. The diffusion models and results (expressions for L_{AA}, L_{AB} and L_{BB}) are given in § 4 for dilute alloys and § 5 for concentrated alloys.

1.3.4. Correlation effects

For most diffusion mechanisms the successive atomic jumps are not independent; as a result, the last term of eq. (30), $P = 2 \sum\sum \overline{x_i x_j}$, does not vanish. The *correlation factor* is defined as:

$$f = \frac{D_{\text{actual}}}{D_{\text{random}}} \tag{38}$$

and from eq. (30) we obtain:

$$f = 1 + \left(2 \sum_{i=1}^{n-1} \sum_{j=i+1}^{n} \overline{x_i x_j} \right) \Big/ \sum_{i=1}^{n} \overline{x_i^2} \tag{39}$$

Thus the expression for D, eq. (33), becomes:

$$D_{\text{actual}} = f\frac{\Gamma l^2}{6} \tag{40}$$

In order to calculate f we have to evaluate $P = 2\sum\sum \overline{x_i x_j}$, which will depend on the diffusion mechanism. BARDEEN and HERRING [1951] were the first to point out that point-defect diffusion mechanisms involve a non-random-walk motion for the atoms, and they calculated the correlation factor f for a vacancy mechanism.

The first useful estimation for f with the vacancy mechanism yields $f = 1 - 2/z$, where z stands for the coordination number of the lattice. Since, at each jump, the vacancy has the probability 1/z to perform a backward jump, a fraction 2/z of the number of jumps performed by a given tracer atom is lost, giving rise to an efficiency factor equal to $1 - 2/z$. This argument cannot be used as such for evaluating the correlation factor for solute diffusion, because the exchange frequency with a solute atom w_2 differs from that with the solvent w_0 and because the solvent jump frequencies themselves are altered in the immediate neighbourhood of the solute (see § 4.1). As a consequence, the walk of the defect around the solute must be considered in more detail. Since the pioneering work of BARDEEN and HERRING, numerous studies have been published on this topic; we refer the reader to the books or articles by ADDA and PHILIBERT [1966], MANING [1968] and LE CLAIRE [1970a].

The principal techniques used for the calculation of f are:

(i) *Computer simulations;* $\overline{X^2_{\text{actual}}}$ is obtained by Monte Carlo simulations and compared to X^2_{random}. For more details see § 1.5.2.

(ii) *The pair association method*; this technique is described in § 4; the fluxes are calculated from the diffusion model and by comparing with the macroscopic expressions we obtain D_{actual} and then f with eq. (38). This technique can only be used for dilute alloys.

(iii) *The random walk method*; this is the calculation of f from the expression (39). In this type of calculation it is necessary to evaluate the return probabilities of the defect on the neighbouring sites of the atom after the first exchange with this atom. To obtain these probabilities, several methods have been used:

– The BARDEEN and HERRING [1951] technique;
– the matrix method (LE CLAIRE and LIDIARD [1956], MULLEN [1961], HOWARD [1966]);
– the electrical analogue method (COMPAAN and HAVEN [1956, 1958]);
– the integral methods, which have now superseded the previous ones. The return probabilities are evaluated through 3–D integrals which are easily computed in a few seconds with a very high accuracy. Tackling with a slightly different problem, the ancestor paper introducing such integrals for random walk probabilities (MCCREA and WHIPPLE [1940]) has been followed much later by others more directly devoted to correlation calculations (MONTET [1973], BENOIST *et al.* [1977]; KOIWA [1978], ISHIOKA and KOIWA [1980]).

For self-diffusion, f is independent of temperature in isotropic materials (for vacancy mechanism $f = 0.72$ for bcc, 0.78 for fcc and hcp, 0.5 for diamond lattice; for divancancy

mechanism f = 0.475 for fcc and hcp lattice). For impurity diffusion see § 4.

In some cases the knowledge of the correlation factor can allow us to choose among several of the mechanisms of diffusion; it is then a very useful quantity, but as we will see later, experiment does not yield f alone. What is measured is the *isotope effect*, E, from which it is not obvious how to extract f (§ 1.4.3.3).

1.3.5. The limitation of Fick's Law

We present here a first restriction of Fick's Law, which is related to the discontinuous nature of the lattice (MARTIN and BENOIST [1977]). Let us consider the case of one-dimensional diffusion; the rate equations for an atomic plane n are:

$$\frac{dC_n}{dt} = \Gamma\left(C_{n+1} - 2C_n + C_{n-1}\right) \tag{41}$$

where Γ is the atomic jump frequency and C_i the concentration for the i^{th} plane.

We have to compare the solution of this rate equation, which takes into account the discontinuous nature of the lattice, with the macroscopic equation:

$$\frac{\partial C}{\partial t} = D\frac{\partial^2 C}{\partial x^2} \tag{42}$$

Let us suppose an infinite medium with an initial concentration variation according to a sine form:

$$C_{(0)} = C_1 + \left(C_2 - C_1\right)\sin\frac{2\pi x}{\lambda}$$

The solution will be:

$$C_{(t)} = C_1 + \left(C_2 - C_1\right)\left(\sin\frac{2\pi x}{\lambda}\right)e^{-\alpha t} \tag{43}$$

when $t \to \infty$, the concentration becomes homogeneous, $C \to C_1$.

By substituting eq. (43) in eqs. (41) and (42), we obtain:

$$\alpha_R = 2\Gamma\left[1 - \cos\frac{2\pi a}{\lambda}\right], \quad \alpha_F = \left(\frac{2\pi}{\lambda}\right)^2 D \tag{44}$$

where a is the interatomic distance, subscript R stands for the solution of eq. (41) and F for the solution of Fick's Law, eq. (42).

In expanding $\cos(2\pi a/\lambda)$ and taking into account the fact that $D = \Gamma a^2$ for this one-dimensional diffusion, we obtain:

$$\alpha_R = \left(\frac{2\pi}{\lambda}\right)^2 D\left[1 - \frac{2}{4!}\left(\frac{2\pi a}{\lambda}\right)^2 + \frac{2}{6!}\left(\frac{2\pi a}{\lambda}\right)^2 \ldots\right] \tag{45}$$

We clearly see by comparing eqs. (44) and (45) that the solutions of the rate equations and of Fick's equation are identical only when $2\pi a/\lambda << 1$, i.e., for large wavelengths.

Since a concentration profile can be expanded in a Fourier series, the short-wavelength components will evolve in a different manner than predicted by Fick's Law. This effect will be noticeable only for very short wavelengths (a_R and a_F differ by 3% for $\lambda = 10a$ and by 0.03% for $\lambda = 100$ a).

1.4. Jump frequency and diffusion coefficient calculation

We have shown above, eqs (33) and (40), that the diffusion coefficient is given as a function of the jump frequency Γ of the diffusing species. Its calculation comes therefore into the determination of this frequency, which itself can be done in the framework of the statistical mechanical theory of fluctuations (LANDAU and LIFSHITZ [1984], FLYNN [1972]). In fact the jump of an atom can be viewed as a particular fluctuation of the local energy density during which the system undergoing diffusion passes from a stable position to another over a barrier of higher energy, the so-called *saddle hypersurface* in the configurational space spanned by the 3 N position variables.The statistics of the fluctuations of the local energy density therefore control the jump frequency. The nature of this saddle hypersurface is defined by the nature of the crystalline lattice and by the mechanism at work (see § 1.1). Let us particularize for example to the case of a vacancy mechanism, the other cases being easily handled in the same framework.

1.4.1. Vacancy concentration

In this case the relevant fluctuation can be decomposed into two steps: the formation of the vacancy and the jump of a neighbouring atom into the vacancy. The probability to observe a defect on a neighbouring site of the atom under consideration is given by:

$$P_v = P_0 \exp\left(-G_v/kT\right)$$

with G_v the free enthalpy of the system containing the vacancy plus N atoms and P_0 a normalizing constant. The relative probability with respect to the non defective state, i.e. the vacancy concentration is therefore:

$$c_v = \exp\left(-\left(G_v - G_0\right)/kT\right) \tag{46}$$

with G_0 the free enthalpy of the perfect crystal. In the so-called quasi-harmonic approximation, which in most cases works fairly well up to near the melting point (LUTSKO *et al.* [1988]), these free enthalpies are given by:

$$G = W + kT \sum_{\alpha=1}^{3(N-1)} Ln\left(\frac{\hbar\varpi_\alpha}{k\,T}\right) + P_{ext}V$$

with W the potential energy of the system in the relevant state, the third term correspond to the work of the external pressure P_{ext} on the actual volume and the second, the so-called vibrational entropy, corresponds to a summation over the 3 (N−1) non-zero normal eigenfrequencies ϖ_α. The enthalpy difference in (46) takes now the form:

$$\Delta G_F = \Delta H_F - T\Delta S_F = W_v - W_0 + kT \sum_{\alpha}^{3(N-1)} Ln\left(\frac{\varpi_\alpha^v}{\varpi_\alpha^0}\right) + P_{ext}\left(V_v - V_0\right) \tag{47}$$

References: p. 651.

in which the eigenfrequencies ϖ_α^ν and ϖ_α^0 pertain to the system with and without a vacancy respectively; and V_ν and V_0 to the volume with and without the defect.

1.4.2. Vacancy jump

In order to handle the second step, the vacancy jump, two theories have been put forth and later refined, the theory of Rate Processes (WERT and ZENER [1949], VINEYARD [1957]), and the Dynamical Theory (RICE [1958], SLATER [1959], FLYNN [1968]). As will become clear, these two approaches emphasize different aspects of the jump, and are complementary rather than contradictory.

1.4.2.1. Rate theory of jumps. The probability of finding a vacancy as a first neighbour of an atom is a static property and as such the statistical thermodynamical treatment given above is rigorous. This is no longer the case for the jump which has a strong dynamic character: the jump proceeds as an hamiltonian trajectory in the phase space and the successive positions during the jump are strongly correlated. However, it is not possible to solve for them down to a calculation of the frequencies, so we need approximations. In the rate theory one neglects completely the dynamical aspects: the successive positions of the system during the jump are viewed as independent static positions with an occupancy given by their equilibrium statistical weight all along the jump path, including the saddle position. The dynamical correlations between successive positions are lost, and therefore the jumping particle has no "memory". Moreover the saddle hypersurface is supposed to be planar as a consequence of the hypothesis of harmonic interatomic interactions even at the saddle position.

The jump frequency of a vacancy, or the frequency in one direction for an atom (eq. 32), is defined as the *flux* J_S crossing the saddle hypersurface S, for a unit occupancy of the stable position, which in our example includes a vacancy on the proper site:

$$\Gamma_\nu = J_S/P_\nu \quad \text{with} \quad J_S = \int_0^\infty P_S s' \mathrm{d}s$$

where s is the unstable normal coordinate perpendicular to the saddle hypersurface S, s′ the corresponding "velocity" and P_S as above the statistical weight along S defined by:

$$\begin{aligned} P_S &= P_0 \exp\left\{-\left(G_S\right)/kT\right\} \\ G_S &= W_S + kT \sum_{\alpha=1}^{3(N-1)-1} \mathrm{Ln}\left(\frac{\hbar\varpi_\alpha^S}{k\,T}\right) + P_{\mathrm{ext}} V_S \end{aligned} \tag{48}$$

Now we have for the migration frequency:

$$\begin{aligned} \Gamma_\nu &= \frac{k\,T}{h} \exp\left\{-\left(G_S - G_V\right)/kT\right\} \\ G_S - G_V &= W_S - W_\nu + kT \sum_{\alpha=1}^{3(N-1)-1} \mathrm{Ln}\left(\frac{\hbar\varpi_\alpha^S}{k\,T}\right) - kT \sum_{\alpha=1}^{3(N-1)} \mathrm{Ln}\left(\frac{\hbar\varpi_\alpha^0}{k\,T}\right) + P_{\mathrm{ext}}\left(V_S - V_\nu\right) \end{aligned} \tag{49}$$

Notice that in this expression the eigenfrequencies ϖ_α^S corresponding to motions

restricted to the saddle hypersurface do not correspond one-to-one to the frequencies in the stable position, ϖ_α^0. Indeed the new modes of the system close to the saddle point have no counterpart in the perfect nor in the defective system in the stable position. Moreover the first product contains one fewer frequency than the second, for the reaction coordinate s is quenched at the saddle value. A more homogeneous formula is generally written as:

$$\Gamma_v = \nu_0 \exp\{-(G_S - G_V)/kT\} = \nu_0 \exp\{-(\Delta G_M)/kT\}$$
$$\Delta G_M = W_S - W_v + kT \operatorname{Ln}\left\{\nu_0 \prod_{\alpha^S}^{3(N-1)-1} \varpi_\alpha^S / \prod_{\alpha^0}^{3(N-1)} \varpi_\alpha^0\right\} + P_{\exp}(V_S - V_v) \tag{50}$$

which shows clearly that the so-called "attempt frequency", ν_0, has no physical meaning on its own, but only as a couple with the migration entropy. From (33) and (50) one recovers the well known expression of the diffusion coefficient in cubic structures:

$$D = \nu_0 a^2 \mathrm{f} \exp\left(\frac{\Delta S_F + \Delta S_M}{k}\right) \exp\left(-\frac{\Delta H_F + \Delta H_M}{kT}\right) \tag{51}$$

where, by comparison with eq. (50), one defines ΔS_M and ΔS_F, respectively the defect migration and formation entropies, ΔH_M and ΔH_F, the corresponding enthalpies, *'a'* the lattice parameter.

As said above, in this approach the dynamic aspect of the jump is neglected. However the system follows during the jump an hamiltonian trajectory in the phase space and its successive positions are therefore correlated. These short time correlations have two effects, multiple jumps one the one hand (DA FANO and JACUCCI [1977], DE LORENZI and ERCOLESSI [1992]) which can be viewed as a new diffusion mechanism, the existence of unsuccessful jumps on the other, in which the jumping particle turns back just after having passed the saddle point. Following BENNETT [1975] these unsuccessful events could amount to 10% of the jumps foreseen by the rate theory up to near the melting point in a Lennard–Jones crystal, but to a larger value for other kinds of interaction (GILLAN *et al.* [1987]). The main origin of this inefficiency lies in the anharmonicity of actual interatomic interactions allowing for a curved rather than planar saddle hypersurface; according to FLYNN [1987], a curved hypersurface can be crossed twice. An improvement to the Vineyard approach as been proposed by TOLLER and col. [1985] by considering the full manifold of the newtonian *trajectories* in the phase space, and not simply the *positions* of the system in the configuration space. Topological considerations allow to count now only the *successful trajectories* as a subset of all possible ones, instead of counting only the static state of the system in the saddle hypersurface, as in the rate theory approach. Using the first non-harmonic term, of third order, for describing the curvature of the saddle hypersurface, a part of the above mentioned 10% discrepancy is shown to be recovered, but the Molecular Dynamics method is needed to account for the remainder (FLYNN [1987]).

1.4.2.2. Dynamic theory of jumps. Contrarily to the rate theory, in the dynamic one the jump frequency is directly deduced from the atomic dynamics, the phonon contribution to the fluctuations of the atomic positions, and not from an occupancy hypothesis about the

states in configurational space. In this approach one defines a 1D reaction coordinate measuring the progress of the jump along the jump direction, according to the scalar product:

$$x = (\delta s_0 - \delta s_{col}) \cdot n$$

where δs_0 and δs_{col} are the 3D displacements with respect to the stable positions s_0 and s_{col}, respectively of the jumping atom and of the saddle point, and n the unit 3D vector along the jump path. The position s_{col} is generally defined as the center of gravity of the atoms defining the saddle gate. All these coordinates fluctuate as a result of the random superposition of phonons. The contribution of a phonon of frequency ϖ, wave vector k and branch λ to x is given by:

$$x(t) = \left(u^0_{\varpi\lambda} . n\right)\left(1 - \exp\left(i . k\ s_{col}\right)\right)\exp\left(i\left(k . s_0 - \varpi t\right)\right) \tag{52}$$

where $u^0_{\varpi\lambda}$ is the 3D amplitude vector of the phonon.

Last, it is assumed that the jump necessarily proceeds to completion, once a certain critical value δ of x has been reached. δ remains in the theory an adjustable parameter, which is supposed to depend only on the crystalline structure of the lattice.

It can be shown that upon superposition of harmonic vibrations of frequencies ν_i and amplitude x^0_i, the critical value δ is reached from below at a frequency w given by:

$$w = \left(\sum_i \left(\nu_i x_i^0\right)^2 / \sum_i \left(x_i^0\right)^2\right)^{1/2} \exp\left(-\delta^2 / \sum_i \left(x_i^0\right)^2\right)$$

The effect of the various phonons in (52) can be evaluated using $k_\lambda = \varpi_\lambda / v_\lambda$ in a Debye model, v_λ being the sound velocity along the phonon branch λ. At high temperature, $\hbar\varpi_\lambda / kT < 1$; denoting by $\varepsilon_{\varpi\lambda}$ the energy in the mode ϖ, λ, one has:

$$\left|u^0_{\varpi\lambda}\right|^2 = \frac{2\varepsilon_{\varpi\lambda}}{NM\varpi^2} \sim \frac{2kT}{NM\varpi^2}$$

and the summation over ϖ and λ gives:

$$w = \left(\tfrac{3}{5}\right)^{1/2} \nu_D \exp\left(-\frac{\delta^2}{kT}\ \frac{15M}{2\left(3v_l^{-2} + v_t^{-2} + v_{t'}^{-2}\right)}\right) \tag{53}$$

where v_l, v_t and $v_{t'}$ reflect the longitudinal and transverse sound velocities, ν_D is a mean Debye frequency and M the mass of the particles.

As in the rate theory approach, one recovers an Arrhenius-like form of the diffusion coefficient with the migration activation energy defined in the second bracket.

It is also possible to express this result as a function of the elastic constants, since $v^2 = c/\rho$ with ρ the specific mass. Using a properly weighted mean of the elastic moduli, c, and taking Ω as the atomic volume, FLYNN proposes:

$$w = \left(\tfrac{3}{5}\right)^{1/2} . \nu_D \exp\left(-\frac{c\,\Omega\,\delta^2}{kT}\right) \tag{53'}$$

Using a value of $\delta = .32$ for fcc metals and $\delta = .26$ for bcc ones, a quite good agreement

is found with experimental values of migration energies (FLYNN [1968]). Other values are sometimes used (SCHULTZ [1991]).

The most severe drawback of this approach lies in the implicit assumption that the normal modes remain untouched during the jump. Its main interest relies in its ability to handle the migration including the effects of the actual crystal dynamics. The summation in (52) can now be made without any approximation thanks to the availability of complete dispersion relations for various metals and to the development of the numerical simulations, allowing for example a deeper understanding of the bcc metals (see section 3.2).

1.4.3. Macroscopic parameters of diffusion

1.4.3.1. Variation with temperature. For self-diffusion in isotropic media, f is independent of T, so that from eq. (51), D has the well-known *Arrhenius form*:

$$D = D_0 \exp\left(-\frac{Q}{kT}\right) \quad \text{with} \quad D_0 = \nu_0 a^2 \, \mathrm{f} \exp\left(\frac{\Delta S_F + \Delta S_M}{k}\right) \quad \text{and} \quad Q = \Delta H_F + \Delta H_M$$

D_0 is the *frequency factor* and Q the *activation energy*.

For impurity diffusion, f depends on T and, strictly speaking, D has no longer the Arrhenius form, but if we want still to recast its variation into the form of an Arrhenius law, we can define Q as:

$$Q = -k \frac{\partial \log D}{\partial(1/T)} \quad \text{hence we obtain:} \quad Q = \Delta H_F + \Delta H_M - C$$

and $$D_0 = \nu_0 \, a^2 \, \mathrm{f} \exp\left(\frac{\Delta S_F + \Delta S_M}{k}\right) \exp\left(-\frac{C}{kT}\right) \quad \text{with} \quad C = k \frac{\partial \log \mathrm{f}}{\partial(1/T)}$$

If C depends on T, Q and D_0 will also depend on T but it is experimentally observed that C is small and more or less constant so that impurity and self-diffusion behaviours are qualitatively similar.

As a matter of fact, the Arrhenius plot (log D versus 1/T) is often curved; the departure from a straight line is more or less substantial (curvature only at high temperature, continuous curvature, two straight lines with different slopes). In general, the activation energy increases with T. Several explanations are possible:

(1) The enthalpy and entropy terms depend on T (GILDER and LAZARUS [1975], VAROTSOS and ALEXOPOULOS[1986]).

(2) Diffusion occurs by more than one mechanism. This is the case:
- for non homogeneous media; e.g. grain boundary + volume diffusion;
- when several types of jumps occur (DA FANO and JACUCCI [1977]);
- when several defects contribute to the diffusion. Monovacancies are responsible for most of the diffusion processes and, at the present time, the curvatures at high temperature are generally ascribed to the increasing contribution of the divacancies (SEEGER and MEHRER [1970]). If several defects contribute to the diffusion we have:

$$D = \sum_i D_i$$

D is the measured diffusion coefficient and D_i the contribution to the diffusion of the i th defect.

(3) There is an intrinsic domain at high temperature and an extrinsic domain at low temperature; this is mainly the case for semiconductors and ionic crystals. At high temperature (*intrinsic* region) the point-defect concentration is only a function of the temperature, whereas at low temperature (*extrinsic* region) the defect concentration is mainly controlled by the impurity content. More complex situations can occur for complex mechanisms (HOOD [1993])

Typically, for metals and alloys, D_0 is in the range of $10^{-6} - 10^{-4}$ m^2/s and Q in the range of 100–600 kJ/mole (~ 1–6 eV), depending on the melting point of the material.

1.4.3.2. Variation with pressure. According to eqs. (50) and (51) the pressure derivative of the activation enthalpy ΔG_M defines an activation volume ΔV along:

$$\left(\frac{\partial \log D}{\partial P}\right)_T \sim -\frac{(V_v - V_0) + (V_S - V_v)}{kT} = -\frac{\Delta V_F + \Delta V_M}{kT} \tag{54}$$

We have neglected the ∂ log f/∂P and all ∂ log ϖ_λ/∂P terms; the former is strictly zero for self-diffusion and the latter are generally small, of the order of 10^{-2} Ω (Ω is the atomic volume), with respect to the volume variation due to defect formation. $\Delta V = \Delta V_F + \Delta V_M$ is the *activation volume*, where ΔV_F and ΔV_M are the *defect formation* and *migration volumes*, respectively. In general, ΔV_M is small so that ΔV_F is not very different from ΔV. Typically ΔV varies from 0.5 to 1.3 Ω at least in the case of a monovacancy mechanism; in some cases ΔV is very small or even negative, which can be an indication of an interstitial-type mechanism.

1.4.3.3. Variation with atomic mass. From an experimental point of view, the *isotope effect* E is obtained by measuring simultaneously the diffusion coefficients D_α and D_β of isotopes α and β of the same element with masses m_α and m_β. It can be shown that E is given by:

$$E = \frac{D_\alpha/D_\beta - 1}{\left(m_\beta/m_\alpha\right)^{1/2} - 1} = f\Delta K \tag{55}$$

where f is the correlation factor. It is assumed that only the frequency ν of the isotope-vacancy exchange is altered by the mass difference according to:

$$\frac{\mathrm{d\ Ln}(\nu)}{-\frac{1}{2}\,\mathrm{d\ Ln}(m)} = \Delta K$$

where ΔK is the fraction of the kinetic energy in the unstable mode residing in the jumping atom. Its value is therefore smaller than 1, of the order of .8 to .9 for self-diffusion in simple fcc metals, and reflects the collective nature of the saddle position crossing during the jump (LE CLAIRE [1966]). Equation (55) holds if, and only if, f has the form:

$$f = \frac{u}{u + \nu}$$

where u is a term which depends on all the frequencies involved but ν. For fcc materials BAKKER [1971] has shown that eq. (55) is valid for vacancy, divacancy and impurity-vacancy pair mechanisms. For more complicated mechanisms such as the Miller mechanism, eq. (55) is no longer valid (see LE CLAIRE [1970a] and PETERSON [1975]). This is also the case for the the vacancy mechanism in ordered alloys with a **B2** structure.

Isotope effect measurements can contribute to identification of the diffusion mechanism through the correlation factor; but we have to know ΔK. Theoretical values of ΔK can be calculated in the framework of the above mentioned jump theories. Unfortunately they are not really sufficiently quantitative for that purpose. An expression has been established by LE CLAIRE [1966], which allows ΔK to be estimated if the defect formation volume ΔV_F is known:

$$\Delta K \sim \left(1 + \tfrac{\xi}{3}\left|(1 - \Delta V_F)\right|\right)^{-1} \tag{56}$$

In this expression, ξ is the number of neighbouring atoms when the jumping atom is in saddle-point position and ΔV_F is expressed as a fraction of the atomic volume. For more details about the isotope effect we refer the reader to LE CLAIRE [1970a], PETERSON [1975] and FLYNN [1987]).

1.5. Numerical simulation approaches

Thanks to the huge progresses of the power of the modern computers as well as of the presently available models of interatomic interactions, the numerical simulation route is now routinely used in diffusion studies (ADDA and CICCOTTI [1985]). The main goal of this approach is twofold. On the one hand numerical simulations are providing well-controlled experiments and allow a proper check of the validity of the various theoretical tools depicted above. Moreover, if realistic interatomic interactions are available, they provide a fairly reliable substitute to actual experiments. This is now almost the case for simple metals with s and p electrons (see for example GILLAN [1989]). On the other hand, like numerical methods, they easily allow for a full treatment of the actual problem: no approximation is needed, and the full anharmonicity can be introduced, which proves to be particularly important in diffusion studies due to the high temperatures involved and the strongly N-body character of the events.

The Molecular Dynamics (M.D.) and the Monte Carlo (M.C.) methods are the most used simulation tools. As explained in the previous paragraph the main observables of the diffusion theory, formation and migration energies for instance or the diffusion coefficient itself, appear as thermodynamic ensemble averages in the phase space of the system. Both of these methods aim therefore to furnish a full set of atomic configurations *using a properly choosen bias* for selecting the most important parts of the phase space, i.e. each configuration will be given a weight according to its Boltzmann factor in the proper ensemble.

References: p. 651.

In M.D., by solving the Newton equations of motion the full trajectory of the system in the phase space is built, and the proper weighting of the possible configurations follows as a consequence of the hamiltonian equations. The ensemble averages can be calculated as time averages thanks to the ergodic hypothesis. In M.C., a set of possibly uncorrelated configurations is built by *randomly moving* the particles according to a rule designed for achieving the proper importance sampling. The notion of trajectory, as well as of time scale, is therefore lost to a large extent.

1.5.1. Molecular Dynamics method

For a broad coverage of the field the interested reader can find almost everything in the following references: CICCOTTI and HOOVER [1986], ALLEN and TILDESLEY [1987], MEYER and PONTIKIS [1991].

In this method the hamiltonian equations of motion are solved by stepwise numerical integration for a system of N particles interacting by a properly chosen potential energy function U. This function can have any degree of complexity (and realism!) from the early empirical sum of interactions between pairs of atoms (GIBSON *et al.* [1960], RAHMAN [1964]), to the most recent quantum-mechanics-based N body potentials where the full contribution of the electrons to the cohesive energy of the system is taken into account (CAR and PARRINELLO [1985], LAASONEN [1994]). Periodic boundary conditions are generally used by repeating on all sides of the primitive system replicas of itself. In this way the spurious effects of free surfaces are avoided. Even in the largest simulations the maximum size is of the order of 10^6 atoms for a maximum duration lower than 10^{-9} seconds of actual time.

The first M.D. simulations were done at constant volume V and total energy E, in the microcanonical ensemble, noted NVE, but more recently new methods appeared which allow to produce trajectories in other ensembles: constant enthalpy (ANDERSEN [1980]), constant stresses (PARRINELLO and RAHMAN [1981]), constant temperature (NOSE [1984], HOOVER [1985]). One must be nevertheless careful when using these new ensembles since the dynamics of the fluctuations introduced is generally no longer the actual one. If needed, special techniques can be used, tailored for studying rare events or non equilibrium systems (BENNETT [1975], CICCOTTI [1991]).

Once a well-equilibrated system has been prepared, the thermodynamic average of the various physical observables can be calculated according to:

$$< f >= \lim_{\tau \to \infty} \frac{1}{\tau} \int_0^{\tau} f(t) dt$$

The observable f, determined as a function of time along the trajectory, can be an energy, enthalpy, temperature, pressure or stress, any correlation function, as well as the mean squared atomic displacement, of special interest here.

In diffusion studies, M.D. has been used either in a direct approach or in an indirect one. In the first the mean squared displacement of the atoms is directly computed from the record of the successive atomic positions. Albeit conceptually simple, this approach is limited by the available computing resources to calculation of diffusion coefficients

higher than 10^{-11} m²/s at most, which limits its application to the studies of liquids (RAHMAN [1964]), or of interstitial diffusion at a quite high temperature (GILLAN [1986], GENDRE *et al.* [1991]). In the indirect approach the M.D. is used for studying the elementary events of the diffusion: the atomic mechanism at work in a given material (BENNETT [1975], DOAN and ADDA [1987], DELAYE and LIMOGE [1993a]), and its various thermodynamic properties, e.g. formation and migration energies, entropies and volumes or associated local modes (WILLAIME [1990], DELAYE [1993]). At a high temperature, the jump frequencies of the defects can also be directly calculated, allowing for a direct check of the validity of the usual theoretical approaches in the diffusion theory.

1.5.2. Monte Carlo method

Now the notion of trajectory is lost: a set of successive configurations Π_i is generated by *randomly* moving one or several particles of a system. As in M.D., the system contains N particles interacting by a properly chosen potential energy function U (the limitations over N are of the same order as in M.D.), and periodic boundary conditions also are frequently used. The configurations resulting from these random moves will be taken as acceptable according to various rules which ensure that the set of configurations contains each state according to its thermodynamical weight in the proper ensemble (for a complete review of the field see VALLEAU and WHITTINGTON [1977] or BINDER ref. S, in the 'Further Reading' list). Such a set forms a Markov chain. It can be shown that it is sufficient that the acceptance rule, or transition probability p_{ij} between states Π_i and Π_j, satisfies the microscopic detailed balance:

$$\pi_j \cdot p_{ji} = \pi_i \cdot p_{ij}$$

for the various states Π_i will be represented in the stationary Markov chain proportionally to their proper Boltzmann weight π_i. Various acceptance rules have been devised, the most popular of which is the Metropolis scheme according to which:

$$\begin{aligned} &a)\quad p_{ij} = 1 && \text{if } W_j < W_i \\ &b)\quad p_{ij} = \exp\left(-\frac{W_j - W_i}{kT}\right) && \text{if } W_j > W_i \end{aligned} \tag{57}$$

if W_i and W_j are the potential energies of states Π_i and Π_j.
As a matter of fact the thermal averages are obtained simply as:

$$< f >= \frac{1}{m} \sum_{1}^{m} f(\Pi_i)$$

with m the length of the Markov chain. The precise form of the acceptance rule influences the rate of convergence towards the limit chain, but does not alter the stationary behaviour. In this approach one of the key point is the source of the random numbers used i) to generate the successive configurations ii) to decide of the acceptance or not in case 57b). The art of building "good" generators of pseudo-random numbers is a quite sophisticated one (see for example KNUTH [1968]). The best one for the present

purpose is probably the so-called "Feedback Shift Register" method (ZIERLER [1959], LEWIS and PAYNE [1973]).

The same comments apply here as in § 1.5.1 with respect to the extension of the method, originally developed for the canonical ensemble, to isoenthalpic, isostress or even Grand Canonical ones by using the proper weight. One of the subtleties of the M.C. method is that the time variable has disappeared, since successive configurations in the chain are not necessarily related by a physically possible path. However, this drawback can be removed (BOCQUET [1987], LIMOGE and BOCQUET [1988]).

Except for the dynamic aspects, the use of M.C. is identical to that of M.D.: defect structure and properties, thermodynamical averages calculation. Moreover, the M.C. approach is particularly well-suited for studying the properties of random walks. Indeed, in a random walk model, the full dynamics of the jump is condensed in a set of frequencies, allowing to calculate by the direct method the diffusion coefficient in a very efficient way. This method has proved to be particularly useful in complex systems, like concentrated alloys, disordered materials etc., where analytical solutions for random walk are not available (MURCH and ZHANG [1990]).

2. *Experimental methods*

We shall review the different techniques which allow the diffusion coefficients D to be measured; for the heats of transport and effective valence measurements the reader is referred to § 6. Two kinds of methods are used to measure D: macroscopic methods, which are based on Fick's Law, and microscopic methods. With the former, we compare the experimental concentration profiles (or a quantity which depends on it) with the appropriate solution of Fick's Law. The latter takes advantage of the fact that many physical phenomena depend on the atomic jumps (for instance, NMR or Mössbauer signals) and can be used to measure atomic jump frequencies. For the microscopic methods it is, in general, necessary to know the diffusion mechanism precisely in order to be able to deduce the jump frequency from the measured signal, whereas the macroscopic methods yield D without any assumption on the diffusion mechanism. Moreover it is not granted that the jumps detected are actually the ones involved in macroscopic diffusion (a drawback of spectroscopic techniques), nor that they are involved in the same manner as in actual diffusion (case of relaxation studies). But the macroscopic methods entail a macroscopic displacement of the atoms and thus a large number of jumps. At low temperatures, for small values of D, it is then necessary to perform long anneals. Conversely, because they only involve a small number of jumps, the microscopic methods require much shorter durations and they allow the variation of D with time to be studied for systems which are not in equilibrium (systems under irradiation, after quenching, during plastic deformation, etc.). For a given system the combination of both kinds of techniques can help to determine the diffusion mechanism (see for instance BRÜGGER *et al.* [1980]). We will successively discuss these two types of techniques.

2.1. Macroscopic methods

Most frequently the quantity which is measured is the concentration $C(x)$ at point x, and the resulting concentration profile is compared with the appropriate solution of Fick's Law; but any quantity which depends on the concentration or on the flux can allow the determination of the diffusion coefficient. In the first part we focus on methods which determine the profile $C(x)$; in the second part we briefly discuss other macroscopic techniques. For more details see ADDA and PHILIBERT [1966], or PHILIBERT [ref. C)].

2.1.1. D from the $C(x)$ curve

2.1.1.1. C(x) by sample sectioning. Generally the $C(x)$ profile is obtained by sectioning the diffusion zone and measuring the quantity of the diffusing species in each slice (thickness Δx).

For *sectioning*, several techniques can be used:
Mechanical sectioning with precision lathe (10 μm, 5×10^{-16} m^2/s), microtome (1 μm, 5×10^{-18} m^2/s) or grinding machine (1 μm, 5×10^{-18} m^2/s).
Chemical or electrochemical attack (50 Å, 10^{-22} m^2/s).
Sputtering by ionic bombardment (10 Å, 5×10^{-24} m^2/s).
The numbers in parentheses indicate, respectively, the minimum thickness of the slices and the minimum diffusion coefficient which can be obtained in practice.

The slice thickness, Δx, and the values of x can be measured by weighing; when Δx is too small, weighing becomes inaccurate and other techniques (optical methods, Talystep) have to be used. The techniques most frequently employed for the *determination of the concentration* $C(x)$ are activity counting (for the radioactive species) and mass spectrometry. Each of them can, in principle, be utilized with one of the sectioning methods described previously. They are very sensitive, especially activity counting which allows the detection of atomic fractions as small as 10^{-10}. Ionic sputtering is associated with mass spectrometry in commercial apparatus (ionic analyzers or SIMS, i.e. secondary ion mass spectrometry, see ch. 10, table 4) and with activity counting in several devices (see for instance GUPTA [1975]); both allow the determination of diffusion coefficients as small 5×10^{-24} m^2/s.

2.1.1.2. Non-destructive techniques. As a matter of fact all these techniques are methods of analysis which could be associated with the sectioning of the sample but they also allow the determination of the profiles without sectioning.

The Castaing microprobe (electron microprobe analyzer). A thin electron beam ($\phi \sim 1\mu m^2$; analyzed zone $\sim 1\ \mu m^3$) stimulates the X-fluorescence radiation of the element to be studied (ch. 12, § 2.2); the profile $C(x)$ can be obtained by analyzing the sample along the diffusion direction. This technique is convenient for studying chemical diffusion. The sensitivity is of order of 10^{-3} and it is not possible to measure diffusion coefficients smaller than 10^{-15} m^2/s.

Nuclear reactions. The surface of the sample is bombarded with particles (α, protons, etc.) which induce a nuclear reaction with the element to be studied; the energy spectrum of the out-going particles created by this nuclear reaction allows the determination of the

concentration profile $C(x)$. These techniques are convenient for the analysis of light nuclei.

Back-scattering. As previously, the surface of the sample is bombarded and one studies the energy spectrum of the elastically back-scattered particles, from which it is possible to obtain the concentration profile. In contrast with nuclear reaction methods, the back-scattering method is convenient for the analysis of heavy nuclei.

For more details about these two last methods we refer the reader to the writings of ENGELMANN [1977], PHILIBERT [ref. C)] and CHU *et al.* [1978].

2.1.2. Other macroscopic methods

There are numerous macroscopic techniques which allow the determination of diffusion coefficients from measurements of properties depending on matter transport; one obtains generally as a result the *chemical diffusion coefficient.* The most important of these methods are the following:

– Measurement of the quantity of matter leaving or crossing a sample. This method is much employed for gases and volatile products.

– Measurement of the growth rate of a new phase. When the growth is controlled by diffusion it is possible to calculate D from the growth kinetics. This is fully explained by SCHMALZRIED [1974].

– Measurements of compaction and deformation kinetics. Sintering of powders and creep of crystals are in some cases controlled by bulk diffusion; it is then possible to deduce D from compaction or deformation kinetics (ch. 31, § 2.2).

– Measurements of the evolution of the concentration modulation by X-rays (or electrical resistance). This method was initially developed by COOK and HILLIARD [1969] and used for amorphous systems by ROSENBLUM *et al.* [1980], GREER and SPAEPEN [1985]. A film of periodic composition is deposited by evaporation or sputtering; this film tends to homogenize on heating, according to the solution given in § 1.3.5. The kinetics can be followed by X-rays and

$$D = -\frac{\lambda^2}{8\pi^2}\frac{\mathrm{d}}{\mathrm{d}t}\left(\ln\frac{I(t)}{I_0}\right)$$

where I is the intensity of the satellite peak in the neighbourhood of the central spot. It is also possible to follow this kinetics using the measurement of the electrical resistance of the sample; this provides a very convenient measurement tool in complex environments, like high pressures or irradiation (WONNELL *et al.* [1992]).

This technique allows the determination of very small coefficients of diffusion ($\sim 10^{-27}$ m^2/s).

The *Gorsky effect,* in spite of its being a macroscopic method, will be described in the next section, together with relaxation phenomena.

2.2. Microscopic (or local) methods

The methods described here pertain to two groups: on the one hand, studies of relaxation kinetics in out-of-equilibrium samples, on the other hand various spectroscopic methods involving transition matrices disturbed by atomic jumps.

2.2.1. Relaxation methods

The reader can find a very detailed theory of relaxation properties in solids as well as experimental results in NOWICK and BERRY [1972].

2.2.1.1. Thermodynamic aspects of relaxation. The internal energy of a system is defined by the state variables, stresses, temperature, fields, etc., and by a set of n internal variables, labelled v_i, the equilibrium values of which, v_i^e, are fixed by the values of the state variables. These internal parameters can be, for example, the order parameters in an alloy or the populations of the various energy levels that a system can occupy. If one of the state variables changes suddenly, the various internal variables which are coupled with it will relax to the new equilibrium values. In the cases of interest here, the diffusional mobility D controls the relaxation towards equilibrium. We can then measure a relaxation time τ, related to D by

$$D = k\frac{a^2}{\tau}$$

where a is a distance characteristic of the lattice, and k is a constant depending on the specific model involved.

The internal energy varies according to:

$$dU = TdS + dU_{ext} - \sum_i U_i dv_i \tag{58}$$

where dU_{ext} is the energy supplied by the external forces and the dv_i stand for the variations of the internal variables. U_i is the ordering energy associated with the i^{th} internal variable.

If the deviations from equilibrium, $v_i - v_i^e$, are not too large, the U_i can be expanded as

$$U_i = -\sum_j U_i^j \left(v_j - v_j^e\right) \tag{59}$$

When the time evolution of the v_i's is first-order, one speaks of relaxation phenomena. In this case:

$$\frac{dv_i}{dt} = -\sum_j w_i^j \left(v_j - v_j^e\right) \tag{60}$$

One sees easily that it is always possible to find a set of n normals modes V_i evolving in time as:

$$V_i(t) = V_i^e\left[V_i(t=o) - V_i^e\right]\exp\left(-t/\tau_i\right) \tag{61}$$

In eq. (61), τ_i is the relaxation time of the i th normal mode. In many cases the homogeneity of the sample is not perfect and, instead of a single-valued τ_i, we observe a distribution $\pi(\tau_i)$ of times, corresponding either to the distribution of atomic environments or to the various relaxation paths.

References: p. 651.

In diffusion studies of metals and alloys, the most frequently used external influences are mechanical stresses, magnetic field or temperature jumps.

2.2.1.2. Anelasticity. In the case of mechanical stresses one speaks of *anelasticity*. Two solicitation modes are used in these studies. The first one is the *mechanical after-effect*: a static stress (or strain) is applied and the strain (stress) relaxation is followed in time. The application for example of a constant stress leads to an instantaneous elastic response defining the *unrelaxed modulus* M_0. Afterwards the system displays a relaxation of the strain which corresponds at infinite time to the *relaxed modulus* M_∞. The after-effect anelasticity is then defined by three physical quantities:

– the relaxation intensity: $\Delta = (M_0 - M_\infty)/M_\infty$;

– the mean relaxation time $\bar{\tau}$;

– the width of the relaxation time spectrum β.

In many cases the experimental data are well fitted with a Gaussian spectrum (NOWICK and BERRY [1972]):

$$\pi(\tau) = \left(\beta\sqrt{\pi}\right)^{-1} \exp\, -\left(\ln\left(\tau/\bar{\tau}\right)/\beta\right)^2$$

The second mode is the *internal friction mode*. In this case, stress and strain are periodic with a frequency ω according to:

$$\sigma = \sigma_0 \exp i\omega t,\ \varepsilon = \varepsilon_0 \exp i(\omega t - \varphi)$$

The *phase factor* φ between stress and strain expresses the energy dissipation due to anelasticity. One can show that φ is related to $\bar{\tau}$ by:

$$\tan\varphi \sim \frac{\omega\bar{\tau}}{1 + (\omega\bar{\tau})^2} \tag{62}$$

The phase factor displays a Debye resonance versus ω, or versus temperature variation through the temperature dependence of $\bar{\tau}$; the maximum value, φ_{max}, is obtained for $\omega\bar{\tau} = 1$. In real experiments the measurements are made either in forced, or in free, damped oscillations. One can then measure the energy absorbed per cycle, $\delta w/w$, or the magnification factor at the resonance Q (inverse of Full Width at Half Maximum (FWHM) of the ε_0^2- *versus*-ω curve) as a function of temperature. In the free case one measures the logarithmic decrement $\delta = \ln\,[\varepsilon(t)/\varepsilon(t+T)]$, where T is the oscillation period.

All these physical quantities are related by:

$$2\pi \sin\varphi \sim \frac{2\pi}{Q} \sim 2\delta \sim \frac{\delta w}{w} \qquad \text{and} \qquad 2\mathrm{tg}\varphi_{max} \sim \frac{\Delta}{(1+\Delta)^{1/2}} \tag{63}$$

The study of the value of φ versus ω, at various temperatures, gives the relaxation time $\bar{\tau}$ versus temperature. We deduce D, the diffusion coefficient, as

$$D = \frac{k\,a^2}{\bar{\tau}}$$

A great variety of experimental set-ups have been used. The reader will find many references in NOWICK and BERRY [1972]. The most commonly used are the torsion pendulum, either in internal friction or in after-effect mode, and the resonant bar at higher frequency. The corresponding D's which can be measured are given in table 1.

2.2.1.3. Snoek relaxation. In body-centered cubic metals the interstitial defect has a tetragonal symmetry, in both octahedral and tetrahedral sites. Owing to this lower symmetry it can give rise to an anelasticity effect, the so-called *Snoek effect* (SNOEK [1939]). In most cases experimental results are, in bcc metals, in good agreement with the octahedral model (see fig. 7 and § 4.2.1). Under a uniaxial tensile stress σ along the Oz axis, there is a splitting of the energy levels of the three kinds of sites S_x, S_y, S_z, in favor of S_z sites. The ordering energy [eqs. (58) and (59) is: $U_i = \gamma\sigma$, where γ is the lattice parameter variation along Oz axis due to the redistribution from S_x and S_y to S_z sites. The associated internal variable is $v = (n_z - n/3)$, n and n_z being the total atomic fraction and the atomic fraction of solute on S_z sites, respectively. Taking Γ as the total solute frequency jump, one easily shows that $\Gamma = 2/(3\bar{\tau})$, and D is given by

$$D = \frac{a^2}{36\,\bar{\tau}} \tag{64}$$

where a is the lattice parameter. (See also ch. 22, § 4.3.)

2.2.1.4. Zener relaxation. In face-centered cubic metals, an interstitial solute has the same symmetry as the lattice. Therefore there is no anelasticity associated with interstitial solutes. On the other hand, a pair of substitutional solute atoms B of non-zero size effect in a solvent metal A represents a defect of orthorhombic symmetry. Their reorientation under stress then gives rise to an anelastic relaxation which can be seen in all lattices of higher symmetry. ZENER [1943, 1947] was the first to point out the existence of an internal friction peak in a 70:30 α-brass, which he further analyzed as the effect of the reorientation of solute pairs (now called the *Zener effect*). LE CLAIRE [1951] has analyzed the kinetics of their reorientation and shown how it allows the solute jump frequencies to be determined. Nevertheless this model in terms of solute pairs suffers from several weaknesses:

– Contrary to Snoek relaxation, the Zener effect can be observed only in concentrated alloys, because of its dependence on the square of the B concentration. The description in terms of isolated pairs therefore becomes less satisfactory.

– Several parameters of the relaxation (the anisotropy, the temperature dependence of D) are badly accounted for by the pair model.

– The solute mobility alone is involved in Le Claire's analysis of the kinetics. However, NOWICK [1952] has shown that the mobility of both species is needed to produce a relaxation.

Clearly we need a full description of the ordering under stress to give a good account of the Zener effect. LE CLAIRE and LOMER [1954] and WELCH and LE CLAIRE [1967] have given a solution to this problem in the framework of Cowley's order parameters (up to the second-nearest neighbours for the latter authors). The most elaborate analysis of the kinetics for the first model is due to RADELAAR [1970]. He simultaneously calculated

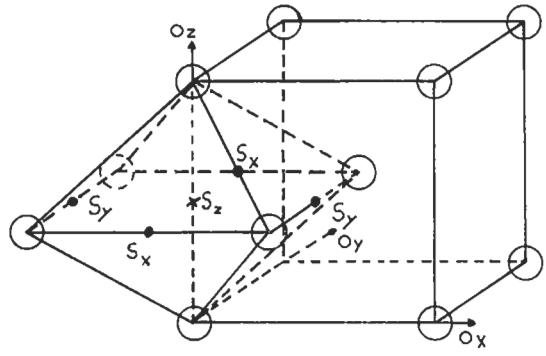

Fig. 7. Characteristics of octahedral interstitial sites in bcc lattices. There are three kinds of sites S_x, S_y and S_z. For an S_z site the first-neighbour distance in the z direction is $a/2$ and $a/\sqrt{2}$ in the xOy plane.

τ_R, the relaxation time for ordering, and $D^{AB}_{A^*}$ and $D^{AB}_{B^*}$, the tracer diffusion coefficients of respectively A* and B* in the alloy:

$$\tau_R \sim a^2 g(\alpha)\left(C_A/D^{AB}_{B^*} + C_B/D^{AB}_{A^*}\right) \tag{65}$$

where $g(\alpha)$ is a smooth function of α, the short range order parameter. No equivalent analysis exists for Welch and Le Claire's model.

One clearly sees that the (approximate) formula (65) does not allow one diffusion coefficients alone to be deduced from τ_R values. The relaxation time appears to be a "Zener-averaged" function of the various atomic jump frequencies and not that particular arrangement which gives the diffusion coefficients. In most cases for example, τ_R appears to be a thermally activated quantity, the activation energy of which is lower than that of either $D^{AB}_{B^*}$ or $D^{AB}_{A^*}$ (NOWICK and BERRY [1972]).

Nevertheless, while the use of Zener relaxation in measuring diffusion coefficients is a delicate task, this effect is of paramount interest in studies of the behaviour of point defects in alloys in, or out of, equilibrium (BERRY and OREHOTSKY [1968], BALANZAT and HILLAIRET [1980]).

2.2.1.5. Gorsky effect. Any defect B which produces a lattice dilatation is also able to give rise to an anelastic relaxation. This is the well known *Gorsky effect* (GORSKY [1935]) the complete theory of which was given by ALEFELD *et al.* [1970]. Indeed, the migration of positive (resp. negative) dilatation centres down (resp. up) a macroscopic strain gradient produces a relaxation of stresses, which is detectable if the diffusion coefficient is high enough (VÖLKL [1972]).

One easily shows that the diffusion coefficient D_{B^*} of the B defect is related to the relaxation time τ_R by (ALEFELD *et al.* [1970]):

$$D_{B^*} = \frac{1}{\varphi \tau_R}\left(\frac{d}{\pi}\right)^2 \tag{66}$$

where d is the length of the diffusion zone and φ the thermodynamic factor (§ 1.2.2). The main interest of the Gorsky relaxation is to give access to D_{B^*} without the need of any diffusion model. Note that here the length scale is d, the sample size, and not a, the atomic size [eqs. (64) or (65)]. We see in table 1 that this method is well suited for high diffusion coefficients.

2.2.1.6. Magnetic relaxation in ferromagnetic alloys. In ferromagnetic alloys the local interactions between a magnetic momentum and local order give rise to relaxation phenomena similar to those observed under stress. Their origin is to be found in the *induced anisotropy energy*, the theory of which was built up by NEEL [1951, 1952, 1954] and TANIGUCHI [1955]. We have an ordering energy U_i given by [see eqs. (58) and (59)]:

$$U_i = w \cos^2 \theta \tag{67}$$

where θ is the angle between the local moment and the symmetry axis of the defect under consideration. The origin of w lies in the perturbation by the defect of i) exchange integrals between magnetic atoms ii) spin–orbit coupling.

This anisotropy energy gives rise to three kinds of relaxations.

Table 1
Diffusion coefficient ranges accessible through different techniques.

Method	Relaxation time τ or Frequency ω	Range of D_{B^*} accessible (m^2/s)
Elastic after-effect (Zener or Snoek)	$10 < \tau < 10^5$ s	$10^{-25} < D_{B^*} < 10^{-21}$
Internal friction (Zener or Snoek)	1 Hz $< \omega < 10^5$ Hz	$10^{-20} < D_{B^*} < 10^{-15}$
After-effect and internal friction in Gorsky relaxation	Approximately same as above	$10^{-12} < D_{B^*} < 10^{-8}$
Torque measurement (magnetic anisotropy method)	$10 < \tau < 10^5$ s	$10^{-25} < D_{B^*} < 10^{-21}$
NMR field gradient	–	$10^{-13} < D_{B^*} < 10^{-8}$
Pulsed NMR	$10^{-7} < \tau < 0.1$ s	$10^{-19} < D_{B^*} < 10^{-13}$
Mössbauer	–	$10^{-15} < D_{B^*} < 10^{-11}$
Neutron scattering	–	$10^{-12} < D_{B^*} < 10^{-9}$

The first, analogous to the Snoek relaxation, is due to reorientation of interstitial impurities in bcc crystals during a change of field direction. The relationship between jump frequency, relaxation time and diffusion coefficient is the same as in the Snoek relaxation.

The second is the analogue of the Gorsky effect. In a domain wall the interaction between the magnetostrictive stresses and the strain field of interstitials can be minimized by diffusion through the wall. This diffusion gives rise to an after-effect. The relaxation

References: p. 651.

time is a factor $(\delta/a)^2$ larger than the preceding one (as in the mechanical case), δ being the domain wall thickness (KRONMÜLLER [1978]).

The third can be called a *magnetic Zener effect* and is due to the ordering of ferromagnetic alloys in a magnetic field. The theory was built up by NEEL [1954] in a quasi-chemical model and by VILLEMAIN [1970] with inclusion of second-nearest neighbour order. The link between relaxation time and diffusion is as difficult to establish as in the Zener effect. However, the sensitivity is extremely high and allows study of diffusion at exceedingly low defect concentrations ($10^{-8} - 10^{-10}$ vacancy fraction, CHAMBRON and CAPLAIN [1974]). (See also ch. 29, § 5.3.3.3).

2.2.1.7. Kinetics of short-range ordering. Any physical property sensitive to atomic order can be used to follow the kinetics of ordering and therefore to study atomic mobility: resistivity (RADELAAR [1966], BARTELS [1987], YU and LÜCKE [1992]), X ray-, electron- or neutron diffraction (PENISSON and BOURRET [1975]). Nevertheless we need to relate quantitatively the order parameter and the measured quantity. Further, the link between ordering kinetics and diffusion coefficients is as difficult to establish as in the Zener effect.

2.2.2. Spectroscopic methods

2.2.2.1. Nuclear magnetic resonance. In a static magnetic field $\mathbf{H}_0$ (say 10^3 Gauss) a nuclear spin of magnitude I takes a precession motion at the Larmor frequency ω_0. Simultaneously the degeneracy of the $2I+1$ energy levels is raised. A macroscopic sample is an assembly of nuclear spins and will then display a magnetic moment along $\mathbf{H}_0$, M_z, and a transverse part $M_\perp$, zero at equilibrium. If we apply a transverse radio-frequency magnetic field $H_\perp$ with a pulsation ω near ω_0, this field will induce transitions between the $2I+1$ Zeeman levels of each spin. Experiments show, and theory confirms in many cases (ABRAGAM [1961]), that the time evolution of the total moment of the sample $\mathbf{M}$ is given by the *Bloch equation*:

$$\frac{\partial \boldsymbol{M}}{\partial t} = \gamma \boldsymbol{M} \Lambda \boldsymbol{H} - \frac{M_\perp}{T_2} - \frac{M_z - M_z^{eq}}{T_1} + \nabla\left[D.\nabla\left(\boldsymbol{M} - \boldsymbol{M}^{eq}\right)\right] \tag{68}$$

where γ is the gyromagnetic ratio, $\mathbf{M}^{eq}$ the equilibrium value of the magnetic moment and D the diffusion coefficient of the nuclei. T_1 is the relaxation time of the longitudinal part M_z and corresponds to an energy transfer between lattice and spins system. T_2 is the relaxation time of the transverse part $M_\perp$. The values of T_1 and T_2 are fixed by various interactions between spins, either direct or indirect via electrons. On each nuclear site these interactions create a local field (approx. 1 Gauss) which fluctuates, due to atomic vibrations and jumps. It induces transitions between levels and then settles their lifetime. However, if the frequency of the atomic displacements becomes of the order of magnitude of the frequency of the precession motion due to this local field, the spins will be sensitive only to the time average of it. This average is zero and the lifetime is no longer limited by interactions: this is the so-called *motional narrowing* of absorption lines, which explains part of the variation of T_1 and T_2 with temperature.

Equation (68) shows that two techniques can be used to determine diffusion coefficients. Firstly, the last term of eq. (68) gives a time evolution of M when the sample is put into a field gradient G according to:

$$M_{\perp}(t) = M_0 \exp\left(-\frac{t}{T_2} - \frac{1}{3} D\gamma^2 G^2 \tau^2 t\right)$$

The measurements of $M_{\perp}$ versus time t then gives D without any further hypothesis (ABRAGAM [1961]).

We can also measure either the width of absorption lines in steady-state resonance (ω near ω_0), or the decay of M_z and $M_{\perp}$ parts with time after the perturbation by a "pulse" of $H_{\perp}$ field. In this last case, the decays fit the laws $M_z = M_0\,[1 - \exp(-t/T_1)]$ or $M_{\perp} = M_0 \exp(-2t/T_2)$. Now the BLOEMBERGEN *et al.* theory [1948] expresses T_1 and T_2 in terms of Fourier transforms of the time correlation function of dipolar interactions (the main interaction in many cases) due to nuclear motions. We then have to postulate a diffusion mechanism, to calculate correlation functions and to compare it with experimental T values in order to deduce a diffusion coefficient.

The original work of Bloembergen was done for diffusion in liquids and later extended to the case of random walk and defect mechanism in lattices (TORREY [1954]), including correlation effects (WOLF [1979]). Self-diffusion in aluminum was measured by NMR by SEYMOUR [1953] and by SPOKAS and SLICHTER [1959].

2.2.2.2. Mössbauer effect. Gamma rays can be emitted or absorbed by excited nuclei. According to the Heisenberg principle, and controlled by the half-life time τ of the nuclei, the width $\Gamma = \hbar/\tau$ of the corresponding lines can be very narrow, of the order of 10^{-9} eV for example. Owing to the recoil energy of the emitter, the emission line of free nuclei is shifted by a much larger amount. This shift then prevents the resonant absorption by other nuclei. On the other hand, if the emitter is embedded in a crystal a part of the emissions occurs without recoil. This is the Mössbauer effect. In this case resonant absorption can occur. However, if one of the emitting or absorbing nuclei is moving, either by thermal vibration or diffusion jumps, the line is broadened by self-interference effects. This broadening is the main effect which has been used to give access to atomic mobility. More precisely, SINGWI and SJÖLANDER [1960a] have shown that the emission, or absorption, cross-section is given by:

$$\sigma(\omega) = \frac{\sigma_0 \Gamma}{4\hbar} \int \exp\left[i(Kr - \omega t) - \frac{\Gamma}{2\hbar}|t|\right] G_s(r,t)\,\mathrm{d}r\,\mathrm{d}t \tag{69}$$

where $G_s(r,t)$ is the Van Hove autocorrelation function and K the wave vector of the γ photon of frequency $2\pi/\omega$. In a classical system G_s gives the probability of finding at (r,t) a particle located initially at (0,0). Therefore $G_s(r,t)$ contains all the information about diffusion processes. SINGWI and SJÖLANDER [1960a, b] have given the theory of diffusion broadening in the case of liquids and of random jumps on an empty lattice (i.e. interstitial case). In the last case the broadening is given by:

$$\Delta\Gamma = \frac{12\hbar}{b^2} D(1 - \alpha) \quad \text{and} \quad \alpha = \frac{1}{N} \sum_{n=1}^{N} \exp(iKR_n) \tag{70}$$

References: p. 651.

where b is the jump distance and R_n the N possible jump vectors. Equivalent formulas have been given for the vacancy mechanism (WOLF [1983]). This dependence can give very valuable informations about the anisotropy of diffusion (FLINN [1980]), as well as on the jump vectors (SEPIOL and VOGL [1993a]). Nevertheless the constraints of: (i) high recoilless fraction (large detectable signal), and (ii) measurable $\Delta\Gamma/\Gamma$, say between 10^{-1} and 10^{2}, limit the available tracers to ^{57}Fe, ^{119}Sn, ^{151}Eu and ^{161}Dy (JANOT [1976]).

The other aspects of the Mössbauer spectroscopy, the so-called hyperfine interactions, isomeric shift, magnetic dipolar and electric quadrupolar interactions, have also been used for studying the various jump frequencies of interstitial iron atoms in Al, Fe, Zr, Nb (YOSHIDA [1989]).

2.2.2.3. Quasi-elastic neutron scattering. A monoenergetic neutron beam can be scattered by nuclei embedded in a solid without any energy transfer, that is, without phonon emission or creation. This is the exact parallel, in the case of neutrons, of the Mössbauer effect for γ photons. More precisely, VAN HOVE [1954] has shown that eq. (69) gives the incoherent scattering differential cross-section for scattering vector K and energy transfer ω. In this case Γ has to be taken as zero, and σ appears to be the (r,t) Fourier transform of G_s. Therefore atomic motions, as given by $G_s(r,t)$, induce a broadening of the elastic peak, the measurement of which versus ω gives access to atomic mobility. The formula (70) works for describing the K and jump vectors dependences of the broadening.

Two experimental techniques can be used (SPRINGER [1972]). For the first, one uses small K values, corresponding to large r, where $G_s(r,t)$ is well represented by:

$$G_s(r,t) = (4\pi Dt)^{-3/2} \exp\left(-r^2/4Dt\right)$$

The quasi-elastic peak then has a Lorentzian shape with a FWHM of $2\,\hbar\,K^2\,D$. The use of this method, at low K, is therefore limited by the energy resolution of spectrometers.

In the second method, one starts from a diffusion model which allows G_s to be calculated. One then fits the parameters of the model to scattering measurements at various K vectors, using the K dependence of the broadening. If one works with fairly large K, then small r, the method is very sensitive to the details of the jump mechanism, (PETRY and VOGL [ref. M)], VOGL *et al.* [1989]).

Neutron scattering techniques, owing to an energy resolution of the spectrometers much more limited than in the case of Mössbauer spectroscopy ($\sim 10^{-7}$ with back-scattering geometry, against $\sim 10^{-9}$ eV), are best suited for fast diffusion, like that of hydrogen in metals (GISSLER [1972]), sodium self-diffusion (AIT SALEM *et al.* [1979]) or high temperature studies in β-Ti, a fast diffuser (PETRY *et al.* [1991]).

3. *Self-diffusion in pure metals*

The pure metals are undoubtedly the most studied with regards to their point defects and diffusion properties. The traditional distinction was between *normal* and *anomalous self-diffusion,* the latter taking place in about ten body-centered cubic metals. A detailed review on this point of view can be found in PETERSON [1978]. However, there has been

deep progress in the understanding of this aspect in the last years, and the paradigm has now changed to distinguish between diffusion in close-packed phases, i.e. fcc and hcp ones, as opposed to diffusion in bcc ones.

Diffusion parameters for various pure elements have been gathered in table 2.

According to LE CLAIRE [1976], normal self-diffusion complies with the three following empirical rules:

– the diffusion coefficient obeys the Arrhenius law: $D = D_0 \exp(-Q/kT)$;

– the D_0 values range from 5×10^{-6} to 5×10^{-4} m^2/s;

– the activation energy is related to the melting temperature by the expression: $Q = 34T_M$, (Q in calories per mole), or $0.14\ T_M$ (Q in kJ/mole), where T_M is the melting point of the metal (in Kelvin). This behaviour, forming the base of the Van Liempt relation, is well obeyed by compact metals (see fig. 8a for fcc ones). In bcc structures the dispersion is much greater (fig 8b).

All these properties can be qualitatively understood in the framework of the above mentioned theories of diffusion by the vacancy mechanism, keeping in mind that a proper formation energy for a vacancy has to be related to the cohesive energy of the material and therefore to its melting point.

The term of anomalous diffusion was formerly reserved for describing ten systems which present very low values of the frequency factor D_0 and of the activation energy Q: β-Ti, β-Zr, β-Hf, γ-U, ε-Pu, γ-La, δ-Ce, β-Pr, γ-Yb and β-Gd. All these metals also display a more or less important curvature of the Arrhenius plot (fig. 9b).

However, one often observes a slight positive curvature in the Arrhenius plot even in the so-called normal metals (Al, Ag, Au, Cu and Ni); it is frequently restricted to high temperatures but sometimes it is present over the whole temperature range. This curvature is always upward.

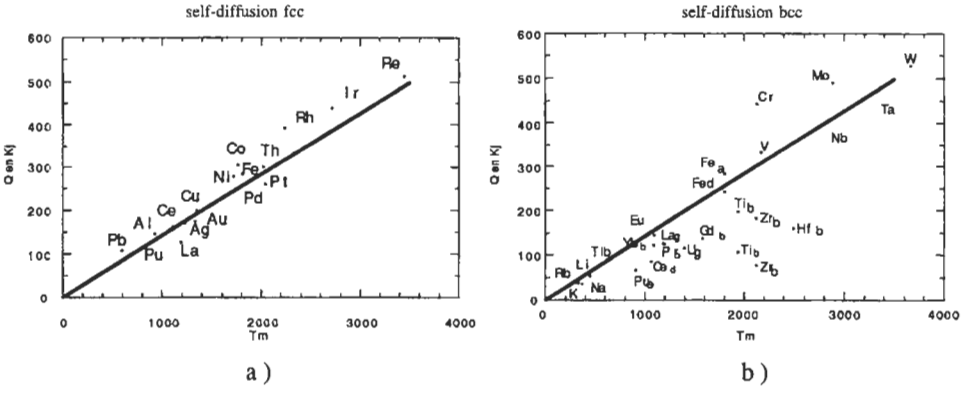

Fig. 8. Van Liempt relation for metals. Fig 8a) fcc metals, fig 8b) bcc metals. The straight line represents the Van Liempt relation: $Q = 0.14\ T_M$ in kJ/mole. bcc structures are widely dispersed around the line, contrarily to fcc ones.

References: p. 651.

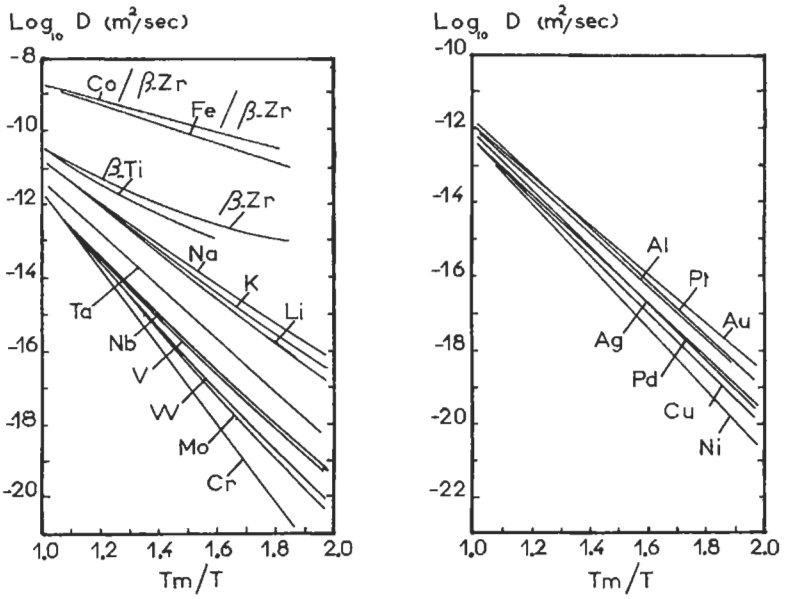

Fig. 9. Diffusion coefficients in an Arrhenius plot normalized to the melting point of the element considered. a) in fcc metals; the range of diffusion values is quite narrow and the curvatures, if any, are small. b) same curves in bcc metals; the diffusion coefficient varies widely from one element to the other according to a systematics controlled by the row number in the Mendeleev classification, the curvatures also are frequently strong.

3.1. Self-diffusion in fcc and hcp metals

The vacancy assumption for the diffusion in these metals is now well accepted by everyone (but see also § 4.2.2). Nevertheless there are still some controversies as regard to the origin of the possible curvature of the Arrhenius plots. In order to explain this curvature, three hypotheses can be retained among all the possibilities which have been discussed in § 1.4.3.1.:

– A vacancy mechanism occurs over the whole temperature range but because of a strong thermal expansion coefficient for the vacancy, (GILDER and LAZARUS [1975]), or due to the variation of the elastic constants with the temperature, (VAROTSOS and ALEXOPOULOS [1986]), D_0 and Q increase with temperature.

– Both vacancies and divacancies contribute to the diffusion, with an increasing participation of the latter at high temperatures (SEEGER and MEHRER [1970]).

Table 2
Self-diffusion parameters for pure elements.

Element (see comments at end)	C.S.	T_m (K)	D_0 (m^2s^{-1})$\times 10^4$	Q (kJ/mole)	Temp. range (K)	$Q = .1422T_m$ Van Liempt	$D(T_m)(m^2s^{-1})$	D (ph. tr.) (m^2s^{-1})	Reference
Ag	fcc	1234	$D_{01} = 0.046$ $D_{02} = 3.3$	$Q_1 = 169.8$ $Q_2 = 218.1$	594–994	175.5	4.9×10^{-13}		REIN and MEHRER (1982)
Al	fcc	933	2.25	144.4	673–883	132.7	1.85×10^{-12}		BEYELER and ADDA (1968)
Au	fcc	1336	0.084	174.1	1031–1333	190	1.3×10^{-12}		HERZIG *et al.* (1978)
Be	hex	1560	$\perp$ c 0.52 // c 0.62	157.4 165	836–1342 841–1321	221.8 id	2.79×10^{-10} 1.85×10^{-10}		DUPOUY *et al.* (1966)
Ca	bcc	1116	8.3	161.2	773–1073	158.7	2.36×10^{-11}		PAVLINOV *et al.* (1968)
Cd	hex	594	$\perp$ c 0.18 // c 0.12	82 77.9	420–587 id	84.5 id	1.11×10^{-12} 1.69×10^{-12}		MAO (1972)
Ce γ $T<999$	fcc	γ/δ 999	0.55	153.2	801–965	152.3*		5.37×10^{-13} (999 K)	DARIEL *et al.* (1971)
Ce δ $T>999$	bcc	1071	0.007	84.7	1018–1064	152.3	4.9×10^{-11}	2.36×10^{-11} (999 K)	LANGUILLE *et al.* (1973)
Co	fcc	1768	2.54	304	944–1743	251.4	2.65×10^{-13}		LEE *et al.* (1988)
Cr	bcc	2130	1280	441.9	1073–1446	302.9	1.86×10^{-12}		MUNDY *et al.* (1981)
Cu	fcc	1357	$D_{01} = 0.13$ $D_{02} = 4.6$	$Q_1 = 198.5$ $Q_2 = 238.6$	1010–1352	193	5.97×10^{-13}		BARTDORFF *et al.* (1978)
Er	hex	1795	$\perp$ c 4.51 // c 3.71	302.6 301.6	1475–1685 id	255.2	7.05×10^{-13} 6.2×10^{-13}		SPEDDING and SHIBA (1972)
Eu	bcc	1099	1	144	771–1074	156.2	1.43×10^{-11}		FROMONT and MARBACH (1977)
Fe α $T<1183$	bcc	α/γ 1183	121	281.6	1067–1168	257.2*		4.45×10^{-15} (1183 K)	GEISE and HERZIG (1987)
Fe γ $1183<T<1663$	fcc	γ/δ 1663	0.49	284.1	1444–1634	257.2*		1.4×10^{-17} (1183 K) 5.83×10^{-14} (1663 K)	HEUMAN and IMM (1968)
Fe δ $T>1663$	bcc	1809	2.01	240.7	1701–1765	257.2	2.25×10^{-11}	5.5×10^{-12} (1663 K)	JAMES and LEAK (1966)

Element	C.S.	T_m (K)	D_0 (m^2s^{-1}) $\times 10^4$	Q (kJ/mole)	Temp. range (K)	$Q = .1422T_m$ Van Liempt	$D(T_m)(m^2s^{-1})$	D (ph. tr.) (m^2s^{-1})	Reference
Gd β	bcc	1585	0.01	136.9	1549–1581	225.4	3.07×10^{-11}		FROMONT and MARBACH (1977)
Hf α $T<2013$	hex	α/β 2013	$\perp$ c 0.28 // c 0.86	348.3 370.1	1538–1883 1470–1883	355.5*		2.56×10^{-14} 2.14×10^{-14} (2013 K)	DAVIS and MCMULLEN (1972)
Hf β $T>2013$	bcc	2500	0.0011	159.2	2012–2351	355.5	5.19×10^{-11}	8.13×10^{-12} (2013 K)	HERZIG *et al.* (1982)
In	tetr	430	$\perp$ c 3.7 // c 2.7	78.5 78.5	312–417 id	61.1 id	1.08×10^{-13} 7.85×10^{-14}		DICKEY (1959)
Ir	fcc	2716	0.36	438.8	2092–2664	386.2	1.3×10^{-13}		ARKHIPOVA (1986)
K	bcc	336	$D_{01} = 0.05$ $D_{02} = 1$	$Q1 = 37.2$ $Q2 = 47$	221–335	47.8	1.32×10^{-11}		MUNDY *et al.* (1971)
La β $T<1134$	fcc	β/γ 1134	1.5	188.8	923–1123	169.6*		3×10^{-13} (1134 K)	DARIEL *et al.* (1969)
La γ $T>1134$	bcc	1193	0.11	125.2	1151–1183	169.6	3.62×10^{-11}	1.88×10^{-11} (1134 K)	LANGUILLE and CALAIS (1974)
Li	bcc	454	$D_{01} = 0.19$ $D_{02} = 95$	$Q1 = 53$ $Q2 = 76.2$	220–454	64.5	3.13×10^{-11}		HEITJANS *et al.* (1985)
Mg	hex	922	$\perp$ c 1.75 // c 1.78	138.2 139	775–906	131.1	2.59×10^{-12} 2.37×10^{-12}		COMBRONDE and BRÉBEC (1971)
Mo	bcc	2893	8	488.2	1360–2773	411.4	1.22×10^{-12}		MAIER *et al.* (1979)
Na	bcc	371	$D_{01} = 57$ $D_{02} = 0.72$	$Q1 = 35.7$ $Q2 = 48.1$	194–370	52.7	1.75×10^{-11}		MUNDY (1971)
Nb	bcc	2740	0.524	395.6	1354–2690	389.6	1.5×10^{-12}		EINZIGER *et al.* (1978)
Ni	fcc	1726	$D_{01} = 0.92$ $D_{02} = 370$	$Q1 = 278$ $Q2 = 357$	815–1193	245.4	9.35×10^{-13}		MAIER *et al.* (1976)
Pb	fcc	601	0.887	106.8	470–573	85.4	4.63×10^{-14}		MILLER (1969)
Pd	fcc	1825	0.205	266.3	1323–1773	259.5	4.9×10^{-13}		PETERSON (1964)

Element	C.S.	T_m (K)	D_0^- (m^2s^{-1})$\times 10^4$	Q (kJ/mole)	Temp. range (K)	$Q=.1422T_m$ Van Liempt	$D(T_m)$(m^2s^{-1})	D (ph. tr.) (m^2s^{-1})	Reference
Pr β $T>1068$	bcc	1205	0.087	123.1	1075–1150	171.3	4×10^{-11}		DARIEL *et al.* (1969)
Pt	fcc	2042	$D_{01}=0.06$ $D_{02}=0.6$	$Q1=259.7$ $Q2=365$	850–1265	290.3	1.4×10^{-12}		REIN *et al.* (1978)
Pu β $395<T<480$	m	β/γ 480	0.0169	108	409–454	129.8*		2.98×10^{-18} (480 K)	WADE *et al.* (1978)
Pu γ $480<T<588$	ort	γ/δ 588	0.038	118.4	484–546	129.8*		4.95×10^{-19} (480 K) 1.15×10^{-16} (588 K)	WADE *et al.* (1978)
Pu δ $588<T<730$	fcc	δ/δ' 730	0.0517	126.4	594–715	129.8*		3.05×10^{-17} (588 K) 4.66×10^{-15} (730 K)	WADE *et al.* (1978)
Pu ε $T>753$	bcc	913	0.003	65.7	788–849	129.8	5.22×10^{-11}	8.3×10^{-12} (753 K)	CORNET (1971)
Rb	bcc	312	0.23	39.3	280–312	44.4	6.05×10^{-12}		HOLCOMB and NORBERG (1955)
Re	hex	3453		511.4	1520–1560	491			NOIMANN *et al.* (1964)
Rh	fcc	2239		391	903–2043	318.4			SHALAYEV *et al.* (1970)
Sb	trig	904	$\perp$ c 0.1 // c 56	149.9 201	773–903	128.5	2.17×10^{-14} 1.36×10^{-14}		CORDES and KIM (1966)
Se	hex	494	$\perp$ c 100 // c 0.2	135.1 115.8	425–488	70.2	5.18×10^{-17} 1.1×10^{-17}		BRÄTTER and GOBRECHT (1970)
Sn	tetr	505	$\perp$ c 21 // c 12.8	108.4 108.9	455–500	71.8	1.29×10^{-14} 6.9×10^{-15}		HUANG and HUNTINGTON (1974)
Ta	bcc	3288	0.21	423.6	1261–2993	467.5	3.9×10^{-12}		WERNER *et al.* (1983)
Te	trig	723	$\perp$ c 20 // c 0.6	166 147.6	496–640	102.8	2.03×10^{-15} 1.3×10^{-15}		WERNER *et al.* (1983)
Th α $T<1636$	fcc	α/β 1636	395	299.8	998–1140	287.7*			SCHMITZ and FOCK (1967)
Ti α $T<1155$	hex	α/β 1155	6.6×10^{-5}	169.1	1013–1149	275.8*		1.48×10^{-16} (1155 K)	DYMENT (1980)

Element	C.S.	T_m (K)	D_0 (m^2s^{-1}) $\times 10^4$	Q (kJ/mole)	Temp. range (K)	$Q = .1422T_m$ Van Liempt	$D(T_m)$(m^2s^{-1})	D (ph. tr.) (m^2s^{-1})	Reference
Ti β $T>1155$	bcc	1940	$D(m^2s^{-1}) = 3.5\times10^{-4}\times \exp(-328/RT)\times\exp\{4.1\ (T_m/T)^2\}$		1176–1893	275.8	3.11×10^{-11}	5.4×10^{-14} (1155 K)	KÖHLER and HERZIG (1987)
Tl α $T<507$	hex	α/β 507	$\perp$ c 0.4 // c 0.4	94.6 95.9	420–500	82*		7.16×10^{-15} 5.2×10^{-15} (507 K)	SHIRN (1955)
Tl β $T>507$	bcc	577	0.42	80.2	513–573	82	2.3×10^{-12}	2.29×10^{-13} (507 K)	CHIRON and FAIVRE (1985)
U α $T<941$	ort	α/β 941	0.002	167.5	853–923	199.8*		1×10^{-16} (941 K)	ADDA and KIRIANENKO (1962)
U β $941<T<1048$	tetr	β/γ 1048	0.0135	175.8	973–1028	199.8*		2.35×10^{-16} (941 K) 2.33×10^{-15} (1048 K)	ADDA *et al.* (1959)
U γ $T>108$	bcc	1405	0.0018	115.1	1073–1323	199.8	9.46×10^{-12}	3.29×10^{-13} (1048 K)	ADDA and KIRIANENKO (1959)
V	bcc	2175	1.79 26.81	331.9 372.4	1323–1823 1823–2147	309.3	3.05×10^{-12}		ABLITZER *et al.* (1983)
W	bcc	3673	$D_{01} = 0.04$ $D_{02} = 46$	$Q_1 = 525.8$ $Q_2 = 665.7$	1705–3409	522.3	1.7×10^{-12}		MUNDY *et al.* (1978)
Y α $T<1752$	hex	α/β 1752	$\perp$ c 5.2 // c 0.82	280.9 252.5	1173–1573	256.4		2.19×10^{-12} 2.43×10^{-12} (1752 K)	GORNY and ALTOVSKII (1970)
Yb α $T<993$	hex	α/β 993	0.034	146.8	813–990	156*		6.4×10^{-14} (993 K)	FROMONT *et al.* (1974)
Yb β $T>993$	bcc	1097	0.12	121	995–1086	156	2.08×10^{-12}	5.18×10^{-12} (993 K)	FROMONT *et al.* (1974)
Zn	hex	693	$\perp$ c 0.18 // c 0.13	96.3 91.7	513–691	98.5	9.92×10^{-13} 1.59×10^{-12}		PETERSON and ROTHMAN (1967)
Zr α $T<1136$	hex	α/β 1136	no value	Curved Arrh. plot	779–1128	302*		$\approx5\ 10^{-18}$ (1136 K) 6.14×10^{-14} (1136 K)	HORVATH *et al.* (1984)
Zr β $T>1136$	bcc	2125	$D(m^2s^{-1}) = 3\times10^{-5}\times \exp(-3.01/RT)\times \exp\{3.39(T_m/T)^2\}$		1189–2000	302	1.37×10^{-11}		HERZIG and ECKSELER (1979)

Comments on table

These self diffusion data have been extracted from the compilation by MEHRER *et al.* (Ref. B).

Column 1: Symbol of the metal.

Column 2: Crystal stucture. bcc = body centered cubic, fcc = face centered cubic, hex = hexagonal, m = monoclinic, ort = orthorhombic, tetr = tetragonal, trig = trigonal.

Column 3: Melting temperature. For the phases which do not melt (for instance Ce γ, Fe α etc.) we have given the temperature of the phase transition.

Column 4: Experimental D_0. The value in m^2s^{-1} is multiplied by 10^4 (so that it is in cm^2s^{-1}).
For some of the metals the Arrhenius plot is curved and D has the form: $D = D_{01}\exp(-Q_1/RT) + D_{02}\exp(-Q_2/RT)$, in these cases D_{01} and D_{02} are given (they are also multiplied by 10^4).
For Ti and Zr which have strongly curved Arrhenius plots special expressions are given for D (in m^2s^{-1}without any multiplying factor).

Column 5: Experimental Q in kJ $mole^{-1}$. Same remarks as for column 4.

Column 6: Temperature range of the experimental determination of D.

Column 7: Empirical value of Q according to the Van Liempt relation. For the phases which do not melt this value is followed by an *.

Column 8: Value of D at the melting point.

Column 9: For metals which display several phases the values of D are given at the temperature boundaries of the phase. For instance U_β is stable between 941 and 1048 K, D values at these temperatures are given in column 9.

Column 10: References.

– A vacancy mechanism occurs and the curvature is due to the dynamical correlation between successive jumps (vacancy double jumps) (DA FANO and JACUCCI [1977]).

Experimentally the following data are available: frequency factor D_0, activation energy Q, isotope effect E and activation volume ΔV. When the Arrhenius plot is curved, we notice that D_0 and Q increase with T whereas E decreases; for example, for silver self-diffusion, E decreases from 0.72 to 0.58 when T increases from 673 to 954°C. Any of the three assumptions can explain these experimental data: the decrease with temperature of the isotope effect is obvious for the mixed vacancy–divacancy mechanism since the correlation factor for the divacancy mechanism is smaller than for the vacancy mechanism. As a result, since the contribution of the divacancies to the diffusion increases with T, the apparent correlation factor and then the isotope effect will decrease. But this variation of E with T can also be explained with the two other assumptions. Likewise the variation of D_0 and Q with T is compatible with all three hypothesis. The variations of ΔV with P and T have not been frequently studied; in the case of silver ΔV increases with T, but remains constant for gold and aluminium. The increase with T has been interpreted as resulting from an increase of the divacancy contribution at high temperatures (REIN and MEHRER [1982]).

However, measurements of defect properties after quenching can only be understood if vacancies *and* divacancies are present (PETERSON [1978]); in addition, the analysis of tracer and NMR data on self-diffusion in sodium seems also to favour the mixed vacancy–divacancy mechanism (BRÜNGER *et al.* [1980]). Although these two statements are not very general *a consensus does exist in favour of the mixed vacancy–divacancy mechanism*. Thus, in general when the Arrhenius plots are curved the data are fitted by assuming a two-defect mechanism; in addition a possible dependence of enthalpies and entropies on temperature is sometimes taken into account (see for instance SEEGER and

MEHRER [1970] or PETERSON [1978]). Nevertheless the discussion is still open, since divacancies might also be formed *during* the quench, and the role of divacancies is among the "Unsolved Problems" for some experts (MUNDY [1992]).

In hcp metals the limited number of available data is compatible with a slight decrease of the ratio of the activation energies of the diffusion parallel to perpendicular to the c axis with increasing *c/a* ratio, the activation energies being the same in the ideal lattice (HOOD [1993]).

3.2. Diffusion in bcc metals

Self-diffusion in bcc metals presents three characteristics which do not comply with the previous picture. At first there is a much larger scatter of the diffusivity in bcc metals than in the compact phases, and some of them display an unusually large absolute value of D (fig. 9b); second, they frequently exhibit much larger curvatures than the fcc or hcp systems, much to large to be accounted for by a divacancy contribution; last they show a systematic variation of D with the position in the classification which has to be explained, e.g. metals of the same column, like Ti, Zr, Hf in the group 4, have for all of them a very small activation energy and a large curvature (fig 9b). Many explanations have been proposed in order to account for these anomalies: strong contribution of short-circuits, presence of extrinsic vacancies due to impurities, interstitial mechanisms, etc. All these assumptions have been ruled out by experiments. The very origin of this behaviour is now recognized to be linked to the electronic structure of the metal and to the structural properties of the bcc lattice.

At first the diffusion mechanism is now proved by quasi elastic neutron scattering experiments, to be the vacancy one with nearest-neighbour jumps, either in sodium (AIT SALEM *et al.* [1979]) or in β-Ti (PETRY *et al.* [1991]). A small fraction of N.N.N. jumps could also contribute, the fraction being independent of temperature. The same mechanism very likely is also at work in other bcc metals.

The key point now is the recognition that the bcc structure is intrinsically soft with respect to some specific shear deformations; moreover this intrinsic softness can be enhanced (as in β-Ti) or lowered (as in Cr) according to specific features of the electronic structure controlled by the number of d electrons (HO *et al.* [1983, 1984]). This softness is the very origin of the numerous martensitic phase transformations observed between bcc and hcp or ω phases, under ambient or high pressure in several of the metals displaying a range of stability in the bcc structure. It is also manifested by the presence in the phonon dispersion curves of a whole branch of soft phonons at large wave vector, from the longitudinal $q = 2/3[111]$ to the $q = 1/2[110]$ phonons. These phonons are precisely the ones which control most efficiently both the jump of the vacancy and the martensitic bcc to hcp phase transformation (1/2 [110]) or to ϖ phase (2/3 [111]). Being of low frequency, they contribute to large fluctuations of the reaction coordinate and therefore give rise to a small migration enthalpy as well as to high diffusion coefficients (see § 1.4.2.2 and eq. (52–53)) (HERZIG and KÖHLER [1987], PETRY *et al.* [1991]). Using experimental dispersion curves, in the framework of the dynamical theory, it is possible to calculate migration enthalpies in good agreement with the

experimental values (SCHOBER *et al.* [1992]). In this respect the 1/2[110] phonon is twice as efficient as the 2/3[111] one to promote the jump (WILLAIME [1991]).

Moreover, using inelastic neutron diffraction methods, the 1/2[110] phonon has been shown to be strongly anharmonic and to soften as temperature decreases in the "most curved" metals (Ti, Zr and Hf) (PETRY and col. [1991]). In this approach the curvature of the Arrhenius plots also can be qualitatively explained, as well as the decrease of the isotopic effect with decreasing temperature (from 0.285 at 916°C to 0.411 at 1727°C in Zr), in contrast with the data of isotope effects in self-diffusion in other structures.

In this picture the whole of the effect appears to be due to the migration term, being small and T-dependent. However we can also expect that these soft phonons will be linked with large relaxations around the vacancy, corresponding to specific features also for the formation contribution in bcc metals. Indeed it is recognized (SCHULTZ [1991], SCHOBER *et al.* [1992]) that in this respect Cr displays an anomalously large formation enthalpy and Ti an anomalously small one. In Cr the 1/2[110] phonon softens with increasing temperature. Since the diffusion activation enthalpy appears to be a constant in the whole temperature range, the formation enthalpy should then increase with T according to the preceding analysis (SCHOBER *et al.* [1992]). The analysis of the electronic structure of bcc metals indeed allows for a systematic variation of the vacancy properties with the number of d electrons: due to the presence of a quasi-band gap in the band structure for a number of electrons of 4, and a maximum around 2, the above mentioned variations of formation terms can be understood (WILLAIME and NASTAR [1994]).

Negative activation volumes have been found for δ-Ce and ε-Pu, pointing possibly to an interstitial diffusion mechanism resulting from specific electronic structure effects (CORNET [1971]).

In alkali metals the migration enthalpy is very low, of the order of one tenth of the formation part (SCHULTZ [1991]). The calculated vacancy formation enthalpy also forms a very important part of the experimental activation enthalpy, or is even greater than it. An interpretation in term of a Zener ring mechanism (see § 1.1.1), has been recently proposed (SEEGER [1993]).

3.3. Prediction of the self-diffusion coefficients

There are three possible ways to predict the diffusion coefficients:
- by theoretical calculations;
- by simulation (see § 1.5.)
- by empirical laws.

3.3.1. Theoretical calculations of D

Using one of the theories given in paragraph 1.4 and 1.5, the calculation of the enthalpies and entropies of formation and migration of the defect involved in the diffusion mechanism allows the determination of the diffusion coefficient. The techniques used in this type of calculation are beyond the scope of this review and we refer the

reader to the general references at the end of this chapter and to specialized treatises, for instance GERL and LANNOO [1978] (see also ch. 18 by WOLLENBERGER).

3.3.2. Empirical relations

Empirical relations are numerous, and we only present the most important;

– *The Zener formula* (ZENER [1951]). This has been established for interstitial solutions and therefore deals only with migration. The idea is that the migration free enthalpy is due to the elastic work required to strain the lattice so that the interstitial can jump. The relation has been empirically extended to self-diffusion. This expression relates the entropy of diffusion ΔS to the activation energy Q via Young's modulus (or shear modulus):

$$\Delta S = \frac{\lambda \beta Q}{T_M}$$

where λ is a constant which depends on the lattice ($\lambda = 0.55$ for fcc and 1 for bcc); $\beta = -\mathrm{d}\,(\mu/\mu_0)/\mathrm{d}\,(T/T_M)$, where μ is Young's modulus (or shear modulus) and μ_0 the value of μ at 0 K; T_M is the melting temperature. The review by LAZARUS [1960] shows that there is a pretty good agreement between experimental and calculated values of ΔS.

– *The Varotsos formula* (VAROTSOS [1978], VAROTSOS and ALEXOPOULOS [1986]). This is based on the idea that the free enthalpy of diffusion has the form $\Delta G = CB\Omega$, where C is a constant which depends on the lattice, B is the bulk modulus (the inverse of the compressibility χ) and Ω the atomic volume. Thus for cubic materials:

$$D = a^2 \nu \exp\left(-\frac{CB\Omega}{kT}\right) \qquad B = \frac{1}{\chi} = -V\frac{\partial P}{\partial V}$$

The agreement with experimental data seems fairly good.

– *Other empirical relations.* These include the *Van Liempt relation*: $Q = 32\ T_M$ (at present one prefers $Q = 34\ T_M$); the *Nachtrieb relation*: $Q = 16.5\ L_M$ (at present one prefers $Q = 15.2\ L_M$), L_M is the latent heat of melting; finally the *Keyes relation*: $\Delta V = 4\chi Q$, where ΔV is the activation volume.

4. *Self- and solute-diffusion in dilute alloys*

This section recalls the expressions of the tracer diffusion coefficients, correlation factors, and phenomenological coefficients L_{ij}'s as functions of the atomic jump frequencies in the frame of standard models which are today widely accepted as good descriptions of impurity effect in diffusion studies. The two methods which have been currently used in the past to establish the expression of the L_{ij}'s are also briefly reviewed. Finally, it is recalled how to determine the atomic jump frequencies starting from the experimental determination of various macroscopic quantities, together with the difficulties usually encountered.

The first part of this section deals with the substitutional alloys for which the vacancy mechanism is expected to be dominant. A short second part deals with the interstitial

dumbbell mechanism in substitutional alloys, since this case is encountered in irradiation experiments. The third part deals with those alloys which do not meet the requirements of a "normal" diffusion behaviour and in which the solute diffusivity is often much larger than the solvent diffusivity.

4.1. Vacancy diffusion in dilute A-B alloys

4.1.1. Standard models for bcc and fcc alloys

In the fcc lattice, the difference between the first and second neighbour distances is large enough to allow us to ignore the interaction between a solute atom and a vacancy beyond the nearest-neighbour distance. The same dissociative jump frequency w_3 is therefore attributed to the three possible dissociative jumps (fig. 10) which separate a vacancy from a neighbouring solute atom; w_4 is the frequency of the reverse jump. w_2 stands for the solute-vacancy exchange and w_1 for the vacancy jump around the solute atom which does not break the solute-vacancy complex. w_0 is a jump not affected by the solute atom. Detailed balancing implies that:

$$w_4/w_3 = \exp(-E_B/kT)$$

where E_B is the binding energy of the vacancy–solute pair (E_B is negative for an attractive binding). This is the so-called "five-frequency model".

All the physical quantities which will be compared to experimental diffusion data in dilute alloys are functions of only three independent ratios of these five jump frequencies, namely w_2/w_1, w_3/w_1 and w_4/w_0.

In the bcc lattice, conversely, the second-neighbour distance is close to the first-neighbour distance and the solute–vacancy interaction energy is not negligible at the second-neighbour distance. Four distinct dissociative frequencies are defined for a vacancy escaping from the first-neighbour shell (w_3, w_3' and w_3'') and from the second-neighbour shell (w_5). The frequencies of the reverse jumps are w_4, w_4', w_4'' and w_6, respectively (fig. 11). The solute–vacancy exchange frequency is w_2. If we denote the interaction energies at the first- and second-neighbour distances by E_{B1} and E_{B2}, respectively, detailed balancing requires that:

$$w_4'/w_3' = w_4''/w_3'' = \exp(-E_{B1}/kT)$$

$$w_6/w_5 = \exp(-E_{B2}/kT)$$

$$w_6 w_4/w_5 w_3 = w_4'/w_3'$$

The calculation of tracer diffusion coefficients has never been performed with the whole set of frequencies. Simplifying assumptions have always been made to reduce the large number of unknown parameters.

– *MODEL I* assumes that $w_4' = w_4'' = w_6 = w_0$. These equalities imply in turns $w_3' = w_3''$ and $w_3 w_5 = w_3' w_4$. All the physical quantities which will be compared to experimental data can be expressed as function of w_3/w_3' and w_2/w_3' only.

— *MODEL II* restricts the interaction to first neighbour distances and assumes that $w_3 = w_3' = w_3''$ and $w_5 = w_6 = w_0$. These equalities imply $w_4 = w_4' = w_4''$. The physical

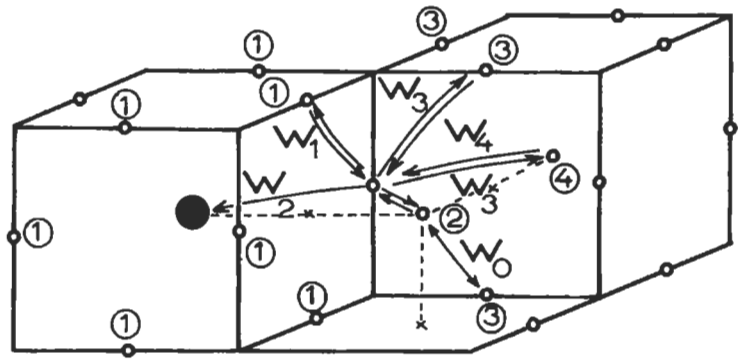

Fig. 10. Standard five-frequency model for solute diffusion in fcc lattices by a vacancy mechanism. The encircled figures denote more and more distant shells of neighbours around the solute atom (solid circle).

quantities which are to be compared with the experimental data are function of w_2/w_3 and w_4/w_0 only.

4.1.2. Kinetic expressions of the phenomenological coefficients L_{AA}, L_{AB}, L_{BA} and L_{BB}

The purpose of the calculation is to express these coefficients as functions of the jump frequencies, the solute and vacancy concentrations, and the various interaction energies between the species. Two methods have been used so far.

4.1.2.1. Kinetic theory. In this theory, also-called pair association method, the stationary fluxes J_A, J_B and J_V are calculated in the presence of a constant electric field E, which biases the jump frequencies of the vacancy. The bias can take two distinct values, ε_A and ε_B, according to the chemical nature of the atom which exchanges with the vacancy. Hence:

$$w_2^{\pm} = w_2(1 \pm \varepsilon_B), \qquad w_i^{\pm} = w_i(1 \pm \varepsilon_A) \text{ for } i \neq 2$$

where the superscript ± stands for a jump fequency in the direction of the electric field (+) or in the reverse direction (–). It can be shown that ε_A and ε_B are proportional to the thermodynamic forces $Z_A^* eE$ and $Z_B^* eE$, respectively, which act upon the species A and B. The final kinetic expressions of the fluxes are then compared with the phenomenological expressions in order to deduce the L_{ij}'s.

For an fcc lattice, the calculation has been carried out at first order in C_B and to an increasing degree of accuracy by including more and more distant shells from the solute (HOWARD and LIDIARD [1963], MANNING [1968], BOCQUET [1974]). For a bcc lattice the calculation has been published in the frame of the two approximations quoted above (SERRUYS and BREBEC [1982b]). For both structures, the common form of the results is the following:

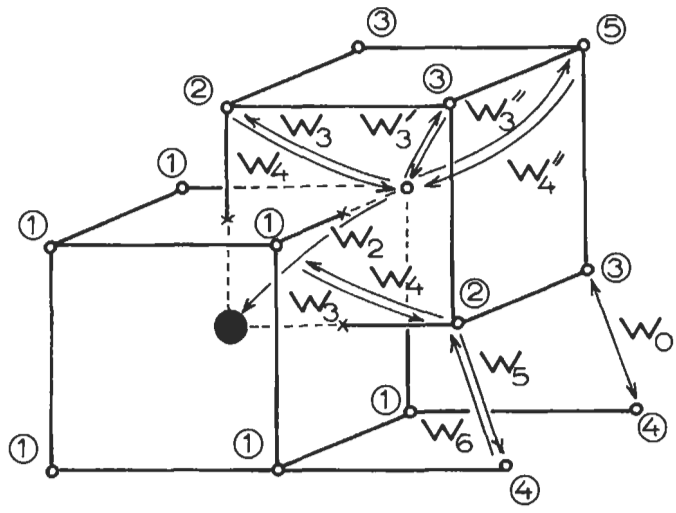

Fig. 11. Standard model for solute diffusion in bcc lattices by a vacancy mechanism.

$$L_{AA} = \frac{nD_{A^*}(0)}{f_0 kT}\left(1 + b_A C_B\right)$$

$$L_{AB} = L_{BA} = \frac{nC_B D_{B^*}(0)}{kT} G$$

$$L_{BB} = \frac{nC_B D_{B^*}(0)}{kT}$$

where n is the number of lattice sites per unit volume; D_{A^*} (0) and D_{B^*} (0) are the solvent and solute tracer diffusion coefficients in pure A ($C_B = 0$); G is the *vacancy wind* term L_{AB}/L_{BB} which accounts for the coupling between J_A and J_B through the vacancy flux J_V. Tables 3 and 4 summarize the expressions of D_{A^*} (0), D_{B^*} (0), b_A and G for both structures. A comprehensive series of papers by FRANKLIN and LIDIARD [1983, 1984], and LIDIARD [1985, 1986] gives a full account of a synthetic reformulation for this method.

The function **F**, always smaller than unity, is a correction to the escape frequency w_3 or w_3' which accounts for that fraction of the vacancies which finally returns in the neighbourhood of a tracer atom: the same function appears in the expression of the correlation factor and in the phenomenological coefficients for all the models where the solute vacancy interaction is restricted to a first neighbour distance (fcc model and bcc model II). More functions appear in the other case (bcc model I). The accuracy in the calculation of these functions increases with the size of the matrix used for the random walk calculation of the defect. The first evaluations (MANNING [1964]) have been recently revised by integral methods (KOIWA and ISHIOKA [1983]). In the same way, the

Table 3
Theoretical expressions of various quantities entering the phenomenological coefficients in an fcc lattice ($f_0 = 0.78145$)

$$D_{A^*} = 2s^2 C_v w_0 f_0, \qquad D_{B^*}(0) = 2s^2 C_v \frac{w_4}{w_3} w_2 f_B;$$

$$u = w_2/w_1, \qquad v = w_3/w_1, \qquad w = w_4/w_0;$$

$$D_{A^*}(C_B) = D_{A^*}(0)(1 + b_1 C_B);$$

$$f_B = (2 + 7\mathbf{F}v)/(2 + 2u + 7\mathbf{F}v);$$

$$b_1 = -34 + 16\frac{X_3}{f_0} + \frac{w}{f_0}\left(4\frac{X_1}{v} + 14X_2\right);$$

$$G = \frac{(3v - 2) + (7 - 7\mathbf{F})v(1/w - 1)}{1 + 3.5\mathbf{F}v};$$

$$b_A = -19 + w(4/v + 14) - \frac{14(1 - \mathbf{F})(1 - w)\left[3v - 2 + (1 + u + 3.5v)(1/w - 1)\right] + (w/v)(3v - 2)^2}{1 + u + 3.5\mathbf{F}v};$$

$$7\mathbf{F} = 7 - \frac{10w^4 + 180.3122w^3 + 924.3303w^2 + 1338.0577w}{2w^4 + 40.1478w^3 + 253.3w^2 + 595.9725w + 435.2839}$$

C_v is the vacancy concentration in pure A; s is the jump distance.

expression of the linear enhancement factor for self-diffusion b_1 contains coefficients X_1, X_2 and X_3 for the fcc lattice and X_1, X_2, X_3 and X_4 for the bcc one: these coefficients are functions of the partial correlation factors for the different solvent jump types in the vicinity of an impurity; they reduce identically to f_0 when all the jumps frequencies are equal, that is, for the case of self-diffusion. They have been numerically tabulated for the fcc lattice (HOWARD and MANNING [1967]) as well as for the bcc lattice (LE CLAIRE [1970b], JONES and LE CLAIRE [1972]). Defining a larger number of solvent jump types, revised and more accurate values have been obtained recently (ISHIOKA and KOIWA [1984]).

4.1.2.2. Linear response method. In the linear response method, a time-dependent (but spatially uniform) external field E(t) is applied to the alloy and instantaneous values of the fluxes J_A, J_B and J_V are calculated. It is shown that the calculation of the L_{ij}'s reduces to the solution, by a Green's function method, of closely related random-walk problems in the unperturbed (E = 0) state of the system. This general formalism has been adapted for the first time to mass transport in solids (ALLNATT [1965]): all the possible trajectories of the vacancy around the tracer atom are automatically taken into account and not only those contained in a few coordination shells, as was done in the pair association method.

The formalism has been illustrated by an application to various cubic structures (ALLNATT [1981], OKAMURA and ALLNATT [1983a]) and has confirmed (and generalised) the results previously obtained by the kinetic method, namely the general

Table 4
Theoretical expressions of various quantities entering the phenomenological coefficients in a bcc lattice ($f_0 = 0.72714$)

$$D_{A^*}(0) = \frac{4}{3} s^2 C_v w_0 f_0 \qquad D_{B^*}(0) = \frac{4}{3} s^2 C_v w_2 \frac{w_4'}{w_3'} f_B \qquad f_B = \frac{7\mathbf{F}w_3'}{2w_2 + 7\mathbf{F}w_3'}$$

$$D_{A^*}(C_B) = D_{A^*}(0)(1 + b_1 C_B)$$

Quantity	Expression	
	Model I	Model II
u	w_3/w_3'	w_4/w_0
v	w_2/w_3'	w_2/w_3
b_1	$-38 + \dfrac{6X_1 u + 8X_2}{f_0} + \dfrac{6X_3 + 18X_4}{f_0}$	$-38 + \dfrac{6X_1 + 8X_2}{f_0} u + \dfrac{6X_3 + 18X_4}{f_0}$
$\mathbf{F}_2$	$(u-2)^2 + 2\mathbf{F}_4(u-2)(u-1) + 3\mathbf{F}_3(3u + 3.096)$	
$\mathbf{F}_3$	$\dfrac{(u-1)^2}{u + 0.8082}$	
$\mathbf{F}_4$	$\dfrac{u + 0.1713}{u + 0.8082}$	
G	$-2\dfrac{(u-2) + \mathbf{F}_4(u-1)}{7\mathbf{F}\, A_1}$	$2\dfrac{u - 7(1-\mathbf{F})(u-1)}{7\mathbf{F}u}$
b_A	$7 + 6u - 2\dfrac{\mathbf{F}_2 + 2\mathbf{F}_3 v}{2v + 7\mathbf{F}}$	$-15 + 14u\left[1 - (1-F)\left(\dfrac{u-1}{u}\right)^2\right] - 2\dfrac{u^2 - 7(1-\mathbf{F})(u-1)^2}{(2v + 7\mathbf{F})u}$
$7\mathbf{F}$	$\dfrac{2u^2 + 5.175u + 2.466}{u + 0.8082}$	$\dfrac{3u^3 + 33.43u^2 + 97.38u + 66.06}{u^3 + 8.68u^2 + 18.35u + 9.433}$

forms for the phenomenological coefficients, and the number of distinct functions $\mathbf{F}$ to be used (ALLNATT and OKAMURA [1984]). Finally, the equivalence between the kinetic and linear response methods has been demonstrated by LIDIARD [1987], and ALLNATT and LIDIARD [1987a]: the former theory focusses on the jumps of a given chemical

References: p. 651.

species when paired to the defect which causes its migration and is well suited to dilute alloys where such pairs can be easily defined; the latter follows the path of a given species by separating it into a direct part when in contact with a defect, and a correlated part where the immobile species waits for the return of the defect. It is more general and can be applied to concentrated alloys (see below § 5).

4.1.3. Experimentally accessible quantities

We restrict ourselves to the experiments which are commonly used to deduce the vacancy jump frequencies at the root of the models for bcc and fcc lattices.

The measurements performed on pure solvent A consist in determining:
– the solvent and solute tracer diffusivities $D_{A^*}(0)$ and $D_{B^*}(0)$;
– the isotope effect for solute diffusion, $f_B \Delta K_B$. The ΔK_B factor must be evaluated in some way to extract f_B. Several theories have tried to determine ΔK_B as a function of the ratio m_B/m_0 where m_B and m_0 are the masses of the solute and of the solvent respectively (ACHAR [1970], FEIT [1972]): but they apparently do not fit with the experiments performed in lithium (MUNDY and MCFALL [1973]).

The measurements of alloying effects are performed on dilute A-B alloys and comparison is made with the same quantities determined in pure A, in order to extract the slope of the linear resulting variation. These measurements usually determine:
– The linear enhancement factor b_1 for solvent tracer diffusion $D_{A^*}(C_B)$, defined by

$$D_{A^*}(C_B) = D_{A^*}(0)(1 + b_1 C_B).$$

Tables 3 and 4 give the expressions for the enhancement factor b_1 which contain the coefficients X_1, X_2 and X_3 for the fcc lattice and X_1, X_2, X_3 and X_4 already defined above.

The solute diffusion coefficient D_{B^*} also varies linearly with the solute concentration, according to:

$$D_{B^*}(C_B) = D_{B^*}(0)(1 + B_1 C_B).$$

The expression of B_1 has been calculated only in the frame of simplified models which do not take into account the solvent partial correlation factors in the presence of solute pairs. But it introduces additional frequencies of the vacancy in the vicinity of two solute atoms (which were not necessary for b_1) as well as the binding energy between solute atoms. A thorough overview has been presented recently on this point (LE CLAIRE [1993]). It is experimentally observed that b_1 and B_1 often have the same sign and are roughly of equal magnitude whenever the diffusion mechanism is the same for A^* and B^* in the alloy (it is not true in Pb-based alloys, § 4.2.2). This means physically that the preponderant effect of the solute is to increase (or decrease if b_1, is negative) the total vacancy concentration, which affects solvent and solute diffusivity roughly to the same extent.
– The linear enhancement factors b_M and b_T for the shift of inert markers and solvent tracer markers in an electric field. If we denote the rates of these shifts by V_M and V_T, b_M and b_T are defined according to:

$$V_M(C_B) = V_M(0)(1 + b_M C_B), \quad V_{A^*}(C_B) = V_{A^*}(0)(1 + b_T C_B)$$

b_M and b_T have been calculated as functions of the vacancy jump frequencies (DOAN [1972]; BOCQUET [1973]; DOAN and BOCQUET [1975]; LIMOGE [1976a]) and are given by:

$$b_T = b_A + 1 + f_0 G \frac{Z_B^*}{Z_A^*} \frac{D_{B^*}(0)}{D_{A^*}(0)} \qquad b_M = b_A + f_0 \frac{D_{B^*}(0)}{D_{A^*}(0)} \left[\frac{Z_B^*}{Z_A^*}(1 + G) + G \right]$$

– The vacancy wind term $G = L_{AB}/L_{BB}$ can be measured from the solute enrichment or depletion in the neighbourhood of a sink (ANTHONY [1971, 1975]) or by combining tracer diffusion experiments with Kirkendall shift measurements in differential couples A + A – B (HEUMANN [1979]; HOSHINO *et al.* [1981a]; HAGENSCHULTE and HEUMANN [1989]).

4.1.4. Determination of vacancy jump frequencies

Jump frequencies depend on the interatomic potential which should, in principle, be deduced from ab-initio calculations. Unfortunately an accurate knowledge of these potentials is far from being currently acquired, except for particular systems, and one usually proceeds differently. Jump frequencies are instead fitted to the experimental results.

As already mentioned, diffusion data yield only three jump frequency ratios for an fcc lattice and only two for a bcc one; thus only three independent measurements are required in the former case and two in the latter. Any additional result is highly desirable and is used to check the consistency of the experiments. If this consistency cannot be maintained in view of a new result, this may mean that one (or more) experimental results are not worthy of confidence or that the model does not correctly represent the experimental system.

All the dilute alloys of fcc structure, for which we know the jump frequency ratios, are displayed in table 5. Whenever the number of experiments is equal to three, one reference only is quoted. When the experimental data are redundant, several references are given. The error bars on the final values of these ratios are large: at least 50% for the best cases, up to an order of magnitude for the worst. We have to keep in mind that any ratio which departs too much from unity (say less than 10^{-2} or larger than 10^2) may be an indication that the weak perturbation assumption at the root of the model is violated in the alloy under consideration. A similar table of jump frequency ratios has been published elsewhere (HERZIG *et al.* [1982]). For bcc alloys, similar tables can be found in fairly recent reviews (LE CLAIRE [1978], AGARWALA [1984]).

The search for the frequency ratios is not always straightforward, as can be seen from the following examples:

– Al-Cu: the value of the self-diffusion coefficient is still today highly controversial. At 585 K it is measured or evaluated to be 1.66 10^{-13} m^2/s (FRADIN and ROWLAND [1967]), 3.03 10^{-13} m^2/s (SEEGER *et al.* [1971]), 3.66 10^{-13} m^2/s (BEYELER and ADDA [1968]), 3.73 10^{-13} m^2/s (LUNDY and MURDOCK [1962]) and 4.51 10^{-13} m^2/s (PETERSON and ROTHMAN

Table 5
Jump frequency ratios for dilute fcc alloys.

Alloy	T(K)	D_{B^*}/D_{A^*}	f_B	b_1	b_T	G	Ref.	w_2/w_1	w_3/w_1	w_4/w_0
Ag–Cd	1060	3.8	0.41	4			c	2.6	0.3	0.85
	1133	3.28	0.71	9.2			b	0.49	0.07	0.52
	1153	3.18		6.5	−12		a	0.5	0.07	0.46
	1197	2.96	0.62	13.7			b	1.7	0.8	1.7
Ag–In	1064	5.7	0.35	17.5			c	4.7	0.7	1.9
Ag–Sn	1043	5.8	0.46	15.6			c	1.8	0.2	1.1
Ag–Zn	1010	4.1	0.52	12.6			d	1.53	0.27	1.15
	1153	3.9	0.57	12.7			d	1.54	0.39	1.30
	1153	3.9		12.7	6		a	1.20	0.26	1.12
Au–In	1075	8.6	0.26	71			e	212	45	5.5
	1175	7.5	0.26	49			e	40	7.3	4.2
Au–Sn	1059	16.4	0.16	130			e	NO SOLUTION		
		16.4	0.16	73			f	1.5	1.2	6.3
	1129	12.93		73		−0.5	n	31.2	4.2	7.1
Au–Zn	1058	6.2	0.15	24			e	942	85	2.9
	1117	5.7	0.15	23			e	973	85	2.6
Cu–Au	1133	1.15	0.9	8.1			g	0.2	0.1	0.6
Cu–Cd	1076	10.2		35		−0.7	h	0.1	1	3
	1076	10.2	0.22	35			h	7.6	0.6	2.8
Cu–Co	1133	0.81	0.85	0			g	2	4.2	1.2
	1133	0.81	0.88	0			g	0.3	0.4	0.76
Cu–Fe	1293	1.1	0.8	−5			i	0.4	0.09	0.3
Cu–In	1005	13.3		42		−0.71	j	18	0.5	3
	1089	11.4		43		−0.57	j	11	1	4
	1089	12	0.07	43			e	33	0.8	3.2
Cu–Mn	1199	4.2	0.36	5			c	3.4	0.35	0.95
Cu–Ni	1273	0.36		−5		0.07	k	0.2	1	1
	1273	0.36		−5.3		0.12	l	0.27	0.42	0.53
Cu–Sb	1005	24.1		79		−1.2	j	15	0.40	5
Cu–Sn	1014	15.5		40		−1.06	j	13	0.2	2
	1014	17	0.15	40			e	7.5	0.14	1.7
	1089	13.6		48		−0.84	j	7	0.33	3
	1089	14.1	0.15	48			e	11	0.5	3.3
Cu–Zn	1168	3.56	0.47	7.3			m	2.5	0.5	1.2
	1168	3.3		8		−0.22	k	3	0.5	1
	1220	3.4	0.47	8.8			m	3.6	0.9	1.5

[a] DOAN and BOCQUET [1975]; [b] BHARATI and SINHA [1977]; [c] HERZIG *et al.* [1982]; [d] ROTHMAN and PETERSON [1967]; [e] HILGEDIECK [1981]; [f] REINHOLD *et al.* [1980]; [g] ECKSELER and HERZIG [1978]; [h] HOSHINO *et al.* [1981b]; [i] BOCQUET [1972]; [j] HOSHINO *et al.* [1982]; [k] HIRANO [1981]; [l] DAMKÖHLER and HEUMANN [1982]; [m] PETERSON and ROTHMAN [1971]; [n] HAGENSCHULTE and HEUMANN [1989].

[1970]). Using ANTHONY's result, which establishes that no detectable solute redistribution occurs in the neighbourhood of a vacancy sink, very different values of $G = L_{AB}/L_{BB}$ are deduced according to the value which is retained for the self-diffusion coefficient. It is easy to check that one obtains $G = -0.4; -0.01; +0.203; +0.226$, and $+0.43$, respectively. The jump frequency ratios which stem from such scattered values of G are highly different of course; in addition they do not fit with the measurement of inert marker shifts in dilute alloys (LIMOGE [1976a]).

Finally, according to SEEGER *et al.* [1971], 40% of the total diffusivity at 858 K is due to divacancies. This fact cannot be ignored any longer, and a revised version of the atomic model should be presented to take properly into account the contribution of the divacancies to diffusion and electromigration.

– Au-Sn: the extracted value for b_1 is sometimes very sensitive to the way chosen for the fitting whenever $D_{A^*}(C_B)$ exhibits a pronounced curvature. A rough fitting extracts a value which is not compatible with the other data and does not allow to deduce the jump frequency ratios (HERZIG and HEUMANN [1972]); a more careful fitting gives reasonable values (REINHOLD *et al.* [1980]). It must be noted however that the direct measurement of the vacancy flow factor G at a slightly different temperature on dilute couples yields noticeably different values (HAGENSCHULTE and HEUMANN [1989]): the departure from the previous ones cannot be accounted for by the small temperature difference, or would imply unusually high activation energies for these frequency ratios.

Although the partial correlation factors are not analytically known, it is possible to check the internal consistency of the experimentally determined quantities in the frame of a given diffusion mechanism. For instance, once the ratio D_{B^*}/D_{A^*} is known, a constraint on the possible values for u,v and w is imposed, which in turn, restrains the possible range for other quantities like b_1 or G. For instance, b_1 is kept to a minimum if the vacancy spends most of its time in exchanging with the solute ($u = w_2/w_1 \to \infty$) and keeping the exchanges with the solvent to the lowest possible value which is compatible with the solute diffusion ($v = w = 0$). Assuming that $X_3 = f_0$ and using the tabulated value $X_1(u \to \infty, v = w = 0) = 0.4682$ yields (MILLER [1969]):

$$b_1^{\min} = -18 + 1.945 \frac{D_{B^*}}{D_{A^*}}$$

If the experimental value for this term is noticeably smaller, it means that the vacancy mechanism alone cannot account for the diffusional behaviour of the system and that, probably, other diffusion mechanisms must be looked for. A similar limitation has been established for the bcc structure, although no simple analytical formula is available (LE CLAIRE [1983]). In the same spirit, it has been shown that the vacancy flow term G in bcc alloys ranges from –2 to a maximum value which depends on the same ratio D_{B^*}/D_{A^*} and on the model (I or II) to be chosen (IIJIMA *et al.* [1985]).

– Pb-Cd: self-diffusion in lead meets the usual requierements of normal diffusion. On the other hand, the solute diffusivity is roughly 20 times larger than the solvent diffusivity: this fact alone is not an indisputable proof that another mechanism is operating. MILLER

[1969] pointed out that the linear enhancement factor b_1 exhibited a value which was noticeably smaller than b_1^{min}. This is the reason why he proposed a new mechanism with interstitial-vacancy pairs (§ 4.2.2).

Like the fcc alloys, there are several bcc systems in which the b_1 factor is too small to be compatible with the high value of the solute-to-solvent diffusivity ratio, namely Zr-based alloys (Co, Cr, Fe), Ti–Co, Nb–Fe and U–Co. The isotope effect measurements, when available in these systems (ABLITZER [1977]; ABLITZER and VIGNES [1978]), are not compatible with the frequency ratios in the frame of a pure vacancy mechanism: another mechanism resting on a dissociative model similar to MILLER's one for Cd in Pb is commonly thought to come into play.

4.1.5. Determination of the solute–vacancy binding energy

The only relevant quantity for determining the binding energy E_B of the solute–vacancy complex is the ratio w_4/w_3, which cannot be deduced from the knowledge of w_2/w_1, w_3/w_1 and w_4/w_0.

DIRKES and HEUMANN [1982] worked out a simple procedure for simulating the vacancy trajectory around the solute and proposed to extract from this trajectory the desired quantity. It is true that the only knowledge of the ratios w_2/w_1, w_3/w_1 and w_4/w_0 is sufficient to determine, at each step of a Monte Carlo simulation, the direction of the most probable next jump. But these authors used an incorrect definition of the vacancy concentration on a first neighbour site of the solute. This concentration is not related to the number of times that the vacancy was located on a first-neighbour site of the solute, but rather to the time the vacancy actually spent on this site.

This definition needs the knowledge of the mean residence time of the vacancy on each site (that is, the inverse of the total escape frequency from this site). It is easily checked that the fraction of the total time which has been spent on a first-neighbour site involves one more independent frequency ratio w_1/w_0 (BOCQUET [1983a]). Moreover, the assumption $w_2 + 4w_1 + 7w_3 = 12w_0$ which is invoked here and there in the diffusion literature for the fcc alloys has no physical justification and is totally arbitrary.

Diffusion experiments by themselves are not sufficient to determine this binding energy. Experiments of another kind must be added: for instance a direct determination of the total vacancy concentration in a dilute alloy, by comparing the macroscopic thermal expansion and the increase in lattice parameter as already done for Al–Ag and Al–Mg (BEAMAN *et al.* [1964]; BEAMAN and BALLUFFI [1965]).

4.2. Dumb-bell interstitial diffusion in dilute A-B alloys

The self-interstitial atom in a compact structure is too large to content itself with an octahedral or tetrahedral position as smaller solute atoms do; it minimizes the distortion of the surrounding lattice by sharing a lattice site with a neighbouring atom and making up a dumb-bell-shaped defect denoted by I_{AA} aligned along <100> (<110>) direction in a fcc (bcc) structure. The migration mechanism involves a translation to a first neighbour site combined to a rotation of its dissociation axis (see chap. 18). The diffusion coeffi-

cient of a substitutional solute atom has been calculated with this mechanism at work for bcc and fcc lattices, under the assumption that it can be incorporated into the defect under the form of a mixed dumb-bell I_{AB} which does not possess necessarily the same symmetry (BOCQUET [1983b, 1991]); the phenomenological coefficients have been calculated for the fcc lattice by the kinetic method (ALLNATT *et al.* [1983]) as well as by the linear response one (OKAMURA and ALLNATT [1986], CHATURVEDI and ALLNATT [1992], SINGH and CHATURVEDI [1993]). But these models cannot be checked experimentally as thoroughly as in the vacancy case, since the frequencies cannot be determined by a clever combination of diffusion experiments; the interstitial defects are necessarily produced by irradiating the solid, and their contribution to diffusion is intricately linked with that of thermal and irradiation-produced vacancies.

4.3. A-B alloys with a high solute diffusivity

4.3.1. Purely interstitial solutes

Light elements like H, C, N, O are known to dissolve interstitially in many bcc and fcc metals. No theoretical criterion has yet been found to predict with confidence the localization of the interstitial atom in the host lattice. In many bcc metals C, O and N are believed to be located on octahedral sites; but dual-occupancy models (octahedral + tetrahedral position) have been invoked to account for the upward curvature of their Arrhenius plot at high temperatures (FARRARO and MCLELLAN [1979]). For the case of hydrogen, a simple empirical rule has been proposed (SOMENKOV and SHIL'STEIN [1979]): H dissolves in the tetrahedral position in all the host metals which have an atomic radius larger than 0.137 nm (Sc, Ti, Y, Zr, Nb, La, Hf, Ta, W) and in the octahedral position for the others (Cr, Mn, Ni, Pd). Vanadium is the link between the two groups and is believed to have a dual occupancy. In Fe, H is expected to be located in octahedral sites although no clear experimental proof has ever been given. The insertion into the host lattice is accompanied by a (generally) large distortion of the surroundings, which can give rise to Snoek-type or Gorsky-type relaxations (§ 2.2).

Although in an interstitial location, the solute atom is believed to interact with vacancies of the host; the diffusivity and the phenomenological coefficients have been calculated with the linear response method (OKAMURA and ALLNATT [1983b]).

The diffusivity of such interstitials in metals has been measured over orders of magnitude by complementary techniques (relaxation methods, tracers, out-gassing, etc...). The Arrhenius plot is straight or exhibits a small curvature at high temperatures. This curvature has been tentatively explained by different models (FARRARO and MCLELLAN [1979]), either a single mechanism with a temperature-dependent activation energy or several mechanisms (or defects) acting in parallel.

For very light interstitials like hydrogen and its isotopes, or the positive muon μ^+, quantum effects play a significant role at low temperatures. Several regimes are expected to be observed in the following order with increasing temperature (STONEHAM [1979]; KEHR [1978]):

(i) *coherent tunneling*, the interstitial propagates through the lattice like a free electron;

(ii) *incoherent (or phonon-assisted) tunneling*, the ground state levels of an occupied and an unoccupied interstitial site have different energies; the tunneling process requires the assistance of phonons which help to equalize the levels of neighbouring sites;
(iii) *classical regime*, the jumping atom receives from the lattice the amount of energy which is required to overcome the potential barrier of the saddlepoint configuration;
(iv) *high-temperature regime*, the residence time on a site is comparable to the time of flight between two neighbouring sites.

The second and third regimes have been observed in many systems. Whether coherent tunneling can actually be observed in real systems or not is still controversial (STONEHAM [1979]; GRAF *et al.* [1980]).

Let us mention the reversed isotope effect which is observed in fcc metals at low temperatures: tritium is found to diffuse faster than deuterium, which diffuses faster than hydrogen. Several models have been proposed to account for this anomaly (TEICHLER [1979]; KAUR and PRAKASH [1982]). See also ch. 18, § 3.3.2.7 for the interaction of self-interstitials with solute atoms.

4.3.2. Complex diffusion mechanisms

The most widely studied case is that of dilute Pb-based alloys.

In lead, several solute atoms (Cu, Ag, Au, Pd, Ni, Zr) diffuse from 10^3 to 10^6 times faster than the solvent tracer. Other elements (Na, Bi, Sn, Tl) diffuse roughly at the same rate. A third group (Cd, Hg) diffuses at rates between the two extremes. It is well established that these properties are in no way related to any short-circuit diffusion path and that they reflect a bulk property. We already mentioned in § 4.1.4 why a pure vacancy mechanism should be rejected for cadmium diffusion in lead.

The high value of the diffusivities led many investigators in the past to think in terms of an interstitial-like diffusion mechanism; it can be shown however, by particular examples, that a purely interstitial mechanism would not yield a value of the linear enhancement factor b_1 consistent with experiment. This is why many authors proposed more complex mechanisms involving interstitial-vacancy complexes, interstitial clusters, and today the consensus is roughly as follows:
– very fast diffusers dissolve partly as substitutionals and partly as interstitials in lead. The total diffusivity is therefore the sum of both contributions; pairs made up of an interstitial solute and a host vacancy are expected to play a dominant role; the phenomenological coefficients L_{ij} have been calculated for this mechanism (HUNTLEY [1974], OKAMURA and ALLNATT [1984]);
– multidefects (interstitial solute atoms sharing one substitutional lattice site) are necessary to account for the diversity of experimental results, especially for the signs and the orders of magnitude of the linear enhancement coefficients b_1 and B_1 (WARBURTON [1975], KUSUNOKI *et al.* [1981]), as well as for the low value of the isotope effect measurements;
– solute atoms which diffuse roughly as fast as the solvent dissolve presumably as substitutionals (except Sn: DECKER *et al.* [1977]);

A general and detailed atomic model including all these defects is still lacking, apart from an attempt by VANFLEET [1980]. The reader is referred to an extensive review by

WARBURTON and TURNBULL [1975].

Lead is not a unique case however, since similar problems arise in other polyvalent metals like Sn, In or Tl (WARBURTON and TURNBULL [1975]; LE CLAIRE [1978]), in the α-phase of Zr, Ti and Hf (HOOD [1993], NAKAJIMA and KOIWA [1993], KÖPPERS *et al.* [1993]), in bcc metals like Nb (ABLITZER [1977]; SERRUYS and BREBEC [1982a]), and for rare-gas diffusion (He) in fcc metals like Au, Ni, Al (WILSON and BISSON [1973]; MELIUS and WILSON [1980]; SCHILLING [1981]). The interaction energy between the smaller solutes and the intrinsic point defects of the host, namely the vacancy one, is believed to be high (above 1 eV); this feature, when combined with a very low solubility in the host, can lead to behaviours, which have puzzled the experimentalists for long. The general interpretation (KÖPPERS *et al.* [1993]) distinguishes three different temperature ranges: in the first (high-temperature) one, the native intrinsic vacancies are more numerous than those trapped by the impurity atoms, and the self-diffusion is normal; at intermediate temperatures (second range), the extrinsic vacancies trapped by the impurity atoms become dominant, and the apparent activation energy for self-diffusion is markedly decreased; at the lower temperatures (third range) where the impurity atoms precipitate into clusters, the number of trapping sites is reduced to such an extent that the intrinsic defects play again the dominant role. It ensues an unusual downward curvature of the Arrhenius plot over the low and intermediate temperature ranges. Depending on the ratio of the melting temperature to the α–β transformation temperature, the interaction energies between impurity and vacancies and between impurities themselves, not all the three regimes are automatically observed. In α-Zr, which has been for long the archetype, the (practically unavoidable) Fe impurity has been found to give rise to the regimes 2 and 3 with the downward curvature observed for self- as well as solute-diffusion; the determining experiments have been carried out only recently since ultra-high purity Zr was not available before (HOOD [1993]). For α-Hf, only regimes 1 and 2 are observed, but the impurity which is responsible of the upward curvature is not yet identified (KÖPPERS *et al.* [1993]). At last for α-Ti, the impurity is believed to be oxygen which is easily incorporated into this highly reactive metal (NAKAJIMA and KOIWA [1993]).

5. *Diffusion in concentrated alloys*

We shall restrict ourselves to binary alloys. The first two sections are devoted to the diffusion of A* and B* tracer atoms in homogeneous disordered and ordered alloys. The third section will deal with chemical diffusion, that is, diffusion in the presence of chemical gradients.

5.1. Diffusion of A* and B* tracers in homogeneous disordered alloys

5.1.1. Experimental results

Diffusion measurements in concentrated binary alloys are legion, but only few alloys have been investigated throughout the whole composition range: Ag–Au (MALLARD *et al.* [1963]), Au–Ni (KURTZ *et al.* [1955]; REYNOLDS *et al.* [1957]), Co–Ni (MILLION and KUCERA [1969, 1971], HIRANO *et al.* [1962]); Cu–Ni (MONMA *et al.* [1964]), Fe–Ni

(CAPLAIN and CHAMBRON [1977], MILLION *et al.* [1981]), Fe–Pd (FILLON and CALAIS [1977]), Ge–Si (MCVAY and DUCHARME [1974]), Nb–Ti (GIBBS *et al.* [1963]; PONTAU and LAZARUS [1979]), Pb–Tl (RESING and NACHTRIEB [1961]). For Fe–Ni, the diffusion has been studied both through a magnetic relaxation method which yields apparent values for the formation and migration energies of the vacancy and by tracers.

Two general trends can be outlined:

– The same kind of empirical correlation as for self-diffusion in pure metals are observed between the preexponential factors D_0 and the activation energy Q, or between Q and the melting temperature T_m of the alloy.

– The diffusion coefficients $D_{A^*}^{AB}$ and $D_{B^*}^{AB}$ for a given temperature and composition do not differ by more than one order of magnitude. When they do, it might be an indication that the diffusion mechanism for the two tracers is not the same (Ge–Si or Pb–Tl). Some cases still offer matter for controversy, like Ge–Si alloys (PIKE *et al.* [1974]). For brevity, $D_{A^*}^{AB}$ and $D_{B^*}^{AB}$ will be denoted by D_{A^*} and D_{B^*} in what follows.

5.1.2. Manning's random alloy model

In this model, the simplest which can be thought of, the alloy is assumed to be random and the vacancy exchanges at rate w_A with A atoms, and w_B with B atoms, whatever the detailed atomic configuration of the local surroundings (fig. 12). The most important finding lies in the fact that the vacancy no longer follows a random walk; its successive jumps are correlated and a vacancy correlation factor f_V smaller than unity shows up in the final expressions (MANNING [1968], [1971]):

$$D_{A^*(B^*)} = \lambda s^2 C_V f_{A(B)} w_{A(B)} \qquad D_V = \lambda s^2 f_V \bar{w}$$

where $f_v = (C_A w_A f_A + C_B w_B f_B)/f_0$ and $f_0 = M_0/(M_0 + 2)$ is the correlation factor for self-diffusion, $\bar{w} = C_A w_A + C_B w_B$, and finally, $f_{A(B)} = M_0 f_v\, \bar{w}/(M_0 f_v\, \bar{w} + 2w_{A(B)})$ for A(B).

Consistent expressions of the phenomenological coefficients L_{ij} have been established in this frame:

$$L_{AA} = n \frac{C_A D_{A^*}}{kT}\left(1 + \frac{2C_A D_{A^*}}{M_0 D^*}\right)$$

$$L_{AB} = L_{BA} = 2n \frac{C_A C_B D_{A^*} D_{B^*}}{kTM_0 D^*}$$

$$L_{BB} = \frac{nC_B D_{B^*}}{kT}\left(1 + \frac{2C_B D_{B^*}}{M_0 D^*}\right)$$

where n is the average number of sites per unit volume, and D^* is the average $C_A D_{A^*} + C_B D_{B^*}$. At last it can be easily shown that the vacancy wind corrections showing up in the expressions of the intrinsic diffusivities [see eqs. (17)] are given by:

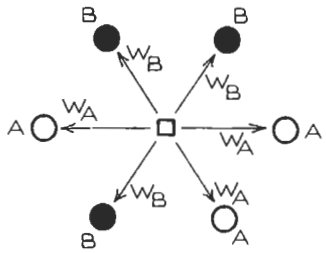

Fig. 12. Manning's random alloy model.

$$r_A = 1 + 2\frac{C_A(D_{A^*} - D_{B^*})}{M_0 D^*}$$

$$r_B = 1 + 2\frac{C_B(D_{B^*} - D_{A^*})}{M_0 D^*}$$

The L_{ij}'s are not independent since they are functions of D_{A^*} and D_{B^*} only; they obey the relationship:

$$L_{AB} = \frac{f_0(L_{AA} + L_{BB})}{2(1 + f_0)}\left[\left(1 + 4\frac{(1 - f_0^2)L_{AA}L_{BB}}{f_0^2(L_{AA} + L_{BB})^2}\right)^{1/2} - 1\right]$$

The same expressions have been later recovered following two different routes:

i) in a formal derivation resting on two macroscopic assumptions related to the invariance of the functional relationship between mobility and flux between the pure substance and the average alloy (LIDIARD [1986]);

ii) in a mean-field treatment of the diffusion problem, resting on the adoption of a preliminary consistency equation over the diffusivities, namely:

$$C_A D_{A^*} + C_B D_{B^*} = f_0 C_v D_v$$

the right-hand side of the above equality being nothing but the tracer self-diffusivity in the average alloy (BOCQUET [1987]).

Manning's approximation appeared fascinating and very appealing since the only independent quantities are the easily accessible tracer diffusivities. It has been the object of very numerous Monte Carlo simulations, which can take into account the detailed occupancy of the sites surrounding the vacancy and can check the accuracy of the approximation. These simulations essentially show that the approximation is indeed quantitatively excellent over the whole concentration range, as long as the disparity between the jump frequencies is not too large, say $10^{-3} < W_A/W_B < 10^3$ (BOCQUET [1973], DE BRUIN *et al.* [1975], [1977], ALLNATT and ALLNATT [1984]). An analytical more sophisticated method for the self-consistent decoupling of the kinetic equations has been worked out and yields the same conclusion (HOLDSWORTH and ELLIOTT [1986], ALLNATT [1991]). Even in dilute alloys, the approximation turns out to be satisfactory

for all quantities but the linear enhancement factor b_1 (ALLNATT and LIDIARD [1987b]).

In the same spirit, the same kind of approximation has been worked out for the dumbbell interstitial mechanism in random two-frequency alloys on fcc and bcc lattices. Although no simple analytical expressions can be established for the tracer diffusivities (BOCQUET [1986]), a similar functional dependence of the L_{ij}'s versus the D_{i*}'s as above can be proposed after replacing f_0 by the product $f_0\mu_0$ (BOCQUET [1987]), where μ_0 is the ratio of the tracer average squared jump length to that of the defect. $\mu_0 = 1/2$ for fcc structures and 7/15 for bcc ones (BOCQUET [1983b, 1991]). The numerical simulations show a good agreement only in special cases for the fcc lattice, and a disagreement for all the cases investigated in the bcc lattice (BOCQUET [1990b]): the reason for these discrepancies has not been elucidated so far, in spite of a recent treatment involving the more sophisticated linear response method (CHATURVEDI and ALLNATT [1994]).

5.1.3. Atomic models for diffusion in non-random disordered alloy

The attempts to improve the alloy model beyond the random approximation and to include the effect of short-range ordering on diffusion have historically followed two different routes.

The first one consisted in extending the dilute alloy models by including more and more solute clusters of increasing size together with the corresponding modifications of the solute and solvent jump frequencies in their neighbourhood. This route turned out to be not well fitted to this purpose, due to the rapidly increasing number of unknown parameters which yielded intractable results, together with the intrinsic impossibility to deal with cluster overlap (BOCQUET [1973]); only rough approximations can be proposed by selecting a few solute clusters which are believed to have a dominant influence (FAUPEL and HEHENKAMP [1987]). But this choice is totally arbitrary and physically unjustified; as a consequence, this route has now been abandoned.

The second route, at the expense of some loss of accuracy, approximates the effect of the local surroundings on the height of the potential barrier by using a small number of pair interaction energies for the stable (E_{ij}) and the saddle-point (E'_{ij}) configurations. The merit of such a description lies in the fact that it connects simply and consistently the thermodynamics (reflected in the E_{ij}'s) and the kinetic behaviour of the alloy (reflected in the E'_{ij}'s). The model was used first to account for the kinetics of short-range ordering in Ag–Au alloys (RADELAAR [1968, 1970]) and Fe–Ni alloys (CAPLAIN and CHAMBRON [1977]). Later it was improved to take into account correlation effects in short-range ordered alloys (STOLWIJK [1981], ALLNATT and ALLNATT [1992]): the analytical formula obtained for the tracer diffusivities and the associated correlation factors are in fair agreement with Monte-Carlo simulations over a reasonably large range of the thermodynamic parameter mastering the order, namely $[2\,E_{AB} - (E_{AA} + E_{BB})]/kT$. The agreement deteriorates to some extent for the lower temperatures where systematic departures show up.

Independently from the search for better expressions of the D_{i*}'s, a systematic investigation of the phenomenological coefficients L_{ij}'s has been carried out numerically by simulating non-random alloys using such pair energies; and the most intriguing result of the last ten years is that the functional dependence of the L_{ij}'s upon the D_{j*}'s

established by Manning for random alloys is still preserved in non-random ones with a fairly good quantitative agreement (MURCH [1982a, 1982b, 1982c], ZHANG *et al.* [1989a], ALLNATT and ALLNATT [1991]), except at the lower temperatures or dilute concentrations; the latter restrictions are not a surprise, since they correspond to those actual situations where the departure from randomness is expected to be the largest. The basic reason for such an agreement is still not understood. Following previous tentative papers (HEUMANN [1979]; DAYANANDA [1981]), an active research effort has recently been undertaken to establish more general relationships between the L_{ij}'s and the various diffusivities (tracer, chemical) (ALLNATT and LIDIARD [1987c], LIDIARD *et al.* [1990], QIN and MURCH [1993a]).

Before closing this section, the main limitations of such models in the present state of the art must be recalled:

– they do not calculate D_{A^*} and D_{B^*} but only the activation energies for diffusion Q_{A^*} and Q_{B^*}, with the correlation effects included in the best case. The preexponential factors D_{0A} and D_{0B} are not known and are arbitrary assumed to remain constant, since no model is available which would account for their variations throughout the whole composition range.

– they use pair energies and assume implicitly that the energy of the alloy can be summed in this way, which is not always true (namely, transition metals). Even if effective pair energies can be defined, the electronic theory of alloys must be used to predict the variations of these pair energies as function of the composition on physically grounded arguments for each specific alloy (DUCASTELLE [1978]).

– finally, they cannot have any predictive power: while pair energies in the stable position can be deduced from thermodynamic measurements, saddle-point pair energies conversely can only be deduced from experiments involving diffusion jumps, that is, from the diffusion experiments themselves.

5.2. Diffusion of A^* and B^* tracers in ordered binary alloys

In the last ten years, intermetallics have been the object of intensive study for their attractive practical properties: some of them are indeed characterized by a high melting temperature, high elastic limit (see ch. 24), high resistance against corrosion and (or) creep (LIU *et al.* [1992]). Before reviewing in more detail the different ordered structures, some preliminary and general ideas should be recalled here.

The progress in the understanding of phase stability from *ab initio* calculations based on the local density functional approximation (LDF) has allowed research people to address very basic points, namely, the physical reasons leading a given alloy to adopt a well-defined structure or symmetry. Such calculations are able to explain the reason why Ti Al_3 is tetragonal (DO_{22}), while Ti_3 Al is hexagonal (DO_{19}) and Ti Al is cubic ($L1_0$); or why Ni_3 Al ($L1_2$) exists whereas there is no corresponding close-packed phase for Ni Al_3 (PETTIFOR [1992]). However, the problem of the point defects has not yet been addressed.

The existence of the so-called constitutional (or structural) defects is probably connected to the preceding point but has not yet received an unambiguous experimental

References: p. 651.

confirmation as well as a firmly grounded theoretical explanation. Starting with the simple case of the B2 structure as an illustration, the stoichiometric A-B alloy is perfectly ordered at 0 K and the N_A (N_B) atoms occupy the α (β)-sites. When the temperature is raised, several kinds of defect are believed to appear:
– *antistructure* or *substitutional defects*: A atoms can occupy β-sites and are denoted A_β, their number is $N_{A\beta}$, B atoms can occupy α-sites (B_α, $N_{B\alpha}$);
– *vacancies* denoted by V_α on α-sites and V_β on β-sites. Depending on the atomic interactions, the alloy will choose preferentially one type of defect or the other (or some combination of the two). Up to this point, these defects have been introduced as a pure manifestation of thermal excitation in a stoichiometric alloy.

However, for a non-stoichiometric alloy, one must think of the way to accommodate the departure from stoichiometry. The same defects (antistructure atoms or vacancies) have been also invoked; but in this case they are expected to be much more numerous than in the thermal case, since their concentrations will be of the order of the stoichiometry offset (up to several percent) and to survive even at O K unlike thermal ones. The difficult point in looking at actual systems at finite temperatures is to decide which part of the observed vacancies or antisite defects has a thermal origin and which part has a structural one. The undisputable fingerprint of structural defects (their non-null concentration at 0 K) is unfortunately very difficult to use practically: in many systems indeed, high concentrations of vacancies (at room temperature and above) have undoubtedly been evidenced by a careful comparison between density and lattice parameter measurements: but their apparent migration energy has often be found to be large, and one cannot safely state that equilibrium properties rather than quenched-in defects ones are measured. Phenomenological models like bond-breaking pictures (NEUMANN [1980], KIM [1991]) or the Miedema "macroscopic atom" model (DE BOER *et al.* [1988]) using rough expressions for configurational entropies cannot claim to be anything but guiding approximations to decide which type of defect is most likely to appear. A rapidly growing number of model defect calculations using semi-empirical potentials is presently observed (CLERI and ROSATO [1993], REY-LOSADA *et al.* [1993]) but the approximations involved are probably still too crude to solve this question. The problem requires undoubtedly accurate *ab initio* calculations of ground-state energies, together with a minimisation procedure which would allow charge transfers (KOCH and KOENIG [1986]), local relaxations as well as the settlement of an arbitrary vacancy concentration: such calculations would tell us whether the ternary (A,B,V) is most stable in the investigated lattice structure at low temperatures or whether a phase separation between ordered phases of other symmetries (and, or) concentrations occurs. If the existence of these *structural vacancies* can be theoretically proven, one must remember however that their properties are in no way different from those of the so-called *thermal* ones although they have received a different name. Indeed, the total vacancy concentration at finite temperatures minimizes the free-energy of the alloy: but in the present case, the existence of two sublattices and of suitable atomic interactions implies that the result of the calculation is more sensitive to a small variation of the composition, than to a temperature change, unlike the case of the disordered alloy at the same concentration.

Tracer diffusion measurements are still performed and are still highly desirable, as a

first insight into the transport mechanisms. Correlation factors have been calculated in various structures and for various jump mechanisms (BAKKER [1979], ARITA *et al.* [1989], WEILER *et al.* [1984], SZABO *et al.* [1991]). While isotope effects were measured with the hope of determining the jump mechanism, it was shown later that, for B2 structures, such a measurement does not yield the correlation factor (ZHANG *et al.* [1989b]); this is rather unfortunate since these (very difficult) experiments have been performed only on alloys with this symmetry (PETERSON and ROTHMAN [1971], HILGEDIECK and HERZIG [1983]).

Spectroscopic methods like nuclear magnetic resonance (NMR), quasi-elastic Mössbauer line broadening (QEMLB) and quasi-elastic neutron scattering (QENS) appear today as the best candidates to clarify the atomic diffusion mechanisms in ordered alloys; NMR techniques measure the frequency (ies) of the diffusing species (TARCZON *et al.* [1988]), while QEMLB and QENS give besides access to the individual jump vectors (see § 2.2.2 and VOGL *et al.* [1992]). Although some intermediate modelling is still necessary for the final interpretation, they yield the most confident information gained so far. The most important result obtained up to now is that diffusion in ordered structures seems to proceed simply via nearest-neighbour jumps of a vacancy defect. Finally, the ability of the positron annihilation (PA) technique to measure vacancy concentration with confidence is also being currently improved (BALOGH *et al.* [1992]).

The preceding point helps to solve old ill-formulated problems about the migration mechanisms in ordered alloys. The 6–jump cycle was initially designed for transporting atoms without altering the long-range order (MCCOMBIE and ELCOCK [1958], ELCOCK [1959], HUNTINGTON *et al.* [1961]): this condition is unnecessarily stringent since local and thermally activated fluctuations of the long-range order (LRO) must necessarily occur in a real system, the only requirement being the conservation of the average LRO through detailed balancing: this remark has been the starting point of a new formalism (Path Probability Method or PPM) for the evolution of cooperative systems (KIKUCHI [1966]; SATO [1984]). The 6–jump cycle is thus not necessary. Moreover, it is also very improbable: many computer simulations show that such cycles never go to completion and are destroyed while underway by strongly correlated backward jumps (ARNHOLD [1981]). In the same way, the triple defect has been introduced only for thermostatistical reasons (large difference between vacancy formation energies on both lattices): but it was implicitly thought that it should migrate as a whole, that is, without dissociating. This unnecessary constraint has led previous investigators to imagine a mechanism of highly concerted vacancy jumps (STOLWIJK *et al.* [1980], VAN OMNEN and DE MIRANDA [1981]), which has never been clearly evidenced neither experimentally nor theoretically.

At last, a growing body of practical knowledge has been gained through the use of macroscopic measurements like chemical diffusivity (DAYANANDA [1992]), kinetics of long range order recovery after irradiation or plastic deformation (CAHN [1992]), internal friction (GHILARDUCCI and AHLERS [1983]), degradation of superconducting temperature in A_{15} compounds (BAKKER [1993]): these experiments yield effective quantities which are of importance for mastering the practical properties of these materials. But a detailed atomistic model is still lacking which would link these effective energies to the usual parameters deduced from tracer diffusion experiments.

References: p. 651.

For sake of space, the reader will be referred to a recent compilation of experimental results (WEVER [1992]).

5.2.1. Ordered alloys with B2 structure

The B2 structure has been more extensively studied than the others: it is made of two interpenetrating simple cubic lattices, α and β. Each α-site is surrounded by eight first-neighbour β-sites and conversely. The existing alloys belong to two distinct groups:

(i) In the first group (AgCd, AgMg, AgZn, AuCd, AuZn, BeCu, BeNi, CuZn, NiZn) the defects are mainly antistructure defects on *both* sublattices (A_β and B_α) the departure from stoichiometry is compensated by A_β defects for A-rich alloys and B_α defects for B-rich alloys. The apparent formation energy E_F^V of thermal vacancies can be different on the two sublattices.

(ii) In the second group (CoAl, FeAl, NiAl, PdAl, CoGa, NiGa, PdIn), for which α will denote the sublattice of the transition metal A, maintenance of equal α and β site numbers allows formation of paired defects only ($A_\beta + B_\alpha$ or $V_\alpha + V_\beta$). If V_β costs more energy than $A_\beta + V_\alpha$, then $V_\alpha + V_\beta$ converts into the triple defect $A_\beta + 2V_\alpha$. Symmetrically, if B_α costs more than $2V_\alpha$ (mainly due to size effects), then $B_\alpha + A_\beta$ converts also into the same triple defect. The departure from stoichiometry is therefore compensated in two different ways: for an A-rich alloy the major defect is A_β; for a B-rich alloy, the major defect is V_α. In the latter case, very high structural vacancy concentrations on one sublattice are expected and (indeed) experimentally observed (up to 10% in CoGa on the gallium-rich side). All the theoretical calculations performed so far (e.g., EDELIN [1979]) are based on a zeroth-order treatment (BRAGG and WILLIAMS [1934]); not withstanding their crudeness, they account qualitatively well for all the presently known experimental situations, provided reasonable values of the adjustable pair energies E_{ij} are chosen.

A first and simple explanation has been proposed to account for the fact that a particular alloy belongs to the first or to the second group (NEUMANN [1980]). Using a crude bond-breaking picture, this author shows that the number of substitutional defects is dominant whenever the mixing enthalpy ΔH_f is (algebraïcally) higher than –0.3 eV/atom; the number of triple defects is dominant otherwise. It is very gratifying to ascertain that this correlation is very well obeyed. The existence of structural defects (namely in CoGa) has been however questioned recently on the basis of a similar model (KIM [1991]): but the controversy rests entirely on the relative values of the bond energies, which are nothing but phenomenological parameters and which cannot be extracted from experimental quantities by undisputable procedures.

In a growing number of experimental systems, a combination of lattice parameter and sample length measurements (SIMMONS and BALLUFFI's technique; ch. 18, § 2.2.2.2) yields the *total* vacancy concentration *increase* between a reference state at room temperature and the high temperature state: (CoGa: VAN OMNEN and DE MIRANDA [1981]; AlFe: HO and DODD [1978], PARIS and LESBATS [1978]; GaNi: HO *et al.* [1977], CoSc and InPd: WAEGEMAEKERS [1990]). The concentration of vacancies for the reference state is determined by a density measurement at room temperature. PA techniques have also been used, which confirm the previous determinations. But the concentration of anti-site defects is usually not directly reachable through spectroscopic

methods; only an indirect determination of their number is possible if such defects can be associated with some macroscopically measurable quantity. As an example, from the measurement of the quenched-in magnetisation of a Co–Ga alloy, the number of antisite atoms Co_{Ga}, which are the only Co atoms to be surrounded by like neighbours and, as such, are assumed to be the only ones to bear a magnetic moment, is indeed found equal to half of the number of vacancies. This beautiful result points strongly in favor of the very existence of the triple defect in this alloy (LO CASCIO [1992]).

Other experimental techniques are necessary in order to gain a sharper insight into the defect populations on each sublattice. First results have been obtained through positron annihilation in CuZn (CHABIK and ROZENFELD [1981]) or direct observation in a field ion microscope in AlFe (PARIS and LESBATS [1975]); but extracting meaningful values from the raw data requires a delicate analysis of positron trapping at vacancies for the first technique, and a careful analysis of image contrast for the second.

5.2.1.1. Experimental results. Most of the experiments measured the tracer diffusion coefficients D_{A^*} and D_{B^*} as a function of temperature and composition. The reader is referred to a recent compilation for the detailed results and references (WEVER [1992]]. Without entering into details, the following trends can be outlined:

– At constant composition, the activation energy for diffusion is higher in the ordered than in the disordered phase (when it exists). There is a break of the Arrhenius plot at the critical temperature T_c of ordering, and a large fraction of the increase in activation energy is due to correlation effects. In the ordered phase, the Arrhenius plot is often more or less curved (KUPER *et al.* [1956]). Simple models show that the migration and formation energies (E_M, E_F) of the vacancy and, therefore, the total activation energy Q, exhibit a quadratic dependence upon the long-range order parameter S (GIRIFALCO [1964]):

$$E_M = E_M^0\left(1 + \alpha_M S^2\right) \quad E_F = E_F^0\left(1 + \alpha_F S^2\right) \quad \text{and} \quad Q = Q_0\left(1 + \alpha_D S^2\right).$$

The experiments are not entirely conclusive however:

– In CuZn, the diffusion *coefficients* of Cu^* and Zn^* tracers (KUPER *et al.* [1956]) have been plotted logarithmically as function of $(1+\alpha_D S^2)/T$ (GIRIFALCO [1964]). The Arrhenius plot is a straight line only if the *theoretical* values S_{BW} of the long-range order parameter (BW stands for Bragg and Williams) are arbitrarily replaced by the *experimental* values S_{exp} which have been determined by X-ray measurements. It has been checked however that S_{exp} is not well accounted for by a Bragg–Williams approximation and that a more sophisticated treatment including short-range order (SRO) must be used instead (COWLEY [1950]). An interesting observation is that S^2_{Cowley} is equal to S_{BW} at the same temperature: therefore the quadratic dependence of Q upon S^2_{exp} can be interpreted as a linear dependence of Q on S_{BW} as well. The last difficulty lies in the fact that, as already mentioned above, most of the change in the activation energy comes from the temperature dependence of the correlation factor, which is not included in Girifalco's analysis.

– In AlFe alloys, the migration energy of the vacancies which have been retained by quenching varies roughly as S^2 (RIVIERE and GRILHE [1974]). But it is clear from the data that the results, within the error bars, can as well be accounted for by a linear law.

– In CoFe alloys, the observation of a Portevin–Le Chatelier effect is related to vacancy

migration and the effective migration energy varies quadratically over a large range of S extending from 0.1 to 0.9 (DINHUT *et al.* [1976]).

– At constant temperature, the diffusion coefficients vary with composition and exhibit a minimum at stoichiometry (or in the close neighbourhood of stoichiometry). This minimum is more or less pronounced (V-shaped curve for AgMg or AlNi) and corresponds to a maximum of the activation energy. The existence of this maximum is understandable, since the formation and migration energies of the vacancy are both increasing functions of the long-range order parameter which goes through a maximum at stoichiometry. D_{A^*} and D_{B^*} differ by no more than a factor of two or three for the alloys in which the defects are predominantly of substitutional type (AgMg, AuCd, AuZn).

– For alloys belonging to group ii), a marked asymmetry between hypo-and-hyper stoichiometric compositions is exhibited: very high vacancy contents show up which correspond to an excess of B component (Ga in NiGa and CoGa; Al in FeAl or CoAl). The difference between D_{A^*} and D_{B^*} is more pronounced than above for the alloys (between one and two orders of magnitude).The apparent vacancy formation energy is usually low (typically 0.4 eV per vacancy), and a minimum shows up at stoichiometry. An effective migration energy can also be determined by following the kinetics of thermal equilibration through the macroscopic length of the sample: the previous analysis of NiGa and CoGa in terms of two diffusion mechanisms (nearest-neighbour plus next-nearest-neighbour jumps: VAN OMNEN and DE MIRANDA [1981]) has been recently revisited: with the only assumption that the departure from the equilibrium value of the vacancy concentration follows a first order kinetics, it turns out that a simple vacancy mechanism with NN jumps only can account fairly well for the observed kinetics (WAEGEMAEKERS [1990]). A puzzling result however is that the sum of the effective formation and migration enthalpies is approximately equal to the activation energies for tracer diffusion in NiGa, but significantly lower in the case of CoGa.

5.2.1.2. Atomic mechanisms for diffusion in ordered B_2 alloys. Several atomic mechanisms have been proposed: nearest-neighbour (NN) or next-nearest-neighbour (NNN) jumps. The triple-defect (TD) has been unnecessarily assumed to migrate as a whole and the migration of the divacancy $2V_\alpha$ was supposed to occur through a correlated sequence of NN vacancy jumps with species A and NNN vacancy jumps with B. The direct determination of jump vectors has been performed only very recently on FeAl alloys. The most probable path for Fe diffusion consists of sequences of two consecutive NN jumps, implying a transitory residence on a β-site and resulting in the net displacements along <110>, <100> and <111> depicted on figure 13a (SEPIOL and VOGL [1993b]).

5.2.2. Ordered alloys with $L1_2$ structure

The $L1_2$ structure of the A_3B compound is such that the B component occupies one of the four sc lattices which make up the host fcc lattice: each B atom has twelve nearest-neighbour A atoms, whereas each A atom has four unlike neighbours and eight like ones. Due to this last property, it is commonly believed that A should diffuse

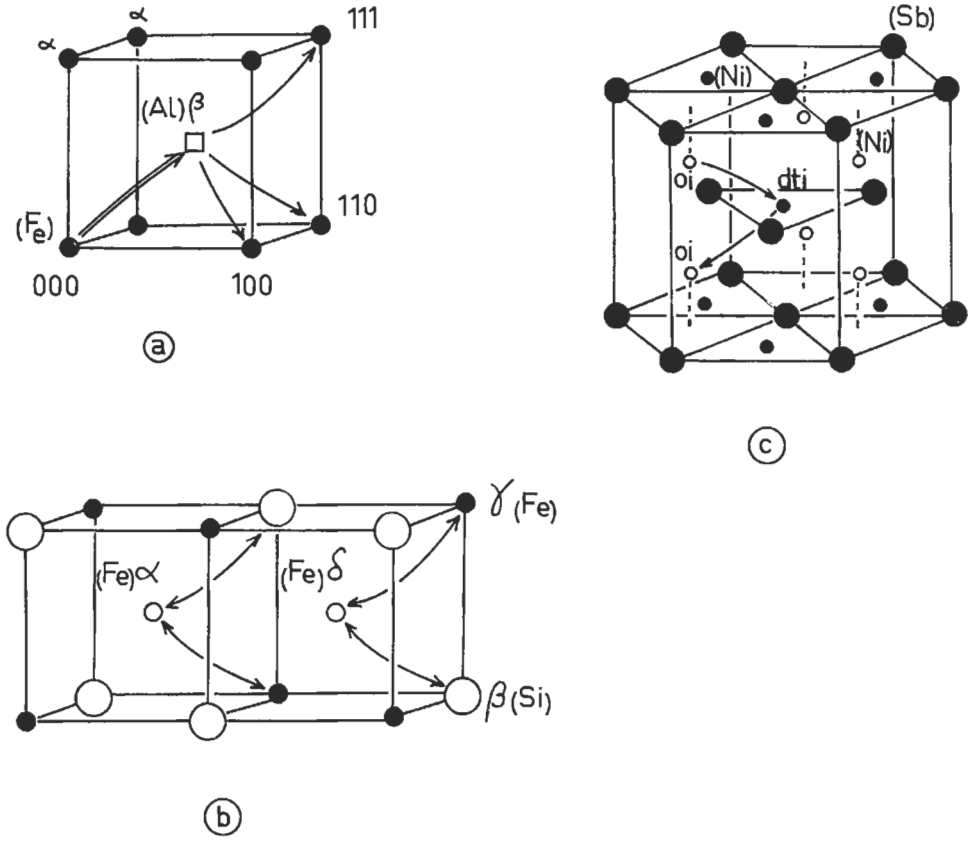

Fig. 13. Observed jump mechanisms for ordered alloys by QEMLB: (a) B2 structure with a → b → a jump sequences; (b) DO_3 structure with $\alpha \leftrightarrow \beta$, $\alpha \leftrightarrow \gamma$, $\beta \leftrightarrow \beta$ and $\gamma \leftrightarrow \delta$ jumps; (c) B8 structure with (oi) ↔ (dti) jumps.

markedly faster than B species: it has been experimentally checked only recently on Ni_3Ge where Ni (as well as Fe or Co tracer) diffusivity is indeed found to be one order of magnitude larger than Ge diffusivity (YASUDA *et al.* [1993]). Direct measurements of vacancy concentrations in Ni_3Al suggest that mainly antistructure atoms accommodate the departure from stoichiometry (AOKI and IZUMI [1975]): model calculations with the embedded atom method (EAM) agree with this picture and predict low vacancy concentrations on both sublattices, with a marked preference for the sublattice of the major component (FOILES and DAW [1987]; XIE and FARKAS [1994]); the same results are suggested by EAM calculations for Cu_3Au (JOHNSON and BROWN [1992]). It is worth noticing that Ni_3Al is the only alloy in which the vibrational entropy has been *measured* in the ordered and disordered phase (ANTHONY *et al.* [1993]): the reduction in entropy when passing to the ordered phase is equal to 0.3 k_B per atom. In Co_3Ti alloys, on the

Ti-poor side, the diffusivity of Co tracer increases with approaching stoichiometry and the isotope effect, which can be shown to equal $f\Delta K$ in $L1_2$ structures (ITO *et al.* [1990]), is small (ITOH *et al.* [1989]).

5.2.3. Ordered alloys with $L1_0$ structure

The $L1_0$ compound AB is such that the (001) planes of the host fcc lattice are alternately filled with A and B atoms. In TiAl alloys, the diffusion of Ti tracer complies the empirical rules of normal diffusion in compact structures (KROLL *et al.* [1993]) and no structural vacancies are expected from PA measurements on either side of the stoichiometric composition (SHIRAI *et al.* [1992]).

5.2.4. Ordered alloys with DO_3 structure

The DO_3 structure for this A_3B compound can be viewed as the occupancy by B atoms (Al, Si, Sn, Sb) of a fcc lattice (named β), the parameter of which is twice that of the host bcc lattice; the others sites belong to three other fcc lattices with the same lattice parameter (α, γ, δ) which are occupied by A atoms (Fe, Ni, Cu, Ag). A_α and A_δ have 4 $A_\gamma + 4B_\beta$ as first neighbours, while A_γ and B_β have $4A_\alpha + 4A_\delta$ (fig. 13b). As a consequence, B atoms have only unlike nearest neighbours. The major component has generally the larger diffusivity which increases with increasing the concentration of the minor component: Cu_3Sn (PRINZ and WEVER [1980], ARITA *et al.* [1991]); Cu_3Sb (HEUMANN *et al.* [1970]), Ni_3Sb (HEUMANN and STÜER [1966]). QEMLB in stoichiometric Fe_3Si (SEPIOL and VOGL [1993a]) and QENS in $Ni_{3-\varepsilon}Sb_{1+\varepsilon}$ (SEPIOL *et al.* [1994]) indicate that the transition metal (Fe, Ni) atoms diffuse by NN jumps between α, γ and δ sublattices; the departure from stoichiometry for $Fe_{3+\varepsilon}Si_{1-\varepsilon}$ is accommodated by antisite Fe_β which are shown to participate also strongly to diffusion. PA measurements in $Fe_{3+\varepsilon}Al_{1-\varepsilon}$ cannot separate V_{Fe} from V_{Al} and gives an apparent vacancy formation energy of 1.2 eV (SCHAEFER *et al.* [1990]): structural vacancies are not expected from the data.

5.2.5. Ordered alloys with B8 structure

The B8 structure for this AB compound is made of a compressed hcp lattice for the B component (In, Sn, Sb, As, Ge) with a *c/a* ratio of the order of 1.3; the A component (Ni) occupies either the octahedral interstices (oi) or the doubly tetrahedral ones (dti). Antistructure atoms Ni_{In} are however believed in NiIn. The large number of (oi) + (dti) sites allows the compounds to accommodate a significant positive departure of Ni atoms from stoichiometry, while still maintaining high concentrations of vacancies on the (oi) sites as large as several percent, even for Ni-rich alloys. The Ni* diffusivity is roughly 10^2 times that of Sb* (HÄHNEL *et al.* [1986]) or Sn* (SCHMIDT *et al.* [1992a, 1992b]). The determination of Ni jump vectors in NiSb compounds shows that Ni atoms jumps essentially from (oi) to (dti) sites, the vacancies on (oi) sites being crucial for allowing easy (dti) to (oi) backward jumps (fig 13c). Direct (oi–oi) or (dti–dti) jumps are excluded (VOGL *et al.* [1993]).

5.2.6. Ordered alloys with $B3_2$ structure

The $B3_2$ structure for this AB compound is made of two interpenetrating diamond lattices. Only two ordered alloys have been investigated so far, namely β-Li-Al and β-Li-In. Structural vacancies V_{Li} and antisite Li_{Al} (or Li_{In}) are believed to be the dominant defects, both defects coexisting at stoichiometry with noticeable concentrations. Li diffusion studied by NMR relaxation exhibits an activation energy of the order of one tenth of an eV and a diffusion coefficient in the range 10^{-6}–10^{-7} cm^2s^{-1} at room temperature. A significant interaction is found between the immobile Li_{Al} or Li_{In} antisite atom and the vacancy on the Li sublattice (attraction for the first, repulsion for the second). (TARCZON *et al.* [1988], TOKUHIRO *et al.* [1989]).

5.2.7. Ordered alloys with A15 structure

The A15 structure for this A_3B compound is made of a bcc lattice for B atoms (Ga, Sn, Au, Si), together with a split interstitial A-A (A = Nb, V, Cr) dissociated along <100>, <010> and <001> directions in the faces (001), (100) and (010) of the elementary cubic cell, respectively. When bringing together the cubic cells, the split interstitials make up linear chains along the corresponding directions. The only alloy in which both diffusivities have been measured is V_3Ga: the activation energy of the transition element is high (4.3 eV), and Ga, which is found to diffuse in grain-boundaries with an unexpectedly high activation energy, is probably the slowest component in bulk diffusion (BAKKER [1984]). Superconductivity occurs along the chains of the transition metal; the thermal disorder, which is believed to be mainly antistructural by analogy with Nb_3Sn (WELCH *et al.* [1984]), can be retained by quenching from higher temperatures: it degrades the superconducting transition temperature T_c in a reversible way, since a subsequent annealing restores the original value. A simple model relates the drop of T_c to the amount of antistructural defects (the vacancies, which are necessary for atomic transport, are neglected) (FÄHNLE [1982]]. An apparent formation energy of 0.65 eV for antisite defects is deduced from the variation of T_c with the quenching temperature (VAN WINKEL *et al.* [1984]). The healing kinetics of T_c, attributed to vacancy bulk migration, is dominated by the slowest bulk diffusivity of Ga atoms: it has been measured at different temperatures with an apparent migration energy of 2.2 eV; however one is left with the contradiction that Ga is the slowest component with the lower activation energy (VAN WINKEL and BAKKER [1985]). Further studies on these compounds are currently in progress (LO CASCIO *et al.* [1992]).

5.3. Chemical diffusion

When diffusion takes place in a region of the sample where the chemical gradients cannot be ignored, the diffusion coefficients of the various components are no longer constant, as in homogeneous alloys, but depend on space and time through the composition.

In what follows, we examine the case of chemical diffusion and the Kirkendall effect in binary alloys. The reader is referred to more extensive reviews for the case of multiphase and multi-component systems (ADDA and PHILIBERT [1966], KIRKALDY and

YOUNG [1987]). The interdiffusion of two elements having different partial molar volumes implies a volume change of the sample which must be taken into account for an accurate measurement of chemical diffusivities (BALLUFFI [1960]). The change of the average atomic volume in neighbouring parts of the sample induces however the birth and the development of stresses, which are usually partially released by some amount of plastic deformation. The inclusion of such effects in the analysis of Kirkendall effects started only recently and is currently under progress (STEPHENSON [1988]; SZABO *et al.* [1993]); they will be ignored in what follows.

5.3.1. Chemical diffusion in binary systems and Kirkendall effect

5.3.1.1. Description and interpretation of a typical experiment. The simplest diffusion experiment to carry out consists in clamping together two pieces of pure metals A and B, to anneal this couple long enough and to determine, at the end of the run, the concentration profile all along the sample. What is observed is a spreading of the initially step-like profile together with a shift of the initial welding interface (defined by inert markers such as oxide particles or tungsten wires) with respect to the ends of the couple which have not been affected by the diffusion (fig. 14). This shift results from the *Kirkendall effect* and finds its origin in the fact that the diffusivities D_A and D_B are not equal. Indeed, if D_A is larger than D_B, species A penetrates into B at a faster rate than B into A: as a consequence, the B-rich part of the sample must increase its volume to accommodate the net positive inward flux of matter. This increase will be achieved at the expense of the A-rich part by shifting the interface towards A. This observation was reported for the first time by SMIGELKAS and KIRKENDALL [1947] on copper–zinc alloys: the zinc is the faster diffuser and the welding interface (called *Kirkendall plane*) shifts towards the zinc-rich side of the couple. This experiment was a milestone in the history of solid-state diffusion: it definitely ruled out the assumption of a direct exchange $A \leftrightarrow B$ mechanism which was formerly proposed and which would have implied equal diffusivities for both species.

It must be noted that a Kirkendall effect has also been observed in fluids: it is expected indeed to be very general, since the first convincing interpretation of the phenomenon is not based on any detailed mechanism for matter transport (DARKEN [1948]).

The simultaneous measurements of the displacement rate v of the Kirkendall plane and of the chemical diffusivity $\tilde{D}$ in that plane yield the intrinsic diffusion coefficients D_A and D_B for the composition of the Kirkendall plane. In order to know D_A and D_B at several concentrations, one should prepare the corresponding number of differential couples, which are made of two alloys with different compositions. In fact it can be shown that a single experiment is needed, provided that a complete set of inert markers has been inserted on both sides of the welding interface (CORNET and CALAIS [1972]).

In what follows we suppose that the observed effect is unidirectional, and that only one space coordinate x is needed, in conjunction with the time variable t, to describe the evolution of the system. The transformation $x/\sqrt{t} \rightarrow \lambda$ in Fick's second Law shows that the solution C(x,t) can be expressed as a one-variable function $C(\lambda)$. We know from

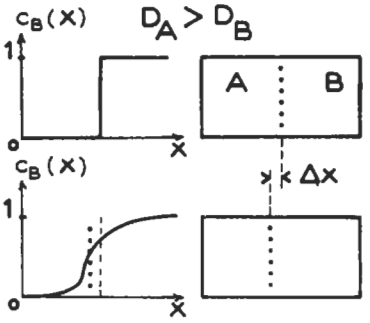

Fig. 14. Kirkendall effect experiment with a diffusion couple made of two pure metals A and B.

experiment that the Kirkendall plane has a constant concentration during the diffusion anneal, and accordingly that it is characterized by a constant value of λ. As a consequence, the Kirkendall shift Δx varies as $\sqrt{t}$; no exception to this simple law has ever been reported.

A similar behaviour has also been observed for any inert marker which is not located in the Kirkendall plane at $t=0$; after a time lag, the duration of which depends on the distance from the Kirkendall plane, the inert marker starts moving with the same time law (LEVASSEUR and PHILIBERT [1967]; MONTY [1972]).

Up to now no atomic mechanism for matter transport has been mentioned; but if we know it, something more can be said about the Kirkendall plane.

We suppose in the following that the vacancy mechanism is operating. In all the experiments performed so far, the inert markers are invariably made of materials which have a high melting temperature. The formation and migration energies of the vacancy in such materials are significantly larger than in the surrounding matrix. As a consequence, the markers are impermeable to the vacancy flux. Under this condition, it can be shown that such a marker shifts along with the lattice planes (KRIVOGLAZ [1969]), whatever the type of its interface with the matrix (coherent or incoherent). Thus the measurement of the Kirkendall shift is nothing but the measurement of the lattice plane shift.

The above formalism can be easily enlarged to account for the case in which the average atomic volume varies with the concentration of the alloy (BALLUFFI [1960]).

5.3.1.2. Vacancy wind effect — Manning's approximation. In the original formulation of the Kirkendall effect, the flux J_A of species A stems only from the chemical potential gradient $\nabla\mu_A$ of species A (DARKEN [1948]).

At infinite dilution, the solid solution becomes ideal ($\varphi = 1$) and the intrinsic diffusion coefficient D_A must tend towards the tracer diffusion coefficient D_{A^*} . Hence:

$$D_A = D_{A^*} \cdot \varphi, \qquad D_B = D_{B^*} \cdot \varphi.$$

These relationships are known as *Darken's equations*; we know however, from the thermodynamics of irreversible processes, that the off-diagonal term cannot be neglected. More general expressions can be established [see eqs. (6)]:

$$D_A = \frac{kT}{n}\left(\frac{L_{AA}}{C_A} - \frac{L_{AB}}{C_B}\right)\varphi \quad D_B = \frac{kT}{n}\left(\frac{L_{BB}}{C_B} - \frac{L_{BA}}{C_A}\right)\varphi$$

There is no simple way to relate theoretically the L_{ij}'s to experimentally accessible quantities such as tracer (or intrinsic) diffusion coefficients. This has been done only in the particular case of a simplified random-alloy model (MANNING [1968]) for which $\varphi = 1$. These expressions are arbitrary assumed to hold even for a non-random alloy where the thermodynamic factor φ is no longer unity. Hence the final expressions for the intrinsic diffusivities are still given by eqs. (17) with the random values of the *vacancy wind* corrections r_A and r_B recalled in § 5.1.2. Hence:

$$\tilde{D} = \left(C_A D_{B^*} + C_B D_{A^*}\right)\varphi\left[1 + 2\frac{C_A C_B\left(D_{A^*} - D_{B^*}\right)^2}{M_0 D^*\left(C_A D_{B^*} + C_B D_{A^*}\right)}\right]$$

The last term in the brackets is called a *vacancy wind* term since it reflects the coupling between the transport of species A and B through the vacancy flux. We note that Manning's equations predict a chemical diffusion coefficient $\tilde{D}$ always larger than that given by Darken's equations. The match of both sets of equations with experimental results will be reviewed in the following section.

Before closing this section, a last remark should be made concerning the structure of Darken's or Manning's expressions: in both sets of equations the thermodynamic factor φ enters in a multiplicative way. In some cases the variations of φ with the respect to concentration or temperature may outweigh the variations of other factors. This situation can be met accidentally as in Au-80 at % Ni (REYNOLDS *et al.* [1975]) but is also expected to happen in well-defined situations: for any alloy which tends to unmix at low temperatures, φ goes through zero at the top of the coexistence curve at some critical temperature T_c. It is easy to show that the maximum of the coexistence curve is such that the second derivative of the molar free energy, d^2f/dC_B^2, vanishes. A short derivation yields:

$$\frac{d^2 f}{dC_B^2} = \frac{kT}{C_A C_B}\left(1 + \frac{d\log\gamma_A}{d\log C_B}\right) = \frac{kT}{C_A C_B}\varphi$$

where γ_A is the activity coefficient of species A.

A convincing illustration of a vanishing $\tilde{D}$ has been reported for Nb-34 at % H (VÖLKL and ALEFELD [1978]). At critical temperature T_c, the Arrhenius plot of $\tilde{D}$ bends downwards and $\tilde{D}$ falls several orders of magnitude, whereas the Arrhenius plot of the hydrogen tracer diffusion exhibits a normal behaviour. This phenomenon is called *critical slowing down*; the top of the coexistence curve is the very point where the alloy hesitates between two conflicting forms of behaviour:

– high-temperature behaviour where all the concentration fluctuations flatten out ($\tilde{D} > 0$);
– low-temperature behaviour where the concentration fluctuations of large wave-lengths are amplified ($\tilde{D} < 0$) in order to allow the system to decompose into two phases of different compositions (spinodal decomposition).

5.3.1.3. Experimental check of vacancy wind effect. Let us recall first that accurate measurements are difficult: in many cases the Kirkendall shift is of the same order of magnitude as the diameter of the inert markers; cavities are often observed on the side of the faster diffusing species, indicating a local vacancy supersaturation; the thermodynamic factor is not known better than within 5–10 percent (ELDRIDGE and KOMAREK [1964]). The departure of the actual experimental conditions from the theoretical assumptions (vacancies everywhere at thermal equilibrium, purely unidirectional fluxes, etc.) probably induce further errors of unknown magnitude.

Only a few systems have been explicitly studied to compare Manning's and Darken's formulations, namely: AgAu (MEYER [1969], DALLWITZ [1972], MONTY [1972], AgCd (BUTRYMOWICZ and MANNING [1978], IORIO *et al.* [1973], AlNi (SHANAR and SEIGLE [1978], AuCu (HEUMANN and ROTTWINKEL [1978], CuZn (SCHMATZ *et al.* [1966], TiVa (CARLSON [1976]). Without entering into great detail, two general trends can be extracted from these studies:

– In most cases, Manning's vacancy wind correction to Darken's expressions for D_A and D_B improves the agreement of the experimentally measured values of the Kirkendall shift Δx and of the ratio D_A/D_B with the corresponding calculated quantities. "Calculated" means that D_A and D_B are evaluated by plugging the experimental values of D_{A^*}, D_{B^*} and φ into Manning's or Darken's equations.

– However, whereas the ratio D_A/D_B is fairly well accounted for, the individual values of D_A and D_B are often larger than the calculated ones (by a factor of two in the case of AuCu!) and the experimental Kirkendall shift has also a tendency to be larger than the theoretical one. (Except for AlNi, where $\tilde{D}_{meas}$ is smaller than $\tilde{D}_{theor}$ for both models.)

The reason for the discrepancy is not yet clearly understood. As pointed out by CARLSON [1978], Manning's correction to Darken's expressions holds only for a random alloy, a condition which is never fulfilled in real systems. But, as outlined above, Manning's approximation is quantitatively reasonable even in the non-random case; the problem of the experimental accuracy should be clarified first.

5.3.2. Ternary alloys

The expressions of the three matter fluxes J_1, J_2, J_3 in the lattice reference frame introduce nine independent phenomenological coefficients (or intrinsic diffusion coefficients if the chemical potentials gradients are expressed as concentration gradients). Neglecting the vacancy concentration C_v against the matter concentrations C_1, C_2 and C_3 and eliminating one of the concentrations (say C_3) yields flux expressions with only six independent new coefficients. Expressing at last, the three fluxes in the laboratory reference frame, together with the condition $J_1^0 + J_2^0 + J_3^0 = 0$ we are finally left with only four independent chemical diffusion coefficients $\tilde{D}_{11}^3$, $\tilde{D}_{12}^3$, $\tilde{D}_{21}^3$, $\tilde{D}_{22}^3$, the superscript '3' recalling that C_3 is the dependent concentration and is evaluated through $C_3 = 1 - C_1 - C_2$ and the tilde (~) recalling that interdiffusion coefficients are determined (BOCQUET [1990a]). A beautiful analytical approach has been worked out on simplified systems, where the above diffusion coefficients are assumed to be concentration independent, a condition which holds in practice whenever the terminal concentrations of the diffusion couples are close to one another (differential couples). This analysis enlightens all the

characteristic features to be encountered in the practical studies of ternaries, namely, the existence of maxima in the concentration–penetration curves, the possible occurrence of zero-flux planes, together with the general properties of diffusion paths (THOMPSON and MORRAL [1986]). The extension to concentration dependent diffusivities can be made straightforwardly with the help of numerical methods.

6. *Electro- and thermomigration*

At temperatures where diffusion is noticeable, atoms of a pure metal, or of an alloy, are caused to drift by a gradient of electric potential or temperature. We saw (§ 4.1.2) that this phenomenon, also called the *Soret effect* in the case of thermal gradients, has been used to study phenomenological coefficients. It has also been used practically to purify some refractory metals. Last, but not least, it is a way to study the electronic structure of point defects (vacancies, impurity atoms) at high temperatures and its variation during a jump. Careful reviews of all aspects of electromigration can be found in VERBRUGGEN [1988] and HO and KWOK [1989].

6.1. Thermodynamic aspects

Starting with the equations (1)–(5) in § 1.2.2., if J_e and J_q are the electron and the heat flux, respectively, we define (DOAN [1971]) the valency and the heat of transport by:

$$z_A^* = \left(\frac{J_e}{J_A}\right)_{J_B=E=0} \quad \text{and} \quad q_A^* = \left(\frac{J_q}{J_A}\right)_{J_B=\nabla T=0} \tag{71}$$

The effective valence Z_A^* and the reduced heat of transport Q_A^* introduced in § 1.2.2. are then given by:

$$Z_A^* = z_A - z_A^* \quad \text{and} \quad Q_A^* = q_A^* - \Delta H_{FV} \tag{72}$$

and the equivalent relations for the B component.

The form of Q_A^* is due to the effect of the temperature gradient on the vacancies. It is derived under the hypothesis of a local equilibrium concentration of vacancies. It has therefore no counterpart in the electric field case. Any deviation from this equilibrium (see § 8) invalidates the comparison between microscopic evaluations of q* and experimental Q*.

In self-diffusion, B stands for an isotope of A, so eqs. (1)–(5) give, in the case of electromigration:

$$J_{A^*} = -D_{A^*}\nabla n_{A^*} + Z_A^* \frac{eE}{kT} n_{A^*} \frac{D_{A^*}}{f_0}$$

where f_0 is the self-diffusion correlation factor. The thermomigration case is given by an analogous equation, Q_A^* and $-\nabla T/T$ replacing Z_A^* and E.

Such self-diffusion experiments then give access to the true values Z_A^* and Q_A^*. For solute diffusion, one calculates easily (dropping the ∇n_{B^*} term):

$$J_B = n_B D_{B^*} \frac{eE}{kT}\left[Z_B^* + Z_A^* \frac{L_{AB}}{L_{BB}}\right] = Z_B^{**} n_B D_{B^*} \frac{eE}{kT}$$

Measurements can then give access only to the *apparent* effective valence Z_B^{**} (or heat of transport Q_B^{**}). This value differs from the true one, Z_B^*, by the vacancy wind term $Z_A^* L_{AB}/L_{BB}$ (MANNING [1968]). The ratio L_{AB}/L_{BB} varies approximately from +2 to –2 and can then give a very large correction to Z_B^*, especially in polyvalent solvents. Equations (1)–(5) are written in the lattice frame, and so are defined the Z_B^{**} and Q_B^{**} values. But if the fluxes are, for some reason, measured in another reference frame, they give access to other values of coupling coefficients. For example in the laboratory frame, one obtains:

$$J_B^0 = n_B D_{B^*} \frac{eE}{kT}\left(Z_B^{**} - \frac{D_{A^*}}{D_{B^*}} Z_A^{**}\right)$$

where the bracketed term defines the apparent effective valence in the fixed frame.

6.2. Microscopic analysis

Atoms in a metal under a gradient of potential or temperature are submitted to a force which has a double origin. On one hand, one finds a static part called *direct* in the electric case, or *intrinsic* in the thermal one. The direct force is due to the unscreened action of the electric field on the true ionic charge [eq. (72), term z_A] and the intrinsic contribution corresponds to the enthalpy transfer due to an atomic jump (WIRTZ [1943], BRINKMAN [1954], LE CLAIRE [1954]). In this approximation the heat of transport q_A^* [eq. (72)] is nothing else than a part of the migration enthalpy (HUNTINGTON [1968]). On the other hand electrons and phonons in metals are highly mobile carriers, either thermal or electrical. Therefore their scattering at atoms which are neighbours of a vacancy gives rise to a second contribution: the electron or phonon *breeze*.

In the case of electromigration FIKS [1959] and HUNTINGTON and GRÖNE [1961] have given a model of this scattering part, treating electrons as semiclassical particles. BOSVIEUX and FRIEDEL [1962] have used the free-electron model in the Born approximation to give a quantum-mechanical expression of the z* term. More rigorous treatments of this term have been developed later, either in the framework of the linear response theory, or of the muffin-tin approach (KUMAR and SORBELLO [1975], TURBAN *et al.* [1976], SCHAICH [1976], RIMBEY and SORBELLO [1980], GUPTA [1982], VAN EK and LODDER [1991]). Controversies are still running on the existence either of a screening effect in z*, which could partially or exactly cancel the direct force (TURBAN *et al.* [1976], LODDER [1991]), or other contributions behind the carrier scattering (GUPTA [1986]). However all these treatments give essentially the same basic results, their main interest being to define more precisely the range of validity for the preceding models. The results are the following:

(i) For a free electron gas the scattering part of the effective valence is given by:

$$Z_i^* = -\frac{z_A}{2}\left[100\,\frac{\Delta\rho_i^{\text{saddle}} + \Delta\rho_i^{\text{stable}}}{\rho_0} - f_0\right] \tag{73}$$

where $\Delta\rho_i^{\text{saddle}}$ and $\Delta\rho_i^{\text{stable}}$ are the residual resistivities (expressed in $\mu\Omega$cm per at%) of atoms of species i (i = B or A) in saddle or stable position (their sum, $\Delta\rho_i^{\text{saddle}} + \Delta\rho_i^{\text{stable}}$, is denoted by $\Delta\rho_{E_M}$ in table 8, below); ρ_0 is the matrix resistivity and f_0 is a correction term due to the neighbouring vacancy (zeroed for an interstitial solute). We find that in normal metals, owing to the order of magnitude of Δr and ρ_0, the (possible) direct term is completely negligible.

(ii) In polyvalent metals, or transition metals, with a hole conductivity, one has to take into account the details of the Fermi surface and of the scattering atom, electron velocities, wave function character, anisotropic scattering. Schematically two opposite contributions like eq. (73) are found, one for electrons and one for holes, which yields a partial compensation between them. The link with the residual resistivities is lost. In that case, the effective valence is much lower, and the calculations are quite involved (FIKS [1973], HUNTINGTON and HO [1963], LIMOGE [1976b], GUPTA [1982], VAN EK and LODDER [1991]).

The situation is more troublesome in thermomigration. FIKS [1961], GERL [1967] and SORBELLO [1972] have calculated the phonon scattering contribution. The result, as given by Gerl, is a positive term, of the order of 100 kJ/mole (or lower after CROLET [1971]) and linear in temperature, contrary to SCHOTTKY's calculation [1965]. The electron term is more firmly established and according to GERL [1967]:

$$q_{el}^* \propto Z^*$$

and so gives a negative contribution in normal metals. The final Q^* is then the result of the compensation between four terms, and theoretical calculations are very questionable (DOAN *et al.* [1976]). Some years ago, it was proposed to use directly the thermodynamic definition of q* eq. (71) to calculate it (GILLAN [1977]); but this way has not been much followed till now to give quantitative results.

6.3. Experimental methods

In electro- or thermotransport, three techniques have been used. In the first, one measures the total atomic flux $J_a + J_b = -J_v$. This is done by measuring the displacement of inert markers with respect to the ends of the sample. This method can be used only for self-diffusion but is able to yield a good accuracy if vacancy elimination conditions are well controlled (GERL [1968]; LIMOGE [1976a]).

In the second method one establishes a steady state between the external force, either E or ∇T, and the induced concentration gradient. Measurement of the contration profile gives access to effective valence, or heat of transport, *in the laboratory frame* (fig. 15a). The accuracy is generally not very high and the method is restricted to solute diffusion. Moreover the assumptions concerning the equilibrium vacancy concentration must be

carefully checked.

In the third method one uses a thin deposit of tracer between two bulk samples of solvent. This deposit will spread (§ 1.2.5.), as a Gaussian in electromigration, and simultaneously displace (fig. 15b) due to the external force. This displacement with respect to the welding interface gives the coefficient Z**, or Q**. The accuracy is very high and the method is as suitable for self-diffusion as for solute diffusion (GILDER and LAZARUS [1966], DOAN [1971]), although its use in thermomigration needs some care (CROLET [1971]).

6.4. Experimental results and discussion

The reader can find an exhaustive review of experimental results on electromigration in PRATT and SELLORS' monograph [1973]. For thermomigration he is referred to ORIANI's article [1969], see also WEVER [1983].

Let us first discuss thermomigration results.

6.4.1. Thermomigration

In table 6, the heat of transport q_B^* for interstitial solutes are displayed: this case does not raise of course the delicate problem of the vacancy local equilibrium! It can be noticed first that q_B^* has generally the same sign for all solutes in a given solvent. There is also some correlation between Z_B^* and q_B^*, but opposite to the one predicted by Gerl's model. According to NAKAJIMA *et al.* [1987] there is a good correlation between the q_B^* and the migration enthalpies of the three isotopes of Hydrogen in V, Nb and Ta. In table 7, we display the heat of transport in self-diffusion in common metals. The strong scattering of the experimental values can be seen at once, either for a given

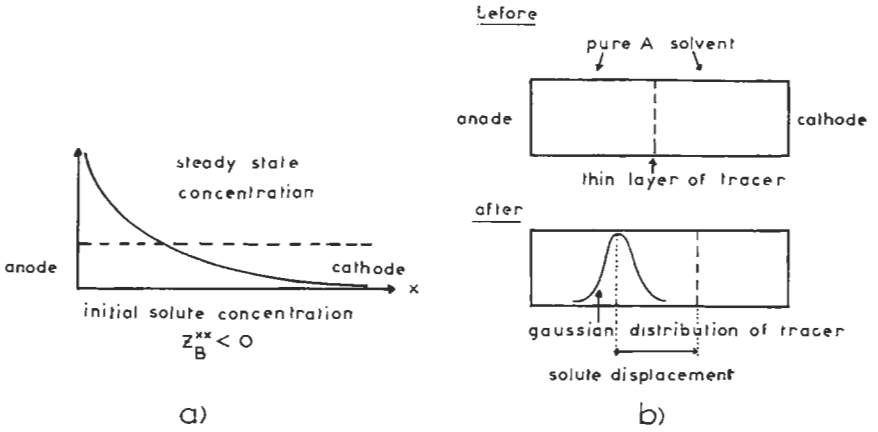

Fig. 15. Experimental methods in electro- and thermomigration. (a) Steady state method: initially the sample has a homogeneous solute concentration; during the current flows a steady-state gradient of concentration is established, the force due to the current flow being equilibrated by the force due to the gradient. (b) The tracer, initially deposited as a thin layer, is spread as a Gaussian in electromigration and also displaced as a whole with respect to the welding interface.

References: p. 651.

Table 6
Effective valences and heats of transport of interstitial impurities.

Solvent	Solute	Z_B^*	q_B^* (kJ/mole)
Ti	H	−1 [e]	+21.7 [b]
	C	>0 [a]	–
	O	<0 [a]	–
V	H	1.5 [d]	1.4 [j]
	O	1 to 1.5 [e]	17 to 29 [e]
	N	–	17 to 29 [e]
	C	–	−42 [i]
Fe_α	H	0.25 [a]	−33 to −23 [b]
	D	0.4 [a]	−33 to −23 [b]
	C	4.3 [a]	−71 to −100 [b]
	N	5.7 [a]	−75 [b]
Ni	H	0.5 [a]	−6.3 to −0.8 [b]
	D	0.7 [a]	−6.3 to −0.8 [b]
	C	–	–
Y	H	−0.3 to −0.9 [a]	–
	N	−0.9 to −2.8 [a]	–
	O	−1.2 to −2.6 [a]	–
Zr_β	C	>0 [a]	–
	N	–	>0 [b]
	O	<0 [a]	–
Nb	H	2.5 [d]	12 [j]
	C	0.6 [a]	54 [h]
	O	6.5 to −2 [a]	−67 [f]
Pd	H	>0 [a]	–
Ta	H	0.5 [d]	28.5 [j]
	O	0 to 2 [g]	−20 to −80 [g]
	N	–	−10 to −40 [g]

[a] PRATT and SELLORS [1973]; [b] ORIANI [1969]; [c] MARECHE *et al.* [1979]; [d] ERCKMANN and WIPF [1976]; [e] MATHUNI *et al.* [1976]; [f] PETERSON and SMITH. [1982]; [g] MATHUNI *et al.* [1979]; [h] CARLSON and SCHMIDT [1981]; [i] UZ and CARLSON [1986]; [j] NAKAJIMA *et al.* [1987].

element or for similar elements. This underlines the experimental difficulties and also a possible departure from equilibrium of the vacancy distribution (§§ 1.2.2, 6.1 and 8.1). Transition metals display large Q_A^* values. This has been explained by HUNTINGTON [1966] as the result of additive contributions of electrons and holes, contributions which are of opposite sign in electromigration, leading to small Z*.

6.4.2. Electromigration

In table 6 are also given the Z_B^* values for interstitial solutes. As in thermomigration, most interstitial solutes migrate in the same direction in a given solvent. The hole

Table 7
Thermomigration — effective heats of transport in self-diffusion, after ORIANI [1969].

Metal	Q_A^* (kJ/mole) [a]
Na	−6.3
Al	−6.3 to −8.4; +46
Cu	−22.6; 0; +16.7
Ag	0
Au	−27; 0
Pb	+8.8
Zn	−0.8; 0; +9.6 to 14.6
Fe_α / Fe_γ	<0; 0; +38 to 314
Co	+221 to +1380
Ni	<0
Pt	+38 to +56
Ti	<0; +773
Zr	−29 to −502

[a] For some elements there are several experimental values from different authors, separated by commas.

contribution is clearly seen in transition metals with hole conductivity. In table 8 are displayed Z_B^* of various solutes in copper, silver and aluminium. We have also shown the residual resistivities $\Delta\rho_M$ given by resistivity measurements in dilute alloys and $\Delta\rho_{EM}$ deduced from electromigration studies using relation (73) (LIMOGE [1976b]). Unlike thermomigration, we see that our predictive understanding of the electron breeze term is fairly good in these quasi free-electron metals, provided experimental resistivities are used. The solute valence effect, varying as $z_B(z_B - z_A)$, is for example well reproduced in copper and silver. The case of aluminium is less satisfactory, probably owing to (i) a badly accounted-for vacancy wind effect and (ii) fairly strong band-structure effects in this polyvalent metal. For the same reason the solvent and the various solutes have low Z^* in lead, smaller than in Al (ROCKOSCH and HERZIG [1983]). Transition metal solutes give rise to large valences due to the formation of a virtual bound level.

6.5. Electromigration in short-circuits

Migration under external forces, mainly an electric field, takes place also in diffusion short-circuits, such as surfaces and grain boundaries (GB) (ADAM [1971]). A first manifestation of this phenomenon is the *induced migration of GB* under an electric field.

This result is now well established both at high temperatures, $T/T_m > 0.7$ (LORMAND [1970]) and at lower temperatures, $T/T_m \sim 0.3$ (HAESSNER *et al.* [1974]). The interpretation however is not clear; namely, it is not obvious how to deduce the migration of an atomic configuration, such as a GB, from the sum of the forces exerted on the constituent atoms. A second manifestation, of great technological impact, is the large matter transport along short circuits in the samples which have a high ratio (surface + GB

Table 8
Valence effect in solute electromigration in normal solvents
(after LIMOGE [1976b]).

Solvent	Solute	Z_B^* (a)	$\Delta\rho_{EM}$ [b] ($\mu\Omega$cm/at%)	$\Delta\rho_M$ [c] ($\mu\Omega$cm/at%)
Copper	Cu	− 8	0.98	0.33
(1300 K)	Ag	− 6	0.62	0.35
	Cd	− 9	1.14	1.31
	In	− 16	2.36	3.95
	Sn	− 30	5.13	8.3
	Sb	− 40	6.64	10.9
Silver	Ag	− 7.5	0.43	0.38
(1150 K)	Zn	− 18.7	2.1	2.9
	Cd	− 30	3.8	2.2
	In	− 43.5	5.7	6.1
	Sn	− 69	9.9	11.6
	Sb	− 103	15	15
Aluminium	Al	− 13.7	0.73	<0.9
(900 K)	Cu	− 6.2	0.26	1.5
	Ag	− 17.3	1.01	2.1
	Cd	− 16.9	1.02	1.5
	Au	− 19.4	1.21	>2.2
	Fe	− 148	9.9	11.6

[a] Z_B^* is the true effective valence.
[b] The resistivity sum $\Delta\rho_{EM}$ is deduced from Z_B^* by eq. (73).
[c] $\Delta\rho_M$ is the resistivity sum as directly measured.

area)/(bulk). This is the case for the very thin stripes of evaporated aluminium used as electrical connections in solid-state electronic devices, run through by current density as high as 10^6 Amp/cm^2. The local divergences of atomic fluxes (triple junctions, hot points) tend to develop vacancy supersaturations and stresses, leading to the formation of voids and hillocks. Rapid breaking or short-circuits intervene, even at low temperatures (D'HEURLE [1971]). Experiments done under well-controlled conditions, for solute diffusion in silver bicrystals (MARTIN [1972]) or in thin aluminium films (D'HEURLE and GANGULEE [1972]), do not show any striking difference between volume and grain boundary valences. Nevertheless, a theory of the GB electromigration force remains to be built. The addition of some solutes (copper, chromium, magnesium) that segregate and/or precipitate at grain boundaries, can enhance the life time by orders of magnitude (D'HEURLE and GANGULEE [1972]). The precise role of these solute is not well understood (LLOYD [1990], SMALL and SMITH[1992]).

6.6. Electromigration as a purification process

Reviews of this topic have been done by PETERSON [1977] and FORT [1987]. The basis of the method is very simple: if a solute impurity displays a non-zero effective apparent valence Z_B^{**}, it will segregate to one end of a sample, of length l, during an

electromigration experiment (see fig. 15a). There remains then a depleted, purified, zone elsewhere. But as the time needed is proportional to $4l^2/(Z_B^* D_b)$, one easily sees that this method is especially efficient for interstitial solutes, or in the liquid state. In fact it has been used mainly for interstitial gaseous impurities in refractory metals, but also for transition metal solutes in Zr (ZEE [1989]) or rare earth (FORT [1987]).

7. *Diffusion along short-circuits*

Short-circuits consist of all the regions of the lattice which have lost their perfectly ordered structure: dislocations, grain boundaries and interfaces, free surfaces. They have in common the following properties:
– The diffusivity is much higher than in the bulk and is detectable in a temperature range where bulk diffusion is negligible.
– The disordered regions interact chemically with the point defects, the diffusing species and with the components of the alloy: the concentrations in the short-circuits are different from those in the bulk.
– They can be modified by the diffusion process itself, which can lead to changes in the ledge and kink densities on a surface, diffusion-induced migration of a grain boundary, etc.
– Their detailed atomic structure is often unknown; when an approximate knowledge is available (as in the case of low-index surfaces), the structure always appears very complex. Extensive simulation work in the last ten years have tried to correlate the macroscopic properties of the boundary (energy per unit area, cleavage fracture energy) to basic microscopic properties (compacity and orientation of the crystalline planes brought into contact) through the use of various semi-empirical potentials: the densest planes seem generally to give rise to low energy grain-boundaries with high cleavage fracture energy (see WOLF [1990a, 1990b, 1991] and references therein). However, no relationship with the behaviour at higher temperatures is available, where point defect generation and possible reconstruction are expected.
– The properties of point defects at surfaces and grain boundaries (formation and migration energies, interaction with the substrate or with other defects) are not yet firmly established.

We recall first the phenomenological approach which has been fruitfully used to interpret grain-boundary diffusion experiments, as well as some recent progress in this area. We next treat the atomistic approach to grain-boundary diffusion and will mention the use of molecular dynamics calculations. The case of surface diffusion will be treated separately.

7.1. Phenomenological approach

The basic idea of the continuous models consists of modeling the (one-) two-dimensional short-circuit as a (pipe) slab, along which the diffusion coefficient D' is much larger than that in the bulk D.

The diffusion equations are then written in both media with suitable matching

conditions at the interfaces. For the grain boundary depicted in fig. 16, the two following equations are written:

$$\frac{\partial c}{\partial t} = D\Delta c \quad |x| > a$$

for the balance equation in the bulk; 2a is the thickness of the boundary, and

$$\frac{\partial c'}{\partial t} = D' \frac{\partial^2 c'}{\partial y^2} + \frac{D}{a} \frac{\partial c}{\partial x}\Big|_{a+\varepsilon} \quad |x| < a, \varepsilon \to 0^+$$

for the balance equation in the grain boundary; the first term is the usual flux divergence term along the y direction; the second term accounts for the lateral exchanges between the slab and the bulk; the concentration inside the boundary is assumed independent of x.

The matching conditions at the interface $x = \pm a$ depend on the problem under consideration:

– for self-diffusion, $c' = c$,

– for solute diffusion $c' = kc$, where k is the grain-boundary segregation factor and under the assumption that c' remains much smaller than the solute concentration inside the boundary at saturation. For the case of a grain boundary in a concentrated alloy or the case of an interface in a two-phase system, the reader is referred to BERNARDINI and MARTIN [1976]. (See also ch. 13 concerning equilibrium grain-boundary segregation, especially § 4).

The solution has been calculated only under simplifying assumptions pertaining to the geometry of the short-circuit or the type of the source. Only one isolated short-circuit is considered; it is assumed to be perpendicular to the surface where the source is deposited.

– Whenever the source is of finite thickness, its concentration is uniform along the plane $y = 0$; the surface diffusion coefficient of the deposited species is taken to be infinitely

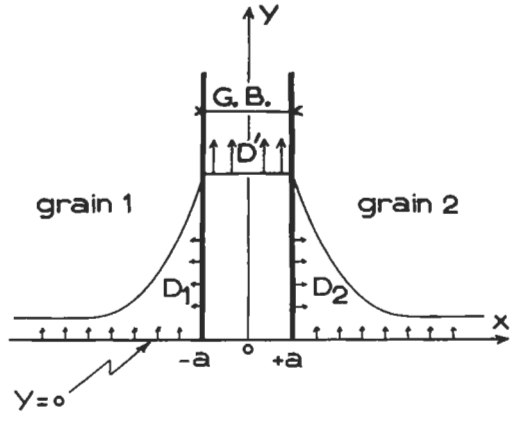

Fig. 16. Equiconcentration profile in the continuous model of grain-boundary diffusion. The slab thickness is 2a; $y = 0$ is the plane of the tracer deposit.

fast to prevent any depletion of the tracer in the area where the short-circuit emerges from the bulk.

7.1.1. Semi-infinite bicrystal

The problem of an infinite source (constant surface concentration) has been solved in an approximate way by FISHER [1951] and in exact form by WHIPPLE [1954]. The problem of the finite source has been solved by SUZUOKA [1961a, b, 1964].

The theoretical quantity which is used to analyze the experiments is not the concentration C(x,t) but its integral $\overline{C}$ along a plane at depth y from the surface:

$$\overline{C}(y,t) = \int_{\infty}^{-a} C(x,y,t)\mathrm{d}x + \int_{+a}^{-a} C'(y,t)\mathrm{d}x + \int_{a}^{\infty} C(x,y,t)\mathrm{d}x$$

It is ascertained that:

– The grain-boundary diffusion coefficient D′ cannot be directly determined, because it shows up in all the expressions in the form 2akD′. A separate measurement of k and an evaluation of 2a is needed to go further.

– The overall shape of the solution is practically independent of the initial condition (infinite source or thin layer) provided that the quantity $b=(D'/D)[ka/(Dt)^{1/2}]$ is large enough (in practice, larger than 5). In that case, log $\overline{C}$ varies as $y^{6/5}$ (LE CLAIRE [1963]). A more detailed discussion of the validity of the above solution can be found elsewhere (MARTIN and PERRAILLON [1979]).

7.1.2. Semi-infinite crystal with an isolated dislocation

A revised version of the calculation has been proposed (LE CLAIRE and RABINOVITCH [1981]). It is shown that log $\overline{C}$ varies linearly with y for distances which are large compared to the penetration depth into the bulk $[y > 4(Dt)^{1/2}]$:

$$\frac{\partial \log \overline{C}}{\partial y} = -A \Big/ \left(k\, a^2 \frac{D'}{D} - a^2 \right)^{1/2}$$

where A is a slowly varying function of the time and a the radius of the pipe. The slope of the straight line is thus nearly independent of time in the case of diffusion along an isolated dislocation pipe: this is in contrast with the case where the dislocations are closely arranged into walls or boundaries and in which the slope varies as $t^{-1/4}$ (LE CLAIRE [1963]). The calculation of correlation effects in dislocation pipe diffusion requires an atomistic modelling of the dislocation core: the two attempts made so far on simple structural models show that the usual form of the correlation factor can be used even in the case where bulk and pipe diffusivities are widely different (ROBINSON and PETERSON [1972], QIN and MURCH [1993b, 1993c]). Molecular Dynamics (MD) simulations of vacancy and interstitial diffusion along a dissociated edge dislocation in copper show that the mobility of the interstitial defect is much larger than that of the vacancy; but that their respective contribution to mass transport are comparable; at last, the existence of the stacking-fault ribbon extends the dimensionality of their migration path to 2–D, slowing down their mobility accordingly (HUANG *et al.* [1991]).

References: p. 651.

7.1.3. Short-circuit networks

In actual crystals, short-circuits are present in high concentration and their orientations with respect to the diffusion direction are more or less random. They make up some kind of connected network along which diffusion is much faster than in the bulk. Three diffusion regimes can be distinguished, according to the bulk penetration depth $(Dt)^{1/2}$ being smaller than, equal to or larger than a characteristic length l of the network: l is the average diameter of the grains in the case of a grain-boundary network and the average distance between two pinning points in the case of a dislocation network (HARRISON [1961]):

(i) When bulk diffusion is totally negligible and when the penetration depth along the network is larger than l, the concentration profile is expected to be similar to a bulk diffusion profile with D′ instead of D. This is called *Harrison's C regime.*

(ii) When bulk diffusion is not negligible but $(Dt)^{1/2}$ remains much smaller than l, the short-circuits do not interact with each other: no significant amount of the diffusing species which has diffused through and out of a first short-circuit ever reaches another short-circuit. It can be shown that an approximate value of $2akD'$ (or ka^2D') can be deduced from plotting log $\bar{C}$ as a function of y (LEVINE and MACCALLUM [1960]): this is called *Harrison's B regime.*

(iii) Whenever the bulk diffusion depth is larger than l, the diffusion fields of neighbouring short-circuits overlap and none of the solutions quoted above can be used. This is *Harrison's A regime.* A simple expression of the effective diffusivity D_{eff} can be proposed, taking into account the fraction f of the lattice sites which belong to the short-circuits (HART [1957]):

$$D_{eff} = fD' + (1 - f)D$$

A detailed mathematical analysis of the penetration profiles versus dislocation density shows that the effective diffusion coefficient D_{eff} is reasonably given by Hart's formula, as soon as the bulk penetration distance $(Dt)^{1/2}$ is larger than 10 l; this limit, which is grounded on a firmer basis, is one order of magnitude lower than that determined by Harrison (LE CLAIRE and RABINOVITCH [1983]). The same analysis shows further that the influence of existing dislocation densities upon the determination of bulk diffusivities in pure metals performed so far should be negligible (LE CLAIRE and RABINOVITCH [1982]).

Harrison's classification has been later extended to the case where the grain boundaries are moving at rate V (CAHN and BALLUFFI [1979]); Harrisson's A regime is encountered whenever $(Dt)^{1/2}$ or Vt is larger than l; Harrison's B regime is split into distinct regimes according to the velocity of the grain boundary; Harrison's C regime remains untouched.

Let us mention that a continuous approach has been proposed for Harrison's A regime (AIFANTIS [1979]; HILL [1979]). A diffusion field is associated with each family of high-diffusivity paths. The total solution results from the superposition of these diffusional fields, which are connected with each other and with the bulk through quasi-chemical reactions. Interesting new features have been predicted, in particular a non-Fickean character of the diffusion in simple cases.

7.1.4. Experimental results

The reader is referred to the compilation of experiments by MARTIN and PERRAILLON [1979]. It is observed that:

– For self-diffusion, the apparent activation energy in a grain boundary is roughly 0.4–0.6 times the activation energy for bulk diffusion.

– For solute diffusion, the apparent activation energy includes the interaction energy of the solute with the boundary.

– For diffusion along the interface separating two phases of different chemical compositions, the results are still too scarce and somewhat controversial. The first experiments in Ag–Fe (BONDY *et al.* [1971]; JOB *et al.* [1974]) or Ag–Cu (PERINET [1975]) showed unusually large activation energies; recent experiments in α/γ interfaces of stainless steels (JUVE–DUC *et al.* [1980]), however, exhibit activation energies which agree fairly well with the activation energy for diffusion along grain boundaries of the γ-phase.

7.2. New advances in grain-boundary diffusion

7.2.1. Impurity effects

This topic is treated in chapter 13, § 5.2.

7.2.2. Diffusion-induced grain-boundary migration (DIGM)

The diffusion of two chemically different species along a grain boundary may under certain conditions induce a lateral displacement of this boundary (DIGM). In the same way, a thin liquid film (during sintering for instance) often migrates towards one grain at the cost of the other (LFM). Contrarily to the initial observations, the condition of a vanishingly small lattice diffusion is not a prerequisite; and the displacement is observed in a fairly large temperature range and for an increasing number of alloy systems. This lateral movement (perpendicular to the grain-boundary plane) is not necessarily uniform along the boundary and as a consequence the latter is very often distorted. The swept area which is left in its wake has a different chemical composition from that of the bulk (fig. 17) and may correspond to a better mixing of the alloy or to phase separation. The *driving force* of this evolution is still highly controversed. A first series of models attributes its origin to the free energy decrease which accompanies the change in chemical composition of the swept area (FOURNELLE [1991]). In a second series of models, the driving force stems from the release of elastic energy: the solute diffusing in the grain-boundary leaks out of the latter and changes the composition of the nearby zone, building up a coherency strain with respect to the undiffused bulk (a situation which prevails only if the bulk diffusivity of the solute is not too large, that is, if the solute does not migrate as fast as an interstitial); the elastic constants are generally anisotropic and the amount of elastic energy will necessarily be different in the two adjacent grains. The grain with the higher elastic energy will shrink and dissolve at the benefit of the other by the sweeping movement of the boundary or of the liquid film (BAIK and YOON [1990]). In both cases, the free energy loss over-compensates the energy increase due to the increase of the grain boundary surface. The only *mechanism* proposed so far invokes the climb of grain-boundary dislocations (BALLUFFI and CAHN

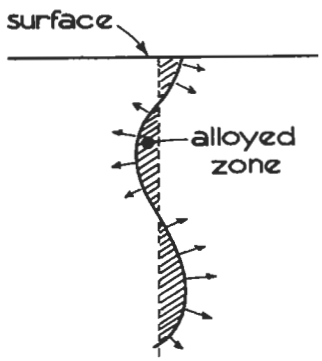

Fig. 17. Lateral displacement of a grain boundary due to a Kirkendall effect along the boundary. The hatched regions have a composition different from that of the surrounding matrix. The dashed line is the initial position of the boundary.

[1981]); it embodies no driving force in itself but offers only a means to move laterally the boundary. It holds however only for DIGM and not for LFM. Beautiful experiments on carefully oriented Cu bicrystals (symmetrical and asymmetrical tilt boundaries) immersed in Zn vapor suggest that the coherency strain model, together with the climb of dislocations in the core of the grain boundary, accounts only roughly for the experimental results concerning the low misorientations (KING and DIXIT [1990]); but the results depend heavily on the detailed structure of the boundary which varies while changing its orientation during the experiments. On the other hand, the calculated elastic effects are often found to be much too low to be consistent with the heavy curvatures of the boundaries sustained in many experiments (LIU *et al.* [1989], KUO and FOURNELLE [1991]); this observation points back to the relevance of the chemical effects.

7.3. Atomistic approach to diffusion in short-circuits

7.3.1. Atomic model for grain-boundary diffusion

The continuous approach has proved its efficiency for interpreting the experimental results which have been collected up to now. However, it raises several questions:
– What is the grain boundary thickness? How can it be defined in a precise way?
– What is a diffusion coefficient inside a grain-boundary?
– Is the assumption of local equilibrium between the bulk and the grain boundary justified?
– What does the solution looks like for very short times, i.e. , times smaller than a jump period in the bulk?

BENOIST and MARTIN [1975a, b]) were able to answer these questions with the following simple model. The grain boundary is modelled as a (100) plane of a simple cubic array, in which the atom jump frequency is Γ' and is supposed to be larger than the jump frequency Γ of the atom in the rest of the lattice. Γ_i and Γ_0 stand for the atom

jump frequencies from the bulk into the grain-boundary and conversely. The starting transport equation is written as follows:

$$\frac{\partial C(r,t)}{\partial t} = \sum_{r'} \left[C(r',t)\Gamma_{r'\to r} - C(r,t)\Gamma_{r\to r'} \right],$$

where C(r,t) stands for the tracer concentration on site r at time t; $\Gamma_{r'\to r}$ for the jump frequency from site r′ to site r; $\Sigma_{r'}$ is extended to sites r′ which are first neighbours of site r. The solution is calculated with a boundary condition corresponding to the instantaneous source of the continuous approach. The main results can be summarized as follows:

– In the limit of large bulk penetration (more precisely, a large number of jumps in the bulk, i.e. $t >> 1$), the solution is equivalent to Suzuoka's solution (see § 7.1.1).

The expression for the parameter β is:

$$\beta = \frac{D'}{D}\frac{ka}{(Dt)^{1/2}} = \frac{\Gamma'}{\Gamma}\frac{\Gamma_i}{\Gamma_0}\frac{1}{2(\Gamma t)^{1/2}}.$$

Since the bulk diffusion coefficient is Γb^2 (b is the lattice parameter), the comparison of the two solutions yields $D' = \Gamma' b^2$; the segregation factor k is equal to Γ_i/Γ_0 and the grain-boundary thickness is b.

In the case where the grain boundary is modelled as p parallel planes, it is found that its thickness is pb. It must be noticed that this thickness is not altered even if the bonds between the sites in the bulk and the sites in the boundary are stretched perpendicularly to the boundary plane. The "thickness" of the grain-boundary is not related to the actual atomic relaxations at the grain-boundary but only to the *number* of high-diffusivity paths which are available for the tracer.

– In the limit of a small penetration depth into the bulk, the identification with the continuous solution is impossible. At very short times ($\Gamma t < 0.1$) the exact solution tends towards a Gaussian with $\Gamma' b^2$ as diffusion coefficient.

This model has been modified to account for more realistic grain-boundary structures, but still disregard the correlation effects. We refer the reader to the original papers (COSTE *et al.* [1976]).

For long, the sophistication of the modelling has been several steps forward with respect to the available experimental information. Only recently, an impressive series of grain-boundary Ag diffusivity measurements, using a clever accumulation method of improved accuracy, has been undertaken in Au bicrystals of well-controlled tilt angle (MA and BALLUFFI [1993a]); the diffusion coefficients (and the activation energies as well) do not exhibit any cusp at those particular orientations which correspond to coincidence site lattice boundaries (CSLB) of short-period and low-Σ. This was taken as an indication that the core of the boundary is made up of several structural units derived from relatively short-period delimiting boundaries which are nearby in the series; in this picture, the change in tilt angle is reflected in a continuous change in the mixture of these structural units. An atomistic modelling resting on the embedded atom method (EAM) suggests that vacancy, direct interstitial and intersticialcy mechanisms are

probable candidates for matter transport along the boundary. The change in activation energy experimentally observed is accounted for by additional jumps of higher energies (MA and BALLUFFI [1993b]). At last, the magnitude of the correlation factor for the intersticialcy mechanism is found to be roughly equal to that of the vacancy one. Thus, a relatively large correlation factor is no longer the indisputable fingerprint of a vacancy mechanism at work, contrarily to previous findings (ROBINSON and PETERSON [1972]). This last result, together with that concerning the diffusion in a dissociated dislocation, suggests that the vacancy mechanism is not necessarily the dominant mass transport mechanism, as thought before from preliminary simulation work (BALLUFFI *et al.* [1981]; KWOK *et al.* [1981]; CICCOTTI *et al.* [1983]). It is worth mentioning however that the activation volume for self-diffusion in a tilt boundary of Ag bicrystals is consistent with the vacancy mechanism (MARTIN *et al.* [1967]).

7.4. Surface diffusion

Although free surfaces can actually play the role of short-circuits for bulk diffusion (inner surfaces of cavities, surfaces along a crack), they have been mostly studied for their own sakes.

We shall not repeat hereafter the continuous approach which has been already used for interface or grain-boundary diffusion; grain 2 in fig. 16 has only to be replaced by vacuum and the exchanges between the surface and the vacuum suppressed. As in the case of a grain boundary, the characteristic quantity which appears in equations is δD_s, where δ is the "thickness" of the surface layer and D_s the surface diffusion coefficient. We will focus in the following on the atomistic point of view.

7.4.1. Atomic structure and point defects

A surface is essentially made up of terraces which are portions of low-index surfaces; these terraces are separated by ledges of atomic height, along which kinks are present (*TLK* model: fig. 18). Ledges and kinks have a double origin:

– A geometrical one, to provide the misorientation of the actual surface with respect to the dense planes of the terraces (Θ and α angles in fig. 18).

– A thermally activated one for entropy purposes.

Such a description is thought to hold in a range of low temperatures where the formation free energy of ledges is large enough to keep their thermal density at a low level and where reconstruction or faceting are not observed (in practice between 0 K and $0.5T_m$).

As predicted by BURTON *et al.* [1951] a dramatic change in the surface topology occurs at some transition temperature T_R, at which the formation free energy of the ledges vanishes (or becomes very small): as a consequence the surface becomes delocalized (ch. 8, § 5.1). This transition (called *roughness transition*) is due to a large number of steps of increasing height which make the edges of the terraces indistinguishable. This has been clearly illustrated by Monte Carlo simulations on (100) surfaces of a simple cubic lattice (LEAMY and GILMER [1974]; VAN DER EERDEN *et al.* [1978]) Figure 17 of ch. 8 shows examples of LEAMY and GILMER's computations. T_R is roughly

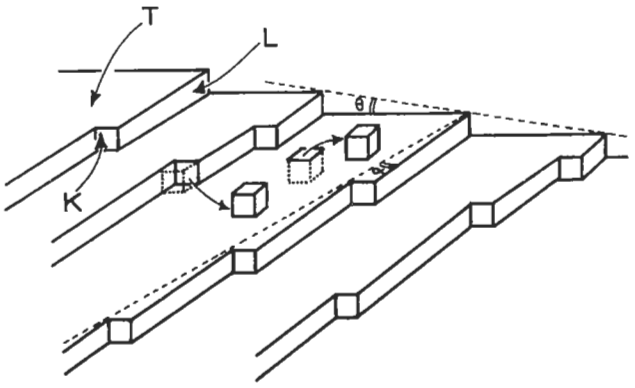

Fig. 18. Terrace–Ledge–Kink (TLK) model for low-index surfaces. The formation of adatoms (the extra atoms bulging out from the plane of a low-index surface) and advacancies (the anti-defects to adatoms) is represented.

given by

$$T_R = 0.5\varepsilon/k,$$

where ε is the strength of the first-neighbour bond. This transition has indeed been observed on several metals using He scattering spectroscopy (for a recent overview, see LAPUJOULADE [1994]). In what follows, we restrict ourselves to surfaces maintained below T_R.

Point defects are also present, namely adatoms and advacancies (see fig. 18); they can be created pairwise at a site of a terrace or separately at a ledge or a kink. The latter case is energetically favoured with respect to the others and is thought to be dominant. Multi-defects can also form by clustering adatoms or advacancies.

Theoretical calculations of point-defect properties on low-index surfaces have so far been performed first with very crude potentials (WYNBLATT and GJOSTEIN [1968]; PERRAILLON *et al.* [1972]; FLAHIVE and GRAHAM [1980a]), and later, refined with atomic potentials derived from the embedded atom method (EAM) (THOMPSON and HUTTINGTON [1982], DESJONQUERES and SPANJAARD [1982], LIU *et al.* [1991], LIU and ADAMS [1992], SANDERS and DE PRISTO [1992]). It is worth noticing that their results do not differ very much, even quantitatively: this is undoubtedly an indication that the formation energies of point defects depend only on very fundamental and simple properties of the surfaces (like the number of lateral neighbours or the packing):

– The formation and migration energies for adatoms and advacancies are found to be highly sensitive to surface orientation.

– The formation energies for both kinds of defect are comparable, except for the (100) surface of an fcc lattice, where the formation energy of the advacancy is significantly smaller than the corresponding energy for the adatom. Therefore, both defects are expected to contribute significantly to matter transport. They will be created in roughly equal amounts, either separately at kinks or pairwise at terrace sites.

– The migration energies have been mainly calculated for adatoms on fcc and bcc

surfaces, and for the vacancy on Cu (PERRAILLON *et al.* [1972]) and Ni (LIU and ADAMS [1992]) surfaces; the advacancy is in most cases the slower-diffusing defect.

For fcc lattices, the migration energies of adatoms increase roughly with increasing surface roughness: $E_m(111) < E_m(113) \sim E_m(331) < E_m(001) < E_m(210)$. For bcc lattices, the migration energies are roughly in the following order: $E_m(110) \sim E_m(211) \sim E_m(321) < E_m(310) < E_m(001) < E_m(111)$. It is worth noticing however that, due to the presence of the defect concentration term, the *surface self-diffusivities* are not necessarily in the same order: a compensation effect occurs, which pairs a low migration to a large defect formation energy (on the (111) surface of fcc lattice, namely). As a result, the surface diffusivity of Ni is expected to be noticeably larger on (113) and (133) surfaces than on any other (LIU and ADAMS [1992]).

A further difficulty stems from the fact that diffusion is expected to be highly anisotropic on non-perfect surfaces: the migration energy along dense rows or in deep channels is usually smaller than the migration energy across these rows or channels. This may obscure the ordering of low-index surfaces with respect to their migrational properties.

Diffusion is thought to take place through individual jumps only at very low temperature and to exhibit a marked anisotropy due to atomic roughness ($T < 0.15T_m$). At higher temperatures, several new mechanisms have been proposed: jumps to more distant neighbours, contribution of multidefects performing collective jumps caused by a strong forward dynamical correlation. Exchange mechanisms involving two or more atoms are believed to play a significant role since they imply a smaller distortion of the surrounding than the hopping of a single atom: after having been observed and simultaneously calculated for the change of channel of the diffusing adatom (BASSETT and WEBBER [1978], HALICIOGLU and POUND [1979]), they have been invoked for the crossing of steps on (111) Al surfaces (STUMPF and SCHEFFLER [1994]), and even recently for the mere migration on (100) Cu (HANSEN *et al.* [1993], BLACK and TIAN [1993]) or the dimer migration on (100), (110) and (111) Ir (SHIANG and TSONG [1994]). Similar mechanisms have also been proposed for bulk or surface diffusion of semi-conductors (PANDEY [1986], FEIBELMAN [1990], KAXIRAS and ERLEBACHER [1994]). All these mechanisms had been previously observed in molecular dynamics calculations on fcc Lennard–Jones crystals (TULLY *et al.* [1979]; DE LORENZI *et al.* [1982]). At last, at still higher temperatures, a delocalization of the adatom is predicted, which spends most of its time in flight rather than on equilibrium sites. The theory of atomic jump at a surface rests on the same model as that for the bulk, namely the reaction rate theory, which considers the saddle point configuration as a possible equilibrium fluctuation; but the dynamical corrections (multiple crossings of the saddle surface, dynamical forward correlation leading to multiple jumps) have been treated slightly differently, starting from the flux–flux correlation function formalism used in the theory of chemical reactions (CHANDLER [1978, 1986, 1988], VOTER and DOLL [1985]). Only recently, a more phenomenological theory has been developed, which covers all the diffusive regimes from the lower temperatures (individual jumps) to the higher ones ((2–D flight of a nearly free adatom over the surface): the particle is described by a continuous equation of motion, including an effective friction term which accounts for the interaction with the

vibrating substrate (ALA–NISSILA and YING [1992]). Quantum effects are easily taken into account and reproduce the diffusion by tunneling expected for very light atoms (H) on metal surfaces (HAUG and METIU [1991], ZHANG *et al.* [1990]).

The next step in the analysis is to deduce a macroscopic *surface diffusion coefficient* D_S as a function of the individual *atomic* jump frequencies (that is, including the defect concentrations) which have been measured or calculated. Following CHOI and SHEWMON [1962], one is intuitively led to write it as:

$$D_S = \frac{1}{4} \sum_{i=1}^{p} \Gamma_i d_i^2$$

where p is the total number of jump types, Γ_i and d_i their frequency and length. However, this expression holds only under restrictive conditions:

– All the diffusion mechanisms must contribute independently to matter transport. At each step, the diffusing atom should be allowed to make a choice between all the p available jump types which are at its disposal.

– All the sites of the surface should be equivalent. The defects should be in equilibrium everywhere and their concentrations should be uniform all over the surface, with no preferential occupancy or trapping sites. This requirement can only be met for close-packed perfect surfaces with no ledges or kinks, e.g., a (111) surface in the fcc lattice.

Real surfaces are not perfect: ledges and kinks are thought to trap the defects. Moreover the jump frequency for the motion along a ledge is different from the frequency for jumping over the ledge. If ledges and kinks could be uniformly distributed over the surface, the equivalence of the surface sites would be maintained and the same expression of D_S could still be used.

As a matter of fact, we know that the misorientation of a real surface from a perfect one is provided by one (or more) periodic array(s) of ledges and kinks. This periodicity (as opposed to uniformity) contradicts the assumption of equivalence between sites, and a new analysis has to be carried out. This has been done only for (310), (h10) and (h11) surfaces (h is any positive integer) of the fcc lattice (COUSTY *et al.* [1981]; COUSTY [1981]), thanks to the atomistic approach which has been already worked out for grain-boundary diffusion (BENOIST and MARTIN [1975a, b]): the method consists of defining a new unit supercell containing all the different types of sites and making up such a basic pattern that it can be used to generate the surface sites by translations in two directions. Effective jump frequencies across this cell, in the direction of the ledges and perpendicularly to them, can be determined by matching the solution of the discrete approach to Suzukoa's solution with the same boundary conditions. The exchanges of matter between bulk and surface are taken into account; but, in its present form, this model requires the knowledge of the atom jump frequencies out of (and into) all the different types of surfaces sites, which is far beyond the scarce experimental information presently available. Careful tracer measurements have been performed on such Cu surfaces, yielding the diffusion coefficients parallel $D_{//}$ and perpendicular $D_{\perp}$ to the steps. The main result is that $D_{\perp}$ is found not to depend on the step density; conversely, $D_{//}$ increases linearly with it, and is thought to decrease with the kink density along the steps.

References: p. 651.

7.4.2. Experimental results

7.4.2.1. Microscopic data. The Field Ion Microscope (FIM) technique (ch. 10, § 5.2.1.) has provided an irreplaceable insight into the migration mechanisms and migration energies of adatoms deposited on low-index surfaces. Table 9 sums up the experimental values (rounded to the nearest tenth of an eV for simplicity) which have been obtained on W (COWAN and TSONG [1975], GRAHAM and EHRLICH [1974, 1975], FLAHIVE and GRAHAM [1980b]), Ni (TUNG and GRAHAM [1980]), Rh (AYRAULT and EHRLICH [1974]) and Pt (BASSETT and WEBBER [1978]). Solute adatoms diffusing on surfaces have been reviewed (EHRLICH and STOLT [1980]), and the modification of self-diffusion on surfaces to which impurities have segregated is treated in ch. 13, § 5.2. An interesting and recently published overview must be quoted (EHRLICH [1994]). Calculated values have not been included since they are intrinsically short-lived and submitted to the fluctuations of the continuous theoretical improvements appearing on the scientific market.

The anisotropy of the adatom jump frequency, which is theoretically expected from the geometrical structure of the surface, is often observed. But it depends on the chemical nature of the diffusing adatom: on the (110) surface of Pt, Au adatoms diffuse only along channels parallel to <110> whereas Pt and Ir adatoms diffuse two-dimensionally with no noticeable anisotropy (BASSETT and WEBBER [1978]).

All the calculations performed so far indicate that diffusion should be very easy on (111) surfaces of fcc metals; this is experimentally observed for Rh but not for Ni, and this difference is not yet understood.

Recent FIM experiments have measured the trapping energy of a self-adatom to a foreign one buried in the first surface layer (KELLOG [1994]); a complex exchange mechanism has also been observed for Re deposited on an (100) Ir surface (CHEN and TSONG [1994]); the trapping energy, when measured, is large and comparable to (or even higher than) the migration energy on the surface.

Remarkable results have been obtained by the promising technique of He scattering spectroscopy, since not only the frequencies but also the jump vectors are measured. The diffusion anisotropy (and, thus, the crystalline character) is maintained on (110) surfaces of Pb close to the melting point: jumps along close-packed rows are more frequent and often multiple, when compared to transverse ones. The resulting diffusion coefficient is larger than that in the bulk liquid phase (FRENKEN *et al.* [1990]); this result is not in agreement with recent simulations on metallic Cu aggregates suggesting that partial surface melting might occur at high temperatures (NIELSEN *et al.* [1994]). The diffusion of isolated Na atoms on (100) Cu surfaces proceeds via a significant fraction of multiple jumps between 200 K and 300 K (ELLIS and TOENNIES [1993]); but the extraction of a migration energy requires a careful separation of the vibrational and of the diffusional component of the observed spectra (CHEN and YING [1993]).

We must remember however that such data, although of importance, cannot be used to deduce straightforwardly an absolute value of the surface diffusion coefficient D_S or any information about its possible anisotropy, for two reasons:

Table 9
Experimental values of migration energies of self-and-solute adatoms on various low-index planes obtained by FIM technique (in eV).

Diffusing adatom	Studied surface (// and ⊥ stand for parallel and perpendicular to dense rows)					
	W (110)	*W* (211)//	*W* (321)//			
W	0.9	0.75	0.85			
Ta	0.75	0.5	0.7			
Re	1.	0.85	0.9			
Ir	0.75	0.6				
Pt	0.65					
Mo		0.55				
	Rh (100)	Rh (110)//	Rh (110)⊥	Rh (111)	Rh (113)//	Rh (133)//
Rh	0.9	0.6	0.9	0.15	0.55	0.65
		Pt (110)//	Pt (110)⊥		Pt (113)//	Pt (133)//
Pt		0.85	0.8		0.7	0.85
Au		0.65			0.55	
Ir		0.8	0.8		0.75	
	Ni (100)	Ni (110)//	Ni (110)⊥	Ni (111)	Ni (113)//	Ni (133)//
Ni	0.65	0.25	0.3	0.35	0.3	0.45

– The surface diffusion coefficient D_S incorporates the concentration of defects, which cannot be reached by the FIM technique since the diffusing atom is deposited from a vapour onto the surface at a temperature where no matter exchange between the bulk and the surface is allowed: the adatom is therefore in high supersaturation and its formation energy cannot be measured with this technique. On the other hand, the formation energy of advacancies has been tentatively measured above room temperature by positron annihilation on copper and silver. The values which are reported are close to 1 eV within experimental uncertainty, that is, only 20% lower than the corresponding energy in the bulk (LYNN and WELCH [1980]). But an appropriate model for the state of a positron at a metallic surface is not presently available and the validity of this technique for probing the advacancies is still questioned (KÖGEL [1992], STEINDL *et al.* [1992]).
– The surface diffusion coefficient D_S is usually measured at a range of much higher temperatures where other diffusion mechanisms may come into play.

7.4.2.2. Macroscopic data. Mass transfer experiments consist in measuring the rate at which a solid changes its shape (at constant volume) in order to minimize its surface free energy. Several techniques can be used: thermal grooving of a grain boundary (MULLINS and SHEWMON [1959]), blunting of a sharp tip observed by conventional transmission electron microscopy (NICHOLS and MULLINS [1965a]) or scanning tunneling microscopy (DRECHSLER *et al.* [1989]), decaying of an isolated (or of a periodic array of) scratch (es) (KING and MULLINS [1962]; NICHOLS and MULLINS [1965b], JAUNET *et al.* [1982]). The possible contributions of bulk diffusion or the evaporation–condensation mechanism must be subtracted to deduce the part due to surface diffusion only. This technique does not yield the surface diffusion coefficient D_S but the product $\gamma_S D_s$ (where γ_S is the surface tension) or, more precisely, some average of this product over the

References: p. 651.

orientation of all the facets making up the macroscopic profile.

A second technique involves the use of a radioactive tracer and consists in measuring the concentration profile of the diffusing species on surfaces of well-defined orientation: it has been used for pure copper (COUSTY *et al.* [1981], GHALEB [1983]). This technique does not yields D_s but the product δD_s where δ is some "thickness" of the surface layer in the continuous approach. For both techniques two crucial points must be checked throughout the diffusion run:

– The absence of any impurity or any two-dimensional superstructure of impurities, both of which might significantly alter the diffusion rate (BONZEL [1976]).

– The absence of any reconstruction of the surface: this point can only be checked for the radiotracer technique, because mass transfer experiments are performed on surfaces, the profile of which evolves in time.

Three points must be noted: (i) The apparent activation energy for self-diffusion is systematically and significantly larger than the migration energy of adatoms which is measured with the FIM technique. The difference is attributed to the energy which is required to form the defects contributing to matter transport. This means physically that the density of defect sources and sinks (steps, kinks) is probably large enough to insure the equilibrium defect concentration throughout the experiment at such temperatures. (ii) The self-diffusion Arrhenius plot is often curved (RHEAD [1975]). If this curvature is not an artefact of the experimental techniques, several explanations can be proposed: contribution of several kinds of defects (advacancies and adatoms, clusters of adatoms, etc.), contribution of multiple jumps, formation of thermal kinks (NEUMAN and HIRSCHWALD [1972]), local melting of the surface (RHEAD [1975]). (iii) Whether the crystallographic structure of the surface induces a marked anisotropy of the surface diffusion coefficient or not is still a matter of controversy: at 0.6 T_m on (110) surfaces of pure nickel, the scratch-decaying technique shows a rather large anisotropy (between one and two orders of magnitude: BONZEL and LATTA [1978], JAUNET *et al.* [1982]), whereas the tracer technique for copper self-diffusion (COUSTY [1981]) or for silver diffusion on copper (ROULET [1973]) exhibits only small differences (at most a factor of 4).

Another route has been followed with diffusion studies at higher coverages ranging from several tenths of a monoatomic layer to several layers (thick deposites) (BUTZ and WAGNER [1979]): these experiments yield a chemical diffusion coefficient, implying the intervention of significant adsorbate–adsorbate interactions. Extensive numerical simulations have been performed to explain how to determine the pronounced maximum of the diffusion at compositions corresponding to ordered structures (BOWKER and KING [1978a, b], UEBING and GOMER [1991], TRINGIDES and GOMER [1992]).

Several points remain somewhat obscure today:

– in the presence of various contaminants (Bi, S, Cl) the surface self-diffusivity can be increased by orders of magnitude and reach much higher values than those typical of bulk liquid state, as high as 10^{-4} m^2/s (RHEAD [1975]). As a rule, chemical interactions of non-metallic character play an important role and give rise to very high surface diffusivities on ionic crystals like alkali-halides for instance (YANG and FLYNN [1989]).

- surface electromigration of metallic adatoms on semi-conductor surfaces differs markedly from the bulk case; the electrostatic field is 10^3 times *larger*, whereas the

current density is 10^3 times *smaller*. As a result, the electrostatic driving force on the solute adatom is much larger than the wind force from the charge carriers, and the metallic ions move in most cases towards the cathode. However, the reversal of the migration direction for Al on (111) Si as a function of the deposited layer thickness is not understood (YASUNAGA [1991]).

– the connection between diffusion and the possible existence of precursor effects in wetting is not understood (ADDA *et al.* [1994]).

8. *Diffusion under non-equilibrium defect concentrations*

Up to now we have discussed diffusion problems involving point defects in thermal equilibrium. In particular, we focused mainly on vacancies; but in some conditions, often of a great technological importance, a high supersaturation of point defects, interstitials and vacancies, can be sustained in steady state. With respect to diffusion, an acceleration of kinetics is the main phenomenon to be observed. Interstitials however have in most cases a high formation enthalpy, and therefore a zero equilibrium concentration. In the case where interstitials are created, apart from an acceleration, new phenomena which are unknown at equilibrium can appear, as we shall see in § 8.3.2.

If point defects are created in a material exceeding their thermal equilibrium concentration, a supersaturation will build up, which results from a competition between creation and elimination, and enhances the diffusion. The new diffusion coefficient can often be written as :

$$D_{acc} = k_v D_v C_v + k_i D_i C_i \tag{74}$$

where k_i, and k_v are coefficients depending on the various jump frequencies of the defects, D_i and D_v are their diffusion coefficients and C_i and C_v their *total* concentrations. The problem of enhanced diffusion is then to calculate the actual C_i and C_v according to the experimental conditions of creation and elimination.

Many situations are now known in materials science where this situation prevails. Without claiming to be exhaustive, we mention the following cases: (i) If vacancy sinks are not very efficient in a sample submitted either to a quench or to a temperature gradient, we can observe a vacancy supersaturation. (ii) Such a supersaturation can also be created in an alloy by vacancy injection from the surface by a Kirkendall mechanism due to preferential depletion of one of the components, by dissolution or oxidation (BURTON [1982], STOLWIJK *et al.* [1994]). (iii) Point defects are also created during plastic deformation. (iv) Under irradiation by energetic particles, a high level of supersaturation can be sustained.

In all these cases the point defect supersaturation is able to accelerate the diffusion and to induce various phase transformations. Let us look first at those cases which involve vacancies only.

8.1. Quenched-in vacancies

Vacancy sinks include free surfaces, dislocations and grain boundaries. Vacancies can

References: p. 651.

also be lost for diffusion by agglomeration as dislocation loops, stacking fault tetrahedra or voids. In some cases (very low dislocation density or surface oxidation for example), the sinks become ineffective, and a supersaturation builds up in the volume which in turn enhances diffusion beyond the thermal equilibrium value. A very important example of the role of quenched-in vacancies is given by the kinetics of age-hardening in alloys displaying precipitation-hardening. We know that GP zone formation is far too rapid to be accounted for by thermal diffusion only: the role of quenched-in vacancies was stressed early (GUINIER [1959]) and later the importance of vacancy-solute complexes (GIRIFALCO and HERMAN [1965]) was recognized in the so-called "vacancy pump" model.

Another very interesting application is the enhancement after a quench of the ordering kinetics in alloys. This phenomenon is at the root of a method for studying defect properties in metals by relaxation measurements (§ 2.2: see also ROBROCK [1981]).

The quenched-in vacancies could also be at work in samples undergoing diffusion under strong thermal gradients (MATLOCK and STARK [1971]). These authors measured the heat of transport of aluminium and found Q^*_{Al} values of 46 kJ/mole in a single crystal and –8.4 kJ/mole in a polycrystalline sample, pointing to the importance of the vacancy formation enthalpy in eq. (72). The same conclusion was drawn from measurements of solute diffusion in a temperature gradient in aluminium or silver (MCKEE and STARK [1975]), SHIH and STARK [1978]). In all these cases, grain boundaries are apparently the only efficient vacancy sinks. The polycrystalline sample is then at equilibrium but not the single crystal. In this last case the hot end imposes its vacancy concentration to the cold one. Therefore the diffusion coefficient is fixed by (i) the hot-end vacancy concentration, (ii) the local vacancy mobility, and is then strongly enhanced in the cold part of the sample. The same effect has been recently observed by HEHENKAMP [1993] in silver using radiotracer measurements and the positron annihilation method. The level of supersaturation observed is of the order of 50 to 100. One can wonder wether at these levels, nucleation of cavities or vacancy clusters should not occur, since they have already been observed in Kirkendall's or electromigration experiments at much lower supersaturations in the same material (MONTY [1972]). Moreover carefully controlled experiments failed to detect such an effect in aluminium, either by measuring the local silver diffusion coefficient at different places along the gradient (BREBEC [1977]), or by measuring the actual vacancy sink activity also all along the gradient by a method using the deplacement of inert markers (LIMOGE [1976a]). Indeed the establishment of a strong enough temperature gradient in a metallic sample is a difficult task, and artefacts are not always avoided, giving rise to an actual gradient much less than expected.

8.2. Cold-work-induced defects

It is now firmly established that during plastic deformation, point defects, probably mainly vacancies, are created by dislocation interactions (WINTENBERGER [1959], FRIEDEL [1964], GONZALES *et al.* [1975a, b]). Two main origins have been proposed. The first one correspond to the annihilation of sufficiently elongated dipoles of edge dislocations which "evaporate" as defects, and the second to non conservative motion of

jogs. The first process is believed to occur mainly in the walls of the dislocation cell structure observed during fatigue experiments or in persistent slip bands (P.S.B.). If we neglect the thermal elimination of defects, a typical concentration could amount to 10^{-3} at. (ESSMAN and MUGHRABI [1979]). However, the very high dislocation density in that case probably prevents such a high supersaturation level (RUOFF and BALLUFFI [1963]). In the second case the production rate could amount to 10^{-6} at. in typical low cycle fatigue experiments, and elimination occurs by diffusion to the walls of the cell or by sweeping by the moving dislocations (TSOU and QUESNEL [1983]). The supersaturation can be quite large at not too high temperatures. Whatever the production mechanism, these excess vacancies have been shown to produce cavity nucleation and growth during fatigue tests in various alloys (ARNAUD *et al.* [1985]). It is then clear that diffusion will be also accelerated, but that any attempt to determine this enhancement by classical *macroscopic* methods (§ 2.1) is hopeless. Artefacts due to surface roughness induced by the slip bands (RUOFF [1967]) or pipe diffusion in dislocation will always screen the actual effect. However, this enhancement can be rendered visible by a local method sensitive to a small number of jumps, such as the Zener effect (NEUMANN *et al.* [1961]) or GP zone formation kinetics (KELLY and CHIOU [1958]). Indeed an acceleration of diffusion has been observed by N.M.R. (see § 2.2.2.1.) in a deformed NaCl crystal (DETEMPLE *et al.* [1991]). The same phenomenon is believed to be at the origin of the dynamic boron segregation at grain boundaries in microalloyed steels: the excess vacancies created during rolling (deformation rates of 1 – 10/sec.) drag the boron atoms to boundaries by a flux coupling mechanism (MILITZER *et al.* [1994]).

8.3. Irradiation-induced defects

The knowledge of the various effects of the irradiation of solids by energetic particles, electrons, neutrons, ions, or photons, is of paramount importance in several domains of materials science: nuclear industry, microelectronics or surface treatment, among others. The topic has been reviewed several times, but not exclusively, by ADDA *et al.* [1975], SIZMAN [1978], ROTHMAN [1981], BREBEC [1990], WOLLENBERGER *et al.* [1992], MARTIN and BARBU [1993]. The domain encompasses three main topics: radiation-enhanced diffusion, segregation and precipitation and phase changes, all of them being generally more or less present simultaneously in any radiation environment.

8.3.1. Irradiation-enhanced diffusion

Fig. 19 shows the result of a diffusion measurement by a tracer method in nickel under self-ion irradiation at an energy of 300 KeV. Three parts can be seen in this graph: thermal diffusion at high temperature; between 1000 K and 700 K, a radiation-enhanced domain corresponding to a thermally activated regime with a lower activation energy; and below 700 K, an athermal part. The efficiency of this last mode is quite high, the resulting squared displacement amounting to 125 A^2/dpa. (MÜLLER *et al.* [1988]). Clearly the origins of the enhancement must be multiple in order to explain this behaviour.

References: p. 651.

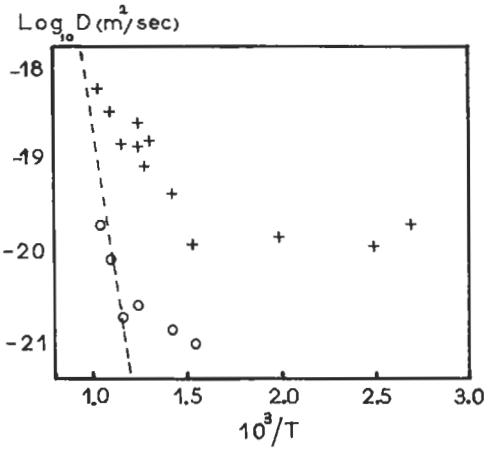

Fig. 19. Self-diffusion coefficient in nickel under self-ion irradiation at 1.2 10^{-2} dpa/s, full symbols, or 1.2 10^{-4} dpa/s, empty dots, dashed line thermal self-diffusion.

8.3.1.1. Defect creation. Under irradiation by energetic particles, the atoms of an alloy suffer elastic and inelastic collisions with the projectiles. Except for very high densities of energy transfer, of the order of several KeV/Angström (BARBU *et al.* [1991]), the electronic excitations are not expected to produce defects. On the contrary the part of the energy which is transfered elastically to a target atom (the primary knocked atom or P.K.A.) will displace it, if the transfer is higher than a threshold E_d of the order of 20 to 50 eV in metals. A Frenkel pair is then created, a lattice vacancy on the initial site and an interstitial on the arrest position. If the energy received by the P.K.A. is high enough, it will in turn act as a projectile and initiate a *cascade of displacements*, also called a *displacement spike*, in the target. The interstitials being created generally at the end of a replacement collision sequence (R.C.S.) will be found at the periphery of the cascade and the vacancies form a dense core at the center. The higher the collisionnal cross section between the moving atoms and the atoms at rest, the more frequent the collisions and the denser the cascade. However a new picture has appeared recently according to which the cascade core is in fact in a molten state, the so-called *thermal spike*, since the mean kinetic energy of the atoms in the cascade core during 10^{-11} sec can amount approximately to 1 eV. This picture is mainly based on Molecular Dynamics simulation results (DIAZ DE LA RUBIA *et al.* [1987]). In this picture the vacancy creation is the result of the ultra fast quench of the molten core, the interstitials are created either by the few R.C.S. escaping from the melt or by a new mechanism of interstitial loops punching from the melt (DIAZ DE LA RUBIA and GUINAN [1992]).

The number of defects created is generally given in the literature with respect to the formula $N_d = KT_D/2E_D$ (TORRENS and ROBINSON [1972]) where T_D is the elastic energy given to the lattice and K an efficiency factor near 0.8. However as soon as the energy of the P.K.A. is higher than a few keV, the vacancy rich core contains too many defects, and collapses more or less into clusters, even at liquid He temperature. The number of

detectable defects is therefore reduced to roughly one third of the above mentioned N_d (AVERBACK *et al.* [1978]). At higher temperatures the defects start to diffuse thermally, and their very inhomogeneous distribution triggers an efficient elimination, either by vacancy-interstitial recombination or by clustering. Finally the fraction of defects able to produce radiation enhanced diffusion is further reduced down to a few percents of N_d in the case of dense cascades. The efficiency of the radiations for producing the so-called freely migrating defects is therefore decreasing from 1 MeV electrons, which are producing only isolated Frenkel pairs with an efficiency of 1, to the heavy ions and even more neutrons which give rise to an efficiency going down to a few 10^{-3} (WIEDERSICH [1990]). (See also ch. 18, § 4.)

8.3.1.2. Collisional diffusion. This effect is also frequently called *Ion-Beam Mixing*, and has been recently reviewed (AVERBACK and SEIDMAN [1987], REHN and OKAMOTO [1989], CHENG [1990]). Indeed, inside a collision cascade the atoms, as a result of the collisions or of the molten state of the matter, will experience an enhanced diffusion not solely due to the presence of point defects. Four origins have been proposed for this new mobility: i) the direct displacement of the knocked atoms, ii) the displacement under subthreshold collisions of the defects already present, iii) the activated jumps of the same defects in the intense thermal field of the spike, iv) the diffusion in the molten core. The first term has been repeatedly shown to give rise to too low a mobility, some A^2/sec at most under heaviest ion irradiations, for explaining the kinetics of ion-beam mixing (LIMOGE *et al.* [1977], SERAN and LIMOGE [1981], BARCZ *et al.* [1984]), despite careful theoretical modeling (LITTMARK and HOFFER [1980]). Nevertheless this negative result has been recently questioned, at least in low Z matrices (KOPONEN [1991]). In the second approach (SERAN and LIMOGE [1981]), the vacancy defects are expected to jump under subtreshold collisions along dense rows ([110] in fcc metals), i. e. involving an energy lower than E_d. Taking into account the actual vacancy concentration in the cascade the above mentioned order of magnitude (fig. 19) is easily explained without any further assumption. The third approach also furnishes the proper order of magnitude provided the migration enthalpy is reduced to roughly one third of the normal value (KIM *et al.* [1988]). The differences between these last two approaches is probably rather small, and they can be viewed as different points of view on the same phenomenon, since each of them rely on a highly idealized description of the state of the matter inside the core, discrete energy transfers in the first case, and equilibrium thermal effects in the second. In the fourth model, atoms are diffusing in the liquid core of the cascade (JOHNSON *et al.* [1985]). Assuming even in the liquid state a thermally activated diffusion scaling with the cohesive energy of the solid, and taking into account the thermodynamical factor in the liquid (see eq. (7)), a qualitative agreement with experimental results can be obtained.

Nevertheless the present authors have the feeling that several well established results (correlation between mixing efficiency and characteristics of diffusion by a *vacancy mechanism in the solid*, no effects of the solute atomic mass on the mixing (KIM *et al.* [1988])), are not well accounted for in this approach. On the one hand the actual mixing is probably the result of the superposition of at least the first three effects; on the other hand we are still lacking of a proper model for the physical structure of the cascade core, for which neither the liquid droplet nor the heavily damaged solid are perfectly adapted concepts.

References: p. 651.

8.3.1.3. Diffusion by thermally activated jumps. This mode of diffusion enhancement, usually called radiation-enhanced diffusion (R.E.D.), can be observed in a medium temperature range, fig. 19, where it is controlled by the thermally activated jumps of the freely migrating defects created by the irradiation. According to the § 8.3.1.2. the denser the cascade, the higher the plateau due to ion-beam mixing, and therefore the narrower the domain of R.E.D. The contribution of the free defects to diffusion is controlled by the equation (74). Two methods have been used for calculating the defect concentrations C_v and C_i. The first is the Monte Carlo simulation method (DORAN [1970], LANORE [1974]). We have no space to discuss it here and refer the reader to the original articles. The other one, a quasi-chemical approach, was initially proposed by LOMER [1954] and progressively refined since. The ingredients of Lomer's model are the following:
– production rate G of spatially uncorrelated point defects (the so called freely migrating ones)
– motion by random walk with coefficients D_i and D_v
– annealing by mutual recombination at a rate K_r, at fixed sinks (supposed to be *uniformly distributed*) at rates K_i and K_v, or at surfaces, generally treated as a boundary condition
– only pure metals where considered in the initial formulation, but now the extension at least to dilute alloys has been done, in the limit of a solution remaining homogeneous.

Since interstitials are present the set of equation (1)–(3) (§ 1.2.2.) has to be completed. The necessary coefficients have been calculated by BARBU [1980] and ALLNATT *et al.* [1983] for fcc dilute solutions (see also § 4.2 and § 5.1.2 for concentrated alloys). It can be shown using a proper thermodynamic model of the solution that the four fluxes can be written:

$$\begin{aligned}
\Omega J_B &= -D_{BI}\nabla C_I - D_{BV}\nabla C_V - \left(M^V_{BB} + M^I_{BB}\right)\nabla C_B \\
\Omega J_V &= -D_{VB}\nabla C_B - D_{VV}\nabla C_V \\
\Omega J_I &= -D_{IB}\nabla C_B - D_{II}\nabla C_I \\
J_A &= -J_B + J_I - J_L
\end{aligned} \tag{75a}$$

These equations define i) in the absence of solute concentration gradients the diffusion coefficient of the defects D_{VV} and D_{II}, written above D_v and D_i for simplicity, ii) in the absence of defect concentration gradients the diffusion coefficient of B, $M^V_{BB} + M^I_{BB}$, which can be put easily in the form (74). If the solute concentration remains homogeneous, the defect concentrations are then solutions of the following equations:

$$\begin{aligned}
\frac{\partial C_V}{\partial t} &= G - \mathrm{Div}\left(\Omega J_V\right) - K_r C_i C_v - K_v\left(C_v - C_v^0\right), \\
\frac{\partial C_i}{\partial t} &= G - \mathrm{Div}\left(\Omega J_I\right) - K_r C_i C_v - K_i C_i
\end{aligned} \tag{75b}$$

where C_V^0 is the concentration of thermal vacancies.

These equations have generally to be solved numerically. Nevertheless, far from the surface, after a very complex transient regime, the duration of which is of the order of

1/K, with K the lower of K_v and K_i, one obtains under the hypothesis of the interstitials being the more mobile defects, a steady-state regime characterized by:
– $D_iC_i = D_v\,(C_v - C_v^0)$ when elimination at sinks prevails
– $C_i = C_v - C_v^0$ when mutual recombinations prevail
– $C_v \sim (G/D_v)^{1/2}$ at low temperatures, i.e., for dominant mutual recombination
– $C_v \sim (G/D_v)\,L$ at high temperatures, i.e., for dominant sink elimination, where L is the mean distance between sinks. At very high temperatures, $T/T_m \geq 0.5$, the defect mobility is sufficient to prevent any noticeable defect supersaturation, and the enhancement is negligible. In table 10 are given the main characteristics of D_{acc} [see eq. (74)] in Lomer's model. To analyze the experiments it must be kept in mind that in most cases they are done near the surface: a correction is then necessary (ERMERT *et al.* [1968]).

In dilute solid solutions we can observe rather severe effects on defect mobility whenever i) a strong defect-solute attractive interaction exists, ii) the pair is immobile (in the case where the pair cannot migrate without dissociating). These two conditions are not linked to one another for the vacancy, but are for the dumbbell interstitial in fcc structures, except may be for very small solutes. In this case the so-called caging effect induces a strong decrease of the mobility of the interstitial defect in the alloy, as long as the concentration is not higher than the percolation limit in the given structure. Beyond this limit the defect can find diffusion paths which do not break the pair (BOCQUET [1986]).

The enhancement being noticeable only at low temperatures, that is at low mobility, D_{acc} will be lower than 10^{-18} m^2/s, and the experiments are very difficult. This fact, as well as the badly known actual level of freely migrating defects, can explain the fairly general discrepancy which has been observed for long between the tracer experiments and the predictions of Lomer's model. The measured values were generally too high, either in self or solute diffusion (ADDA *et al.* [1975], BREBEC [1990]). However, Lomer's model also rests on numerous approximations, for example in the calculations of the various rate terms, K, K_i or K_v, particularly in concentrated alloys [eq. (74)].

Relaxation methods, however, are well suited to this case, owing to their high sensitivity, and their ability to follow all along the kinetics during the complex transient

Table 10
Characteristics of D_{acc} in Lomer's model [eq. (74)]; after ADDA *et al.* [1975]

Régime of elimination	Activation energy of D_{acc}			Dose-rate dependence (G = dose rate)
	Term due to interstitials	Term due to vacancies	Total	
Recombination only in the transient regime	$\frac{1}{2}H_m^i$	$H_m^v - \frac{1}{2}H_m^i$	complex	$G^{1/2}$
Elimination on sinks	0	0	0	G
Elimination both by recombination and on sinks	$\frac{1}{2}H_m^v$	$\frac{1}{2}H_m^v$	$\frac{1}{2}H_m^v$	$G^{1/2}$

H_m^i and H_m^v are the migration enthalpy of, respectively, the interstitial and the vacancy.

References: p. 651.

regime preceding the stationary state. The results of HALBWACHS [1977], HALBWACHS and HILLAIRET [1978] and of HALBWACHS *et al.* [1978a, b] on Ag–Zn alloys by Zener relaxation display a good agreement with the predictions of Lomer's model, if one assumes that, in these alloys, the vacancies are less mobile than interstitials. The use of electron irradiations avoided the ambiguity of the actual level of freely migrating defect production. This result, confirmed by electron-microscopy studies (REGNIER and HALBWACHS [1980]), has given the first evidence of the large pairing effect on the interstitial mobility in solid solutions.

The tracer experiment which has probably for the first time evidenced the R.E.D. in self-diffusion is the one depicted in fig. 19. The authors have been able to adjust in a coherent manner on the experimental results the various parameters entering the model; in particular they invoke a temperature dependent sink density and an efficiency for the production of freely migrating defects amounting to 1.5% only of the Kinchin and Pease value, in agreement with the recent simulation results on defect production in cascades.

8.3.2. Irradiation-induced segregation and precipitation

Irradiation-induced segregation, leading eventually to precipitation in *undersaturated* alloys, is now a well established phenomenon in a large number of systems (for a quite recent review of experimental results see RUSSELL [1985], also ENGLISH *et al.* [1990]). We display in table 11 the characteristics of such precipitation in a few binary alloys. This effect has to be clearly distinguished from a simple radiation-enhanced precipitation in an *oversaturated* alloy.

At a given defect creation rate G, the segregation or the precipitation of a non-equilibrium phase appear in a well defined temperature interval (see figs. 20 and 21). A new variable, or more precisely a new control parameter, has to be added to the classical phase diagram: the defect creation rate (or irradiation flux), in addition to temperature, pressure and composition (ADDA *et al.* [1975]).

Two ways have been explored to explain these results. The first one is a constraint-equilibrium one: the stored energy due to point defects might displace the free enthalpy curves, to such an extent that it renders stable under irradiation a phase which is normally unstable. Careful calculations of this effect have shown that the order of magnitude of the possible displacement is too low to explain the great majority of the results (BOCQUET and MARTIN [1979]). In the second approach, initially proposed by ANTHONY [1972] for vacancies, the elimination of irradiation-created point defects by diffusion to sinks, like surfaces or dislocations, results in defect fluxes which induce, through the flux coupling terms, local solute supersaturations. These supersaturations can grow beyond the solubility limit, resulting in a precipitation. Indeed both terms D_{BV} and D_{BI} (eq. 75a)), if positive, can give rise to such a segregation.

Many authors have developed this idea for dilute alloys and proposed more or less approximate expressions for the coupling terms due to interstitials (OKAMOTO and WIEDERSICH [1974], JOHNSON and LAM [1976], BARBU [1978, 1980]).

As shown in table 11, two forms of segregation or precipitation have been observed, and can be explained in the present framework. The first one is *heterogeneous*, and occurs on sinks, either pre-existing to, or created by, the irradiation. The most elaborate

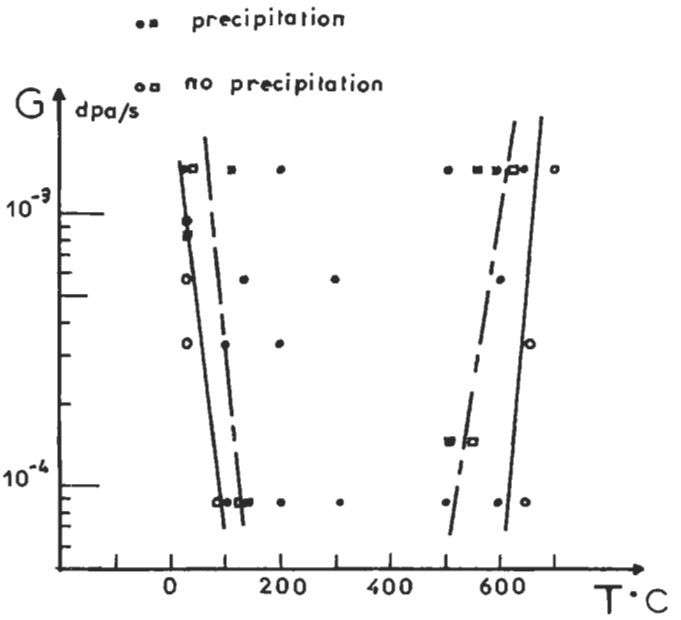

Fig. 20. "Phase diagram", in a flux-temperature section, for the system Ni–Si irradiated by 1 MeV electrons (after BARBU and MARTIN [1977]). Solid line: precipitation borderline for a concentration of 6 at% Si, dashed line idem for 2 at% Si.

numerical solutions of the above set of equations give a fairly good account of experimental results. In particular, the role of sinks, dislocation loops or surfaces is well understood. Nevertheless in this approach the position and the slope of the low-temperature borderline remains to be explained (BARBU [1978]). In all theses models the solute supersaturation results from a balance between the interstitials, which always carry the solute down the gradient and the vacancies, which can act in both directions (BARBU [1980]). At higher temperatures the phenomenon disappears owing to the lowering of the defect supersaturation.

A second kind of precipitation, *the homogeneous precipitation*, was discovered later (table 11), where precipitates are not associated with any pre-existing defect sink. By studying the stability of the set of equations (75) with respect to concentration fluctuations, CAUVIN and MARTIN ([1981], [1982]) have been able to show that, due to the recombination term, the homogeneous solution can become unstable with respect to small concentration fluctuations, giving rise to solute precipitation. Before reaching this instability, the system may become metastable with respect to the growth of large enough precipitates. The analysis of the nucleation problem taking into account the supersaturation of defects, allows to calculate a solubility limit under irradiation. Models have been proposed for incoherent precipitates of oversized solutes (MAYDET and RUSSELL [1977]), or coherent ones, wether over- or under-sized (CAUVIN and MARTIN [1981], [1982]), the latter providing a good agreement with results obtained in Al–Zn

References: p. 651.

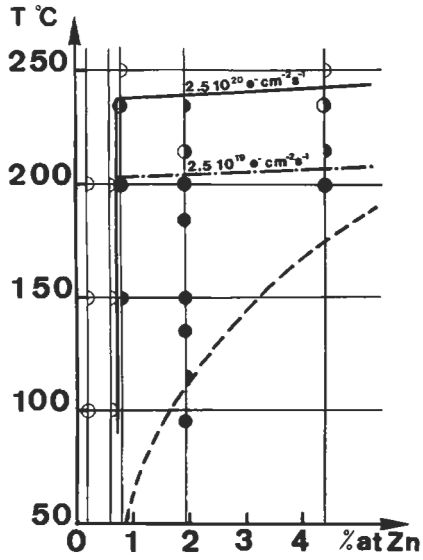

Fig. 21. Solvus line in the Al–Zn system under 1 MeV electron irradiation (after CAUVIN and MARTIN [1981]). Open half-circles: no precipitation; solid half-circles: precipitation at low, or high, flux; dashed line: solvus line without irradiation.

Table 11
Binary alloys where radiation-induced precipitation has been found.

Alloy	Projectile	Precipitate	Morphology
Ni–Be	Ni^+ ions	β-NiBe	at interstitial dislocation loops
Ni–Si	neutrons	γ'-Ni_3Si	at interstitial dislocation loops
	Ni^+ ions	γ'-Ni_3Si	at interstitial dislocation loops
	electrons	γ'-Ni_3Si	at interstitial dislocation loops
	H^+ ions	γ'-Ni_3Si	homogeneous, coherent, in regions of non-uniform defect production
Ni–Ge	electrons	γ'-Ni_3Ge	at cavities or dislocations lines
Al–Zn	neutrons	β-Zn	homogeneous precipitation
	electrons	GP zones + β-Zn	homogeneous precipitation
Al–Ag	electrons	{100} silver-rich platelets	homogeneous precipitation
Pd–W	H^+, N^+ ions	bcc W	at dislocation loops
	electrons	Pd_8 W	homogeneous
W–Re	neutrons	χ-WRe_3	homogeneous
Cu–Be	electrons	G.P. zones + γ	homogeneous
Mg–Cd	electrons	Mg_3Cd	?

alloys under electron irradiations. The origin of this mode of precipitation is to be found in the enhanced recombination probability for the defects in solute rich zones in case of attractive solute-defect interaction.

The theoretical situation is less favourable for concentrated alloys since the available models both for the thermodynamics and for the phenomenological coefficients are much less safe (see § 5.1.2). They are generally based on the random alloy model of MANNING [1971] and discard the specific trapping effects of solutes on the interstitials. As a consequence they do not introduce properly the coupling terms (WIEDERSICH *et al.* [1979]), The more elaborate treatments still suffer from restrictive assumptions (BOCQUET [1987], LIDIARD *et al.* [1990]). The interest of treating the thermodynamics of the alloy and the dynamics at the same level of approximation, has been evidenced by GRANDJEAN *et al.* [1994], who where able to reproduce a whole segregation profile in NiCu alloys.

8.3.3. Irradiation-induced phase transformations

In the two preceding paragraphs we have sketched specific models for irradiation enhanced diffusion and segregation/precipitation phenomena. More generally an alloy under irradiation can be described as a *dissipative dynamical system* which can display a very rich behaviour in response to an irradiation: the system will develop an evolving microstructure with voids, dislocations loops, precipitates, displaying, or not, steady states. The nature and the relative stability of these states can be studied thanks to a whole bunch of methods like deterministic approaches, Langevin equations, Master equation, Monte Carlo simulation, ... which allow to draw dynamical phase diagrams. These topics however are too far from the point of view of the diffusion and the interested reader can found in the specific section of the bibliography the relevant references.

Irradiation-induced segregation and phase transformations are further discussed in ch. 18, § 4.7.

9. *Diffusion in amorphous metallic alloys*

The study of diffusion properties in amorphous metallic alloys (A.M.A.), has been quite active in the past ten years both because these materials have been used as models of disorder for more complex glasses, like oxide ones, but also because they pose an interesting question from the point of view of solid-state physics: what level of structural disorder is sufficient and/or necessary for invalidating the notion of point defect (LIMOGE *et al.* [1982])? The reader is referred to recent reviews (AKTHAR *et al.* [1982], ADDA *et al.* [1987], MEHRER and DÖRNER [1989] and LIMOGE [1992b]), and to the general references on metallic glasses given at the end. The topic is still highly controversial on some points, so the present authors will try, as everybody engaged in the hottest debates, to separate as clearly as possible the established facts from more subjective interpretations.

References: p. 651.

9.1. A primer of metallic glasses

Whatever the preparation mode, vapor condensation, ultrafast quench, it is now recognized that after a proper annealing a unique metastable equilibrium structure is obtained. We have given in fig. 22 a schematic picture of the evolution of the viscosity and self-diffusion in a supercooled liquid during a quench. Two parts are clearly distinguishable. First a high-temperature one, above the so-called glass transition T_g, where the system flows. The diffusion mechanism is of a collective type and, as far as it can be checked, the Stokes–Einstein relationship is obeyed. In this part the well-known WILLIAMS–LANDEL–FERRY [1955] expression works as a mere fit at least as well as any other expression; in particular it describes rather well the near divergence of the viscosity at a finite temperature T_0, which gives rise to the phenomenon of the glass transition. Around T_g a rather abrupt change is observed and a new regime sets in, which has all the characteristics of a mobility in solids. In the following, we will be interested in this latter part, that is, sufficiently below T_g.

As a consequence of these very rapid quenches the glassy alloys are metastable, and as compared to silicate glasses, more "meta" than "stable". As soon as an enhanced temperature allows a sufficient mobility they evolve in a twofold manner. On the one hand they relax towards the (hypothetical) equilibrium liquid structure, probably becoming locally more ordered, and therefore decreasing the mobility. On the other hand if sufficiently large fluctuations of topological and chemical order can form, they will crystallize; the crystallization is controlled by diffusion.

The study of diffusion is thus a quite difficult task. First the allowed (mobility × time) window is very limited by the onset of crystallization: most of the measurements are for example done in a temperature range of less than 100 K, and over two decades of D at most, the total penetration being typically less than 100 nm in tracer experiments. Needless to say, the D values obtained are at the lower limit of the available techniques, imperatively restricting the temperature range where diffusion can be studied. As a second drawback, during this short time the structure itself will evolve: a proper preliminary anneal is generally needed for obtaining a reasonably stabilized structure. This minimum requirement as not been always met in the first studies. Finally, a characteristic feature of the glasses is the wide distribution of physical properties prevailing in non translationally invariant systems. As probed by local methods (see § 2.2) activation energy spectra are frequently found with halfwidth of the order of tenths of an eV.

Glassy alloys have now been discovered in a great number of systems. With respect to diffusion two families only have been studied: the M–Me group where M is a late transition metal or a noble one (or a mixing of them), and Me a metalloid in a concentration between 15% and 25% at.; and the M–M group, alloying an early transition metal (and big) with a late (and small) one in a broader composition range, from 20% to 80% at. approximately. The level of local order is thought to be much more developed in the first class than in the second. As a consequence the properties of the two groups are possibly different. (See also ch. 19, § 4).

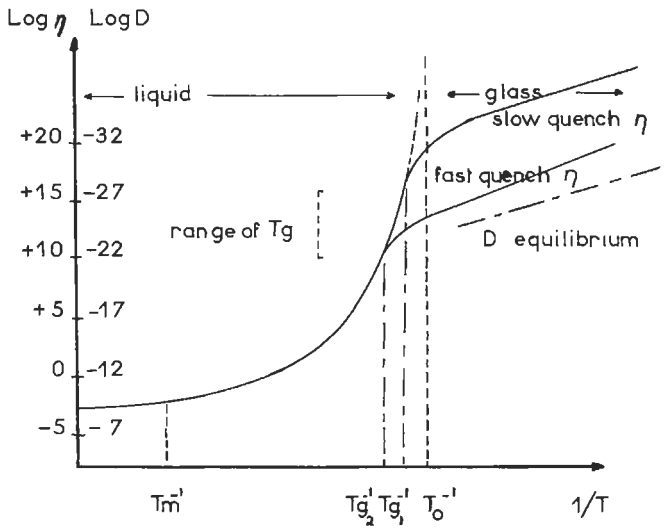

Fig. 22. Viscosity (η) and diffusion (D) evolutions during two rapid quenches of a liquid. Above T_g, in the liquid range, η and D obey the Stokes–Einstein relation. Below T_g, depending on the quench rate, the isoconfigurationnal viscosity evolves according to the "slow" or the "fast" curve. The Stokes–Einstein relationship is no longer obeyed, the diffusion being generally much underestimated.

9.1.1. Experimental portrait of the diffusion behaviour

I) At first, a thermally activated equilibrium diffusion can be defined in all these materials, after a proper annealing. One of the most intriguing characteristics of the diffusion in A.M.A. is its "normal" behaviour: diffusion is arrhenian versus T (but on a quite limited temperature range), and not dispersive (penetration plots are gaussian and D does not depend on time). Apparently D is controlled by a single activation energy Q, or by a very narrow distribution (but see § 9.3), in contradiction with local measurements (see above, § 2.2).

In table 12 a non exhaustive set of tracer determinations of self-and-solute diffusion measurements in various alloys have been gathered. They have been choosen according to the level of confidence the present authors can reasonably have in them. A few of them displaying quite unrealistic diffusion parameters have however been kept in order to give a clue to the possible uncertainty remaining in the other ones.

II) In the first class the best measurements have converged toward i) a Q value of the order of 0.7 to 0.8 of an equivalent solute solvent couple in the crystalline state, ii) the D_0 are within ± 2 orders of magnitude of the corresponding terms. Nevertheless in the first row the D_0 value of the P^{32} tracer (5.10^{-15} m^2/sec!) is a reminiscence of the stone age in the studies of glassy metals during which the D_0 where supposed to be able to cover 38 (!) orders of magnitude (LIMOGE *et al.* [1982]). The same comment applies probably also to P diffusion in the second row; in both cases the value of the P *diffusion coefficient* is nevertheless *in the same range* as the one of the other tracers.

III) In the second class the diffusion of the late T.M. (Fe, Co, Ni, Cu), small atoms,

References: p. 651.

occurs with a Q nearly equal to the one prevailing in the α-Zr, but not in the α-Ti matrix, and a D_0 of the same order, albeit a bit smaller. A marked correlation has been found (HAHN and AVERBACK [1988]) between the value of D and the size of the solute, reminiscent of the one observed in the crystalline α-Zr or α-Ti matrices (HOOD [1978]). The diffusivity of small solutes is orders of magnitude larger than the diffusivity of big ones. With regard to the mobility of the early T.M. (big atoms) the situation is quite confusing: as probably the mobility is related to the size of the tracer, the results for Au, Ag, Zr and Hf in the various Zr-rich alloys are not consistent, contrarily to the Ti-based alloys, where the recent results are more in line with the behaviour of the first group (row 10). More generally neither for the small nor for the big solutes is the consistency between nearby alloys in the same laboratory (rows 11 and 12) or for similar systems in different laboratories (rows 7, 8 and 9) satisfactory. The possibility to deduce from these results safe values for the activation energies, and even more for the D_0, is not obvious.

Among the experiments which cast a specific light on the possible atomic mechanisms the following results have been obtained.

IV) The isotopic effect has been measured for Co diffusion in a CoFeNbB alloy; it decreases during the relaxation, from 0.5 to 0.1 in a well-relaxed glass (RÄTZKE *et al.* [1992]).

V) The activation volume has been determined in a FeNiPb glass for chemical diffusion yielding a value of 1 Ω (LIMOGE [1987], [1990]), in a CoFeNbB alloy for the Co tracer, yielding a result of –0.06 Ω (RÄTZKE and FAUPEL [1992]), and last in a series of NiZr alloys in which the activation volume for the Co tracer varies rather strongly with the concentration from 0.8 to 1.6 Ω (HÖFLER *et al.* [1993]).

VI) Under irradiation, diffusion is enhanced. This has been shown in the first group, using either electron irradiation, that is producing only isolated Frenkel pairs and excluding cascade mixing, (BARBU and LIMOGE [1983]), or heavy ions (TYAGI *et al.* [1991a]), and also in the second group using electrons (LIMOGE [1987]) or heavy ions too (AVERBACK and HAHN [1988]). When measured, the flux dependence is sublinear, of the order of 1/2, pointing *in crystals* to a recombination regime (see § 8.3.1.3). Irradiations at low temperature (30 K) followed by isochronal annealings produce stages similar to the ones in crystalline metals (AUDOUARD and JOUSSET [1979]).

VII) Positron annihilation spectroscopy, possibly due to the competition between vacancy trapping and a high level of volume trapping, does not provide a clear answer, but the results are not incompatible with the existence of vacancy defects in both kind of alloys (TRIFTHÄUSER and KÖGEL [1987]).

VIII) As sketched on the figure 22, the Stokes–Einstein relationship is not obeyed *below* T_g. On the contrary, the viscosity deduced from creep measurements evolves as t^{-1} whatever the duration of the experiment (LIMOGE *et al.* [1882], LIMOGE and BREBEC [1988]), at least in the first group of alloys: with regard to the deformation there is no "equilibrium" structure on any accessible time scale. But the activation energies of diffusion and viscosity are generally very similar.

IX) Hydrogen diffusion has been reviewed by KIRCHEIM [1988]. It has been much studied in PdSi and NiTi alloys by various methods. The main characteristic is that D

Table 12
Diffusion parameters in various metallic glasses.

Alloy	Tracer	D_0 m²/sec	Q_{eV}	$Q_{crystal}$ (eV)	Reference
$Fe_{40}Ni_{40}P_{14}B_6$	Fe^{59}	1.0×10^{-3}	2.0	2.9	a
	P^{32}	5.5×10^{-15}	.81		a
	Fe^{56}	2.7×10^{-2}	2.4	2.9	b
$Fe_{40}Ni_{40}B_{20}$	P^{32}	$1.0\times10^{+4}$	3.1		b
	Ni^{63}	4.0×10^{-4}	2.14		c
	Au	1.9×10^{-4}	2.09		d
$Fe_{80}B_{20}$	Fe^{59}	4.6×10^{-5}	2.1		e
$Pd_{77}Cu_6Si_{17}$	Au	1.2×10^{-5}	1.78		d
	Fe^{59}	3.1×10^{-7}	1.5		e
$Fe_{91}Zr_9$	Zr^{95}	2.1×10^{-3}	2.5		e
	Co^{57}	8.0×10^{-7}	1.52		f
$Co_{89}Zr_{11}$	Au^{195}	7.9×10^{-1}	2.84		
$Co_{74}Ti_{26}$	B^{11}	1.77×10^{-7}	1.63		g
	Co^{60}	3.7×10^{-7}	1.42	1.52 (α Zr)	h
	Ni^{63}	1.7×10^{-7}	1.47	.8 (α Zr)	h
$Ni_{50}Zr_{50}$	Cu	1.2×10^{-6}	1.69		i
	Au	4.8×10^{-6}	2.09		i
	Hf	8×10^{-17}	.75		j
	Ag	1.2×10^{-14}	.82		k
$Cu_{50}Zr_{50}$	Au	1.3×10^{-7}	1.55		k
$Ni_{40}Ti_{60}$	B	7.4×10^{-4}	2.05		l
	Be	1.7×10^{-3}	2.2		l
	Fe	2.5×10^{-3}	2.33	1.2 (α-Ti)	l
	Si	5.8×10^{-4}	2.35		l
$Fe_{28}Zr_{72}$	Fe^{59}	2.6×10^{1}	2.6		e
	Fe^{59}	6.0×10^{-1}	2.3	< 1	e
$Fe_{24}Zr_{76}$	Zr^{95}	7.0×10^{6}	3.2	3.1	e

[a] VALENTA *et al.* [1981]; [b] HORVATH *et al.* [1985]; [c] TYAGI *et al.* [1991b]; [d] AKTHAR *et al.* [1982]; [e] HORVATH *et al.* [1988]; [f] DÖRNER and MEHRER [1991]; [g] LA VIA *et al.* [1992]; [h] HOSHINO *et al.* [1988]; [i] HAHN and AVERBACK [1988]; [j] WU [1991]; [k] STELTER and LAZARUS [1987]; [l] SHARMA *et al.* [1993].

increases with the H concentration with a concomitant decrease of both activation energy and D_0 term. The diffusion in a $Pd_{81}Si_{19}$ alloy can be lower at low concentration than in the crystalline phase, but higher at high concentration (LEE and STEVENSON [1985]). These results can be understood by assuming a distribution of site energies for H, the lowest being filled first and acting like traps which decrease D. A gaussian distribution is usually assumed (KIRCHHEIM *et al.* [1982]), although in-elastic and quasi-elastic neutron scattering are more in agreement with bimodal distributions (RUSH *et al.* [1989]). This bimodal distribution has been seen by H permeation studies in a NiTi system (KIM and STEVESON[1988]).

References: p. 651.

9.1.2. Mechanism proposals

We enter here a more subjective part. Three possibilities are presently explored, namely the so-called collective mechanism, the point defect route and the free volume approach. Lacking space, we will not present here the free volume approach (COHEN and TURNBULL [1961], SPAEPEN [1981]) since in its present state, it is basically an inconsistent *vacancy model* (LIMOGE [1992a)]), which moreover contradicts point VIII) above (among others).

Five reasons are generally invoked to support the proposal of a collective mechanism: i) the difficulty to figure out a defect in the absence of a lattice, ii) the extreme values of the D_0's, iii) the arrhenian behaviour, iv) the small value of the isotope effect, v) the slightly negative value observed for the activation volume in one alloy. The D_0's have been shown particularly to be correlated with the Q's, with a correlation coefficient quite different from the one prevailing in crystals, obtained through Zener's model (§ 3.3.3). This unusual coefficient has been taken as the indication of a new mechanism at work (SHARMA *et al.* [1989]). The points i) ii) iii) iv) will be developed in the next two paragraphs. We have no explanation for the experimental contradictions on point v), except that diffusion under pressure is an extremely difficult task in itself, and *systematic errors* (surface oxidation, thermal gradients, ...) are not easy to avoid, particularly in the glassy systems for the reasons given above. Moreover negative activation volumes are difficult to understand in compact phases. We nevertheless have the feeling that the strongest motivation for that proposal is simply that the glassy state can be obtained in a continuous evolution from the liquid state, making the transposition very natural, despite the break in the D versus 1/T plot in fig. 22. No proposal has been made for describing the diffusion event at an atomic level.

The defect proposal is based on the following ideas: i) a sufficient amount of *local order* in amorphous metallic alloys for defining a defect, ii) a close analogy for D_0 and Q between crystalline and credible results in many glasses, for similar compositions, iii) the existence of irradiation effects, iv) the activation volume measurements, v) from point VIII) above different defects are involved in diffusion and creep, vi) the defect viewed as an energy density fluctuation which must exist in a glass as in any other thermodynamic system. A vacancy defect has been proposed for the first group of alloys and possibly for the large atoms in the second, and an interstitial defect for the small solutes in the second group.

We have no room here to discuss these proposals in detail and the interested reader can find quite extensive developments in the reviews quoted at the beginning, or in the general references given at the end. We would like to emphasize that almost all of these arguments are mere *analogies*. In order to get firmer conclusions we need to develop a better understanding of the atomic mechanism itself, and of its statistical properties. This is the purpose of the following two paragraphs, chiefly in the case of the vacancy proposal for which the most developed studies have been done.

9.2. Simulation approach of the self-diffusion process

The direct simulation of the diffusion, generally by Molecular Dynamics, is a delicate

task since the lowest accessible values of D are of the order of 10^{-11} m^2/s given the present-day limitations of the computing possibilities, to be compared to the 10^{-20} m^2/s which is the typical goal. The direct simulations are therefore limited to the *liquid* range, giving few informations on the *solid* one. The other way is to devise a (and of course if possible all) probable atomic mechanism(s), involving a defect or not, and to study its properties, coming back to macroscopic diffusion using the proper statistical theory.

In the first approach it has been shown several times recently that when the diffusion becomes of the order of 10^{-11} m^2/s, the diffusion *in the liquid* turned progressively from a collective behaviour to a jump one, involving three to five atoms (MIYAGAWA *et al.* [1988], WAHNSTROM [1991]). In the absence of any activation energy determination for these jumps, it is not possible to determine wether they are still active at the much lower temperatures which are of interest here, and which role they could play in diffusion. It is also not possible to build a proper statistical theory for them.

Several works have attempted to characterize point defects in simple models of glasses, using mostly Lennard–Jones interactions (BENNETT *et al.* [1979], DOYAMA *et al.* [1981], LAAKONEN and NIEMINEN [1988, 1990]). These studies generally denied any interest in the notions of interstitial or vacancy, since the latter disappeared quite rapidly after their introduction into a model glass at a non-zero temperature. However, given the small size of the systems studied in simulation, and the possibility that a glass contains sources and sinks for the various possible defects, this elimination is possibly normal if the temperature is high enough to allow the defect to jump (LIMOGE and BREBEC [1988]). This is indeed what has been observed in a careful statistical study of the properties of vacancies in a Lennard–Jones glass: it has been shown that it is possible to define a vacancy defect in this simple model glass (DELAYE and LIMOGE [1992, 1993a, 1993b]). These vacancies are associated with a high level of local order, of a spherical nature in this case. They can jump as soon as the temperature is high enough, and these jumps are frequently collective like those observed in crystalline metals at high temperature, involving from three to five atoms. The least ordered regions in the glass act as defect sources and sinks, and this characteristic feature persists over duration quite long with respect to the duration of a jump sequence. The thermodynamical properties of the vacancy (formation and migration energies, entropies and volumes) were shown to be in quite good agreement with the knowledge gained in actual glasses. We have shown in figure 23 an example of these thermodynamic properties.

Using the results of the theory of the random walk on a random lattice (see § 9.4) LIMOGE [1992b)] and LIMOGE *et al.* [1993] have been able to build a model for the vacancy-mediated diffusion in amorphous metals in reasonable agreement with the experimental results.

The goal now is to check wether the other mechanisms which can be imagined, can be characterized and inserted in a statistical model in a similar way, to compare them with the experiments.

9.3. Random walk on a random array

Due to the lack of translational symmetry, in an amorphous solid the local properties

References: p. 651.

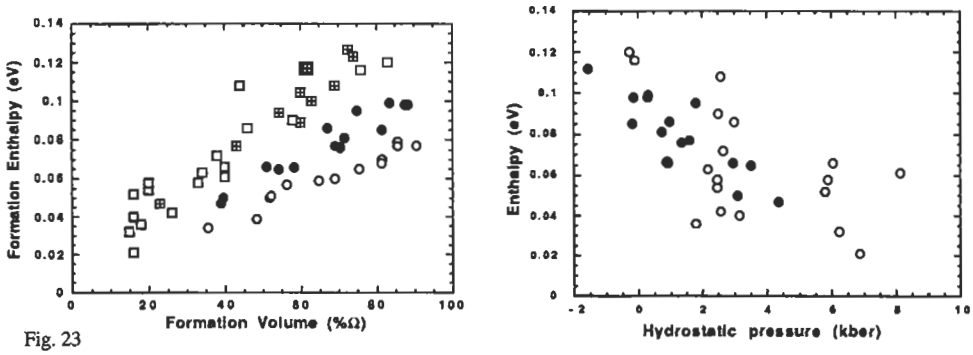

Fig. 23

a. Formation enthalpies, in eV, versus formation volumes, % of an atomic volume.
Rapidly quenched system: □ at 2.5 kbar.
Slowly quenched system: ⊙ at 0. kbar; ● at 0.8 kbar; ⊞ at 2.5 kbar.

b. Same formation enthalpies as in figure 8a but versus local pressure:
Rapidly quenched system: ⊙ at 2.5 kbar.
Slowly quenched system: ● at 0.8 kbar

are distributed. In our case the activation energies determined by local probes show a more or less broad spectrum (BALANZAT [1980], RETTENMEYER *et al.* [1986]), corresponding to a very large spreading of the jump frequencies. The site and the saddle point energies display such a distribution. However they have very different properties and effects upon diffusion, at least in a 3–D space: the saddle disorder tends to accelerate diffusion but the site one slows down a tracer particle. It has only recently be realized that the opposite effects of the two kinds of disorder should produce qualitatively new kinds of behaviour. A theory of the interstitial diffusion at low concentration, combining an analytical approach and Monte Carlo simulations, for the random walk on an energetically random lattice has been built (LIMOGE and BOCQUET [1988, 1989, 1990, 1993]. The main results are the following:

– with respect to long range diffusion, the two kinds of disorder *do not add but more or less compensate each other*. The diffusion coefficient of a tracer particle can be calculated in a mean field approximation as:

$$D^{\infty} = \exp\left(-\beta\left(\overline{\varepsilon_c} - \overline{\varepsilon_s}\right)\exp\left(\frac{1}{2}\beta^2\left(f\sigma_c^2 - \sigma_s^2\right)\right)\right) \tag{76}$$

for gaussian distributions of site and saddle point energies, described by their mean value, $\overline{\varepsilon_S}$ and $\overline{\varepsilon_C}$, and their variances, σ_s and σ_c; f is a slowly varying function of $\beta\sigma_c$ as well as of the nature of the underlying lattice, the high temperature limit of which is unity.

– for values of the σ's compatible with the experimental orders of magnitude, as deduced from the relaxation measurements, the non gaussian regime cannot be detected by *macroscopic diffusion* measurements since the dispersive regime lasts at most a few

jumps, but is accessible to local probes. Once more the two disorders do not add, but the saddle one appears to be dominant, with regard to the dispersive behaviour.

It is clear from the equation (76) that the residual term (exp $(\beta^2(f\sigma_c^2 - \sigma_s^2)/2)$ can be without proper judgement incorporated into an *apparent* D_0, thus appearing very much different from the true pre-exponential factor which is related to an activation entropy (in the above model D_0 equals 1); depending on the nature of the dominant disorder, very large or very low apparent D_0 are obtained. Using the experimental orders of magnitude, the expected deviations can amount to very large values, say of the order of $10^{\pm 3}$, even for undetectable residual curvatures of the Arrhenius plots. Finally, it is interesting to note that in a non perfectly compensated case, one can easily demonstrate that the result of this effect is a Zener-like correlation between the *apparent preexponential term and the apparent activation energy*, the order of magnitude of which is exactly what is found in the experimental results (LIMOGE [1992b]).

All the features of diffusion in amorphous metals can therefore be taken into account at the present day in the framework of the standard defect-mediated models. Of course, this cannot exclude that other mechanisms could compete and be even more efficient, for example the collective relaxation events mentioned above. The proper treatment of these other possibilities, collective or not, is a matter for years to come.

Note added in proof: A very recent work (OLIGSCHLEGER and SCHOBER [1995]) based on M. D. simulations in model glasses reported on the existence of collective relaxation events of low energy, which could partly answer our questions, if transposable to diffusion.

References

ABLITZER, D., 1977, Phil. Mag. **36**, 391.
ABLITZER, D., J. P. HAEUSSLER and K. V. SATHYARAJ, 1983, Philos. Mag. **A47**, 515
ABLITZER, D., and A. VIGNES, 1978, J. Nucl. Mater. **69–70**, 97.
*ABRAGAM, A., 1961, The Principles of Nuclear Magnetism (University Press, Oxford).
ACHAR, B. N. N., 1970, Phys. Rev. **B2**, 3848.
ADAM, P., 1971, Z. Naturf. **26a**, 40.
ADDA, Y., M. H. AMBROISE and F. BARBIER, 1994, Defect and Diffusion Forum **155–156**, 511.
ADDA, Y., M. BELEYER and G. BREBEC, 1975, Thin Solid Films **25**, 107.
ADDA Y., G. BREBEC, R. P. GUPTA and Y. LIMOGE, 1987, in ref. J), p.349.
ADDA. Y. and G. CICCOTTI, 1985, Rapport C. E. A. R-5328.
ADDA, Y. and A. KIRIANENKO , 1959, J. Nucl. Mater. **1**, 120
ADDA, Y. and A. KIRIANENKO, 1962, J. Nucl. Mater. **6**, 130
ADDA, Y., A. KIRIANENKO and C. MAIRY, 1959, J. Nucl. Mater. **3**, 300
*ADDA, Y. and J. PHILIBERT, 1966, La diffusion dans les solides (Presses Universitaires de France. Paris).
AGARWALA, R. P., 1984, Mat. Sc. Forum, **1**, 15.
AIFANTIS, E. C., 1979, Acta Metall. **27**, 683.
AIT SALEM, M., T. SPRINGER, A. HEIDEMANN and B. ALEFELD, 1979, Phil. Mag. **A39**, 797.
AKTHAR, D., B. CANTOR and R. W. CAHN, 1982, Acta Metall. Mater., **30**, 1571.
ALA-NISSILA, T. and S. C. YING, 1992, Progress in Surface Science **39**, 227.
ALEFELD, G., J. VÖLK and G. SCHAUMANN, 1970, Phys. Stat. Sol. **37**, 337.
ALLNATT, A. R., 1965, J. Chem. Phys. 43, 1855.
ALLNATT, A. R., 1981, J. Phys. **C14**, 5453.

ALLNATT, A.R., 1991, Phil. Mag. **A64**, 709.
ALLNATT, A.R. and E.L. ALLNATT, 1984, Phil. Mag. **A49**, 625.
ALLNATT, A.R. and E.L. ALLNATT, 1991, Phil. Mag. **A64**, 341.
ALLNATT, A.R. and E.L. ALLNATT, 1992, Phil. Mag. **A66**, 165.
ALLNATT, A.R., A. BARBU, A. D. FRANKLIN, A. B. LIDIARD, 1983, Acta Metall **31**, 1307.
ALLNATT, A.R. and A.B. LIDIARD, 1987a, Rep. Progr. Physics, 50, 373.
ALLNATT, A.R. and A.B. LIDIARD, 1987b, Acta Metal. **35**, 1555.
ALLNATT, A.R. and A.B. LIDIARD, 1987c, Phil. Mag. Letters **56**, 231.
ALLNATT, A.R. and Y. OKAMURA, 1984, Non-traditional Methods in Diffusion, ed. G.E. Murch, H.K. Birnbaum and J.R. Cost (N.Y.: Met. Soc. AIME), 237.
ANDERSEN H.C., 1980, J. Chem. Phys., **72**, 2384.
ANTHONY, T.R., 1971, Impurity Currents Generated by Vacancy Currents in metals, in: Proc. Conf. Atomic transport in Solids and Liquids, Marstrand (1970), eds. A. Lodding and T. Lagerwall (Zeitschrift für Naturforschung, Tübingen) p. 138.
ANTHONY, T.R., 1972, Solute Segregation and Stresses Generated around Growing Voids in Metals, in : Conf-71060, Proc. Conf. Radiation-induced Voids in Metals, Albany (1971), eds. J.W. Corbett and L.C. Ianniello (USAEC, Oak Ridge) p. 630.
ANTHONY, T.R., 1975, in ref. D), p. 353.
ANTHONY, L., J.K. OKAMOTO and B. FULTZ, 1993, Phys. Rev. Letters **70**, 1128.
AOKI, K. and O. IZUMI, 1975, Phys. Stat. Sol. **a82**, 657.
ARITA, M., M. KOIWA and S. ISHIOKA, 1989, Phil. Mag. **A60**, 563.
ARITA, M., H. NAKAJIMA, M. KOIWA and S. MIURA, 1991, Mat. Trans., JIM, **62**, 32.
Arkhipova, N.K., S.M. Klotsman, I.P. Polikarpova, A.N. Timofeev and P. Shepatkovskii, 1986, Fiz. Met. Metalloved **62**, 1882.
ARNAUD, B., LE HAZIF R. and MARTIN G., 1985, Acta Metall., **33**, 1105.
ARNHOLD, V., 1981, Inaugural dissertation, Münster.
ASKILL, J., 1971, Phys. Stat. Sol. **8**, 587.
AUDOUARD, A. and J.C. JOUSSET, 1979, Rad. Eff. Lett., **50**, 9.
AVERBACK, R.S., R. BENEDEK and K.L. MERKLE, 1978, Phys. Rev. B, **18**, 4156.
AVERBACK, R.S. and H. HAHN, 1988, Phys. Rev. B, **37**, 10833.
Averback, R.S. and H.J. Höfler, 1993, Def. Diff. Forum., **95–98**, 1131.
AVERBACK, R.S. and D.N. SEIDMAN, 1987, **15–18**, 963.
AYRAULT, G. and G. EHRLICH, 1974, J. Chem. Phys. **60**, 281.
BAIK, Y.-J. and D. N. YOON, 1990, Acta Metall. Mater. **38**, 1525.
BAKKER, H., 1971, Phys. Stat. Sol. **44**, 369.
BAKKER, H., 1979, Phil. Mag. **A40**, 525.
BAKKER, H., 1984, J. Less-Common Metals **99**, 257.
BAKKER, H., 1993, Defect and Diffusion Forum **95–98**, 803.
BALANZAT, M., 1980, Scr. Metall., **14**, 173.
BALANZAT, M., and J. HILLAIRET, 1980, The Zener relaxation: A Convenient Tool to Study Vacancy Sources and Sinks in a Metal Lattice, in: Proc. Conf. Internal Friction and Ultrasonic Attenuation in Solids, Manchester (1980), ed. C.C. Smith (Pergamon Press, New York) p. 123.
BALLUFFI, R.W., 1960, Acta Metall. **8**, 871.
BALLUFFI, R.W., and J.W. CAHN, 1981, Acta Metall. **29**, 493
BALLUFFI, R.W., T. KWOK, P.D. BRISTOWE, A. BROKMAN, P.S. HO and S. YIP, 1981, Scripta Metall. **15**, 951.
BALOGH, A.G., I. DESZI, J. PELLOTH, R.A. BRAND, W. KEUNE and W. PUFF, 1992, Materials Science Forum **105–110**, 897.
BARBU, A., 1978, Thèse, Univ. Nancy.
BARBU, A., 1980, Acta Metall. **28**, 499.
BARBU, A., DUNLOP A., LESUEUR D. and AVERBACK R.S., 1991, Europhys. Lett., **15**, 37
BARBU, A., and Y. LIMOGE, 1983, Acta Metall., **31**, 559.
BARBU, A., and G. MARTIN, 1977, Scripta Metall. **11**, 771.
BARCZ, A.J., B.H. PAINE and M.A. NICOLET, 1984, Appl. Phys. Lett., **44**, 45.

BARDEEN, J. and C. HERRING, 1951, Diffusion in Alloys and the Kirkendall Effect, in : Atom Movements, ed. J. H. Hollomon (ASM, Cleveland, OH) p. 87.
BARCZ, A. J., PAINE B. N. and NICOLET M. A., 1984, App. Phys. Lett., **44**, 45.
BARTDORFF, D., G. NEUMANN and P. REIMERS, 1978, Philos. Mag. **38**, 157.
BARTELS, A., 1987, Mat. Sci. Forum **15–18**, 1183.
BASSETT, D. W. and P. R. WEBBER, 1978, Surf. Sci. **70**, 520.
BEAMAN, D. R., and R. W. BALLUFFI, 1965, Phys. Rev. **137**, 917.
BEAMAN, D. R., R. W. BALLUFFI and R. O. SIMMONS, 1964, Phys. Rev. **A134**, 532.
BENNETT, C. H., 1975, in ref. D), 73.
BENNETT, C. H., P. CHAUDHARI, V. MORUZZI and P. STEINHARDT, 1979, Phil. Mag. **A40**, 485.
BENOIST, P., and G. MARTIN, 1975a, Thin Solid Films **25**, 181.
BENOIST, P., and G. MARTIN, 1975b, J. Physique. Colloq. **C4**, 213.
BENOIST, P., J. L. BOCQUET and P. LAFORE, 1977, Acta Metall. **25**, 265.
BERNARDINI, J. and G. MARTIN, 1976, Scripta Metall. **10**, 833.
BERRY, B. S., and J. L. OREHOTSKY, 1968, Acta Metall. **16**, 683.
BEYELER, M., and Y. ADDA, 1968, J. Physique **29**, 345.
BHARATI, S., and A. P. B. SINHA, 1977, Phys. Stat. Sol. (a) **44**, 391.
BLACK, J. E. and Z.-J. TIAN, 1993, Phys. Rev. Letters **71**, 2445.
BLOEMBERGEN, N., E. M. PURCELL and R. V. POUND, 1948, Phys. Rev. **73**, 679.
BOCQUET, J. L., 1972, Acta Metall. **20**, 1347.
BOCQUET, J. L., 1973, Thèse, Univ. Paris-Sud.
BOCQUET, J. L., 1974, Acta Metall. **22**, 1.
BOCQUET, J. L., 1981, C.E.A. (Saclay, France) Internal Report, R-5112.
BOCQUET, J. L., 1983a, J. Phys. **F13**, L33.
BOCQUET, J. L., 1983b, Phil. Mag. **A47**, 547.
BOCQUET, J. L., 1986, Acta Metall. **34**, 571.
BOCQUET, J. L., 1987, Res Mechanica **22**, 1.
BOCQUET, J. L., 1990a, in ref. G), p. 87.
BOCQUET, J. L., 1990b, CEA-Report-R-5531
BOCQUET, J. L., 1991, Phil. Mag. **A63**, 157.
BOCQUET, J. L. and G. MARTIN, 1979, J. Nucl. Mater. **83**, 186.
BONDY, A., P. REGNIER and V. LEVY, 1971, Scripta Metall. **5**, 345.
BONZEL, H. P., 1976, CRC Crit. Rev. Solid State Sci. **6**, 171.
BONZEL, H. P. and E. E. LATTA, 1978, Surf. Sci. **76**, 275.
BOSE, A., G. FROHBERG and H. WEVER, 1979, Phys. Stat. Sol. (a) **52**, 509.
BOSVIEUX, C. and J. FRIEDEL, 1962, J. Phys. Chem. Solids **23**, 12.
BOWKER, M. and D. A. KING, 1978a, Surf. Sci. **71**, 583.
BOWKER, M. and D. A. KING, 1978b, Surf. Sci. **72**, 208.
BRAGG, W. L. and E. J. WILLIAMS, 1934, Proc. Roy. Soc. **A145**, 699.
BRÄTTER, P. and H. GOBRECHT, 1970, Phys. Status Solidi **37**, 869
BREBEC, G., 1977, unpublished work.
BREBEC, G., 1978, Diffusion Atomique, in : Defauts Ponctuels dans les Solides (Les Editions de Physique, Orasy) p. 181.
BREBEC, G., 1990, in ref. G), p.339.
BREITLING, H. M., and R. F. HUMMEL, 1972, J. Phys. Chem. Solids **33**, 845.
BRINKMAN, J. A., 1954, Phys. Rev. **93**, 345.
BRÜNGER, G., O. KANERT and D. WOLF, 1980, Solid State Commun. **33**, 569.
BURTON, B., 1982, The Interaction of Oxidation with Creep Processes, in : Single Crystal Properties, vol. B1, ed. D. J. Fisher (Trans. Tech. S. A., Rockport) p. 1.
BURTON, M. K., N. CABRERA and F. C. FRANK, 1951, Phil. Trans. Roy. Soc. **A243**, 299.
BUTRYMOWICZ, D. B. and J. R. MANNING, 1978, Metallurg. Trans. **9A**, 947.
BUTZ, R. and H. WAGNER, 1979, Surf. Sci. **87**, 69 and 85.
CAHN, J. W., 1967, Trans. AIME **242**, 166.

CAHN, J. W. and R. W. BALLUFFI, 1979, Scripta Metall. **13**, 499.
CAHN, R. W., 1992, Ordered Intermetallics: Physical Metallurgy and Mechanical Behaviour, C. T. Liu, R. W. Cahn and G. Sauthoff Eds.,Kluwer Academic Publishers, 511.
CAPLAIN, A. and W. CHAMBRON, 1977, Acta Metall. **25**, 1001.
CARLSON, O. N. and F. A. SCHMIDT, 1981, J. Less-Common Met. **79**, 97.
CARLSON, P. T., 1976, Metallurg. Trans. **7A**, 199.
CARLSON, P. T., 1978, Metallurg. Trans. **9A**, 1287.
CAR R. and PARRINELLO M., 1985, Phys. Rev. Lett., **55**, 2471.
*CARSLAW, H. S. and J. C. JAEGER, 1959, Conduction of Heat in Solids (Clarendon Press; Oxford)
CAUVIN, R., 1981, C. E. A. report R-5105.
CAUVIN, R. and G. MARTIN, 1981, Phys. Rev. **B23**, 3322 and 3333.
CAUVIN, R. and G. MARTIN, 1982, Phys. Rev. **B25**, 3385.
CHABIK, St. and B. ROZENFELD, 1981, Appl. Phys. **25**, 143.
CHAMBRON, W., and A. CAPLAIN, 1974, Acta Metall. **22**, 357.
CHANDLER, D., 1978, J. Chem. Phys. **68**, 2959.
CHANDLER, D., 1986, J. Stat. Phys. **42**, 49.
CHANDLER, D., 1988, Faraday Discuss. Chem. Soc. **85**, 341.
CHATURVEDI, K. L., and A. R. ALLNATT, 1992, Phil. Mag. **A65**, 1169.
CHATURVEDI, K. L., and A. R. ALLNATT, 1994, Phil. Mag. **A70**, 657.
CHEN, C., and T. T. TSONG, 1994, Phys. Rev. Letters **72**, 498.
CHEN, L. Y., and S. C. YING, 1993, Phys. Rev. Letters **71**, 4361.
CHENG, Y. T., 1990, Mater. Sci. Rep., **5**, 45.
CHIRON, R., and G. FAIVRE, 1985, Philos. Mag. **A51**, 865.
CHOI, J. Y., and P. G. SHEWMON, 1962, Trans. Met. Soc. AIME **224**, 589.
CHU, W. K., J. W. MAYER and M. A. NICOLET, 1978, Backscattering Spectrometry (Academic, New York).
CICCOTTI G., 1991, in ref. R), p. 119.
CICCOTTI, G., M. GUILLOPE and V. PONTIKIS, 1982, in ref. I), p. 415.
* CICCOTTI G. and W. G. HOOVER, 1986, Molecular Dynamics simulations of Statistical Mechanical Systems, (North Holland, Amsterdam).
CLERI, F. and V. ROSATO, 1993, Phil. Mag. Letters **67**, 369.
COHEN M. H. and D. TURNBULL, 1961, J.Chem. Phys., **34**, 120.
COMBRONDE, J. and G. BRÉBEC, 1971, Acta. Metall. **19**, 1393.
COMPAAN, K. and Y. HAVEN, 1956, Trans. Farad. Soc. **52**, 786.
COMPAAN, K. and Y. HAVEN, 1958, Trans. Farad. Soc. **54**, 1498.
COOK, H. E. and J. E. HILLIARD, 1969, J. Appl. Phys. **40**, 2191.
CORDES, H., and K. Kim, 1966, J. Appl. Phys. **37**, 2181.
CORNET, J. A., 1971, J. Phys. Chem. Solids, **32**, 1489.
CORNET, J. F. and D. CALAIS, 1972, J. Phys. Chem. Solids **33**, 1675.
COSTE, V., P. BENOIST and G. MARTIN, 1976, Calcul de la Fréquence Moyenne de Saut des Atomes le long de Joints de Grains à Structure Périodique, in: Proc. 19ème Colloque Métall., La Diffusion dans les Milieux Condensés, Théories et Applications, Saclay 1976 (INSTN, Saclay, France) p. 507.
COUSTY, J., 1981, Thèse, Univ. Paris-Sud; Internal Report CEA-R-5143 (Saclay).
COUSTY, J., R. PEIX and B. PERRAILLON, 1981, Surf. Sci. **107**, 586.
COWAN, P., and T. T. TSONG, 1975, Phys. Lett. **53A**, 383.
COWLEY, J. M., 1950, Phys. Rev. **77**, 669.
*CRANK, J., 1956, The Mathematics of Diffusion (Clarendon Press, Oxford).
CROLET, J. L., 1971, Thèse, Univ. Paris-Sud.
DA FANO, A., and G. JACUCCI, 1977, Phys. Rev. Lett. **39**, 950.
DALLWITZ, M. J., 1972, Acta Metall. **20**, 1229.
DAMKÖHLER, R., and Th. HEUMANN, 1982, Phys. Stat. Sol. (a) **73**, 117.
DARIEL, M. P., D. DAYAN and A. LANGUILLE, 1971, Phys. Rev. **B4**, 4348.
DARIEL, M. P., G. EREZ and G. M. J. SCHMIDT, 1969, Philos. Mag. **19**, 1045.
DARKEN, L. S., 1948, Trans. AIME **175**, 184.

DAVIS, R.E., and W.D. MCMULLEN, 1972, Acta Metall. **20,** 593.
DAYANANDA, M.A., 1981, Acta Metall. **29**, 1151.
DAYANANDA, M.A., 1992, in 'Ordered Intermetallics: Physical Metallurgy and Mechanical Behaviour', Liu, C. T., CAHN R.W. and SAUTHOFF G. Eds, Kluwer Academic Publishers (Boston), 465.
DE BOER, F.R., R. BOOM, W.C.M. MATTENS, A.R. MIEDEMA and A. K. NIESSEN, 1988, Cohesion in Metals: Transition Metal Alloys (NorthHolland, Amsterdam).
DE BRUIN, H.J., A. BAKKER and L.P. VAN DER MEY, 1977, Phys. Stat. Sol. **b82**, 581.
DE BRUIN, H.J., G.E. MURCH, A. BAKKER and L.P. VAN DER MEY, 1975, Thin Solid Films **25**, 47.
DECKER, D.L., J.D. WEISS and H.B. VANFLEET, 1977, Phys. Rev. **B16**, 2392.
*DE GROOT, S.R., and P. MAZUR, 1969, Non-Equilibrium Thermodynamics (North-Holland, Amsterdam).
DELAYE, J.M., 1993, PhD Thesis, Univ. Paris VI.
DELAYE, J.M., and Y. LIMOGE, 1992, Europhys. Lett., **20,** 421.
DELAYE, J.M., and Y. LIMOGE, 1993a, J. Phys. I, **3,** 2063.
DELAYE, J.M., and Y. LIMOGE, 1993b, J. Phys. I, **3,** 2079.
DE LORENZI, G., and F. ERCOLESSI, 1992, Europhys. Let., **20**, 349.
DE LORENZI, G., G. JACUCCI and V. PONTIKIS, 1982, Surf. Sci. **166**, 391.
DESJONQUERES, M.C. and D. SPANJAARD, 1982, J. Phys. **C15**, 4007.
DETEMPLE, K., O. KANERT, K. LINGA MURTY and J. Th.M. DE HOSSON, 1991, Rad. Eff. Def. Sol., **119–121**, 771.
D'HEURLE, F.M., 1971, Proc. IEEE **59**, 1409.
D'HEURLE, F.M., and A. GANGULEE, 1972, Solute effects on Grain Boundaries, Electromigration and Diffusion, in: The Nature and Behaviour of Grain-Boundaries, ed. H. Hu (Plenum, New York).
DIAZ de la RUBIA, T., R.S. AVERBACK, R. BENEDEK and W.E. KING, 1987, Phys. Rev. Lett., **59**, 1930.
DIAZ de la RUBIA, T. and M.W. GUINAN, 1992, Mat. Sci. Forum, **97–99**, 23.
DICKEY, J.E., 1959, Acta Metall. **7,** 350.
DINHUT, J.F., T. BONOU and P. MOINE, 1976, Acta Metall. **24**, 445.
DIRKES, H. and Th. HEUMANN, 1982, J. Phys. **F12**, L 67.
DOAN, N.V., 1971, Thèse, Univ. Paris-Sud.
DOAN, N.V., 1972, J. Phys. Chem. Solids **33**, 2161.
DOAN, N.V., 1978, Dynamique Moléculaire, in: Défauts Ponctuels dans les Solides (Les Editions de Physique, Orsay) p. 285.
DOAN N.V., and Y. ADDA, 1987, Phil. Mag. A, **56**, 269.
DOAN, N.V., and J.L. BOCQUET, 1975, Thin Solid Films **25**, 15.
DOAN, N.V., and J.L. BOCQUET and Y. LIMOGE, 1976, Diffusion sous Champ Electrique et Gradient de Température, in: Proc. 19ème Colloque Métall., La Diffusion dans les Milieux Condensés, Théories et Applications, Saclay 1976 (INSTN, Saclay, France) p. 911.
DOMIAN, H.A., and H.I. AARONSON, 1965, Simultaneous Diffusion of Silver and Magnesium in Stoichiometric Monocrystalline b-AgMg, in: Diffusion in Body-Centered Cubic Metals (ASM, Cleveland, OH) p. 209.
DONALDSON, A.T., and R.D. RAWLINGS, 1976, Acta Metall. **24**, 285.
DORAN, D.G., 1970, Rad. Eff. **2**, 249.
DÖRNER W., and H. MEHRER, 1991, Phys. Rev. B, **44**, 101.
DOYAMA M., R. YAMAMOTO and H. SHIBUTA, 1981, Proc. Int. Conf. R.Q.4, Sendaï 1981, p. 781.
DRECHSLER, M., B.L. BLACKFORD, A.M. PUTNAM and M.H. JERICHO, 1989, Colloque de Physique **C8**, Supplt n°11, **50**, 223.
DUCASTELLE, F., 1978, Electronic Structure and Equilibrium Properties of Metals and Alloys, in: Solid State Phase Transformations in Metals and Alloys, Aussois, 1978, (Les Editions de Physique, Orsay) p. 51.
DUPOUY, J.M., J. MATHIE and Y. ADDA, 1966, Mem. Sci. Rev. Metall. **63,** 481.
DYMENT, F., 1980, in: Titanium 80, Proc. 46th Int. Conf. on titanium, Eds. H. Kimura and O. Izumi, Kyoto p. 519.
ECKSELER, H., and C. HERZIG, 1978, Phys. Stat. Sol. (b) **85**, 185.
EDELIN, G., 1979, Acta Metall. **27**, 455.
*EHRLICH, G., and K. STOLT, 1980, Ann. Rev. Phys. Chem. **31**, 603.
EHRLICH, G., 1994, Surface Science **299/300**, 628.

EINSTEIN, A., 1905, Ann. Phys. **17**, 549.
EINZIGER, R. E., J. N. MUNDY and H. A. HOFF, 1978, Phys. Rev B,**17**, 440.
ELCOCK, E. W., 1959, Proc. Roy. Soc. (London) **73A**, 250.
ELDRIDGE, J. and K. L. KOMAREK, 1964, Trans. AIME **230**, 226.
ELLIS, J., and J. P. TOENNIES, 1993, Phys. Rev. Letters **70**, 2118.
ENGELMANN, C., 1977, Analyse par Observation Directe des Réactions Nucléaires. Rétrodiffusion de Particles Chargées, in: Les Techniques de l'Ingénieur, ed. C. Engelmann, p. 2561.
ENGLISH, C. A., S. M. MURPHY and J. M. PERKS, 1990, J. Chem. Soc. Far. Trans., **86**, 1263.
ERCKMANN, V., and H. WIPF, 1976, Phys. Rev. **37**, 341.
ERMERT, U., W. RUPP and R. SIZMANN, 1968, Thermal and Radiation-Enhanced Self-Diffusion in Gold Single Crystals at low Temperature, in: Proc. Int. Conf. Vacancies and interstitials in metals, Jülich, 1968 (KFA Jülich) p. 30.
ESSMAN, U., and MUGHRABI H., 1979, Phil. Mag. A, **40**, 731.
FÄHNLE, M. 1982, J. Low Temp. Phys. **46**, 3.
FARRARO, R., and R. B. MCLELLAN, 1979, Mat. Sci. Eng. **39**, 47.
FAUPEL, F. and T. HEHENKAMP, 1987, Acta Metall. **35**, 771.
FEIBELMAN, P. J., 1990, Phys. Rev. Letters **65**, 729.
FEIT, M. D., 1972, Phys. Rev. **B45**, 2145.
FIKS, V. B., 1959, Fiz. Tverd. Tela **1**, 16.
FIKS, V. B., 1961, Sov. Phys. Solid. State. **3**, 724.
FIKS, V. B., 1973, Fiz. Metall. Metalloved. **36**, 253.
FILLON, J., and D. CALAIS, 1977, J. Phys. Chem. Solids **38**, 81.
FISHER, J. C., 1951, J. Appl. Phys. **22**, 74.
FLAHIVE, P. G., and W. R. GRAHAM, 1980a, Surf. Sci. **91**, 449.
FLAHIVE, P. G., and W. R. GRAHAM, 1980b, Surf. Sci. **91**, 463.
FLINN, P. A., 1980, Diffusion in Solids and Liquids, in: Application of Mössbauer Spectroscopy VII, ed. R. L. Cohen (Academic, New York) p. 393.
FLYNN, C. P., 1968, Phys. Rev. **171**, 682.
*FLYNN, C. P., 1972, Point Defects and Diffusion (Clarendon Press, Oxford) p. 306.
FLYNN, C. P., 1987, in ref. J), p. 281.
FOILES, S. M., and M. S. DAW, 1987, J. Mater. Res. **2**, 5.
FORT, D., 1987, J. Less. Com. Met., **134**, 45.
FOURNELLE, R. A., 1991, Materials Science and Engineering **A138**, 133.
FRADIN, F. Y., and T. J. ROWLAND, 1967, Appl. Phys. Lett. **11**, 207.
FRANK, F. C., and D. TURNBULL, 1956, Phys. Rev. **104**, 617.
FRANKLIN, A. D., and A. B. LIDIARD, 1983, Proc. R. Soc. Lond. **A389**, 405.
FRANKLIN, A. D., and A. B. LIDIARD, 1984, Proc. R. Soc. Lond. **A392**, 457.
FRENKEN, J. W. M., B. J. HINCH, J. P. TOENNIS and C. WÖLL, 1990, Phys. Rev. **B41**, 938.
FRIEDEL, J., 1964, Dislocations, (Pergamon, Oxford).
FROHBERG, G., 1971, Habilitationsschrift, Berlin, p. 132.
FROMONT, M., A. LANGUILLE and D. CALAIS, 1974, J. Phys. Chem. Solids, **35**, 1367.
FROMONT, F. and G. MARBACH, 1977, J. Phys. Chem. Solids **38**, 27.
GEISE, J., and Ch. Herzig, 1987, Z. Metallkd, 291.
GENDRE, P., Y. LIMOGE and J. L. BOCQUET, 1991, Rapport C.E.A. R-5548.
GERL, M., 1967, J. Phys. Chem. Solids **28**, 725.
GERL, M., 1968, Thèse, Orsay.
GERL, M., and M. LANNOO, 1978, Structure Electronique, in: Defauts Ponctuels dans les Solides (Les Editions de Physique, Orsay) p. 29.
GHALEB, D., 1983, Thèse, Univ. Paris-Sud.
GHILARDUCCI, A. and M. AHLERS, 1983, J. Phys. F: Met. Physics **13**, 1757.
GIBBS, G. B., D. GRAHAM and D. H. TOMLIN, 1963, Phil. Mag. **8**, 1269.
GIBSON J. B., A. N. GOLAND, M. MILGRAM and VINEYARD G., 1960, Phys. Rev., **120**, 1229.
GILDER, H. M., and D. LAZARUS, 1966, Phys. Rev. **145**, 507.

GILDER, M., and D. LAZARUS, 1975, Phys. Rev. **B11**, 4916.
GILLAN, M.J., 1977, J. Phys. C, **10**, 1641.
GILLAN, M.J., 1986, J. Phys. C, **19**, 6169.
GILLAN, M.J., 1989, J. Phys. Condens. Mater., **1**, 689.
GILLAN, M.J., J.H. HARDING and R.J. TARENTO, 1987, J. Phys. C, **20**, 2331.
GIRIFALCO, L.A., 1964, J. Phys. Chem. Solids **24**, 323.
GIRIFALCO, L.A. and H. HERMAN, 1965, Acta Metall. **13**, 583.
GISSLER, W., 1972, Ber. Bunsen Gesell. **76**, 770.
GONZALES, R., J. PIQUERAS and L.I. BRU, 1975a, Phys. Stat. Sol. **29**, 161.
GONZALES, R., J. PIQUERAS and L.I. BRU, 1975b, Mat. Sci. Eng. **20**, 95.
GORNY, D.S., and R.M. ALTOVSKII, 1970, Fiz. Met. Metalloved. **30**, 85.
GORSKY, W.S., 1935, Z. Phys. der Sowjetunion **8**, 457.
GRAF, H., G. BLAZER, E. RECKNAGEL, A. WEIDINGER and R.I. GRYNSZPAN, 1980, Phys. Rev. Lett. **44**, 1333.
GRAHAM, W.R., and G. EHRLICH, 1974, Surf. Sci. **45**, 530.
GRAHAM, W.R., and G. EHRLICH, 1975, Thin Solid Films **25**, 85.
GRANDJEAN, Y., P. BELLON and G. MARTIN, 1994, Phys. Rev. **B50**, 4228.
GREER, A.L., and F. SPAEPEN, in Synthetic modulated structures, 1985, ed. L.L. Chang and B.C. Giessen, (Academic Press. New York).
GUINIER, A., 1959, Adv. Solid State Phys. **9**, 293.
GUPTA, D., 1975, Thin Solid Films **25**, 231.
GUPTA, D., 1982, Phys. Rev., **25**, 5188.
GUPTA, D. and D.S. LIEBERMAN, 1971, Phys. Rev. **B4**, 1070.
GUPTA, D., D. LAZARUS and D.S. LIEBERMAN, 1967, Phys. Rev. **153**, 863.
GUPTA, R.P., 1982, Phys. Rev. **B25**, 5188.
GUPTA, R.P., 1986, Sol. Stat. Com., **59**, 219.
HAESSNER, F., S. HOFMANN and H. SECKEL, 1974, Scripta Metall. **8**, 299.
HAGENSCHULTE H., and Th. HEUMANN, 1989, Defect and Diffusion Forum, **66–69** (DIMETA-88), 459.
HAHN, H., and R.S. Averback, 1988, Phys. Rev. B, **37**, 6533.
HAHN, H., R.S. Averback and H.M. Shyu, 1988, J. Less Comm. Metals, **140**, 345.
HÄHNEL, R., W. MIEKELEY and H. WEVER, 1986, Phys. Stat. Sol. **a97**, 181.
HALBWACHS, M., 1977, PhD Thesis, Université de Grenoble.
HALBWACHS, M., and J. HILLAIRET, 1978, Phys. Rev. **B18**, 4927.
HALBWACHS, M., J. HILLAIRET and S.R. COST, 1978a, J. Nucl. Mater. **69–70**, 776.
HALBWACHS, M., J.T. STANLEY and J. HILLAIRET, 1978b, Phys. Rev. **B18**, 4938.
HALICIOGLU, T., and G.M. POUND, 1979, Thin Solid Films **57**, 241.
HANCOCK, G.F., and B.R. MCDONNELL, 1971, Phys. Stat. Sol. (a) **4**, 143.
HANSEN, L.B., P. STOLTZE, K.W. JACOBSEN and J.K. NÖRSKOV, 1993, Surface Science **289**, 68.
HARRISON, L.G., 1961, Trans. Farad. Soc. **57**, 1191.
HART, E.W., 1957, Acta Metall. **5**, 597.
HÄSSNER, A., and W. LANGE, 1965, Phys. Stat. Sol. **8**, 77.
HAUG, K., and H. METIU, 1991, J. Chem. Phys. **94**, 3251.
HEHENKAMP, T., 1981, Microchim. Acta Suppl. **9**, 15.
HEITJANS, P., A. KÖRBLEIN, H. ACKERMANN, D. DUBBERS, F. FUJIWARA and H.J. STÖCKMANN, 1985, J. Phys. F **15**, 41.
HERZIG, Ch., and H. ECKSELER, 1979, Z. Metallkd. **70**, 215.
HERZIG, Ch., H. ECKSCLER, W. BUSSMANN and D. CARDIS, 1978, J. Nucl. Mater. **69–70**, 61.
HERZIG, C., and Th. HEUMANN, 1972, Z. Naturforschung, **27a**, 1109.
HERZIG, C., and U. KÖHLER, 1987, in ref. J), p.301.
HERZIG, Ch., L. MANKE and W. BUSSMAN, 1982, in: Proc. of Yamada Vth Conf. on point defects and defect interactions in metals, Eds. J.I. Takamura, M. Doyama and M. Kiritani (Univ. of Tokyo Press), p. 578.
HERZIG, C., H.J. ROCKOSCH and R. HILGEDIECK, 1982, in ref I), p. 330.
HEUMANN, T., 1979, J. Phys. **F9**, 1997.
HEUMANN, Th., and R. IMM, 1968, J. Phys. Chem. Solids **29**, 1613.

HEUMANN, T., H. MEINERS and H. STÜER, 1970, Z. Naturforsch. **25a**, 1883.
HEUMANN, T., and Th. ROTTWINKEL, 1978, J. Nucl. Mater. **69–70**, 567.
HEUMANN, T., and H. STÜER, 1966, Phys. Stat. Sol. **15**, 95.
HILGEDIECK, R., 1981, Inaugural dissertation, Münster.
HILGEDIECK, R., and C. HERZIG, 1983, Zeit. Metallkunde **74**, 38.
HILL, J. M., 1979, Scripta Metall. **13**, 1027.
HIRANO, K., 1981, Jump Frequency on Impurity Diffusion in Cu Based on New Data, in: Proc. Yamada Conf. V. - Point Defects and Defect Interactions in Metals, Kyoto (Japan), eds. J. I. Takamura, M. Doyama and M. Kiritani (Univ. of Tokyo Press, 1982) p. 541.
HIRANO, K., R. P. AGARWALA, B. L. AVERBACH and M. COHEN, 1962, J. Appl. Phys. **33**, 3049.
HO, K., and R. A. DODD, 1978, Scripta Metall. **12**, 1055.
HO, K., M. A. QUADER, F. LIN and R. A. DODD, 1977, Scripta Metall. **11**, 1159.
HO, K. M., C. L. FU and B. N. HARMON, 1983, Phys. Rev. B, **28**, 6687.
HO, K. M., C. L. FU and B. N. HARMON, 1984, Phys. Rev. B, **29**, 1575.
HO, P. S., and T. KWOK, 1989, Rep. Prog. Phys., **52**, 301.
HÖFLER H. J., R. S. AVERBACK, G. RUMMEL and H. MEHRER, 1992, Phil. Mag. Lett., **66**, 301.
HOLCOMB, D. F., and R. E. NORBERG, 1955, Phys. Rev. **98**, 1074.
HOLDSWORTH, P. C. W., and R. J. ELLIOTT, 1986, Phil. Mag. **A54**, 601.
HOOD, G. M., 1978, J. Phys. F, **8**, 1677.
HOOD, G. M., 1993, in ref. K), p. 755.
HOOVER, W. G., 1985, Phys Rev A, **31**, 1695.
HORVATH, J., F. DYMENT and H. MEHRER, 1984, J. Nucl. Mater. **126**, 206.
HORVATH, J, J. OTT, K. PFAHLER and W. ULFERT, 1988, Mater. Sci. Eng., **97**, 409.
HORVATH J., K. PFAHLER, W. ULFERT, W. FRANK and H. MEHRER, 1985, J. de Phys., **46**, 645.
HOSHINO K., R. S. AVERBACK, H. HAHN and S. J. ROTHMAN, 1988, Def. Dif. Forum, **59**, 225.
HOSHINO, K., Y. IIJIMA and K. HIRANO, 1981a, Phil. Mag. **A44**, 961.
HOSHINO, K., Y. IIJIMA and K. HIRANO, 1981b, Isotope Effect and Diffusion of Cadmium in Copper, in: Proc. Yamada Conf. V. - Point Defects and Defect Interactions in Metals, Kyoto (Japan), eds. J. I. Takamura, M. Doyama and M. Kiritani (Univ. of Tokyo Press, 1982) p. 562.
HOSHINO, K., Y. IIJIMA and K. HIRANO, 1982, Acta Metall. **30**, 265.
HOWARD, R. E., 1966, Phys. Rev. **144**, 650.
HOWARD, R. E., and A. B. LIDIARD, 1963, J. Phys. Soc. Jap. **18**, Suppl. II, 197.
*HOWARD, R. E., and A. B. LIDIARD, 1964, Rep. Prog. Phys. **27**, 161.
HOWARD R. E., and J. R. MANNING, 1967, Phys. Rev. **154**, 561.
HUANG, F. M., and H. B. HUNTINGTON, 1974, Phys. Rev. **B9**, 1479.
HUANG, J., M. MEYER and V. PONTIKIS, 1991, Phil. Mag. **A63**, 1149.
HUNTINGTON, H. B., 1966, Bull. Am. Phys. Soc. **11**, 265.
HUNTINGTON, H. B., 1968, J. Phys. Chem. Solids. **29**, 1641.
HUNTINGTON, H. B., and A. R. GRÖNE, 1961, J. Phys. Chem. Solids **20**, 76.
HUNTINGTON, H. B., and S. C. HO, 1963, J. Phys. Soc. Jap. **18**, Suppl. II, 20.
HUNTINGTON, H. B., N. C. MILLER and V. NERSES, 1961, Acta Metall. **9**, 749.
HUNTLEY, F. A., 1974, Phil. Mag. **30**, 1075.
IIJIMA , Y., S. I. USHINO and K. I. HIRANO, 1985, Phil. Mag. Letters **A52**, L37.
IORIO, N. R., M. A. DAYANANDA and R. E. GRACE, 1973, Metallurg. Trans. **4**, 1339.
ISHIOKA, S., and M. KOIWA, 1978, Phil. Mag. **A37**, 517.
ISHIOKA, S., and M. KOIWA, 1980, Phil. Mag. **A41**, 385.
ISHIOKA, S., and M. KOIWA, 1984, Phil. Mag. **A50**, 505.
ITO, T., S. ISHIOKA and M. KOIWA, 1990, Phil. Mag. **A62**, 499.
ITOH, T., H. NAKAJIMA, Y. NAKAMURA, M. KOIWA and S. YAMAGUCHI, 1989, Defect and Diffusion Forum **66–69**, 509.
JAMES, D. W., and G. M. LEAK, 1966, Philos. Mag. **14**, 701.
JANOT, C., 1976, J. Physique **37**, 253.
JAUNET, J., C. WALDBURGER and J. PHILIBERT, 1982, Surface Science **121**, 452.

JOB, B., J. MATHIE and P. REGNIER, 1974, Acta Metall. **22**, 1197.
JOHNSON, R. A., and N. Q. LAM, 1976, Phys. Rev. **B13**, 4364.
JOHNSON, R. A., and J. R. BROWN, 1992, J. Mat. Res. **7**, 3213.
JOHNSON, W. L., Y. T. CHENG, M. VAN ROSSUM and M. A. NICOLLET, 1985, N.I.M. B, **7–8**, 657.
JONES, M. J., and A. D. LE CLAIRE, 1972, Phil. Mag. **26**, 1191.
JUVE-DUC, D., D. TREHEUX and P. GUIRALDENQ, 1980, Mat. Sci. Eng. **42**, 281.
KAUR, R., and S. PRAKASH, 1982, J. Phys. **F12**, 1383.
KAXIRAS, E., and J. ERLEBACHER, 1994, Phys. Rev. Letters **72**, 1714.
KEHR, K. W., 1978, Theory of the Diffusion of Hydrogen in Metals, in: Hydrogen in Metals, eds. G. Alefeld and J. Völkl (Springer, Berlin) vol. 1, p. 197.
KELLOG, G. L., 1994, Phys. Rev. Letters **72**, 1662.
KELLY, A., and C. CHIOU, 1958, Acta Metall. **6**, 565.
KIKUCHI, R., 1966, Progr. Theor. Phys. Suppt **35**, 1.
KIM, J. J., and D. A. STEVENSON, 1988, J. non Cryst. Sol., **101**, 187.
KIM, S. J., M. A. NICOLLET, R. S. AVERBACK and D. PEAK, 1988, Phys. Rev. B, **37**, 38.
KIM, S. M., 1991, J. Mat. Res. **6**, 1455.
KING, A. H., and G. DIXIT, 1990, J. de Physique (France), Colloque C1, **51**, 545.
KING, R. T., and W. W. MULLINS, 1962, Acta Metall. **10**, 601.
KIRCHHEIM, R., 1988, Prog. Mat. Sci., **32**, 261.
KIRCHHEIM, R., F. Sommer and G. Schluckebier, 1982, Acta. Metall. **30**, 1059.
*KIRKALDY, J. S., and D. J. YOUNG, 1987, Diffusion in the Condensed State (The Institute of Metals, London).
KNUTH, D. E., 1968, The Art of Computer Programming, (Addison Wesley, Reading).
KOCH, J. M., and C. KOENIG, 1986, Phil. Mag. **B54**, 177.
KÖGEL, G. 1992, Materials Science Forum **105–110**, 341.
KÖHLER, U., and Ch. HERZIG, 1987, Phys. Status Solidi (b) **144**, 243.
KOIWA, M., 1978, Phil. Mag. **45**, 1327.
KOIWA, M., and S. ISHIOKA,1983, Phil. Mag. **A47**, 927.
KOPONEN, I., 1991, Nuc. Instr. and Methods, **B61**, 394.
KÖPPERS, M., C. HERZIG, U. SÖDERVALL and A. LODDING, 1993, in ref. K), p. 783.
KRIVOGLAZ, M. A., 1969, Phys. Met. and Metallogr. **28**, 1.
KROLL, S., N. A. STOLWIJK, C. HERZIG and H. MEHRER, 1993, in ref. K), p. 865.
KRONMÜLLER, H., 1978, Magnetic After-Effects, in: Hydrogen in Metals, eds. C. Alefeld and J. Völkl (Springer, Berlin) vol. 1, p. 289.
KUMAR, P., and R. S. SORBELLO, 1975, Thin Solid Films **25**, 25.
KUO, M., and R. A. FOURNELLE, 1991, Acta Metall. Mater. **39**, 2835.
KUPER, A. B., D. LAZARUS, J. R. MANNING and C. T. TOMIZUKA, 1956, Phys. Rev. **104**, 1536.
KURTZ, A. D., B. L. AVERBACH and M. COHEN, 1955, Acta Metall. **3**, 442.
KUSUNOKI, K., K. TSUMURAYA and S. NISHIKAWA, 1981, Trans. Japan. Inst. Met. **22**, 501.
KWOK, J., P. S. HO, S. YIP, R. W. BALLUFFI, P. D. BRISTOWE and A. BROKMAN, 1981, Phys. Rev. Lett. **47**, 1148.
LAAKKONEN, J., and R. M. Nieminen, 1988, J. Phys. C, **21**, 3663.
LAAKKONEN, J., and R. M. Nieminen, 1990, Phys. Rev., B, **41**, 3978.
LAASONEN, K., 1994, Mater. Sci. Forum, **155–156**, 149.
LA VIA F., K. T. F. JANSSEN and A. H. READER, 1992, Appl. Phys. Lett., **60**, 701.
LAM, N. Q., N. V. DOAN, L. DAGENS and Y. ADDA, 1983, J. Phys. **F13**, 1369.
LANDAU L., and E. LIFSHITZ, 1984, Physique Statistique, 3rd edition, (ed. Mir, Moskow).
LANGUILLE, A., and D. CALAIS, 1974, J. Phys. Chem. Solids **35**, 1461.
LANGUILLE, A., M. P. DARIEL, D. CALAIS and B. COQBLIN, 1973, Mem. Sci. Rev. Metall. **70**, 241.
LANORE, J. M., 1974, Rad. Eff. **22**, 153.
LAPUJOULADE, J., 1994, Surf. Sci. Rep. **20**, 191.
LAZARUS, D., 1960, Solide State Phys. **10**, 71.
LEAMY, H. J., and G. H. GILMER, 1974, J. Cryst. Growth **24/25**, 499.
LE CLAIRE, A. D., 1951, Phil. Mag. **42**, 673.

LE CLAIRE, A. D., 1954, Phys. Rev. **93**, 344.
LE CLAIRE, A. D., 1958, Phil. Mag. **3**, 921.
LE CLAIRE, A. D., 1963, Brit. J. Appl. Phys. **14**, 351.
LE CLAIRE, A. D., 1966, Phil. Mag. **14**, 271.
LE CLAIRE, A. D., 1970a, Correlation Effects in Diffusion in Solids, in: Physical Chemistry, an Adavanced Treatise, eds. H. Eyring, D. Henderson and W. jost (Academic, New York) vol. 10, ch. 5.
LE CLAIRE, A. D., 1970b, Phil. Mag. **21**, 819.
LE CLAIRE, A. D., 1976, Le Point Actuel sur la Théorie de la Diffusion, Anomalies de Diffusion, in: Proc. 19ème Colloque Métall., La Diffusion dans les Milieux Condensés, Théories et Applications, Saclay, 1976 (INSTN, Saclay, France).
LE CLAIRE, A. D., 1978, J. Nucl. Mater. **69–70**, 70.
LE CLAIRE, A. D., 1983, in ref. I), p. 82.
LE CLAIRE, A. D., 1993, in ref. K), p. 19.
LE CLAIRE, A. D., and A. B. LIDIARD, 1956, Phil. Mag. **1**, 518.
LE CLAIRE, A. D., and W. M. LOMER, 1954, Acta Metall. **2**, 731.
LE CLAIRE, A. D., and A. RABINOVITCH, 1981, J. Phys. **C14**, 3863.
LE CLAIRE, A. D., and A. RABINOVITCH, 1982, J. Phys. **C15**, 3455.
LE CLAIRE, A. D., and A. RABINOVITCH, 1983, J. Phys. **C16**, 2087.
LEE, Ch. G., Y. IIJIAMA and K. HIRANO, 1988, The Ninth Japan Symposium Thermophysical properties, p. 1.
LEE Y. S., and D. A. STEVENSON, 1985, J. non Cryst. Sol., **72**, 249.
LEVASSEUR, J., and J. PHILIBERT, 1967, C. R. Acad. Sci. Paris **264**, Sér. C, 277.
LEVINE, H. S., and C. J. MACCALLUM, 1960, J. Appl. Phys. **31**, 595.
LEWIS T. G., and W. H. PAYNE, 1973, J. Ass. Comp. Mach., **20**, 456.
LIDIARD, A. D., 1985, Proc. R. Soc. Lond. **A398,** 203.
LIDIARD, A. D., 1986, Proc. R. Soc. Lond. **A406,** 107.
LIDIARD, A. D., 1987, Proc. R. Soc. Lond. **A413,** 429.
LIDIARD A. B., G. E. MURCH, Z. QUIN and L. ZHANG, 1990, Phil. Mag. A, **62**, 595.
LIMOGE, Y., 1976a, Thèse, Univ. Paris-Sud.
LIMOGE, Y., 1976b, Electromigration dans l'Aluminium, in: Proc. 19ème Colloque de Métall., La Diffusion dans les Milieux Condensés, Théories et Applications, Saclay, 1976 (INSTN, Saclay, France) p. 971.
LIMOGE, Y., 1987, Mat. Sci. Forum, **15–18**, 517.
LIMOGE, Y., 1990, Acta Metall., **38,** 1733.
LIMOGE, Y., 1992a, Scr. Metall., **26**, 809.
LIMOGE, Y., 1992b, Defect and Diffusion Forum, **83**, 145.
LIMOGE, Y., and J. L. BOCQUET, 1988, Acta Metall., **36**, 1717.
LIMOGE, Y., and J. L. BOCQUET, 1989, Diff. Def. Data, **66–69**, 269.
LIMOGE, Y., and J. L. BOCQUET, 1990, Phys. Rev. Lett., **65**, 60.
LIMOGE, Y., and G. BREBEC, 1988, Acta Metall., **36,** 665.
LIMOGE, Y., G. BREBEC and Y. ADDA, 1982, in ref. I), p. 285.
LIMOGE, Y., J. M. DELAYE and J. L. BOCQUET, 1994, Proc. of the 1993 A.S.M./T.M.S. Meeting, Pittsburg, October 1993, ed. H. Jain, D. Gupta, The Min. Met. Mat. Soc., Warrendale, P.A., 79.
LIMOGE, Y., J. L. SERAN and R. SEGUIN, 1977, in Proc. 8th Int. Conf. on X-Ray Optics and Microanalysis, (Boston, MA., U.S.A.).
LITTMARK, U., and W. O. HOFFER, 1980, N.I.M., **168**, 329.
LIU, C. L., and J. B. ADAMS, 1992, Surface Science **265**, 262.
LIU, C. L., J. M. COHEN, J. B. ADAMS and A. F. VOTER, 1991, Surface Science **253**, 334.
LIU, C. T., R. W. CAHN and G. SAUTHOFF, 1992, Ordered Intermetallics: Physical Metallurgy and Mechanical Behaviour, Kluwer Academic Publishers (Boston).
LIU, D., W. A. MILLER and K. T. AUST, 1989, Acta Metall. **37**, 3367.
LO CASCIO, D. M., 1992, Thesis (Amsterdam).
LO CASCIO, D. M. R., P. I. LOEFF and H. BAKKER, 1992, J. Phys.: Condensed Matter **4,** 7441.
LODDER, A., Sol. Stat. Com., 1991, **79**, 143.
LOMER, W. M., 1954, AERE Report T/R 1540.

LORMAND, G., 1970, Thèse, Lyon.
LLOYD J.R., 1990, App. Phys. Let., **57**, 1167.
LUNDY, T.S., and J.F. MURDOCK, 1962, J. Appl. Phys. **33**, 1671.
LUTSKO, J.F., D. WOLF and S.J. YIP, 1988, J. Chem. Phys., **88**, 6525.
LYNN, K.G., and D.O. WELCH, 1980, Phys. Rev. **B22**, 99.
MA, Q., and R.W. BALLUFFI, 1993, Acta Metall. Mater. **41**, 133.
MA, Q., and R.W. BALLUFFI, 1994, Acta Metall. Mater. **42**, 1.
MA, Q., C.L. LIU, J.B. ADAMS and R.W. BALLUFFI, 1993, Acta Metall. Mater. **41**, 143.
MAIER, K., H. MEHRER, E. LESSMANN and W. SCHÜLE, 1976, Phys. Status Solidi (b) **78**, 689.
MAIER, K., H. MEHRER and G. REIN, 1979, Z. Metallkd **70**, 271.
MALLARD, W.C., A.B. GARDNER, R.F. BASS and L.M. SLIFKIN, 1963, Phys. Rev. **129**, 617.
MANNING, J.R., 1964, Phys. Rev. **136**, A 1758.
*MANNING, J.R., 1968, Diffusion Kinetics for Atoms in Crystals (Van Nostrand, Princeton).
MANNING, J.R., 1971, Phys. Rev. **B4**, 111.
MANNING, J.R., 1978, Bull. Am. Phys. Soc., **23**, 287.
MAO, C., 1972, Phys. Rev. **B5**, 4693.
MARECHE, J.F., J.C. RAT and H. HEROLD, 1979, Z. Phys. Chem. Neue Folge **115**, 137.
MARTIN, G., 1972, Phys. Stat. Sol. **14**, 183.
MARTIN, G., and A. BARBU, 1993, in ref. Z), p. 179.
MARTIN, G., and P. BENOIST, 1977, Scripta Metall. **11**, 503.
MARTIN, G., D.A. BLACKBURN and Y. ADDA, 1967, Phys. Stat. Sol. **23**, 223.
MARTIN, G., and P. PERRAILLON, 1979, Measurements of Grain Boundaries Diffusion, in: Grain Boundary Structure and Kinetics, ASM Materials Science Seminar 1979 (ASM, Metals Park, OH) p. 239.
MATANO, C., 1933, Jap. J. Phys. **8**, 109.
MATHUNI, J., O.N. CARLSON, E. FROMM and R. KIRCHHEIM, 1976, Metallurg. Trans. **7A**, 977.
MATHUNI, J., R. KIRCHHEIM and E. FROMM, 1979, Acta Metall. **27**, 1665.
MATLOCK, J.H., and J.P. STARK, 1971, Acta Metall. **19**, 923.
MAYDET, S.I., and K.C. RUSSELL, 1977, J. Mater. Nuc., **64**, 101.
MCCOMBIE, C.W., and E.W. ELCOCK, 1958, Phys. Rev. **B2**, 1451.
MCCREA, W.H., and F.J.W. WHIPPLE, 1940, Proc. Roy. Soc. Edinb. **60**, 281.
MCKEE, R.A., and J.P. STARK, 1975, Acta Metall. **23**, 1145.
MCVAY, G.L., and A.R. DUCHARME, 1974, Phys. Rev. **B9**, 627.
MEHRER H., and W. DÖRNER, 1989, Defect and Diffusion Forum, **66–69**, 189.
MELIUS, C.F., and W.D. WILSON, 1980, Rad. Eff. **53**, 111.
MEYER, R.O., 1969, Phys. Rev. **181**, 1086.
MILITZER, M., W.P. SUN and J.J. JONAS, 1994, Acta Metall. Mater., **42**, 133.
MILLER, J.W., 1969, Phys. Rev. **181**, 1095.
MILLION, B., and J. KUCERA, 1969, Acta Metall. **17**, 339.
MILLION, B., and J. KUCERA, 1971, Czech. J. Phys. **B21**, 161.
MILLION, B., J. RUZICKOVA, J. VELISEK and J. VRESTAL, 1981, Mat. Sc. Eng. **50**, 43.
MIYAGAWA, H., Y. HIWATARI, B. BERNU and J.P. HANSEN, 1998, J. Chem. Phys., **88**, 3879.
MONMA, K., H. SUTO and H. OIKAWA, 1964, J. Japan. Inst. Met. **128**, 192.
MONTET, G.L., 1973, Phys. Rev. **B7**, 650.
MONTY, C., 1972, Thèse, Univ. Paris-Sud.
MULLEN, J.G., 1961, Phys. Rev. **124**, 1723.
MÜLLER A., V. NAUNDORF and M.P. MACHT, 1988, J. Appl. Phys., **64**, 3445.
MULLINS, W.W., and P.G. SHEWMON, 1959, Acta Metall. **7**, 163.
MUNDY, J.N., 1971, Phys. Rev **B3**, 2431.
MUNDY, J.N., 1992, in ref. E), p. 1.
MUNDY, J.N., H.A. HOFF, J. PELLEY, S.J. ROTHMAN, L.J. NOWICKI and F.A. SCHMIDT, 1981, Phys. Rev. **B24**, 658.
MUNDY, J.N., and W.D. MCFALL, 1973, Phys. Rev. **B7**, 4363.
MUNDY, J.N., T.E. MILLER and R.J. PORTE, 1971, Phys. Rev **B3**, 2445.

MUNDY, J. N., S. J. ROTHMAN, N. Q. LAN, H. A. HOFF and L. J. NOWICKI, 1978, Phys. Rev. **B18,** 6566.
*MÜNSTER, A., 1966, Thermodynamique des Processus Irréversibles (Presses Universitaires de France, Paris).
MURCH, G. E., 1982a, Phil. Mag. **A45**, 941; 1982b, Phil. Mag. **A46**, 565; 1982c, Phil. Mag. **A46**, 575.
MURCH G. E., and L. ZHANG, 1990, in ref. G), p. 251.
NACHTRIEB, N. H., and G. S. HANDLER, 1954, Acta Metall. **2**, 797.
NAKAJIMA, H., M. YOSHIOKA and M. KOIWA, 1987, Trans. Jap. Inst. Metals, **28**. 949.
NAKAJIMA, H., and M. KOIWA, 1993, in ref. K), p. 775.
NEEL, L., 1951, J. Phys. Rad. **12**, 339.
NEEL, L., 1952, J. Phys. Rad. **13**, 249.
NEEL, L., 1954, J. Phys. Rad. **14**, 225.
NEUMAN, G., and W. HIRSCHWALD, 1972, Z. Phys. Chem. Neue Folge **Bd.8**, 515.
NEUMANN, C. H., D. LAZARUS and D. B. FITCHEN, 1961, J. Phys. Chem. Solids **20**, 170.
NEUMANN, J. P., 1980, Acta Metall. **28**, 1165.
NICHOLS, F. A., and W. W. MULLINS, 1965a, J. Appl. Phys. **36**, 1826.
NICHOLS, F. A., and W. W. MULLINS, 1965b, Trans. AIME **233**, 1840.
NIELSEN, O. H., J. P. SETHNA, P. STOLTZE, K. W. JACOBSEN and J. K. NØRSKOV, 1994, Europhys. Letters **26**, 51.
NOIMANN, Kh., G. KLOZE and I. L. SOKOL'SKAYA, 1964, Sov. Phys. Solid State **6,** 1369.
NOSE S., 1984, Mol. Phys., **52**, 255.
NOWICK, A. S., 1952, Phys. Rev. **88**, 925.
*NOWICK, A. S., and B. S. BERRY, 1972, Anelastic Relaxation in Crystalline Solids (Academic, New York).
OKAMOTO, P. R., and H. WIEDERSICH, 1974, J. Nucl. Mater. **53**, 336.
OKAMURA, Y., and A. R. ALLNATT, 1983a, J. Phys. **C16**, 1841.
OKAMURA, Y., and A. R. ALLNATT, 1983b, Phil. Mag. **A48**, 387.
OKAMURA, Y., and A. R. ALLNATT, 1984, Phil. Mag. **A50**, 603.
OKAMURA, Y., and A. R. ALLNATT, 1986, Acta Metall. **34**, 189.
OLIGSCHLEGER, C., and H. R. SCHOBER, 1995, Sol. State Comm. **93,** 1035.
ORIANI, R. A., 1969, J. Phys. Chem. Solids **30**, 339.
PANDEY, K. C., 1986, Phys. Rev. Letters **57**, 2287.
PARIS, D., and P. LESBATS, 1975, Scripta Metall. **9**, 1373.
PARIS, D., and P. LESBATS, 1978, J. Nucl. Mater. **69–70**, 628.
PARRINELLO M., and A. RAHMAN, 1981, J. App. Phys., **52**, 7182.
PAVLINOV, L. V., A. M. GLADYSHEV and V. N. BYKOV, 1968, Fiz. Met. Metalloved. **26,** 823.
PERINET, F., 1975, Rapport CEA-4657, Saclay.
PENISSON, J. M., and A. BOURRET, 1975, Mise en Odre de l'Alliage Fe–Ni, in: Proc. 4th Int. Conf. on High-Voltage Electron Microscopy, Toulouse (1975), eds. B. Jouffrey and P. Favard (Sté Française de Microscopie Electronique, Paris) p. 205.
PERRAILLON, B., I. M. TORRENS and V. LEVY, 1972, Scripta Metall. **6**, 611.
PETERSON, D. T., 1977, Electromigration as a Purification Process, in: Electro- and Thermotransport in Alloys, eds. R. E. Hummel and H. B. Huntington (AIME, New York) p. 54.
PETERSON, D. T., and M. F. SMITH, 1982, Metallurg. Trans. **13A**, 821.
PETERSON, N. L., 1964, Phys. Rev. **A136**, 568.
PETERSON, N. L., 1975, in ref. D), p. 115.
PETERSON, N. L., 1978, J. Nucl. Mater. **69–70**, 3: Proc. Int. Conf. on the Properties of Atomic Defects in Metals, Argonne (1976), eds. N. L. Peterson and R. W. Siegel.
PETERSON, N. L., and S. J. ROTHMAN, 1967, Phys. Rev. **163**, 645.
PETERSON, N. L., and S. J. ROTHMAN, 1970, Phys. Rev. **B1**, 3264.
PETERSON, N. L., and S. J. ROTHMAN, 1971, Diffusion and Correlation Effects in Copper-Zinc Alloys, in: Proc. Conf. Atomic Transport in Solids and Liquids, Marstrand (1970), eds. A. Lodding and T. Lagerwall (Zeitschrift für Naturforschung, Tübingen) p. 248.
PETRY W., A. HEIMING, C. HERZIG, and J. TRAMPENAU, 1991, Def. Diff. Forum, **75**, 211.
PETTIFOR, D. G., 1992, in: Ordered Intermetallics: Physical Metallurgy and Mechanical Behaviour, C. T. Liu, R. W. CAHN and G. SAUTHOFF, eds., Kluwer Academic Publishers (Boston), 47.
PIKE, G. E., W. J. CAMP, C. H. SEAGER and G. L. MCVAY, 1974, Phys. Rev. **B10**, 4909.

PONTAU, A. E., and D. LAZARUS, 1979, Phys. Rev. **B19**, 4027.
*PRATT, J. N., and R. G. R. SELLORS, 1973, Electrotransport in Metals and Alloys, in: Diffusion and Defect Monograph Series, ed. F. H. Wöhlbier (Trans. Tech. Publications, Aedermannsdorf, Switzerland).
*PRIGOGINE, I., 1947, Etude Thermodynamique des Phénomènes Irréversibles (Desoer, Liège).
PRINZ, N., and H. WEVER, 1980, Phys. Stat. Sol. **a61**, 505.
QIN, Z., and G. E. MURCH, 1993a, Phil. Mag. **A67**, 757.
QIN, Z., and G. E. MURCH, 1993b, Phil. Mag. **A67**, 369.
QIN, Z., and G. E. MURCH, 1993c, Phil. Mag. **A67**, 381.
RADELAAR, S., 1966, J. Phys. Chem. Solids **27**, 1375.
RADELAAR, S., 1968, Phys. Stat. Sol. **27**, K23.
RADELAAR, S., 1970, J. Phys. Chem. Solids **31**, 219.
RAHMAN, A., 1964, Phys. Rev., **136**, 405.
RÄTZKE K., and F. FAUPEL, 1992, Phys. Rev. B, **45**, 7459.
RÄTZKE K., P. W. HÜPPE and F. FAUPEL, 1992, Phys. Rev. Lett., **68**, 2347.
REGNIER, P., and M. HALBWACHS, 1980, Electron Micros. **4**, 204.
REHN, L. E., and P. R. OKAMOTO, 1989, N.I.M. B, **39**, 104.
REIN, G., and H. MEHRER, 1982, Phil. Mag. A, **45**, 467.
REIN, G., H. MEHRER and K. MAIER, 1978, Phys. Status Solidi (a) **45**, 253.
REINHOLD, U., A. NEIDHARDT, G. KRAUTHEIM and A. ZEHE, 1980, Phys. Stat. Sol (a) **61**, K13.
RESING, H. A., and N. H. NACHTRIEB, 1961, J. Phys. Chem. Solids **21**, 40.
RETTENMEYER, F., E. KISDI-KOSZO and H. KRONMÜLLER, 1986, Phys. Stat. Sol. A, **93**, 597.
REY-LOSADA, C., M. HAYOUN and V. PONTIKIS, 1993, Mat. Res. Soc. Symp. Proc. **291**, 549.
REYNOLDS, J. E., B. L. AVERBACH and M. COHEN, 1957, Acta Metall. **5**, 29.
RHEAD, G. E., 1975, Surf. Sci. **47**, 207.
RICE, S. A., 1958, Phys. Rev., **112**, 804.
RIMBEY, P. R., and R. S. SORBELLO, 1980, Phys. Rev. **B21**, 2150.
RIVIERE, J. P., and J. GRILHE, 1974, Phys. Stat. Sol. (a) **25**, 429.
ROBINSON, J. T., and N. L. PETERSON, 1972, Surf. Sci. **31**, 586.
ROBROCK, K. H., 1981, Mechanical Relaxation Studies of Point Defects in Metals, in: Internal Friction and Ultrasonic Attenuation in Solids, Lausanne (1981), J. Physique **C15**, 709.
ROCKOSCH H. J., and C. HERZIG, 1983, Zeit. Metall., **74**, 94.
ROSENBLUM, M. P., F. SPAEPEN and D. TURNBULL, 1980, Appl. Phys. Lett. **37**, 184.
ROTHMAN, S. J., 1981, in ref. V), p. 189.
ROTHMAN, S. J., and N. L. PETERSON, 1967, Phys. Rev. **154**, 552.
ROULET, C., 1973, Surf. Sci. **36**, 295.
RUOFF, A. L., 1967, J. Appl. Phys. **38**, 3999.
RUOFF, A. L., and R. W. BALLUFFI, 1963, J. Appl. Phys. **34**, 2862.
RUSH, J. J., T. J. UDOVIC, R. HEMPELMANN, D. RICHTER and G. DRIESEN, 1989, J. Phys., **1**, 1061.
RUSSELL, K. C., 1985, Prog. Mater. Sci., **28**, 229.
SANCHEZ, J. M., and D. DE FONTAINE, 1975, Phys. Rev. Lett. **35**, 227.
SANDERS, D. E., and A. E. DEPRISTO, 1992, Surface Science **260**, 116.
SATO, H., 1984, in: Non-Traditional Methods in Diffusion, TMS Conf. Proc., 283.
SCHAEFER, H.-E., R. WÜRSCHUM, M. SOB, T. ZAK, W. Z. YU and W. ECKERT, 1990, Phys. Rev. **B41**, 11869.
SCHAICH, W. L., 1976, Phys. Rev. **B13**, 3350.
SHARMA, S. K., and P. MUKHOPADHYAY, 1990, Acta Metall., **38**, 129.
SCHILLING, W., 1978, J. Nucl. Mater. **69–70**, 465.
SCHILLING, W., 1981, Diffusion of Helium in Metals, in: Proc. Yamada Conf. V: Point Defects and Defect Interactions in Metals, Kyoto (Japan, 1981), Eds. J. I. Takamura, M. Doyama and M. Kiritani (Tokyo) p. 303.
SCHMALZRIED, H., 1974, Solid State Reactions (Academic, New York) ch. 7.
SCHMATZ, D. J., H. A. DOMIAN and H. I. AARONSON, 1966, J. Appl. Phys. **37**, 1741.
SCHMIDT, H., G. FROHBERG and H. WEVER, 1992a, Acta Metall. Mater. **40**, 3105.
SCHMIDT, H., G. FROHBERG, W. MIEKELEY and H. WEVER, 1992b, Phys. Stat. Sol. **b171**, 29.

SCHMITZ, F., and M. FOCK, 1967, J. Nucl. Mater. **21,** 317.
SCHOBER H. R., PETRY W. and TRAMPENAU J., 1992, J. Phys. Condens. Mater., **4,** 9321.
SCHOTTKY, G., 1965, Phys. Stat. Sol. **8,** 357.
SCHULTZ, H., 1991, Mat. Sci. Eng., **A 141,** 149.
SEEGER, A., 1976, The Interpretation of Radiation Damage in Metals, in: Proc. Conf. Fundamental Aspects of Radiation Damage in Metals, Gatlinburg, USA (1975), eds. M. T. Robinson and F. W. Young Jr. (ERDA Report CONF-751006, Oak Ridge) vol. 1, p. 493.
SEEGER, A., 1993, in ref. K), p. 147.
SEEGER, A., and H. MEHRER, 1970, Analysis of Self-Diffusion and Equilibrium Measurements, in: Vacancies and Interstitials in Metals, eds. A. Seeger, D. Schumacher, W. Schilling and J. Diehl (North-Holland, Amsterdam) p. 1.
SEEGER, A., D. WOLF and H. MEHRER, 1971, Phys. Stat. Sol. (b) **48,** 481.
SEPIOL, B., and G. VOGL, 1993a, Phys. Rev. Letters **71,** 731.
SEPIOL, B., and G. VOGL, 1993b, Defect and Diffusion Forum **95–98,** 831.
SEPIOL, B., O. G. RANDL, C. KARNER, A. HEIMING and G. VOGL, 1994, J. Phys.: Condens. Matter **6,** L43.
SERAN, J. L., and Y. LIMOGE, 1981, Surf. Sci., **107,** 176.
SERRUYS, Y., and G. BREBEC, 1982a, Phil. Mag. **A45,** 563.
SERRUYS, Y., and G. BREBEC, 1982b, Phil. Mag. **A46,** 661.
SEYMOUR, E. W. F., 1953, Proc. Phys. Soc. (Lond.) **A66,** 85.
SHALAYEV, V. I., I. B. TKACHENKO, V. A. PAVLOV, N. I. TIMOFEYEV and A. V. GUSHCHINA, 1970, Fiz. Metal. Metalloved **39,** 1061.
SHANKAR, S., and L. L. SEIGLE, 1978, Metallurg. Trans. **9A,** 1467.
SHARMA, S. K., S. BANERJEE, K. JAIN and A. K. JAIN, 1989, J. Mater. Res., **4,** 603.
SHARMA, S. K., M. P. MACHT and V. NAUNDORF, 1993, Def. Dif. Forum, **95–98,** 1145.
SHIANG, K.-D., and T. TSONG, 1994, Phys. Rev. **B49,** 7670.
SHIH, S., and J. P. STARK, 1978, Phys. Rev. **B18,** 711.
SHIRAI, Y., K. MATSUMOTO, M. YAMAGUCHI, K. FUKUDA, R. TANIGUCHI and S. TSUKUI, 1992, Materials Science Forum **105–110,** 1229.
SHIRN, G. A., 1955, Acta Metall. **3,** 87.
SHOLL, C. A., 1981, J. Phys. C., **14,** 2723.
SINGH, R., and D. K. CHATURVEDI, 1993, Phys. Rev. **B48,** 16366.
SINGWI, K. S., and A. SJÖLANDER, 1960a, Phys. Rev. **120,** 1093.
SINGWI, K. S., and A. SJÖLANDER, 1960b, Phys. Rev. **119,** 863.
SIZMANN, R., 1978, J. Nucl. Mater. **69–70,** 386.
SLATE N. B., 1959, The theory of unimolecular reactions, (Cornell Univ. Press).
SMALL, M. B., and D. A. SMITH, 1992, Appl. Phys. Lett., **60,** 3235.
SMIGELKAS, A. D. and E. O. KIRKENDALL, 1947, Trans. AIME **171,** 130.
SNOEK, J. L., 1939, Physica **6,** 591.
SOMENKOV, V. A., and S. S. SHIL'STEIN, 1979, Prog. Mater. Sci. **24,** 267.
SORBELLO, R. S., 1972, Phys. Rev. **B6,** 4757.
SORBELLO, R. S., 1975, Comm. Solid. State Phys. **6,** 117.
SPAEPEN, F., 1981, in Les Houches Lectures XXV, eds. M. Kléman and J. P. Poirier, (North Holland), p. 136.
SPEDDING, F. H., and K. Shiba, 1972, J. Chem. Phys. **57,** 612.
SPOKAS, J. J., and C. P. Slichter, 1959, Phys. Rev. **113,** 1462.
*SPRINGER, T., 1972, Quasi-elestic Neutron Scattering for the Investigation of Diffusive Motion in Solids and Liquids (Springer, Berlin).
STELTER, E., and D. LAZARUS, 1987, Phys. Rev. B, **36,** 18, 9545.
STEPHENSON, B., 1988, Acta Metall. **36,** 2663.
STEINDL, R., G. KÖGEL, P. SPERR, P. WILLUTZKI, D. T. BRITTON and W. TRIFTSHAUSER, 1992, Mater. Sc. Forum, **105–110,** 1455.
STOLWIJK, N. A., 1981, Phys. Stat. Sol. (b) **105,** 223.
STOLWIJK, N. A., BRACHT H., HETTWER H. G., LERCH W., MEHRER H., RUCKI A. and JÄGER W., 1994, Mater. Sci. Forum, **155–156,** 475.

STOLWIJK, N. A., M. VAN GEND and H. BAKKER, 1980, Phil. Mag. **A42**, 783.
STONEHAM, A. M., 1979, Hyperfine Interactions **6**, 211.
STUMP, R., and M. SCHEFFLER, 1994, Phys. Rev. Letters **72**, 254.
SUZUOKA, T., 1961a, Trans. Japan Inst. Met. **2**, 25.
SUZUOKA, T., 1961b, Trans. Japan Inst. Met. **2**, 176.
SUZUOKA, T., 1964, J. Phys. Soc. Jap. **18**, 839.
SZABO, I. A., M. KOIWA and S. ISHIOKA, 1991, Phil. Mag. **A63**, 1137.
SZABO, I. A., I. DARUKA and D. L. BEKE, 1994, Defect and Diffusion Forum **155–156**, 289.
TANIGUCHI, S., 1955, Sci. Rep. Res. Inst. Tohoku Univ. **A7**, 269.
TARCZON, J. C., W. HALPERIN, S. C. CHEN and J. O. BRITTAIN, 1988, Mat. Sc. Eng. **A101**, 99.
TEICHLER, H., 1979, Hyperfine Interactions **6**, 251.
THOMPSON, M. D., and H. B. HUNTINGTON, 1982, Surf. Sci. **116**, 522.
THOMPSON, M. S., and J. E. MORRAL, 1986, Acta Metall. **34**, 339.
TOKUHIRO, T., S. SUSMAN, T. O. BRUN and K. J. VOLIN, 1989, J. Phys. Soc. Jap. **58**, 2553.
TOLLER, M., G. JACUCCI, G. DE LORENZI and C. P. FLYNN, 1985, Phys. Rev. B, **32**, 2082.
TORRENS, I. M., and M. T. ROBINSON, 1972, Computer Simulation of Atomic Displacement Cascades in Metals, in: Proc. Conf. Radiation-Induced Voids in Metals, Albany (1971), eds. J. W. Corbett and L. C. Ianello (USAEC, Oak Ridge) p. 739.
TORREY, H. C., 1954, Phys. Rev. **96**, 690.
TRIFTSHÄUSER, W., and G. KÖGEL, 1987, in ref. DD), p. 218.
TRINGIDES, M. C., and R. GOMER, 1992, Surf. Sci. **265**, 283.
TSOU, J. C., and D. J. QUESNEL, 1983, Mat. Sci. Eng., **59**, 99.
TULLY, J. C., G. H. GILMER and M. SHUGARD, 1979, J. Chem. Phys. **71**, 1630.
TUNG, R. T., and W. R. GRAHAM, 1980, Surf. Sci. **97**, 73.
TURBAN, L., P. NOZIERES and M. GERL, 1976, J. Physique **37**, 159.
TYAGI, A. K., M. P. MACHT and V. NAUNDORF, 1991a, J. Mater. Nucl., **179–181**, 1026.
TYAGI, A. K., M. P. MACHT and V. NAUNDORF, 1991b, Acta Metall. Mater., **39**, 609.
UEBING, C., and R. GOMER, 1991, J. Chem. Phys. **95**, 7626.
UZ, M., and O. N. CARLSON, 1986, J. Less. Com. Met., **116**, 317.
VALENTA, P., K. MAIER, H. KRONMULLER and K. FREITAG, 1981, Phys. Stat. Sol., **105**, 537, and **106**, 129.
VALLEAU, J. P., and S. G. WHITTINGTON, 1977, in ref. O), 137.
VAN DER EERDEN, J. P., P. BENNEMA and T. A. CHEREPANOVA, 1978, Prog. Cryst. Growth Charact. **1**, 219.
VANFLEET, H. B., 1980, Phys. Rev. **B21**, 4340.
VAN EK, J., and A. LODDER, 1991, J. Phys., **3**, 7307 and 7331.
VAN HOVE, L., 1954, Phys. Rev. **95**, 249.
VAN OMNEN, A. H., and J. DE MIRANDA, 1981, Phil. Mag. **A43**, 387.
VAN WINKEL, A., A. W. WEEBER and H. BAKKER, 1984, J. Phys. F: Met. Phys. **14**, 2631.
VAN WINKEL, A., and H. BAKKER, 1985, J. Phys. F: Met. Phys. **15**, 1565.
VAROTSOS, P. A., 1978, J. Phys. **F8**, 1373.
*VAROTSOS P. A., and K. D. ALEXOPOULOS, 1986, Thermodynamics of point defects and their relation with bulk properties, (North Holland).
VERBRUGGEN, A. H., 1988, IBM J. Res. Dev., **32**, 93.
VILLEMAIN, P., 1970, 3rd Cycle Thesis, Grenoble University.
VINEYARD, G. H., 1957, J. Phys. Chem. Sol., **3**, 121.
VOGL, G., C. H. KARNER, O. RANDL, B. SEPIOL and D. TUPPINGER, 1992, Ordered Intermetallics: Physical Metallurgy and Mechanical Behaviour, C. T. Liu, R. W. Cahn and G. Sauthoff Eds., Kluwer Academic Publishers, 497.
VOGL, G., W. PETRY, T. FLOTTMANN and A. HEIMING, 1989, Phys. Rev. B, **39**, 5025.
VOGL, G., O. G. RANDAL, W. PETRY and J. HÜNECKE, 1993, J. Phys.: Condensed Matter **5**, 7215.
VÖLKL, J., 1972, Ber. Bunsen Gesell. **76**, 797.
VÖLKL, J., and G. ALEFELD, 1978, Diffusion of Hydrogen in Metals, eds. G. Alefeld and J. Völkl (Springer, Berlin) vol.1, p. 231.
VOTER, A. F., and J. DOLL, 1985, J. Chem. Phys. **82**, 80.

WADE, W. Z., D. W. SHORT, J. C. WALDEN and J. W. MAGANA, 1978, Metall. Trans. **9A**, 965.
WAEGEMAEKERS, A. A. H. J., Thesis (Amstersdam 1990).
WAHNSTROM, G. H., 1991, Phys. Rev., **A44**, 3752.
WARBURTON, W. K., 1975, Phys. Rev. **B11**, 4945.
WARBURTON, W. K., and D. TURNBULL, 1975, in ref. D), p. 171.
WEILER, D., H. MEHRER and N. A. STOLWIJK, 1984, Phil. Mag. **A50**, 559.
WELCH, D. O., G. J. DIENES and O. W. LAZARETH, 1984, J. Phys. Chem. Solids **45**, 1225.
WELCH, D. O., and A. D. LE CLAIRE, 1967, Phil. Mag. **16**, 981.
WERNER, M., H. MEHRER and H. SIETHOFF, 1983, J. Phys. C: Solid State Phys. **16**, 6185.
WERT, C. A., and C. ZENER, 1949, Phys. Rev., **76**, 1169.
WEVER, H., 1983, Zeit. Metall., **74**, 1.
WEVER, H., 1992, Defect and Diffusion Forum, **83**, 55.
WHIPPLE, R. T. P., 1954, Phil. Mag. **45**, 1225.
WIEDERSICH, H., 1990, Rad. Eff. Deff. Solids, **113**, 97.
WIEDERSICH, H., P. R. OKAMOTO and N. Q. LAM, 1979, J. Mater. Nuc., **83**, 98.
WILLAIME, F., and C. MASSOBRIO, 1990, in Atomic Scale Calculations of Structure in Materials, eds. M. S. Daw and M. A. Schluter, (MRS Soc., Pittsburgh), p. 295.
WILLAIME, F., 1991, to be published.
WILLAIME, F., and M. NASTAR, 1994, private communication.
WILLIAM, M. L., R. F. LANDEL and J. D. FERRY, 1955, J. Am. Chem. Soc., **77**, 3701.
WILSON, W. D., and C. L. BISSON, 1973, Rad. Eff. **19**, 53.
WINTENBERGER, M., 1959, Acta Metall. **7**, 549.
WIRTZ, K., 1943, Z. Phys. **44**, 231.
WOLF, D., 1979, Spin Temperature and Nuclear Spin Relaxation in Matter (Clarendon Press, Oxford).
WOLF, D., 1980, J. Phys. Chem. Solids **41**, 1053.
WOLF, D., 1983, Phil. Mag. A, **47**, 147.
WOLF, D., 1990a, J. Mater. Res. **5**, 1708.
WOLF, D., 1990b, J. Appl. Phys. **69**, 185.
WOLF, D., 1991, Phil. Mag. **A63**, 1117.
WOLLENBERGER, H., V. NAUNDORF and M. P. MACHT, in ref. L), p. 201.
WONNELL, S. K., J. M. DELAYE, M. BIBOLE and Y. LIMOGE, 1992, J. Appl. Phys., **72**, 5195.
WU, H. M., 1991, Effect of Atomic Size on Diffusion in Metallic Glasses, Ph. D. thesis, Illinois Univ.
WYNBLATT, P., and N. A. GJOSTEIN, 1968, Surf. Sci. **12**, 109.
XIE, Z.-Y., and D. FARKAS, 1994, J. Mat. Res. **9**, 875.
YANG, M. H., and C. P. FLYNN, 1989, Phys. Rev. Letters **62**, 2476.
YASUDA, H., H. NAKAJIMA and M. KOIWA, 1993, Defect and Diffusion Forum **95–98**, 823.
YASUNAGA, H., 1991, Surf. Sci. **242**, 171.
YOSHIDA, Y., 1989, Hyper. Int., **47**, 95.
YU, G., and K. LÜCKE, 1992, Acta Metall. Mater. **40**, 2523.
ZEE, R. P., 1989, J. Phys., **1**, 5631.
ZENER, C., 1943, Trans. AIME **152**, 122.
ZENER, C., 1947, Phys. Rev. **71**, 34.
ZENER, C., 1951, J. Appl. Phys. **22**, 372.
ZHANG, L., W. A. OATES and G. E. MURCH, 1989a, Phil. Mag. **B60**, 277.
ZHANG, L., W. A. OATES and G. E. MURCH, 1989b, Phil. Mag. **A59**, 171.
ZHANG, Z., K. HAUG and H. METIU, 1990, J. Chem. Phys. **93**, 3614.
ZIERLER, N., 1959, J. Soc. Ind. Appl. Math., **7**, 31.

Further reading

The references in the preceding list marked with an asterisk can also be used for general reading.

Diffusion data

A) All numerical results concerning diffusion are gathered in: Diffusion and Defect Data (DDD), eds. F. H. Wohlbier and D. J. Fisher (Trans. Tech. Publications, Aedermannsdorf, Switzerland), a review which appears three times a year.

B) A comprehensive issue of the Landolt–Börnstein New Series (vol. 26), Ed. O. Madelung (Springer-Verlag, 1990) is devoted to "Diffusion in Solid Metals and Alloys".

General references

C) PHILIBERT, J., 1991, Atom movements, diffusion and mass transport in solids, (Editions de Physique, Les Ulis, France).

D) Diffusion in Solids - Recent Developments, 1975, eds. A. S. Nowick and J. J. Burton, (Academic, New York).

E) Diffusion in Solids: unsolved Problems, 1992, Ed. G. E. Murch, (Trans. Tech. Pub., Aedermansdorf).

F) Atomic Transport in Solids, A. R. Allnatt and A. B. Lidiard, 1993, (Cambridge Univ. Press).

G) Diffusion in Materials, 1990, NATO ASI Series n° E 179, eds. A. L. Laskar, J. L. Bocquet, G. Brebec and C. Monty, (Kluwer, Dordrecht).

H) Proc. Int. Conf. on Atomic Defects in Metals, Argonne (1976), eds. N. L. Peterson and R. W. Siegel, J. Nucl. Mater. **69–70** (1978).

I) Proc. Int. Conf. on Diffusion in Metals and Alloys, 1982, Tihany (Hungary), eds. F. J. Kedves and D. L. Beke, 1983, Diff. and Defect Monograph, n° **7**.

J) Proc. Int. Conf. on Vac. and Int. in Metals and Alloys, 1986, Berlin, 1987, Mater. Sci. Forum, **15–18**.

K) Proc. Int. Conf. on Diffusion in Materials, 1992, Kyoto (Japan), 1993, Def. Diff. Forum, **95–98**.

L) Diffusion Processes in Nuclear Materials, 1992, ed. R. P. Agarwala, (North Holland, Amsterdam).

Spectroscopic measurement methods

M) Petry, W., and G. Vogl, 1987, Mater. Sci. Forum, **15–18**, 323.

N) Vogl, G., 1990, Hyper. Int., **53**, 197.

Molecular Dynamics and Monte Carlo simulations

O) Berne B. J., 1977, Statistical Mechanics, part A and B, modern Theoretical Chemistry 5 and 6, (Plenum, New York).

P) Hansen, J. P., and I. R. McDonald, 1986, Theory of Simple Liquids, 2nd ed., (Academic, London).

Q) Allen M. P., and D. J. Tildesley, 1987, Computer Simulation of Liquids, (Clarendon, Oxford).

R) Meyer, M., and V. Pontikis, 1991, Computer Simulation in Materials Science, (Kluwer).

S) Binder, K., 1992, The Monte Carlo Method in Condensed Matter Physics, (Springer, Berlin).

Diffusion under stresses and stress gradients

T) Larché, F. C., and J. W. Cahn, 1982, Acta Metall. **30**, 1835, and references therein.

Diffusion in thin films

U) Balluffi, R. W., and J. M. Blakely, 1975, Thin Solid Films **25**, 363.

V) Martin, G., and B. Perraillon, 1976, Diffusion dans les milieux limités, in: Proc. 19ème Colloque de Métall., La Diffusion dans les Milieux Condensés, Théories et Applications, Saclay 1976 (INSTN, Saclay, France) p. 367.

Precipitation under irradiation

W) Phase Stability under Irradiation, Proc. of the Fall Meeting of AIME, Pittsburgh (1980), eds. J. R. Holland, L. K. Mansur and D. I. Potter (The Metallurgical Society of AIME, Warrendale, 1981).

X) Phase transformations and Solute Redistribution in Alloys during Irradiation, ed. F. V. Nolfi, Jr. (Applied Science Publishers, Barking, UK).

Y) Phase Stability under Irradiation, K. C. Russell, Prog. Mater. Sci., 1984, **28**, 229.

Z) Materials under Irradiation, Solid State Phenomena, 1993, **30** & **31**.

Alloys under irradiation as dynamical systems

AA) Non Linear Phenomena in Materials Science, ed. L. Kubin and G. Martin, Vol. 1, 1988, Vol. 2, 1992, Vol. 3, 1995 (Trans. Tech. Pub., Aedermansdorf, Switzerland).

Amorphous metallic Alloys

There are two famillies of conferences devoted to A.M.A.:

BB) the "LIQUID and AMORPHOUS METALS" serie the last of which have been published as follows: L.A.M. VI, 1988, Zeits. Phys. Chem. Neue Folge, **156–157**; L.A.M. VII, 1990, J. non Cryst. Sol., **117–118**; L.A.M. VIII, 1993, J. non Cryst. Sol., **156–158.**

CC) the "RAPIDLY QUENCHED METALS", series which have been published as: **R.Q.5**" Rapidly Quenched Metals", 1985, eds. S. Steeb and H. Warlimont, (North Holland, Amsterdam); **R.Q.6**, 1988, Mater. Sci. Eng., **97–99**; R.Q.7, 1991, Mater. Sci. Eng., **A133–134**; **R.Q.8**, 1994, Mater. Sci. Eng., **A179–180.**

DD) Amorphous and Liquid Materials, 1987, ed. E. Luscher, G. Fitsch and G. Jacucci, NATO ASI Series E n° 118, (Martinus Nijhoff Pub.).

Diffusion in Grain Boundaries

EE) Fundamentals of Grain and Interphase Boundary Diffusion, 1989, eds. I. Kaur and W. Gust, (Ziegler Press, Stuttgart).

FF) Handbook of Grain and Interphase Boundary Diffusion, 1989, eds. I. Kaur, W. Gust and L. Kozma, (Ziegler Press, Stuttgart).

CHAPTER 8

SOLIDIFICATION

H. BILONI

Laboratorio de Entrenamiento Multidisciplinario
para la Investigación Tecnológica (LEMIT-CIC)
1900 La Plata
Argentina

and W. J. BOETTINGER

National Institute of Standards & Technology
Gaithersburg
MD 20899-0001
USA

R. W. Cahn and P. Haasen†, eds.
Physical Metallurgy; fourth, revised and enhanced edition

1. Introduction

In this chapter, we give a general view of the formation of the solid from its melt. This process is generally driven by the extraction of heat from the melt and the first section deals with heat flow during conventional casting, directional solidification, and rapid solidification processing. Next, the fundamentals of the freezing process are treated under the headings: i) Thermodynamics of solidification, ii) Nucleation, iii) Interface attachment kinetics, iv) Solute distribution for planar and nearly planar solid–liquid (S–L) interfaces, v) Cellular and dendritic growth and vi) Polyphase solidification. Subsequently, fluid flow and associated phenomena are discussed. The last portion of the chapter deals with the application of these fundamentals to conventional and continuous casting, welding processes, manipulation of structure and new and emerging solidification processes. Rapid solidification is not treated separately, but is included in the headings above in an attempt to provide a general understanding of the solidification process as the solidification rate is increased.

2. Heat flow in solidification

When hot metal is poured into a mould, the rate at which it can lose heat is controlled by a number of thermal resistances. Figure 1 shows schematically the thermal conditions for a simple geometry of solidifying metal. In different parts of the metal-mould system heat transfer may occur by conduction, convection or radiation. The formal treatment of this problem involves considerable complexity as a consequence of the continuous generation of latent heat at the moving S–L interface, the nature of the S–L interface geometry which can be cellular or dendritic for alloys, and the variation of the physical properties of the metal-mould system with temperature. The major impediments to the removal of the latent heat are the solidifying metal itself, the metal-mould interface, and the mould. For these, the solidification process is primarily controlled by heat diffusion and Newtonian heat transfer across the mould-metal interface. Many numerical software packages are now available to solve the heat flow problem and are becoming more widely used to treat the complex shapes involved in industrial foundry applications.

In the following sections we describe heat transfer inside the solid/liquid metal system, heat transfer to the mould, examples of heat flow analysis in 1-D and more complex geometries, as well as software developments and the use of controlled solidification geometries for research purposes.

2.1. Heat transfer within the solid/liquid metal system

If the system under consideration involves an interface between solid and liquid that has a relatively smooth shape, as in the case of solidification of pure substances or dilute alloys, it is convenient to treat the phases as two different media. For pure conduction heat diffusion equations are applied separately to the solid and liquid.

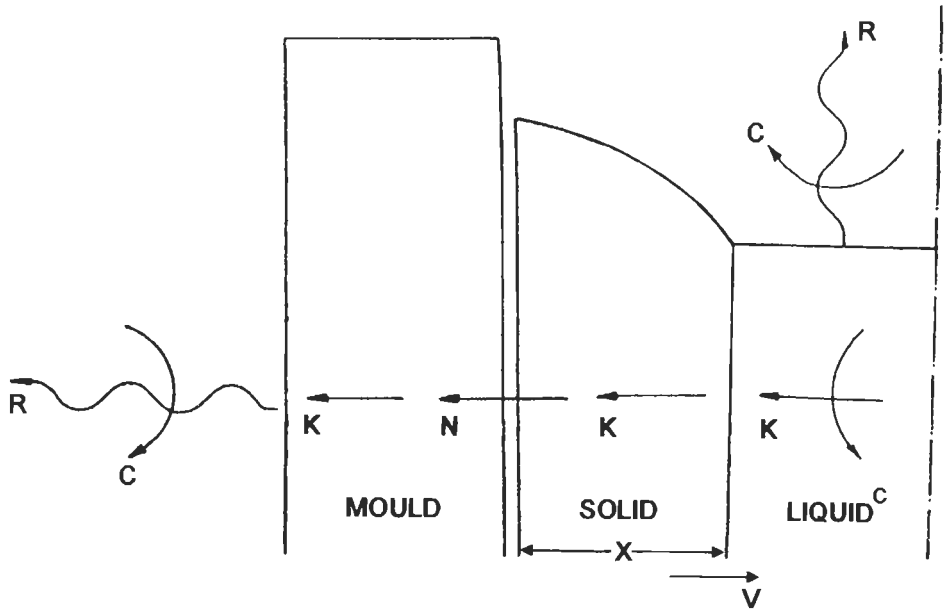

Fig. 1. Thermal conditions for solidification of a simple geometry of a pure superheated liquid metal. In the figure, K corresponds to heat transfer by conduction, N to Newtonian heat transfer across the mould–metal interface, C to convective heat transfer, and R to heat transfer by radiation.

$$div\left[K_S\, grad\, T_S(\vec{x},t)\right] = C_p^S \frac{\partial T_s(\vec{x},t)}{\partial t}, \tag{1}$$

$$div\left[K_L\, grad\, T_L(\vec{x},t)\right] = C_p^L \frac{\partial T_L(\vec{x},t)}{\partial t}, \tag{2}$$

and the heat flux and temperatures are matched at the S–L interface using

$$K_S G_S - K_L G_L = LV, \tag{3}$$

$$T_L = T_S = T_i \tag{4}$$

where K_S = solid thermal conductivity, K_L = liquid thermal conductivity, G_S = normal component of the thermal gradient in solid, G_L = normal component of the thermal gradient in the liquid, V = normal velocity of the S–L interface, T_i = interface temperature which may depend on curvature and V (see § 5), T_L = liquid temperature, T_S = solid temperature, C_p^L = volumetric liquid specific heat, C_p^S = volumetric solid specific heat, and L = volumetric latent heat.

Convection within the melt can also be important and influences solidification at both the macroscopic and microscopic levels. At the macroscopic level it can change the shape of the isotherms and reduce the thermal gradients within the liquid region. Also the

References: p. 830.

local solidification conditions, macrosegregation, and microstructure can be affected by convection. In particular the orientation of columnar dendritic structure, the occurrence of the columnar-to-equiaxed (CET) transition and nucleation initiated by dendrite arm detachment are all influenced by convection (see § 9).

When solidification of alloys that exhibit a large solidification range are treated, a *mushy zone* (see § 7) is usually present. In this case the solid and liquid phases are often treated as a single domain (RAPPAZ and STEFANESCU [1988] and RAPPAZ [1989]). The heat diffusion equation to be solved is

$$div\left[K(T)\,grad\,T(\vec{x},t)\right] + \dot{Q} = C_P(T)\frac{\partial T(\vec{x},t)}{\partial t}, \tag{5}$$

where $K(T)$ is the thermal conductivity, $C_p(T)$ is the volumetric specific heat and $\dot{Q}$ is the heat source term associated with the phase change.

$$\dot{Q} = L\frac{\partial f_S(\vec{x},t)}{\partial t}, \tag{6}$$

with $f_S(\vec{x},t)$ being the solid fraction. To solve eq. (5) a relationship for $f_S(\vec{x},t)$ must be known.

The simplest and most widely used method assumes that f_S depends only on T. Then eqs. (5) and (6) can be combined as

$$div\left[K(T)\,grad\,T(\vec{x},t)\right] = \left[C_P(T) - L\frac{df_S}{dT}\right]\frac{\partial T(\vec{x},t)}{\partial t}. \tag{7}$$

This equation can be rewritten according to two different numerical techniques. When the *specific heat method* is considered the equation is

$$div\left[K(T)\,grad\,T(\vec{x},t)\right] = C_P^e(T)\frac{\partial T(\vec{x},t)}{\partial t}, \tag{8}$$

where C_P^e is an altered specific heat

$$C_P^e(T) = \left(C_P(T) - L\frac{df_S}{dT}\right), \tag{9}$$

that includes the latent heat. When the *enthalpy method* is used, instead of treating the temperature as a variable, the volumetric enthalpy H is adjusted and equation (7) becomes

$$div\left[K(T)\,grad\,T(\vec{x},t)\right] = \frac{\partial H(\vec{x},t)}{\partial t} \tag{10}$$

where

$$H(T) = \int_0^T C_P(T')dT' + L\left[1 - f_S(T)\right]. \tag{11}$$

RAPPAZ [1989] discussed the advantages and disadvantages of using the equivalent

specific heat method (eq. (8)) and the latent heat method (eq. (10)). In standard macroscopic modeling of solidification the relationship $f_S(T)$, C_p^e (T), or $H(T)$ can either be deduced from DTA-type measurements or from a simple solute model as that of SCHEIL [1942] to be discussed in § 6.

More complex methods, where f_S is not simple a function of T, must be considered if the details of nucleation and growth or solid diffusion (BRODY and FLEMINGS [1966]) are to be coupled to the macroscopic heat flow (RAPPAZ [1989]). For example, for columnar dendritic growth, f_S depends on the local isotherm velocity and temperature gradient, as well as the temperature.

2.2. Heat transfer at the metal-mould interface

The heat flow from the solidifying metal is often limited by the metal-mould thermal resistance. This resistance is quantified by the value of the heat transfer coefficient, h_i, defined by

$$q = h_i(T_{iS} - T_{iM}), \tag{12}$$

corresponding to a Newtonian heat transfer model where q is the heat flux across the interface, T_{iS} is the metal temperature and T_{iM} the mould temperature, both at the metal-mould interface. When the melt first enters into contact with the mould wall, the mould surface is at a low temperature and the liquid is at the melting point plus the superheat. The thermal contact is not perfect and the h_i value depends on the complex nature of the contact between metal and mould as shown in fig. 2a. Also important are the thermal resistance imposed by any coating present on the mould surface (BILONI [1977]) and the "air gap" that often develops between the mould surface and the solidifying metal due to metal shrinkage (DAS and PAUL [1993]). Consequently, the physical nature of the thermal contact can change with time and from point to point and may also depend on the wetting capacity of the melt, existence of oxides, grease, etc.

HO and PEHLKE [1984], [1985] and CAMPBELL [1991a], [1991b] give a clear picture of the heat flow at the metal-mould interface including the origin, development, and nature of the so called "*air gap*". The following facts must be considered:
1) When the metal enters the mould, good contact exists between the molten metal and the mould surface as PRATES and BILONI [1972] and MORALES *et al.* [1979] proved through the analysis of the casting surface structure. Contact occurs at the peaks of the mold surface roughness where large supercooling creates *predendritic nuclei* (BILONI and CHALMERS [1965]). The application of pressure enhances the contact and the h_i value can be increased dramatically (CAMPBELL [1991a]). 2) After the creation of a solidified layer with sufficient strength, the casting and mould both deform due to thermal contraction and the contact is reduced to isolated points at greater separations than that determined by the surface roughness. The interface gap starts to open and the conduction across the interface decreases drastically. Consequently, the h_i value falls by more than one order of magnitude. When radiation is neglected, the important mechanism becomes the conduction of heat through the gas phase in the gap. In this case $h_i = K_f/e$, where e is the equivalent thickness averaged over the metal-mould interface and K_i an effective thermal

References: p. 830.

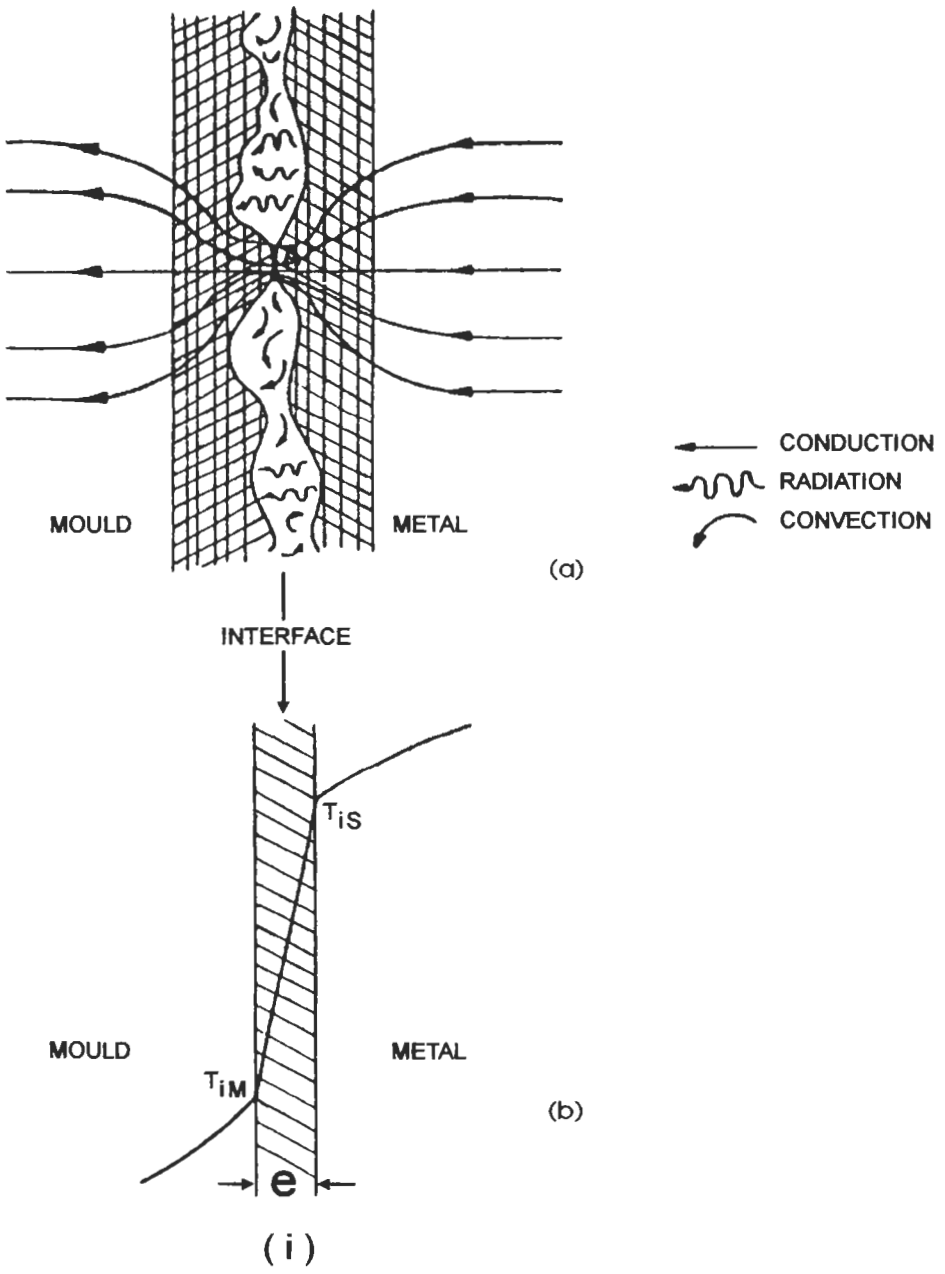

Fig. 2. Nature of the thermal contact between the metal and the mould and equivalent Newtonian model of the metal–mould interface. (a) The complex nature of the contact and different types of heat transfer occurring at the interface are shown schematically. At point A good local contact assures a higher heat conduction. As a consequence, h_i will locally be higher than at the rest of the metal–mould interface. (b) The equivalent Newtonian model is based on an effective value of the gap, e, to yield an average value of h_i.

conductivity of the gas. Then, h_i corresponds to an *average value* represented by the equivalent model of fig. 2b but local values can be considerably different. The important aspects for modelling h_i are the identity of the gas in the gap and the gap thickness.

HO and PEHLKE [1984] and CAMPBELL [1991a], [1991b] discuss the nature of the gas in the gap. For iron and steel castings in sand moulds, the gas present is likely to be hydrogen. This is significant, because of the high thermal conductivity of hydrogen, which is of the order of seven times greater than for air. For metallic moulds the lower H content in the gap will result in a lower thermal conductivity, but the h_i value may still be twice that of air (CAMPBELL [1991b]). These conclusions must be considered seriously when h_i values are estimated for heat transfer calculations.

The width of the gap is treated as a thermal expansion effect of the casting and the mould. If the mould expansion is considered homogeneous, transient heat flow consideration yields (CAMPBELL [1991a]) that e/D is proportional to

$$a_c(T_m - T) + a_M(T_{Mi} - T_o), \tag{13}$$

where e = gap size, D = casting diameter, T_m = freezing point, T_{Mi} = temperature of the mould interface, T_o = original temperature of the mould, a_c = casting thermal diffusivity, a_M = mould thermal diffusivity.

However, in general, there will be powerful geometrical effects and the gap thickness can change differently in various parts of the mould. Therefore, the situation in shaped casting is complicated as CAMPBELL [1991b] affirms and has yet to be tackled successfully by theoretical models. Indeed HO and PELKE [1984] and [1985] demonstrate the difference in h_i value obtained for chilling surfaces located at the top or bottom of a cylindrical Al casting.

MEHRABIAN [1982] reported the measurement of h_i in splat cooling, in pressurized aluminium against a steel mould and in liquid die casting against a steel mould. He estimates that an upper limit exists for practically achievable heat transfer between liquid and substrates of about $h_i = 10^5$–10^6 J/m^{2}Ks. Table 1 gives the order of magnitude of h_i for different conditions of a metal in contact with a mould.

Careful measurements and analysis are necessary to obtain accurate heat transfer coefficients. Using thermocouple measurements and numerical solution of the *inverse heat conduction problem*, HO and PEHLKE [1985] have obtained h_i values that show the onset of gap formation, and its time evolution.

More recently HAO *et al.* [1987] performed experiments with ductile iron and discussed the effect on h_i of the expansion of graphite precipitated during the solidification period. SHARMA and KRISHMAN [1991] discussed the effect of the microgeometry of moulds considering several combinations of V grooves upon the mould or chill surface. DAS and PAUL [1993] determined h_i in castings and quenching using a solution technique for inverse problems based on the Boundary Element Method (BEM).

2.3. Heat flow in one dimensional solidification geometries

Two examples of the analysis of one dimensional heat flow during solidification are given here. The first is often applicable in ordinary casting processes, while the second applies to rapid solidification.

References: p. 830.

2.3.1. Freezing at mould wall

The pioneering work by PIRES *et al.* [1974] analytically treated the case where the effects of a finite heat transfer coefficient at the metal-mould interface and conduction in the both metal and mould are important. Later, GARCIA and PRATES [1978] and GARCIA *et al.* [1979] obtained similar results. CLYNE and GARCIA [1980] reviewed the analytical solutions, known now as the "Virtual Adjunct Method" (VAM), and described various limiting cases. The basic assumptions are: i) Conductive heat flow is unidirectional with semi-infinite metal and mould regions. ii) The Newtonian interface resistance is represented by a heat transfer coefficient, h_i, which remains constant throughout the process. The important case of variable h_i is not treatable by exact analytical methods. iii) The metal solidifies with a planar S–L interface that remains at the equilibrium melting point. iv) The metal solidifies with zero superheat in the liquid. v) Convection currents and radiation losses are assumed to be small. vi) The thermal properties of the metal and mould do not change with temperature. The analytical solution for the solidification time, t_S, as a function of the distance solidified, X, has the form:

$$t_S(X) = AX^2 + BX \tag{14}$$

where

$$A = \frac{1}{4\phi^2 a_S}, \tag{15}$$

$$B = \frac{L\rho_S}{h_i(T_m - T_o)} \tag{16}$$

with ϕ evaluated numerically from the equation

$$\phi \exp(\phi^2)[M + \operatorname{erf}\phi] = \frac{1}{\sqrt{\pi}L^+}. \tag{17}$$

Here, a_S is the thermal diffusivity of the solid metal, $M = (K_S C_p^S / K_M C_p^M)^{1/2}$ = mould constant, subscripts or superscripts S and M refer to solidified metal and mould,

Table 1
Order of magnitude of heat-transfer coefficient, h_i, for different processes. MEHRABIAN [1982].

Process	h_i (J/m^{2}Ks)
Massive mould, polished	4×10^3
Massive mould, coated	7.5×10^2
Cooled mould, polished	5×10^3
Cooled mould, coated	10^3
Pressure-Cast	3×10^3–3×10^4
Die-cast	5×10^4
Drop-smash	10^4–10^5
Splat-cooling	10^5–10^6

respectively, C_p is the volumetric specific heat, and L^+ is the dimensionless latent heat given by $L/C_S(T_m-T_0)$. The two terms in eq. (14) describe respectively: (i) the time necessary to solidify a metal of specified thickness if h_i were infinite, that is, if the thermal contact between metal and mould were perfect and (ii) the time necessary to solidify a metal of specified thickness if the thermal conductivity of the mould and metal were large and $h_i \neq \infty$, that is, the second term only considers the effect of the Newtonian thermal resistance at the metal-mould interface. PIRES *et al.* [1974] and GARCIA and PRATES [1978] successfully checked eq. (14) for the particular case of efficient refrigeration of the chill mould in unidirectional solidification of Sn, Pb, Zn and Al. In this case, $M \cong 0$ giving a more simplified form of the general solution. GARCIA *et al.* [1979] extended the experiments to moulds where $M \neq 0$. These authors calculated the h_i value from the experimental curves, $X=f(t_S)$, through eq. (16).

GARCIA and CLYNE [1983] consider that in the case of Al–Cu alloys, having an appreciable temperature range of solidification, this method can be used without major modification. An analytical treatment that takes account of the mushy zone has been developed by LIPTON *et al.* [1982]. In addition, the VAM method has been extended to freezing processes involved in certain types of splat cooling (CLYNE and GARCIA [1981]). When the effects of superheat are considered, numerical methods are necessary, as shown for example by HILLS *et al.* [1975].

2.3.2. Rapid freezing in contact with a cold substrate with initial melt supercooling

Rapid cooling of a melt often causes the liquid phase to be cooled below the melting point. The interplay of liquid volume to be frozen, melt supercooling and external heat transfer to a cold substrate controls the solidification speed as in splat cooling. Theoretical details of this process have been examined numerically by CLYNE [1984]. A major complication occurs for heat flow analysis when high solidification velocities are involved even for pure materials. The temperature of the S–L interface T_i, cannot be treated as a constant, equal to the melting point, T_m, but rather it is a function of the interface velocity. As a result, the heat flow analysis depends on the details of this function, which are even more complicated for dendritic growth and for alloys (see § 5 and 7). CLYNE [1984] treats the case of a pure metal freezing with a smooth (non-dendritic) S–L interface governed by a kinetic law for the interface velocity given by $V=\mu(T_m-T_i)$ where μ is the linear interface attachment coefficient taken as 4 cm s^{-1} K^{-1} (see § 5).

Calculations show the importance of the initial supercooling ΔT on the development of high solidification velocities. Large values of ΔT can develop if nucleation on the substrate is difficult. Figure 3 (from CLYNE [1984]) shows temperature-time plots at two positions inside a 50 μm thick layer of an Al melt cooling in contact with a substrate with $h_i = 10^6$ Wm^{-2} K^{-1}. For example, at a position 5 μm from the substrate, the temperature in the liquid drops until nucleation occurs near the substrate at a dimensionless supercooling $\Delta\theta = \Delta T/(L/C_p^L) \cong 0.4$, which he assumes to be predicted from homogeneous nucleation theory (see § 4). The temperature at this position then rises rapidly as the S–L interface proceeds from the substrate towards the 5 μm position. After the

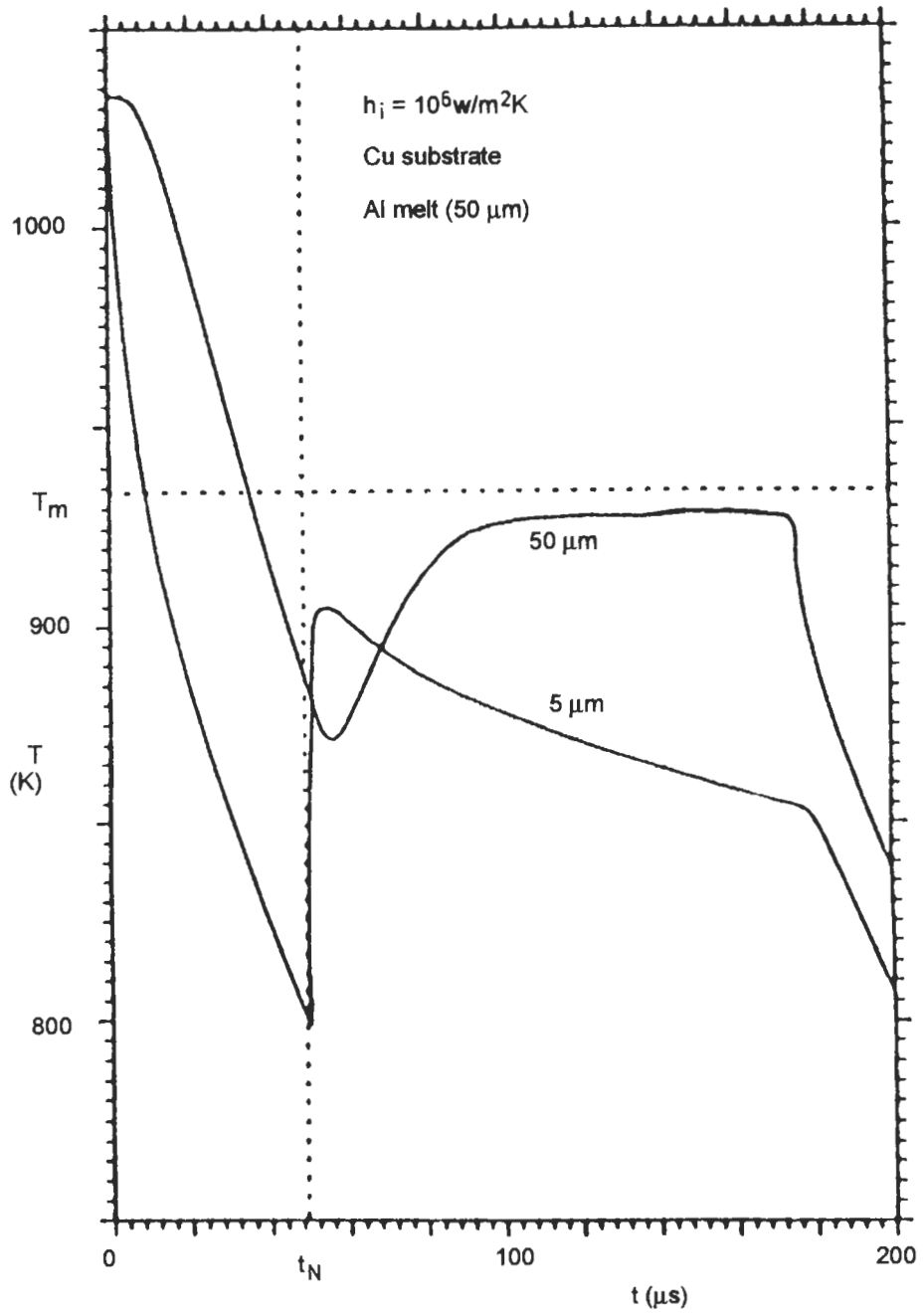

Fig. 3. Calculated temperature–time histories for two positions within a liquid layer 5 and 50 μm from a chilling substrate. Nucleation occurs at the substrate surface at time, t_N, at an undercooling of $-0.4\,L/C_p^L$. The recalescence after the passing of the liquid–solid interface is evident at both positions. CLYNE [1984].

interface passes the 5 μm position, the temperature falls slowly. A plot for the temperature at the 50 μm position shows a smaller initial drop in temperature followed by a gradual rise as the interface approaches. The supercooling of the interface when it passes the 5 and 50 μm position is approximately 25 and 5 K respectively which correspond to interface velocities of 100 cm s^{-1} and 20 cm s^{-1}. Thus, the initial supercooling produces a much higher solidification rate close to the chill than would be possible without initial supercooling.

2.4. Heat flow in more complex solidification geometries

In general the analysis given above is useful for one-dimensional heat flow. In more complicated geometries there are several aspects that lead to difficulties, including the nonlinearity of the heat transfer problem due to the latent heat of fusion, the geometric complexity of shaped castings, the disparities in thermal properties between the metal and mould. Also the treatment of temperature dependent properties and heat transfer coefficient. In this framework, the techniques of *numerical modeling* are necessary.

From the pioneering work of HENZEL and KEVERIAN [1965], applying successfully the Transient Heat Program (THP) to heavy steel cast production, an explosive growth of computer modeling techniques have arisen, especially in the last 15 years (BERRY and PEHLKE [1988]). As a result macroscopic modeling of solidification processes are well developed and different processes can be treated. We shall present here the application of these methods in two cases: controlled directional solidification and rapid solidification of atomized metal droplets into powder. In § 10 we discuss the application of numerical modeling of heat flow to welding and continuous casting processes.

2.4.1. Heat flow in controlled directional solidification of metals

Although a number of variations in the construction of DS equipment has been described in the literature, in many cases the process used is the Bridgman technique where a cylindrical crucible is moved through at a fixed temperature gradient, G_L, with a constant translation velocity V^*. It is often assumed that the interface will remain stationary with respect to the furnace during most of the growth period and that the growth velocity of the interface, V, is equal to that of the crucible or the moving furnace (V^*). However, CLYNE [1980a], [1980b] combined experimental investigation of commercial purity Al with mathematical modeling to determine the relationship between the interface and the traverse speed. He used a finite difference model to investigate a number of facets of the process. It was calculated that V can differ from V^* by 50% or more over a significant distance in some cases. The difference between V and V^* was found to increase as the thermal diffusivity of the metal increases. The model was used to examine the conditions under which the departure from ideal behavior would be significant and some practical steps were suggested to eliminate this problem.

2.4.2. Powder solidification

LEVI and MEHRABIAN [1982] examined theoretically the heat flow during rapid cooling of metal droplets. Relationships were established between atomization paramet-

ers, growth kinetics, and interface velocity. They developed a numerical solution based on the enthalpy method for simulating the solidification process from a single nucleation event occurring at the powder surface and their results are compared with the trends predicted from a Newtonian cooling model. They also discuss the implications of single vs. multiple nucleation events. Their results stressed the importance of the initial supercooling, ΔT, when nucleation occurs, on the development of high solidification velocities. Figure 4 adapted by BOETTINGER and PEREPEZKO [1985] from LEVI and MEHRABIAN [1982] shows the interface temperature and interface velocity as solidification proceeds from one side of the droplet to the other, increasing the fraction solid. The curves shows the case of an initial supercooling of $\Delta\theta = 0.5$ (~182 K for Al) for various values of h_i. The velocity starts at a high value (>3 m/s) and slows as the interface moves across the droplet. This decrease in velocity is due to the evolution of the latent heat at the S–L interface and the resultant reduction in the interface supercooling. The effect of changing the heat transfer coefficient by two orders of magnitude is primarily to alter the velocity after the fraction solid exceeds the dimensionless initial supercooling (0.5 in this case). Growth at small fraction solid is controlled primarily by heat flow inside the powder particle, while growth at large fraction solid is controlled by external heat flow. If no initial supercooling were present, the growth velocities across the entire particle would be near those seen at large fraction solid (fig. 4), which are typically less than 10 cm/s.

2.5. Software packages

Different numerical methods have been used to treat solidification. RAPPAZ [1989] discusses five main computational techniques: i) The finite difference method (FDM) with or without the alternative implicit direction (ADI) time stepping scheme, ii) The finite element method (FEM), iii) The boundary element method (BEM), iv) The direct finite difference method (DFDM), v) The control volume element method (VEM). He discussed the basic advantages and/or inconveniences of these methods using schematic 2-dimensional enmeshments that are associated with the five main computational techniques. OHNAKA [1991] analyzed solidification for a thermal conduction model and reviewed critically these computational techniques. BERRY and PEHLKE [1988] give a comprehensive view of the steps to be taken when solidification modeling is used, stressing the fact that the thermophysical properties and details about mould material are often poorly known. Indeed, conditions such as moisture, property dependence on temperature, etc., would require an almost limitless data base. Software packages permit, through suitable interactions, the generation of maps displaying the variation of specific criteria functions that affect casting soundness, such as local temperature gradient, freezing time, front speed or cooling rate.

DANTZIG and WIESE [1986] and WIESE and DANTZIG [1988] have focused on a technique to reduce the computation time involved in FEM methods for sand castings. Considering that the number of nodes located within the mold is far greater than those within the casting, the authors replace the sand mold by a set of boundary conditions applied at each element on the surface of the casting. This method was initially proposed by NIYAMA [1977] and later by WEI and BERRY [1980] and is known as the *Q-Dot*

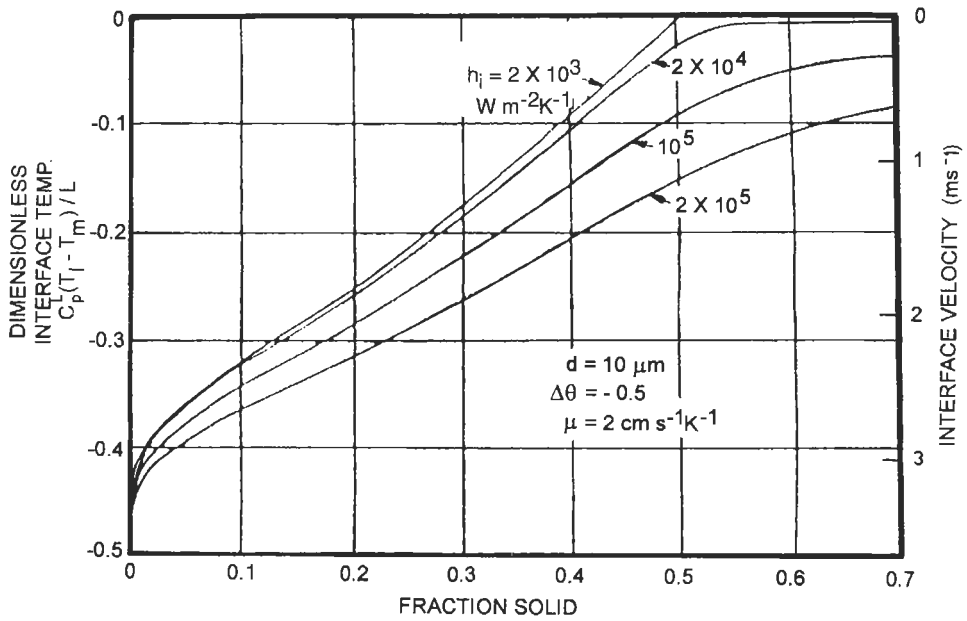

Fig. 4. Calculated interface temperature (LEVI and MEHRABIAN [1982]) for the solidification of a powder particle initially undercooled by $1/2\ L/C_p^L$. The temperature rises and the velocity falls as growth proceeds from the point of nucleation on the powder surface across the powder particle. The effect of various values of the heat transfer coefficient h_i is also shown. The velocity scale on the right was added by BOETTINGER and PEREPEZKO [1985].

method. More recently DANTZIG and LU [1985] and DANTZIG and WIESE [1985] developed the Boundary Curvature Method (BCM). In both techniques the heat flow from the surface of the casting is treated using a library of special functions, related to the local geometry, which contain the information about heat flow from that shape into a mould material. The BCM method seems to adapt better to arbitrary shapes in three dimensions than the *Q-Dot method.* DANTZIG and WIESE [1986] present an example of a complex casting (a cylinder block section) stressing the fact that this problem would have required much greater computation time without the BCM.

2.6. Experimental methods involving controlled solidification

The difficulties associated with predicting external heat transfer in casting has lead to the development of two research techniques of controlled solidification: unidirectional solidification and solidification with prescribed bulk supercooling. Much of the understanding of solidification laws comes from unidirectional solidification experiments based on the simple principle that the extraction of latent heat must be achieved without allowing the melt to supercool sufficiently to permit the nucleation of crystals ahead of the solidification front. In practice this requires a heat sink that removes heat from the

solid and a heat source that supplies heat to the melt. The extensive use of such techniques by CHALMERS and his school (CHALMERS [1964], [1971]) produced the basis of modern understanding in solidification. The basic heat flow objectives are to obtain a unidirectional thermal gradient across the interface and to move it so that the interface moves at a controlled rate. For a planar S–L interface the gradients are related by eq. (3). Based on this idea different techniques have also been developed to obtain single crystals employed for research purposes. FLEMINGS [1974] gives details of the different techniques used. Heat flow in controlled directional solidification (DS) is treated in § 2.4.1.

Another directional controlled process corresponds to the extraction of heat via a botton chill. Growth occurs in a direction parallel and opposite to the heat flux direction. In this situation a better control of microstructure and properties is obtained in comparison with conventional casting. However the microstructure is not uniform as in the Bridgman method, because V and G decrease with the distance from the chill. It is possible to improve the microstructure uniformly by programmed furnace temperature and withdrawal rates.

The above examples of controlled solidification do not involve bulk liquid supercooling. However, when a crystal is nucleated at a specified temperature and grows freely into the liquid, the bulk supercooling ΔT plays a major role in determining the structure observed during the solidification process. This type of study has been performed with both low and high supercooling and important structural information has been obtained in organic material analogues (GLICKSMAN [1981]) and metallic alloys (FLEMINGS and SHIOHARA [1984], WILLNECKER *et al.* [1989], [1990]). More details will be given in § 11.

3. *Thermodynamics of solidification*

3.1. Hierarchy of equilibrium

The process of solidification cannot occur at equilibrium. However it is clear that different degrees of departure from full equilibrium occur and constitute a hierarchy which is followed with increasing solidification rate. This hierarchy is shown in Table 2 (BOETTINGER and PEREPEZKO [1985]).

The conditions required for global equilibrium, (i), are usually obtained only after long term annealing. Chemical potentials and temperature are uniform throughout the system. Under such conditions no changes occur with time. Global equilibrium is invoked for descriptions of solidification that apply the lever rule at each temperature during cooling to give the fraction of the system that are liquid and solid as well as the compositions of the (uniform) liquid and solid phases. This situation is only realized during solidification taking place over geological times.

During most solidification processes, gradients of temperature and composition must exist within the phases. However one can often accurately describe the overall kinetics using diffusion equations to describe the changes in temperature and composition within

Table 2
Hierarchy of Equilibrium.

i.	Full Diffusional (Global) Equilibrium
	a. No chemical potential gradients (composition of phases are uniform)
	b. No temperature gradients
	c. Lever rule applicable
ii.	Local Interfacial Equilibrium
	a. Chemical potential for each component continuous across the interface
	b. Phase diagram gives compositions and temperatures only at Solid–Liquid interface
	c. Correction made for interface curvature (Gibbs–Thomson Effect)
iii.	Metastable Local Interfacial Equilibrium
	a. Important when stable phase cannot nucleate or grow fast enough
	b. Metastable phase diagram (a true thermodynamic phase diagram missing the stable phase or phases) gives the interface conditions
iv.	Interfacial Non-Equilibrium
	a. Phase diagram fails to give temperature and compositions at interface
	b. Chemical potentials are not equal at interface
	c. Free energy functions of phases still lead to criteria for the "impossible" (Baker and Cahn [1971])

each phase and using the equilibrium phase diagram to give the possible temperatures and compositions for boundaries between the phases, e.g., at the solidification interface. The Gibbs–Thomson effect is included to determine shifts in equilibrium due to the curvature of the liquid–solid interface. This condition is called the local equilibrium condition, (ii) in table 2.

For a dilute alloy the liquidus and solidus of the phase diagram can often be represented as straight lines (fig. 5). The local equilibrium condition for a curved interface is given in this case by

$$T_i = T_m + m_L C_L^* - T_m \Gamma K_m \tag{18}$$

and

$$C_S^* = k_o C_L^*, \tag{19}$$

where T_i and T_m are the interface temperature and pure solvent melting temperature, m_L is the liquidus slope, C_L^* and C_S^* are the compositions at the interface of the liquid and solid, Γ is the ratio of the liquid–solid surface energy to the latent heat per unit volume, K_m is the mean curvature of the interface (defined as positive when the center of curvature is in the solid), and k_o is the equilibrium partition coefficient.

Local equilibrium is never strictly valid, but it is based on the notion that interfaces will equilibrate much more quickly than will bulk phases. The conditions described in (ii) of Table 2 are widely used to model the majority of solidification processes that occur in castings. For example, under the assumptions of fast diffusion in the liquid phase, negligible diffusion in the solid phase, and local equilibrium at the interface, the Scheil Equat-

References: p. 830.

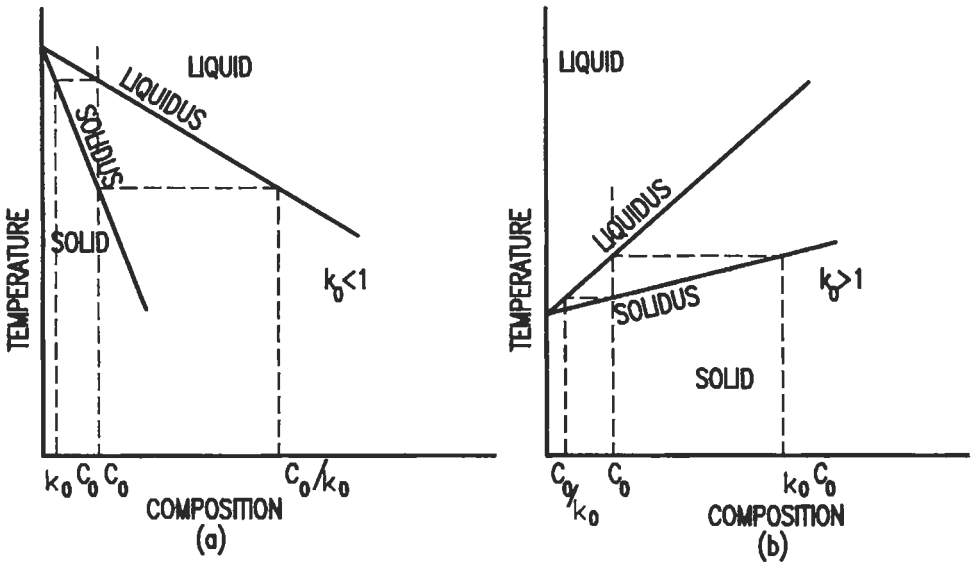

Fig. 5. Solidus–liquidus relationships for dilute binary alloys. For a liquid composition of C_0 the equilibrium solid composition is k_0C_0. For a solid of composition, C_0, the equilibrium liquid composition is C_0/k_0.

ion (see § 7.3) gives a reasonable first approximation to the "nonequilibrium" dendritic coring or microsegregation in conventional castings. Clearly phase diagrams constitute an essential part of the data base for the modeling and analysis of solidification problems.

Metastable equilibrium, (iii) in Table 2, can also be used locally at interfaces and is important in ordinary metallurgical practice. For example, one can understand the microstructural change of cast iron from the stable gray form (austenite and graphite) to the metastable white form (austenite and cementite) with increasing solidification rate (and interface supercooling) using information from the stable and the metastable phase diagrams combined with a kinetic analysis (JONES and KURZ [1980]). The eutectic temperature and composition for white cast iron are well defined thermodynamic quantities just as they are for gray cast iron. Metastable equilibrium is represented by a common tangent construction to the molar free energy vs. composition curves for the liquid, austenite, and cementite phases and thus minimizes the free energy as long as graphite is absent. When solidification is complete, a two phase mixture of austenite and cementite can exist in a global metastable equilibrium. The concept of local metastable equilibrium is especially important during rapid solidification (PEREPEZKO and BOETTINGER [1983], PEREPEZKO [1988]) because some equilibrium phases, especially those with complex crystal structures, have sluggish nucleation and/or growth kinetics and are absent in rapidly solidified microstructures.

An example of a metastable phase diagram superimposed on a stable phase diagram is given in fig. 6 for the Al–Fe system. If Al_3Fe is absent, phase boundaries involving a metastable phase, Al_6Fe, which is isomorphous with Al_6Mn, are obtained. In particular a metastable eutectic, $L \rightarrow Al + Al_6Fe$ occurs. Transitions of microstructures involving

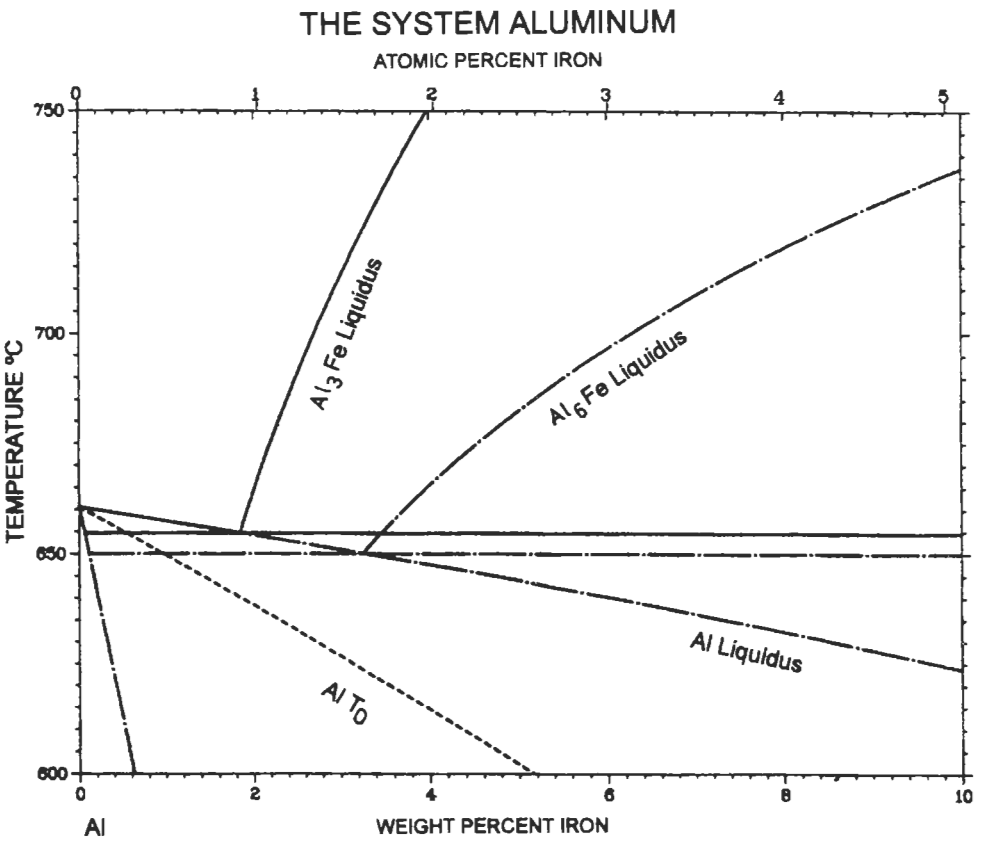

Fig. 6. Calculated Al-rich portion of the stable Al–Fe phase diagram is shown by solid lines. If Al_3Fe is absent, a metastable phase diagram (dot-dashed lines) involves a eutectic L→Al+Al_6Fe. The T_0 for the solidification of Al solid solution is shown dashed. The solvus curves are omitted for clarity. MURRAY [1983a].

Al_3Fe to those involving Al_6Fe have been observed with increasing solidification speed by ADAM and HOGAN [1972] and by HUGHES and JONES [1976]. The competitive growth kinetics of the two can also be analyzed using the stable and metastable phase diagrams.

For local equilibrium, whether stable or metastable, the chemical potentials of the components for the liquid and solid are equal across the interface. In Table 2, however, another situation is described in (iv), and relates to a situation where chemical potentials can not be approximated as being equal across an interface growing at a high rate and large supercooling. These rapid growth rates can trap the solute into the freezing solid at levels exceeding the equilibrium value for the corresponding liquid composition present at the interface. Thus the chemical potential of the solute increases upon being incorporated in the freezing solid in a process called *solute trapping*. This increase in chemical potential of the solute across the interface must be balanced by a decrease in chemical potential of the solvent in order for crystallization to occur; i.e., to yield a net decrease

in free energy (BAKER and CAHN [1971]). The free energy change during solidification, ΔG, is given by

$$\Delta G = \left[\left(\mu_S^A - \mu_L^A\right)\left(1 - C_S^*\right) - \left(\mu_S^B - \mu_L^B\right)C_S^*\right], \tag{20}$$

where μ_S^A and μ_S^B are the chemical potentials for species A and B in the solid, and μ_L^A and μ_L^B are the chemical potentials in the liquid. These potentials are functions of the temperature and solid or liquid composition (C_S^* or C_L^*) at the interface during solidification. Despite the loss of interface equilibrium during rapid solidification, the free energy functions of the solid and liquid phases and their associated chemical potentials can be used to define the possible range of compositions that can exist at the interface at various temperatures. This restriction is obtained by the requirement that ΔG be negative. Figure 7 shows the region of allowable solid compositions at the interface for a fixed liquid composition, C_L^*, at the interface as a function of interface temperature (BOETTINGER [1982]). Such allowable regions can be calculated from a thermodynamic model of the system of interest.

3.2. T_0 curves

For any selected pair of liquid and solid compositions, a thermodynamic temperature can be described that is the highest temperature where crystallization can occur as shown in fig. 7. However one often considers a limiting case, called *partitionless solidification*, which is favored at very high solidification rate, where the composition of the solid formed at the interface, C_S^*, equals the composition of the liquid at the interface, C_L^*. The T_0 temperature is the highest temperature where this can occur (APTEKAR and KAMENETSKAYA [1962]), (BILONI and CHALMERS [1965]). This is the temperature where the molar free energies of the liquid and solid phases are equal for the composition of interest; i.e., the temperature where $\Delta G = 0$ for $C_S^* = C_L^*$ in Equation (20). As illustrated in fig. 7, a T_0 curve represents only part of the thermodynamic information available, when solidification occurs without local equilibrium.

T_0 curves exist for the liquid with stable or metastable phases, and lie between the liquidus and solidus for those phases. In fact for dilute alloys the slope of the T_0 curve is $m_L\,[(\ln k_0)/(k_0 - 1)]$. Figure 8 shows schematically, possible T_0 curves for three eutectic phase diagrams (BOETTINGER [1982]). An important use of these curves is to determine whether a bound exists for the extension of solubility by rapid melt quenching. If the T_0 curves plunge to very low temperatures as in fig. 8a, single phase α or crystals with composition beyond their respective T_0 curves cannot be formed from the melt. In fact, for phases with a retrograde solidus, the T_0 curve plunges to absolute zero at a composition no greater than the liquidus composition at the retrograde temperature, thus placing a bound on solubility extension (CAHN *et al.* [1980]). Experiments on laser-melted doped Si alloys seem to confirm this bound (WHITE *et al.* [1983]). Eutectic systems with plunging T_0 curves are good candidates for easy metallic glass formation. An alloy in the center of such a phase diagram can only crystallize into a mixture of solid phases with different compositions regardless of the departure from equilibrium. The diffusional kinetics of this separation from the liquid phase frequently depresses the

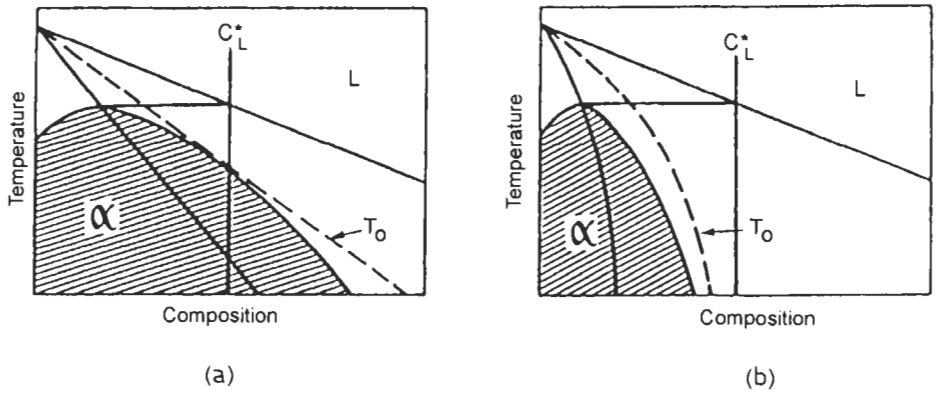

Fig. 7. The shaded regions indicate thermodynamically allowed solid compositions that may be formed from liquid of composition at various temperatures. The T_0 curve gives the highest temperature at which partitionless solidification ($C_L^* = C_S^*$) can occur. In (b) the T_0 temperature plunges and partitionless solidification is impossible for liquid of composition C_L^*. BOETTINGER [1982].

solidification temperature to near the glass transition, T_g, where an increased liquid viscosity effectively halts crystallization.

In contrast, alloys with T_0 curves which are only slightly depressed below the stable liquidus curves, as in fig. 8b, c, make good candidates for solubility extension and unlikely ones for glass formation. In fig. 8b the crystal structures of α and β are different and the T_0 curve cross, whereas in fig. 8c the crystal structures are the same and the T_0 curve is continuous across the diagram. At temperatures and liquid compositions below the T_0 curves, partitionless solidification is thermodynamically possible. Ni–Cr and Ag–Cu are examples of the behavior in fig. 8b and c.

4. Nucleation

4.1. Nucleation in pure liquids

Nucleation during solidification can be defined as the formation of a small crystal from the melt that is capable of continued growth. From a thermodynamic point of view the establishment of a S–L interface is not very easy. Although the solid phase has a lower free energy than the liquid phase below T_m, a small solid particle is not necessarily stable because of the free energy associated with the S–L interface. The change in free energy corresponding to the liquid–solid transition must therefore include not only the change in free energy between the two phases but also the free energy of the S–L interface. From a kinetic point of view it is possible to arrive at the same result on the basis that the atoms at the surface of a very small crystal have a higher energy than the surface atoms of a larger crystal (CHALMERS [1964]). Therefore, the equilibrium temperature at which atoms arrive and leave at the same rate is lower for a very small

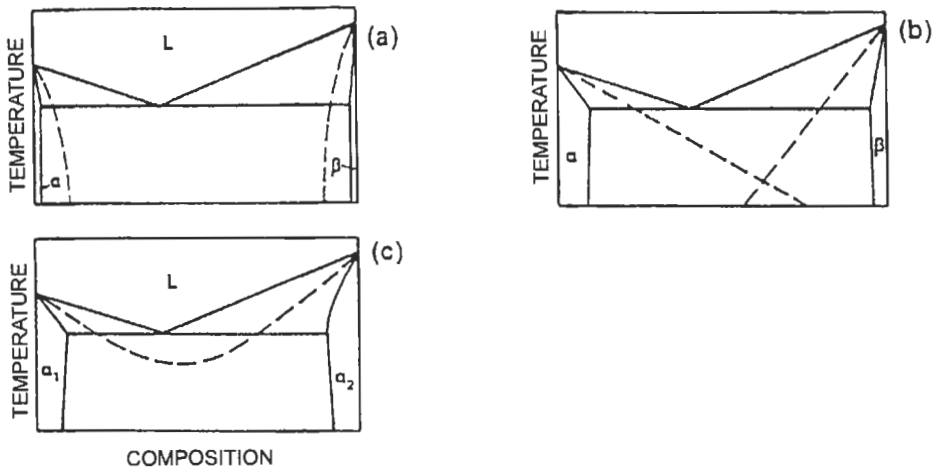

Fig. 8. Schematic representation of T_0 curves for liquid to crystal transformations in three types of eutectic systems. BOETTINGER [1982].

crystal than for a larger one. Consequently for each temperature below T_m, a solid particle can be in equilibrium with the liquid when its radius of curvature has a particular value, known as the *critical radius*. Because at higher supercooling there is more bulk free energy to compensate for the surface free energy, the critical radius decreases with increasing supercooling.

On the other hand, at any supercooling, there exists within the melt a statistical distribution of atom clusters or embryos of different sizes having the character of the solid phase. The probability of finding an *embryo* of a given size increases as the temperature decreases. *Nucleation* occurs when the supercooling is such that there are sufficient embryos with a radius larger than the *critical radius* (HOLLOMON and TURNBULL [1953]).

4.1.1. Calculation of the critical radius and energy barrier

The change in the free energy per unit volume, ΔG, to form a solid embryo of spherical shape of radius, r, from liquid of a pure material involves the variation of the volume free energy and the surface free energy associated with the S–L interface and is given by

$$\Delta G = \Delta G_v + \Delta G_i = -\frac{4}{3}\pi r^3 \frac{L\Delta T}{T_m} + 4\pi\gamma_{SL} r^2, \tag{21}$$

where ΔG_v is the change in free energy on solidification associated with the volume and ΔG_i is the free energy associated with the interface, γ_{SL} is the S–L interfacial free energy, L is the latent heat per unit volume and ΔT is the supercooling. The critical radius, r^*, occurs when ΔG has a maximum given by the condition, $d(\Delta G)/dr = 0$, as

$$r^* = \frac{2\gamma_{SL}T_m}{L\Delta T}. \tag{22}$$

Figure 9, due to KURZ and FISHER [1989], gives a comprehensive picture of the variation of the free energy of an embryo as a function of its radius and ΔT: (a) At temperatures T greater than T_m both ΔG_v and ΔG_i increase with r. Therefore the sum ΔG, increases monotonically with r. (b) At the melting point, $\Delta G_v = 0$ but ΔG_i still increases monotonically. (c) Below the equilibrium temperature the sign of ΔG_v is negative because the liquid is metastable while the behavior of ΔG_i is the same as in (a) and (b). At large values of r, the cubic dependence of ΔG_v dominates over ΔG_i and ΔG passes through a maximum at the critical radius, r^*. When a thermal fluctuation causes an embryo to become larger than r^*, growth will occur as a result of the decrease in the total free energy. Nucleation in a homogeneous melt is called *homogeneous nucleation* and from eq. (21) the *critical energy of activation* for an embryo of radius r^* is given by

$$\Delta G^* = \frac{16}{3}\pi \frac{\gamma_{SL}^3 T_m^2}{L^2 \Delta T^2}. \tag{23}$$

The unlikelihood that statistical fluctuations in the melt can create crystals with a large radius is the reason why nucleation is so difficult at small values of the supercooling. Thus, homogeneous nucleation is only possible for high supercooling (on the order of 0.25 T_m) according to the HOLLOMON and TURNBULL [1953] theory. However small contamination particles in the melt, oxides on the melt surface or contact with the walls of a mould may catalyze nucleation at a much smaller supercooling and with fewer atoms required to form the critical nucleus. This is known as *heterogeneous nucleation*.

In fig. 10, homogeneous and heterogeneous nucleation are compared for a flat catalytic surface and isotropic surface energies. For this simple case, the embryo is a spherical cap that makes an angle θ with the substrate given by

$$\gamma_{cL} - \gamma_{cS} = \gamma_{SL} \cos\theta, \tag{24}$$

where γ_{cL} is the catalyst–liquid interfacial free energy and γ_{cS} the catalyst–solid interfacial free energy. At a supercooling, ΔT, the critical radius of the spherical cap is again given by eq. (22), but the number of atoms in the critical nucleus is smaller than that for homogeneous nucleation as a consequence of the catalytic substrate. Indeed the thermodynamic barrier to nucleation ΔG^* is reduced by a factor $f(\theta)$ to

$$\Delta G^* = \frac{16}{3}\pi \frac{\gamma_{SL}^3 T_m^2}{L^2 \Delta T^2} f(\theta) \tag{25}$$

where

$$f(\theta) = \frac{(2 + \cos\theta)(1 - \cos\theta)^2}{4}. \tag{26}$$

If nucleation occurs in a scratch or a cavity of the catalytic substrate, the number of atoms in a critical nucleus and the value of ΔG^* can be reduced even more. For a planar catalytic surface, the reduction in the free energy barrier compared to that for homo-

References: p. 830.

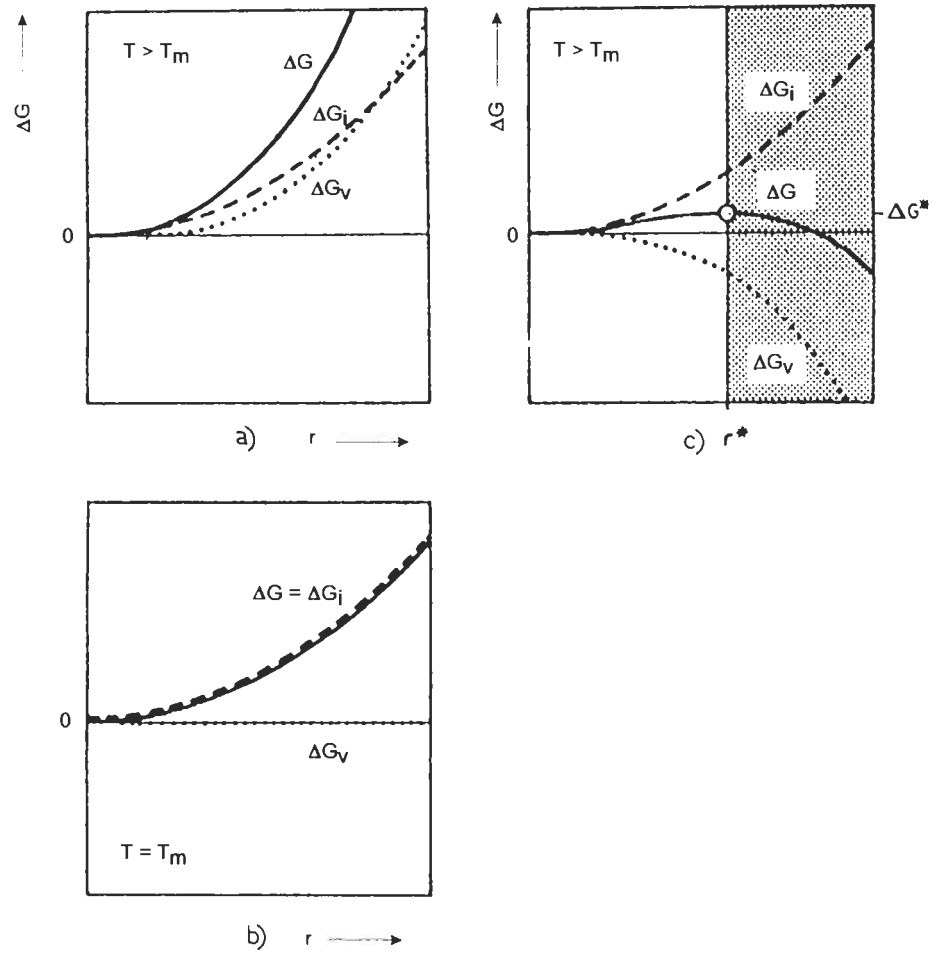

Fig. 9. Volume, surface and total values of the free energy of a crystal cluster as a function of radius, r, at three temperatures: (a) $T > T_m$, (b) $T = T_m$, and (c) $T < T_m$. KURZ and FISHER [1989].

geneous nucleation depends on the contact angle. Any value of θ between 0° and 180° corresponds to a stable angle. When $\theta = 180°$, the solid does not interact with the substrate, $f(\theta) = 1$ and the homogeneous nucleation result is obtained. When $\theta = 0°$, the solid "wets" the substrate, $f(\theta) = 0$, and $\Delta G^* = 0$. As a result, solidification can begin immediately when the liquid cools to the freezing point. From the classical heterogeneous nucleation point of view, a good nucleant corresponds to a small contact angle between the nucleating particle and the growing solid. According to eq. (24) this implies that γ_{cS} must be much lower than γ_{cL}. However, in general, the values of γ_{cS} and γ_{cL} are not known and, therefore it is rather difficult to predict the potential catalytic effectiveness of a nucleant. TILLER [1970] pointed out that there is no clear insight into what deter-

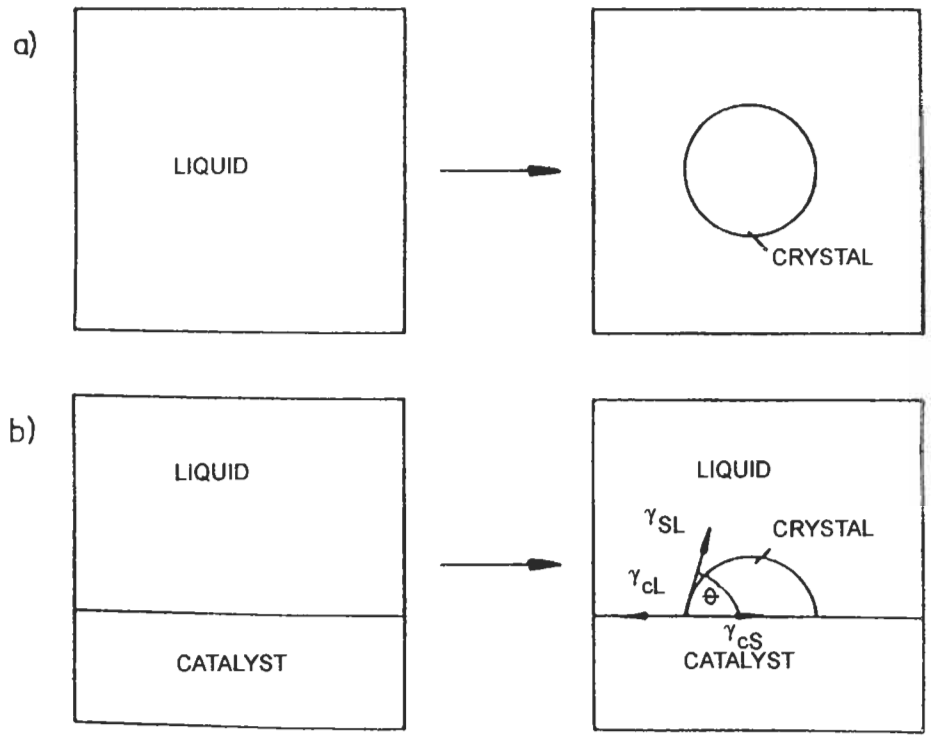

Fig. 10. Schematic comparison of (a) homogeneous and (b) heterogeneous nucleation of a crystal in a supercooled liquid. The interface energies are assumed to be isotropic and in (b) the catalytic surface is assumed to be flat.

mines θ and how it varies with (i) lattice disregistry between substrate and the stable phase, (ii) topography of the catalytic substrate surface, (iii) chemical nature of the catalytic surface and, (iv) absorbed films on the catalytic substrate surface.

4.1.2. Nucleation rate

The rate of homogeneous nucleation, I, is the number of embryos formed with a size that just exceeds the critical value per unit time per unit volume of liquid. Similarly, the heterogeneous nucleation rate is considered per unit area of active catalytic site. To determine the rate of nucleation, it is necessary to find expressions for the number of embryos that have critical size and the rate at which atoms or molecules attach to the critical nucleus.

By considering the entropy of mixing between a small number, N_n, of crystalline clusters, each of which contains n atoms, and N_L atoms of the liquid, an expression for the equilibrium number of clusters with n atoms can be obtained as,

$$\frac{N_n}{N_L} = \exp\left(-\frac{\Delta G_n}{k_B T}\right), \tag{27}$$

where k_B is Boltzmann's constant, ΔG_n is the value of ΔG, obtained from eq. (21) for a cluster of radius, r, containing n atoms. In particular, the number, N_n^*, of clusters of critical radius, r^*, is given by

$$\frac{N_n^*}{N_L} = \exp\left(-\frac{\Delta G_n^*}{k_B T}\right), \tag{28}$$

where ΔG_n^* corresponds to the critical size cluster.

If one can assume that an equilibrium number of critical nuclei can be maintained in the melt during the nucleation process, the homogeneous nucleation rate (#nuclei/time/volume) is then given by

$$I = K_1 \nu \frac{N_n^*}{N_L}, \tag{29}$$

where K_1 is a constant involving the product of the number of atoms per unit volume and the number of atoms on a nucleus surface, and where ν is the rate at which atoms can attach to the critical embryos. This is called the steady state nucleation rate. The value for ν is usually thought to scale with D_L/a_0^2, where D_L is the diffusion coefficient in the liquid and a_0 is the atomic jump distance. For metals, this attachment rate is fairly independent of temperature and so

$$I = K_2 \exp\left(-\frac{K_3}{T\Delta T^2}\right), \tag{30}$$

K_2 typically has a value of $10^{42}/\mathrm{m}^3\mathrm{s}$. For nonmetallic melts, where the diffusion coefficient in the liquid can depend strongly on temperature,

$$I = K_4 \exp\left(\frac{\Delta G_n^* + \Delta G_d}{k_B T}\right), \tag{31}$$

where K_4 includes the pre-exponential factor for diffusion, and ΔG_d is the activation energy for diffusion. For heterogeneous nucleation, similar expressions can be developed but is described per unit area of catalytic surface.

An evaluation of eq. (30) shows that as the supercooling is increased, I increases very rapidly at a critical supercooling in the range of 0.2 T_m to 0.4 T_m. Changes in the pre-exponential term in eq. (30) by orders of magnitude do not appreciably affect the calculated supercooling for sensible nucleation rates. This rapid rise in nucleation rate with temperature effectively defines a *nucleation temperature*.

During rapid cooling of the melt especially to large supercoolings in glass forming alloys, atomic transport may be too slow to maintain an equilibrium number of clusters. This requires the examination of transient nucleation theory and effectively introduces a

delay time into nucleation kinetics that can be important during glass formation or during devitrification as described by THOMPSON *et al.* [1983].

One of the major assumptions of the classical nucleation theory is that the free energy per unit volume and free energy per unit surface area are independent of the size of the embryo. Since the interface between solid and liquid is usually considered to be diffuse on the level of a few atomic dimensions (see § 5), embryo that are a few atomic dimensions in radius cannot be described classically. This leads to a radius (or temperature) dependence of the surface energy as shown by LARSON and GARSIDE [1986] and SPAEPEN [1994]. PEREPEZKO [1988] has pointed out that if θ approaches zero for a heterogeneous nucleation process, the thickness of the spherical cap can approach atomic dimensions, even when the cap radius is much larger, a fact that would also necessitate a nonclassical approach to heterogeneous nucleation.

4.2. Effect of melt subdivision

When a volume of liquid metal is converted to an array of liquid droplets, large supercoolings prior to solidification are often obtained in many of the droplets. This fact leads to a method for the study of nucleation and to understand the supercooling often obtained in metal droplets created by atomization. For the study of nucleation this method was pioneered by TURNBULL and CECH [1950] and continued most notably by PEREPEZKO and ANDERSON [1980]. An example of the effect of supercooling on microstructure development is given for atomized Al–8%Fe alloys by BOETTINGER *et al.* [1986].

If the nucleating sites contained within a given liquid volume are distributed randomly, the arrangement of nucleants among the droplets may be described by a Poisson distribution. For this case the nucleant free droplet fraction, X, is represented by $X = \exp(-mv)$ where m is the average number of nucleants per volume in the melt and v is the droplet volume. Based on experience with droplet emulsion samples (PEREPEZKO and ANDERSON [1980]), supercooling effects become measurable for size refinement below about 100 μm diameter and can become appreciable for powder sizes less than about 10 μm. This suggests that typical values for nucleant densities within the volume of a melt must be in the range from about 10^6–10^9 cm^{-3}. The relatively sharp selection of a given X value (e.g., $X = 0.9$) with the droplet volume indicates the important role of size refinement in achieving large supercooling. Similar relationships can be developed for surface nucleant distributions.

4.3. Experiments on nucleation in pure metals

PEREPEZKO and ANDERSON [1980] have summarized the principal techniques for nucleation experiments conducted at slow cooling rates as shown in fig. 11. The most common corresponds to the dispersion of a pure metal into droplets within a suitable medium. For metals that melt below 500°C, organic fluids with added surfactants are used to form the droplet dispersion. In addition to the isolation of nucleants discussed above, the surfactant probably plays a role in rendering some nucleates inactive. For systems with high melting points, molten salts and glasses have been employed. In both

References: p. 830.

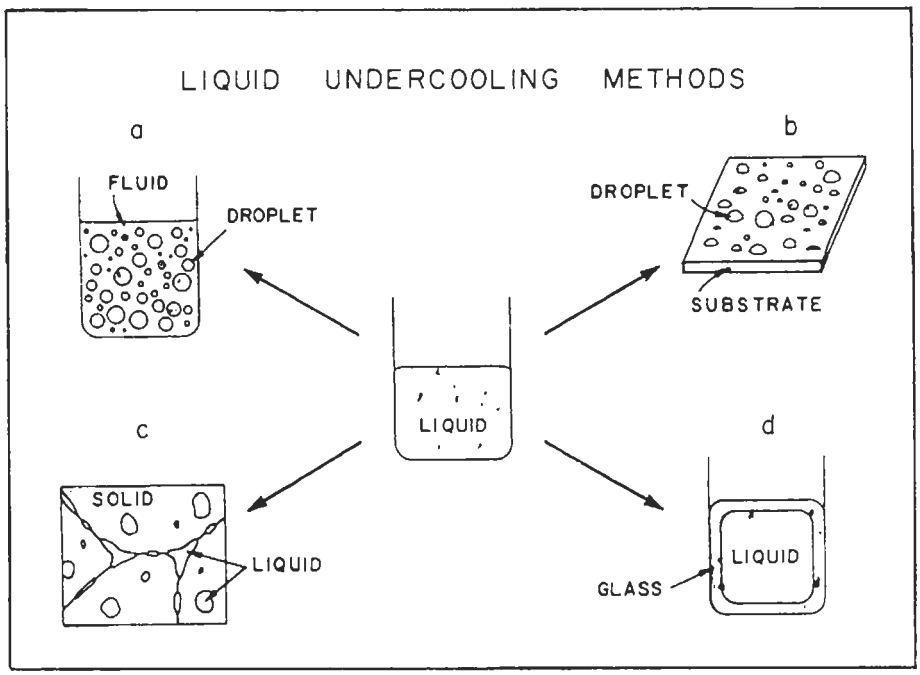

Fig. 11. Sample configuration for different supercooling methods. (after PEREPEZKO and ANDERSON [1980]).

cases, independence and separation of droplets are maintained by a thin inert coating which must be non-catalytic to nucleation. Such dispersions of droplets can be thermally cycled in a DTA or DSC to determine the supercooling of the majority of droplets prior to nucleation. PEREPEZKO [1984] summarizes the maximum supercoolings obtained by his coworkers and by previous work. Maximum supercoolings in the range of 0.3–0.4 T_m are typically obtained. Often maximum supercoolings are used to compute the liquid–solid surface energy using the homogeneous nucleation temperature. Such procedures can provide only a lower bound on the value of the surface energy, unless it is known that the nucleation is indeed homogeneous. It may be that heterogeneities still limit the observed maximum supercoolings in most metals.

In practice the predictive capability of nucleation theory is limited by the unavailability of data for liquid–solid surface energy, which appears in the nucleation rate expression as γ_{SL}^3, and by a lack of knowledge about the catalytic sites present in liquid metals and alloys. Improvements in the independent experimental determination of γ_{SL} for metals would be invaluable in allowing a clearer evaluation of theoretical interface models and more reliable nucleation and growth rate calculations. While the measurements of surface energy using techniques such as grain boundary grove experiments (for example GUNDUZ and HUNT [1985] and HARDY *et al.* [1991]) is preferable, the difficulty of these measurements has led to the development of theoretical models. SPAEPEN [1975] and SPAEPEN and MEYER [1976] estimate the surface energy based on

the configurational entropy of a structural transition that enforces polyhedral atomic packing in the interfacial region. Their result is equivalent to the expression

$$\gamma_{SL} = \frac{\alpha(T/T_m)L}{\left(\frac{V_m}{N_a}\right)^{1/3}}, \tag{32}$$

where N_a is Avogadro's number, V_m is the molar volume and α is a numerical factor related to the atomic packing (0.866 for fcc and hcp and 0.71 for bcc metals). KIM *et al.* [1988a], [1988b] have used this model to calculate homogeneous nucleation rates for the fcc and bcc phases for all compositions in Fe–Ni alloys. Due primarily to the higher α values for fcc as described above, nucleation of fcc phase is predicted to dominate in these alloys even for compositions where bcc has a higher liquidus. Indeed this is confirmed in their own experiments in 3–30 μm size powders as well as in the earlier work of CECH [1956].

4.4. Alloy nucleation

For a binary alloy, ΔG_v in eq. (21) depends not only on the temperature but also on the composition of the liquid and of the solid nuclei. Thus for a given liquid composition, critical values of nucleus composition as well as size are required to determine ΔG^*. If the surface energy and $f(\theta)$ are constants independent of cluster composition, the smallest value of r^* (hence easiest nucleation) is obtained if the composition of the critical cluster maximizes ΔG_v. For alloy nucleation the appropriate expression for ΔG_v is obtained by dividing the expression given in eq. (20) by the molar volume of the solid. It is apparent from eq. (20) that ΔG_v would be maximized for a composition of the solid where $\mu_S^A - \mu_L^A = \mu_S^B - \mu_L^B$; i.e., by a parallel tangent construction as shown in fig. 12. This maximum driving force condition has been proposed (HILLERT [1953], THOMPSON and SPAEPEN [1983]) to find the favoured nucleus composition for a given temperature and liquid composition. In order to use this condition, one must have a thermodynamic model for the alloy of interest; i.e., the free energy functions for the liquid and solid phases must be known. For simple analysis, regular solution models are often employed for the liquid and solid phases. More precise models that fit the measured phase diagram and other thermodynamic data are often available in the literature. In contrast, by including a simple model of the composition dependence of the surface energy, ISHIHARA *et al.* [1986] have shown that the critical nucleus composition can approach the bulk liquid composition at large supercoolings.

Experience with alloy supercooling indicates that the composition dependence of the nucleation temperature, T_N, reflects the composition dependence of liquidus temperature T_L. For example in the Pb–Sb system, the supercooling results shown in fig. 13 reveal that T_N follows a similar trend to T_L even for different T_N levels resulting from catalytic sites of different potency, i.e., different surface coatings (RICHMOND *et al.* [1983]). The maximum ΔG_v condition to determine nucleus composition has been used to successfully predict the composition dependence of measured values of T_N in various alloy systems (THOMPSON and SPAEPEN [1983]).

References: p. 830.

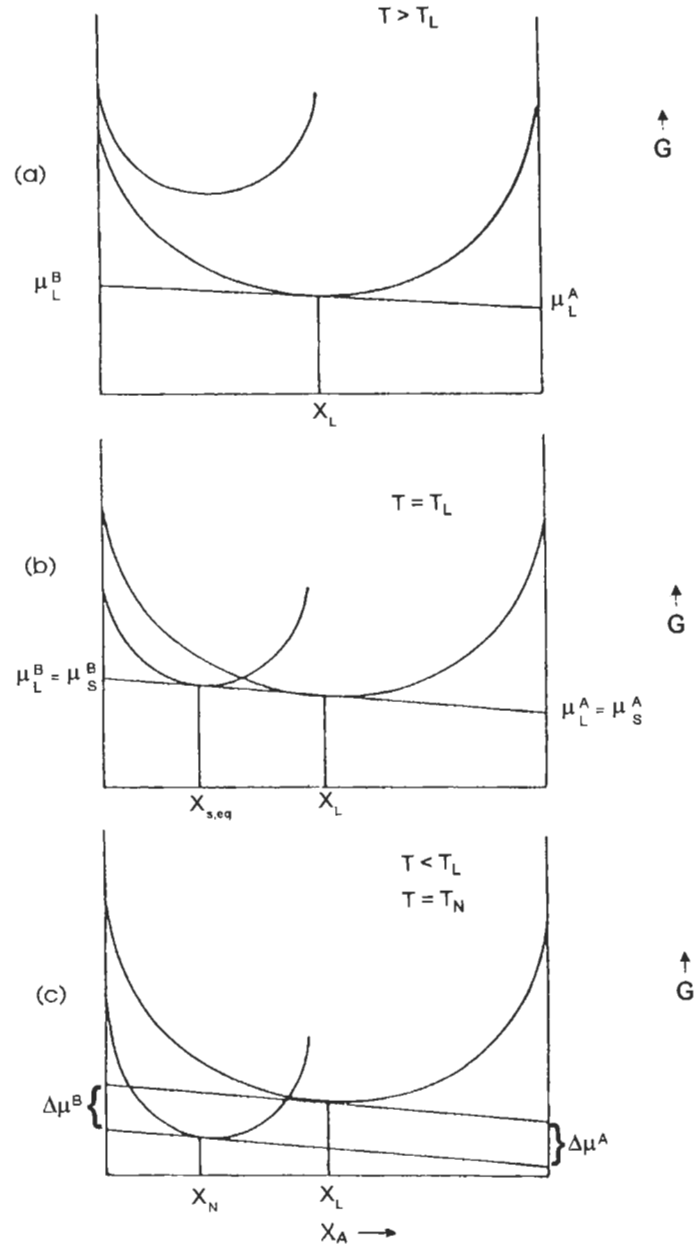

Fig. 12. Schematic free energy versus composition curves for liquid and solid at three temperatures: (a) above the liquidus for composition x_L, (b) at the liquidus, and (c) below the liquidus at an arbitrary nucleation temperature. The composition of a nucleus, x_N, that maximizes the free energy change at the temperature given in (c) is given by the parallel tangent construction. THOMPSON and SPAEPEN [1983]).

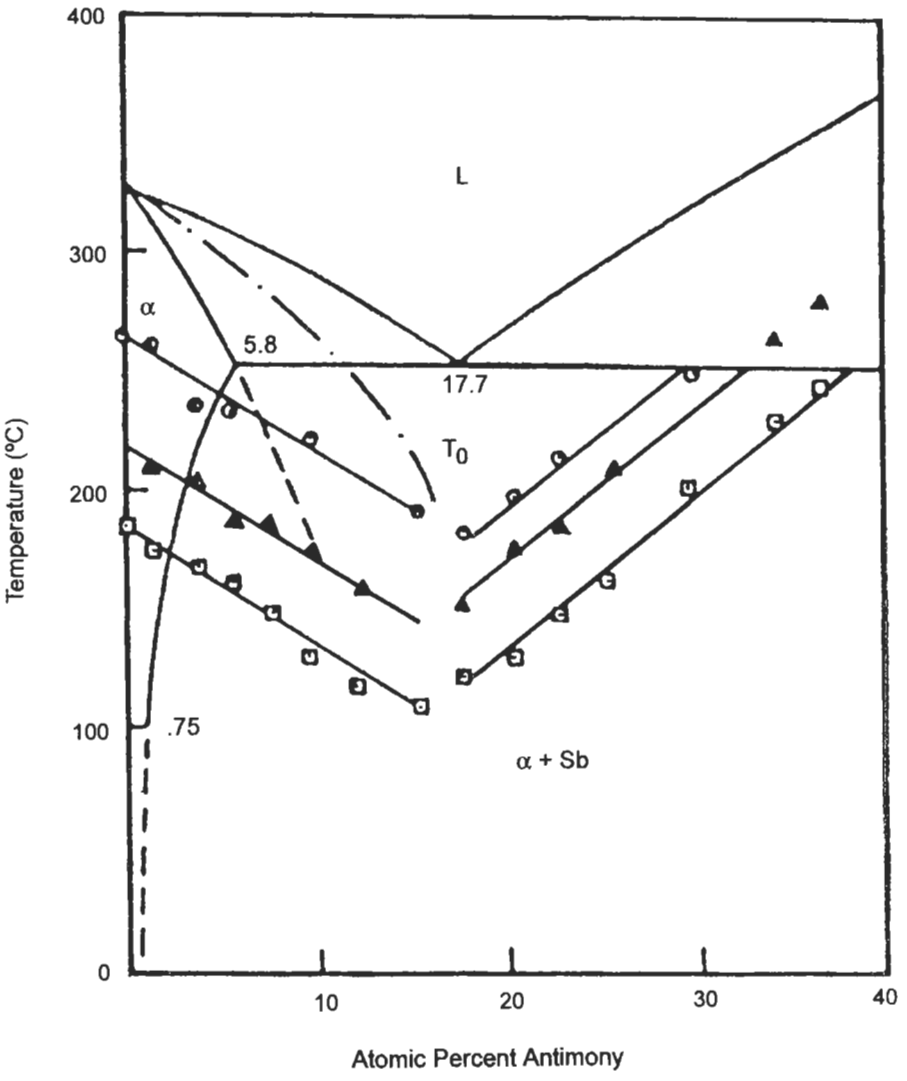

Fig. 13. Summary of nucleation temperatures for Pb–Sb alloys which generally follow the liquidus slope (RICHMOND *et al.* [1983]). Supercooling trends at different levels are produced by different droplet surface coating treatments.

4.5. Experiments on heterogeneous nucleation

While it is clear that most nucleation processes are heterogenous, and the formalism of embryo/substrate interaction is useful, rarely have the heterogeneities been identified

with any certainty. The most common way to control the catalytic substrate is to use binary alloys, typically of the simple eutectic type, and to determine the nucleation temperature of each solid phase in the presence of the other. These experiments can be performed using entrained droplets (SOUTHIN and CHADWICK [1978], with analysis by CANTOR and DOHERTY [1979], MOORE *et al.* [1990], KIM and CANTOR [1991]) or the droplet emulsion technique used extensively by PEREPEZKO and coworkers. A typical thermal cycle for a collection of droplets employed for this purpose is shown in fig. 14. A composition on one side of the eutectic is first melted to determine the characteristic double peaked endotherm corresponding to eutectic ($\alpha+\beta$) and primary phase (β) melting. The sample is then cooled to form solid at T_N and then reheated. After eutectic melting, heating is halted and the sample is equilibrated in the (liquid $+\beta$) two phase field. During subsequent cooling, the nucleation peak observed at T_{het} is then the nucleation temperature of α on β. In Perepezko's work great care was taken to confirm that β was indeed the catalytic surface and that α formed rather than a metastable phase. A summary of such measurements is given in Table 3 where ΔT_{het} is taken as the difference between the eutectic temperature and T_{het}.

One simple idea put forward originally by SUNDQUIST and MONDOLFO [1961] was that of a nonreciprocal potency; i.e., that if α is an effective nucleant for β, then β was an ineffective nucleant for α. Writing two expressions as in eq. (24), one for the contact angle, $\theta_{\alpha\beta}$, of α on a β substrate and one for the contact angle, $\theta_{\beta\alpha}$, of β on an α substrate and eliminating $\gamma_{\alpha\beta}$, it is easy to show that

$$\frac{1+\cos\theta_{\alpha\beta}}{1+\cos\theta_{\beta\alpha}}=\frac{\gamma_{\beta L}}{\gamma_{\alpha L}}. \tag{33}$$

Thus if $\gamma_{\beta L}>\gamma_{\alpha L}$, $\theta_{\alpha\beta}<\theta_{\beta\alpha}$, and β is a more effective substrate for the nucleation of α than α is for β. For example, values of liquid solid surface energy for both Pb and Sn phases in contact with eutectic liquid have been measured by GUNDUZ and HUNT [1985] using the grain boundary groove technique. They find that $\gamma_{SnL}>\gamma_{PbL}$ (132 and 56 erg/cm^2, respectively). Thus the contact angle for nucleation of Pb on a Sn substrate is smaller than the contact angle for Sn on a Pb substrate. Thus both factors in the product, $\gamma^3_{SL}f(\theta)$ in eq. (25), contribute to a lower activation energy for nucleation for Pb on Sn. This is consistent with the results in Table 3 for Pb–Sn.

Recently HOFFMEYER and PEREPEZKO [1988] have intentionally added heterogeneous sites to pure Sn. Using the droplet emulsion technique and by carefully changing the

Table 3
Heterogeneous Nucleation in the Presence of the Primary Phase (PEREPEZKO [1994])

System	Pb–Sn	Pb–Cd	Pb–Sb	Pb–Ag	Bi–Cd	Bi–Ag
Substrate	Pb	Pb	Pb	Pb	Bi	Bi
ΔT_{het}(°C)	80	69	43	27	61	28
Substrate	Sn	Cd	Sb	Ag	Cd	Ag
ΔT_{het}(°C)	22	39	23	40	94	160

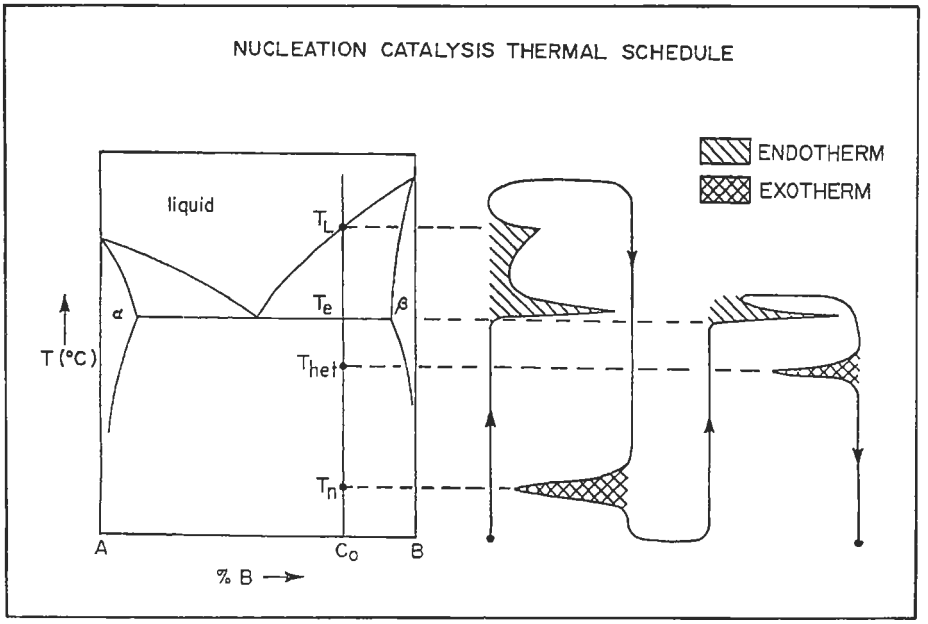

Fig. 14. Example of the interrupted thermal cycle using the droplet emulsion technique that can be used to measure the heterogeneous nucleation temperature, T_{het}, of α phase on a β substrate. PEREPEZKO [1992].

droplet coatings to prove that spurious nucleation by the coating was unimportant, they measured the nucleation temperature of Sn in the presence of various stable oxides, sulphides, and tellurides. The supercooling response of each class was identical even though the lattice disregistry within each class varied. This result indicates that a common surface reaction product may form in each class and catalyze the nucleation process. More details about heterogeneous nucleation and grain refining will be given in § 11.

4.6. Formation of metastable phases by supercooling

One of the most dramatic effects of large supercoolings prior to solidification is the possibility of forming metastable phases. An elegant yet simple example occurs for pure Bi (YOON *et al.* [1986]). A dispersion of Bi droplets was cooled from above the Bi melting temperature of 271°C to approximately 50°C where nucleation took place. Upon reheating the dispersion, melting of a metastable phase occurred at 174°C. If one examines the pressure–temperature diagram for Bi and extrapolates the melting curve for the high pressure Bi(II) phase to atmospheric pressure, one obtains a metastable melting point for Bi(II) very close to 174°C. In addition performing the supercooling experiment with an increase in ambient pressure modified the melting point of the metastable phase in a manner consistent with it being Bi(II). Thus the formation of metastable Bi(II) occured rather than the stable Bi(I) phase at large supercooling.

The bulk free energy change for solidification, ΔG_v (eq. 21) is always largest for the

stable phase. However in the context of the heterogeneous nucleation theory described above, a metastable phase may make a smaller contact angle with a particular catalytic site than does the stable phase. Thus the barrier for nucleation of a metastable phase may be smaller than the barrier for the stable phase. Of course one must always supercool below the melting point of the metastable phase in order for ΔG_v for the metastable phase to be negative. Similarly metastable phases have been formed in alloy systems. In fact in the Pb–Sn system, by avoiding the nucleation of the stable Sn phase, the metastable Pb liquidus and solidus curves have been measured more than 80K below the Pb–Sn eutectic temperature as shown in fig. 15 (FECHT and PEREPEZKO [1989]). When nucleation did occur in this supercooled state, a metastable phase was formed.

4.7. Grain size predictions in castings

Perhaps one of the most elusive problems in the prediction of cast microstructure involves the grain size. THEVOS *et al.* [1989] and STEFANESCU *et al.* [1990] have found it necessary to postulate respectively the existence of a distribution of catalytic sites or a cooling rate dependence for the number of sites to predict accurately the grain size of castings. This subject will be discussed in more detail in § 9 and 11.

5. *Interface kinetics*

As mentioned in § 3, local equilibrium is often a good approximation for interface conditions during growth of metals and alloys under casting conditions. Here we quantify the degree of nonequilibrium (interface supercooling) required to move an interface between a crystal and a melt at a given velocity. First we describe pure materials and then describe alloy effects focussing on the nonequilibrium incorporation of solute into a growing crystal at high solidification velocity.

5.1. Pure materials

The nature of the S–L interface and the rate at which atoms attempt to join the crystal can have a decisive influence on the kinetics and morphology of crystal growth. For solidification of a pure material, the parameter which governs the atomic or molecular attachment kinetics is the interface supercooling, ΔT_k, which is the difference between the thermodynamic melting point and the interface temperature. The dependence of ΔT_k on growth velocity is the subject of this section. The discussion of bulk supercooling and supersaturation and their effect on transport of heat and solute will be addressed in later sections on dendritic and polyphase growth.

An interface can advance by two basic processes depending on the nature of the S–L interface. (i) Non-uniform (or lateral growth) advances the interface by lateral motion of steps that are typically interplanar distances in height. An atom or molecule can attach itself to the solid only at the edge of a step and as a result the crystal only grows by the passage of steps. The relationship between the lateral spreading rate and the effective growth rate normal to the interface is very sensitive to the number and formation

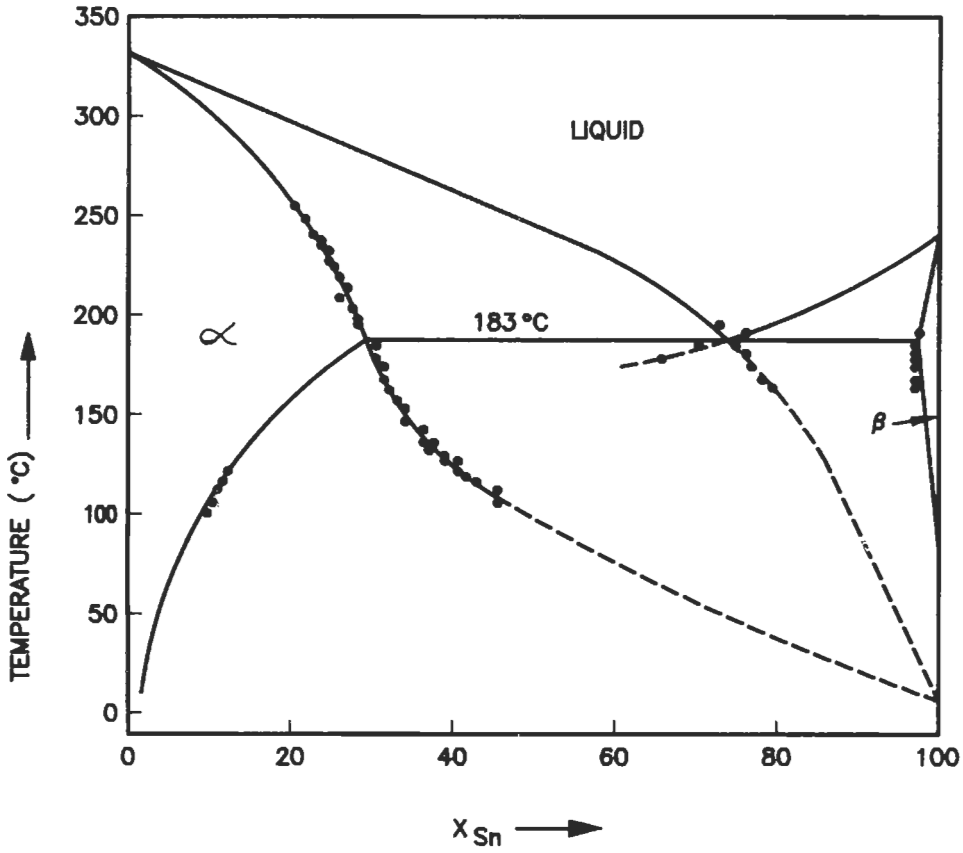

Fig. 15. The stable Pb–Sn phase diagram (solid line), including measured and calculated metastable extensions (dashed line) of liquidus and solidus curves. FECHT and PEREPEZKO [1989].

mechanism of new steps. (ii) Uniform or continuous growth advances the interface without needing steps, that is, growth can equally well proceed from any point. For a given material and supercooling, it is important to determine which type of growth occurs. The supercooling required for lateral growth at a given interface velocity, is typically much larger than that for continuous growth. Moreover, an interface that advances by continuous growth can propagate with a smoothly curved interface on a microscopic scale while lateral growth leads to facets. Whereas growth from the vapor or growth from supersaturated aqueous solutions is easily observed and usually occurs by lateral growth, such atomic scale observations are not usually possible for melt growth. Thus the nature of the S–L interface for metals is the subject of various models. In fact there is strong evidence that most metals freeze by continuous growth.

References: p. 830.

5.1.1. Interface structure

There are two approaches involved in the description of the transition in order from a liquid to a crystal across an interface. In the first, atoms are considered to belong to either the crystal or the liquid and the interface is considered to be sharp. The geometry of the surface that separates the two types of atoms may be smooth or meandering on an atomic scale. The former is called a facetted interface while the later is called a rough interface. In either case the atomic position of atoms in the crystal at the interface are considered to be in perfect crystallographic positions. The second approach includes the additional possibility of a gradual transition in atomic position from the randomness associated with a liquid to the perfect registry of the crystal. This later is called a *diffuse interface*. Indeed if the thickness of the transition layer is of the same order as the roughness, the distinction between rough and diffuse is lost. A facetted interface provides the most difficult situation for growth while a diffuse/rough interface moves most easily. First we describe sharp interface structure models and later describe models based on diffuse interfaces.

JACKSON [1958] has considered a sharp interface model and estimates the conditions when a facetted or a rough interface will occur between liquid and solid. Using a near-neighbor bond model and assuming that a random arrangement of atoms are added to an atomically planar crystal surface, he obtained an expression for the change in free energy as a function of the fraction, x, of the N possible sites occupied by "solid atoms" as

$$\frac{\Delta G}{RT_m} = \alpha^* x(1-x) + x\ln x + (1-x)\ln(1-x), \tag{34}$$

where

$$\alpha^* = \left\{\frac{L_m}{RT_m}\right\}\xi, \tag{35}$$

R is the gas constant, L_m the molar latent heat and ξ is a factor depending on the crystallography of the interface. This factor is always less than 1 and is usually greater than 0.5 and is largest for close-packed planes. This theory has been successfully used to classify and categorize growth morphologies (JACKSON [1971]). Figure 16 shows plots of eq. (34) for different values of α^*. When $\alpha^* < 2$, the minimum value of ΔG occurs at $x = 1/2$; i.e., when half the sites are full. This represents a rough interface. Solidification will then occur by continuous growth because there are so many sites for easy attachment. In these circumstances, from a macroscopic point of view the S–L interface is, in general, non-faceted and may exhibit curvature on a scale much larger than atomic dimensions. When $\alpha^* > 2$, minima in x occur at small and large values of x indicating a interfacial layer with only a few filled (or empty) sites. This represents a smooth (facetted) interface. Solidification must then occur by layer or lateral growth. Planes that are not close-packed have smaller values of ξ and thus for some materials, can exhibit roughness while close-packed planes may be facetted. Planes that are rough will grow faster than the close-packed planes leading to a crystal growth shape composed only of slowly growing close-packed interfaces.

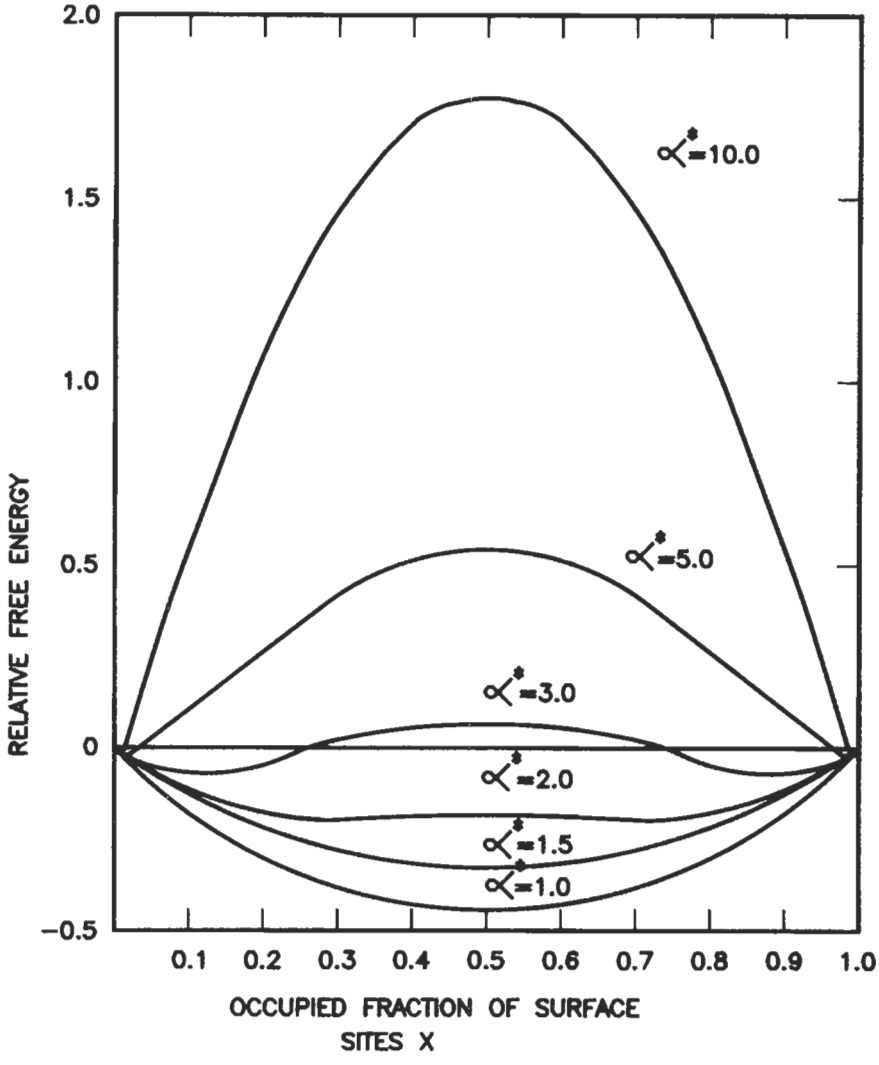

Fig. 16. Change in free energy of a monolayer at the liquid–solid interface as a function of the fraction, x, of sites that are occupied. The value of α^* depends most strongly on the entropy of fusion and to a lesser extent on the crystallographic orientation of the face. JACKSON [1958].

Another approach to interface roughness comes from the consideration of how thermal vibrations affect the surface energy of a step on an otherwise facetted interface (CHERNOV [1984]). It is found that the step energy vanishes when L_m/RT_m falls below a critical value of order unity. When the step energy goes to zero there is no barrier to surface roughening. This analysis gives the same qualitative result as Jackson's approach. Various statistical multilevel models of interface structure and Monte Carlo simulations (TEMKIN

References: p. 830.

[1964, 1969], LEAMY and JACKSON [1971], JACKSON [1974]) also indicate the importance of the ratio L_m/RT_m presented in eq. (35). A common feature of all these models is that the roughness of the interface increases with decreasing L_m/RT_m. Figure 17 shows simulations of an interface at several values of L_m/RT_m (LEAMY and GILMER [1974]).

Molecular dynamics simulations have also been used to model interface structure. Because the position of each atom is computed as a function of time, the approach allows an interface to be diffuse. Indeed simulations show that the transition between liquid and solid for a material with a Lennard–Jones interatomic potential takes place over several atomic layers (BROUGHTON *et al.* [1981]). Such potentials are thought to approximate nondirectional metallic-like bonding. Figure 18 shows the calculated structure of successive (111) layers between the liquid and crystal. In another technique, density functional theory, superposition of ordering waves are employed to represent the local atomic density (OXTOBY and HAYMET [1982]). This method also shows the interface to be several atom layers thick. The expansion relating the free energy to the local density uses order parameters that describe the amplitude of the ordering waves through the interfacial region. This is in fact a generalization of the gradient energy approach of CAHN [1960] except that liquid structure factor data are used to determine the interface thickness and gradient energy coefficient.

5.1.2. Continuous growth

The growth of a rough, sharp interface is called continuous or normal growth because the interface can propagate normal to itself in a continuous manner due to the large number of sites for easy atom attachment. To obtain the velocity-supercooling function for continuous growth of single-component melts, the growth velocity is typically expressed as a product of a factor involving the thermodynamic driving force for solidification and a kinetic prefactor involving the interface mobility:

$$V(T_i) = V_c(T_i)\left[1 - \exp(\Delta G/RT_i)\right], \tag{36}$$

where T_i is the interface temperature and ΔG is the Gibbs free energy change per mole of material solidified (defined to be negative for solidification). The bracketed term in eq. (36) represents a difference between the "forward flux" (liquid → solid) and the "backward flux". The kinetic prefactor, $V_c(T)$, is the rate of the forward flux alone, and corresponds to the hypothetical maximum growth velocity at infinite driving force. Near equilibrium, the exponential can be expanded, resulting in a linear relation between velocity and supercooling:

$$V(T) = V_c(T_m)\frac{L_m \Delta T_k}{RT_m^2}, \tag{37}$$

that is often written as

$$V = \mu \Delta T_k, \tag{38}$$

where μ is called the linear interface kinetic coefficient.

In conventional modeling of interface kinetics (WILSON [1900], FRENKEL [1932],

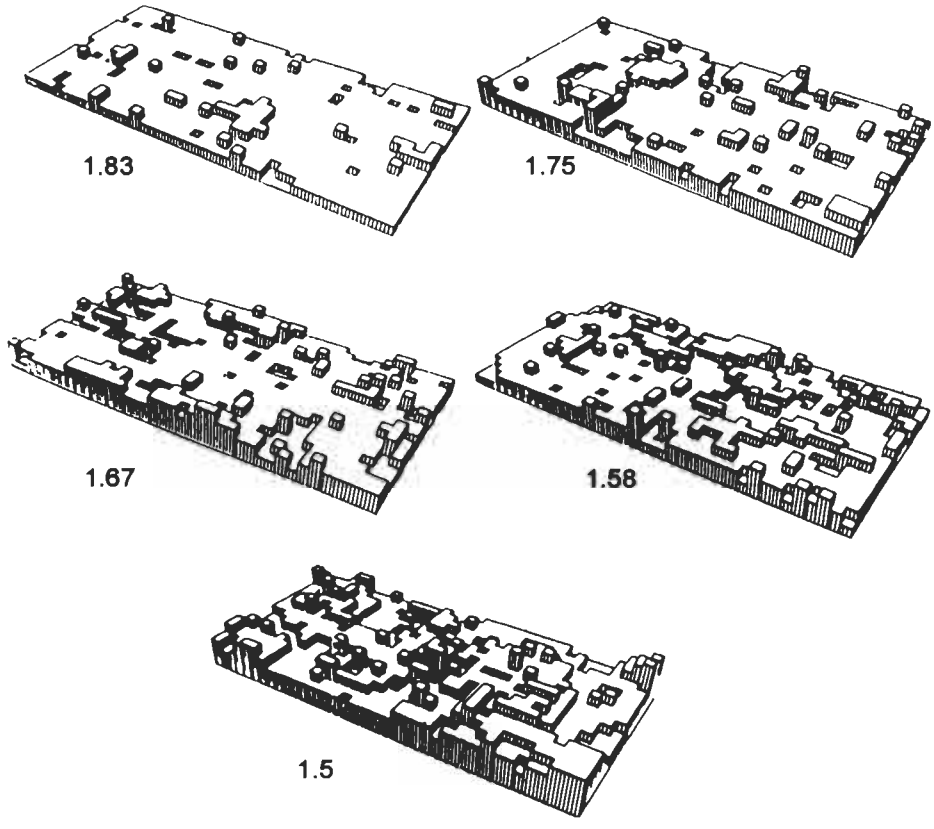

Fig. 17. Surface configuration showing increasing roughness with decreasing values of L_m/RT_m. After LEAMY and GILMER [1974].

TURNBULL [1962], JACKSON [1975]) it is assumed that the rate of the forward reaction, i.e., the rate at which atoms can jump across the interface to join the solid, is similar to the rate at which atoms can diffuse in the melt. Consequently, the kinetic prefactor is assumed to scale with the diffusivity in the liquid:

$$V_c = f_1 D_L/a_0, \tag{39}$$

where a_0 is an interatomic spacing and f_1 is a geometrical factor of order unity. Since the shear viscosity, h_S, of the melt is usually more readily measured, this scaling is often rewritten in terms of h_S using the Stokes–Einstein relation, resulting in:

$$V_c = f_2 k_B T/h_S, \tag{40}$$

where f_2 is another geometrical factor of order unity. Because of the temperature dependence of D_L (or h_S), V will first increase linearly, then go through a maximum and finally decrease as the supercooling increases. This relation has extensive experimental

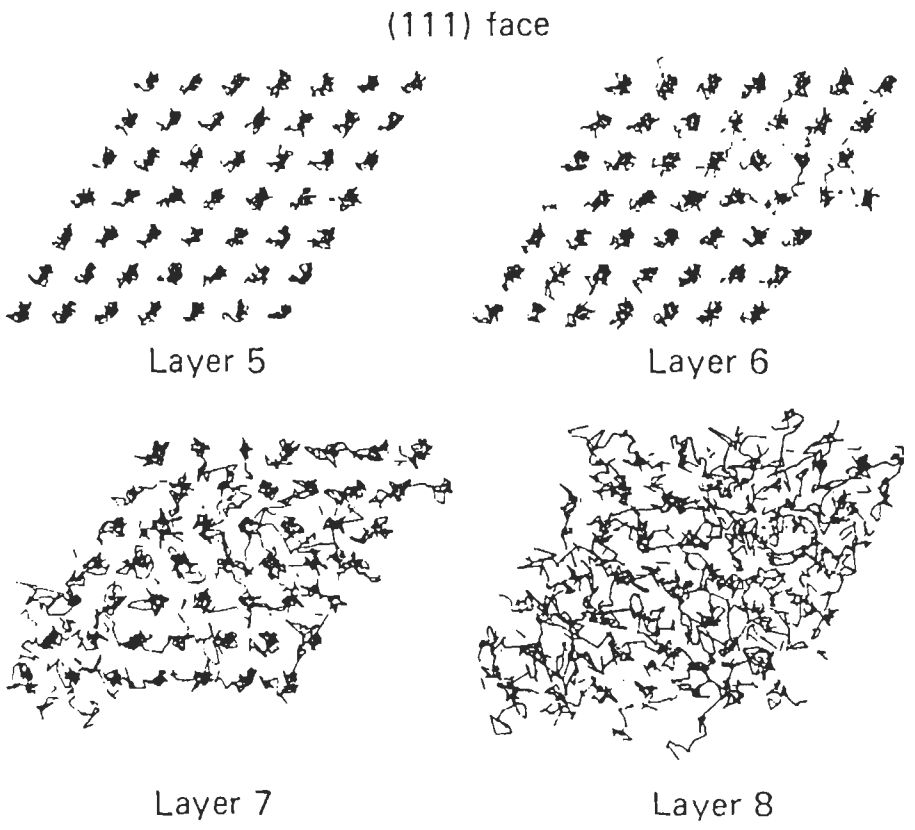

Fig. 18. Trajectories of the molecules in layers parallel to a (111) interface going from solid (layer 5) into the liquid (layer 8) that were obtained by molecular dynamics simulations by BROUGHTON *et al.* [1981].

support for the crystallization of oxide glasses and other covalent materials (JACKSON *et al.* [1967]). However a prefactor that scales with viscosity has never been verified for monatomic melts such as liquid metals (BROUGHTON *et al.* [1982]).

TURNBULL and BAGLEY [1975] pointed out that for simple molecular melts in which the intermolecular potential is largely directionally independent, crystallization events may be limited only by the impingement rate of atoms with the crystal surface and therefore can be much more rapid than diffusive events. According to their *collision-limited growth model*,

$$V_c = f_3 V_S, \tag{41}$$

where V_S is the velocity of sound and f_3 is another numerical factor of order unity. The important consequence is that V_S is about three orders of magnitude greater than D_L/a_0 for typical metallic melts, resulting in a correspondingly more mobile crystal/melt

interface. In addition no maximum is expected in the velocity-supercooling curve. The collision-limited growth model has been confirmed by the analysis of the velocities of rapidly growing dendrites growing into pure Ni melts (CORIELL and TURNBULL [1982]), by molecular dynamics calculations on Lennard–Jones systems (BROUGHTON *et al.* [1982]) and by pulsed laser melting experiments on Cu and Au (MCDONALD *et al.* [1989]). In the molecular dynamics simulation of growth, BROUGHTON *et al.* [1982] approximate their results by eq. (36) with V_c given by $(3k_BT_m/m_w)^{1/2}$ where m_w is the atomic weight. This speed is the average thermal velocity and corresponds to the velocity at which atoms can strike the lattice sites. For Ni at its melting point, this velocity is 8.6×10^4cm/s which is only slightly less than the speed of sound for liquid Ni estimated by CORIELL and TURNBULL [1982]. For Ni at small supercoolings, this value of V_c yields a kinetic coefficient, μ, of 200cm/sK corresponding to negligible interface supercoolings under ordinary solidification conditions. In addition, RODWAY and HUNT [1991] using the Seebeck effect to measure the velocity-interface supercooling relation for Pb have obtained a value of 28 cm/sK for μ that agrees well with that predicted by BROUGHTON *et al.* [1982] using the average thermal speed for this lower melting point material. Both values are orders of magnitude greater than would be predicted for interface kinetics governed by diffusive jumps.

5.1.3. Growth of a diffuse interface

Another approach to modelling continuous growth comes from the consideration of a diffuse interface. MIKHEEV and CHERNOV [1991] have estimated the kinetic coefficient for Pb using this approach. For a gradual transition in the density of atomic planes, the model predicts that the kinetic coefficient is proportional to the thickness of the transition width. Thus a diffuse interface propagates faster at a given level of supercooling than a sharp interface. Spatial and temporal frequency data obtained from bulk liquid structure factor measurements, obtained with neutron scattering experiments on simple monatomic liquids, are employed to estimate the transition width and rate at which atoms can readjust into correct atomic positions. The estimate of the linear kinetic coefficient of 28 cm/sK for Pb is in excellent agreement with the data of RODWAY and HUNT [1991].

An earlier model for a diffuse interface (CAHN [1960], CAHN *et al.* [1964]) also shows the interface mobility to increase with interface thickness. This concept was also incorporated into models for lateral growth (see item 5.1.4.) involving diffuseness of the step edge. In all cases, the diffuseness increases the mobility of the interface over what would be expected for a sharp interface.

5.1.4. Two dimensional nucleation controlled growth

If the interface is atomically smooth and free of any defects, the growth rate is limited by the nucleation of surface clusters. These clusters must form on the interface in order to create the necessary surface steps for lateral growth. The lateral spreading rate is assumed to occur quite rapidly at a speed determined by the continuous growth law described above. The classical theory of two-dimensional nucleation was developed by VOLMER and MARDER [1931]. The growth law (for the formation of cylindrical surface clusters) has the form:

$$V \sim \exp\left\{\frac{-\pi\gamma_e^2 h T_m}{L k_B T \Delta T_k}\right\} \tag{42}$$

where γ_e is the ledge energy per unit area and h is the step height. In the classical theory the constant of proportionality scales with the diffusion coefficient but it could scale with the speed of sound as does the prefactor for continuous growth. According to eq. (42) the growth rate is effectively zero at small supercooling and increases sharply at some critical supercooling. HILLIG [1966] has found that the "constant" of proportionally may in fact depend on ΔT_k. When the number of nuclei is extremely high, the growth is better described by the continuous mechanism.

5.1.5. Growth by screw dislocations

If one or more screw dislocations emerge at the S–L interface it is not necessary to nucleate new layers to provide the sites for lateral attachment. The step generated by each dislocation moves one plane each time it sweeps around the dislocation (FRANK [1949]). It was shown by HILLIG and TURNBULL [1956] that the distance between neighboring turns of the spiral is inversely proportional to ΔT_k, and therefore the total length of step is directly proportional to ΔT_k. For small supercooling, the rate of growth, therefore, will be

$$V \sim (\Delta T_k)^2, \tag{43}$$

because the rate of growth per unit length of step should also be proportional to ΔT_k (CHALMERS [1964]). Figure 19 schematically shows the growth laws for continuous, 2D-nucleation, and screw dislocation-assisted growth laws.

Another source of steps at the S–L interface is the reentrant angle resulting from the emergence of twin planes at the S–L interface. This mechanism is found to be important for Si and Ge. See FLEMINGS [1974].

5.1.6. Transition between continuous growth and facetted growth

The model of CAHN [1960], CAHN *et al.* [1964] predicts a smooth transition from lateral growth at low supercooling to continuous growth at high supercooling. The transition begins at a critical supercooling, ΔT_k^*, and ends at $\pi\Delta T_k^*$. The critical value depends on the surface energy and the degree of diffuseness. For a material with a very diffuse interface, ΔT_k^* may be so small that lateral growth is impossible to observe. An experiment showing the transition predicted by the theory has been performed by PETEVES and ABBASCHIAN [1986] on Ga. The transition to continuous growth occurs at a supercooling of about 4K and a growth rate of about 5 mm/s for the (111) face.

With increasing supercooling other models can also predict a transition to continuous growth. CHERNOV [1984] considers the nucleation of a disk on an otherwise facetted interface. If $L_m/RT_m > 2$ the edge energy is nonzero and the surface is facetted and the growth will be lateral. At some value of increased supercooling, the driving force is comparable to the work of creating a new disk and the moving interface becomes rough. This kinetic roughening then permits growth to proceed in a continuous manner.

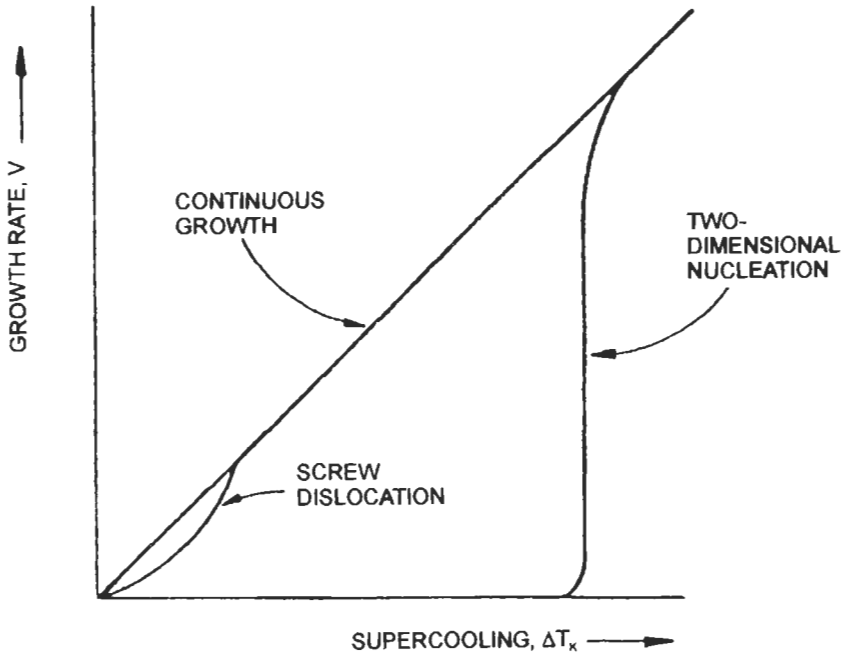

Fig. 19. Growth rate versus interface supercooling according to the three classical laws of interface kinetics.

5.2. Binary alloys

BAKER and CAHN [1971] described the general formalism for the interface conditions for solidification of a *binary* alloy in terms of two response functions. One choice for these functions describes the interface temperature, T_i, and the composition of the solid at the interface, C_S^*. Neglecting orientation effects, these response functions can be written as follows:

$$T_i = T\left(V, C_L^*\right) - T_m \Gamma K_m \tag{44}$$

and

$$C_S^* = C_L^* k\left(V, C_L^*\right), \tag{45}$$

where V is the local interface velocity. The functions $T(V, C_L^*)$ and $k(V, C_L^*)$ must be determined by a detailed kinetic model for the interface. At zero velocity they are very simply related to the phase diagram: $T(0, C_L^*)$ is the equation for the phase diagram liquidus and k(0, C_L^*) is the equation for the equilibrium partition coefficient k_0, which can depend on composition. The dependence of k on curvature is thought to be negligible (FLEMINGS [1974]). The possible forms for the functions T and k are constrained by the condition that $\Delta G < 0$ as described in fig. 7 above. The kinetic partition coefficient can also depend on the crystallographic orientation of the growing interface. If a crystal

grows with a S–L interface having regions that are curved and facetted, the incorporation of solute into the crystal behind the facet can be quite different from the rest of the crystal. BRICE [1973] calls this the *facet effect*. This effect will be neglected in the remainder of this chapter.

Several models for the dependence of the partition coefficient on velocity, eq. (45), have been formulated for continuous growth. The model formulated by BAKER [1970] is quite general. Other theories predict that the partition coefficient changes monotonically from its equilibrium value to unity as the growth velocity increases. In these models the interface partition coefficient is significantly changed from the equilibrium value, k_0, only when a dimensionless growth velocity, V/V_D approaches one. Here V_D is the diffusive speed for atom exchange between the crystal and the liquid. V_D is a ratio of a diffusion coefficient, D_i, for that exchange to the interatomic distance, a_0. The value of this diffusion coefficient should be bounded by those of the liquid and the solid, but experimentally appears to be closer to that of the liquid. Using a value for a liquid diffusion coefficient typical of metals (2.5×10^{-5} cm^2/s) and a length scale of 0.5 nm, V_D should be less than 5 m/s. Experimental evidence (SMITH and AZIZ [1994]) suggests that V_D is in the range between 6 and 38 m/s. Thus in ordinary solidification where $V \ll 1$ m/s the local equilibrium assumption is valid. The functional form of the models of AZIZ [1982] and of JACKSON *et al.* [1980] for non-facetted growth is given by

$$k = \frac{k_0 + V/V_D}{1 + V/V_D}. \tag{46}$$

This expression is valid only for dilute alloys where the composition dependence of k_0 can be neglected. At a velocity of V_D, the partition coefficient is the mean of the equilibrium partition coefficient and unity (see fig. 28a). Because eq. (46) has no dependence on composition, it cannot treat the situation shown in fig. 7b), in which partitionless solidification is impossible for some compositions. The Aziz model has been generalized to treat non-dilute alloys by AZIZ and KAPLAN [1988] and to include the possibility that solute drag dissipates some of the available free energy.

In the continuous growth model of Aziz, the process that accomplishes the formation of the crystal structure from the liquid and the process that establishes the compositions at the interface are considered to be distinct. Indeed for metals, the former may only be limited by the rate at which atoms hit the interface (collision limited growth) whereas the latter process requires diffusive interchanges between liquid and solid to reach equilibrium partitioning. It is this separation of time scales that permits solute trapping at high velocity where there is insufficient time for the diffusive rearrangements before the solute is buried under additional crystal. For this reason the $k(V)$ expression given above involves a diffusion coefficient, whereas the model assumes that the interface temperature equation can be obtained in an identical manner to a pure material, eq. (36), employing eq. (41). It is however necessary to use the value for ΔG obtained for alloys, eq. (20) rather than the simple expression based on ΔT_k.

For dilute solutions, an analytical expression for the interface temperature can be obtained (BOETTINGER and CORIELL [1986]. In this case ΔG from eq. (20) can be given by

$$\frac{\Delta G}{RT_i} = \frac{1-k_0}{m_L}\left(T_m + m_L C_L^* - T_i\right) + C_L^*\left[k_0 - k\left(1 - \ln\left(k/k_0\right)\right)\right]. \tag{47}$$

Expanding eq. (36) for small ΔG gives $V = -V_c(\Delta G/RT_i)$ where V_c is taken here as the speed of sound. One can then summarize the two response functions for a flat interface as follows:

$$T_i = T_m + m_L(V)C_L^* - \frac{RT_m^2}{L_m}\frac{V}{V_c} \tag{48}$$

and

$$C_S^* = kC_L^*, \tag{49}$$

where $m_L(V)$ is given by

$$m_L(V) = m_L\left\{1 + \frac{k_0 - k\left(1 - \ln k/k_0\right)}{1-k_0}\right\}, \tag{50}$$

with k (i.e. $k(V)$) given by eq. (46). For a curved interface, eq. (48) must include an additional term for the Gibbs–Thomson effect. Note that for $V=0$, eq. (48) and (49) revert to the local equilibrium conditions. As k goes to unity, the term in the large brackets in eq. (50) changes the effective liquidus slope from the equilibrium value of m_L to the slope of the T_0 curve, which is $m_L[(\ln k_0)/(k_0-1)]$. The last term in eq. (48) can be identified as a interface kinetic supercooling necessary to drive the formation of the lattice.

Figure 20 shows a plot of the response functions obtained using eqs. (46), (48)–(50) superimposed on a phase diagram including the liquidus, solidus, and T_0 curves. The plot gives the liquid composition at the interface and the interface temperature as a function of interface velocity for a fixed solid composition. This would be the case for directional solidification at different but constant velocities. The figure is based on a phase diagram for Ag–Cu with $T_m = 960°C$, $k_0 = 0.44$ and $m_L = -5.6$ K/at.%, $C_S^* = 5$ at%Cu, $V_D = 5$ m/s, and $V_c = 2 \times 10^3$ m/s. At zero velocity, the composition of the liquid lies on the liquidus curve, a situation that corresponds to local equilibrium. At intermediate velocities (about 1 m/s) the composition of the liquid moves towards the composition of the solid but with an increased interface temperature. At higher velocities the liquid composition continues to approach the solid composition but the interface temperature drops below the T_0 curve. At still higher velocities, where the partition coefficient is essentially unity, the temperature drops sharply with increasing velocity.

This analysis provides a pair of thermodynamically consistent response functions for dilute alloys. For concentrated alloys no simple expressions can be written because k_0 depends on composition. However, given a thermodynamic description of the liquid and solid phases and values for the two kinetic parameters V_D and V_c, the response functions can be calculated numerically (AZIZ and KAPLAN [1988]). Figure 21 shows the result for all compositions of an ideal binary alloy. Effective liquidus and solidus curves are shown for several interface velocities. These curves give the combinations of C_L^*, C_S^*, and T_i

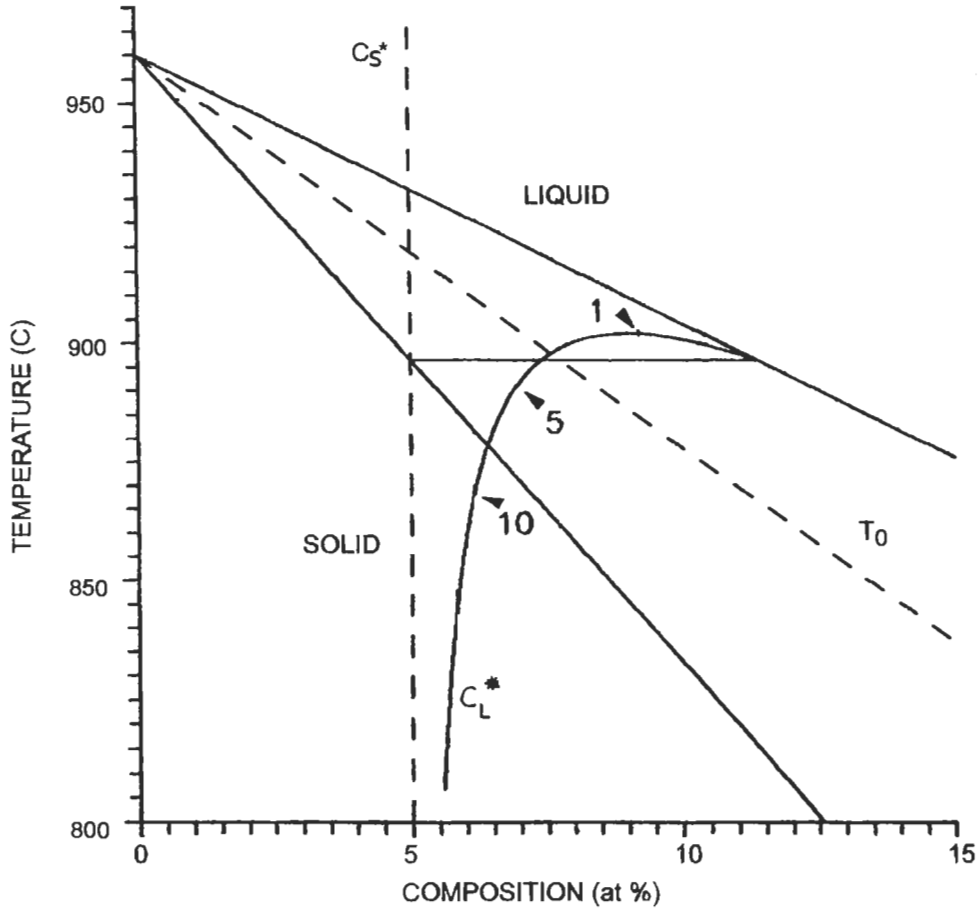

Fig. 20. Plot of interface temperature vs. liquid composition at the interface for a fixed solid composition, (=5 at %), forming at the indicated velocities (in m/s) superimposed on the phase diagram.

possible as interface conditions at the indicated velocities. A related model, which includes solute drag (AZIZ and KAPLAN [1988]), can also be reduced to a simple analytical expression for dilute alloys (AZIZ and BOETTINGER [1994]). Extensive experimental research has been focused on testing these models (KITTL *et al.* [1994]).

These solute trapping ideas have been extended to ordered intermetallic phases by BOETTINGER and AZIZ [1989]. Rapid solidification experiments indicate that some compounds, which are normally ordered at the solidus, can be forced to solidify into the chemically disordered form of the crystal structure (INOUE, *et al.* [1984], HUANG, *et al.* [1986], BOETTINGER *et al.* [1988a)], HUANG and HALL [1989]). The theory treats the trapping of disorder by a consideration of solute trapping on each sublattice of the ordered phase. At high rates, there is insufficient time to proportion the solute onto each

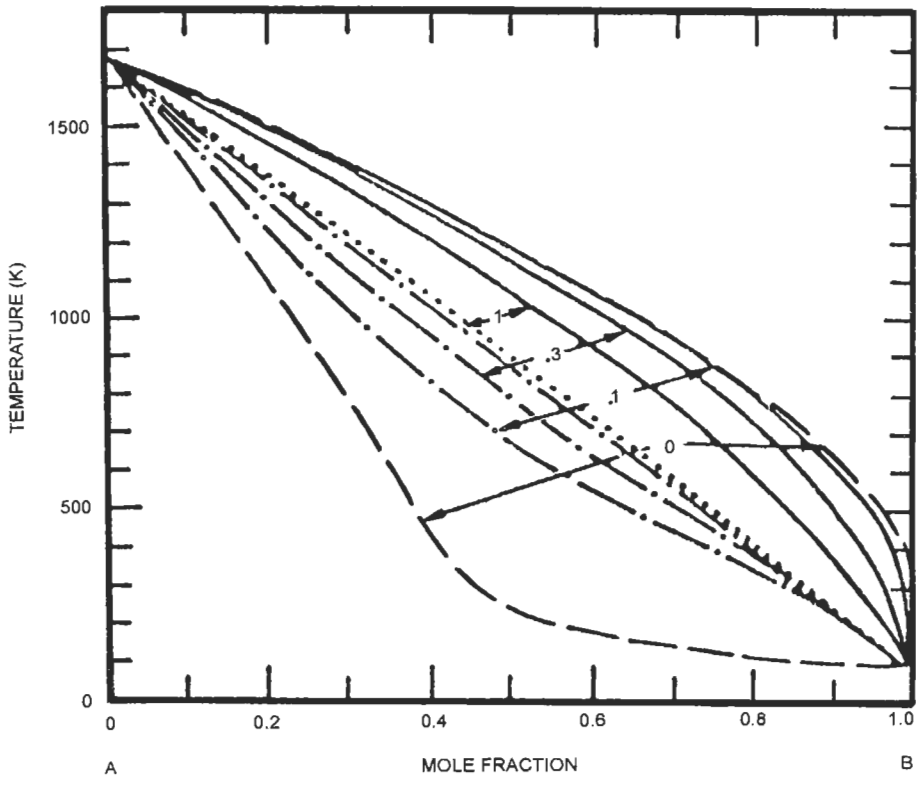

Fig. 21. Kinetic interface condition diagram for ideal liquid and solid with pure component melting points as shown, pure component entropies of fusion equal to R, and $V_C/V_D = 100$. Dashed lines: equilibrium liquidus and solidus labeled zero, dash-dot lines: kinetic liquidus and solidus at different interface velocity given as values of V/V_D, dotted line: T_0 curve. AZIZ and KAPLAN [1988].

sublattice and a chemically disordered crystal can be formed. Often however, this disordered phase reverts to the equilibrium ordered phase during solid state cooling with a resultant microstructure consisting of a high density of antiphase domains. An approximate expression giving the solidification velocity at which the long range order parameter, η, at the liquid solid interface goes to zero is given by

$$V_{\eta \to 0} = V_D[T_c/T_m - 1], \tag{51}$$

where T_m is the melting point of the ordered phase and T_C is the temperature where the solid phase would disorder during heating if melting could be prevented; i.e. the metastable critical temperature for the order–disorder reaction. Clearly the closer T_c is to the melting point, the lower is the velocity to obtain disorder trapping. Strongly ordered compounds cannot usually be disordered by rapid solidification techniques.

References: p. 830.

6. *Solidification of alloys with planar and nearly planar S–L interfaces*

The analysis of the shape of the S–L interface on a scale larger than atomic dimensions begins with a consideration of plane front growth. Plane front growth is used extensively to control the solute distribution that remains in a solid after freezing, especially in the area of crystal growth of materials for electronic applications. It is also important as a starting point to understand the more complex interface shapes involving cellular and dendrite growth. To achieve planar growth, it is necessary to obtain a S–L interface that is both macroscopically and microscopically planar. The former is achieved by controlled directional solidification with good furnace design and avoiding convection in the melt. The latter is achieved by avoiding interface instabilities due to constitutional supercooling (C.S). This section will summarize important work in these two areas.

6.1. General formulation of diffusion controlled growth

In general, the transport of solute during directional solidification in the absence of convection with a planar S–L interface growing in the z-direction is described by the one dimensional diffusion equation

$$\frac{\partial^2 C}{\partial z^2} = \frac{1}{D}\frac{\partial C}{\partial t}, \tag{52}$$

that must be solved for the composition C in the liquid and solid subject to conditions at the interface given by

$$C_S = k_0 C_L \tag{53}$$

and

$$D_S \frac{\partial C_S}{\partial z} - D_L \frac{\partial C_L}{\partial z} = V(C_L - C_S). \tag{54}$$

The use of k_0 in eq. (53) corresponds to the local equilibrium assumption and can be modified for rapid solidification using eq. (46).

6.2. Solute redistribution during one dimensional solidification

Four limiting cases of the diffusional transport and the resultant solute distribution can occur during unidirectional plane front solidification of a rod (fig. 22).

6.2.1. Equilibrium freezing

Here the S–L interface advances so slowly that diffusion in both phases maintains global equilibrium at all time (see § 3). If the phase diagram predicts the solid to be a single phase for the bulk alloy composition, any difference in solid and liquid composition occurring during the solidification process will disappear after solidification is complete (fig. 22a). In more quantatative terms, a *Peclet number* (Pe), defined by

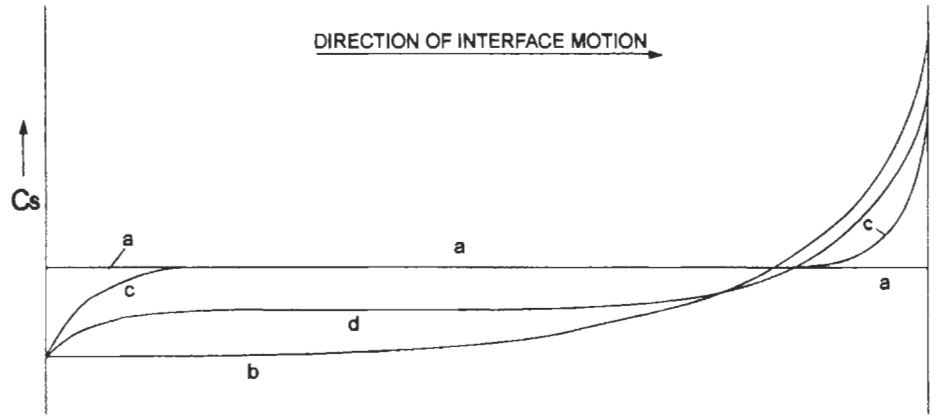

Fig. 22. Solute distribution remaining in the solid *after* one-dimensional solidification: (a) complete diffusion in solid and liquid; (b) complete mixing in liquid-no solid diffusion; (c) diffusion in liquid only; (d) partial mixing in liquid, including convection.

$$P_e = \frac{L_0 V}{D}, \tag{55}$$

for each phase, especially the solid, must be much smaller than unity, where L_0 is the length of the sample. Only under unusual circumstances can the *lever rule* be expected to apply during solidification. One such case is Fe–C growing at very low velocity because of the high solid state diffusivity of C in Fe. In substitutional alloys, equilibrium freezing does not occur in any practical casting or crystal growth situations.

6.2.2. Complete liquid mixing, with no solid diffusion

The conditions considered in this limiting case are: i) complete mixing of the liquid; ii) no solid state diffusion; iii) constant and equal solid and liquid densities; iv) local equilibrium at the S–L interface. The assumption of complete liquid mixing and no solid diffusion is often made because diffusion in the liquid is typically orders of magnitude faster than in the solid. In this case eq. (52) is replaced by a statement of solute conservation. When a fraction of the rod, f_S, is solidified, the concentration of the remaining liquid is found to obey the following differential equation

$$\frac{dC_L}{C_L} = \frac{1 - k_0}{1 - f_S} df_S, \tag{56}$$

which is easily integrated for constant k_0 to

$$C_L = C_0 (1 - f_S)^{k_0 - 1}, \tag{57a}$$

where C_0 is the nominal alloy composition. After freezing is complete, this process leaves a solute distribution in the solid (fig. 22b) given by

$$C_S = k_0 C_0 \left(1 - f_S\right)^{k_0 - 1}, \tag{57b}$$

where now f_S is taken as the fractional distance down the rod. Indeed in this model, the rod geometry with a planar interface is not a necessary assumption if the Gibbs–Thomson effect can be neglected, and the equations are valid for any interface shape as long as f_S is taken as volume fraction. The temperature of the interface can be simply obtained by substituing eq. (57a) into eq. (18).

GULLIVER [1922], HAYES and CHIPMAN [1938], SCHEIL [1942] and PFANN [1952] all developed the same type of equation, also called the "*nonequilibrium lever rule*". Equations (57) can only be considered a limiting case since most real systems have at least some solid state diffusion and some level of incomplete liquid mixing. For alloys containing a eutectic (see § 8) the liquid composition may reach the eutectic composition. In this case, the remaining liquid will freeze as a eutectic mixture. For cases when k_0 depends on composition, eq. (56) can be numerically integrated.

6.2.3. Solid diffusion during solidification

BRODY and FLEMINGS [1966] were the first to account for diffusion in the solid. They retained the assumption of complete liquid mixing, approximated the solute concentration gradient in the solid at the S–L interface and derived the following expressions:

$$C_S^* = k_0 C_0 \left[1 - \frac{f_S}{\left(1 + \alpha_\theta k_0\right)}\right]^{k_0 - 1} \tag{58}$$

and

$$C_S^* = k_0 C_0 \left[1 - f_S\left(1 - 2\alpha_\theta k_0\right)\right]^{\left(k_0 - 1\right)/\left(1 - 2\alpha_\theta k_0\right)}. \tag{59}$$

Equation (58) considers the case where V is constant and eq. (59) considers the case where the growth is parabolic, i.e. $V \sim t^{-1/2}$. The parameter α_θ is a measure of the extent of diffusion of solute in the solid and is defined as:

$$\alpha_\theta = \frac{D_S t_f}{L_0^2}, \tag{60}$$

where t_f = local solidification time, that in the simplest case, where V = constant, is given by V/L_0. BRODY and FLEMINGS [1966] also obtained numerical solutions of the solid diffusion equation.

Equations (58) and (59) are good approximations only when $\alpha_\theta << 1$, i.e., with limited solid diffusion during the solidification process. However problems occur when α_θ becomes larger, as has been demonstrated by FLEMINGS *et al.* [1970]. KURZ and CLYNE [1981] postulated an empirical variable, Ω, applicable for the parabolic growth law, given by

$$\Omega = \alpha_\theta \left[1 - \exp\left(-\frac{1}{\alpha_\theta}\right) - \frac{1}{2}\exp\left(-\frac{1}{2\alpha_\theta}\right)\right]. \tag{61}$$

The value for Ω is then used to replace α_θ in eqs. (58) or (59). This new variable was postulated because it provides two limiting cases corresponding to the ordinary Scheil Equation (no solid diffusion, $\alpha_\theta = 0$ or $\Omega = 0$) and to the lever rule (complete solid diffusion, $\alpha_\theta = \infty$ or $\Omega = 0.5$) respectively.

Another form for Ω with the proper limits was given by OHNAKA [1986]. He approximately solved the diffusion equation under the assumption that the solute distribution in the solid can be represented by a quadratic curve and has derived another form for Ω valid for parabolic growth, given by

$$\Omega = \alpha_\theta / 1 + 2\alpha_\theta. \tag{62}$$

KOBAYASHI [1988] developed an exact analytical solution involving a slowly converging series and showed that the approximate solutions above always underestimate the solute composition at the S–L interface with large deviations when k_0 is small and α_θ is large. Another useful approximation for solid diffusion has been given by WANG and BECKERMANN [1993].

The above analytical solutions have limitations, because all the physical properties must be constant, and C_S can only be calculated at the S–L interface. While this does permit one to calculate the fraction of solid versus temperature curve that is required for heat flow modelling (eq. (7)), it does not give the solute profile that remains in the solid. Numerical solutions can overcome these limitations. BATTLE [1992] gives a review of the several models developed. Among them the recent model of BATTLE and PEHLKE [1990] has approached the one dimensional problem in a general form. The method combines solution of the diffusion equation for heat and solute through out the entire rod using the technique of MEYER [1981]. GANESAN and POIRIER [1989] used numerical calculations of solid diffusion to point out that α_θ can not be treated as a constant during solidification. Consequently, eq. (59) overestimates the extent of diffusion in the solid. This effect is more pronounced when $k_0 \leq 0.4$. Diffusion during solidification is also important when dendritic or cellular dendritic growth is considered. This will be discussed in § 7.

6.2.4. Steady-state diffusion controlled freezing

Another practically important limiting case of one dimensional solidification occurs when all the assumptions described in § 6.2.2. apply, except item i). In this case mixing in the liquid is not complete and is governed by diffusion. Figure 22c shows the resulting solute distribution along the rod after solidification. Three distinct regions occur: an initial transient, a steady-state region and a terminal transient. The first is required to establish the steady state boundary layer of solute ahead of the interface and the third arises from the interaction of the boundary layer with the end of the specimen. The diffusion boundary layer in the liquid ahead of the S–L interface is a region of the system that transports the solute missing from the initial transient in the solid and maintains a constant solid composition in the central region of the rod. The moving boundary layer changes the liquid interface composition from C_0 to C_0/k_0, and disappears at the end of solidification by "depositing" its solute in the final transient. Figure 23 (KURZ and FISHER [1989]) shows the distribution of solute in the liquid and solid along the rod during unidirectional solidification.

References: p. 830.

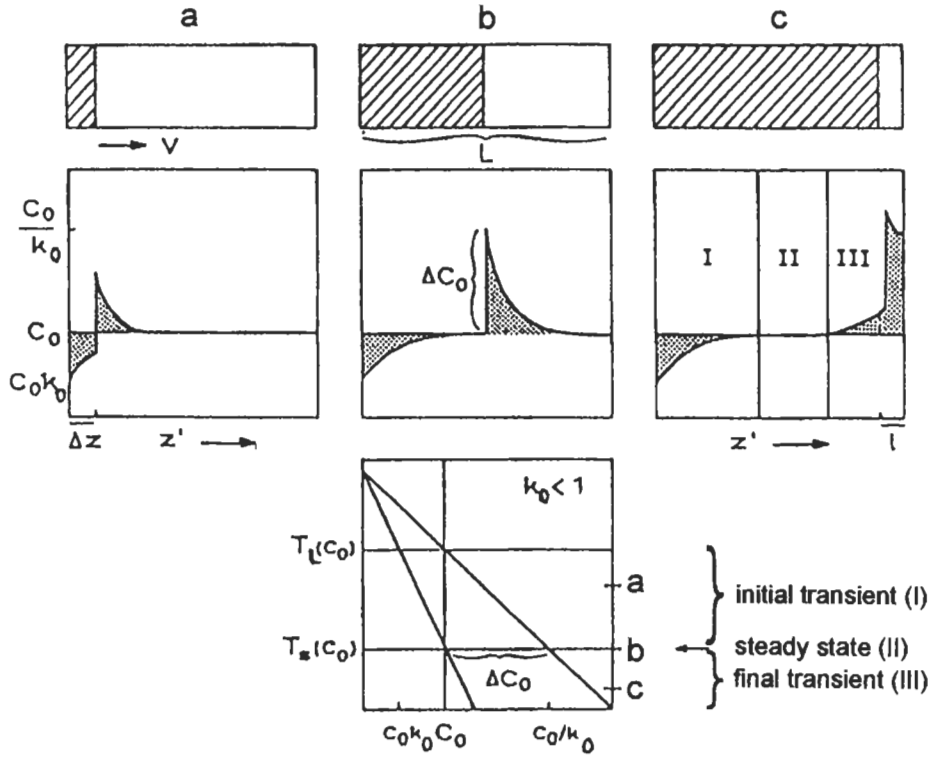

Fig. 23. Development of initial and final transient during steady-state diffusion controlled planar solidification for an alloy of composition C_0. After KURZ and FISHER [1989].

When the steady state condition has been reached in the central region of the bar, the solute distribution in the liquid in front of the interface is given by (TILLER *et al.* [1953]):

$$C_L = C_0\left[1 + \frac{1-k_0}{k_0}\exp\left(-\frac{V}{D_L}z\right)\right], \tag{63}$$

where D_L is the solute diffusion coefficient in the liquid and z the distance from the interface. Note that the liquid concentration at the interface is C_0/k_0 producing a solid composition C_0. In eq. (63) the thickness of the solute rich layer is given by the characteristic distance, D_L/V.

It is quite important to know the extent of each of the three regions shown in fig. 22c. The reader is refered to VERHOEVEN *et al.* [1988], [1989] for a summary of analysis of the initial and final transients.

6.2.5. Convection effects. Freezing with partial mixing in the liquid (Boundary Layer Approach)

Free convection, due to solute or thermal gradients in the liquid, or forced convection,

due to crystal rotation or electromagnetic forces, strongly influence segregation. This subject has been reviewed by various authors: HURLE [1972], CARRUTHERS [1976], PIMPUTKAR and OSTRACH [1981], GLICKSMAN *et al.* [1986], BROWN [1988], FAVIER [1990]. Fluid flow has important technological consequences for the processing of electronic materials where the solute distribution determines the quality of the devices.

The interval between the extreme cases of complete mixing and diffusion controlled freezing was bridged by the pioneering work of BURTON *et al.* [1953]. In this simple approach, a diffusion layer of thickness δ_F is assumed near the interface outside of which the liquid composition is maintained uniform by convection. A general expression for an effective distribution coefficient is then obtained.

$$k_{eff} = \frac{k_0}{k_0 + (1 - k_0)\exp\left[\left(\frac{-V\delta_F}{D_L}\right)\frac{\rho_S}{\rho_L}\right]}. \tag{64}$$

The solute distribution (fig. 22d) is then given by

$$C_S = k_{eff} C_0 (1 - f_S)^{k_{eff}} - 1. \tag{65}$$

Fluid flow affects the solute distribution through the parameter $V\delta_F/D_L$ in eq. (64). For vigorous convection in the liquid, $\delta_F \to 0$, $k_{eff} \to k_0$, and eq. (65) is the same as the Schiel result. For negligible convection, $\delta_F \to \infty$, $k_{eff} \to 1$, and eq. (65) gives a constant solute profile. The model has been quite successful in modeling axial segregation in the presence of laminar and turbulent convection during plane-front growth.

This simple approach, while particularly easy to use, neglects many factors which have been more recently considered. A major effort has been made to include time dependence in the BURTON *et al.* [1953] model when Czochralski and Bridgman crystal growth is considered (WILSON [1978], [1980], FAVIER [1981a], [1981b], (FAVIER and WILSON [1982]). More recently CAMEL and FAVIER [1984a], [1984b] and FAVIER and CAMEL [1986] used an order of magnitude analysis and scaling to examine different flow regimes in terms of dimensionless numbers in Bridgman crystal growth. We defer more complex models of convection until later.

6.2.6. Zone melting

The most important variables in the zone melting process are: (i) zone length; (ii) charge length; (iii) initial distribution of solute in the charge; (iv) vapor pressure and (v) zone travel rate (constant or variable). Manipulation of these variables can produce a large variety of impurity distributions in the solid charge. The most important variation of the method used to obtain high purity metals and semiconductors is *zone refining*. Figure 24 shows a schematic view of a multipass zone refining device, a more efficient system than the single pass system originally developed. The reader is referred to the important contributions of PFANN [1966] concerning this technique as well as the *zone leveling* and the *Temperature Gradient Zone Melting* (TGZM) techniques reviewed by BILONI [1983].

Recently RODWAY and HUNT [1989] established a criterion for optimizing the zone

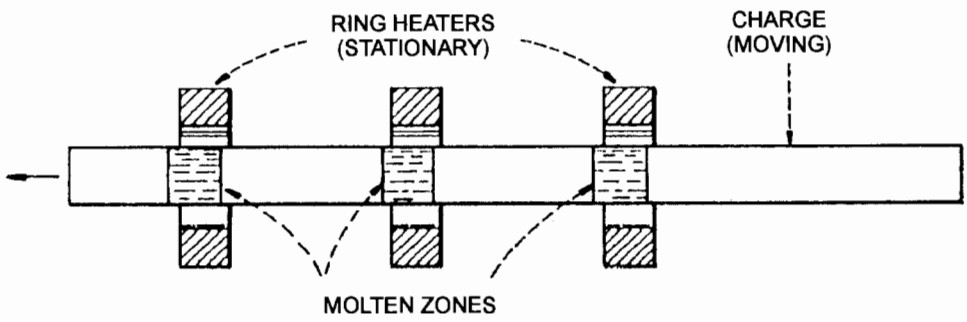

Fig. 24. Schematic of zone-refining, showing three molten zones travelling along an ingot. PFANN [1966].

length during multipass zone refining. The technique has been applied numerically, to model the redistribution in a rod, for various values of k_0. The important conclusions are: (i) a Variable Zone Size along the bar (VZS) during the process, causes a considerable increase in the rate at which the ultimate distribution is approached, compared to a fixed zone size process. This leads to a significant improvement in the usable fraction of the rod. (ii) the optimum zone length at any stage in the process is independent of the k_{eff} value. Consequently for a material containing many impurities with different k_0 values ($k_0 < 1$ or $k_0 > 1$), the VZS is optimum for all of them.

6.3. Lateral segregation

In the previous discussion we have assumed the interface to be planar. In the event that the thermal distribution of the crystal growth apparatus is not perfect, macroscopic curvature of the interface can develop. If convective mixing can be neglected, CORIELL and SEKERKA [1979], and CORIELL *et al.* [1981] have modeled the lateral segregation that will be present for a given shape. Their numerical and analytical results treat the segregation in terms of the distance that the interface deviates from planarity (δ_p), the sample width, the characteristic diffusion distance (D_L/V) and the partition coefficient, k_0. The radial segregation is greatest when k_0 is small and when $\delta_p/(D_L/V) \gg 1$. Detailed calculations of lateral segregation due to convection driven by longitudinal and radial gradients, typical of Bridgman growth upward and downward, are described by CHANG and BROWN [1983]. Experiments performed by SCHAEFER and CORIELL [1984] in the transparent succinonitrile–acetone system show the effect of radial gradients at a S–L interface.

6.4. Morphological stability of a planar interface

In § 6.2 it was assumed that the S–L interface was microscopically planar during solidification. Thus the composition profile induced in the solid varied only in the direction of growth. However even if the heat flow is controlled to be unidirectional and the isotherms are planar, a planar interface may be unstable to small changes in shape. Lateral composition variations can then be induced in the solid on a scale much smaller than the sample width. The morphological stability theory defines the conditions under

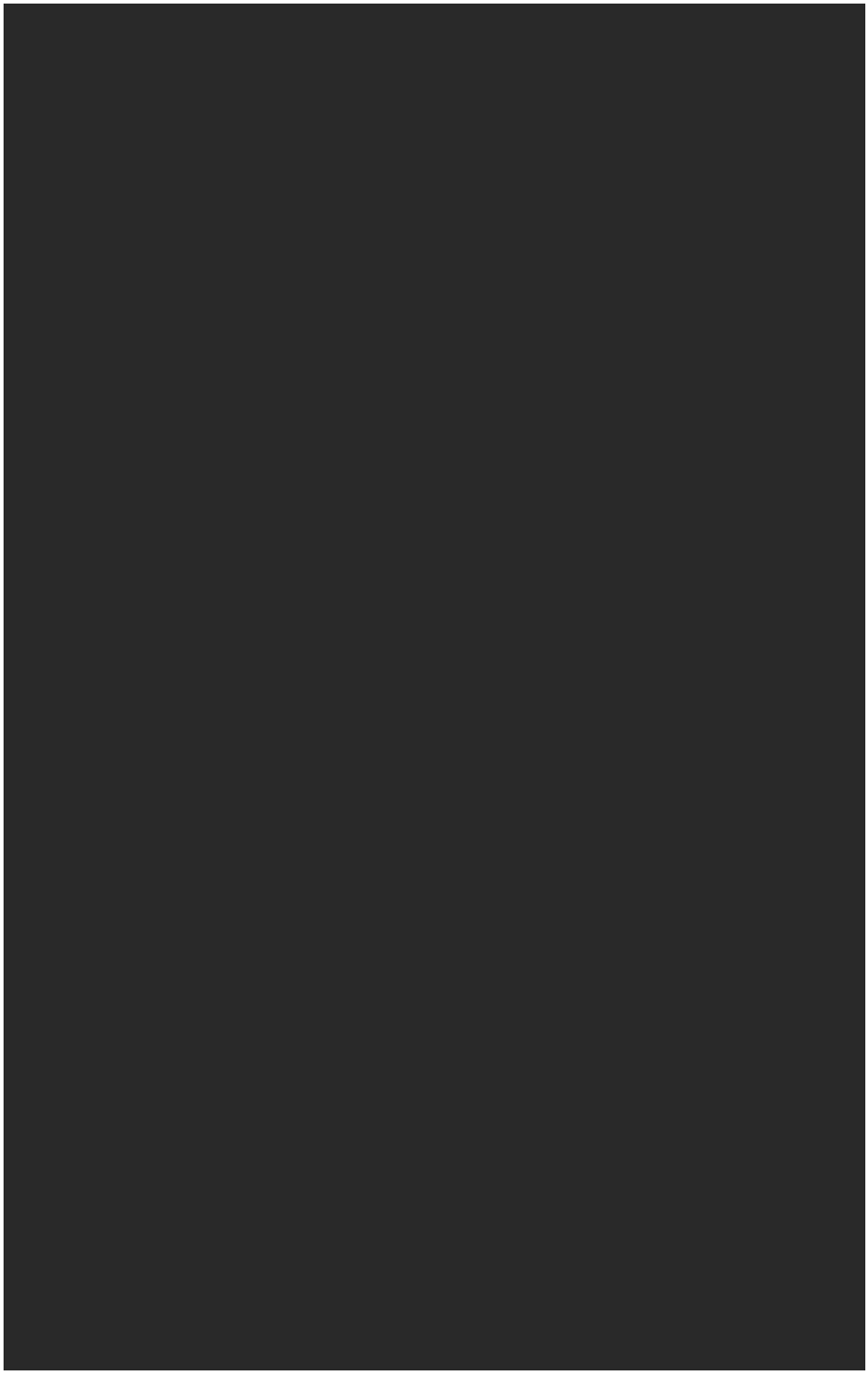

for all values of λ. The conditions giving the stability–instability demarcation ($\sigma = 0$) reduce to an equation with three terms corresponding to the three factors contributing to the overall stability of the interface, the thermal field, the solute field and the capillarity forces. The stability equation is

$$G - m_L G_C \xi_C + \frac{4\pi^2 T_m \Gamma}{\lambda^2} = 0. \tag{67}$$

The parameter G is the conductivity weighted temperature gradient given by

$$G = \frac{K_S G_S + K_L G_L}{2\bar{K}}, \tag{68}$$

where $\bar{K} = (K_L + K_S)/2$ is the mean of the liquid and solid thermal conductivities. The parameter G_c is the composition gradient in the liquid, which for a planar interface moving at constant velocity, is obtained from eq. (63) and is given by

$$G_C = \frac{VC_0(k_0 - 1)}{k_0 D_L}. \tag{69}$$

The parameter ξ_c can usually be set equal to unity. However ξ_c may deviate significantly from unity under rapid solidification conditions, where $V\lambda/2D_L \gg 1$. In general its value is given by

$$\xi_C = 1 + \frac{2k_0}{1 - 2k_0 - \left[1 + \left(\frac{4\pi D_L}{V\lambda}\right)^2\right]^{1/2}}. \tag{70}$$

Technically eq. (67) is correct only when $V\lambda/2a$ is small, where a is the liquid or solid thermal diffusivity. This condition is almost never violated even during rapid solidification. See KURZ and FISHER [1989] for a complete description of this detail.

If the left hand side of eq. (67) is positive, the interface is stable. The first term is stabilizing for positive temperature gradients; if the temperature gradient is negative (growth into an supercooled melt), this term is destabilizing. If a pure material is considered, this is the only possible destabilizing term. Thus a planar interface in a pure material is only unstable for growth into an supercooled melt. The second term represents the effect of solute diffusion in the liquid and, being negative, is always destabilizing. The third term, involving capillarity, has a stabilizing influence for all wavelengths, though its effect is largest at short wavelengths. This is the sort of stabilizing effect to be expected from surface energy which tends to promote an interface shape with the least area, namely a plane.

Figure 26 shows a plot summarizing the stability of a planar interface for dilute Al–Cu alloys. Figure 26a shows the value of σ vs. λ for selected values of G_L, V, and C_0 (200 K/cm, 0.1 cm/s and 0.1 wt%Cu). Under these conditions a range of wavelengths have positive σ, and are therefore unstable. The smallest unstable wavelength is usually referred to as the marginal wavelength and the wavelength with the largest value of σ is

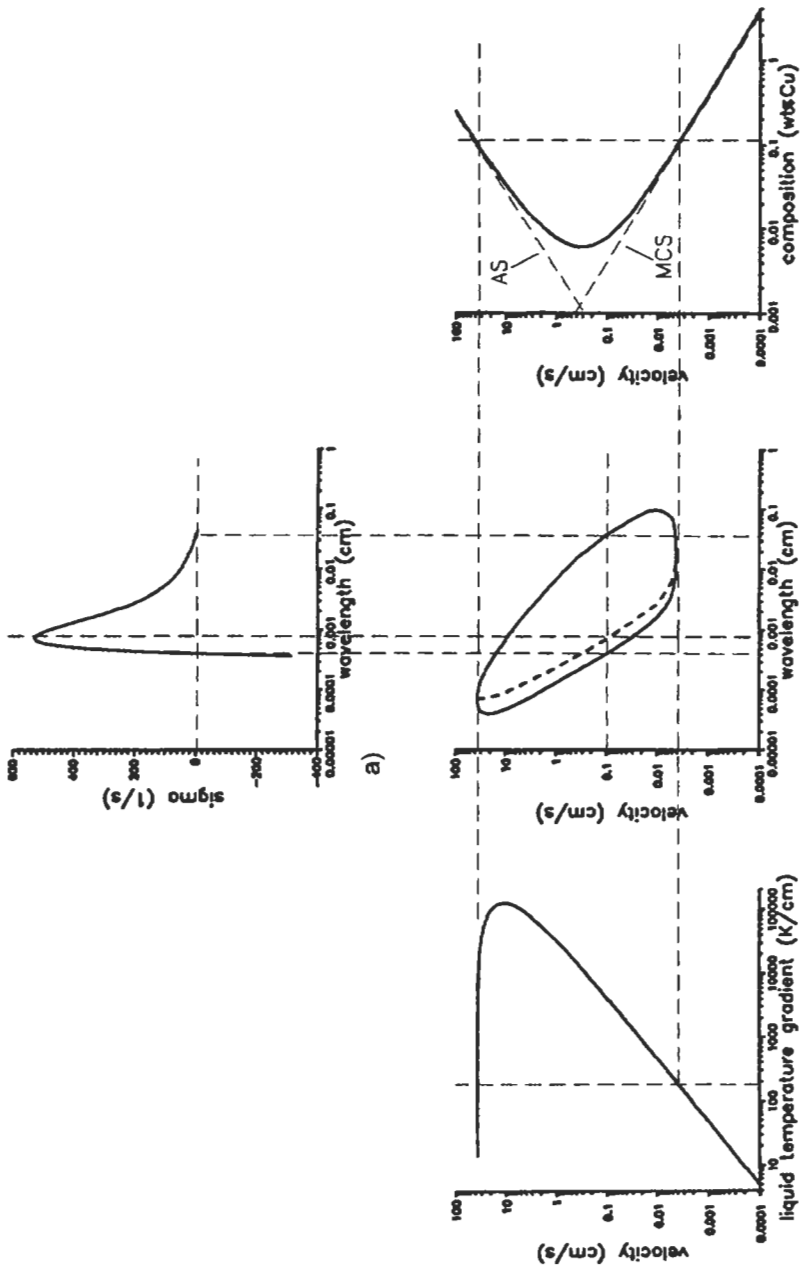

Fig. 26. Summary of the results of interface stability theory for Al-rich Al–Cu alloys. CORIELL and BOETTINGER [1994].

References: p. 830.

called the fastest growing wavelength. For some velocities, $\sigma < 0$ for all λ, and the interface is said to be stable. Figure 26c shows a closed curve of λ and V values for fixed G_L and C_0 (200°K/cm, 0.1 wt%Cu) for which $\sigma = 0$. At values of V and λ inside the closed curve the interface is unstable. Note that instability only exists over a range between two critical velocities. Outside this range, $\sigma < 0$ for all λ and the interface is always stable. Also shown dashed is the wavelength that corresponds to the fastest growing wavelength. Figure 26d shows the two critical velocities as a function of C_0 for fixed G_L (200 K/cm). The curves for the two velocities merge into a smooth curve for low C_0. Instability occurs to the right of the curve. Figure 26b shows the critical velocities as a function of G_L for fixed C_0 (0.1 wt%Cu). Note the insensitivity of the upper velocity stability limit to the value of G_L.

The upper and lower critical velocities may be approximated by two different limiting cases:

(i) If the interface grows at slow velocities, the capillarity forces are small and can be neglected; the stability criterion becomes:

$$G \geq m_L G_C. \tag{71}$$

If, in addition, eq. (68) is coupled with eq. (3), and $VL << 2K_L G_L$, the stability criterion becomes:

$$(K_L/\bar{K})G_L \geq m_L G_C, \tag{72}$$

which is called the *modified constitutional supercooling criterion*. For $K_S = K_L$ this reduces to the *constitutional supercooling criterion* (to be examined in more detail in 6.4.2).

(ii) If the interface grows at high velocity, unstable wavelengths become small and capillarity dominates. In this case, stabilization due to the temperature gradient is negligible and one obtains the *absolute stability condition*:

$$m_L G_C \leq k_0 T_m \Gamma (V/D_L)^2 \tag{73}$$

or

$$V \geq \frac{m_L C_0 (k_0 - 1) D_L}{k_0^2 T_m \Gamma}. \tag{74}$$

The modified constitutional supercooling criterion and the absolute stability criterion serve as asymptotes to the exact result at low and high velocity respectively shown in fig. 26d.

6.4.2. Relationship to constitutional supercooling

The constitutional supercooling criterion obtained by TILLER *et al.* [1953] before the morphological stability theory was developed, serves as a model to understand the major cause of instability. The theory determines if any part of the liquid ahead of a moving interface is supercooled with respect to its local liquidus temperature. The theory considers the solute distribution in front of the interface given by eq. (63) and the

corresponding liquidus temperature for the composition at each point in front of the interface given by

$$T_L(z) = T_m + m_L C_0 \left[1 + \frac{1 - k_0}{k_0} \exp\left(- \frac{V}{D_L} z \right) \right]. \tag{75}$$

The temperature in the liquid ahead of the unperturbed interface due to the temperature gradient, G_L, is

$$T(z) = T_m + \frac{m_L C_0}{k_0} + G_L \, z. \tag{76}$$

Figure 25 considers three possible profiles of the actual temperature. For case (b), the actual temperature is less than the local liquidus temperature $T_L(z)$ (labelled $T_{constitutional}$) for a range of values of z and the liquid is said to be constitutionally supercooled; as a consequence the S–L interface is unstable. Case (a), where the actual temperature exceeds $T_L(z)$, corresponds to a stable S–L interface. Case (c) is the critical condition. It can easily be demonstrated that the interface will be stable for

$$\frac{G_L}{V} \geq \frac{m_L C_0}{D_L} \frac{k_0 - 1}{k_0}. \tag{77}$$

Even though the stability criterion derived from this simple method is very similar to that derived from the more complex treatment, it does not yield any information about the size scale of the instability.

6.4.3. Experiments

Low V — The decrease of the parameter G_L/VC_0 controls [eq. (77)] the evolution of the S–L interface from plane to dendritic. Even when the evolution of the instability is continuous it is possible to recognize discrete stages of the substructure, as shown by many authors using various experimental techniques. BILONI *et al.* [1966] and BILONI [1968] summarize the various methods used: optical observations after liquid decanting, radioactive tracers, and anodic oxidation to produce interference colors. The last method is one of the most sensitive even when extremely dilute alloys such as 99.993% and 99.9993% purity Al were studied (BILONI *et al.* [1965a]). In addition, a quenching technique is often used in order to detect the morphology of the S–L interface through suitable metallography, as used among others by AUDERO and BILONI [1972]. All the techniques are based on the fact that the interface instabilities produce a redistribution of solute that can reveal the origin and development of the instabilities. With increasing CS, corresponding to a decreased value of G_L/VC_0, the following discrete stages may be defined: (i) planar S–L interface; (ii) nodes or depressions at the interface; (iii) elongated or bidimensional cells; (iv) regular hexagonal cells; (v) distorted or branched cells; (vi) dendritic cells or arrayed dendrites.

Many authors have determined experimentally that the CS criterion corresponds reasonably well to the transition from plane to unstable interfaces (CHALMERS [1964],

FLEMINGS [1974]). BILONI *et al.* [1966], through critical experiments with Sn–Pb ($k_0 < 1$) and Sn–Sb ($k_0 > 1$) alloys, were the first to establish that depressions at the S–L interface rather than projections are the first sign of interface instability. Current knowledge of the origin of the instability and its evolution can be summarized as follows:

(i) The first sign of instability is segregation associated with depressions at the interface: grain boundaries, striation boundaries and isolated depressions or *nodes*. These nodes occur in an ordered arrangement in tetragonal Sn base alloys (BILONI *et al.* [1966]) and fcc Pb–Sb alloys (MORRIS and WINEGARD [1969]). However, in Zn–Cd hexagonal close-packed alloys, the first array of nodes is disordered (AUDERO and BILONI [1973]). Alloy crystallography as well as crystal orientation have a large influence on the morphology of the interface formed after the breakdown of the planar interface.

(ii) The grooves associated with grain boundaries and striation boundaries act as built-in distortions of the plane front, and interface breakdowns begin here, spreading outward to other portions of the crystal (SCHAEFER and GLICKSMAN [1970]). The same effect occurs adjacent to the container surface (SATO and OHIRA [1977]).

(iii) The evolution from nodes or depressions at the interface into a regular or hexagonal substructure is obtained as the CS increases. This occurs by the formation of interface depressions that connect the nodes to initially form elongated cells and finally a hexagonal arrangement. This process depends on the alloy crystallography (MORRIS and WINEGARD [1969], BILONI *et al.* [1965b], BILONI *et al.* [1967], AUDERO and BILONI [1973]). Figure 27 corresponds to the evolution from a planar interface to a cellular interface shown by the shape of the decanted interface and by metallographic sectioning slightly behind the interface.

High V — With the development of techniques for rapid solidification over the past twenty five years, the ability to produce microstructures free of cellular and dendritic segregation by increasing the interface velocity as predicted by theory became possible. NARAYAN [1982] summarized the morphological stability results obtained with pulsed laser melting and resolidification in Si alloys. The transition velocities observed were in the m/s range and good agreement with the predictions of the absolute stability velocity if the velocity dependent value of the partition coefficient was used (see section 6.4.4). BOETTINGER *et al.* [1984] showed that in Ag-1 and 5 at% Cu alloys, a transition from cellular structures to plane front growth could be obtained by increasing the growth velocity beyond 0.3 and 0.6 m/s, respectively. These velocities are a factor of two larger than the calculated absolute stability values. However in view of the uncertain materials parameters, the agreement is reasonable. More recently HOAGLUND *et al.* [1991] performed a detailed study using pulsed laser melting and resolidification of Si–Sn alloys. Figure 28 shows the values of $k(V)$ determined and the fit to the morphological stability theory using these measured values of $k(V)$.

6.4.4. Further theoretical developments

Morphological stability theory remains an active area of research. The theory has been extended to include nonequilibrium solute trapping by CORIELL and SEKERKA [1983]. Complex temporally oscillatory instabilities are found. A first order approximation of the results suggests that the absolute stability condition is modified by

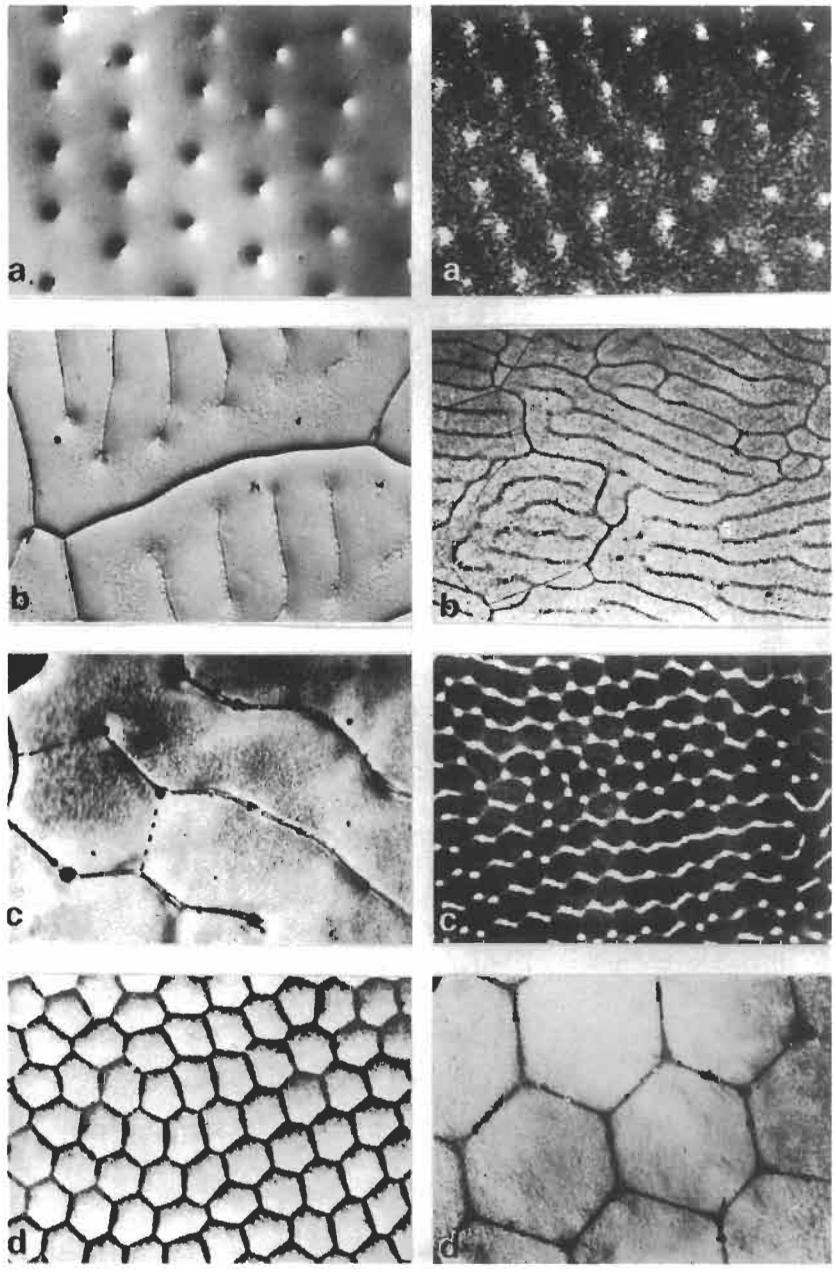

Fig. 27. Evolution of the segregation substructure as a function of constitutional supercooling shown by decanting the interface (left) and slightly behind it by metallographic sectioning (right). The amount of CS increases from (a) to (d). Magnifications: a) left: × 100, right: × 100; b) left: × 100, right: × 50; c) left: × 150, right: × 50; d) left: × 50, right: × 150. BILONI [1970].

References: p. 830.

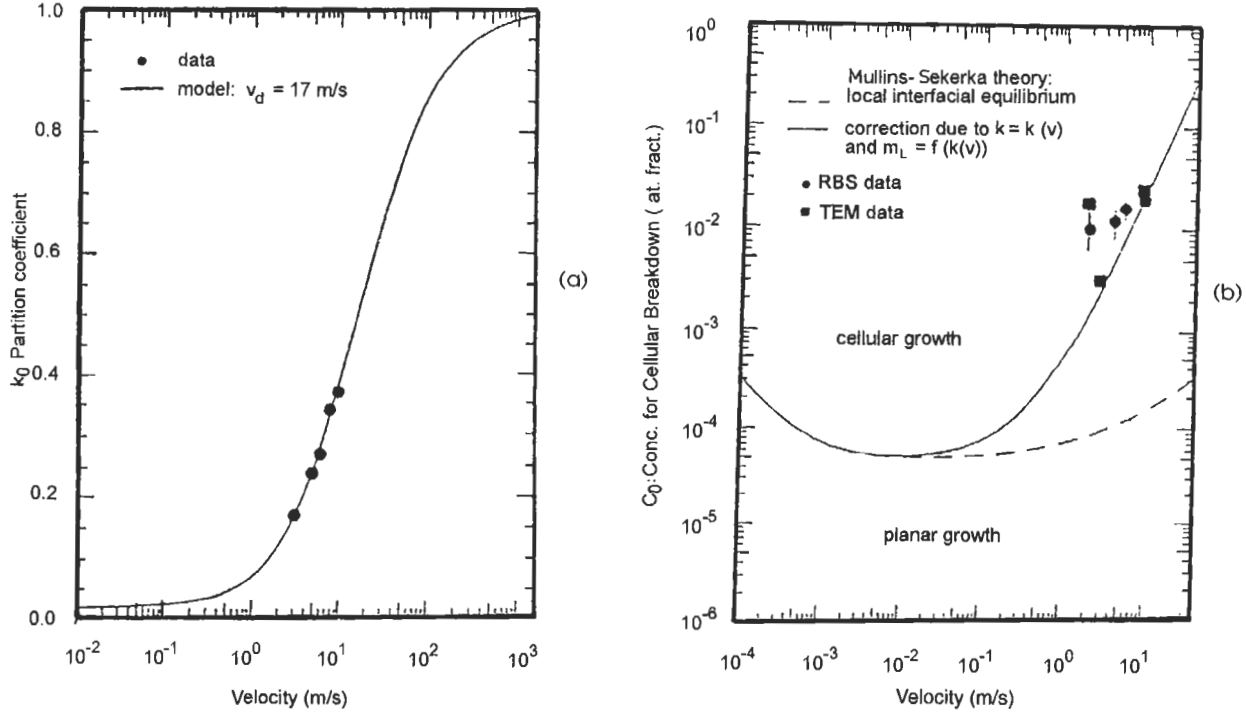

Fig. 28. (a) Velocity-dependence of measured partition coefficient of Sn in (100) Si. $k_0 = 0.016$. Data are fit by eq. (46) with $V_D = 17$ m/s. (b) Critical concentration above which cellular breakdown occurs: dashed curve stability theory using k_0; solid line, stability theory using velocity dependent $k(V)$ and $m_L(V)$. HOAGLUND *et al.* [1991].

substituting the $k(V)$ expression from eq. (46) into eq. (74) and solving implicitly for the critical velocity. This effect reduces the absolute stability velocity compared to what would be calculated on the basis of an equilibrium partition coefficient. The oscillatory instabilities exposed in this analysis and in more detailed studies are related to the banded microstructures observed at high solidification velocities (BOETTINGER *et al.* [1984]) (See § 8.1.7). Other modifications to the linear stability theory include extension to multicomponent alloys (CORIELL *et al.* [1987]), anisotropic thermal conductivities (CORIELL *et al.* [1990]), modification of the latent heat due to heat of mixing effects (NANDAPURKAR and POIRIER [1988]).

Methods for dealing with finite amplitude perturbations and the transition to cellular structures near the lower critical velocity corresponding to the constitutional supercooling condition have been summarized by CORIELL *et al.* [1985]. Two types of behavior are found depending primarily on the value of the partition coefficient (WOLLKIND and SEGAL [1970], CAROLI *et al.* [1982]). If k_0 is near unity, the transition (bifurcation) is supercritical; i.e., a small increase in the velocity past the critical value leads to interface shapes that are only slightly deformed. The wavelength of the instability is close to the fastest growing wavelength of the linear theory. For small values of k_0, the bifurcation is subcritical; i.e., a small increase above the critical value of the linear theory leads to interfaces deformed by a large amount. The wavelength is 2 to 4 times smaller than the fastest growing wavelength predicted by linear theory. The available data on the planar to cellular transition have been reviewed by CHEVEIGNE *et al.* [1988]. Agreement with the above bifurcation concepts was demonstrated. However it has been argued by LEE and BROWN [1993] that the range of velocity where the subcriticallity exists may be too small for experimental observation. They attribute the observation of spacings much smaller than the fastest growing wavelength to the fact that, at velocities only a few percent above the critical velocity, wavelengths up to factors of four smaller than the critical are also unstable. The instability of these smaller wavelengths is evident in the flatness of the bottom of the closed curve in fig. 26c. Indeed the spacing and amplitude of cells that form very close to the critical velocity are very complex (ESHELMAN *et al.* [1988]). However, few practical situations involve velocities that are so carefully controlled. A more detailed discussion of cell and dendrite shapes is deferred to § 7.

6.5. Coupled interface and fluid flow instabilities

Fluid flow is often present during solidification and upsets the diffusion of solute and heat assumed above. Fluid flow during solidification can be caused by the density difference between liquid and solid (shrinkage flow), or by the action of gravity on density gradients within the fluid phase itself. Temperature gradients as well as composition gradients due to solute rejection at the interface induce density gradients. Near a free surface between liquid and gas, temperature and composition variations can lead to gradients in surface energy that can induce flows (Marangoni Effect). This last effect has been shown to be important in some welding situations. Fluid flow can alter the morphological stability of planar interfaces and alter the composition within the interdendritic zone of castings. Flow in the mushy zone will be deferred to § 9.

References: p. 830.

HURLE [1969] and CORIELL *et al.* [1976] first treated the impact of fluid flow on interface stability using the simple boundary layer approach described in § 6.2.5. The thickness of the diffusion boundary layer, δ_F, in front of the planar interface was assumed to be reduced due to flow of an unspecified origin. This reduction increases the value G_c and if δ_F is much larger than the interface perturbation wavelength, alters the stability simply through eq. (67). FAVIER and ROUZAUD [1983] improved this approach with a deformable boundary layer. Flow resulting from radio frequency electromagnetic stirring might be treated using this boundary layer approach.

Complete coupling of the fluid flow and diffusion phenomena near a S–L interface lead to many complex results that influence morphological and fluid stability. These have been summarized by CORIELL and MCFADDEN [1990]. When directional solidification is performed with the liquid above the solid, rejection of a less dense solute can cause a liquid density that increases with height near the interface if the temperature gradient is not sufficiently large and thus cause fluid flow. However even if the overall density decreases with height, convection can still occur when a light solute is rejected. This is termed *double-diffusive convection* due to the fact that heat and solute diffuse with vastly different rates during the flow. A physical argument for the instability can be obtained by considering the forces that act on a small packet of liquid that is given a displacement upward away from the interface into a region of hotter fluid that contains less solute. Because heat transfer is more rapid than solute transfer, the packet will become hotter but remain approximately of the same composition. The displaced packet then finds itself surrounded by liquid of the same temperature but with less solute. The packet is thus less dense than its surroundings and continues to rise. Generally the wavelength of an unstable interface that forms due to the fluid instability are much larger than those of the ordinary morphological instability. However under some conditions, the wavelengths are comparable and complex time dependent oscillations can occur.

Another case of instability can occur even when the rejected solute is more dense than the solvent. Figure 29 shows experiments by BURDEN *et al.* [1973] in which a macroscopic deformation of the S–L interface was observed during growth at very slow rates (1 μm/s). Although these observations were made during cellular and dendritic growth, an analysis by CORIELL and MCFADDEN [1989] for a noncellular interface seems to apply. Instability occurred for wavelengths of the order of millimeters in this case and were determined to be due primarily to the difference in thermal conductivity of the liquid and solid phases. The creation of a slight radial temperature gradient by long wavelength perturbations induces a flow that ultimately leads to the more dense solute accumulating in the depressions in the interface. In the experiments of BURDEN *et al.* [1973], these depressions occurred at the walls of the container and the wavelength was approximately twice the container diameter.

MURRAY *et al.* [1991] studied the effect of time variations of the gravitational force during solutal convection. In the context of experiments in microgravity, this research permits an assessment of the effects of so-called *g-jitter* that occurs during space flight. In space, surface tension driven flows can also become important.

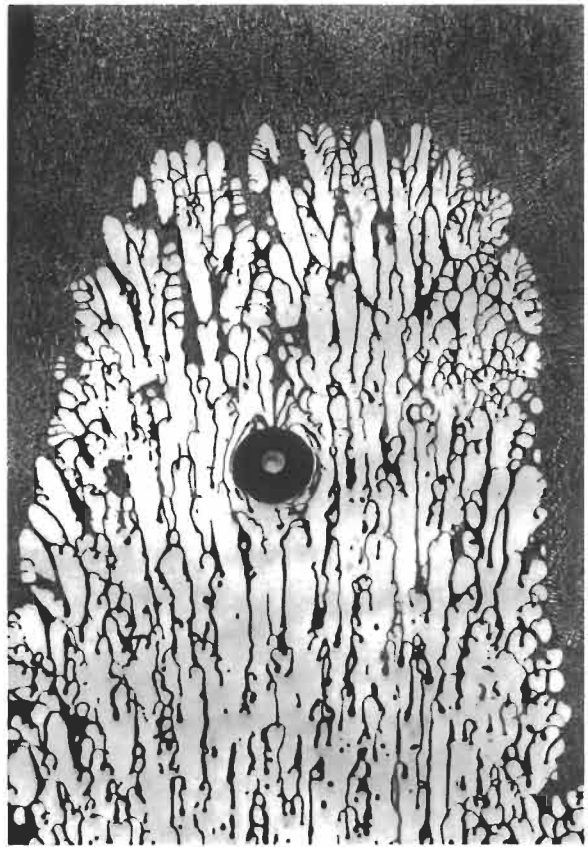

Fig. 29. Macroscopic interface shape across the full sample diameter of 4 mm for an Al-10%Cu alloy grown at $V = 2.8 \times 10^{-4}$ cm/s and $G_L = 60$ K/cm due to solute convection. BURDEN *et al.* [1973].

7. *Cellular and dendritic solidification*

The instability of the planar shape of the liquid solid interface described in § 6.4 leads to solidification by a cellular mechanism and, at conditions further from stability, by a dendritic mechanism. After the passage of the solidification front, a variation of composition remains in the solid on a length scale characteristic of the cellular or dendritic growth that is called microsegregation. This microsegregation pattern typically remains frozen in the solid due to the small ratio of the solute diffusion coefficients in the solid and liquid ($\sim 10^{-4}$ for substitutional solid solutions). In many cases the composition variation is so severe that a second solid phase solidifies in the intercellular or interdendritic regions even though none would be predicted based on a consideration of global equilibrium. The focus of this section is the prediction of the spacings associated with cellular and dendritic growth and the degree of microsegregation produced by that

growth. These spacings are important in the selection of heat treatment times and temperatures for the homogenization of ingots as well as the properties of as-cast materials. Thus the prediction of the microsegregation pattern is a fundamental goal of solidification modeling. Control of practical casting defects such as macrosegregation, porosity and hot tearing must start from an understanding of cellular and dendritic growth.

We will first focus on the theory of growth of an isolated *alloy* dendrite. The case of a pure material can be recovered from this theory by letting the composition go to zero and the reader is referred to a review of dendritic growth of pure materials by GLICKSMAN and MARSH [1993]. For alloys, the relations between dendrite tip velocity, radius, composition and supercooling will be established and compared to existing experiments. TRIVEDI and KURZ [1994] have recently reviewed alloy dendritic growth. The important expression for the tip composition will permit subsequent estimates of the degree of microsegregation. We will then consider the growth of arrays of cells and dendrites and develop an understanding of the factors that control the primary and secondary spacings of fully developed cells and dendrites. Finally we describe microsegregation.

7.1. Alloy dendritic growth

7.1.1. Theory of the tip region

Typically only the region of a growing dendrite near the tip is modelled. Two cases are distinguished: free growth and constrained growth. The model for free dendritic growth treats the situation where an isolated nucleus initiates growth into an uniformly supercooled melt and is often applied to the growth of an equiaxed grain in a casting. The melt temperature far from the dendrite can be taken as the nucleation temperature, T_N and the temperature gradient is negative; i.e., the latent heat flows into the supercooled liquid. The goal is to predict the dendrite tip velocity, V, tip radius, r, tip solid composition, C_S^*, and tip temperature, T^*, as functions of bulk liquid composition C_0 and the bulk supercooling, ΔT, below the liquidus temperature, given by

$$\Delta T = T_m + m_L C_0 - T_N. \tag{78}$$

The model for constrained growth most accurately treats the situation that occurs during directional solidification, where the heat flow is controlled by a moving furnace, and approximates the situation of dendritic growth of columnar grains where heat flows to a cold mould wall. The goal is to predict the dendrite tip radius, tip solid composition and tip temperature for a given liquid alloy composition as functions of velocity and temperature gradient. For constrained growth, the temperature gradient is positive, i.e., the latent heat flows into the solid.

For both free and constrained growth, the diffusion of solute into the liquid ahead of the growing dendrite is treated by assuming that the dendrite tip region has the shape of a paraboloid of revolution. By solving the diffusion equation in the liquid and neglecting solid diffusion, IVANTSOV [1947] has shown that the liquid composition at the dendrite tip C_L^* is given by

$$C_L^* = \frac{C_0}{1-(1-k_0)Iv(P_c)}, \tag{79}$$

where $P_c = Vr/2D_L$, and is called the solute Peclet number. The Ivantsov function, $Iv(P)$, is equal to $P\exp(P)E_1(P)$ where $E_1(P)$ is the first exponential integral of P, a function that is easily available from mathematics tables or software subroutine libraries. (The case of a 2-D (plate) dendrite was also treated and involves complementary error functions.) The composition gradient in the liquid at the tip, G_c^*, is given from the conservation of solute flux condition at the tip as

$$G_c^* = -\frac{V}{D_L}(1-k_0)C_L^*. \tag{80}$$

The treatment of the temperature field is handled differently for free or constrained growth. For free dendritic growth, heat flow in the solid can be neglected, and an Ivantsov solution for the temperature field can be obtained in the liquid. The temperature T^* at the dendrite tip is then given by

$$T^* = T_N + (L/C)Iv(P_t), \tag{81}$$

where $P_t = Vr/2a$ is the thermal Peclet number. The gradient in the liquid at the tip, G_L^*, is given from the conservation of heat flux at the tip as

$$G_L^* = -(2/r)(L/C)P_t = -\left(\frac{L}{C}\right)\left(\frac{V}{a}\right). \tag{82}$$

For constrained growth, the temperature gradient is assumed to be to that imposed by the furnace.

Regardless of the direction of heat flow, the dendrite tip temperature, T^*, must be given by the local interface condition equation evaluated at the velocity and liquid composition present at the tip, viz.,

$$T^* = T_m + m_L(V)C_L^* - \frac{2T_m\Gamma}{r} - \frac{RT_m^2}{L_m}\frac{V}{V_c}. \tag{83}$$

This expression is the same as eq. (48) except for the inclusion of the Gibbs–Thompson supercooling $2T_m\Gamma/r$ for a tip radius of r and includes interfacial non-equilibrium solute trapping effects that are important at high velocity as described in § 5. Letting $m_L(V) = m_L$ and $V_c = \infty$ recovers the local equilibrium condition valid for slow solidification.

For free growth (BOETTINGER *et al.* [1988b]), a combination of eq. (78), (79), (81) and (83) yields

$$\Delta T = \frac{L}{C}Iv(P_t) + m_L C_0\left[1 - \frac{m_L(V)/m_L}{1-(1-k_0)Iv(P_c)}\right] + \frac{2T_m\Gamma}{r} + \frac{RT_m^2}{L_m}\frac{V}{V_c}. \tag{84}$$

This equation connects the values of dendrite growth rate and tip radius that are possible for each value of ΔT. A plot of the relationship is shown in fig. 30. The curve

References: p. 830.

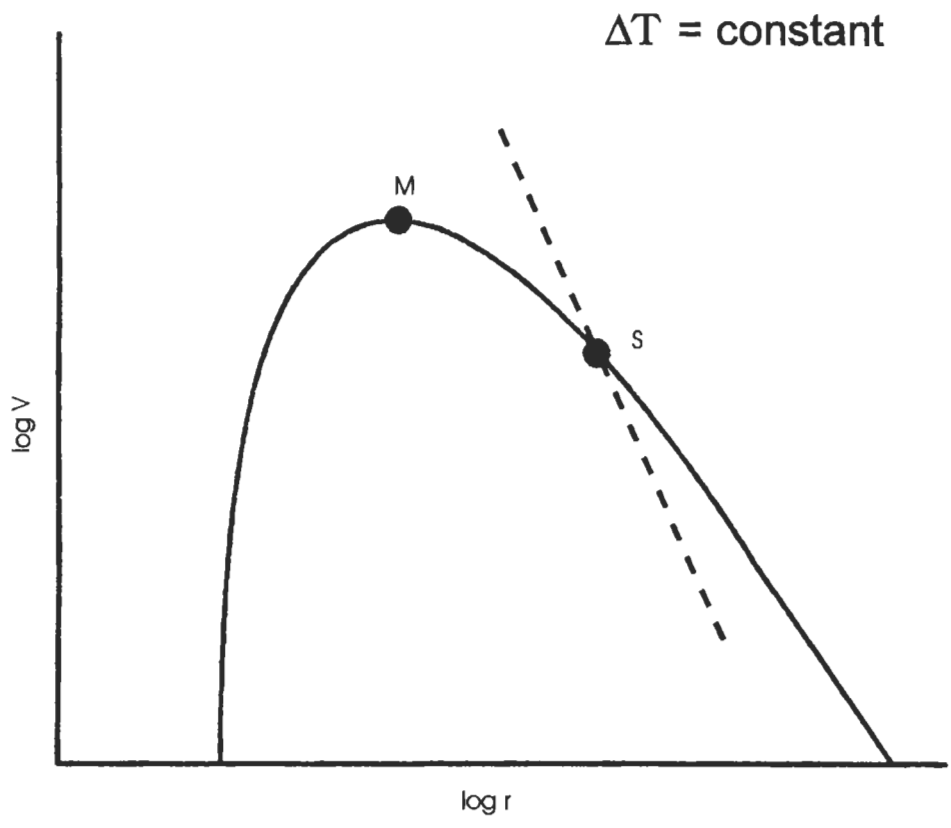

Fig. 30. Relationship between growth velocity and tip radius for dendritic growth for a fixed bulk supercooling as given by eq. (84). Point *M* corresponds to the maximum growth rate hypothesis and point *S* is the operating point of the dendrite correspond to the marginal stability hypothesis, eq. 85, shown dashed.

shows that the growth velocity would be low for small and large values of radius and exhibits a maximum velocity at intermediate values of the radius. At small values of r, the creation of a dendrite tip with high curvature (high surface area) retards growth. At large values of radius, the build-up of heat and solute at the blunt tip is so severe that growth is retarded. Thus intermediate values of radius permit higher growth rates. Experiment has shown that a unique value of velocity and tip radius occur for each value of supercooling. Thus an additional condition is necessary to uniquely specifiy V and r for each supercooling. Similarly for constrained growth, prescribed values of G_L and V also fail to specify the tip radius of the system.

The additional condition required to select the operating point of the dendrite has been the subject of much research. For many years a maximum growth rate hypothesis was employed corresponding to point *M* in fig. 30. Careful experiments by GLICKSMAN

et al. [1976] showed that this hypothesis gave dendrite tip radius values that were too small. Ideas concerning the stability of the tip were first considered by OLDFIELD [1973]. The marginal stability condition of LANGER and MUELLER–KRUMBHAAR [1978] is now commonly used and has been the subject of some experimental validation. It equates the operating tip radius with the minimum unstable wavelength prediction from linear stability theory for a planar interface growing at the same velocity with temperature and composition gradients that are present at the dendrite tip. (These values of the gradients will not in general correspond to those present for planar growth of an alloy of composition C_0). An equation for the tip radius, r, valid for small and large Peclet numbers (BOETTINGER and CORIELL [1986], LIPTON *et al.* [1987]) is given by

$$r^2 = \frac{T_m \Gamma/\sigma^*}{m_L G_c^* \xi_c - G\xi_t} \tag{85}$$

where

$$\xi_t = 1 - \frac{1}{\left(1 + \left(\sigma^* P_t^2\right)^{-1}\right)^{1/2}} \tag{86}$$

and

$$\xi_c = 1 + \frac{2k(V)}{1 - 2k(V) - \left(1 + \left(\sigma^* P_c^2\right)^{-1}\right)^{1/2}}. \tag{87}$$

The parameter σ^* is $1/4\pi^2$. ξ_t and ξ_c can be set equal to unity if P_t and $P_c \ll 1$, but may deviate from unity as the velocity approaches either the constitutional supercooling or absolute stability condition. The parameter G is the conductivity weighted temperature gradient given by

$$G = \frac{K_S G_S + K_L G_L}{K_S + K_L} \tag{88}$$

If the conductivities are equal, G is simply the mean of the liquid and solid temperature gradients. For free dendritic growth, $G_S = 0$, and

$$G = G_L^*/2. \tag{89}$$

For constrained growth, G is determined by the imposed temperature gradient of the furnace. Point S in fig. 30 shows the operating condition given by the marginal stability hypothesis.

Using the marginal stability condition, eq. (85), a complete specification of the dendrite tip can be obtained for free growth or for constrained growth. In the former case, eqs. (79, 80, 82, 89) are used in eq. (85) and solved simultaneously with eq. (84) to numerically determine the tip radius and velocity for a given value of ΔT. For constrained growth, the prescribed values of G and V are used in eqs. (79) (80) and (85) to implicitly give the radius. The radius and velocity are then used to determine C_L^*

References: p. 830.

using eq. (79) and T^* using eq. (83). We refer to the results of this theory as *IV/MS* after the Ivantsov solution using the marginal stability criterion for tip radius selection. A simplified version of this theory for free growth that assumes local equilibrium is given by LIPTON *et al.* [1984].

An example of the results of this theory for free growth into a supercooled melt using corrections for high Peclet numbers and for nonequilirium interface conditions for temperature and compositions is shown in fig. 31 for a Ag-15 wt% Cu alloy (BOETTINGER *et al.* [1988b]). Figure 31a shows the growth velocity versus supercooling relation. The dendrite velocity increases with supercooling. Note the more rapid increase

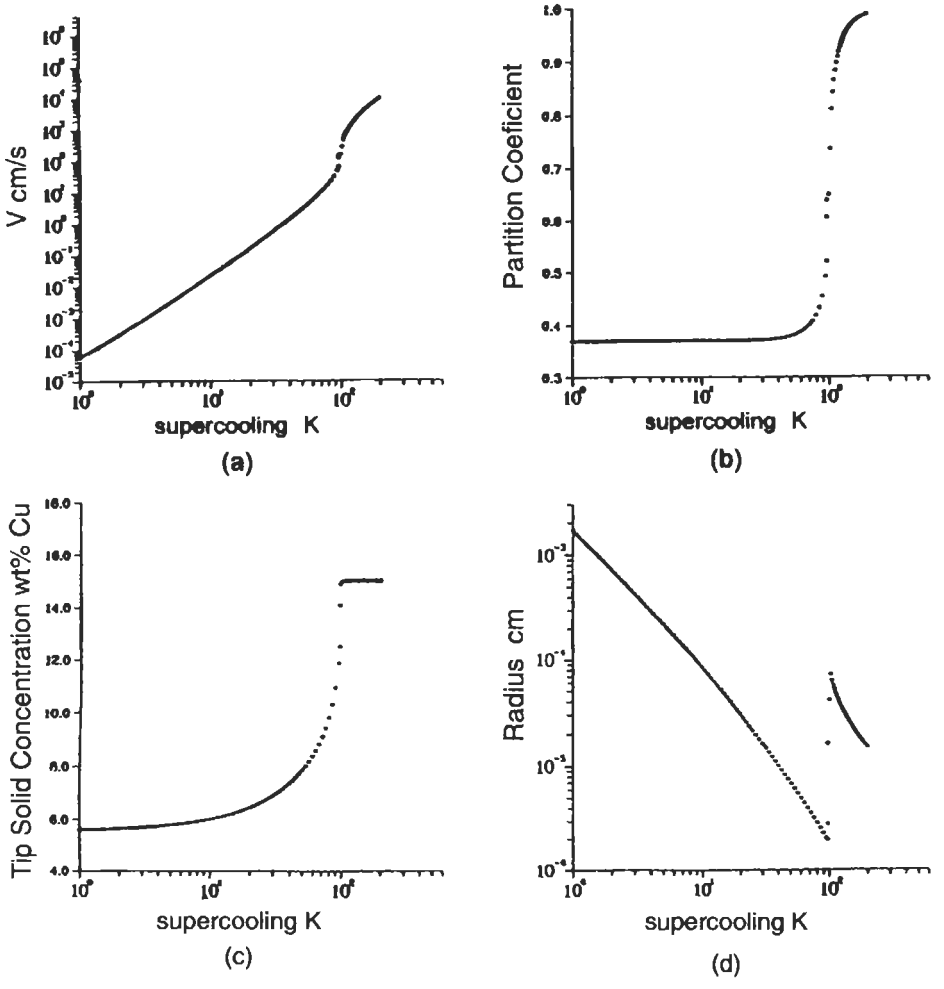

Fig. 31. Results of dendritic growth calculations for free dendritic growth of Ag-15 wt% Cu for various supercoolings below the liquidus, ΔT: (a) growth velocity, V; (b) non-equilibrium partition coefficient, k(v); (c) solid composition at the dendrite tip, ; and (d) tip radius r. BOETTINGER *et al.* [1988b].

in velocity near $\Delta T = 100$ K. Figure 31b shows how the nonequilibrium interface partition coefficient at the tip increases very sharply towards unity due to solute trapping at this same level of supercooling. This indicates the transition to partitionless solidification for the tip. In fact for supercoolings greater than 200 K the dendritic growth rate is the same as that for a pure metal with a melting point equal to the T_0 temperature for a Ag-15 wt% Cu alloy. Figure 31c shows how the composition of the solid at the dendrite tip depends on supercooling. The composition rises from 5.5 wt% Cu (k_0C_0) for low supercooling to 15 wt% Cu for $\Delta T = 100$K. This plot shows how microsegregation in dendritic structures can be reduced by increased supercooling. Finally, fig. 31d gives the dendrite tip radius. The general decline in radius with increased supercooling is sharply arrested at $\Delta T = 100$K as the dendrite tip changes from solute controlled length scales to the larger thermally controlled length scales corresponding to $k(v) \rightarrow 1$.

An example of the results of this theory for constrained growth during directional solidification of Ag–Cu alloys assuming local equilibrium is shown in fig. 32 from KURZ *et al.* [1986]. The calculated tip radius and tip temperature as a function of imposed growth rate for a temperature gradient of 10^5K/cm are given. The general trend for the radius follows $Vr^2 =$ constant for each alloy. However near the constitutional supercooling and absolute stability velocities the tip radius approaches infinity (planar interface) and deviates from this simple law. The tip temperature is close to the liquidus at intermediate velocities and approaches the solidus temperatures at low and high velocity. A very important result from this theory is that the solid composition at the center of a dendrite, $k_0C_L^*$ is only slightly greater than k_0C_0 at intermediate velocity but increases toward C_0 as the velocity approaches the constitutional supercooling and absolute stability velocities. This result impacts the discussion of microsegregation below.

7.1.2. Anisotropy

Clearly anisotropy is important in dendritic growth. Dendrites in cubic materials grow in [100] directions. In the context of the dendrite tip model described above this can be understood by a consideration of the small, but important, anisotropy of the liquid solid surface tension that was neglected above. BLODGETT *et al.* [1974] measured the anisotropy of the liquid–solid surface energy of succinonitrile. They determined that the surface energy had maxima in the [100] directions. To determine the Gibbs–Thomson coefficient, $T_m\Gamma$, for a anisotropic material with surface energy γ_{sL} that depends on orientation θ, the surface energy γ_{SL} is replaced by $(\gamma_{SL} + d^2\gamma_{SL}/d\theta^2)$. This quantity is smallest when γ_{SL} is largest. Therefore through eq. (85), the tip radius would be smaller for growth in the [100] direction than, for example, growth in the [110] direction. This smaller radius leads to more rapid growth in the [100] direction. A more complex expression is necessary if γ_{SL} depends on two angles, as would be the case for a three dimensional dendrite tip.

Despite the success of the marginal stability argument, the choice of the *minimum unstable wavelength (maximum stable wavelength)* rather than a smaller stable value remains somewhat arbitrary. Further analyses by many researchers has been summarized by BILLIA and TRIVEDI [1993]. This work indicates that by including the effect of anisotropic surface energy, only one shape preserving solutions is found to the diffusion

References: p. 830.

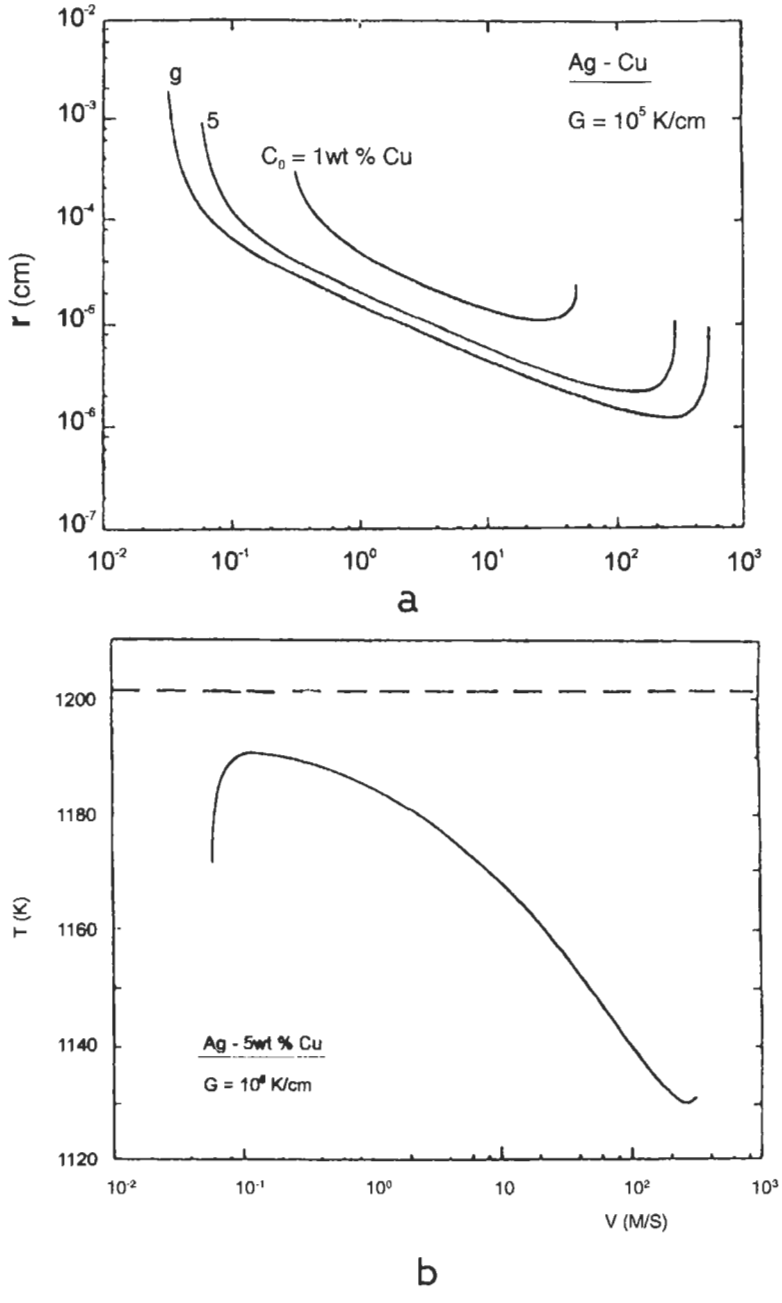

Fig. 32. Calculated dendrite tip radius (a) and tip temperature (b) for Ag–Cu alloys of the noted compositions as a function of velocity for constrained growth at a temperature gradient of 10^5 K/cm. In (b) the liquidus temperature is shown dashed. Local equilibrium was assumed. KURZ *et al.* [1986].

equations that is stable with respect to tip splitting. These considerations are called *microscopic solvability* and specify a unique value of the tip radius. Microscopic solvability predicts that the tip radius will follow essentially the same relationship given by stability analysis except that the value of σ^* depends on the degree of anisotropy in the surface energy. Tests of this model are inconclusive to date.

7.1.3. Approximate theory for low supercooling

For low supercooling, the model presented above can be simplified. For low values of P_c, local equilibrium can be assumed and $Iv(P_c)$ can be approximated by

$$Iv(P_c) \approx P_c, \tag{90}$$

an expression called the hemispherical approximation (KURZ and FISHER [1981]). This approximation leads to a particularly simple expression for the dendrite velocity as a function of supercooling

$$V = \frac{D_L}{\pi^2 m_L C_0 (k_0 - 1) T_m \Gamma} \Delta T^2 \tag{91}$$

with a tip radius given by

$$r = \left(\frac{D_L T_m \Gamma / \sigma^*}{m_L C_0 V (k_0 - 1)} \right)^{1/2}. \tag{92}$$

These relations can be applied to free growth or to constrained growth. However for the latter, the expressions are only valid when the temperature gradient is small. In this case the supercooling, ΔT, in eq. (91) is the difference between the liquidus temperature for the bulk alloy composition and the dendrite tip temperature.

7.1.4. Experiments on dendritic growth

CHOPRA *et al.* [1988] have compared the results of the LIPTON *et al.* [1984] theory to experiments using succinonitrile–acetone transparent alloys. Their results are shown in fig. 33. One of the most interesting results of the theory and experiments is that the addition of a small amount of solute actually increases the growth rate of the dendrites above that for the pure material for fixed bath supercooling below the liquidus. This effect is due to the destabilizing influence (through G_c^* in eq. (85)) of the solute on the dendrite tip. The solute pushes the marginal wavelength and consequently the tip radius to a smaller value and permits the dendrite to grow at a higher speed. With further increased levels of solute, the transport difficulties associated with the solute begin to dominate and the dendritic growth rate slows for a fixed supercooling below the liquidus.

For high supercoolings (100–300 K), several groups have obtained dendritic growth rate data as a function of bulk supercooling for alloys using carefully designed experiments in levitated samples (WU *et al.* [1987] and ECKLER *et al.* [1992]). Good agreement between theory and experiment has been obtained. Figure 34 shows a summary of data and theoretical predictions of the model that incorporates non-equilibrium interface

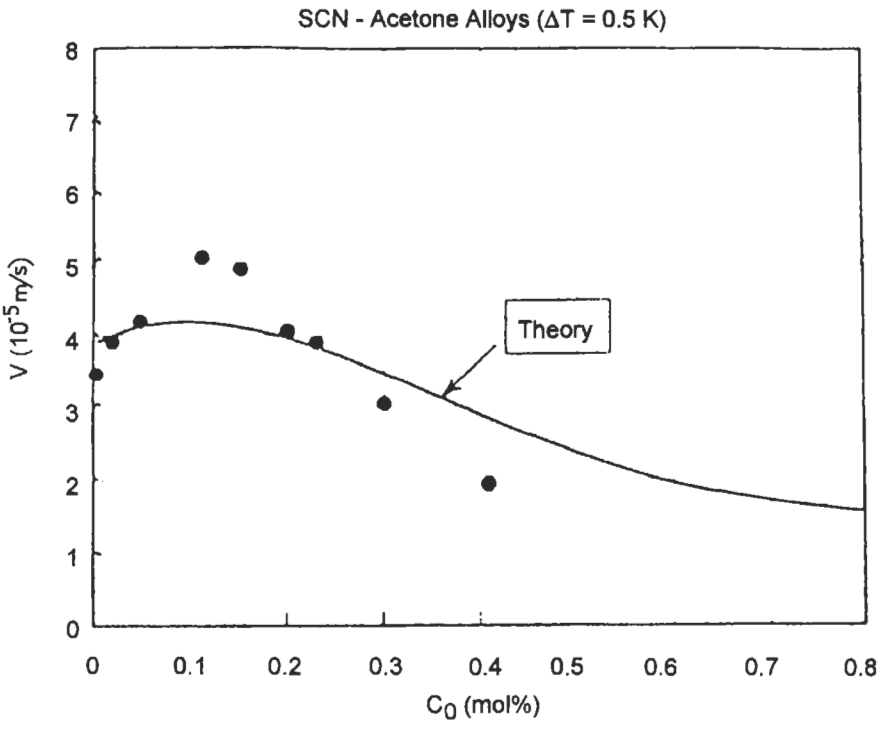

Fig. 33. Comparison of theory and measured dendrite growth velocities as a function of alloy composition for a fixed bulk supercooling below the liquidus of 0.5 K for succinonitrile-acetone alloys. CHOPRA *et al.* [1988].

kinetics for pure Ni and for Ni–B alloys by ECKLER *et al.* [1992]. The abrupt increase in velocity at high supercoolings is associated with the transition from solute controlled dendritic growth to thermally controlled growth brought about by the solute trapping (velocity dependent partition coefficient).

The predictions of the theory for constrained growth have been compared by KURZ *et al.* [1988] to measurements of cell compositions for Ag-15 wt% Cu alloy samples prepared by moving electron beam melting performed by BOETTINGER, *et al.* [1987]. Figure 35 shows bars corresponding to the observed range of composition across cells of the Ag-rich phase as a function of growth velocity. The solid curve shows the results of the present theory. The curve marked IV/MS is the same theory without the inclusion of the velocity dependence of the partition coefficient. The curve BH is the older dendritic growth theory of BURDEN and HUNT [1974a], [1974b] which uses the maximum growth rate hypothesis rather than the marginal stability analysis. It can be seen that the present formulation is closer to the observed experimental data.

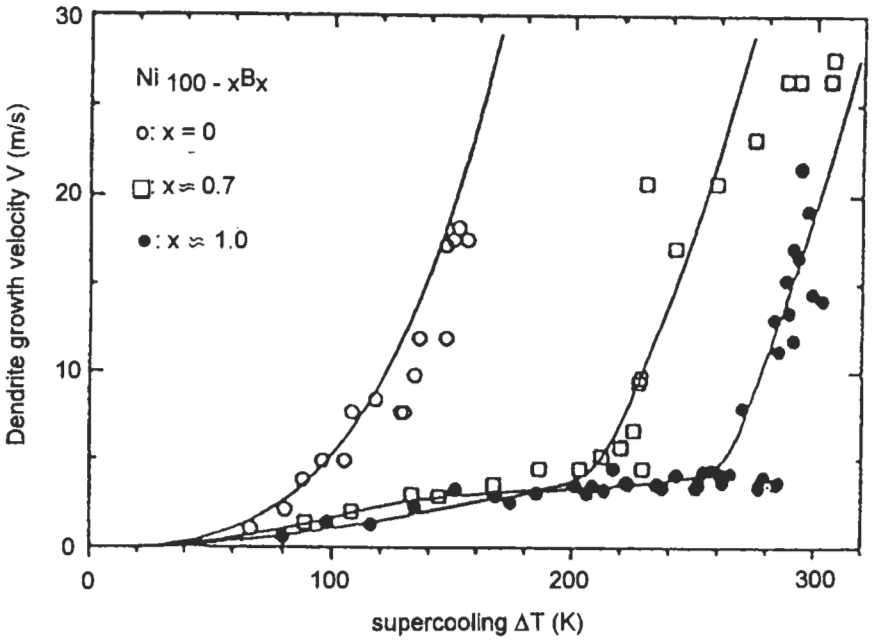

Fig. 34. Comparison of theory and measured dendrite growth velocities as a function of bulk supercooling below the liquidus for pure Ni and two Ni–B alloys. ECKLER *et al.* [1992].

7.2. Cell and dendrite spacings

7.2.1. Numerical calculations of arrayed cell and dendrite primary spacings

During constrained growth cells and dendrites form arrays with a characteristic spacing transverse to the growth direction called the primary spacing. To model the primary spacing, interactions with neighboring cells/dendrites must be considered. In a series of papers, HUNT [1990], LU and HUNT [1992] and LU *et al.* [1994] have performed finite difference calculations to study cell/dendrite shapes and primary spacings during constrained growth. The diffusion equation for solute in the liquid is solved employing local equilibrium. More recently LU *et al.* [1994] use the non-equilibrium interface conditions, eq. (46) and (48), for similar calculations. Computations are performed for single cells and dendrites with radial symmetry in a cylindrical computational domain of various diameters. This geometry is used to approximate a hexagonal array of cells or dendrites with a primary spacing equal to the cylinder diameter. Two classes of solutions were obtained; those with rounded nearly hemispherical interface shapes and those with parabolic interface shapes. The authors associate these two shapes with cells and dendrites respectively. Side branching was not simulated in the dendrite calculations. Multicell calculations where also performed to examine the stability of arrays of cells and dendrites with various primary spacings.

For a very wide primary spacing, only dendritic solutions were obtained and a unique

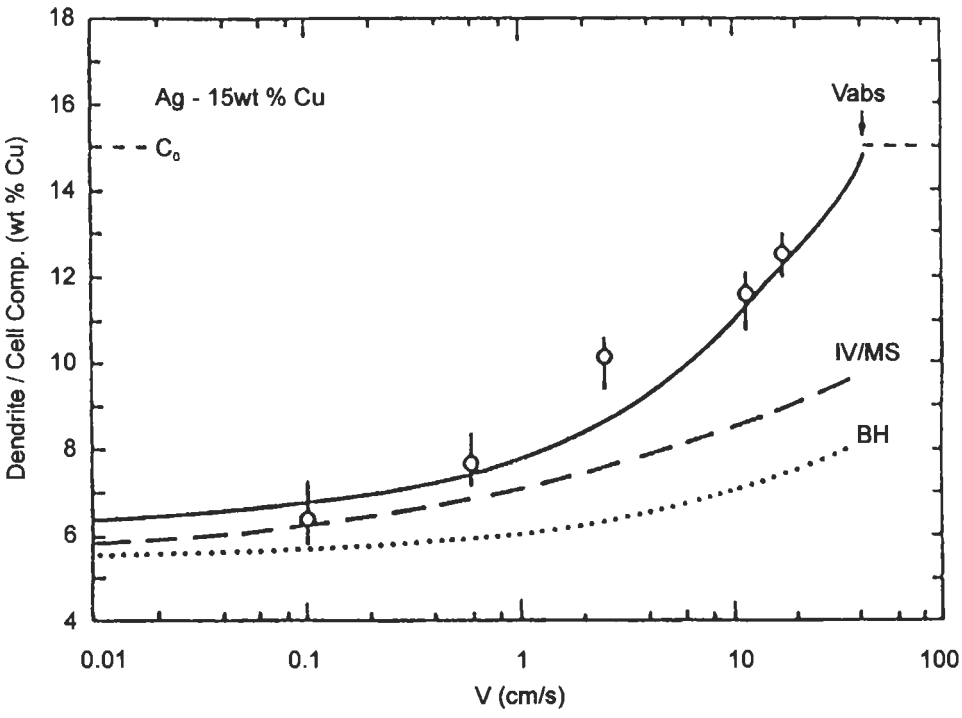

Fig. 35. Measured average composition (circles) of cells of the Ag-rich phase in a Ag-15 wt% Cu alloy as a function of solidification velocity (BOETTINGER *et al.* [1987]). The bars at each velocity represent the range of composition observed for each profile measured by STEM. The three curves are: i) the predictions of dendritic growth theory with velocity dependent partition coefficient, (solid curve), ii) without the velocity dependent partition coefficient, curve labeled IV/MS, iii) the older Burden–Hunt model of dendritic growth (labeled BH). KURZ *et al.* [1988].

value of tip radius was determined for a given set of growth conditions. This computational regime is thought to approximate isolated dendrites. Although the original work (HUNT [1990]) indicated that anisotropic surface energy was not necessary to obtain this unique solution, it was later determined that slight anisotropy was induced by the calculation mesh. Later work (LU and HUNT [1992]) confirmed the important role of anisotropy on the selection of the radius of the tip. The values of radius determined by these calculations can be approximated by the IV/MS model.

For smaller primary spacings, both cell and dendrite solutions could be obtained for the same growth conditions. For each, solutions could be obtained only over a range of primary spacings. The physical processes that define the allowable range of primary spacings are shown in fig. 36. The minimum stable cell spacing is determined by overgrowth of one cell by the adjacent cells. The maximum cell spacing occurs when the cell tips become very flat and on the verge of splitting. For dendrites, the minimum

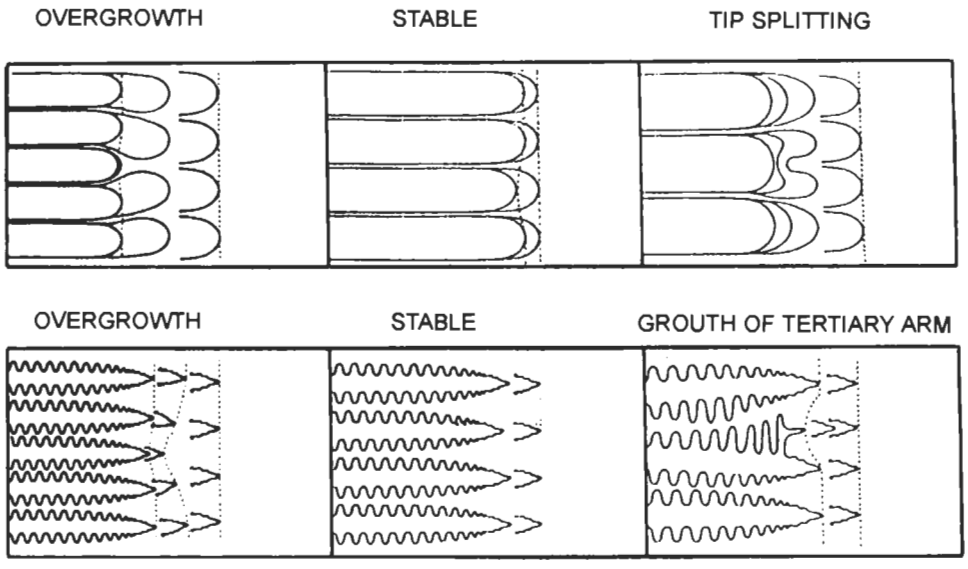

Fig. 36. Schematic illustration of primary spacing adjustment mechanism for cells and dendrites. LU and HUNT [1992].

spacing is also determined by overgrowth. The maximum spacing is assumed to be twice the minimum spacing based on an argument regarding the transition of tertiary arms into new primary arms. An example of the range of primary spacing that could be calculated is shown in fig. 37 and 38 along with experimental data for slow and rapid solidification respectively. The existence of a range of spacings for cells for given growth conditions agrees with observations of ESHELMAN and TRIVEDI [1988]. The predictions of the dendrite tip radius from the IV/MS theory presented above are also shown in fig. 38. It is seen that the primary spacing of the cell solutions is approximately twice the dendrite tip radius from the IV/MS value.

The computations described above do not describe the conditions at the root of cells. The walls of adjacent cells never join and a thin layer of liquid persists far behind the cell tips. UNGAR and BROWN [1985] have performed finite element calculations of deep cells using a composite coordinate technique that allows cell walls to fold over and join at the cell roots. In fact small drop-like structures are found to form at the cell roots that may be indicative of the pinch-off and periodic shedding of liquid droplets. Such shedding of liquid droplets may be the cause of spherical second phase particles that occur in some rapidly solidified alloys, BOETTINGER *et al.* [1988c].

7.2.2. Analytical expressions for primary spacings

Analytical theories of primary spacings often yield a power law expression applicable to a range of solidification conditions not too close to the constitutional supercooling or absolute stability velocities that is given by

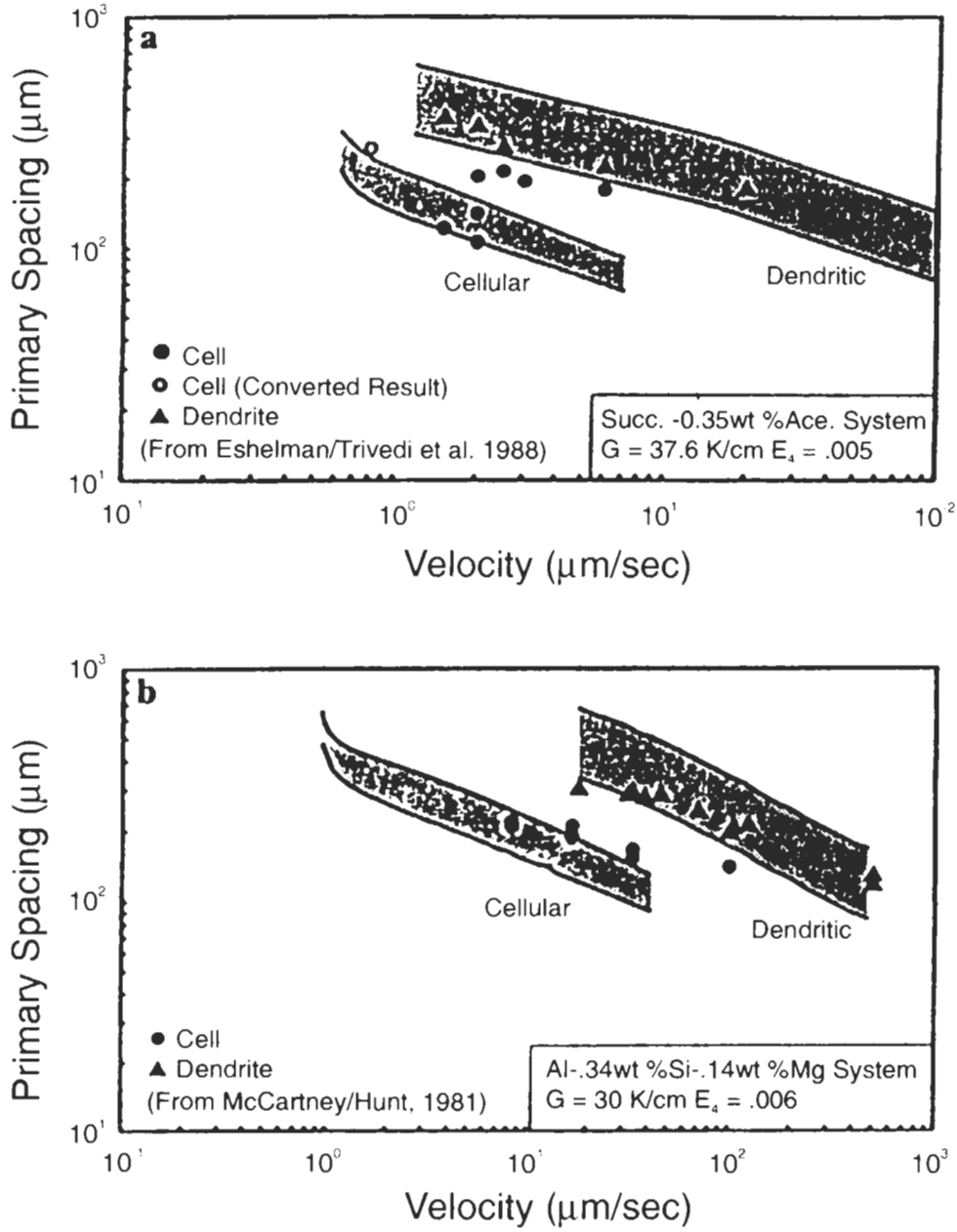

Fig. 37. Comparison of the predicted ranges of cell/dendrite primary spacings with experimental results: (a) succinonitrile-0.35 wt% acetone; (b) Al-0.34 wt% Si-0.14 wt% Mg. E_4 specifies the anisotropy of the surface energy. LU and HUNT [1992].

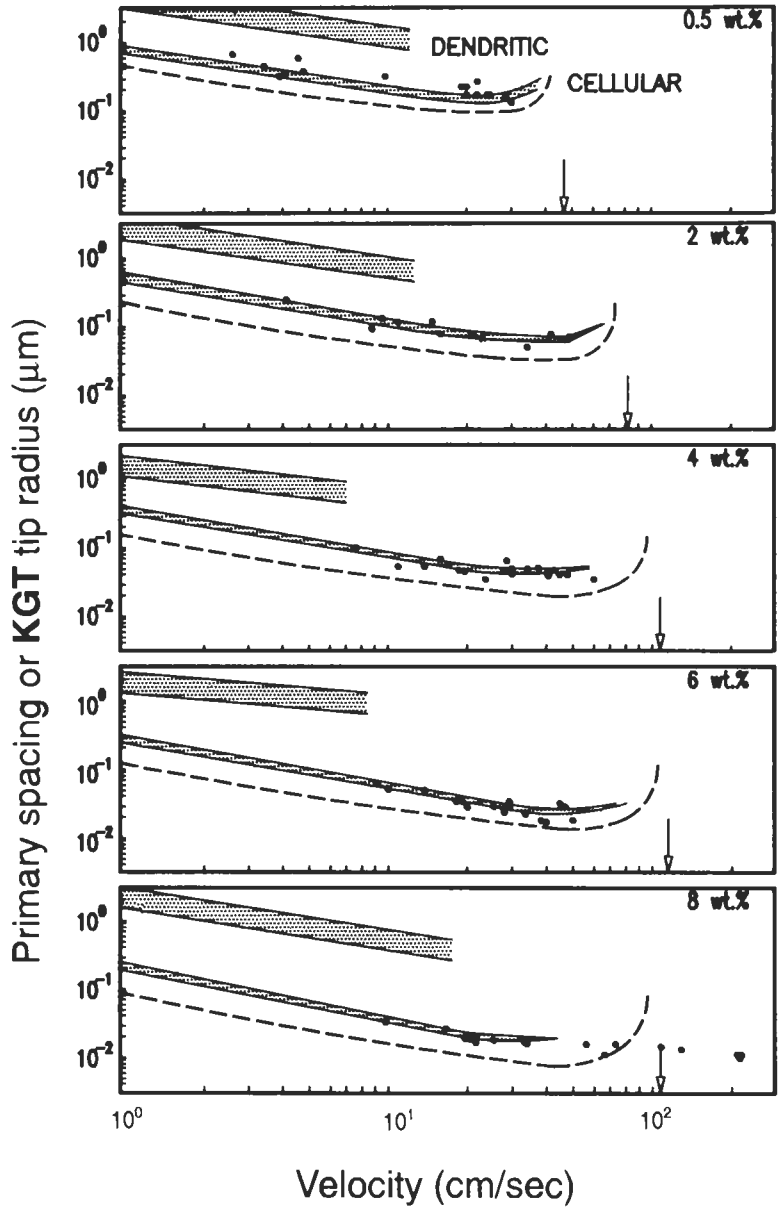

Fig. 38. Comparison of range of predicted primary spacings with experimental data for cell spacings obtained for five compositions of rapidly solidified Al–Fe alloys. The *IV/MS* tip radius is also shown dashed for comparison. LU *et al.* [1994]. The arrow shows the velocity where absolute stability is expected. Data from GREMAUD *et al.* [1991].

$$\lambda_1 = A_1 G_L^{-m} V^{-n}. \tag{93}$$

The result of the model by HUNT [1979] coincides closely with the expression derived by KURZ and FISHER [1981] using quite different assumptions about the dendrite geometry. The values $m = 0.5$ and $n = 0.25$ were obtained by both with the constant, A_1, being proportional to the fourth root of the alloy composition for dilute alloys. Thus for a given V and G_L, the primary spacing is larger for concentrated alloys than for dilute alloys. Traditionally many authors have considered that experimental values of λ_1 are better correlated to the local cooling rate, $G_L V$, such that $m = n \approx 0.5$ (FLEMINGS [1974]; OKAMOTO *et al.* [1975]; OKAMOTO and KISHITAKE [1975]; YOUNG and KIRKWOOD [1975]). On the other hand, in steels a broad discrepancy exists for the values of m and n, although many of the experimental studies have not been performed under controlled solidification conditions. JACOBI and SCHWERDTEFEGER [1976], controlling G_L and V separately, obtained values of $m = 0.25$ and $n = 0.72$. The complexity of modeling primary spacings is indicated by the fact that values of m and n fit to the numerical computations of LU and HUNT [1992] depend on the anisotropy of the surface energy.

Equation (93) is often used in conjunction with microstructural measurements to estimate the freezing conditions for various rapid solidification processing techniques. In view of the complexity of modelling λ_1 and the disparity in experimental values even at slow cooling rates, such an approach should be used with great caution.

7.2.3. Secondary dendrite arm spacing

During dendritic growth of cubic materials, the paraboloid-shape dendrite tip bulges laterally in the four {100} longitudinal planes containing the [100] growth direction. Each bulge then develops perturbations down the length of the dendrite shaft that become secondary arms as shown in fig. 39. The initial spacing of the secondary arms near the tip has been observed in transparent pure materials and alloys (HUANG and GLICKSMAN [1981], TRIVEDI and SOMBOONSUK [1984]). For both constrained and free growth, the spacing near the tip is approximately 2.5 times the tip radius over a broad range of growth conditions. Theoretical work by LANGER and MUELLER–KRUMBHAAR [1981] has also confirmed this relationship, which is related to the question of the tip stability discussed previously.

However as a result of coarsening effects during solidification, the final secondary dendrite spacing in a fully solidified casting is usually much coarser than the one formed near the tip. The observed mechanism of coarsening is the melting or dissolution of smaller arms at the expense of larger arms. Through the Gibbs–Thompson effect, local differences in curvature give rise to slight temperature and/or composition variations along the liquid solid interface. Diffusion of heat and/or solute in response to these differences cause the dissolution of small arms and the growth of others effectively increasing the average spacing of the secondary arms. For dendritic alloys, the process is practically important because it sets the length scale associated with the microsegregation. Indeed, the interplay between microsegregation and the coarsening process has only

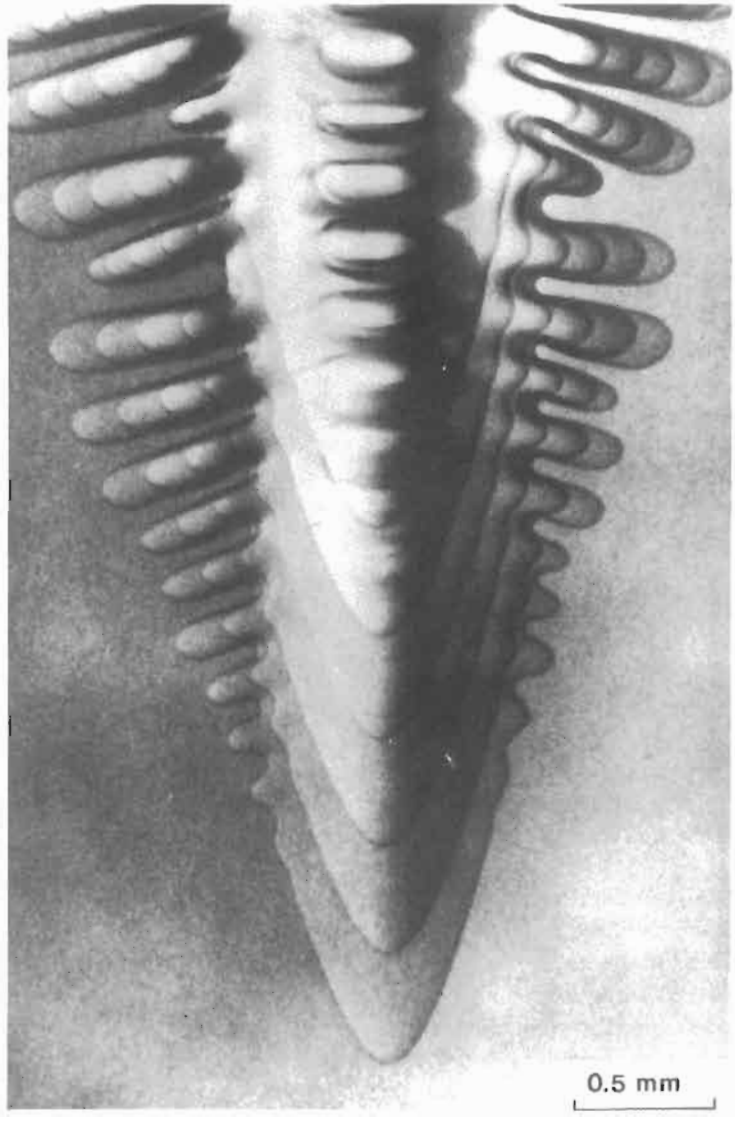

Fig. 39. Superposition of time-lapse photographs of the growth of a succinonitrile dendrite. Sidebranch evolution on the {100} branching sheets is evident. HUANG and GLICKSMAN [1981].

recently been examined (VOLLER and SUNDARRAJ [1993]). Coarsening in some alloys can be so extreme that the dendritic structure can be lost.

For all but the most dilute alloys, the rate of coarsening is determined by the diffusion of solute in the liquid (VOORHEES [1990]). Models were obtained for isothermal coarsening of the secondary arms held in the mushy zone by KATTAMIS *et al.* [1967] and

FEURER and WUNDERLIN [1977]. The latter obtained an expression for the secondary arm spacing, λ_2, given by

$$\lambda_2 = 5.5\left(M^* t_f\right)^{1/3}, \tag{94}$$

where

$$M^* = \frac{T_m \Gamma D_L \ln\left(\frac{C_b}{C_0}\right)}{m_L\left(k_0 - 1\right)\left(C_b - C_0\right)}, \tag{95}$$

where C_b is the final composition of the liquid at the base of the dendrite. When solidification is completed by a eutectic reaction, C_b is equal to the eutectic composition. The numerical factor in eq. (95) depends on the details of the geometry of the coarsening process and the dendritic structure and should be viewed as approximate. For directional solidification the local solidification time can be approximated by

$$t_f = \frac{\Delta T_f}{G_L V}, \tag{96}$$

where ΔT_f is the temperature difference between the dendrite tip and the base of the dendrite. Thus for a given growth velocity and temperature gradient λ_2 decreases with increasing composition.

KIRKWOOD [1985] obtained the above result only when the cooling rate is small compared to $m_L C_0 / t_f$. At larger cooling rates, the strict dependence, $\lambda_2 \sim t_f^{1/3}$, was not obtained and he ascribed the scatter in λ_2 vs. t_f data to this effect. In real solidification processes, coarsening takes place simultaneously with the subsequent increase in the fraction solid during cooling. MORTENSEN [1991a] presents a model that includes this effect.

7.2.4. Cell to dendrite transition

As the solidification velocity is increased for a given alloy composition and temperature gradient, one observes a transition in structure: planar, cellular, dendritic, cellular, planar. The lower and upper transitions between planar and cellular structures are given by the modified constitutional supercooling and the absolute stability criteria, respectively (§ 6.4). The transitions between cellular structures and dendritic structures at intermediate velocities are not well understood. Experimental data for the *low velocity transition* were obtained by TILLER and RUTTER [1956] and CHALMERS [1964] and were fit by the expression

$$G_L V^{1/2} \sim C_0 / k_0, \tag{97}$$

with a constant of proportionality that depends on crystallographic growth direction. Later KURZ and FISHER [1981] proposed the condition

$$G_L / V = \frac{m_L C_0\left(k_0 - 1\right)}{D_L}, \tag{98}$$

which is k_0 times the critical value of G_L/V for the plane to cell transition given by eq. (77).

In experiments by SOMBOONSUK *et al.* [1984], it became clear that cells and dendrites could coexist at the same velocity and that the conditions required for the transition were more difficult to calculate. (See BILLIA and TRIVEDI [1993]). Indeed in Hunt's calculations described above, cell and dendrite structures were found to exist at the same velocity. Hunt postulated that the cell to dendrite transition might occur when the tip temperature for the cell becomes lower than that for the dendrite (fig. 40). This postulate also predicts an upper transition velocity from dendrites back to cells with increasing solidification velocity in the rapid solidification regime. This upper transition is observed experimentally but has received no theoretical treatment.

7.3. Microsegregation

Microsegregation is the pattern of composition variation that remains in a solidified alloy. It includes the composition variation across cells or dendrites as well as the formation of other phases in the intercellular or interdendritic regions. One of the major goals of microsegregation analysis is the prediction of the volume fraction of eutectic or other secondary phases that may form between the cells and/or dendrites of the primary phase.

The simplest approximation for the prediction of microsegregation during dendritic solidification uses the Scheil equation described in § 6.2.2 where the volume under consideration is shown in fig. 41. With this approach no assumptions are necessary

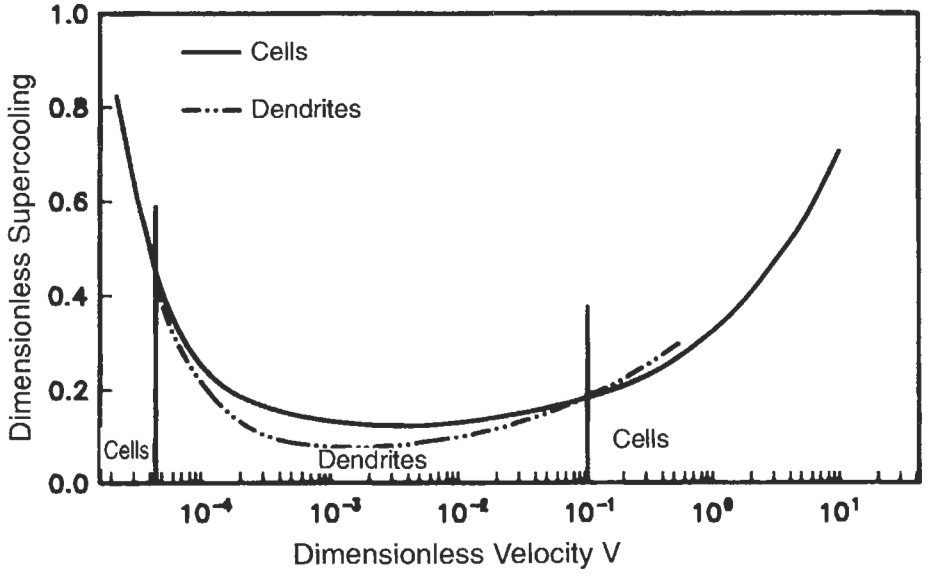

Fig. 40. Dimensionless tip supercooling vs. velocity for cells and dendrites calculated by LU *et al.* [1994]. The velocities where the curves cross define where the cell to dendrite transition is thought to take place.

References: p. 830.

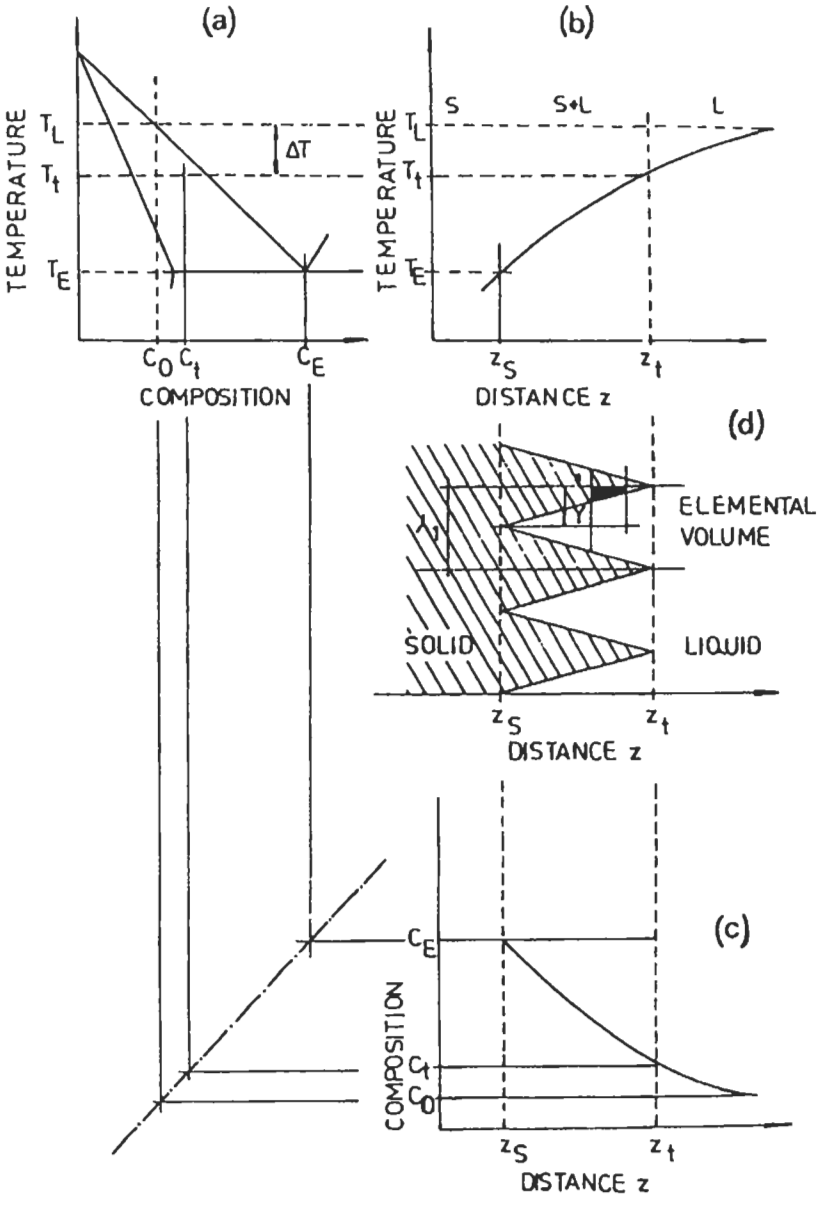

Fig. 41. Conceptual model of cellular/dendritic freezing showing: (a) portion of the phase diagram; (b) schematic temperature distribution in the melt; (c) distribution of solute within the liquid in the mushy zone; (d) representation of plate-like, unbranched dendrites showing the position of a characteristic elemental volume. (After BRODY and FLEMINGS [1966]).

concerning the geometry of the freezing solid until one desires to convert from fraction solid to distance in a cast microstructure. For example, the dependence of fraction solid on distance, r_1 from the center of a cell or dendrite with radial symmetry with a primary spacing, λ_1, can be obtained the expression,

$$f_S = 1 - \left(\frac{r_1}{\lambda_1}\right)^2. \tag{99}$$

Other geometries require other relationships between fraction solid and distance.

The predictions of the Scheil Equation establish an upper bound on the severity of microsegregation, for example, as determined by the predicted fraction of eutectic. Effects that alter the predicted microsegregation are: (a) the variation in cell or dendrite tip composition with growth conditions; (b) the degree of liquid mixing between the cells or dendrites; and (c) diffusion in the solid. All of these effects decrease the severity of microsegregation from that predicted by the Scheil Equation.

One of the first treatments of (a) and (b) was performed by BRODY and FLEMINGS [1966] and BOWER *et al.* [1966]. They assumed complete lateral mixing behind the cell tips and matched the composition gradient in the growth direction with the temperature gradient using the local equilibrium assumption (without curvature). This yields a prediction of the cell tip composition, C_L^*. A mass balance behind the tips was then used to obtain their final result which can be rewritten as

$$C_S = k_0 C_0 \left\{ \frac{1 - C_L^*/C_0}{k_0 - 1} + \left[1 - \frac{k_0\left(1 - C_L^*/C_0\right)}{k_0 - 1} \right] \left(1 - f_S\right)^{k_0 - 1} \right\}, \tag{100}$$

with $C_L^* = C_0(1 - a')$ where $a' = D_L G_L / m_L V C_0$.

Other approaches can be used to obtain the cell/dendrite tip composition along with the same mass balance. SOLARI and BILONI [1980] used the BURDEN–HUNT [1974a], [1974b] model based on the maximum growth rate hypothesis. In this work, $C_L^* = C_0(1 - a' + b')$ with $b' = [T_m \Gamma V(k_0 - 1)/m_L D_L\, C_0]^{1/2}$. Substitution of this value of C_L^* into eq. (100) gives the SOLARI and BILONI prediction. Use of the IV/MS dendrite model to obtain C_L^* would update this approach. The appeal of these approximate treatments is found in two limiting cases. If $C_L^* = C_0$, eq. (100) becomes the Scheil Equation. If $C_L^* = C_0/k_0$, eq. (100) becomes $C_S = C_0$ independent of f_S. This limit corresponds to planar growth where no microsegregation occurs.

GIOVANOLA and KURZ [1990] employ a method that uses the IV/MS prediction for the tip composition without assuming complete mixing between the dendrites near the tip region. They employ a polynomial to connect the tip composition to a composition well behind the tips where the complete mixing assumption is valid. The solid composition vs. fraction solid relation is determined by numerically solving algebraic equations.

The most important feature of microsegregation models that employ dendrite tip kinetics is the alteration of the composition of solid that forms at $f_S = 0$. The Scheil equation implicitly assumes that no solute is built up in front of the dendrite tip. Thus the first solid to form has composition, $k_0 C_0$. Increasing levels of solute in the liquid at the

tip correspondingly increase the amount of solute in the solid along the central dendrite trunk leaving less solute to accumulate in the interdendritic liquid regions at high fraction solid. Thus, for example, the amount of eutectic that forms will be reduced compared to the Scheil prediction.

Solid diffusion during solidification also reduces the amount of microsegregation. One approach is to apply the one-dimensional solid diffusion analysis presented in § 6.2.3 to a small volume in the mushy zone shown in fig. 41. The distance L_0 is then equated with λ_1 or λ_2 depending on whether the microstructure has fully developed secondary arms. When solid diffusion is added to the Scheil approach, one must know how the fraction solid changes with time. For a linear dependence of fraction solid on time, the term $(1-f_S)$ in eq. (100) was changed to $(1-f_S/(1+\alpha_\theta k_0))$ (see eq. 58) as was done by SOLARI and BILONI [1980]. Another approach is to numerically solve the diffusion equation in the solid and liquid (e.g. BATTLE and PEHLKE [1990]). While this approach is more accurate for the treatment of solid diffusion, it ignores the dendritic nature of cast alloys and the details of the solute profile in front of a growing dendrite. Corrections due to solid diffusion are very important for extremely slow solidification or when solid diffusion is very rapid as in the case of interstitial solutes, as for C in steels.

That the Scheil equation gives a good first approximation to dendritic microsegregation in the columnar zone of ingots has been proven, among other authors, by KATTAMIS and FLEMINGS [1965] for low alloy steels and WEINBERG and TEGHTSOONIAN [1972] for Cu-base alloys. CALVO and BILONI [1971], combining anodic oxidation techniques with electron microprobe measurements, obtained a clear map of the solute segregation together with quantitative measurements of the Cu concentration in Al-1% Cu alloys. The corrections to the Scheil approach due to solid diffusion have been tested by BOWER *et al.* [1966] and FLEMINGS *et al.* [1970]. The fraction of eutectic as well as the composition at the center of the dendrite agrees well with predictions using this approach.

In the rapid solidification regime, microsegregation profile must be measured in the TEM due to the small primary spacings. MASUR and FLEMINGS [1982] measured the composition profiles across very fine dendritic cells of Al-4.5% Cu solidified at a very high cooling rate (2×10^5 K/s) and a solidification velocity estimated to be 0.6 m/s. PALACIO *et al.* [1985] and BILONI [1983] analyzed their data using eq. (100) with values of C_L^* from the theory of BURDEN and HUNT [1974a]. Figure 42 shows the measured and *predicted* variation of solid composition as a function of f_S. The segregation profile described by this equation is in close agreement with the experimental results.

Other features of microsegregation profiles however have been noted especially in the rapid solidification regime. Flat solute profiles have been associated with cellular growth at high solute Peclet numbers by BOETTINGER *et al.* [1987]. Solute rich regions at the center of cells have been observed by KATTAMIS [1970] and by BOETTINGER *et al.* [1987]. The recent computation method of LU *et al.* [1994] may yield a better approach to understanding the details of microsegregation over a broad range of growth conditions.

7.4. Solidification of ternary alloys

Practical alloys typically contain many components and a brief discussion of

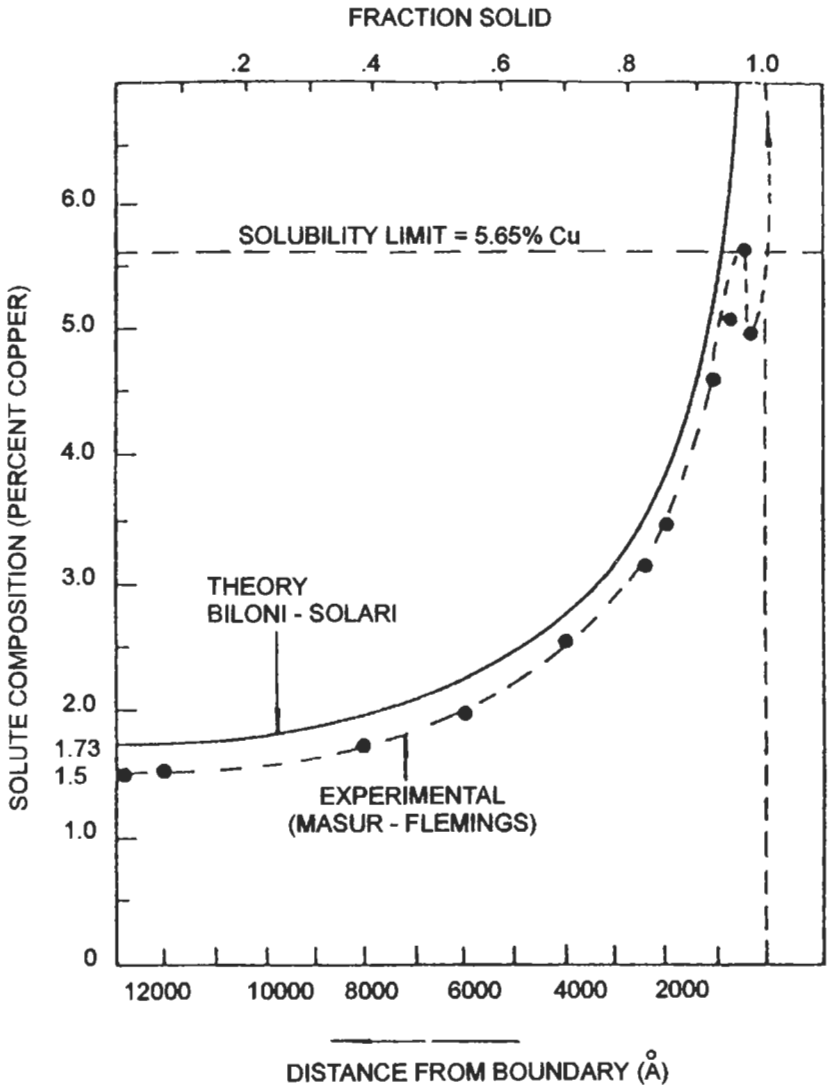

Fig. 42. Comparison between data of MASUR and FLEMINGS [1981] on the composition of a cell from center to periphery in Al-4.5 wt% Cu melt spun ribbon solidified at an estimated growth velocity of 0.6 m/s, and predictions of composition given by eq. (100) due to SOLARI and BILONI [1980].

solidification in ternary alloys is appropriate. A general view of solidification microstructures in a ternary eutectic system has been presented by MCCARTNEY *et al.* [1980a], [1980b] as shown in fig. 43. Depending on the alloy composition, various mixtures of primary phase, monovariant binary eutectic and invariant ternary eutectic can be expected. For the dendritic growth of a primary phase, the Scheil approach can be

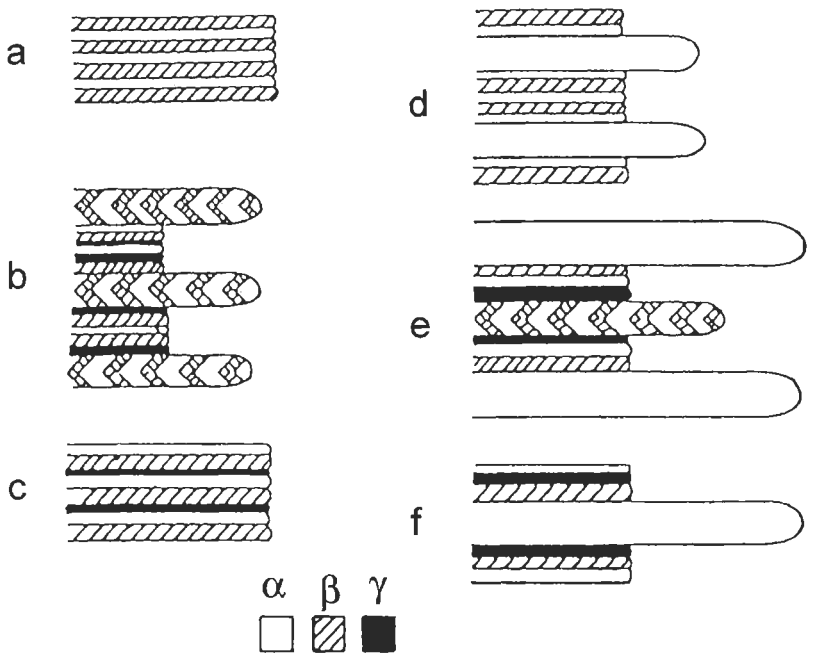

Fig. 43. Possible growth interfaces in a ternary system depending on composition: (a) two phase eutectic (planar growth), (b) two phase cells plus ternary eutectic, (c) three phase eutectic, (d) single phase cells plus binary eutectic, (e) single phase cells, two phase cells and ternary eutectic, (f) single phase cells plus ternary eutectic. McCartney *et al.* [1980a].

utilized, if appropriate, or a dendrite tip model constructed.

The ternary (or higher order) phase diagram is important for either of these approaches. One requires information concerning the relationship between C_{Si}^* and C_{Li}^* for each of the $\underline{i}$ alloying additions. Often values are taken from the binaries, but in general the composition of one species in the solid may depend on the composition of other species as well. This information is given by the tie-lines of the phase diagram that are usually only available through a thermodynamic model of the multicomponent alloy of interest, rather than through experimental studies.

Use of the Scheil approach to determine the solidification path, which is the composition of liquid (and thus solid) as a function of fraction solid, uses a set of equations

$$\frac{dC_{Li}}{df_S} = \frac{(1-k_{0i})C_{Li}}{1-f_S}, \tag{101}$$

that are uncoupled if the k_{0i} $(=C_{Si}/C_{Li})$ do not depend on the composition of the other species. In fact, if the k_{0i} are constants, then for an alloy of initial composition C_{0i},

$$C_{Li} = C_{0i}(1-f_S)^{k_{0i}-1}, \tag{102}$$

for each component during primary solidification. Using the phase diagram, one then determines the fraction solid at which the liquid crosses a monovariant eutectic line. Solidification then follows this line and finally ends with the ternary eutectic. If the solidification path for primary solidification crosses a monovariant peritectic line, solidification switches to single phase growth of the new phase. Calculations of solidification path using full integration of phase diagram tie-lines with the Scheil approach (including solid diffusion) have been conducted by CHEN and CHANG [1992].

For a treatment of the kinetics of the dendrite tip in a multicomponent alloy, Ivantsov solutions are obtained for each solute to determine the composition of each solute at the dendrite tip. The marginal stability criterion for the multicomponent alloy is applied to determine the tip radius as shown by BOBADILLA *et al.* [1988] and RAPPAZ *et al.* [1990].

7.5. New approaches to modeling dendritic growth

Another approach to modeling dendritic growth is the phase-field method (CAGINALP [1986], KOBAYASHI [1991] [1992], WHEELER *et al.* [1992], [1993b]). With this method the interface is treated as being diffuse and the transition from liquid to solid is described by an order parameter called the phase field. For a pure material, equations that govern the phase field and the temperature are solved over a domain of interest without applying boundary conditions along the liquid solid interface. The position of the interface is then determined from the solution as a surface with a constant value of the order parameter intermediate between a homogeneous liquid and solid. This method, which requires time consuming computations on a supercomputer, has succeeded in obtaining realistic dendritic growth forms for pure materials and alloys with no extra conditions required to specify the operating state of the dendrite tip, such as the marginal stability condition, eq. (85). The velocity and tip radius are naturally selected by the solution to the differential equations (WHEELER *et al.* [1993a]). An example of a computed two dimensional alloy dendrite using this method is shown in fig. 44 (WARREN and BOETTINGER [1995]). Presently, computations have been performed using finite difference methods and, due to high computation times, are limited to high supercooling of the order of L/C_p^L.

8. *Polyphase solidification*

The discussion of solidification is now extended to situations where several phases are formed from the melt. Eutectic, peritectic, and monotectic solidification involve the freezing of an alloy at or near a special liquid composition. In a binary system, this special composition is defined thermodynamically as the liquid composition that can be in equilibrium with two other phases at the same temperature. This equilibrium can only occur at a single temperature in a binary system at fixed pressure. For the eutectic and peritectic cases, the liquid is in equilibrium with two solid phases and for the monotectic case, the liquid is in equilibrium with a solid and another liquid phase. The monotectic case involves alloys that exhibit a miscibility gap in the liquid phase.

References: p. 830.

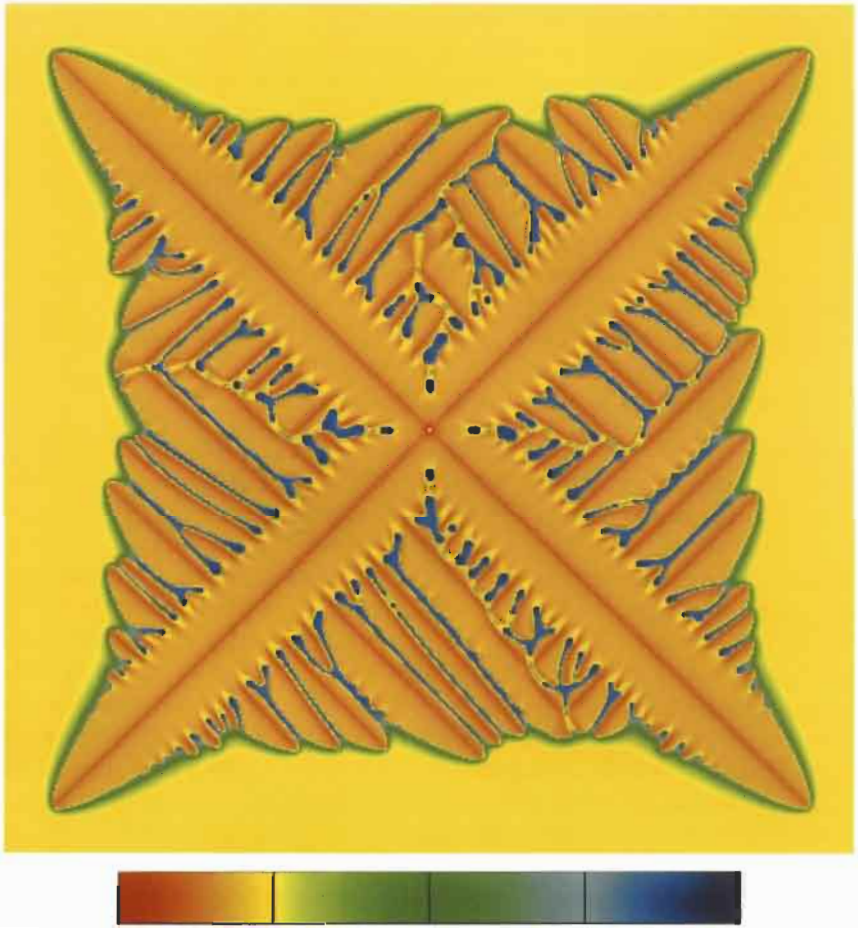

Fig. 44. Simulation of an alloy dendrite growing into a supercooled liquid using the phase-field method. The shadings show variation of composition (atomic fraction Cu) in the liquid and solid for parameters approximating a Ni–Cu alloy with 0.41 atomic fraction Cu. (WARREN and BOETTINGER [1995].)

8.1. Eutectic solidification

In a binary alloy, eutectic solidification converts a liquid simultaneously into two solid phases. Alloys near eutectic compositions are very important in the casting industry due to several characteristics: (i) low liquidus temperatures compared to the pure component melting points that simplify melting and casting operations: (ii) zero or small freezing ranges that effectively eliminate the dendritic mushy zone thereby reducing segregation and shrinkage porosity while promoting excellent mold filling; (iii) possibil-

ities of forming "in-situ" composites. Among the most common eutectic or near-eutectic alloys of industrial importance are cast irons, Al–Si alloys, wear-resistant alloys and solders. In many other practical alloys that freeze dendritically, secondary phases are formed near the end of freezing by eutectic solidification.

Eutectic solidification involves the following stages: eutectic liquid is supercooled and one of the solid phases nucleates, causing solute enrichment in the surrounding liquid and sympathetic nucleation of the second solid phase. Repeated nucleation and/or overgrowth of one solid phase by the other produces a growth center that defines an individual eutectic grain. For many eutectics, solidification proceeds by simultaneous growth of two interspersed solid-phases at a common liquid–solid interface. The solute rejected into the liquid by each phase is taken up by the adjacent phase particles. As solidification proceeds, spatial and crystallographic rotation of the solid phases together with competitive overgrowth of adjacent eutectic grains lead to a stable solidification front, with the surviving eutectic grains having, as much as possible, maximized the solidification rate, minimized the α–β interfacial energy and oriented the α–β interfaces in the heat flow direction. The ability of one solid phase in the eutectic to stimulate nucleation of the other varies widely for different α–β phases and, in general, knowledge about the nucleation process in eutectic solidification remains rather poor (MONDOLFO [1965]). Thus, this section will treat mainly theory and experiments concerning steady state directional solidification, a method which has furnished, as in the case of dilute alloys, a large number of reliable results. Two excellent summaries of the earlier literature on eutectic solidification can be found in reviews by CHADWICK [1963] and HOGAN *et al.* [1971].

8.1.1. Eutectic classification

When a eutectic liquid solidifies, the resulting material generally consists of a dispersed two-phase microstructure that is approximately ten times finer than cells or dendrites formed under the same conditions. The exact arrangement of the two phases in the eutectic microstructure can vary widely, depending on the solidification conditions and the particular eutectic alloy being solidified. HUNT and JACKSON [1966] provided a simple classification scheme according to the interface kinetics of the component phases. A correlation was found between eutectic morphology and the entropies of fusion of the two solid phases, concepts discussed in § 5.1. The classification refers to: non-facetted–non-facetted eutectics (nf–nf); non-facetted–facetted eutectics (nf–f); and facetted–facetted eutectics (f–f). Very little is known about the solidification of f–f eutectics but extensive research has been performed on nf–nf and nf–f eutectics. KERR and WINEGARD [1967] argued that the facetted or nonfacetted nature of the liquid–solid interface of the phases was better described by the entropies of solution of the individual phases because the (eutectic) liquid composition is generally quite different from the solid phase compositions. CROKER *et al.* [1973] examined a large number of eutectic microstructures and in addition found that the volume fraction of the solid phases in the eutectic structure and the growth velocity must also be considered to obtain a good classification scheme.

8.1.2. Non-facetted – Non-facetted eutectics

Eutectic mixtures of two non-facetted phases tend to form regular microstructures

References: p. 830.

consisting of either alternate lamellae of α and β or rods of α embedded in β that grow in a continuous edgewise manner into the melt. Experimentally, it is found that eutectics in which one phase has a very low volume fraction tend to grow in a rod-like manner. This can be explained on the basis that a rod-like structure has lower total α–β surface energy than a lamellar structure when the volume fraction of one of the phases is less than about 0.3. This assumes that the surface energies are isotropic. A 25% anisotropy of surface energy can stabilize lamellar structures at practically any value of volume fraction. In marginal cases, lamellar-to-rod transitions can occur for a given alloy by changing the growth conditions. Three-dimensional analysis of the eutectic structures shows that both phases are continuous in the growth direction over large distances that are called eutectic grains. A eutectic grain can be described approximately as two interpenetrating single crystals of the two component phases having almost constant crystallographic orientation. HOGAN *et al.* [1971] give a thorough discussion of eutectic grains and a summary of the orientation relationships between phases and the habit plane of the α–β interfaces. The orientation relationship and the orientation of the interfaces usually allow for a high degree of fit between the two crystal structures that minimizes the α–β surface energy.

In lamellar or rod eutectic solidification, the two phases, α and β, solidify side by side with an approximately planar and isothermal S–L interface, supercooled ΔT below the equilibrium eutectic temperature. During solidification of an A–B alloy, the A-rich phase rejects B atoms into the liquid and the B-rich phase rejects A atoms. The interaction of the diffusion fields in the liquid in front of the two phases gives rise to the term *coupled growth*, which is commonly used to describe eutectic solidification. At a given solidification rate V, the spacing of the lamellae or rods, λ_E, and the interface supercooling below the eutectic temperature, ΔT, are controlled by a balance between: (i) the necessity for lateral diffusion of excess A and B in the liquid just ahead of the S–L interface, which favors a small interlamellar or interrod spacing, and (ii) the necessity to create α–β interfacial area, which tends to favor large λ_E (fewer interfaces).

Over the years the theory of lamellar or rod growth for the slow solidification velocities found in castings or in directional solidification when $\lambda_E V/2D_L \ll 1$ has been developed by ZENER [1946], HILLERT [1957], TILLER [1958], JACKSON and HUNT [1966], MAGNIN and TRIVEDI [1991]. The situation for rapid solidification is treated below. The basis of the analysis is illustrated in fig. 45. The interface temperature at each interface point is controlled by the velocity at each point, the composition of the liquid at the interface at each point and the curvature at each point. The supercooling below the eutectic temperature, T_E, for each point on the S–L interface (α–L and β–L) can be described by

$$\Delta T = \Delta T_k + \Delta T_D + \Delta T_c. \tag{103}$$

The first term is the interface attachment kinetic supercooling and is usually neglected compared to the other terms. Thus it is assumed that each point on the α–L and β–L interfaces is at local equilibrium. ΔT_D is the supercooling below the eutectic temperature due to the local variation in composition from the eutectic composition. This local variation is approximated by solving the steady-state diffusion equation in the liquid for

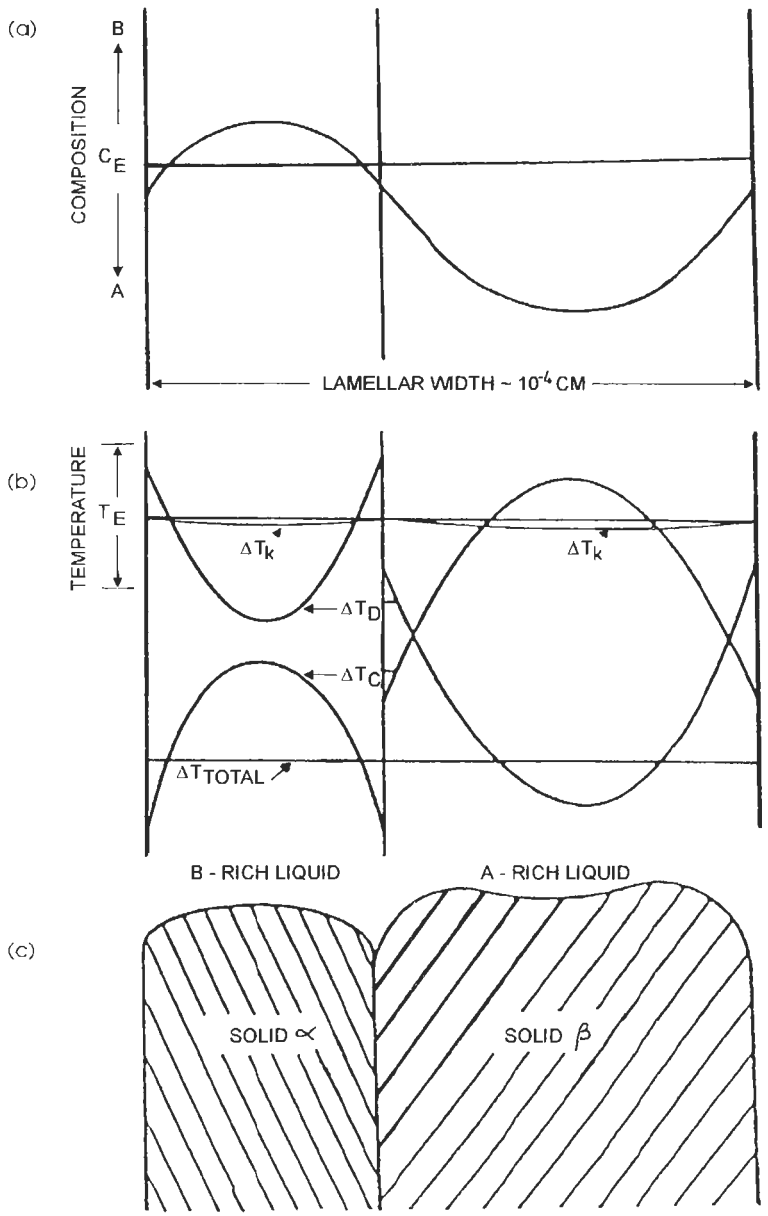

Fig. 45. (a) Liquid composition (% B) across an α–β interface. (b) Contributions to the total supercooling (ΔT) existing at the S–L interface, ΔT_D, ΔT_c, and ΔT_K are the solute, curvature and kinetic supercoolings respectively. (c) Shape of the lamellar S–L liquid interface. HUNT and JACKSON [1966].

a planar α–β interface growing at velocity V and spacing λ_E. ΔT_c is the supercooling due to curvature.

It is then assumed that the total supercooling, ΔT, given by eq. (103) is constant across the interface. Thus across the interface, any variation in ΔT_D must be balanced by a variation in ΔT_c, giving a constant value for $\Delta T = \Delta T_D + \Delta T_c$ at each point of the interface. Due to the solution of the diffusion equation, ΔT_D has a minimum value near the α–β–L groove, and thus ΔT_c has a maximum value there. The radius of curvature is, therefore, smallest near the triple junctions and leads to an interface shape similar to that shown in fig. 45c. JACKSON and HUNT [1966] have shown that the predicted interface shape agrees very well with the interface shape observed in the transparent hexachloroethane–carbon bromide model system.

By averaging the composition deviation from the eutectic composition in the liquid in front of each phase and the interface curvature of each phase (which depends on the width of the phase and the angle the interface makes with the α–β interface), the total supercooling is found to be

$$\Delta T = K_5 \lambda_E V + K_6/\lambda_E, \tag{104}$$

where K_5 and K_6 are constants. For lamellar growth they are given by

$$K_5 = \frac{\overline{m}_L C_0^*}{D_L} \frac{P_E}{f_\alpha f_\beta} \tag{105}$$

and

$$K_6 = 2\overline{m}_L \left(\frac{\Gamma_\alpha \sin\theta_\alpha}{m_{L\alpha} f_\alpha} + \frac{\Gamma_\beta \sin\theta_\beta}{m_{L\beta} f_\beta} \right) \tag{106}$$

with

$$\overline{m}_L = \frac{m_{L\alpha} m_{L\beta}}{m_{L\alpha} + m_{L\beta}} \tag{107}$$

The parameters $m_{L\alpha}$ and $m_{L\beta}$ are the liquidus slopes for the alpha and beta phases, C_0^* is the difference in composition between the solid phases, D_L is the liquid diffusion coefficient, f_α and f_β are the volume fraction of the solid phases in the eutectic, P_E is a series function of the phase fractions and can be approximated (TRIVEDI and KURZ [1988]) by

$$P_E = 0.3383 \left(f_\alpha f_\beta \right)^{1.661}. \tag{108}$$

Γ_α and Γ_β are the Gibbs–Thomson coefficients (surface energy/entropy of fusion per unit volume), and θ_α and θ_β are the angles that the alpha and beta interfaces make with a plane perpendicular to the α–β interface. Because a balance of tensions must exist at the α_E–β_E–L triple point, the solid–solid energy exerts its influence through its effect on these angles. A low value of $\gamma_{\alpha\beta}$ leads to small values for θ_α and θ_β making ΔT_c small.

Very similar expressions are obtained for rod eutectic growth.

Equation (104) is shown schematically for different growth rates in fig. 46. It can be seen that ΔT is biggest for large lamellar spacings because diffusion is difficult, and also for small spacings where curvature effects are dominant. Clearly, the values of λ_E and ΔT are not fixed uniquely by V, yet in experiments it is well established that the value of λ_E generally decreases with increasing V. Hence an additional condition is required to specify the operation point on each λ_E vs. ΔT curve.

The simplest additional condition is obtained by assuming that growth occurs at the minimum ΔT for a given V or, equivalently, a maximum V for a given ΔT. This condition is called the *extremum condition*. Using this condition,

$$\lambda_E^2 V = K_6/K_5, \tag{109}$$

and:

$$\Delta T^2/V = 4K_5K_6. \tag{110}$$

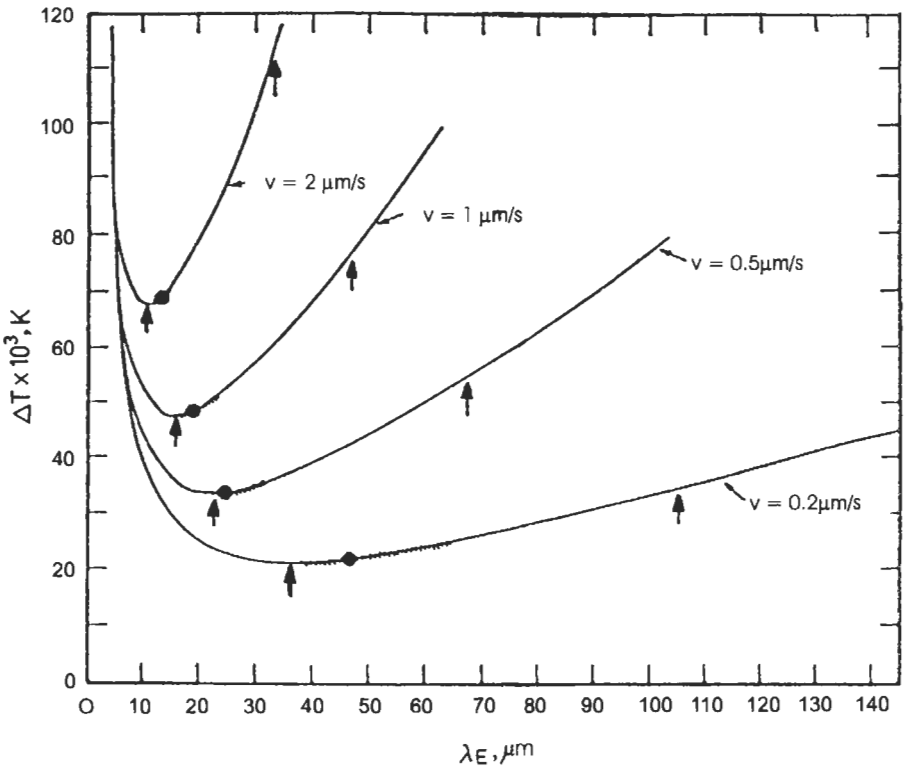

Fig. 46. Interface supercooling, ΔT, as a function of lamellar spacing, λ_E, for different growth rates, V using eq. (104) for CBr_2–C_2Cl_6 organic eutectic. The vertical arrows show the theoretical minimum (extremum) and maximum spacings for stable lamellar growth. The experimentally observed range of spacings (hatch marks) and the mean spacing (filled circles) at the different velocities are shown. (SEETHARAMAN and TRIVEDI [1988]).

References: p. 830.

Many investigators (for example JORDAN and HUNT [1971, 1972], TASSA and HUNT [1976]) have found the average spacing and interface supercooling to be close to the values given by these equations using the extremum condition.

However the use of the extremum condition is rather ad hoc and a more satisfying selection criterion has been sought for years. Indeed the discovery that the dendrite tip radii could not be described by a maximum growth rate hypothesis (see § 7), led to further consideration of this criterion for eutectic growth. Experiments on eutectics (JORDAN and HUNT [1972], SEETHARAMAN and TRIVEDI [1988]) have shown experimentally that a small range of spacings are observed for a given growth rate. They find that the minimum spacing is close to that given by the extremum condition but that the average spacing is somewhat larger than that given by eq. (109). Much research has been focused on defining the allowable range.

The basic concepts were first proposed by JACKSON and HUNT [1966], who indicated that only spacings within a certain range were stable to fluctuations in the shape of the S–L interface as shown in fig. 47. They quoted unpublished work by J.W. CAHN that argued that spacings smaller than that given by the extremum condition are inherently unstable and thus the extremum spacing is expected to be the minimum observed. This instability is due to the pinching off of an individual lamella or rod that locally increases the spacing (fig. 47a). That the extreemum value corresponds to the minimum spacing has been confirmed by extensive theoretical work (LANGER [1980], DAYTE and LANGER [1981] and DAYTE *et al.* [1982].) Less sudden spacing adjustments can occur by the motion of faults (lamellar edges) perpendicular to the growth direction.

A value for the maximum possible spacing at any velocity was first proposed by JACKSON and HUNT [1966]. This maximum spacing also follows a $\lambda_E^2 V$ = constant law. If the spacing exceeds the extremum value by a critical factor, the larger volume fraction phase develops a pocket that drops progressively back from the interface until growth of the other phase ultimately occurs in it (fig. 47b). They took this condition to occur when the slope of the pocket became infinite. For example, this condition yields maximum

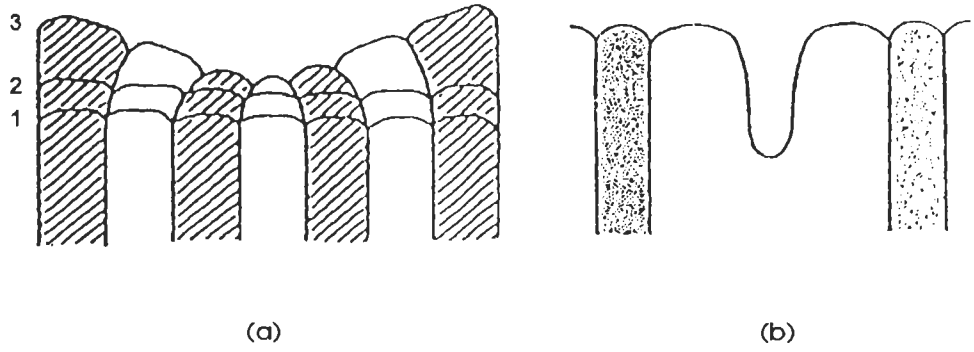

Fig. 47. (a) Schematic illustration of the instability of lamellae with λ_E less than the extremum value. The lamella in the center will be pinched off with time. (b) The shape instability of the interface of one phase that occurs when the spacing becomes too large. A new lamella may be created in the depressed pocket. JACKSON and HUNT [1966]. Figure taken from TRIVEDI and KURZ [1988].

values for the $\lambda_E^2 V$ constant of ten and two times the extremum value for volume fractions of 0.5 and 0.1 respectively. As a consequence of the formation of the new lamella, the local spacing is abruptly reduced by a factor of two. However, the careful experiments of SEETHARAMAN and TRIVEDI [1988] show that the maximum observed spacing is much smaller than this estimate (see fig. 46), giving an average spacing that is only ~20% larger than the extremum value (or minimum stable spacing). Thus the maximum value of spacing occurs before the pocket depression attains infinite slope. While further research is required on this topic, the extremum value is often taken as a good approximation for nf–nf growth. Other stability issues of eutectic growth involving compositions different from the eutectic composition in § 8.1.4 and § 8.1.5.

Convection in the liquid near the interface of a growing eutectic has been found to increase the value of λ_E (JUNZE *et al.* [1984] and BASKARAN and WILCOX [1984]). Flow parallel to the interface distorts the liquid concentration profile in front of the lamellae slightly and alters the diffusion controlled growth. The effect is greatest when the dimensionless parameter, $G_u \lambda_E^2 / D_L$, is large, where G_u is the gradient normal to the interface of the fluid flow velocity parallel to the interface. Vigorous stirring is required to alter the spacing significantly.

8.1.3. Non-facetted–facetted eutectics

The modeling of nf–f eutectics is quite important given the fact that eutectics of technological importance such as Al–Si and Fe–C belong to this class. FISHER and KURZ [1979] and KURZ and FISHER [1979] summarize the main features of (nf–f) eutectic growth. When (nf–f) eutectics are compared with (nf–nf) eutectics, several characteristics can be noted:

i) the degree of structural regularity is much lower and a wide dispersion of local spacing is observed.

ii) for a given growth rate and fraction of phases, the average spacing and the supercooling for growth of a nf–f eutectic are much larger than for a nf–nf eutectic.

iii) for a given growth rate, the supercooling and the spacing decrease as the temperature gradient is increased. No such effect is seen for nf–nf eutectics.

Early investigations introduced interface attachment supercooling for the facetted phase in order to explain the increased supercooling. However STEEN and HELLAWELL [1975] and TOLOUI and HELLAWELL [1976] showed that the kinetic supercooling of Si in Al–Si eutectic is too small to explain the increased eutectic supercooling. Indeed Si in Al–Si and graphite in Fe–C both contain defect planes parallel to the plate growth direction that enable easy growth (twins in Si and rotation boundaries in graphite). TOLOUI and HELLAWELL [1976] suggested that the large supercoolings were due to the difficulties of adjusting the spacing to minimize the diffusion distance. These difficulties are related to the anisotropy of growth of the facetted phase.

Measurement of spacing and supercooling on the model system camphor–naphthalene by FISHER and KURZ [1979] permitted important results to be obtained. The system exhibits two distinct eutectic growth forms: one regular and the other irregular. By assuming that the measured spacing and supercooling for the regular growth were given using the nf–nf theory with the extremum condition, the various materials parameters for

this system were obtained. When ΔT vs. λ_E was plotted for the relevant growth rate, the spacing and supercooling values for irregular growth fell on the same derived theoretical curve for regular eutectic growth but, with spacings much larger than the extremum value. Thus the coarseness of the structure is the cause of the large supercooling of growing nf–f eutectics. Indeed theoretical analysis of the λ_E vs. ΔT curves by MAGNIN and KURZ [1987] that relax the assumption of an isothermal interface made in the nf–nf theory, show a deviation from the nf–nf theory only at very slow growth rates where the constants in eq. (103) become functions of G_L. Thus for growth at more normal speeds, the theory turns to an analysis of why the spacing is so big for nf–f eutectics.

The general argument employed to understand why the average spacing of f–nf eutectics is large focusses on determining the stable range for eutectic spacings at a given velocity. Important contributions have been made by FISHER and KURZ [1980], MAGNIN and KURZ [1987] and MAGNIN *et al.* [1991]. For irregular eutectics the growth directions of different lamellae are not parallel. Thus as growth proceeds, the local spacing decreases between two converging lamellae and increases between diverging lamellae (fig. 48). For converging lamellae, when their separation decreases below the extremum value, one of the lamellae is pinched off, just as for nf–nf growth. For diverging lamellae, when the local spacing increases beyond a critical value, FISHER and KURZ [1980] have suggested that the facetted phases branches into two diverging lamella. The formation of the new lamella decreases the local spacing. The anisotropic growth kinetics

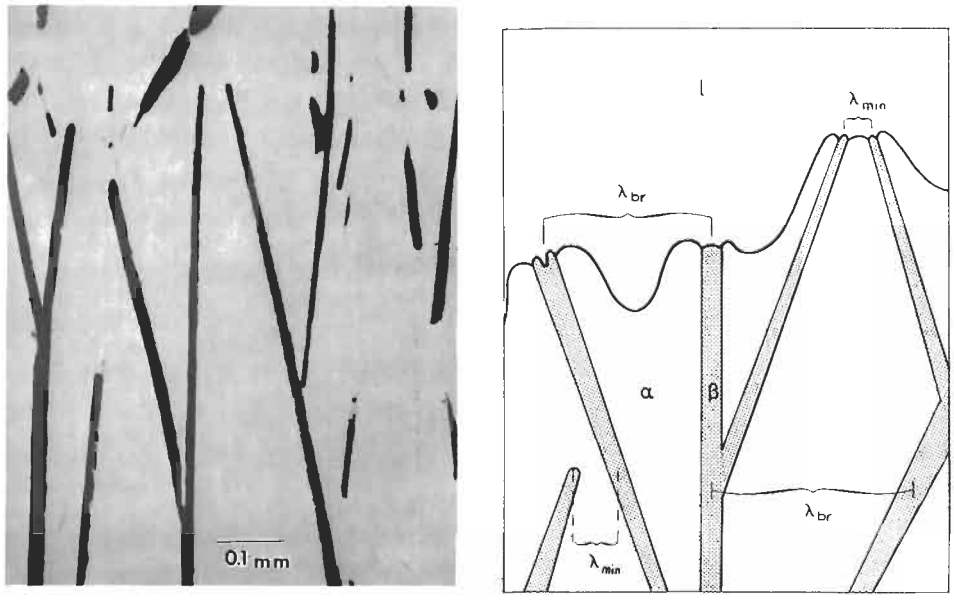

Fig. 48. Proposed growth behavior of irregular eutectics, showing branching at λ_{br} and termination at λ_{ex}. (a) Fe-graphite eutectic growth at $V = 1.7 \times 10^{-2}$ μm/s. (b) schematic representation of solid–liquid interface during growth. MAGNIN and KURZ [1987].

of the facetted phase leads to what is termed *branching-limited growth.* Several criterion have been proposed to determine the maximum value of spacing where the branching takes place (FISHER and KURZ [1980] and MAGNIN and KURZ [1987].) MAGNIN and KURZ [1987] suggest that this branching instability occurs when the facetted phase interface develops a depression of some characteristic depth; e. g., when it drops below a line joining the two triple points for the lamella. The average spacing lies between the minimum spacing and the spacing that cause the branching instability. MAGNIN *et al.* [1991] argue that the mechanism that establishes the minimum and maximum spacings remains undetermined and that the inherently nonsteady solidification of nf–f eutectics plays a fundamental role. Many issues remain to be studied in this area especially those regarding orientation relationships and their relationship to the branching mechanism.

8.1.4. Eutectic cells and dendrites

In addition to consideration of the stability of the eutectic spacing, two other instabilities can influence the microstructure of alloys at or near the eutectic composition. These involve the addition of a ternary impurity or the deviation of the average composition from the thermodynamic eutectic composition in a binary. These will now be discussed in turn.

A ternary impurity added to a binary eutectic can lead to a cellular structure (CHADWICK [1963]). The mechanism is similar to the cellular breakdown in single-phase solidification treated in § 7; for a critical value of G_L/V the average planar S–L interface of the eutectic structure can become unstable and the solidification front becomes corrugated. The cells (often called eutectic colonies) are quite large containing many (10–100) eutectic spacings with the lamellae curving to remain approximately normal to the liquid solid interface. Thus cells are most noticeable for nf–nf eutectics. BERTORELLO and BILONI [1969] propose that the inception of the instability occurs at depressions in the interface due to eutectic grain boundaries or at fault terminations at the S–L interface. It might be noted that near the edge of eutectic colonies there is often a transition to a rod structure.

If an excessive amount of a ternary element is added, the eutectic colony can actually evolve into a two-phase dendrite with secondary arms. In this case, ternary eutectic is usually found between the two-phase dendrite (SHARP and FLEMINGS [1974] (see also fig. 43).

8.1.5. Competitive growth – coupled zone

As a binary alloy with a composition different from the thermodynamic eutectic composition cools from the liquidus to the eutectic temperature, dendritic growth of the primary phase followed by eutectic growth of the remaining interdendritic liquid is expected. However, there is a *range* of alloy composition and growth rate (or interface supercooling) where it is possible to freeze these liquids as eutectic microstructures without dendrites. This range of conditions is known as the *coupled zone.* Pioneering investigations in this field were those of TAMMANN and BOTSCHWAR [1926] and KOFLER [1950] in organic systems, which established that at low or zero temperature gradients, the range of alloy compositions for coupled growth widened with increasing growth

velocity. Later, MOLLARD and FLEMINGS [1967] showed that the widening of the coupled zone was not restricted to high growth rates but, with a positive temperature gradient, could also be obtained at low growth rates with a high G_L/V ratio. Solidification with a high value of G_L/V suppresses the dendritic growth of the primary phase. Other milestones in the development of the knowledge of the coupled zone were the investigations by HUNT and JACKSON [1967], JACKSON [1968], BURDEN and HUNT [1974c], TASSA and HUNT [1976] and KURZ and FISHER [1979].

Taking into account the fact that the description of the microstructural transition from eutectic to eutectic plus dendrites has not yet been successfully modeled using perturbation analysis (JORDAN and HUNT [1971]; HURLE and JAKEMAN [1968]), the coupled zone width can only be obtained using a simpler approach that employs three concepts reviewed by KURZ and FISHER [1979]: For each overall liquid composition, (i) consider all the growth forms possible, i.e., α dendrites, β dendrites, and eutectic. (ii) Analyze the growth kinetics of these forms and determine the interface (or tip) temperatures of the growth forms as a function of V, and possibly of G_L. (iii) Apply the competitive growth criterion, e.g., that the morphology having the highest interface temperature for a given growth rate, or the highest growth rate for a given temperature will dominate. The range of temperatures and compositions, within which eutectic growth is fastest, is called the coupled zone and can be plotted on the phase diagram. The composition range of the coupled zone can also be plotted versus velocity because each value of interface temperature corresponds to a known value of the growth velocity for the dominant growth structure. For growth conditions where the eutectic is not dominant, the microstructure consists of a mixture of dendrites and interdendritic eutectic.

Figure 49 shows an example of a competitive growth analysis for a system involving a f–nf eutectic (the β phase is facetted). The kinetic curves are shown for α dendrites, β dendrites and (planar) eutectic. The curves for the dendrites depend on the value of the

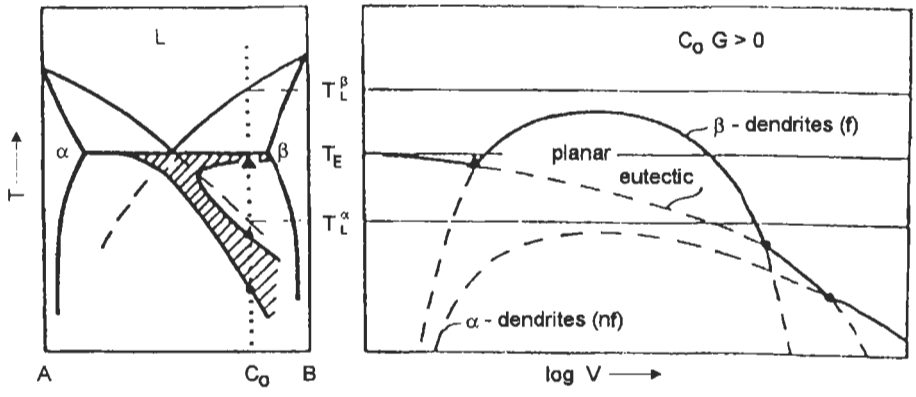

Fig. 49. The origin of the coupled zone (hatched) is understood by considering the variation in eutectic interface temperature and dendrite tip temperatures for an off-eutectic alloy. The dominant microstructure for any composition at a given velocity (or supercooling) is that which grows with the highest temperature (or fastest growth rate given by the solid curves in b). TRIVEDI and KURZ [1988].

temperature gradient and this dependence leads to the decreased interface (tip) temperatures at low velocity and the widening of the coupled zone at high G_L/V ratio. The skewed nature of the coupled zone about the eutectic composition for this f–nf system is due to two factors (KURZ and FISHER [1979]): the nf–f eutectic and the facetted phase dendrite require higher supercooling for a given growth rate than a nf–nf eutectic and a nonfacetted dendrite respectively. The former is due the branching difficulties already discussed and the latter is due to the fact that facetted phase dendrites usually grow as a plate or 2D dendrite rather than a paraboloid or 3-D dendrite. Diffusion of solute away from the tip region of a plate dendrite is more difficult and leads to increased supercooling. Thus for the alloy shown, one expects with increasing growth rate (or supercooling): eutectic, β dendrites (with eutectic), eutectic, and α dendrites (with eutectic). This kind of behavior leads to much confusion if a simplistic, purely thermodynamic view of solidification is employed and leads to difficulty in determining eutectic compositions by purely metallographic methods. For different alloy compositions, the various kinetic curves are raised or lowered leading to a description of the full coupled zone. For a system with a nf–nf eutectic the coupled zone is symmetric about the eutectic composition and the formation of dendrites phase is not observed on the "wrong side" of the eutectic. It is useful to note that near the growth rate where a microstructural transition from dendritic to fully eutectic structure takes place, the interdendritic eutectic will not have an average composition equal to the thermodynamic eutectic composition (SHARP and FLEMINGS [1973]).

The methodology of competitive growth outlined above provides an adequate framework to understand the major features of the transition from eutectic to dendritic growth . However more subtle variations in eutectic microstructure occur under conditions close to the transitions that require a more complete analysis of interface stability. JACKSON and HUNT [1966] observed a tilting of lamellae when the growth rate was suddenly increased. ZIMMERMANN *et al.* [1990] have observed oscillations where the widths of the Al lamellae vary while the Al_2Cu lamellae widths remain fixed in the growth direction in Al-rich Al–Al_2Cu off-eutectic alloys. GILL and KURZ [1993] observed another instability where the widths of both lamellae vary in the growth direction. KARMA [1987] succeeded in simulating these instabilities using Monte Carlo methods. He related the appearance of the instability with increasing velocity to critical values of the concentration gradient in the liquid ahead of the interface.

8.1.6. Divorced eutectics

When the liquid remaining between a primary dendritic phase reaches the eutectic composition, eutectic solidification usually occurs. Typically one observes the same eutectic microstructures already described between the dendrite arms especially if the fraction of liquid remaining between the dendrites when the liquid reaches the eutectic composition is large. If however the fraction of liquid remaining is so small that the width is comparable to the eutectic spacing, the characteristic two-phase structure may not be observed. It is easier for the second phase to form as single particle or layer between the dendrites. This occurs more often for a facetted second phase because coupled nf–f eutectics grow with larger spacings and hence require more space to

develop their characteristic morphology. Thus the final solidified microstructure consists of dendrites or cells with interdendritic single phase. This microstructure is sometimes misinterpreted as resulting from a peritectic reaction in complex alloys where the phase diagram is unknown.

8.1.7. Rapid solidification of eutectic alloys

Rapid solidification produces a very rich variety of microstructures for alloys near eutectic compositions. At extremely high rates of solidification and depending on the thermodynamic structure of the T_0 curves, glass formation or extended crystalline solubility is expected as described in § 3.2, fig. 8. How microstructures and phase distributions evolve from the classical microstructures described above as the solidification velocity is increased has been the subject of intense investigation over the past 15 years.

Eutectic theory – In § 7, the general theory presented for dendritic growth included the modifications necessary to treat high growth rates; viz., modifications of the tip stability condition for high Peclet numbers (of order unity) and the inclusion of non-equilibrium interface conditions (solute trapping). For eutectic growth the Peclet number becomes large at relatively low velocity (~10 cm/s) where the effects of solute trapping are not too important. Thus TRIVEDI *et al.* [1987] recomputed the solute field in the liquid in front of a growing eutectic when the Peclet number is large while maintaining the local equilibrium assumption. The theoretical results are similar to those for nf–nf growth at slow velocity except that the function P_E in eq. (105) depends not only on the volume fractions of the solid phases but also on the Peclet number, the shape of the metastable extensions of the liquidus and solidus curves below the eutectic temperature, and the partition coefficients. Also at high velocity the supercooling can become sufficiently large that the temperature dependence of the liquid diffusion coefficient must be considered (BOETTINGER *et al.* [1984]).

These considerations alter the $\lambda_E^2 V$ "constant" at high speed and the spacing vs. velocity relation (fig. 50) in a way that depends strongly on the equilibrium partition coefficients of the two phases, taken to be equal in the TRIVEDI *et al.* [1987] analysis. Two cases are distinguished depending on whether (a) k_0 is close to unity or (b) k_0 is close to zero. In case (a), the eutectic interface temperature is found to approach the solidus temperature of one of the constituent solid phases as the velocity is increased. During this approach, the eutectic spacing actually *increases* with increasing velocity. Indeed eutectic solidification is replaced by single phase planar growth at high velocities. In case (b) the interface temperature can not reach a metastable solidus curve of either phase. The supercooling becomes so large that the temperature dependence of the diffusion coefficient has a major influence and the spacing decreases with velocity faster than predicted by a constant $\lambda_E^2 V$ value. In both cases there exists a maximum velocity for coupled eutectic growth. In case (a) the eutectic is replaced by single phase growth of one of the phases whereas in case (b) glass formation is possible if the interface temperature reaches the glass transition temperature where the melt viscosity (diffusion coefficient) plummets. In fact, the cases where the k_0's are close to zero are those that would exhibit plunging T_0 curves and lead to glass formation as described in § 3. The symmetry of the coupled zone has an impact on these considerations. Glass formation

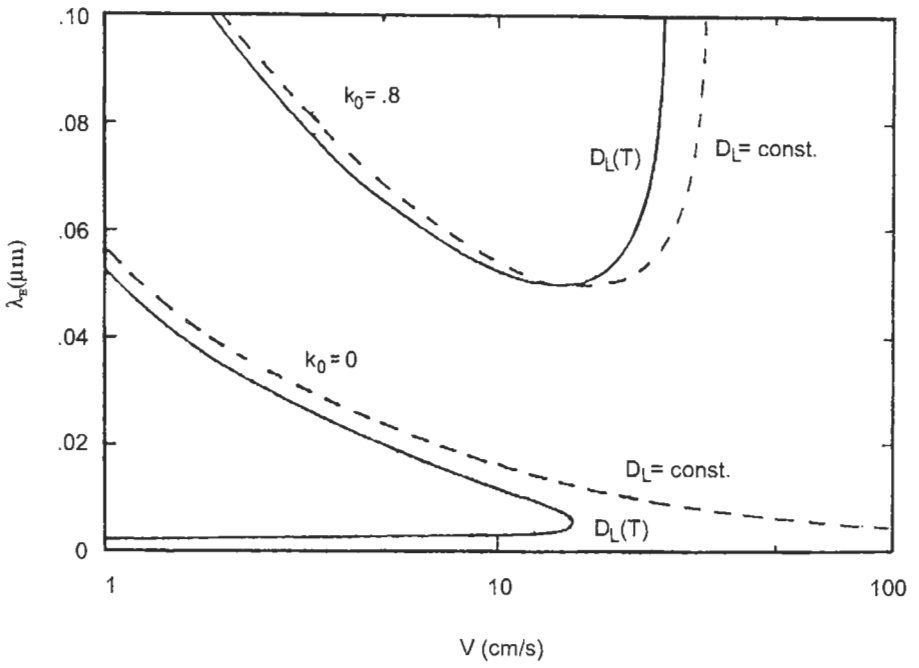

Fig. 50. At high solidification velocities the $\lambda_E^2 V$ "constant" depends on the Peclet number and the relationship between λ_E and V is altered. The changes at high velocity depend strongly on the partition coefficients of the two phases (here taken to be equal). Curves are shown when D_L is assumed constant and when D_L depends on temperature. TRIVEDI *et al.* [1987].

often occurs in systems involving f–nf eutectics. Thus the composition with the smallest maximum growth rate for the eutectic (and hence easiest glass formation) may be shifted towards the direction of the facetted phase. Case (b) may also lead to the formation of a metastable crystalline phase if the eutectic interface temperature drops below the liquidus for such a phase.

Experiments – It is clear from the above that solidification velocity plays a dominant role in controlling microstructure. To control solidification velocity at high rates, surface melting and resolidification employing a moving heat source have been used to create small trails of material that are solidified at speeds close to the scan speed (BOETTINGER *et al.* [1984]). This technique is useful for speeds up to a/d^* where a is the thermal diffusivity and d^* is the diameter of the focussed electron or laser beam. For higher speeds surface melting and resolidification employing a pulsed laser or electron beam must be used. Maps giving the predominant microstructure as a function of speed and alloy composition are then produced. Figure 51 shows such a map for Ag–Cu alloys. Similar maps have been constructed for Al–Al_2Cu (GILL and KURZ [1994]).

In fig. 51 four microstructural domains are obtained: cells/dendrites and eutectic microstructure at slow speed, bands at intermediate speed and microsegregation-free

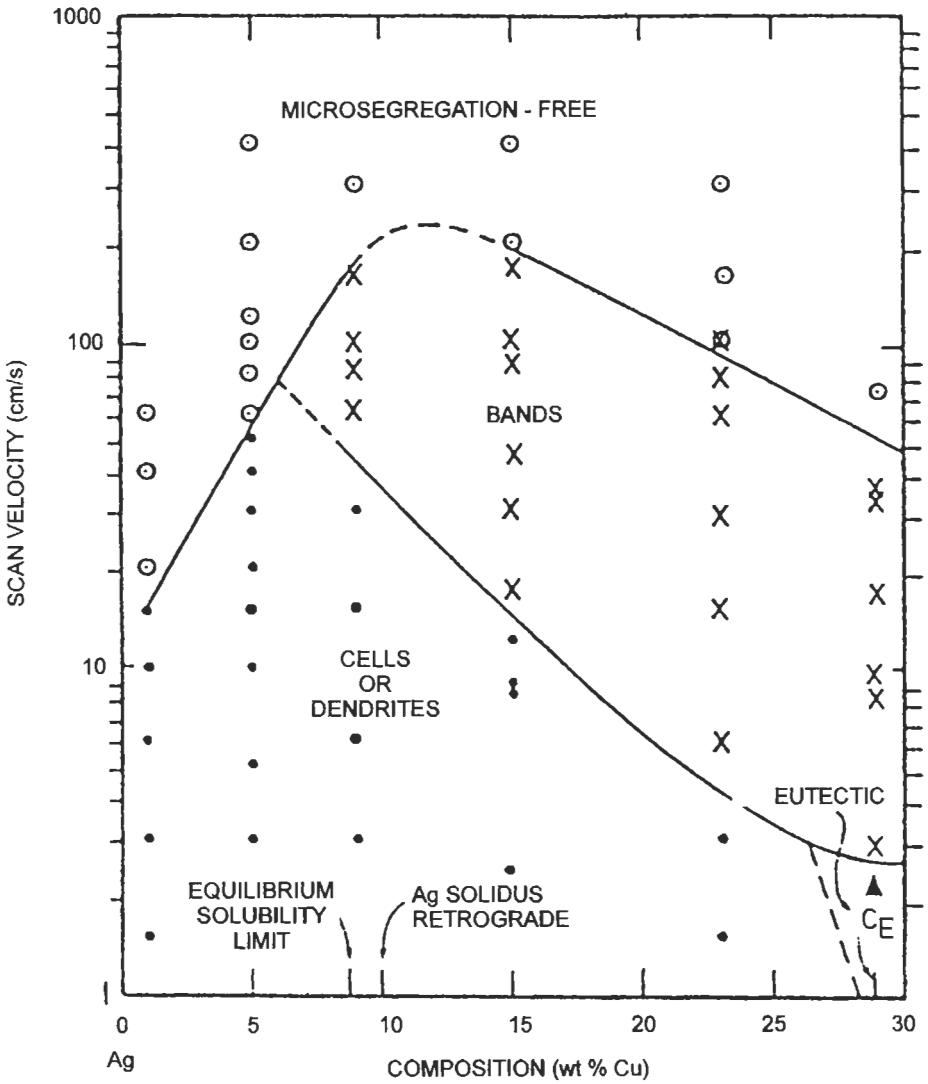

Fig. 51. Experimental results for the variation in microstructure observed for Ag–Cu alloys depending on solidification velocity. BOETTINGER *et al.* [1984].

single phase FCC at high speed. The boundary on the left is due to absolute stability and was described in § 7. Eutectic growth ceases at ~2.5 cm/s generally following the description above except that an intermediate structure of bands is observed before single phase growth dominates at high velocity.

This banded microstructure consist of thin (1 μm) regions *parallel* to the growth front that alternate between cellular solidification and cell-free solidification. The general

character of this structure is due to details of solute trapping (MERCHANT and DAVIS [1990], BRAUN and DAVIS [1991], GREMAUD *et al.* [1991], CARRAD *et al.* [1992]). Ordinarily, interface kinetics requires that the temperature of a planar single phase growth front decrease with increasing velocity. However over the range of velocity where the partition coefficient is approaching unity the interface temperature actually increases with increasing velocity (fig. 20). This reversed behavior is the basic cause of an instability that leads to the banded microstructure. At high speeds in the nondilute Ag–Cu alloys, the microsegregation-free structures are caused by the fact the partition coefficient has gone to unity.

In the Pd–Cu–Si system, maximum growth rates for eutectic and dendritic growth are also observed as shown by BOETTINGER [1981]). However in this case, partitionless growth is not thermodynamically possible and the liquid cools into the glassy state.

Metastable crystalline phase formation – An analysis of growth competition has also been highly successful at explaining observed transitions from microstructures involving stable phases to those involving metastable phases. In the Fe–C system the transition from gray cast iron (Fe-graphite) to white cast iron (Fe–Fe_3C) has been extensively studied (JONES and KURZ [1980]). This transition occurs at relatively slow speeds not normally considered to be rapid. However the same principles can be employed at higher rates for other alloy systems using appropriately modified kinetic laws. The competitive growth analysis must include the dendritic and eutectic growth involving the stable and metastable phases. Figure 52 shows the coupled zones for Al–Al_3Fe (the stable eutectic) and Al–Al_6Fe (the metastable eutectic) summarizing experimental and theoretical work of several groups (ADAM and HOGAN [1972], HUGHES and JONES [1976], GREMAUD *et al.* [1987]). The metastable Al_6Fe phase forms at an increased solidification velocity when the interface temperature drops below about 920K. One of the most striking results of this diagram is the fact that alloys with compositions far on the Fe-rich side of either eutectic can form a microstructure consisting of primary Al at large supercooling and increased velocity; i.e., the Al phase is the first to freeze. Indeed a determination of the powder size dependence of microstructural transitions in Fe-rich Al–Fe alloys from primary Al_3Fe, to eutectic $Al + Al_6Fe$, to primary Al as the powder size decreases is consistent with increasing velocities (supercoolings) calculated for the different size powders (BOETTINGER *et al.* [1986]). Similar microstructural transitions have been observed for other Al based-transition metal alloys. The ability to form a matrix phase of a nf (usually ductile) phase for alloys with a large excess of alloying additions has been a major motivation for alloy development through rapid solidification processing.

8.2. Monotectic solidification

In some metallic systems, the liquid separates into two distinct liquid phases of different composition during cooling. On the phase diagram, the range of temperature and average composition where this separation occurs, as well as the compositions of the two liquid phases are given by a dome-shaped curve that defines the miscibility gap. The maximum temperature of the miscibility gap is called the critical temperature. An example of a miscibility gap is shown in fig. 53 for the Al–In system.

References: p. 830.

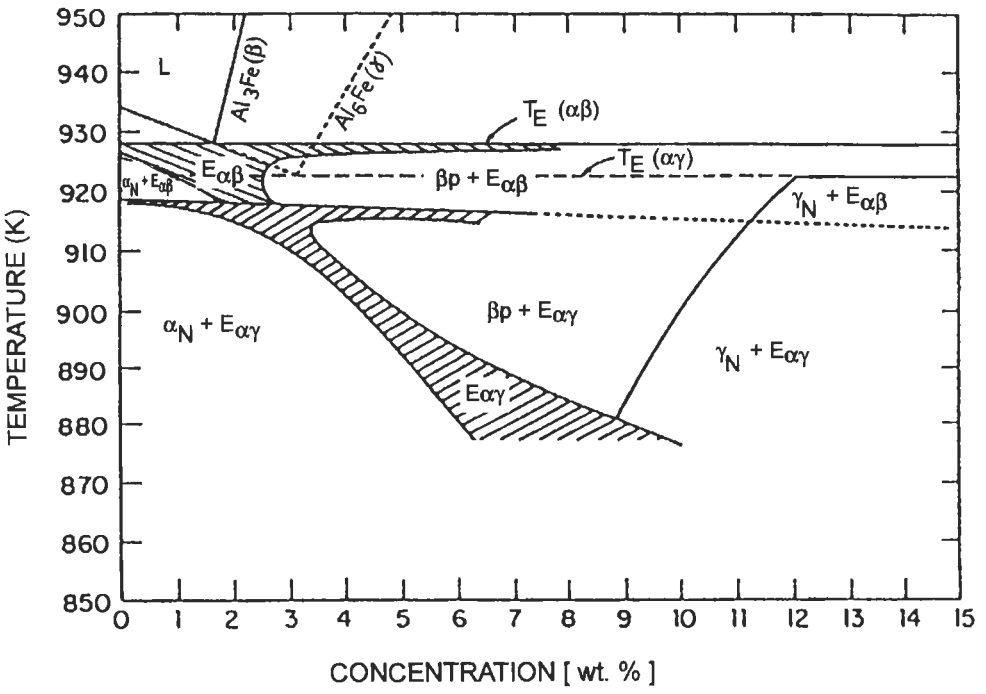

Fig. 52. Theoretical coupled zones for the stable Al–Al_3Fe and metastable Al–Al_6Fe eutectics (hatched). The phases forming outside the coupled zones are also designated. The microstructure present at any value of interface supercooling and average alloy composition has been determine by a competitive growth analysis. TRIVEDI and KURZ [1988]. Subscripts P and N refer to plate (2D) and needle (3-D) dendrites respectively.

Even for alloys outside the miscibility gap, such as for Al-rich alloys in fig. 53, a consideration of the miscibility gap is important in developing an understanding of solidification microstructure. Under ordinary conditions, solidification of these alloys begins with the formation of dendrites of the Al solid phase and enrichment of the liquid remaining between the dendrites with In until the composition reaches the edge of the miscibility gap. This composition (17.3 wt% In, fig. 53) defines the monotectic composition and temperature where the "reaction", liquid $L_1 \rightarrow$ solid S_1 + liquid L_2. Formally this reaction is the same as a eutectic reaction except that on cooling, one of the product phases is a liquid, the liquid defined by the other side of the miscibility gap. At much lower temperatures this liquid usually solidifies in a terminal eutectic reaction $L_2 \rightarrow S_1 + S_2$.

Some sulphide and silicate inclusions in commercial Fe-based alloys are thought to form by monotectic solidification (FLEMINGS [1974]). Free-machining Cu alloys containing Pb also involve this reaction. Considerable research has been focused on directional solidification for fundamental reasons but also because of the potential for producing aligned growth of composites, or (with selective removal of one phase) thin fibers or microfilters (GRUGEL and HELLAWELL [1981]). For this latter purpose it is most

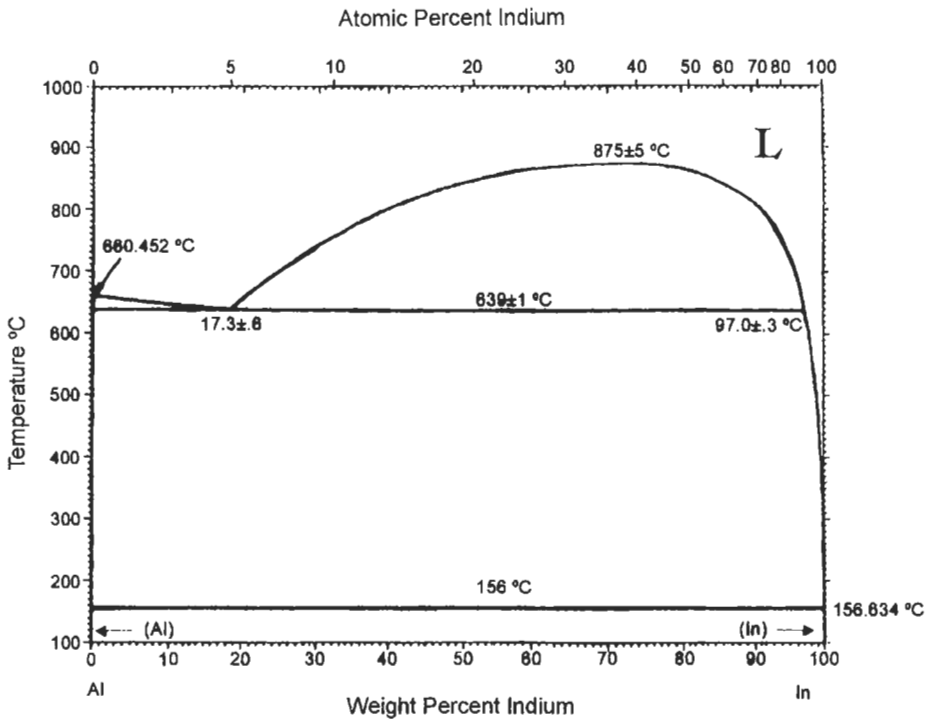

Fig. 53. Al–In monotectic-type diagram. MURRAY [1993b].

important to describe the possibilities of coupled growth of the S_1 and L_2 phases from the L_1 phase of monotectic composition.

8.2.1. Directional solidification of monotectic alloys

As in the case of eutectic solidification, a wide variety of microstructures can be produced by directional solidification of monotectic alloys. Lamellar microstructures are not observed in monotectic systems because the volume fraction of the L_2 phase is usually small. Three types of structures are observed. The first and most interesting and useful, typified by Al–In (GRUGEL and HELLAWELL [1981]), is a regular fibrous or composite structure that consists of closely packed liquid tubes of a uniform diameter embedded in a matrix of the solid phase. These liquid tubes solidify at much lower temperatures to solid rods of In by a divorced eutectic reaction. If the growth rate is increased, the distance between rods decreases, and the structure gives way to a second type of microstructure that consists of discrete droplets of L_2 embedded in a solid matrix. The third type, typified by Cu–Pb (LIVINGSTON and CLINE [1969]), is more irregular consisting of interconnected globules that take on some degree of alignment as the growth rate is increased. Although the L_2 tubes formed at a monotectic reaction are susceptible to

ripening and spheroidization during subsequent cooling, the droplet and irregular structures are not thought to form by coarsening (GRUGEL and HELLAWELL [1981]).

One of the most important considerations for understanding the different microstructures comes from a consideration of whether a stable triple junction can exist between L_1, L_2, and S_1 (CHADWICK [1965]). This condition can only occur if

$$\gamma_{S_1L_1} + \gamma_{L_1L_2} > \gamma_{S_1L_2}. \tag{111}$$

If the inequality is satisfied, regular fibrous structures can be obtained. The eutectic theory for rod growth can then be applied although some modifications are required to treat the increased diffusion in the L_2 phase (GRUGEL and HELLAWELL [1981]). When this inequality is not satisfied, L_2 does not "wet" S_1, and L_1 will tend to coat the interface between L_2 and S_1; i.e., L_1 preferentially wets S_1 to the exclusion of L_2. CAHN [1979] calls this the *perfect wetting case* and during monotectic growth, the L_2 phase will form droplets in the L_1 phase just ahead of the growing S_1 interface. As growth proceeds, the droplets are pushed by the interface and the size of the droplets increase until they reach a critical size where they are engulfed into the growing S_1 solid. The critical size for engulfment is determined by microscopic fluid flow around the droplet. As the solidification velocity is increased, irregular semicontinuous liquid rods can be partially engulfed in the solid as shown schematically in fig. 54. This irregular engulfment is believed to be the origin of the irregular globular microstructure typified by Cu–Pb.

CAHN [1979] showed that in monotectic systems, the perfect wetting case should be expected if the temperature difference between the monotectic temperature and the critical temperature of the miscibility gap is small. Thus irregular composite structures are formed in these systems. When the temperature difference is large, perfect wetting does not occur, a stable triple junction can exist, and regular composite growth is expected. This idea was confirmed by the addition of a ternary element to a binary monotectic alloy. This addition altered the height of the miscibility gap and hence the wetting behavior (GRUGEL and HELLAWELL [1981]). GRUGEL *et al.* [1984] found experimentally that the border between systems with regular and irregular composite

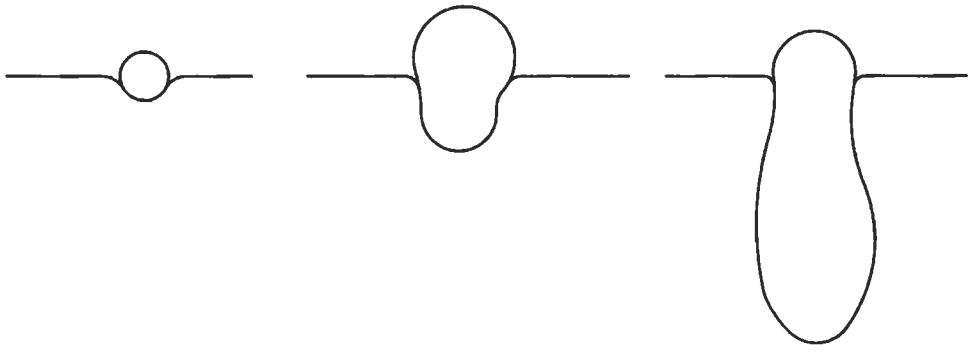

Fig. 54. Schematic sequence to show liquid particle pushing, growth, and engulfment during irregular monotectic growth. GRUGEL *et al.* [1984].

structures occurred when the ratio of the monotectic temperature to the critical temperature is approximately 0.9.

For regular fibrous growth, the spacing varies inversely with the square root of the velocity. GRUGEL *et al.* [1984] showed that the "(spacing)^2 velocity" constant was about an order of magnitude larger for irregular growth than for regular growth. DERBY and FAVIER [1983] have presented a different model for the occurrence of regular and irregular structures similar to those used for irregular eutectics. KAMIO *et al.* [1991] have shown that the value of the temperature gradient has a large effect on the transitions between aligned growth and the formation of droplets.

GRUGEL and HELLAWELL [1981] also examined whether composites could be grown for compositions different than the exact monotectic composition. They found that the dendritic growth of the S_1 phase could be suppressed by sufficiently large values of G_L/V to permit planar composite growth just as for eutectic alloys. Attempts to grow composites with compositions on the other side of the monotectic (within the miscibility gap) failed due to convective instabilities. Reduced gravity experiments have been employed by ANDREWS *et al.* [1992] to avoid these difficulties.

8.2.2. Rapid solidification of monotectic alloys

Some alloys whose phase diagrams do not contain a miscibility gap or a monotectic reaction form microstructures consisting of droplets embedded in a matrix of a primary phase after rapid solidification. If the liquidus curve has a portion where the slope is close to zero, a metastable miscibility gap lies just beneath the liquidus curve. In fact the temperature difference between the liquidus and the metastable critical point is proportional to the liquidus slope (PEREPEZKO and BOETTINGER [1983b]). Thus with the supercooling inherent in many rapid solidification processes, alloy microstructure can be influenced by the presence of the metastable miscibility gap and its associated metastable monotectic reaction. The microstructure of rapidly solidified Al–Be alloys, which consists of fine Be particles in an Al matrix, have been interpreted in this manner (ELMER *et al.* [1994]). In fact even some slowly cooled alloys can exhibit microstructures characteristic of monotectic solidification even though there is no apparent miscibility gap. VERHOEVEN and GIBSON [1978] showed that oxygen impurities raise the metastable miscibility gap in the Cu–Nb system so that it becomes stable and produces droplet microstructures.

8.3. Peritectic solidification

The phase diagram for the Pb–Bi system is shown in fig. 55a. If a liquid with 33% Bi is cooled, and global equilibrium could be maintained (see § 3), the alloy would be composed of $L+\alpha$ at a temperature just above the peritectic temperature of 184°C, denoted T_p, and would be composed of single phase β just below T_p. This gives rise to the notion of a peritectic "reaction" that occurs on cooling that is written as $L+\alpha \rightarrow \beta$. However the diffusion required to accomplish this "reaction" during any realistic solidification process greatly reduces the amount of the β phase formed.

References: p. 830.

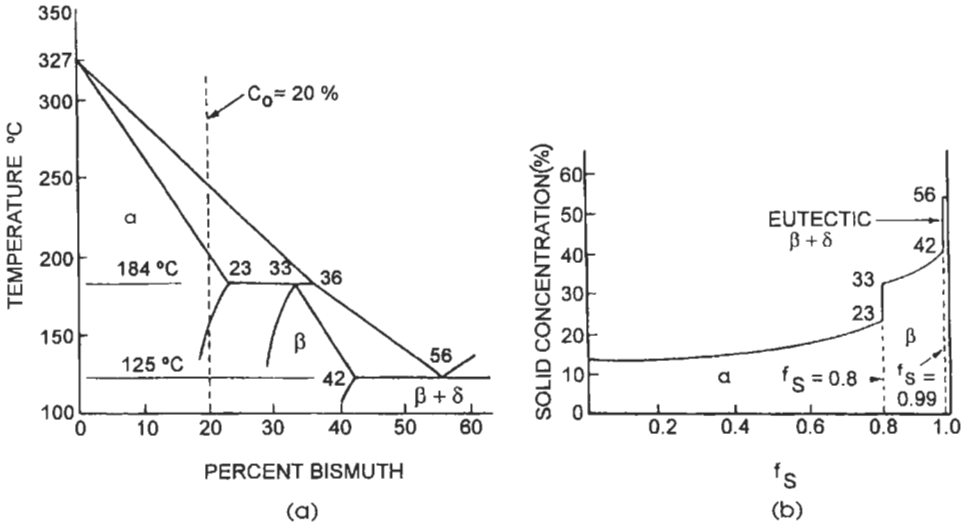

Fig. 55. (a) Pb–Bi peritectic phase diagram. (b) Concentration (% Bi) in the solid according to a Scheil model of solidification. FLEMINGS [1974].

8.3.1. Peritectic solidification during dendritic growth

Under conditions where the α phase grows dendritically, the β phase will usually begin to form along the surface of the α phase. Although the β phase can be formed by three mechanisms, the most important during continuous cooling is the formation of β directly from the melt. The simplest way to treat this situation is to employ the Scheil approach in a small volume of the interdendritic liquid with the usual assumptions: local equilibrium at the solid–liquid interface, uniform liquid composition at each instant (temperature) and no solid diffusion. At small fraction solid, solidification of α phase occurs in the normal way with build up of solute in the liquid between the dendrites following the Scheil equation. When the liquid composition reaches 36%Bi, denoted C_p, solidification switches from the α phase to the β phase. A new value of the partition coefficient given by the β liquidus and solidus must then be employed in the Scheil equation to follow the continued enrichment of the liquid composition in the component Bi. Often one must employ a concentration dependent partition coefficient for the β phase in peritectic systems that requires numerical solution of the differential form of the Scheil equation. The solid composition and the fraction of α and β phases formed by this mechanism using the Scheil model are shown in fig. 55b. For Pb–Bi alloys the final solidification product is eutectic. One notes that using the Scheil approach, *any* alloy composition to the left of 36% will contain α phase in the solidified microstructure. Many systems involve a cascade of peritectic reactions, with solidification switching from phase to phase forming separate layers around the initial α dendrite.

The second and third mechanisms for the formation of β are less important and more difficult to model. The geometry and connectivity of the L, α and β phases determine

their relative importance. Both decrease the fraction of α phase from that predicted above. They have been referred to as the *peritectic reaction* and the *peritectic transformation* by KERR *et al.* [1974]. The peritectic reaction requires that all three phases be in contact with each other. This occurs in the vicinity of the liquid–α–β triple junction and involves partial dissolution of the α phase and solidification of the β by diffusion of solute through the liquid from the L–β boundary to the L–α boundary (fig. 56a). HILLERT [1979] gives an approximate analysis of this process.

The third way that β phase can form, the peritectic transformation, involves solid state diffusion and the motion of the α–β interface during cooling as shown in fig. 56b. This mechanism is very important when the solid diffusion coefficient is large; e.g., for interstitial solutes such as carbon in Fe. Indeed the peritectic reaction in low carbon

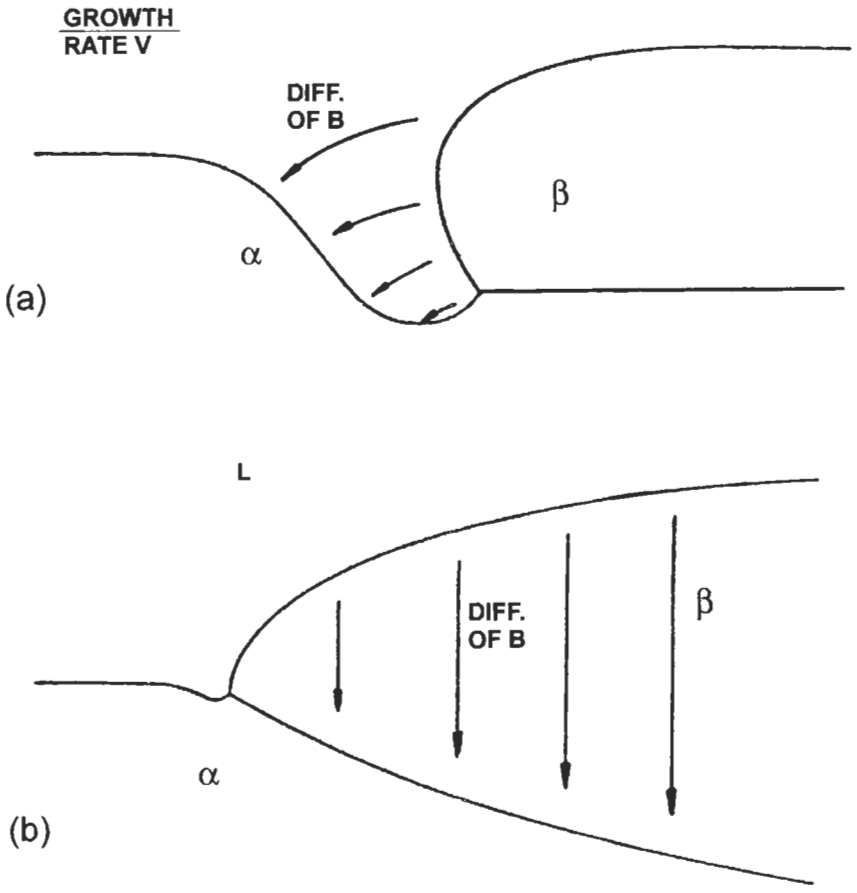

Fig. 56. Peritectic reaction and peritectic transformation on the side of an α dendrite. (a) in the peritectic reaction a second solid phase, β, grows along the surface of the primary phase α by diffusion through the liquid. (b) In the peritectic transformation, diffusion of B atoms through the already formed solid phase β occurs. (After HILLERT [1979]).

References: p. 830.

steels ($L+\delta$–Fe $\rightarrow \gamma$–Fe) seems to go to completion; i.e., no δ–Fe is observed in these alloys. The diffusion problem that governs the motion of the α–β interface involves long range transport of solute from the liquid across the β phase to the α–β interface. At this interface, this flow of solute causes the α phase to dissolve at the expense of the growing β phase. The analysis must use compositions for the interfaces that are given by the $L+\beta$ and $\alpha+\beta$ two phase fields on the phase diagram. HILLERT [1979] has given an approximation for the growth of the β phase by solid state diffusion. Due to the long range diffusion, the thickness of the β phase increases with the square root of time if the interface compositions and diffusion coefficients can be assumed to be independent of temperature.

FREDRIKSSON and NYLEN [1982] have measured the fraction of L, α, and β phases as a function of distance behind the peritectic isotherm by quenching various alloys during directional solidification. The relative contributions of the three mechanisms are analyzed and compared to the measurements. In one alloy (Al–Mn) the β phase did not grow along the L–α interface but grew independently from the melt.

8.3.2. Aligned peritectic growth

Several attempts have been made to grow aligned composites of peritectic alloys by directional solidification. By increasing the temperature gradient or slowing the solidification velocity, it is possible to suppress the dendritic growth of the α phase during directional solidification in peritectic alloys with narrow freezing ranges. When cellular growth of the α phase occurs for alloys whose overall composition falls within the $(\alpha+\beta)$ field, a coarse aligned $(\alpha+\beta)$ two-phase structure can be formed (BOETTINGER [1974]; BRODY and DAVID [1979]).

More interesting were attempts to achieve coupled growth of the α and β phases to produce a fine two-phase structure. It was thought that if the G_L/V ratio were large enough to suppress cellular solidification of the α phase and force a planar solidification front that coupled growth of the two solid phases might be possible. This would also require that the composition of the liquid near the interface be maintained near C_p, a liquid composition from which both α and β could form. However coupled growth has never been observed in peritectic alloys. Instead, coarse alternating bands of α and β form from the melt. (BOETTINGER [1974]; OSTROWSKI and LANGER [1979]; TITCHENER and SPITTLE ([1975]).

BOETTINGER [1974] analyzed the supercooling-velocity-spacing relation for hypothetical coupled growth in a peritectic alloy and showed that it was intrinsically unstable. The formation of bands can be understood through an examination of the stable and metastable liquidus and solidus curves for the α and β phases (HILLERT [1979]). In fig. 57, an alloy of the indicated composition can solidify to single phase α at a planar interface at temperature T_1 if the β phase does not nucleate. Alternately the same alloy composition can solidify to single phase β at a planar interface temperature at T_2 if α does not nucleate. Thus two steady state solidification situations are possible. However each situation is precarious in that nucleation of the other phase can occur in front of the growing phase. The system is extremely sensitive to minor growth rate fluctuations that leads to solidification that alternates between α and β. This situation has been recently analyzed by TRIVEDI [1995].

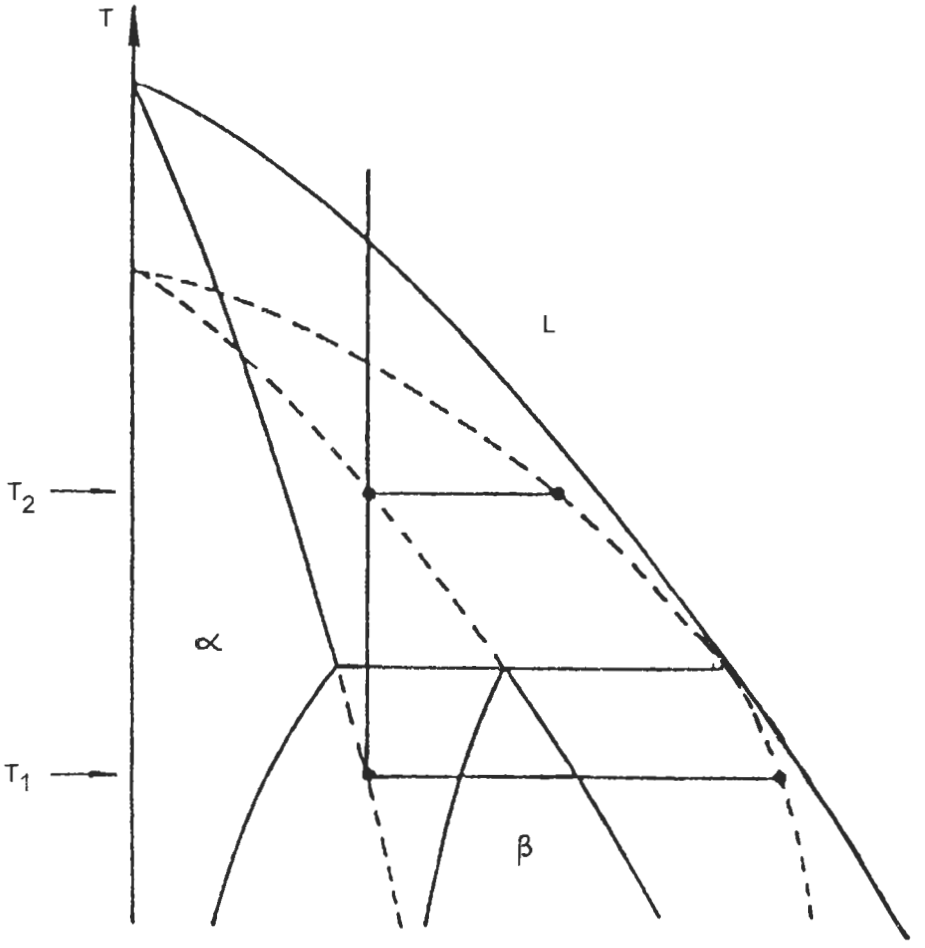

Fig. 57. Peritectic phase diagram with metastable extensions of α and β liquidus and solidus curves below and above the peritectic temperature respectively. For an alloy of the composition of the vertical line, planar steady-state growth of either α or β is possible at the temperatures T_1 and T_2 respectively. After HILLERT [1979].

8.3.3. Rapid solidification of peritectic systems

As shown in fig. 57, the metastable liquidus curve of the α phase below the peritectic temperature must lie below the stable β liquidus. However when compared to a eutectic system, the metastable liquidus is relatively close to the stable β liquidus. Thus there exists considerable opportunity for the formation of the α phase directly from the melt at modest levels of supercooling at compositions where it is not expected. Whether or not this happens depends on the competition of nucleation and growth kinetics for the α and β phases. An example of this kind of behavior is found in the classic experiments of CECH [1956] on solidification of small droplets (3–30 μm) of Fe–30%Ni alloys in a drop tube. This system contains a peritectic reaction, L + bcc → fcc. Experiments showed that

bcc was formed from the melt (and not by solid state transformation) at compositions with high Ni content where only fcc should have formed. In contradiction to the experimental facts, analysis of the dendritic growth kinetics of the competing fcc and bcc structures showed that fcc would be the favored product phase at all supercoolings for Fe–30%Ni (BOETTINGER [1988]). This result is due primarily to the fact that the partition coefficient for bcc is much larger than for fcc. On the other hand, analysis of the nucleation behavior indicates that bcc is favored over fcc if the nucleation is homogeneous or if the contact angle on heterogeneities is greater than about 45° (KELLY and VANDERSANDE [1987]). Thus only nucleation can explain the observed bcc structure.

In alloys containing a cascade of peritectic reactions, the close proximity of stable and metastable liquidus curves can also explain why one or more phases may be skipped over in the layer structure that coats the initial dendritic phase in rapidly solidified alloys.

9. *Fluid flow and casting structure*

The flow of molten metal or alloy is an important consideration during casting. Although the requirements for mold filling especially in narrow cross sections have been considered for centuries, the importance of flow during the freezing process has been recognized much more recently. In this section we consider: i) the general origins of fluid flow in castings; ii) the development of casting macrostructure (grain structure); iii) the macrosegregation observed in ingots and castings due to flow in the mushy zone; and iv) the formation of porosity and inclusions. Finally, the foundry concept of *fluidity* associated with the mould filling capability of alloys will be described.

9.1. Transport processes and fluid flow in casting

There are many sources of material transport that can occur during solidification: i) residual flow due to mold filling, ii) thermal and solute driven bouyancy convection, iii) convection due to expansion or contraction upon solidification, iv) floating or settling of free crystals, v) dendritic breakage and transport, vi) convection driven by thermocapillary forces, vii) pushing of equiaxed crystals by the columnar solidification front, viii) external forces (pressure, rotation, magnetic fields).

COLE [1971] and WEINBERG [1975] extensively studied the flow in the fully liquid part of castings. Weinberg's use of radioactive tracers techniques proved to be very sensitive and overcame the handicap of other experiments performed with transparent model liquids having much lower thermal conductivity than metals. Convection has the largest effect on thermal transport and macrostructure when the S–L interface (position of dendrite tips) is parallel to the gravity vector. Thus horizontal solidification is dramatically affected by convection due to the horizontal temperature gradients. Flows in metals and the heat transfer due to the flow can be reduced by the application of a magnetic field due to the induced eddy current that exerts a body force on the fluid. Rotation of ingots gives a effect similar to the application of a magnetic field; here the body force is a Coriolis force that deflects particles of fluid in a direction normal to the axis of rotation, and normal to the direction of fluid motion. On the other hand, an

increase in heat transfer can be accomplished by vigorous fluid motion near the S–L interface. Rotation or oscillations of the crucible, a rotating magnetic field, or electromagnetic field interactions can be used for this purpose (COLE [1971]).

On a more microscopic scale, fluid flow due to a variety of causes has also been associated with dendrite fragmentation and subsequent crystal multiplication during solidification (JACKSON *et al.* [1966] and O'HARA and TILLER [1967]). In alloys the interaction of natural or forced convection with the dendritic substructure can be rationalized as follows. When secondary branches form, they must grow through the solute-rich layer that exists around the primary stalk. The initial growth through this layer is slow. After the branch passes through the layer, it enters the bulk liquid of lower solute concentration and grows more rapidly. The result is a thin neck of the secondary branch near the primary stalk. Any slight increase in the local temperature or shear force due to local fluid flow can detach portions of the dendrites. These crystals may be able to survive in other portions of the liquid and, if the thermal and constitutional conditions are appropiate, subsequently grow. This leads us into a discussion of ingot macrostructure.

9.2. Ingot structure

The classical representation of ingot macrostructure shows three distinct zones: the chill zone, which is a peripheral region near the mould surface composed of small equiaxed grains, the columnar zone and a central equiaxed zone. Inside each grain a substructure of cells, dendrites, and/or eutectic exists. Fluid flow during solidification affects the origin and development of the three zones. Extensive research has been performed because of the important influence of macro- and microstructure of ingots and castings upon mechanical properties.

9.2.1. Chill zone

The formation of the chill zone structure involves complex interactions of liquid metal flow, metal-mould heat transfer, nucleation catalysis and dendritic growth. CHALMERS [1964] suggested that chill zone grains could form by independent nucleation events or by a *copious nucleation* mechanism. BOWER and FLEMINGS [1967], BILONI and MORANDO [1968] and PRATES and BILONI [1972] experimentally simulated the thermal conditions existing in the chill zone using thin samples filled quickly by a vacuum technique. By controlling the fluid flow, BOWER and FLEMINGS [1967] found a dendritic substructure in the chill grains and established that a *grain multiplication (fragmentation)* mechanism induced by melt turbulence during pouring was quite important. They used moulds coated with lampblack which drastically reduces the value of h_i compared to an uncoated Cu mould. In contrast BILONI and CHALMERS [1965] had earlier found chill grains with a different substructure with uncoated moulds. Predendritic nuclei with solute-rich cores were formed by partitionless solidification. BILONI and MORANDO [1968] used an identical device as BOWER and FLEMINGS [1967], but coated only part of the chill surface with lamp black (fig. 58). The region with lampblack had the same substructure as was previously observed by BOWER and FLEMINGS [1967], but the chill grains in the region without the lampblack were smaller and contained a predendritic

References: p. 830.

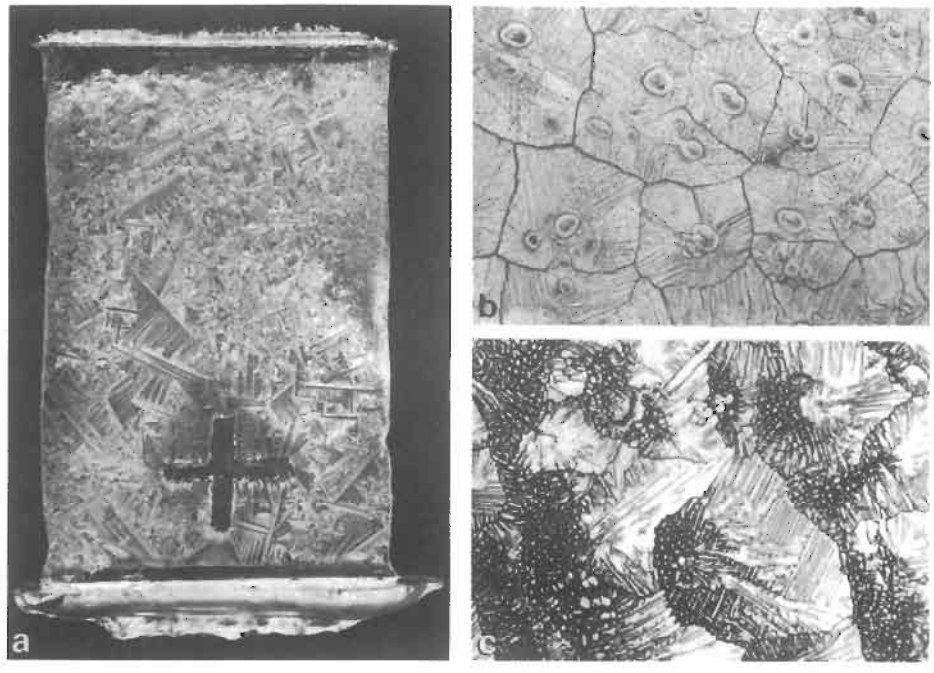

Fig. 58. (a) Chill plate of Al-1% Cu cast in a copper mould coated with lamp black, except in the area of the cross which appears with different reflectivity. (b) Substructure corresponding to the uncoated region of fig. 58a). Each grain has a predendritic region as origin. (c) Substructure corresponding to the coated region; notice the "cells", probably produced by a multipication mechanism, as the origin of the dendrites. BILONI [1980].

substructure. Thus the importance of local values of the heat transfer cannot be neglected even though the grain multiplication mechanism by fragmentation can be active. BILONI [1980] reviewed the origin and development of the chill zone.

The roughness of the mould surface as affected by polishing, machining, or coating can also be important (PRATES and BILONI [1972]). A suitable microprofile design of the surface can promote a specific distribution of predendritic nuclei and fig. 59 (MORALES *et al.* [1979]) shows how the coating microprofile can influence the columnar grains originating from the chill zone.

In summary, a rough surface, a very cold mould, a low pouring temperature and convection currents that stir the melt, all favour a fine grain size in the chill zone through both nucleation and multiplication mechanisms.

9.2.2. Columnar zone

Further from the mould surface, the grain structure evolves into columnar grains growing roughly perpendicular to the mould surface. The origin of the columnar zone was first analyzed by WALTON and CHALMERS [1959]. These authors mention the competitive mechanism through which the favourably oriented grains eliminate those less

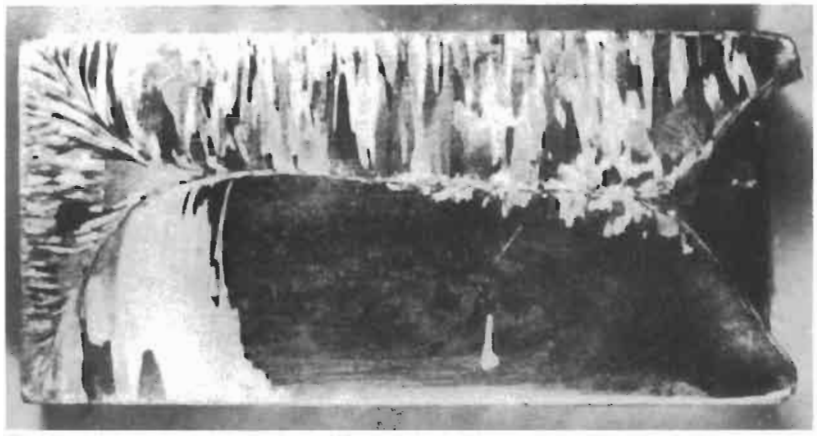

Fig. 59. Longitudinal section of an ingot poured from the bottom (shown to the left), after macroetch. The difference in grain size is due to mould walls with different microgeometries. The small columnar grains start at the asperities of an alumina mould coating presenting a controlled microgeometry; the very large grain started from a wall coated with a very smooth film of lamp black. MORALES *et al.* [1979].

favourably oriented and a texture arises. In fcc and bcc alloys, a preferred <100> orientation is characteristic of the structure.

Figure 60 (RAPPAZ and GANDIN [1993]) schematically shows the competetive columnar growth of three grains. Some equiaxed grains that nucleate and grow in front of the columnar zone are also depicted which will be discussed later. The columnar grains on the left and on the right contain dendrites whose <100> crystallographic orientations are nearly perpendicular to the liquidus isotherm. These dendrites grow with the same velocity V_L, as that of the isotherms. The grain in the middle of the figure, having a deviation of its <100> crystalographic direction from the heat flow direction, grows with a velocity $V_\theta = V_L/\cos\theta$ that is larger than V_L. According to the growth kinetic model of the dendrite tip for constrained growth (§ 7), the faster growing (misoriented) dendrites are characterized by a larger tip supercooling. Thus the tips lie behind those of the better oriented grains. RAPPAZ and GANDIN [1993] give the details of the elimination of the misoriented grains according to the convergence or divergence of the neighbouring grains and the ability or inability to form tertiary arms as shown in fig. 60.

After elimination of misoriented grains, the growth of the columnar front in a casting can be modelled using a macroscopic heat code that solves eq. (7). This requires a fraction solid versus temperature (and other variables) relationship obtained from one of the various dendritic microsegregation models presented in section 7.3. FLOOD and HUNT [1987a] give one approach and the various methods are summarized by RAPPAZ and STEFANESCU [1988] and RAPPAZ [1989].

Several researchers have attempted to provide a more detailed numerical procedure to model the development of the columnar zone including the variation of the transverse

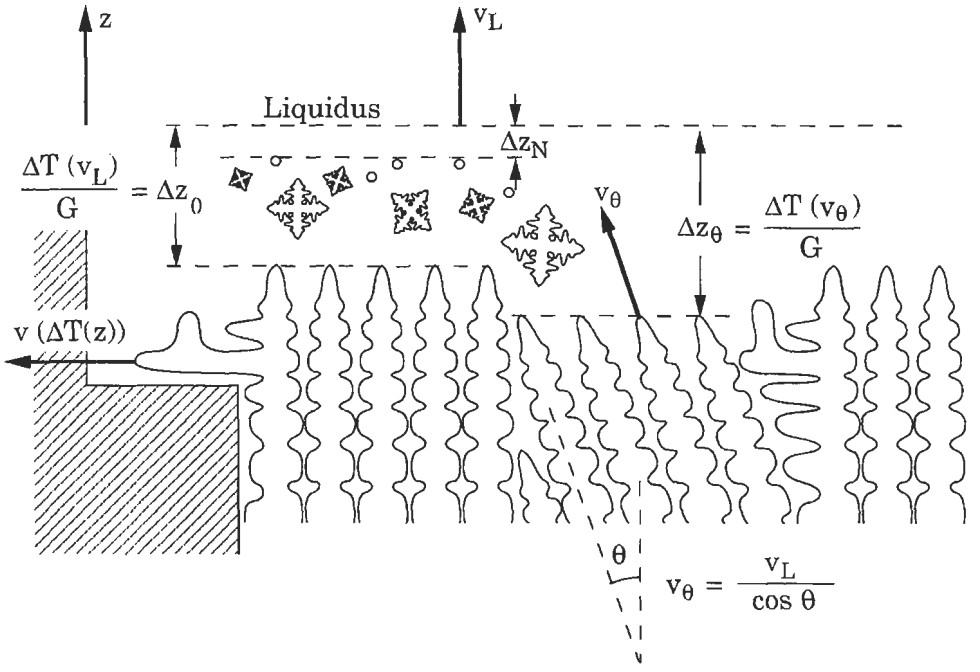

Fig. 60. Competing processes during directional dendritic growth: development of preferred orientation in the columnar region, formation of equiaxed grains ahead of the columnar front. RAPPAZ and GANDIN [1993].

size of columnar grains described by CHALMERS [1964] and to deal with other issues of crystalline anisotropy, and texture formation. BROWN and SPITTLE [1989] and ZHU and SMITH [1992a], [1992b] used Monte-Carlo methods to model the effect of anisotropy. RAPPAZ and GANDIN [1993] developed what they call a *probabilistic model* that includes an orientation variable for each grain and keeps track of the developing grain shape using a cellular automaton technique.

These numerical methods have been able to be compute realistic grain macrostructures as well as crystallographic texture. As predicted by the model, the orientation distribution of the columnar grains narrows as the distance from the mould surface increases and the comparison with the WALTON and CHALMERS [1959] experiments is acceptable. Additionally, the selection of the columnar grains at the chill-columnar transition as well as the columnar extension is also succesfully predicted. This approach is also useful for modeling the grain competition in the grain selector during directional solidification (DS) for the production of modern turbine blades (RAPPAZ and GANDIN [1994]). It must be remembered however, that the success of this approach depends strongly on the input of an accurate nucleation law that generally must be determined from experiments.

Fluid flow can also affect the columnar zone structure. In conventional ingots,

columnar growth may not be perpendicular to the mould wall if convection sweeps past the S–L interface due to horizontal temperature gradients. If convection is diminished through magnetic fields or mould rotation, perpendicular columnar growth can be restored (COLE [1971]).

When columnar growth occurs in concentrated alloys with a low temperature gradient, a substructure other than cellular-dendritic can sometimes appear. Dendrite groups rather than individual dendrites comprise the solidification front. These groups have been called *superdendrites*, where apparently the normal coupling that establishes the primary spacing between dendrites becomes unstable, with certain dendrites grow ahead of their neighbors. (COLE and BOLLING [1968]; FAINSTEIN–PEDRAZA and BOLLING [1975]).

In aluminum-base alloys and under some conditions, another unusual structure can appear. Laminar grains grow from a single origin and form "colonies". These structures have different names in the literature but most commonly are called *feather crystals*. Generally, they appear in continuous or semicontinuous castings and in welding processes. Occasionally they are observed in conventional casting. BILONI [1980], [1983] describes the current knowledge about this structure, which is open to further research.

9.2.3. Equiaxed zone

Equiaxed grains grow ahead of the columnar dendrites and the columnar to equiaxed transition (CET) occurs when these equiaxed grains are sufficient in size and number to impede the advance of the columnar front. Evidence for the collision of the columnar front with equiaxed grains can be found in the work of BILONI and CHALMERS [1965] and BILONI [1968]. When this collision occurs, the heat flow direction in the equiaxed grains changes from radial to unidirectional and a modification of the dendritic substructure can be observed by careful metallography in the solidified samples.

The situation to be modelled therefore corresponds to that shown in fig. 60. The major challenges to predict the columnar to equiaxed transition and the size of the equiaxed zone in castings involve an accurate description of the source of the nuclei and an accurate description of the growth rates of the columnar and equiaxed crystals under the prevailing conditions.

9.2.3.1. Origin of the equiaxed nuclei. Three principal sources of nuclei can be considered. i) *Constitutional Supercooling (CS)* driving heterogeneous nucleation (WINEGARD and CHALMERS [1954]). Because the tips of the dendrites in the columnar grains are at a temperature below the bulk alloy liquidus temperature a region of liquid exists where hetrogenous nuclei may become active. ii) *Big-Bang* mechanism: Equiaxed grains grow from predendritic shaped crystals formed during pouring at or near the mould walls. These crystals are carried into the bulk by fluid flow with some surviving until the superheat has been removed (CHALMERS [1963]). As outlined in § 9.2.1., the origin of the grains could be either by nucleation events or crystal multiplication mechanisms. OHNO *et al.* [1971] has proposed a *separation theory* (OHNO [1970]) for the origin of the equiaxed grains by the big bang mechanism. iii) *Dendritic fragmentation* occurring from the columnar grains (JACKSON *et al.* [1966]), (O'HARA and TILLER [1967]) or from dendritic crystals nucleated at the top of the ingot as a result of the radiation cooling occurring in that region (SOUTHIN [1967]).

References: p. 830.

Many experiments have been performed in metallic alloys and transparent analogues to decide the nucleation mechanism responsible for the equiaxed zone. The available information suggests that in conventional castings there is strong evidence to support the big bang and fragmentation mechanisms, probably a combination of both, in most of the cases where convection is present (MORANDO *et al.* [1970], FLOOD and HUNT [1988]). In these circumstances, the C.S. mechanism would seem not to have a large enough contribution except in the presence of very efficient heterogeneous nuclei. When upward directional solidification experiments are performed and a near-perfect adiabatic lateral mould walls exist, convection is minimized, and the only possible mechanism for equiaxed grain formation is C.S. However, the complete elimination of convection is quite difficult even in this type of growth (CHANG and BROWN [1983], ADORNATO and BROWN [1987]).

9.2.3.2. Columnar to equiaxed transition (CET). If a reliable nucleation model were available, and convection could be ignored, any one of several models could be employed to predict the columnar to equiaxed transition. The model of HUNT [1984] uses selected columnar growth and nucleation models to determine whether the structure will be fully equiaxed or fully columnar. The results depend on whether the temperature gradient is smaller or larger respectively than a critical value given by

$$G_L = 0.617 N_0^{1/2} \left[1 - \left(\frac{\Delta T_n}{\Delta T_c} \right)^3 \right] \Delta T_c, \tag{112}$$

where N_o = density of nucleating sites, ΔT_n = supercooling required for heterogeneous nucleation and ΔT_c = supercooling of the dendrite tips in the columnar grain. This analysis was expanded by FLOOD and HUNT [1987b]. The experimental results by ZIV and WEINBERG [1989] are in close agreement with eq. (112) for Al–3%Cu. Factors which promote a columnar to equiaxed transition by this mechanism are: large solute content (increases the value of ΔT_c for fixed growth conditions), low temperature gradient, which increases the size of the supercooled region in front of the dendritic tips, a small value for ΔT_n (potent nucleation sites), and a large number of nuclei. Hunt's model ignores many complexities of the dendritic growth of equiaxed grains and nucleation was assumed to take place at a single temperature rather than over a range of temperature. It therefore cannot predict the effect of solidification conditions on equiaxed grain size (KERR and VILLAFUERTE [1992]). More detailed models of equiaxed growth employing empirical nucleation laws have been combined with numerical solutions of the heat flow to predict the grain size of fully equiaxed structures (THEVOZ *et al.* [1989], RAPPAZ [1989], STEPHANESCU *et al.* [1990]). These more detailed analyses could be used to predict the columnar to equiaxed transtition. FLOOD and HUNT [1988] have critically reviewed the models and experiments of several researchers.

RAPPAZ and GANDIN [1993] have used the probabalistic model described in § 9.2.2 to simulate the columnar to equiaxed transition. Figure 61a) corresponds to the simulation of the final grain structure of an Al–5%Si casting with no temperature gradients when cooled at 2.3 K/s. Figure 61b) corresponds to an Al–7%Si casting cooled at 2.3 K/s and fig. 61c) to an Al–7%Si casting cooled at 7.0K/s. Comparisons among the

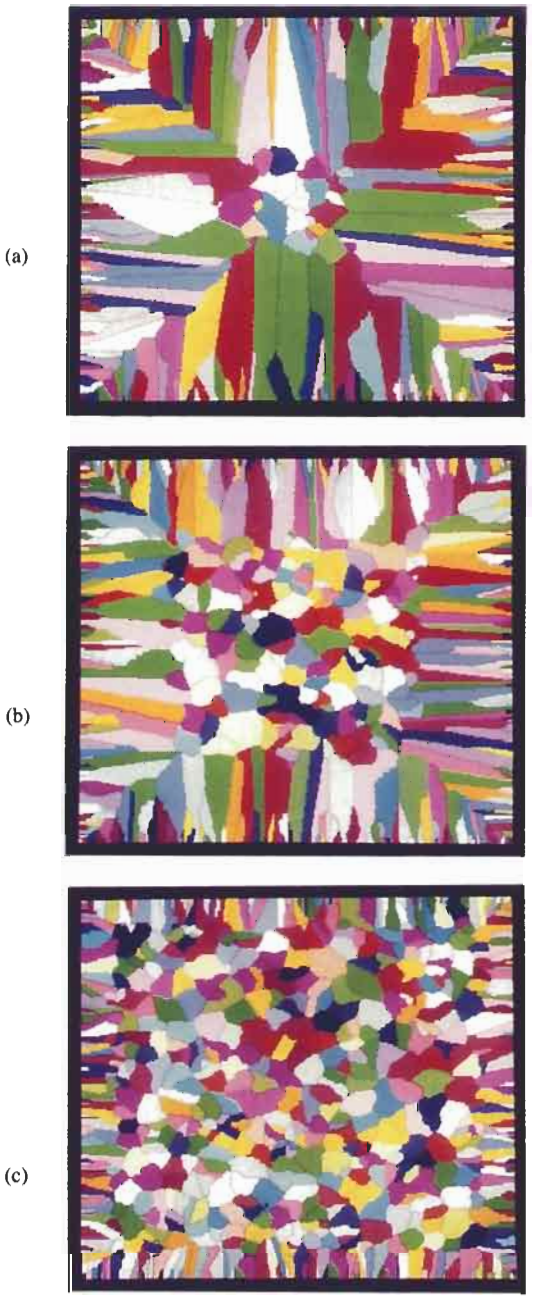

Fig. 61. Simulation of columnar and equiaxed structures by RAPPAZ and GANDIN [1993].

three figures show the effect of the alloy composition and cooling rate upon the grain structure. Very recently RAPPAZ and GANDIN [1994] presented a very comprehensive review of the modeling of grain structure formation in solidification processes.

A set of experiment were performed by BILONI and CHALMERS [1968] which showed that the CET could be stimulated by mechanically disturbing the columnar growth front during upward directional solidification (fig. 62). Experiments were conducted in which the value of $G/V^{1/2}$ decreased with distance down the length of a small ingot. This leads to a columnar to equiaxed transition at some position as previously shown by PLASKETT and WINEGARD [1959] and ELLIOT [1964]. The critical values of $G/V^{1/2}$ obtained by BILONI and CHALMERS [1968] for various Al–Cu alloys are shown in fig. 62 as circles. When the experiment was repeated, but with a periodic disturbance (1 min) of the interface, small equiaxed grains were formed at the position of the disturbance at significantly higher values of $G/V^{1/2}$ as shown by the squares in fig. 62. However this band of equiaxed grains reverted to columnar growth upon further solidification. Presumably the disturbance increased the number of potential growth sites by dendrite fragmentation and acccording to eq. (112) momentarily increased the possibilities for equiaxed growth. However the available growth centers where quickly consumed and the growth reverted to columnar. Finally at a position in the ingot with a low value of $G/V^{1/2}$

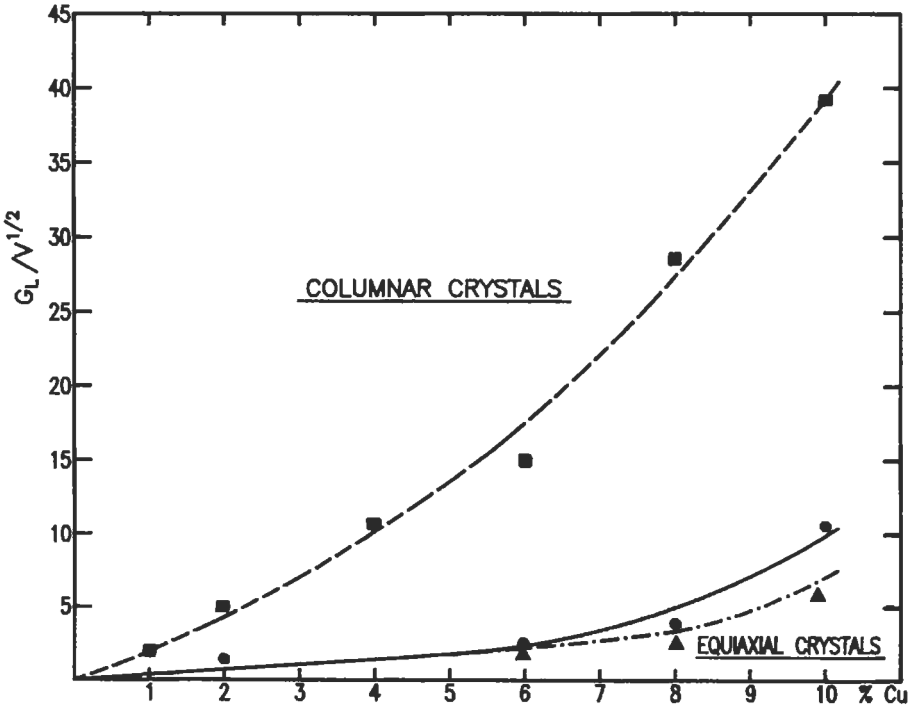

Fig. 62. Critical values of $G/V^{1/2}$ for columnar to equiaxed transition for various Al–Cu alloys. BILONI and CHALMERS [1968].

(triangles, fig. 62) close to that established by the undisturbed experiments, it was found that the equiaxed grains did not revert to columnar grains, but persisted for the remainder of the ingot. These experiments indicate the importance of dendrite fragmentation on the columnar to equiaxed transition.

9.3. Macrosegregation

Macrosegregation is defined as variations in composition that exist over large dimensions, typically from millimeters to the size of an entire ingot or casting. We have already considered one form of macrosegregation in the initial and final transients during planar growth of a rod sample (§ 6.2). However in order to define or measure macrosegregation for dendritically solidified samples, it is necessary to determine an average composition over a volume element that contains several dendrite arms. As we will see, changes in the dendritic microsegregation profile in such a volume element due to settling of free-floating solid or flow of solute-rich liquid in or out of the volume element during solidification will change the average composition of the volume element away from the nominal composition of the alloy. Thus macrosegregation is produced. Figure 63 shows a drawing of a large steel ingot showing some of the major types of macrosegregation commonly found. Positive and negative macrosegregation refer to solute content greater or less than the average.

9.3.1. Gravity segregation

Negative cone segregation has been explained by the settling of equiaxed grains or melted off dendrites into the bottom of a casting if they are of higher density than the liquid. If lighter solids such as nonmetallic inclusions and kish or spheroidal graphite are formed they can float to the upper part of a casting forming positive segregation areas. Centrifugal casting clearly can alter the pattern of macrosegation formed by this mechanism (OHNAKA [1988]). It is important to note that gravity produces negligible macrosegration of a single phase liquid, discrete particles with densities different from the average are necessary.

9.3.2. Interdendritic fluid flow and macrosegregation

The first attempt to create models for macrosegregation due to flow of solute rich material was by KIRKALDY and YOUDELIS [1958]. Later the subject was treated extensively at MIT by FLEMINGS and NEREO [1967]) and MEHRABIAN *et al.* [1970] and has been summarized by FLEMINGS [1974], [1976]. Using a volume element similar to that chosen in fig. 41, a mass balance is performed under the additional possibility that flow of liquid in or out of the volume elements can occur and that the liquid and solid can have different densities. Thus the necessity for flow to feed solidification shrinkage is treated. The result is a modified form of the solute redistribution equation used to describe microsegregation in § 7,

$$\frac{\mathrm{d}f_\mathrm{L}}{\mathrm{d}C_\mathrm{L}} = -\frac{(1-\beta)}{(1-k_0)}\left[1+\frac{\bar{v}\cdot\nabla T}{\varepsilon}\right]\frac{f_\mathrm{L}}{C_\mathrm{L}}, \tag{113}$$

References: p. 830.

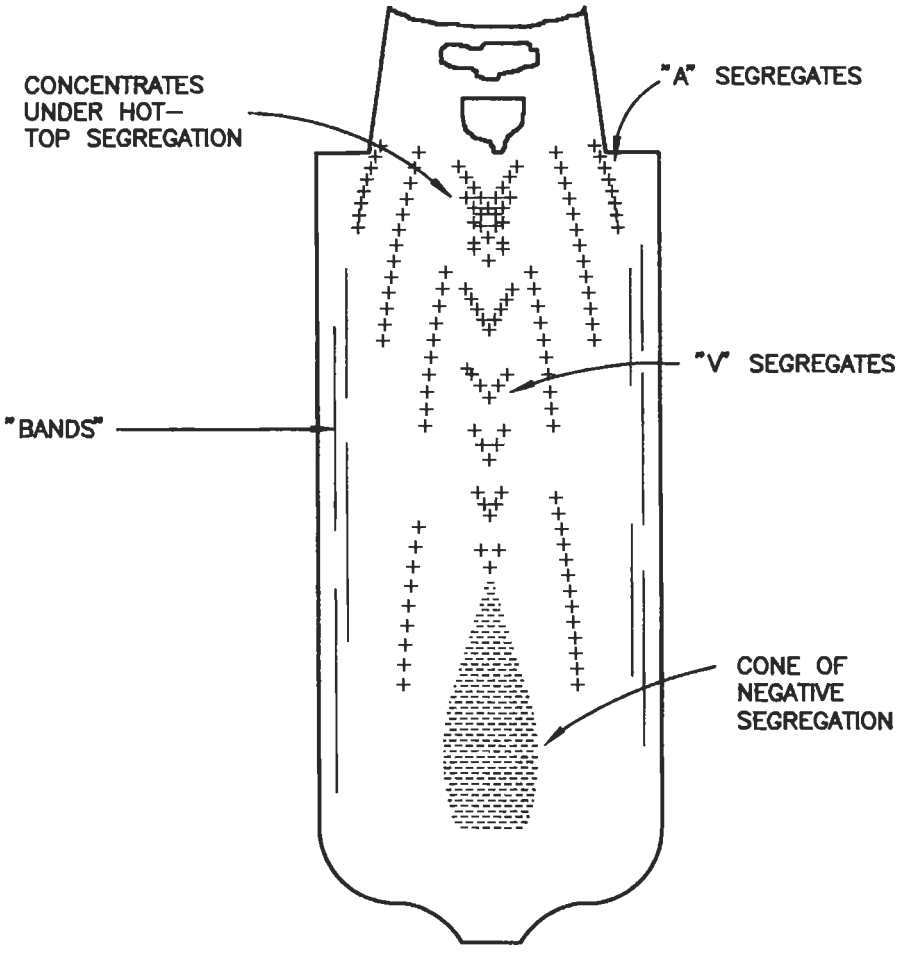

Fig. 63. Different types of macrosegregation in an industrial steel ingot. FLEMINGS [1974].

where: f_L is the fraction of liquid; $\beta = (\rho_S - \rho_L)/\rho_S$ = solidification shrinkage; $\bar{v}$ = velocity vector of interdendritic liquid; ∇T = local temperature gradient vector; ε = local rate of temperature change.

This expression assumes: i) local equilibrium without curvature correction, ii) uniform liquid composition in the small volume of interest, iii) no solid diffusion, iv) constant solid density, v) no solid motion, and vi) absence of voids. In this approach, the appropriate values for $\bar{v}$ and ε at each location must be determined from a separate calculation involving thermal analysis and flow in the mushy zone, which will be outlined below. However given these values for each small volume element, C_L and hence C_S as a function of f_S can be determined along with the fraction of eutectic. The average value of C_S from $f_S = 0$ to 1 gives the average composition at each location in the

casting. The average composition will not in general be equal to the nominal alloy composition.

Several cases can be distinguished. If the interdendritic flow velocity just equals the flow required to feed local shrinkage,

$$\bar{n} \cdot \bar{v} = -\frac{\beta}{1-\beta} \bar{n} \cdot \bar{V}. \tag{114}$$

Then eq. (113) reverts to the Scheil equation and the average composition is equal to the nominal. Here $\bar{n}$ is the unit normal to the local isotherms and $\bar{V}$ is the isotherm velocity. If on the other hand $\bar{n} \cdot \bar{v}$ is greater than or less than this value, negative or positive macrosegregation occurs, respectively. A particularly simple case ocurs at the chill face of a casting. Here $\bar{n} \cdot \bar{v}$ must be zero because there can be no flow into to the chill face. This clearly produces positive macrosegregation (for normal alloys where $\beta > 0$ and $k_0 < 1$). This is commonly observed in ingots and is termed *inverse segregation* (KIRKALDY and YOUDELIS [1958]) because it is reversed from what one would expect based on the initial transient of plane front growth.

In order to compute the fluid velocity of the liquid, the mushy zone is treated as a porous media and *D'Arcy's Law* is used. The pressure gradient and the body force due to gravity control the fluid velocity according to

$$\bar{v} = \frac{K_p}{\eta f_L} \left(\nabla P + \rho_L \bar{g} \right), \tag{115}$$

where:

K_p = specific permeability; η = viscosity of the interdendritic liquid; ∇P = pressure gradient; $\bar{g}$ = acceleration vector due to gravity.

Often, heat and fluid flow in the interdendritic region have been computed by ignoring the fact that the fraction of liquid at each point in the casting depends on the flow itself through eq. (115). This decoupling is thought to cause little error if the macrosegregation is not too severe. FLEMINGS [1974] and RIDDER *et al.* [1981] solved the coupled problem using an iterative numerical scheme for an axisymmetric ingot. In their work the flow in the bulk ingot was also coupled to that in the interdendritic region. Experiments on a model system showed good agreement.

Determining an accurate expression for the permeability of a mushy zone is a difficult problem since the value of K_p depends on interdendritic channel size and geometry. In the case of the mushy zone it has been proposed (PIWONKA and FLEMINGS [1966]) that

$$K_p = \lambda_c f_L^2, \tag{116}$$

where λ_c is a constant depending on dendritic arm spacing. Recently, POIRIER [1987] analysed permeability data available for the flow of interdendritic liquid in Pb–Sn and borneol–paraffin. The data were used in a regression analysis of simple flow models to arrive at relationships between permeability and the morphology of the solid dendrites. When flow is parallel to the primary dendritic arms the permeability depends upon

References: p. 830.

λ_1 (primary arm spacing) but not λ_2 (secondary arm spacing). When flow is normal to the primary arms the permeability depends upon both λ_1 and λ_2. These correlations are only valid over an intermediate range of f_L, roughly between 0.2 and 0.5.

With this model of macrosegregation, FLEMINGS [1974], [1976] was able to explain different types of macrosegregation present in industrial ingots (fig. 63):
a). *Gradual variations in composition from surface to center and from bottom to top* are due to the interdendritic fluid flow with respect to isotherm movement. b) *Inverse segregation* as described above. If a gap is formed between the mould and the solidifying casting surface, a severe surface segregation or *exudation* can arise. c) *Banding* or abrupt variations in composition that result from either unsteady bulk liquid or interdendritic flow, or from sudden changes in heat transfer rate. d) *"A" segregates* or *"freckel"*. These are abrupt and large variations in composition consisting of chains of solute-rich grains. They result from movement of interdendritic liquid that opens channels in the liquid–solid region. Recent work by HELLAWELL [1990] seems to prove that, at least in some cases, the initiation of the channels is at the growth front itself. e) *"V" segregates*. As the fraction solid in the central zone increases in the range of 0.2 to 0.4, the solid network that has formed is not yet sufficiently strong to resist the metallostatic head and fissures sometimes occur. These *internal hot tears* open up and are filled with solute rich-liquid. f) *Positive segregation under the hot top*: Probably occurs during the final stages of solidification when the ingot feeding takes place only by interdendritic flow.

More recently KATO and CAHOON [1985] concluded that void formation can affect inverse segregation. They studied inverse segregation of directionally solidified Al–Cu–Ti alloys with equiaxed grains. MINAKAWA *et al.* [1985] employed a finite difference model of inverse segregation. This model allowed for volume changes due to microsegregation and thermal contractions as well as the phase change.

9.3.3. Further theoretical developments for flow in the mushy zone

Many simplifying assumptions regarding the flow in the mushy zone and its interaction with the bulk flow have been required in the past work. More rigorous approaches have recently been performed. In order to formulate a set of governing equations that determines the flow, temperature and composition fields in the mushy zone as well as in the bulk liquid, two approaches have been employed: *continuum mixture theory* and a *volume averaging technique* as reviewed by VISKANTA [1990] and PRESCOTT *et al.* [1991]. Both approaches have successfully computed macrosegregation patterns in ingots, including freckles. The continuum mixture approach has been used by BENNON and INCROPERA [1987a)], [1987b)], GANESAN and POIRIER [1990], and FELICELLI *et al.* [1991]. The volume averaging technique (BECKERMANN and VISKANTA [1988], NI and BECKERMANN [1991]) may be better suited to flow models involving the formation of equiaxed (free floating) dendritic structures where solid movement must be treated.

9.4. Porosity and inclusions

Porosity and inclusions have a strong effect on the soundness and mechanical properties of castings.

9.4.1. Porosity

For most metals the density of the solid is higher than the liquid. Thus liquid metal must flow toward the solidifying region in order to prevent the formation of voids. Much of foundry practice is involved with the placement of chills and risers that maintain proper temperature gradients to retain an open path of liquid metal from the riser to the solidification front. Indeed the major use of macroscopic heat flow modelling of castings is to identify potential locations in the casting where the solidifying regions are cut off from the risers.

Even if a path of liquid metal remains open to the riser, porosity on the scale of the dendritic structure can still form. When liquid metal flows through the mushy zone to feed solidification shrinkage, the liquid metal pressure in the mushy zone drops below the external atmospheric pressure. The pressure gradient required for flow is given by eq. (115). Microporosity forms when the local pressure in the mushy zone drops below a critical value. Thus detailed prediction of microporosity requires a rather complete description of fluid flow in the mushy zone as does the prediction of macrosegregation. Clearly the larger the freezing range of an alloy and the smaller the temperature gradient, the more tortuous are the liquid channels in the mushy zone. This leads to greatly increased difficulty of feeding the shrinkage and a greater reduction of the liquid metal pressure deep in the mushy zone (far from the dendrite tips).

The critical reduction of the liquid pressure required for the formation of micropores depends on many factors. Indeed the initial formation of a pore is a heterogeneous nucleation problem (CAMPBELL [1991a]) that requires the same consideration as described in § 4, but with pressure substituted for temperature. In principle one needs to know the contact angle of the pore on the solid–liquid interface. It is common to postulate that the critical radius (in the sense of nucleation) of a pore, above which the pore can grow, is related to the scale of the dendrite structure. KUBO and PEHLKE [1985] let the critical radius be equal to the primary dendrite spacing, λ_1, whereas POIRIER *et al.* [1987] relate the critical radius to the space remaining between dendrites. They obtain an expression for the liquid metal pressure where a void can form as

$$P \leq P_G - \frac{4\gamma_{LG}}{f_L}\lambda_1, \tag{117}$$

where P_G is the pressure of gas in the pore if any, and γ_{LG} is the surface energy of the liquid gas interface. If no dissolved gas is present and if the surface energy were zero, porosity would form at locations in the casting where the liquid metal pressure drops to zero. Dissolved gas increases the likelihood of porosity formation whereas the inclusion of the surface energy effect makes it more difficult, possible requiring negative pressure to form a void.

Dissolved gas in a liquid alloy causes porosity because the solubility of gas in liquid metal usually exceeds the solubility in the solid. One can define a partition coefficient for the gas, k_0', as the ratio of the equilibrium solubilities of gas in the solid and the liquid just like any solute. The value of the coefficient as a function of temperature must be known to make predictions. As an alloy solidifies, the dissolved gas is rejected into the

remaining liquid where its level increases. Because the diffusion rate of gas in solid metal is usually quite high, the gas content of the solid phase is usually assumed to be uniform and at the equilibrium concentration. Thus the lever rule can be applied to compute the concentration of gas in the liquid as a function of fraction solid. This increase in the concentration of gas leads to an expression for the equilibrium pressure of the gas in the pores given by

$$P_G = \frac{P'_G}{\left(f_L\left(1 - k'_0\right) + k'_0\right)^2}, \tag{118}$$

where P'_G is the partial pressure of the gas above the melt (given by the initial concentration of gas in the melt (BRODY [1974]). Thus it can be seen how the presence of dissolved gas in the melt (through its effect on P_G) as well as solidification shrinkage both contribute to the formation of dendritic microporosity. This combined effect is particularly important for aluminium castings where the solubility of H in the solid is only tenth of that in the liquid.

Equation (118) for the pressure inside a pore is only valid when the volume fraction of porosity is small. To actually calculate the size and fraction of porosity after solidification is complete, a more complex analysis is required. KUBO and PEHLKE [1985] have calculated the amount and size of the porosity formed in Al-4.5 wt% Cu plate castings containing hydrogen that match experimental measurements. POIRIER *et al.* [1987] perform such calculations for Al–Cu in a directional solidification geometry. ZHU and OHNAKA [1991] have also simulated interdendritic porosity considering both H redistribution in the melt and solidification contraction. With this method, the effect of the initial H content, cooling rate and ambient pressure were simulated.

9.4.2. Inclusions

At present it is very clear that inclusions exert an important influence on fracture behaviour of commercial materials. As a result, this portion of the field of solidification is receiving much greater attention. One type of inclusions, called *primary inclusions*, corresponds to: i) exogeneous inclusions (slag, dross, entrapped mould material, refractories); ii) fluxes and salts suspended in the melt as a result of a prior melt-treatment process; and iii) oxides of the melt which are suspended on top of the melt and are entrapped within by turbulence. These are called primary inclusions because they are solid in the melt above the liquidus temperature of the alloy. In the steel industry a significant reduction of inclusions is obtained by the their floating upward and adhering to or dissolving in the slag at the melt surface. In the aluminum industry filtering has become a common practice and the development of better filters is an important area of research (ROSS and MONDOLFO [1980], APELIAN [1982]).

Secondary inclusions are those which form after solidification of the major metallic phase. Although in industrial practice commercial alloys involve multicomponent systems, a first approach to the understanding of the formation of secondary inclusions has been achieved through the considerations of ternary diagrams involving the most important impurity elements under consideration (FLEMINGS [1974]). Then, the solidifi-

cation reactions occurring during the process, together with the values of the various partition coefficients of the impurity elements in the metallic phase play an important role in the type, size and distribution of inclusions in the final structure. Important ternary systems to be considered are Fe–O–Si, Fe–O–S, and Fe–Mn–S from which the formation of silicates, oxides and sulphides results.

As an example of research in this field FREDRICKSSON and HILLERT [1972], through carefully controlled solidification, were able to determine the formation of four types of MnS inclusions formed by different reactions. CAMPBELL [1991a] and TRAJAN [1988] treat extensively both primary and secondary inclusions and their effect on mechanical properties in ferrous and nonferrous alloys.

An important effect to consider when a moving solidification front intercepts an insoluble particle is whether the inclusion is pushed or engulfed. If the solidification front breaks down into cells, dendrites or equiaxed grains, two or more solidification fronts can converge on the particle. In this case, if the particle is not engulfed by one of the fronts, it will be pushed in between two or more solidification fronts and will be entrapped in the solid at the end of local solidification. STEFANESCU and DHINDAW [1988] reviewed the variables of the process as well the available theoretical and experimental work for both directional and multidirectional solidification. More recently, SHANGGUAN *et al.* [1992] present an analytical model for the interaction between an insoluble particle and an advancing S–L interface. There exists a critical velocity for the pushing-engulfment transition of particles by the interface. The critical velocity is a function of a number of materials parameters and processing variables, including the melt viscosity, the wettability between the particle and the matrix, the density difference as well as the thermal conductivity difference between the particle and the matrix, and the particle size. Qualitatively the theoretical predictions compare favorably with experimental observations.

As an example of the interaction between the formation of inclusions and porosity, MOHANTY *et al.* [1993] present a novel theoretical approach to the nucleation of pores in metallic systems. The proposed mechanism is based on the behavior of foreign particles at the advancing S–L interface. Mathematical analysis has been employed to predict gas segregation and pressure drop in the gap between the particle and the S–L interface. The authors discussed the effect of particle properties and solidification parameters, such as wettability, density, thermal conductivity, solidification rate and S–L interface morphology. They recognize, however, that at present quantitative measurements of materials properties are necessary, in particular for interfacial energies.

9.5. Fluidity

Over the years the foundryman has found it useful to employ a quantity called *fluidity*. The concept arises from practical concerns regarding the degree to which small section sizes can be filled with metal during castings with various alloys. This property is measured through one of several types of fluidity tests. Hot metal is caused to flow into a long channel of small cross section and the *maximum length* that the metal flows before it is stopped by solidification is a measure of fluidity. The solidification process

References: p. 830.

in the channel is under the influence of many variables: metallostatic pressure, heat transfer coefficient, superheat, latent heat of fusion, density of the alloy liquid, viscosity, liquid surface tension, alloy freezing range, and whether the alloy freezes with plane front or with columnar or equiaxed dendrites.

FLEMINGS [1974] reviewed the field and his contributions to the study of fluidity. More recently CAMPBELL [1991a], [1991b] gives a general view of this property and stresses the importance of the factors that influence the fluidity test as they relate to present limitations and future difficulties of numerical modeling of casting. It is worthwhile to follow the approach of CAMPBELL [1991a] who considers three cases: i) *Maximum Fluidity Length*, L_f, determined by an experiment where the cross sectional area of the channel is large enough that the effect of surface tension is negligible; ii) L_f, when surface tension is important, and, iii) *Continuous Fluidity Length*, L_c.

9.5.1. Maximum fluidity

Instead of only determining the total distance travelled, which is the maximum fluidity length, MORALES *et al.* [1977] and AGUILAR RIVAS and BILONI [1980a], [1980b] performed tests on Al–Cu alloys that measured the distance flowed vs. time for different metallostatic pressures, superheats and metal-mould heat transfer coefficients, h_i. In addition, the use of careful metallographic analysis of the fluidity samples gave information about the vein closing mechanism. The measured data have two stages with different slopes. For a given fluidity test, the first stage represents a high percentage of the total distance flowed but depends on variables independent of the true capacity of flow of the metal or alloy, namely, the liquid superheat and the heat transfer coefficient at the metal-channel surface. The second stage, in general, represents a small percentage of the total distance flowed but reflects the intrinsic ability of the metal or alloy to flow. In a complementary study, MORALES *et al.* [1979] determined how the channel microgeometry, as influenced by machining, polishing and coating, affects microstructure and L_f through variations in the local and average heat transfer rates. In summary, the molten metal entering the channel flows until all the superheat is eliminated in the first stage. The liquid can continue to flow primarily because of the delayed cooling due to the latent heat evolution. This second stage is strongly affected by the solidification mechanisms, the $f_S(T)$ relationships, and the nature of the columnar/equiaxed structures.

Until recently all fluidity tests performed in fundamental investigations used binary alloys to establish relationships between L_f and alloy composition (FLEMINGS [1974], CAMPBELL [1991a]). GARBELLINI *et al.* [1990] carried out an extensive study of the fluidity of the Al–Cu rich corner of the Al–Cu–Si ternary system, which serves as a basis for many commercial alloys. This paper developed a correlation between L_f and alloy microstructure in the binary (Al–Cu and Al–Si) and ternary (Al–Cu–Si) systems. CAMPBELL [1991c] discussed this paper expanding on the results. L_f for any composition is a balance among three factors primarily related to the phase diagram: a) the latent heat of the proeutectic phase, i.e., Al, Si or Al_2Cu; b) the amount of interdendritic liquid remaining at the end of the proeutectic solidification; and c) The value of the fluidity for the specific eutectics (binary and/or ternary) that complete solidification. These considerations led to the conclusion that minor changes of compositions can be quite

important, for example for metal matrix composites (MMC) obtained by infiltration. Also due to the latent heat effect, the high fluidity of alloys with proeutectic Si phase in hyper eutectic alloys was confirmed. The important industrial Al–Si alloys do not display a peak fluidity at the eutectic composition. Typically alloys with the smallest freezing ranges show the best fluidity (FLEMINGS [1974], CAMPBELL [1991a]). Small amounts of Si in hypereutectic alloys dramatically increased L_f because of the extraordinarily high latent heat of Si that maintains the fluid state of the alloys for longer times. The relationships that exist between fluidity length and solidification microstructure are open to further research. As examples, there is a large difference in fluidity between binary Al–Al_2Cu, a regular eutectic and Al–Si, an irregular eutectic (GARBELLINI *et al.* [1990]). In eutectic cast irons the fluidity is determined by the morphological changes of the graphite phase as documented by fluidity tests on laminar, vermicular and nodular cast irons (STEFANESCU *et al.* [1988]).

9.5.2. Combined effects of surface tension and fluidity

When the channel section becomes thinner than a critical value, considered to be ~0.30 cm for most metals and alloys by FLEMINGS [1974], the resistance to liquid flow increase because of surface tension. This is particularly critical in technologies such as aerofoils, propellers, and turbine blades (CAMPBELL [1991a]). CAMPBELL and OLLIF [1971] distinguish two aspects of filling thin sections: *flowability*, essentially, following the rules discussed above and *fillability* limited by surface tension.

9.5.3. Continuous fluidity length

Figure 64a is a schematic representation of the solidification into a channel when a nondendritic S–L interface is considered (MORALES *et al.* [1977]). In region I, no solidification occurs; in region II the solidification occurs in the presence of a decreasing amount of superheat. Region III corresponds to the liquid and solid at the melting temperature, i.e. with no superheat. The length, L_c, defines a critical value known as the continuous fluidity length. The physical meaning of L_c has been defined by FELIU *et al.* [1962], who introduce the concept of the flow capacity of a channel. In the case of a very long channel the flow capacity is just the volume of the cast fluidity length L_f. In the case of a channel of intermediate length, the flow capacity is the total of the amount which has flowed through, plus the amount which has solidified in the channel. For a channel shorter than L_c the flow capacity becomes infinity (fig. 64b). CAMPBELL [1991a] gives technological applications of these concepts for different types of alloys and moulds.

10. Solidification processes

This section will treat two conventional solidification processes that have an important impact in current technology: continuous casting and welding.

10.1. Continuous casting

Continuous casting has emerged as one of the great technological developments of

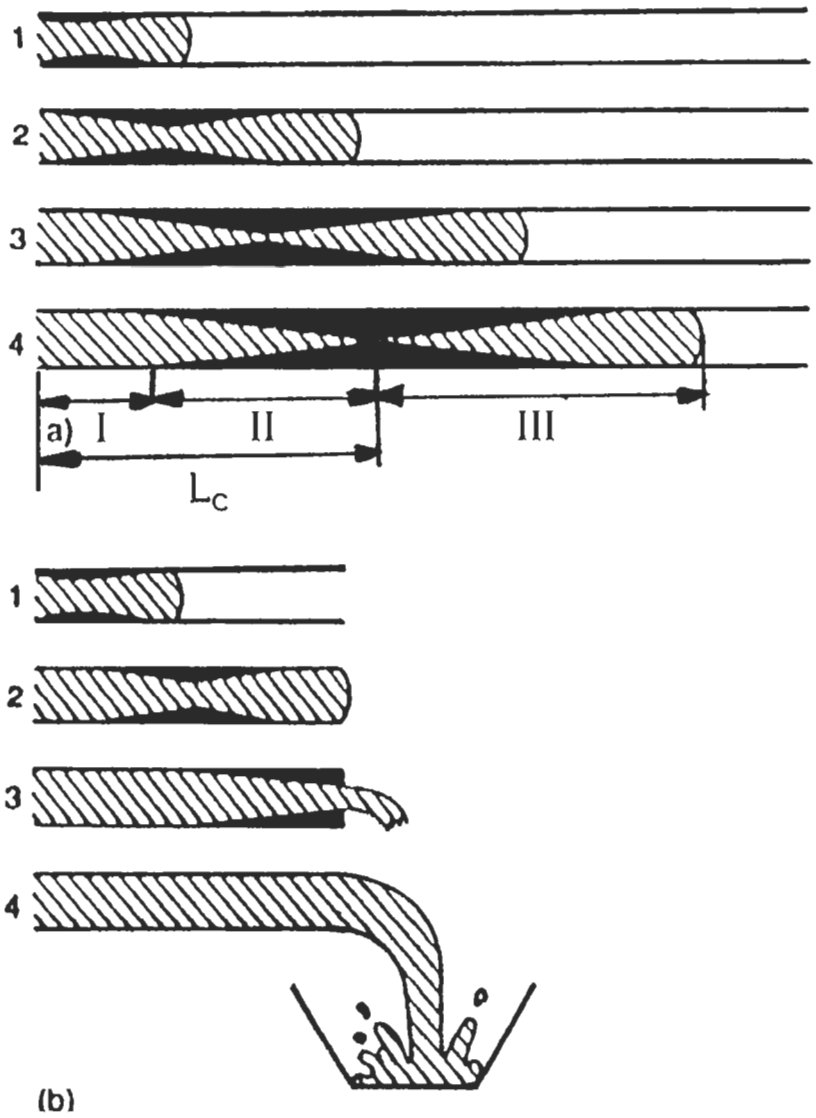

Fig. 64. The concepts of: (a) maximum fluidity length showing the stages of freezing leading to the arrest of flow in a long mould; and (b) the continuous flow which can occur if the length of the mould does not exceed a critical length, defined as the continuous-fluidity length. CAMPBELL [1991a]. In (a) has been included the schematic representation of the solidification considered by MORALES *et al.* [1977].

this century, replacing ingot casting and slabbing/blooming operations for the production of semi-finished shapes: slabs, blooms and billets. More recently even continuous production of single crystals for research and sophisticated technology has been

developed. Excellent reviews of the research and technology involved in this field have been presented by TAYLOR [1975], WEINBERG [1979a] [1979b] and BRIMACOMBE and SAMARASEKERA [1990] for steels and EMLEY [1976] and BAKER and SUBRAMIAN [1980] for aluminum and its alloys. Additionally PEHLKE [1988] and MINKOFF [1986] present comprehensive details of the process both in ferrous and nonferrous alloys together with technical details of the industrial installations currently used.

10.1.1. Continuous casting of steels

Figure 65 shows the main components of a continuous casting machine. Molten steel is delivered from a ladle to a reservoir above the continuous casting machine called a *tundish*. The flow of steel from the tundish into the water cooled mould is controlled by a stopper rod nozzle or a slide gate valve arrangement. To initiate a cast, a starter, or *dummy bar* is inserted into the mould and sealed so that the initial flow of steel is contained in the mould and a solid skin is formed. After the mould has been filled, the dummy bar is gradually withdrawn at the same rate that molten steel is added to the mould. Solidification of a shell begins immediately at the surface of the water cooled copper-mould. The length of the mould and the casting speed are such that the shell thickness is capable of withstanding the pressures of the molten metal after it leaves the mould. Usually a reciprocating motion is superimposed on the downward travel to prevent sticking.

Figure 66 shows schematically the role of fundamental knowledge in analyzing the process for the achievement of quality products (BRIMACOMBE and SAMARASEKERA [1990]). Determination of the *heat flow* is important because it allows the prediction of the shell profile, the pool depth and temperature distribution as a function of casting variables. In the mould heat transfer, the gas gap separating the mould and the strand casting and its relationship to mould heat flux is very important. MAHAPATRA *et al.* [1991a] [1991b] employed measured mould temperatures and mathematical modeling in order to predict formation of oscillations marks, longitudinal or corner depressions and subsurface cracks. Additionally, laboratory experiments and in-plant studies have been undertaken to determine the relationship between spray heat transfer coefficient and spray water flux. As, a result, mathematical models of spray systems have been developed.

The main aspects of solidification that must be understood in continuous casting are: i) the cast structure; ii) growth of the solid shell encasing the liquid pool and, iii) segregation. For the first concern, as with static casting, the structure consists of both columnar and equiaxed grains. The lower the pour temperature, the higher the fraction of equiaxed grains. The equiaxed structure is favoured in the medium carbon range, from about 0.17% to 0.38%C. Also induced fluid flow, for example by electromagnetic stirrers, enhance the growth of equiaxed grains. Shell growth is affected by all the variables that influence the mould heat flux distribution. When microsegregation is considered the models discussed in § 7 can be applied but the macrosegregation associated with the fluid flow during the solidification process is still not completely understood in continuous casting. However it is recognized that the same factors favoring an equiaxed structure diminish the macrosegregation.

Very recently BRIMACOMBE [1993] stressed the challenges of transferring knowledge

References: p. 830.

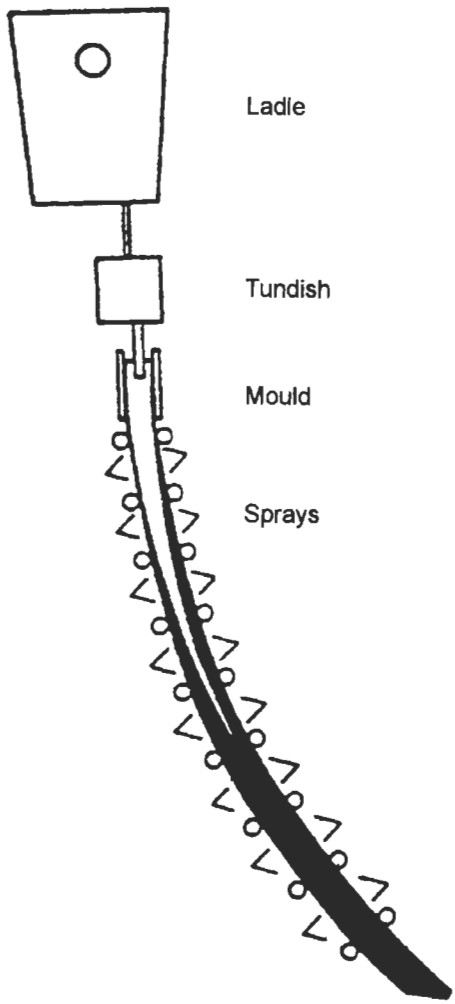

Fig. 65. Schematic diagram of continuous-casting machine. BRIMACOMBE and SAMARASEKERA [1990].

from R & D to the steel continuous casting industry. He suggests the development of *expert systems* in the form of an *intelligent billet casting mould*. This system effectively transfers knowledge on line to the shop floor through the combination of thermocouple and load cell information, signal data recognition based on years of research, mathematical models of heat flow in the solidifying shell and mould, understanding of the mechanism of quality problems, and the formulation of a response to a given set of casting conditions.

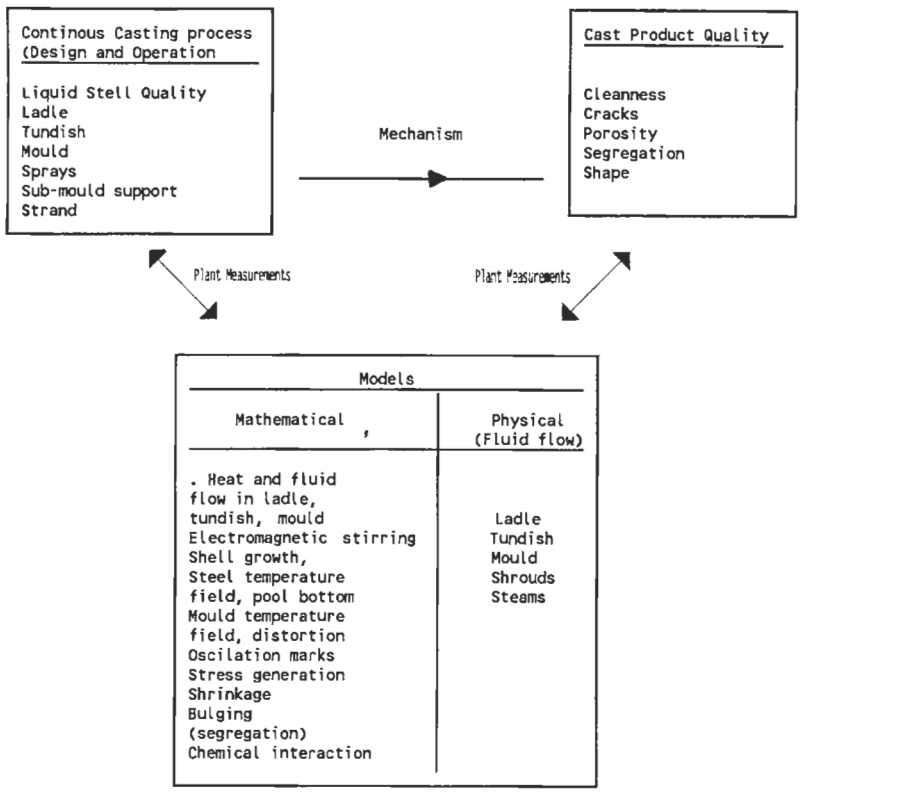

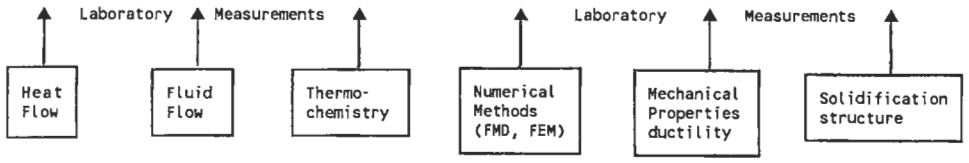

Fig. 66. Knowledge-based approach to analysis of continuous casting. After BRIMACOMBE and SAMARASEKERA [1990].

10.1.2. Continuous casting of light alloys

The principal casting process for light metals, such as Al, is the *direct chill process*. Figure 67 shows a schematic representation of the D.C. casting components for conventional open mould casting, the most common method used for blocks and billets

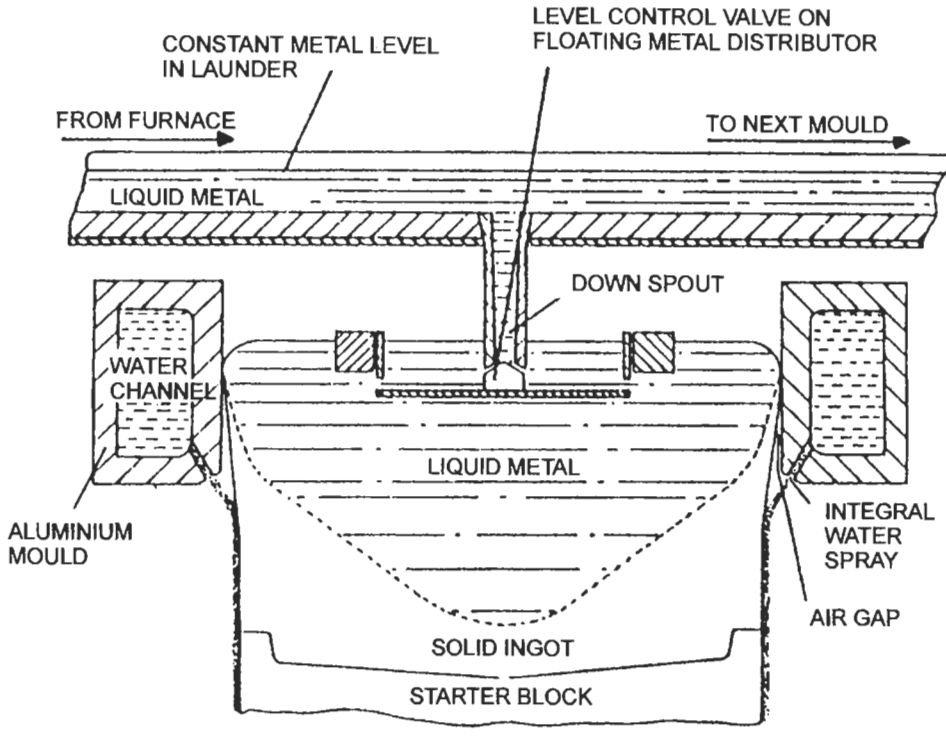

Fig. 67. Schematic diagram of vertical DC casting as commonly practiced. EMLEY [1976].

(BAKER and SUBRAMANIAN [1980]). There are three factors that influence the separation of the ingot shell from the mould: (i) shrinkage at the ingot shell itself; (ii) thermal strain within the ingot shell; (iii) shrinkage in the block section below the mould and the associated mechanical strains in the shell. All are influenced by the primary and secondary water cooling system and can affect the ingot structure, principally at the surface of the ingot. The air gap developed when the shell separates from the mould can give rise to defects of various types. When gap formation occurs there is increased resistance to heat transfer and, consequently, reheating of the skin. Reheating results in macrosegregation, exudation, runouts, retardation of the solidification in the subsurface zone, and variations in the cell/dendrite size of the outer surface of ingots. Zones of coarse dendritic substructure may extend 2–3 cm below the surface. Associated with the coarse cells are large particles of intermetallic constituents, formed by eutectic reactions, which may be exposed by surface machining that is usually performed before fabrication (BOWER *et al.* [1971]). Several methods have been proposed to reduce surface defects. The most succesful are those that reduce the heat extraction at the mould through the control of the microgeometry of the mould surface, for example by machining fine

grooves in the face of the mould. The molten aluminum does not fill the grooves due to surface tension.

More recently, *mouldless electromagnetic casting* has been developed to improve the metal surface quality. Electromagnetic casting was invented by GETSELEV [1971] and the principle behind this process is simple. Molten metal is supported slightly away from a mould by radial electromagnetic body forces concentrated within the upper part of the ingot. These forces are generated by a one-loop induction coil supplied with 5000 A at 2000 Hz (VIVES and RICOU [1985]).

SATO *et al.* [1989], [1991], [1992] studied extensively the production of Al, Al–Cu, and Al–Si rods with different cross-sectional geometries by a mouldless vertical continuous casting process. The main advantages consist of: (i) near net shape material having small and complex cross sectional configuration; (ii) full automation preventing break-out of molten metal and permitting easy start-up and easy shut down; (iii) cast material having unidirectional solidification structures; iv) geometries having changeable cross sectional configuration along their axes.

Elimination of the nucleation source for new crystals during solidification permits long single crystals to be continuously cast. Figure 68 shows the principle of the ingenious Ohno Continuous Casting process (OCC) (OHNO [1986]). The mould is heated to a temperature above the melting point of the metal to prevent the formation of new crystals on the surface of the mould. Cooling is arranged so is that the ingot maintains a small region of molten metal when leaving the mould, which solidifies immediately after leaving the outlet of the mould. If many crystals are nucleated at the end of the dummy, where the ingot begins to solidify, the combination of dendritic growth competition and macroscopic interface curvature eliminates all grains except one having a direction of preferential growth in close proximity to the casting direction. As a consequence a single crystal is formed. The process can also be used with a seed crystal of desired crystal orientation at the end of the dummy. Excellent results have been reported with Al, Pb, Sn, Cu and their alloys (OHNO [1986]). More recently KIM and KOU [1988] and WANG *et al.* [1988] studied the experimental variables of the OCC process and performed numerical modeling of heat and fluid flow. TADA and OHNO [1992] extended the OCC principles to the production of aluminum strips using an open horizontal, heated mould. The method was patented under the name, Ohno Strip Casting process (OSC).

As in most solidification processes, mathematical modelling of continuous casting of nonferrous alloys has also been undertaken. In the particular case of aluminum alloys, SHERCLIFF *et al.* [1994] present a comprehensive review.

10.2. Fusion welding structures

In most metallurgical processes the scientific approach to process improvement is to obtain relations between operational variables, metallurgical structures and properties. However, for many years in fusion welding technology, only relations between operational variables and mechanical properties were considered. In the last thirty years, the scientific approach has begun to be applied in cases where quality assurance is man-

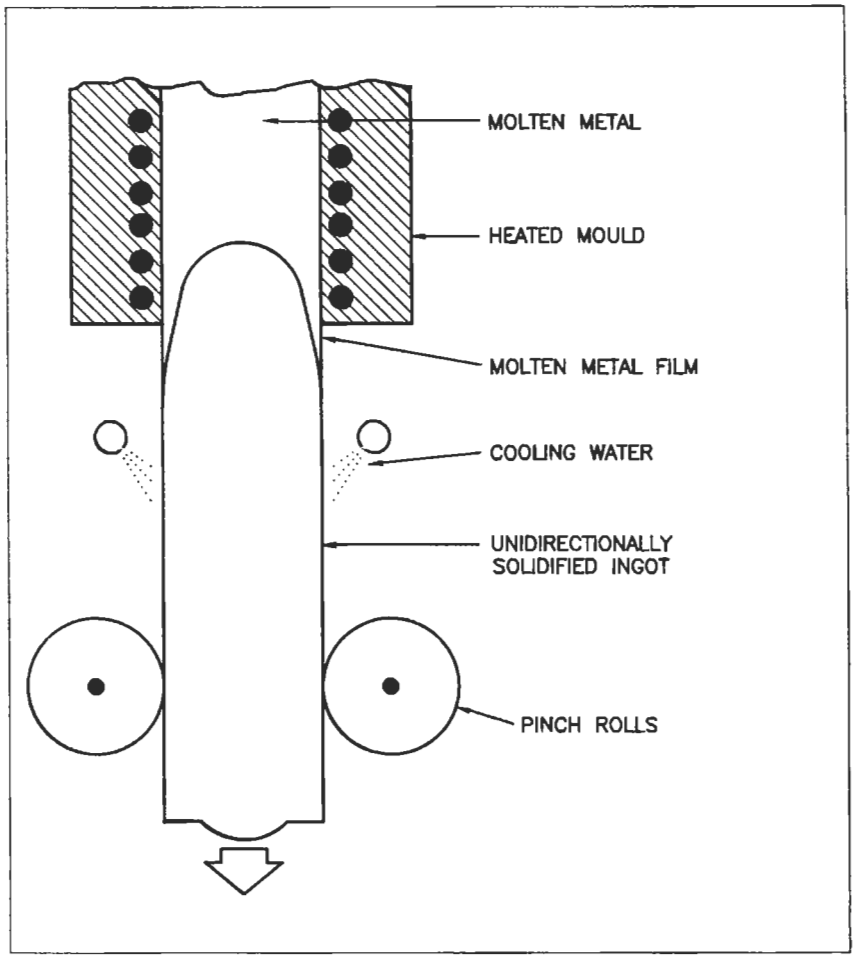

Fig. 68. The principle of the OCC process. After OHNO [1986].

datory for sophisticated technologies.

The fusion welding structure is a result of complex transformations and interactions starting with metal–gas and metal–flux reactions in the liquid state followed by the formation of the *primary structure* by solidification. Pioneering work by SAVAGE and co-workers at R.P.I. initiated the correlation between operational variables and primary structures (SAVAGE *et al.* [1965]). More recently, DAVIES and GARLAND [1975], EASTERLING [1984] and DAVID and VITEK [1989] have presented comprehensive reviews of the correlation between solidification parameters and weld microstructures.

Metallurgically, a fusion weld can be considered to consist of three major zones, namely the *fusion zone* (FZ), the *unmelted heat affected zone* (HAZ) and the *unaffected*

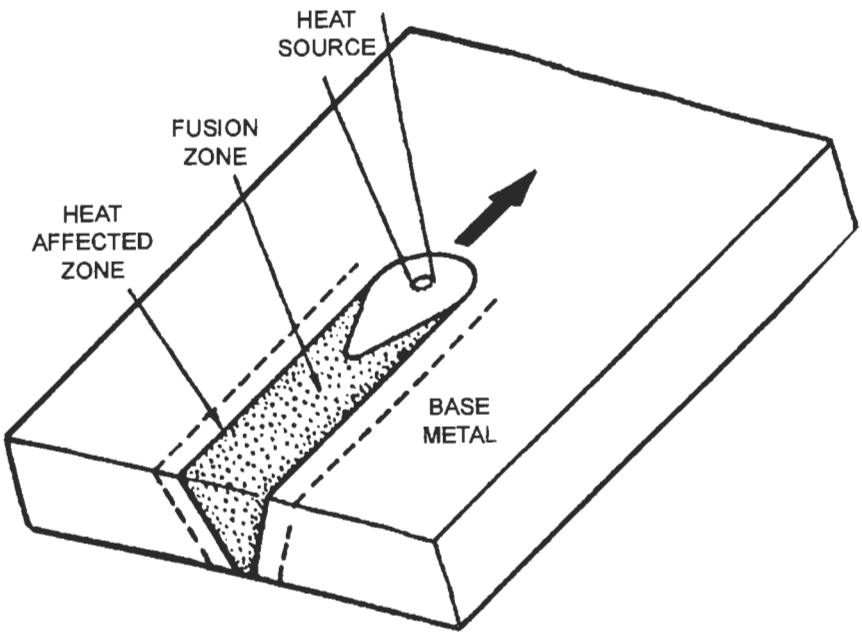

Fig. 69. Schematic diagram showing the three zones within a weldment. After DAVID and VITEK [1989].

base metal (BM), fig. 69. However careful metallographic analysis reveals the zones schematically shown in fig. 70 (SAVAGE and SZEKERES [1967]). The (FZ) can be divided into subzones: the *composite zone* (CZ) and the *unmixed zone* (UZ). In addition between

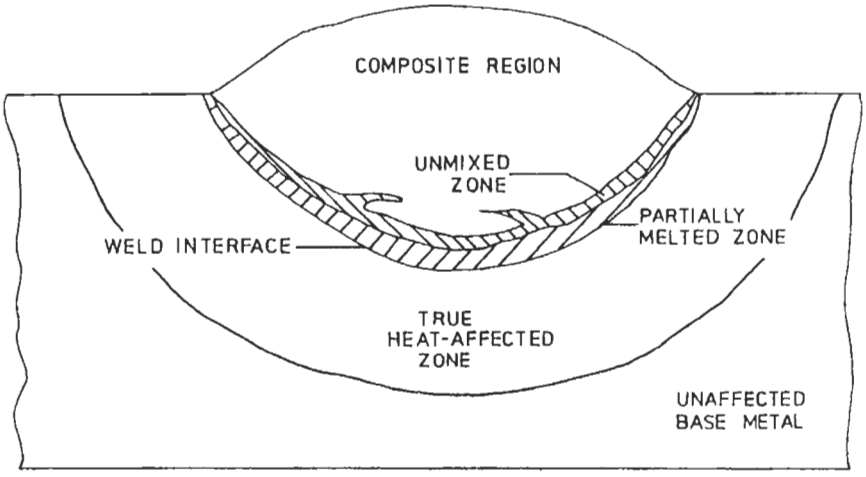

Fig. 70. Schematic representation of the different zones of a weld. After SAVAGE and SZEKERES [1967].

References: p. 830.

the (FZ) and the (HAZ), a *partially melted zone* (PMZ) exists.

The (UZ) appears in welds made with filler metal additions. It is a thin zone composed of base metal that is melted and resolidified without mixing with the filler metal during the passage of the weld puddle. This zone can be the location of initiation sites of microcracking as well as corrosion susceptibility in stainless steel. The PMZ is a region where the peak temperatures experienced by the weldment falls between the liquid and the solidus. As a consequence, only inclusions of low melting point as well as segregated zones can be melted. These areas resolidify and the contraction during the subsequent cooling can be a source of microcracks (BILONI [1983]).

In solidification processes, cooling rates range from 10^{-2}–10^{2} Ks^{-1} in casting technology to 10^{4}–10^{7} Ks^{-1} for rapid solidification technology. Cooling rates in welds may vary from 10–10^{3} Ks^{-1} for conventional processes, but when modern high energy beam processes such as electron beam (EB) and laser welding (LW) are considered cooling rates may vary from 10^{3} to 10^{6} Ks^{-1}. Furthermore the local conditions and cooling rates vary significantly within the weld pool. Therefore weld pool solidification incorporates aspects of both extremes of solidification, i.e. traditional casting as well as rapid solidification. Thus, most of the solidification concepts discussed previously may be applied to the understanding of the different weld microstructures. The most important subjects to be considered are: weld pool geometry and macro- and microstructures of the welds.

10.2.1. Weld pool geometry

Figure 69 schematically describes an autogeneous welding process in which a moving heat source interacts with the metal parts to be joined. The weld pool geometry is a function of the weld speed and the balance between the heat input and the cooling conditions. For arc welding processes the puddle shape changes from elliptical to tear drop shaped as the welding speed increases. For high energy processes such as EB or LW, the thermal gradients are steeper and as a result the puddles are circular at lower speeds becoming more elongated and elliptical in shape as the welding speeds increases. Eventually at high speeds they become tear drop shaped.

The heat transfer equation for a moving heat source was developed by ROSENTHAL [1941]. MINKOFF [1986] and KOU *et al.* [1981] reviewed this type of analytical model of heat transfer for welding. They consider only heat transfer by conduction neglecting the important convective heat transfer existing in the weld pool. In recent years much effort has been focussed on the dynamics of the heat and fluid flow in the weld puddle through experimental work and mathematical modeling. The goal is to reproduce actual weld pool shapes and eventually to develop the capability of predicting weld geometries (DAVID and VITEK [1989], [1992]), (DAVID *et al.* [1994]).

Convection is produced by: a) buoyancy effects; b) electromagnetic forces and, c) surface tension forces. The interactions among these three driving forces have been modeled by WANG and KOU [1987] showing the effects on the shape and weld penetration in G.T.A. (Gas Tungsten Arc) aluminum welds and by ZACHARIA *et al.* [1992] in G.T.A. welding of type 304 stainless steel. It is important to keep in mind that impurities in weld metal are often surface active and alter the surface tension of the liquid metal and its temperature dependence. For pure metals and high purity alloys the surface

tension decreases with increasing temperatures and the resultant flow is outward, away from the center of the weld pool. The result is a wide and shallow weld pool. When surface active elements exist, a positive temperature coefficient of the surface tension can occur in some cases and the resultant inward flow promotes a deeper and narrower weld pool. An example is the presence of small amounts of O and S (less than 150ppm) in stainless steel (HEIPLE *et al.* [1984]).

As already mentioned, computational models have been developed in order to predict the weld pool shape. Figure 71 shows calculated profiles superimposed on a macrograph of a cross section of an aluminum G.T.A. weld (ZACHARIA *et al.* [1988]). Although the correlation is reasonable, improvement of the model is necessary considering that the calculations underestimate the depth of penetration.

10.2.2. Macro- and microstructures of welds

A weld pool solidifies epitaxially from the parent grains in the (PMZ) surrounding it. As a consequence of competitive growth controlled by the orientation of the temperature gradients and the easy growth direction, favourably oriented grains survive. As in castings, a columnar region develops, favoured by the presence of a continuous heat source, which keeps thermal gradients high at the S–L interface. Figure 72 corresponds to an elliptical weld pool. The *local thermal gradient*, G_L and the *local solidification rate*, R_w changes from the fusion line to the weld center line. If crystal growth is considered isotropic (fig. 72a)

$$R_w = V_w \cos\theta_1. \tag{119}$$

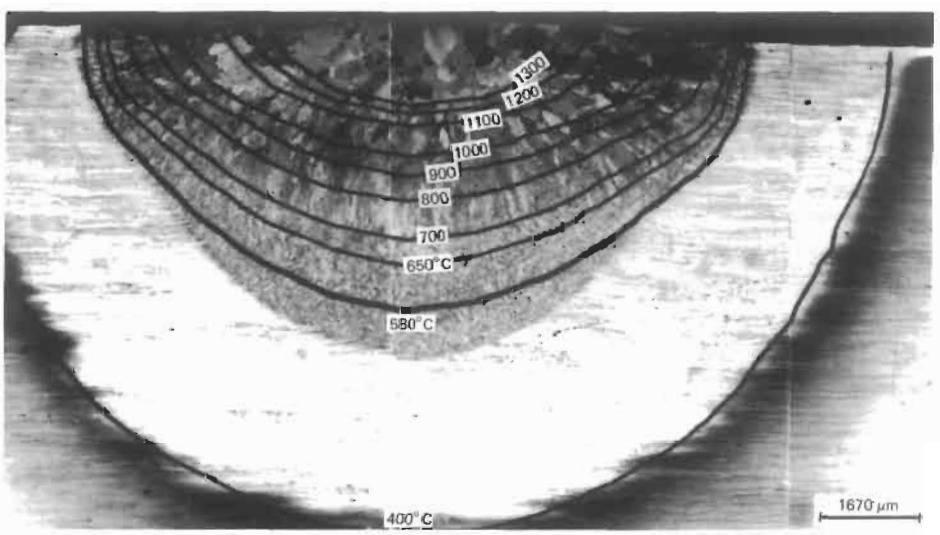

Fig. 71. Calculated temperature profiles superimposed on a macrograph of a cross-section of an aluminium alloy. DAVID and VITEK [1989].

References: p. 830.

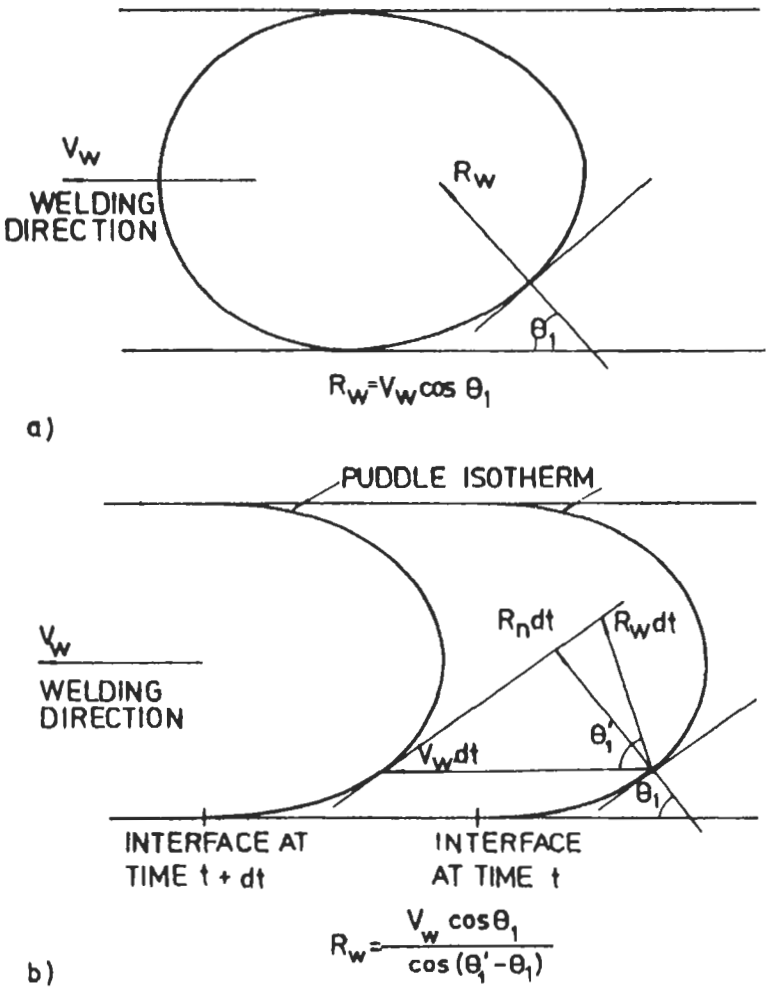

Fig. 72. (a) Solidification rates at different positions of the weld pool if isotropic growth is assumed. (b) Relationship between welding speed and actual growth rate if anisotropic growth is assumed. NAKAWAKA *et al.* [1970].

where V_w is the velocity in the welding direction. If crystal growth is anisotropic, R_w must be corrected according to the expression developed by NAKAGAWA *et al.* [1970],

$$R_w = \frac{R_n}{\cos(\theta_1' - \theta_1)} = \frac{V_w \cos\theta_1}{\cos(\theta_1' - \theta_1)}, \tag{120}$$

where R_n is the growth rate in a direction normal to the isotherm and θ_1' is the angle between the welding direction and the direction of favoured growth (fig. 72b). Thus in welding the solidification rate is greatest on the weld center line where $\theta_1 = 0°$. At this

point the temperature gradients are shallow because of the large distance from the welding heat source.

The liquid pool shape determines the columnar growth direction as well as the solidification rate and thermal gradient into the liquid. Columnar-grain substructures are determined by the S–L interface morphology. Thus, most of the concepts discussed in § 6 and § 7 for unidirectional solidification of alloys and in § 9 for columnar growth in conventional castings can be applied to columnar growth in welding: micro- and macrosegregation, banding, inclusions, porosity, etc. In addition, when situations involving rapid solidification arise, significant departures from local equilibrium at the S–L interface may occur (see § 5) and as a result metastable structures may be obtained. VITEK and DAVID [1992] reported recent research showing that in LW or EB welding, metastable microstructures can be produced in stainless steel welds. Laser surface melting and alloying will be treated in § 11. Regarding the classification of welding macrostructures, PEREZ *et al.* [1981], BILONI [1983] shown schematically nine types of macrostructures obtained with different fusion welding processes. All of them show a columnar zone which may occupy the entire weld, or be accompanied by grains growing along the welding direction, by feathery crystals (see § 9), by equiaxed grains or by mixed coarse and fine grains, the last being characteristic of electroslag welding (PATON [1959]). Recently RAPPAZ *et al.* [1989] and DAVID *et al.* [1990] examined the effect of growth crystallography and dendrite selection on the development of the FZ microstructures. Using single crystals and geometrical analysis that provides a three dimensional relationship between travel speed, solidification velocity and dendrite growth velocity, they were able to reconstruct a three dimensional diagram of a weld pool. The presence of equiaxed grains near the center of welds is believed to be beneficial in preventing solidification cracking and in maintaining good ductility in alloys subjected to brittle fracture. KERR and VILLAFUERTE [1992] reviewed the mechanisms and conditions which give equiaxed grains in castings (see § 9) and compared them to the situation in welds.

11. Structure manipulation and new processes

The concepts discussed in previous sections are the basis used by metallurgists to manipulate microstructure and thus obtain better physical and mechanical properties. However, the manipulation of structure is closely related to the continued development of processing methods. In this section we describe a few examples: single crystal growth from the melt, grain refinement, eutectic modification, rapid solidification, microgravity processing, metal matrix composite fabrication, and semi-solid metal forming.

11.1. Single crystal growth from the melt

Single crystal growth is useful to study the laws governing solidification of metals and alloys, to prepare samples for scientific studies, especially mechanical properties, and for technological devices such as those used in the electronics industries or the production of gas turbine blades. Thus, we consider single crystal production an important example of structure manipulation.

References: p. 830.

CHALMERS [1964] and THORTON [1968] present reviews of the different methods available for single crystal preparation. In general, the same methods can be used for the growth of *bicrystals* if grain boundaries are to be studied. Four main methods and their variations are employed. (i) In the *Bridgman method* the mould containing the melt is lowered through the furnace and the solidification begins either at the lowest point of the mould or on a seed located in the bottom of the mould. (ii) The *Chalmers method* is a variation of the above using a horizontal boat. An advantage of these methods is the fact that the remaining liquid can be decanted by electromagnetic devices. However with horizontal growth, problems arise due to excessive convection during growth (see § 6). (iii) The *Czochralski or pulling method* consists of a melt contained in a crucible and a seed crystal that is lowered into it from above and then slowly rotated and withdrawn. The purpose of the rotation is to maintain axial symmetry of the crystal and decrease the solute enriched layer at the S–L interface. HURLE [1987] discussed the evolution of the method, mathematical modeling, and the advantages and future potential of this technique. (iv) The *floating zone method* employs zone melting principles (PFANN [1966]) and, uses no mould. Essentially, the molten zone is held in place by surface tension forces, sometimes aided by magnetic fields.

In § 6 the importance of maintaining a flat interface has been discussed in detail as well as the relationship between different types of convection and stable interfaces. PIMPUTKAR and OSTRACH [1981] present a comprehensive review of convective effects in crystals grown from the melt, especially when Czochralski and Bridgman methods are considered.

The directional freezing technique has been applied extensively to turbine blade manufacture. The techniques are employed in preparing aligned eutectic structures, directional columnar structures, and single crystal turbine blades. Unlike single crystals grown for electronic applications, single crystal turbine blades solidify with a dendritic structure. Therefore even though the crystallographic orientation of all the dendrites is the same, the turbine blades contain microsegregation and occasionally second phase particles formed by eutectic reactions. PIWONKA [1988] reviewed the different methods used. In the case of single crystal turbine blades, the alloys have no grain boundaries and thus need no grain boundary strengtheners. Elimination of these elements permits solution heat treatment at higher temperatures. Consequently, new high temperature Ni base alloys have been developed having better high temperature properties because they contain a higher percentage of the γ' strengthening phase. In addition, because no grain boundaries exist, monocrystal turbine blades have better corrosion resistance.

11.2. Grain refinement

Various techniques may be used to produce fine grained structures during solidification: thermal methods, innoculation and energy induced methods (BOLLING [1971]). Each of these operates principally through one mechanism: nucleation or multiplication.

11.2.1. Thermal methods

From a thermal point of view we are concerned principally with two possibilities, rapid chilling and bulk supercooling.

(i) ***Chill effect***: when molten metals contact the cold walls of a mould, the melt superheat is removed from the liquid and it becomes locally supercooled. The number of nucleation centres increase and nucleation takes place catastrophically in the liquid. Techniques such as splat cooling (see below) and die casting, as well as applications using chills employ this approach with varying efficiencies according to the sample size. The reader is referred to § 9 regarding the influence of wall microgeometry on the grain size in the chill zone of ingots and castings as well as the columnar zone grain size.

(ii) ***Supercooling methods***: WALKER [1959] published the first observations of grain refinement phenomena due to bulk supercooling. Samples of about 500 g were cooled under a glass slag and/or inert gas atmosphere and were contained in a fused silica crucible to reduce the probability of heterogeneous nucleation on the crucible walls, and, thus, aid the achievement of large supercooling of the melt. With this method Ni samples doped with Ag (to preserve the grain structure) were supercooled in the range from 30 to 285K. From 30 to about 145K of supercooling the grain size decreased monotonically but at this *critical supercooling* (ΔT^*), a sharp decrease in grain diameter from about 20mm to 2mm arose. WALKER [1964] found a similar grain size transition in Co but at $\Delta T^* = 180K$. WALKER measured the pressure pulse associated with the solidification of Ni and found that it showed a maximum in the vicinity of ΔT^*. He suggested that the grain refinement was brought about by homogeneous nucleation in the liquid ahead of the S–L interface due to a transient local elevation in melting temperature caused by the pressure pulse. Subsequently, many researchers tried to understand the grain refinement mechanism associated with high supercooling. Other containerless processes, such as electromagnetic levitation and drop tubes have been used (HERLACH *et al.* [1993]). These authors have analyzed most of the previous results and the proposed mechanisms as well as the effect of minor amount of impurities on the grain refined structure, which can be columnar and/or equiaxed. The large number of proposed mechanisms fall into three broad categories having much overlap: (i) multiple nucleation in the melt arising from a mechanical disturbance of some kind, generally associated with a pressure pulse generated by the solidification itself. (WALKER [1959]; COLLIGAN *et al.* [1961]; GLICKSMAN [1965]; HORVAY [1965], POWELL [1965]). (ii) Dendrite fragmentation arising in a number of possible ways including remelting and mechanical fracture (KATTAMIS and FLEMINGS [1966]; JONES and WESTON [1970a]; MCLEOD [1971]; TARSHIS *et al.* [1971]; SOUTHIN and WESTON [1973], [1974]; KATTAMIS [1976], MCLEOD and HOGAN [1978]; KOBAYASHI and HOGAN[1978]; KOBAYASHI and SHINGU [1988]; DEVAU and TURNBULL [1987]). (iii) Recrystallization of the solidified structure (POWELL and HOGAN [1968], [1969]; JONES and WESTON [1970a], [1970b]).

The study of the segregation substructure of the grains obtained at different supercooling seems to support the fragmentation mechanism. KATTAMIS and FLEMINGS [1966], [1967] and KATTAMIS [1976] observed a gradual change in dendrite morphology from a normal branched form to a more cylindrical form with decreasing side branching as the supercooling increased. At ΔT^*, the transition from coarse columnar grains to fine equiaxed grains was accompanied by a change in the solute segregation pattern from dendritic to spherical. Each of these spherical patterns corresponded to a refined grain. The evolution of the spherical morphology is assumed to occur in two steps: detachment

References: p. 830.

of the secondary dendrite arms and subsequent coarsening into spherical elements during recalescence. Regarding the short time available for the remelting/coarsening mechanism during recalescence, COCHRANE *et al.* [1991] have shown that in drop tube processed Cu–30%Ni and Fe–35%Ni alloys, local solidification times as short as 200 μs cannot retain the dendrite structure formed during the rapid growth phase. In addition, WILLNECKER *et al.* [1989], [1990] measured dendrite growth velocities and grain refinement in Cu–30%Ni and Cu–30%Ni–1%B as a function of supercooling. The addition of 1at % B shifted ΔT^* from 193 to 255 K. The grain refinement transition occurred in both cases at the same supercooling that a sharp change in V–ΔT behavior occurred (fig. 73). These results open the possibility of a link between grain refinement with the onset of complete solute trapping during the rapid growth phase (see § 5). As HERLACH *et al.* [1993] pointed out, there are many issues to be resolved in determining the mechanism responsible for grain refinement in highly supercooled melts and containerless processing. SCHWARZ *et al.* [1994] have presented a simple model of dendrite fragmentation by a Rayleigh instability that appears to predict the correct value for ΔT^* for Cu–Ni alloys.

A variant of the supercooling method uses so-called *denucleation*, a concept introduced by MARCANTONIO and MONDOLFO [1974], working with aluminum alloys. If the nucleants that act at low supercooling can be removed (by centrifuging during freezing, among other methods) a denucleated melt can be supercooled well below its freezing point where it can be made to freeze rapidly on a chosen nucleant. These authors were able to reduce considerably the grain size of commercial purity Aluminum and Al–Mn alloys by this method. Also in Al–Mn alloys the method permits the retention of a higher percentage of Mn in solid solution.

11.2.2. Innoculation methods

One of the most important examples of structure modification in industry is the grain refinement of Al and its alloys using innoculants that increase heterogeneous nucleation (See § 4). A fine grain size in shaped castings ensures the following: (i) mechanical properties that are uniform throughout the material, (ii) distribution of second phases and microporosity on a fine scale, (iii) improved machinability because of (ii), (iv) improved ability to achieve a uniformly anodizable surface, (v) better strength, toughness, and fatigue life, and (vi) better corrosion resistance.

The grain refining inoculants used in the aluminum industry employ so-called "master alloys" containing Al with Ti, B and C. Several mechanisms have been proposed for grain refinement and critical reviews exist in the literature (GLASSON and EMLEY [1968], ROSS and MONDOLFO [1980], PEREPEZKO and LEBEAU [1982], PEREPEZKO [1988], MCCARTNEY [1989]). It is agreed that when master alloys are added to aluminum alloy melts, the aluminum mattrix dissolves and releases intermetallics into the melt, probably Al_3Ti and various borides and carbides. Some compounds appear to act as effective nucleants with disregistry values below 10% and nucleation supercooling of less than about 5°C. In the past, the identities of the active nucleants have typically been studied from thermal and structural results obtained from standard bulk refinement tests. However more recently HOFFMEYER and PEREPEZKO [1989a], [1989b], [1991] utilized the Droplet Emulsion Technique (DET) (see § 4) to produce a fine dispersion of master alloys powders containing innoculant particles. In this way the response of Al to specific

effective and ineffective nucleants can be separated and identified through highly sensitive DTA and metallographic analysis. On the other hand, very recently JOHNSSON

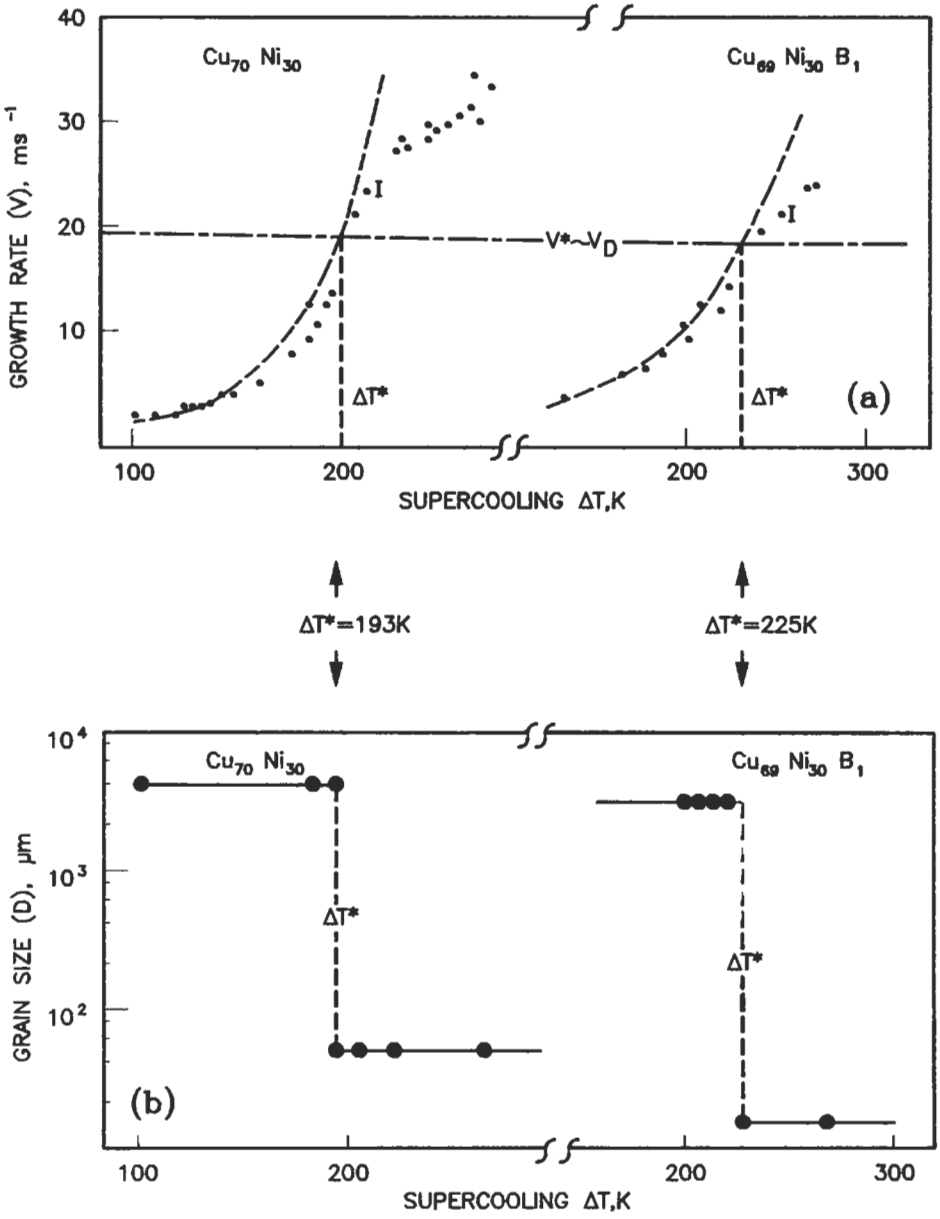

Fig. 73. Dendrite growth velocity and grain diameter as function of supercooling for $Cu_{70}Ni_{30}$ and $Cu_{69}Ni_{30}B_1$. WILLNECKER *et al.* [1990]. See HERLACH *et al.* [1993].

References: p. 830.

et al. [1993] used highly sensitive thermal analysis in bulk experiments to study the mechanisms of grain refinement in high purity Al by master alloys. The use of high purity material and a computer automated thermal analysis technique, permitted them to isolate the effect of the Ti and B containing particles. Both types of work are complementary and promise to elucidate the quite complicated refinement mechanisms.

Despite the uncertainty about the details of nucleation mechanisms, improvements have been made in theory in order to predict the final grain size as a function of the dispersion and density of nucleant particles. MAXWELL and HELLAWELL [1975] and HELLAWELL [1979] treat the ability of a substrate to act as a surface for heterogeneous nucleation simply using the *wetting angle*, θ, without entering into the details of the nucleation mechanism. A comparison is made between the final grain density and the initial nucleant density for various freezing conditions. As the melt cools below the liquidus, two processes take place concurrently. Solid nucleates on the available substrate surfaces at a rate which rises exponentially with the supercooling and, when the temperature has fallen below a certain limit, nucleated particles start to grow and evolve latent heat. The local cooling rate decreases as nucleation and growth accelerate until the temperature reaches a minimum and recalescence begins. The nucleation rate rises rapidly to a maximum at a temperature just before the minimum in the cooling curve. Afterwards the number of nucleation events decreases quickly as the available particles are exhausted and particularly because recalescence begins. Consequently, nucleation is almost complete just beyond the minimum temperature in the cooling curve. Subsequently, there is only growth. The number of grains varies according to the nucleation rate and is determined by the time recalescence begins.

The minimum temperature reached and the recalescence rate are strongly influenced by the growth rate from each nucleation center. MAXWELL and HELLAWELL [1975], and HELLAWELL [1979] employ a purely solute diffusion model for growth of spheres. More recently the *deterministic* model of RAPPAZ [1989] employs a more realistic dendritic growth model to predict final grain size for different inputs of nucleation and cooling conditions. An important effect is how grain size is decreased, for fixed nucleation and cooling conditions, by increasing the level of solute in the alloy. This occurs because of the reduction of the dendritic growth rate with increasing composition as described in § 7. The important effects of convection are not included in these models.

11.2.3. Energy-induced methods

A large number of methods have been employed to refine the grain structure through energy-induced methods that increase nucleation through cavitation or that promote crystal multiplication, principally through mechanical vibration, bubbling agitation, rotating magnetic fields, magnetic–electric interactions and mould oscillation. COLE and BOLLING [1969] and CAMPBELL [1981] present comprehensive reviews in the field. Although cavitation may be responsible for grain refinement under some experimental conditions, today it is generally accepted that the best, and cheapest method of grain refinement using energy-induced methods is to *promote crystal multiplication during the solidification process.* The multiplication occurs primarily by fragmentation of the

incipient dendritic structure by forced convection. FLEMINGS [1991] gives a summary of the possible dendrite fragmentation mechanism existing in the literature.

11.3. Eutectic modification

Among the most important foundry alloys are those based on the Fe–C and Al–Si systems. The mechanical properties of these metal–nonmetal (nonfacetted–facetted) eutectics are dominated by the morphologies in which the non-metals solidify. As nonfacetted–facetted eutectics, the asymmetry of the couple zone must always be considered in the interpretation of microstructure regarding the presence or absence of primary phases as described in § 8.1.5. In both systems the structure can be *modified* either by rapid cooling or by controlled addition of specific elements. The use of elemental additions has an advantage because their effect is essentially independent of the casting section thickness. Thus we shall only discuss modification by additives. The modification of the structure of these alloys and the resultant effect on the mechanical properties is a clear example of the manipulation of the structure based on the application of fundamental principles.

11.3.1. Aluminum–silicon alloys

Many studies have been focussed on the mechanism of modification in Al–Si alloy and several reviews are available (CHADWICK [1963]; SMITH [1968]; HELLAWELL [1970]; GRANGER and ELLIOTT ([1988]). Most important is the change of the morphology of the silicon phase in the eutectic mixture. In unmodified alloys, the Si phase in the eutectic appears as coarse flakes that grow more or less independently of the Al phase. With small additions of alkaline or alkaline earth metals (especially Na and Sr), the Si phase takes on a somewhat finer branched fibrous form that grows at a common liquid–solid interface with the Al phase to form a composite-like structure with improved properties. The easy branching of the modified Si leads to a more regular and finer structure as described in § 8.1.3. Modifiers also change the morphology of primary Si in hypereutectic alloys. Although nucleation studies have been performed (CROSSLEY and MONDOLFO [1966]; ROSS and MONDOLFO [1980]), the modifying effects of Na and Sr are now thought to be growth related (HANNA *et al.* [1984]). Nucleation remains important however, through the addition of Al–Ti–B master alloys to control the Al grain size in hypoeutectic alloys (§ 11.2.2) and through the addition of P (usually Cu–P) to promote heterogeneous nucleation (on AlP) and refinement of primary Si in hypereutectic alloys.

During the growth of unmodified Al–Si eutectic, the Si flakes contains widely spaced {111} twins that provide for easy growth in the [111] direction and difficult growth normal to [111]. This is called twin plane re-entrant edge (TPRE) growth. In modified alloys the Si fibres contain a much higher density of twins that exhibit an internal zig-zag pattern (LU and HELLAWELL [1987], [1988]). Since both Na and Sr are concentrated in the Si phase, these authors proposed a mechanism whereby the modifying elements are adsorbed on the growth ledges spewing out from the re-entrant corner. These adsorbed atoms cause the formation of new twins due to stacking errors on the growing interface due to size mismatch of the Si and the modifier. A hard sphere model for atomic packing

was used to define a critical ratio (1.65) of modifier to Si atomic size that promotes twinning. The growth of the Si is then thought to occur by repeated twin formation in a more isotropic manner than by TPRE governed growth. This more isotropic growth permits the Si fibers to branch and adjust eutectic spacing. The formation of the internal zig-zag twin structure is also consistent with the observation of microfaceting on the Al–Si interface (LU and HELLAWELL [1987]).

MAJOR and RUTTER [1989] proposed that a certain concentration of Sr is required at the interface to achieve modification (CLAPHAM and SMITH [1988]). Below a critical concentration, growth of the Si is by the twin plane re-entrant edge (TPRE) mechanism typical of unmodified eutectic. If growth occurs for a sufficient distance to accumulate Sr concentration at the solid–liquid interface above a critical level, the re-entrant edges are poisoned. Then, new twins form as described above. A continuous cycle of twin formation, TPRE growth, poisoning, new twin formation and so on can occur. More recently QIYANG *et al.* [1991] confirmed the adsorption of Na on $\{111\}_{Si}$ in agreement with the poisoning of the twin re-entrant edges. The phenomenon of overmodification can be explained as complete suppression of the TPRE mechanism resulting from elevated quantities of the modifying addition. In this way, formation of Al bands in overmodified structures (FREDRIKSSON *et al.* [1973]) may be explained.

11.3.2. Cast iron

It is known that cast iron, belonging to the family of high carbon Fe alloys, can solidify according to either the stable iron-graphite system (grey iron) or to the metastable Fe–Fe_3C system (white iron). As a consequence, the eutectic may be austenite–graphite or austenite–cementite (ledeburite). Furthermore, the complex chemical composition of the material has important and powerful effects on the structure of cast iron. Commercial alloys usually contain Si, minor addition of S, Mn and P and usually trace elements such as Al, Sn, Sb and Bi as well as the gaseous elements H, N and O. Both forms of cast irons (white and grey) have technological importance. Several comprehensive reviews and books have been published in the last decades both from fundamental and technological points of view (MORROG [1968a], [1968b]; MINKOFF [1983]; ELLIOT [1988]; STEFANESCU [1988]; CRAIG *et al.* [1988]; HUGHES [1988]; STEFANESCU *et al.* [1988]). Grey iron is the most interesting because of the different morphologies that the graphite can achieve and the resulting differences in mechanical and physical properties. Although semantic problems have confused scientists and foundrymen in the past, a general understanding of the mechanisms of nucleation, growth and modification of the graphite phase has occurred in the last 15 years. In this section, the present status of knowledge in the area will be discussed briefly.

It is known that the growth of the stable Fe–G eutectic is favoured over the metastable Fe_3C eutectic by slow freezing (See § 8.1.7.) or by addition of elements such as Si and Al. These elements increase the temperature difference between the stable Fe–G and metastable Fe–Fe_3C eutectic temperatures. In addition a wide variety of compounds have been claimed to serve as nuclei for graphite, including oxides, silicates, sulphides, nitrides, carbides and intermetallic compounds. Most of the nucleation mechanisms are connected with impurities existing in the melt or with inoculants that promote heterogen-

eous nucleation of the graphite. Although other inoculants are used, Fe–Si alloys are the most powerful and popular (ELLIOT [1988], STEFANESCU [1988]), SKALAND *et al.* [1993]).

11.3.3. Cast iron eutectic morphology

The morphology and characteristic of the eutectic, whether stable or metastable, with or without modification, are very important in determining the physical and thermal properties. Thus, it is worthwhile to consider the most important eutectic structures observed. The microstructure of these major forms are shown for example by STEFANESCU [1988].

White Irons: The metastable unalloyed Fe–Fe_3C ledeburite eutectic is classified as quasi-regular. HILLERT and SUBBARAO [1968] described the mode of growth of the eutectic as well as the orientations arising between Fe_3C and austenite(γ). POWELL [1980] has shown that the eutectic structure can be modified by quenching. By adding Cr or Mg, a plate-like Fe_3C structure associated with equiaxed grains can be achieved (STEFANESCU [1988]).

Grey Irons: For high purity Fe–C–Si alloys, the structure of the Fe–G eutectic is *spheroidal* (SADOCHA and GRUZLESKY [1975]). However in practice the presence of impurities in the melt cause the graphite to take a flake morphology and grey flake iron is considered to be the *characteristic* form from a practical point of view. Modification of this structure gives different graphite morphologies: *nodular*, *compact* or *vermicular*, and *coral*. We shall be concerned only with the growth of eutectic structures without a primary phase and we will refer mainly to the three structures widely used in industry: flake, compact or vermicular, and nodular or spheroidal cast iron.

At present there exists a theory for the mechanisms of the evolution from flake to compact and nodular graphite (MINKOFF [1990]): (i) fig. 74 corresponds to cooling curves for the three types of structure (BACKERUD *et al.* [1975]). The major characteristics of these cooling curves is the increase of supercooling on going through flake, compact and spheroidal graphite forms. The rate of recalescence after nucleation is determined by the nucleation rate and the growth rate. (ii) *Grey flake irons*: the growth of the flake structure is well understood. Once graphite has nucleated, the eutectic cell or colony grows in an approximately radial manner and each flake is in contact with austenite up to the growing edge. The crystals of graphite grow in the close packed strong bonding "a" direction using steps created by rotation boundaries. These rotation boundaries are defects in the crystals in the form of rotations of the lattice around the <0001> axis. According to MINKOFF [1990], the screw dislocations on $\{10\bar{1}0\}$ planes, which have been proposed as an alternative growth mechanism, are inactive (fig. 75a).

ELLIOTT [1988], STEFANESCU [1988] and SKALAND *et al.* [1993] discuss the effect of S and O as promoters of the flake graphite morphology on the basis of their adsorption on the high-energy $(10\bar{1}0)$ plane. Thus, growth becomes predominant in the "a" direction. The result is a *plate like* or *flake* graphite. (iii) *Nodular or Spheroidal Irons*. This is considered a divorced eutectic. Until recently has been widely accepted that the growth of this eutectic begins with nucleation and growth of graphite in the liquid, followed by early encapsulation of these graphite speroids in austenite shells. The result is eutectic grains (often named "eutectic cells") presenting a single nodule (WETTERFALL *et al.*

References: p. 830.

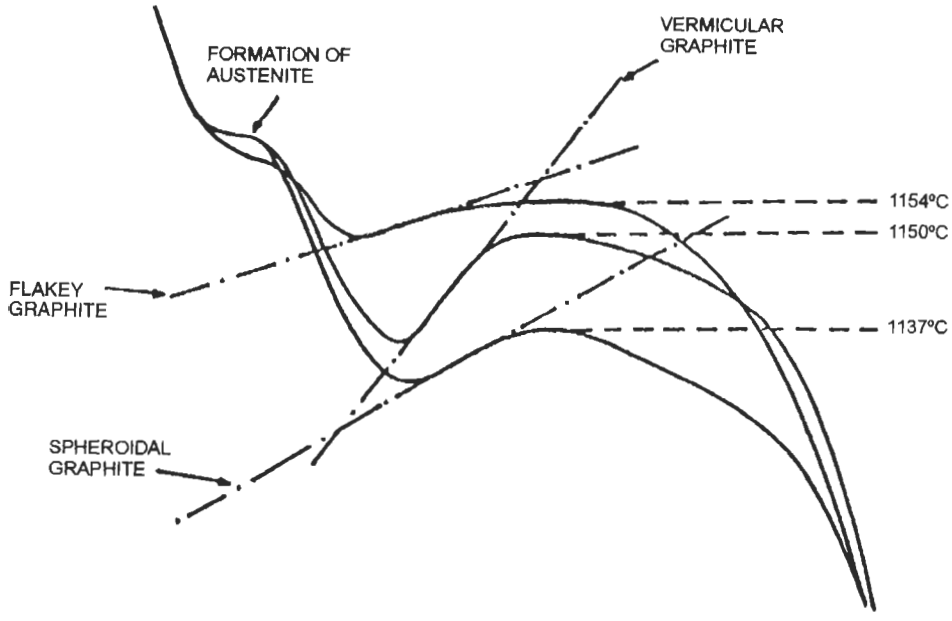

Fig. 74. Cooling curves for laminar, vermicular and nodular cast irons. BACKERUD *et al.* [1975].

[1972]). Thus, it is common practice in the foundry industry to associate the number of nodules to the number of eutectic grains. However recent research by SIKORA *et al.* [1990]) and BANERJEE and STEFANESCU [1991] indicated the existence of simultaneous nucleation of both the dendritic austenite and the spheroidal graphite. The interaction between both phases during solidification gives rise to the formation of eutectic grains presenting several nodules. This is a fact to be taken into account when micromodelling of the structure is attempted. Regarding the spheroidal growth of the graphite, several theories exist in the literature and they have been reviewed by MINKOFF [1983], ELLIOT [1988] and STEFANESCU [1988]. MINKOFF [1990] considers that the relationship among supercooling, melt chemistry and crystalline defects determine the spheroidal growth of the graphite. In this case the screw dislocation mechanism is considered dominant in causing repeated instability of the pyramidal surfaces, so that a radial array of pyramids is formed (fig. 75b). (iv) *Compact or Vermicular Graphite Irons*: This intermediate graphite morphology has been studied extensively due to its technological importance (RIPOSAN *et al.* [1985]). The graphite is interconnected within the eutectic cell but its growth differs from flake graphite. As in the case of spherulitic growth, several theories exist (STEFANESCU [1988], ELLIOT [1988]). The influence of the melt chemistry is very important. The occurence of compact graphite form requires a balance between flake-promoting elements, such as S and O, spheroidizing elements such as Mg, Ce and La, and antispheroidizing elements such as Ti and Al (SUBRAMANIAN *et al.* [1985]).

MINKOFF [1990], in his general approach to the interdependence of supercooling,

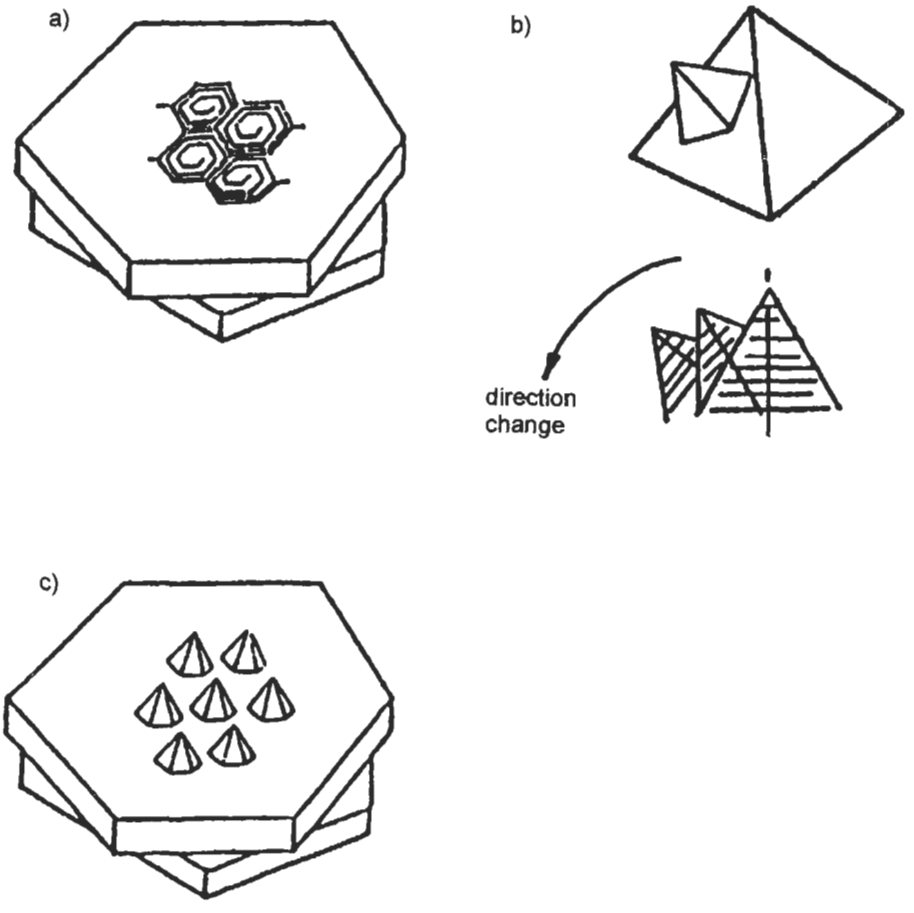

Fig. 75. (a) Mechanism of growth of flake graphite from a rotation boundary which provides steps for the nucleation of (1010) faces. (b) Mechanim of growth of spheroidal graphite by repeated instability of pyramidal surfaces forming a radial array. (c) Mechanism of growth of compacted graphite by development of pyramidal forms on the crystal surface at steps due to screw dislocations. MINKOFF [1990].

chemical composition and crystalline defects, considered that compact or vermicular graphite forms are intermediate between flake and spherulitic formation, and that the rounded morphology of the structure is a result of the thickening of graphite crystals at small values of supercooling by growth from the steps of screw dislocations, which have Burgers vector in the <0001> direction (fig. 75c). We consider that the mechanisms of graphite growth as well as modification by proper chemical agents is an open research field. Recent unidirectional solidification of flake and compact graphite irons with and without "in situ" modification in front of the S–L interface open questions about the forms of crystalline growth of the graphite phase, as well as the influence of the impurities and chemical agents on the surface tension of the Fe–G eutectic phases (ROVIGLIONE and HERMIDA [1994], ROVIGLIONE and BILONI [1994]).

References: p. 830.

11.4. Influence of rapid solidification processes (RSP)

Most of the fundamentals of RSP have been included in § 2–8 and grain refinement due to high supercooling was described in § 11.1.2. The present section considers how RSP can be used to manipulate microstructure.

11.4.1. Experimental and production methods

The evolution of RSP methods goes back to the last century and its potential for the modification of microstructure were initiated by DUWEZ and his collaborators at the beginning of the 60's. They designed the *Duwez Gun*, a device in which a gaseous shock wave smashes a drop of about 10mg of molten alloy into contact with a copper substrate or *chill block* to produce small foils or *splats*. This method usually is called *splat cooling*. These authors were successful in making a continous series of Cu–Ag alloys without any two-phase structure. In the same year the first *metallic glasses* were also discovered (DUWEZ *et al.* [1960]) (see chapter 19, §§ 2 and 3). Much earlier work in the field focused on equipment invention and evaluation, for example, the invention of *melt spinning* by POND [1958]. Subsequently many other methods have been developed and they have been reviewed by JONES [1982], CAHN [1983], LAVERNIA *et al.* [1992], and SURYANARAYANA *et al.* [1991]. In all the methods a *cast* sample is produced where at least one physical dimension is small assuring a rapid removal of the latent heat of fusion by an appropriate heat sink. The methods developed to achieve rapid solidification have been categorized into three main categories, (i) *atomization*, (ii) *chill methods*, and (iii) *self substrate quenching*. (See also detailed discussion in ch. 19, § 3).

In *atomization* a fine dispersion of droplets is formed when molten metal is impacted by a high energy fluid; as a result of the transfer of kinetic energy from the atomising fluid (gas or liquid) to molten metal, atomization occurs. For example LAVERNIA *et al.* [1992] summarize the phenomena associated with the method considering that the size distribution of atomized droplets will depend on: (a) the properties of the material, such as liquidus temperature, density, thermal conductivity, surface tension, heat capacity and heat of fusion; (b) the properties of the gas, such as density, heat capacity, viscosity and thermal conductivity and (c) the processing parameters such as atomization gas pressure, superheat temperature and metal/gas flow ratio. One of the most important applications of the atomization method is powder fabrication. Powder is convenient for subsequent consolidation into near final shapes. Variants of the method include, among others, gas atomization, centrifugal atomization and spark erosion (KOCH [1988]). A recent review by GRANT [1992] indicates that in recent years, atomization processes have been improved, new alloy compositions have been developed, hot isotatic pressing (HIP) has become an important processing tool, and new commercial product areas have emerged.

One extension of the atomization method is *spray atomization and deposition*. Pionneering work in this area was performed by SINGER [1970], [1972]. The general principle of the method is to atomize a stream of molten metal and to direct the resulting spray onto a shaped collector, or mandril. On impact with the collector, the particles, often partially liquid, flatten and weld together to form a high density preform which can be readily forged to form a product. LAVERNIA *et al.* [1992] and GRANT [1992] reviewed

the different variables involved in the method. Additionally, GRANT [1992] reviewed further application of the method to the formation of continuous sheet. It seems clear that high potential exists for continuous forming of steel and other metals as strips, sheet, plate and other forms. Recently ANNAVARAPU and DOHERTY [1993] have developed an understanding of the microstructural development in spray forming.

Chill Methods: *Melt spinning* is the technique most widely used in rapid solidification because it is easy to execute and the quenching rates compare favorably with other available processes. Melt spinning makes possible the production of long narrow ribbons up to a maximum width of 3 mm. This limitation has led to the development of a patented method, *planar flow casting* (fig. 76a), and to renewed interest in the melt *overflow process* originally patented in 1911 by STRANGE (fig. 76b) and now not protected by patents. Both methods can yield large quantities of wide ribbons cooled at rates approaching 10^6 Ks^{-1}.

Self-Substrate Quenching Methods: In this method the main objective is the modification of surface layers by rapid solidification. The heat source is typically a scanned or pulsed laser or electron beam focussed onto the specimen surface to cause rapid melting and resolidification. Spark discharge has also been used as a localized heat source. This field, especially when laser beams are used, have been reviewed among others by DRAPER and POATE [1985] and SURYANARAYANA *et al.* [1991]. Because of the intimate thermal contact within the different regions of the sample, the flow of heat during solidification can be modeled simply by conduction into the underlying cold material. In addition resolidification does not require nucleation: the unmelted portion of a crystalline sample provides a growth source. Then the supercooling that exists in the process is only associated with the S–L interface and is due to kinetics of the growth.

11.4.2. Relationships between RSP and solidification structures

The principal changes which can be brought about in crystalline alloys by RSP include, (i) Extension of solid-state solubility; (ii) refinement of grain size, with possible modification of grain shapes and textures; (iii) reduction or elimination of microsegregation; (iv) formation of metastable phases; (v) achievement of high density of point defects; (vi) surface alloying. Many aspects of RSP have been discussed earlier from thermodynamic and /or kinetic points of view. Several papers and reviews exist for particular metals and alloys as a consequence of the increasing importance of RSP. Among these contributions the reader is referred to LAVERNIA *et al.* [1992] for aluminum alloys; KOCH [1988] for intermetallic compounds; SURYAMARAYANA *et al.* [1991] for titanium alloys; GRANT [1992] for powder production by RSP methods; PAWLOSKI and FUCHAIS [1992] for thermally sprayed materials; DRAPER and POATE [1985] for laser surface alloying; CHEN *et al.* [1988a] [1988b] for laser surface modification of ductile iron. KURZ and TRIVEDI [1989] have modeled the selection of the microstructure under given laser processing conditions.

11.5. Low gravity effects during solidification

The common features of research in this area are the drastic reduction of sedimentation and buoyancy driven convection. Space flight provides solidification research with

References: p. 830.

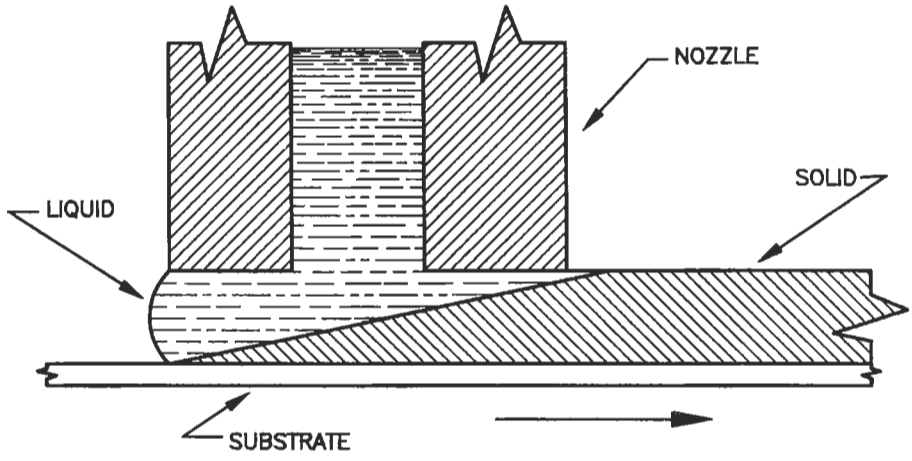

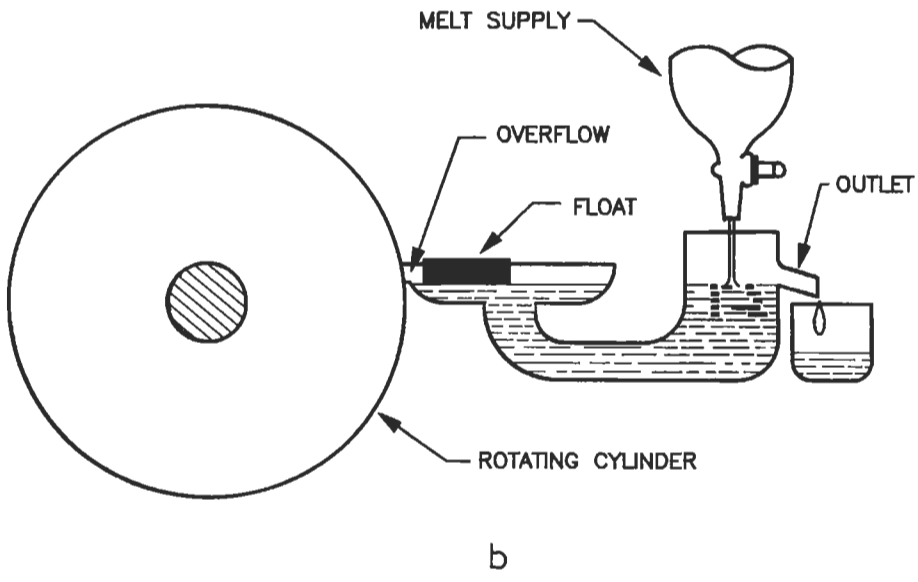

Fig. 76. (a) Planar flow casting in which the nozzle is positioned near the moving substrate to control the thickness of the cast tape. NARASHIMAM [1980]. See LAVERNIA *et al.* [1992]. (b) Melt overflow process as described by Strange in 1911 patent. STRANGE [1911]. See LAVERNIA *et al.* [1992].

long duration access to *microgravity*. However there also exist several short duration free fall facilities. Figure 77 shows the available low-g experimental systems (CURRERI and STEFANESCU [1988]). Both drop tubes and drop towers are used extensively. A *drop tube* is an enclosure in which a molten droplet can solidified while falling freely either in vacuum or in a protective atmosphere. Microgravity conditions are obtained up to a maximum of about 2 s. By contrast in a *drop tower* an entire experimental package, which may include furnace and instrumentation as well as the specimen is dropped within an enclosure. At present the best facilities are at NASA-LRC and at ZARM (Bremen) with drop towers of 145 m and 110 m height where 10^{-6} and 10^{-5} g during free fall times of 5.2 and 4.7 s respectively are obtained. However, the 500 m drop tower planned at Sunagawa (Japan) and the Eurotube-Saar project of 1200 m high drop tower would give microgravity periods of 10 s and 12 s respectively (HERLACH *et al.* [1993]). On the other hand parabolic flight and suborbital sounding rockets (fig. 77) provide microgravity levels between 30 s and 5 min.

The wide variety of experiments and disciplines involved in microgravity research opens a new field where solidification and mechanisms as modified by the near null value of gravity may be studied. On the basis of different reviews (JANSEN and SAHM

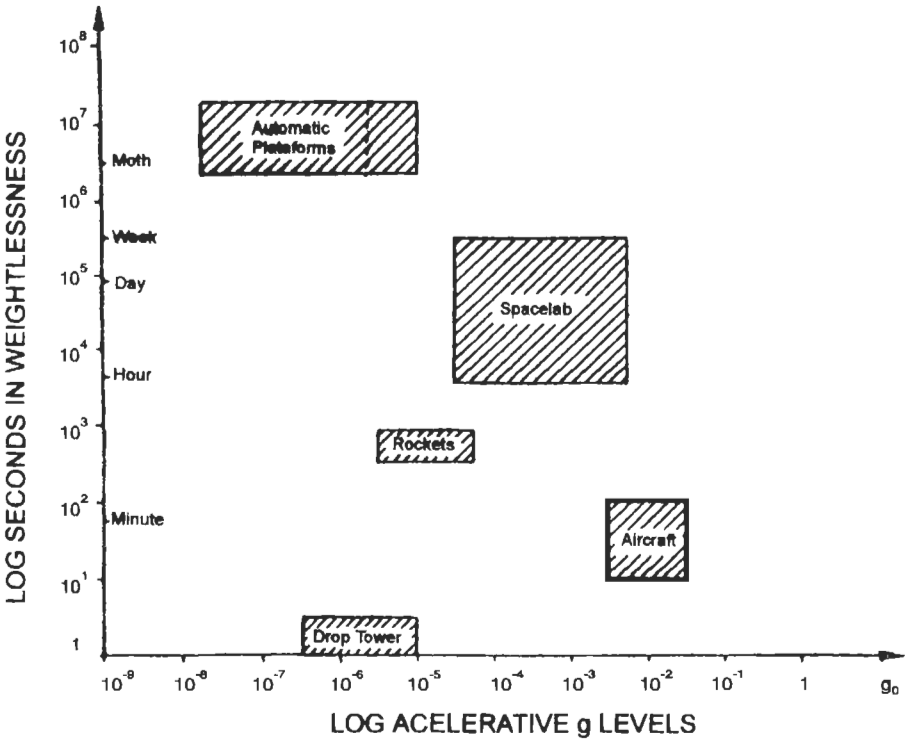

Fig. 77. Regimes of microgravity experimentation in terms of time in weightlessness and accelerative g-levels. CURRERI and STEFANESCU [1988].

References: p. 830.

[1984], MINKOFF [1986], CURRERI and STEFANESCU [1988], HERLACH *et al.* [1993]) among others, and the numerous proceedings of microgravity symposia quoted by the preceding authors, the mechanisms under study can be summarized: (i) distribution of the constituents in the initial fluid phase; (ii) phenomena of mass and heat transfer in the absence of bouyancy-driven convection. The drastic reduction of this source of convection leads to the increased influence of other mechanisms, which in general are masked on earth, namely: a) *Marangoni* convection; b) fluid movement as a result of expansion associated with phase changes or in the presence of electric, magnetic or thermoelectric fields; c) mechanisms of solute redistribution through diffusion; d) damping of temperature fluctuations in the fluid phase; e) effect of the absence of gravity on phase interfaces or meniscuses. iii) Techniques for forming or preparing materials without crucibles, direct formation of whiskers, thin films without substrates, production of hollow spheres with extremely thin walls, and float zone melting with large diameter; iv) in the more specific case of alloys in connection with casting structures: a) convection and solute distribution, b) solidification of off-monotectic and eutectic alloys, c) morphological stability of the S–L interface, d) micro- and macrosegregation, e) grain multiplication and casting structures.

11.6. Solidification processing of metal matrix composites

Thirty years ago KELLY and DAVIES [1965] and CRATCHLEY [1965] summarized their own and other pioneering efforts on metal matrix composites. Recently there has been a surge of interest in using reinforced metal matrix composites as structural materials. ASHBY [1993] indicates that any two materials can, in principle, be combined to make a composite in many geometries. A review of the processes for fabrication of MMCs is presented by GOSH [1990] covering a wide range of materials such as light alloy matrices, high temperature matrices and other special cases such as high thermal conductivity matrices and a variety of particulates, whiskers and fibers as reinforcements. Process methods may be divided as follows (i) liquid metal processes, (ii) solid state processes, (iii) deposition processes and (iv) deformation processes. Of these, solidification processing of MMC is gaining more and more importance because liquid metal is relatively inexpensive, and can flow easily to surround the reinforcing phases and create composites having a wide variety of shapes. ROHATGI [1988] has presented the state of the art related to the technical aspects of solidification processing for metal matrix composite fabrication. MORTENSEN [1991b] and MORTENSEN and JIN [1992] have reviewed the fundamentals. MORTENSEN [1991b] has classified the methods for production of MMCs into four classes on the basis of the mechanism by which the reinforcement and metal are combined (fig. 78 a–d).

1. ***Infiltration***. (fig. 78A) The reinforcement phase is stationary and essentially constitutes a very fine and intricate mould into which the liquid metal flows to fill all open porosity.
2. ***Dispersion processes*** (fig. 78B) The reinforcement phase is discrete and is added to the metal. Entrainment of the reinforcing phase into the melt is affected by agitation, which acts on the reinforcement via viscous shear stresses.
3. ***Spray processes*** (fig. 78C) The metal is divided into molten droplets and sprayed with,

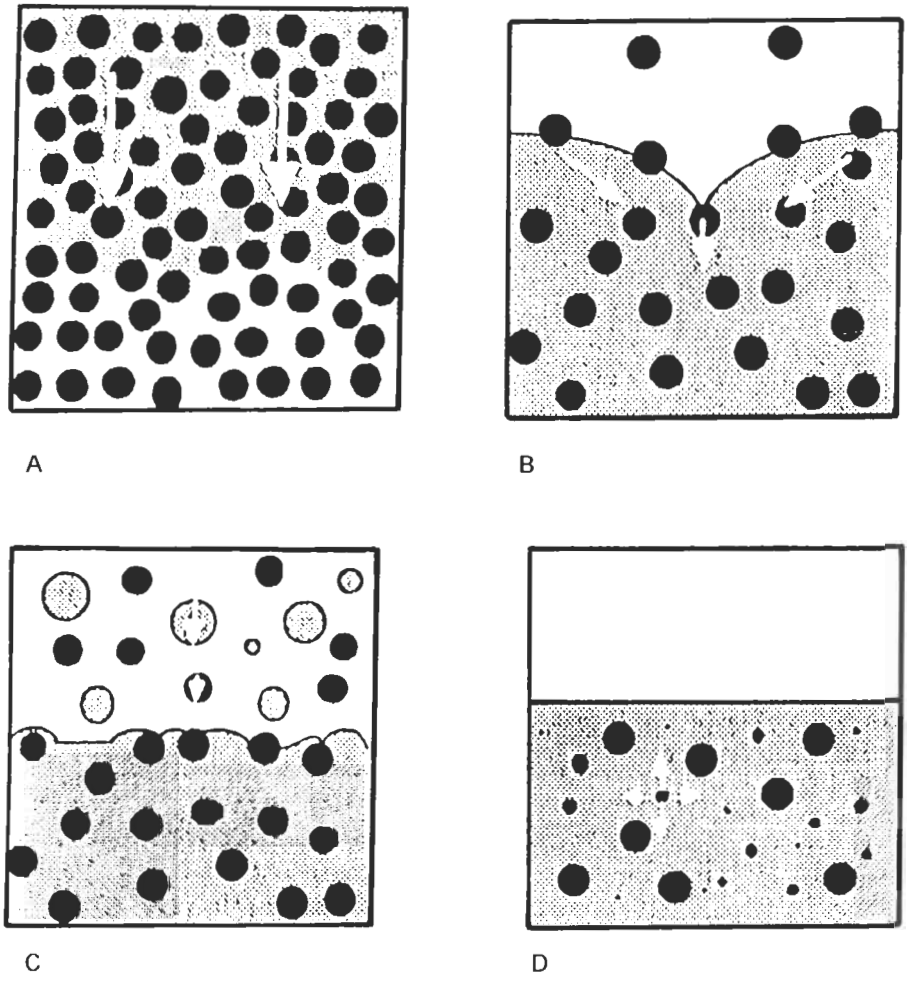

Fig. 78. Schematic representation of the principal classes of metal matrix composite solidification processes: A: infiltration, B: dispersion, C: spray-casting and D: in-situ processes. The reinforcing phase is black, the metal gray. MORTENSEN [1991b].

or onto, the reinforcement. Incorporation of the reinforcement into the matrix is affected by the added surface energy of the metal and the kinetic energy of moving droplets and particles.

4. ***In situ-processes*** (fig. 78D) Essentially consists of obtaining composites via directional solidification. In contrast with the above methods, "in-situ" processes use conventional alloying and not an artificial combination of two phases. Thus the material can have exceptional high temperature capabilities.

MORTENSEN and JIN [1992] present a comprehensive review of the physical phenom-

ena that govern infiltration and dispersion processes, which describes the governing phenomena of the process as being connected with the three main steps of metal matrix composite solidification.

The *first step* involves the interaction between the liquid matrix and the reinforcement material. This step is governing by the *wetting* between the metal and the reinforcing phase that are being combined. In most cases wetting is generally unfavorable and positive pressure and hence external work must be provided to create the composite (MORTENSEN [1991b]). From an elementary thermodynamic analysis a minimum amount of energy W per unit volume of composite is equal to

$$W = A_i(\gamma_{LR} - \gamma_{AR}), \tag{121}$$

where A_i is the surface area of the reinforcement/matrix interface per unit volume of composite; γ_{LR} = reinforcement/molten metal interfacial energy; γ_{AR} = reinforcement/atmosphere interfacial energy. MORTENSEN and JIN [1992] discussed the methods to measure wettability and to improve it namely by: (a) reinforcement pretreatment, (b) alloying modification of the matrix and (c) reinforcement coating. From a chemical point of view, knowledge about the surface of the metal matrix, the reinforcement surface and the interface chemistry as well as the influence of alloy additions and reactive wetting are described.

The *second step* corresponds to fluid flow, heat transfer and solidification phenomena that takes place in the composite material during infiltration and before it is fully solidified. The mechanics of infiltration and thermal and solidification effects, as well as processing of metal matrix composite slurries, (rheology and particle migration) must be considered.

The *third step* corresponds to completion of the solidification process. The solidification of the metal matrix is strongly influenced by the presence of the reinforcing phase that can affect the nucleation, coarsening, microsegregation and grain size. In the case of particulate composites, particle pushing theories and experiments discussed in § 9 are very important.

In conclusion it appears that the solidification processing of MMCs is an open and fascinating research area. It now stands at a point where the most essential phenomena are beginning to be clarified. On the other hand, the engineering potential of metal matrix composites is continuously increasing. Reinforced metals have been introduced in a growing number of applications, ranging from the sports industry, electronics and aerospace to the automotive sector. Current estimates indicate that the number of applications and their commercial significance will grow significantly over the next decade (WHITE and OLSON [1990]).

11.7. Semisolid metal forming processes

When metals or alloys solidify in castings and ingots, a dendritic structure forms that develops cohesion when the alloy is as little as 20% solid. Thereafter strength develops rapidly. When the casting is deformed during solidification, deformation takes place preferentially along grain boundaries; grains slide and roll over one another with small welds forming and breaking. Occasional bending of dendrite arms in the neighbourhood

of the region of deformation also occurs. As deformation proceeds, open fisures may form (*hot tears*) and be fed by liquid. In this case segregated regions, sometimes called *filled hot tears* result, yielding *V* segregates as mentioned in § 9 (FLEMINGS and MEHRABIAN [1971]). In the course of this type of macrosegregation research, METZ and FLEMINGS [1969a], [1969b] performed experiments where small blocks of Al alloys were isothermally sheared. They found negligible strength below about 0.2 fraction solid. SPENCER *et al.* [1972] carried out similar tests of Sn–15pct Pb alloy. Their test apparatus consisted of two grooved, counter-rotating cylinders. Figure 79a) shows the result obtained. Cleverly SPENCER [1971] decided to use the same apparatus to conduct a quite different type of test. Instead of partially solidifying the alloy before beginning the shear, they began the shear above the liquidus and then slowly cooled the alloy into the solidification range (fig. 79b). Two major differences are noted: (i) there is a change from

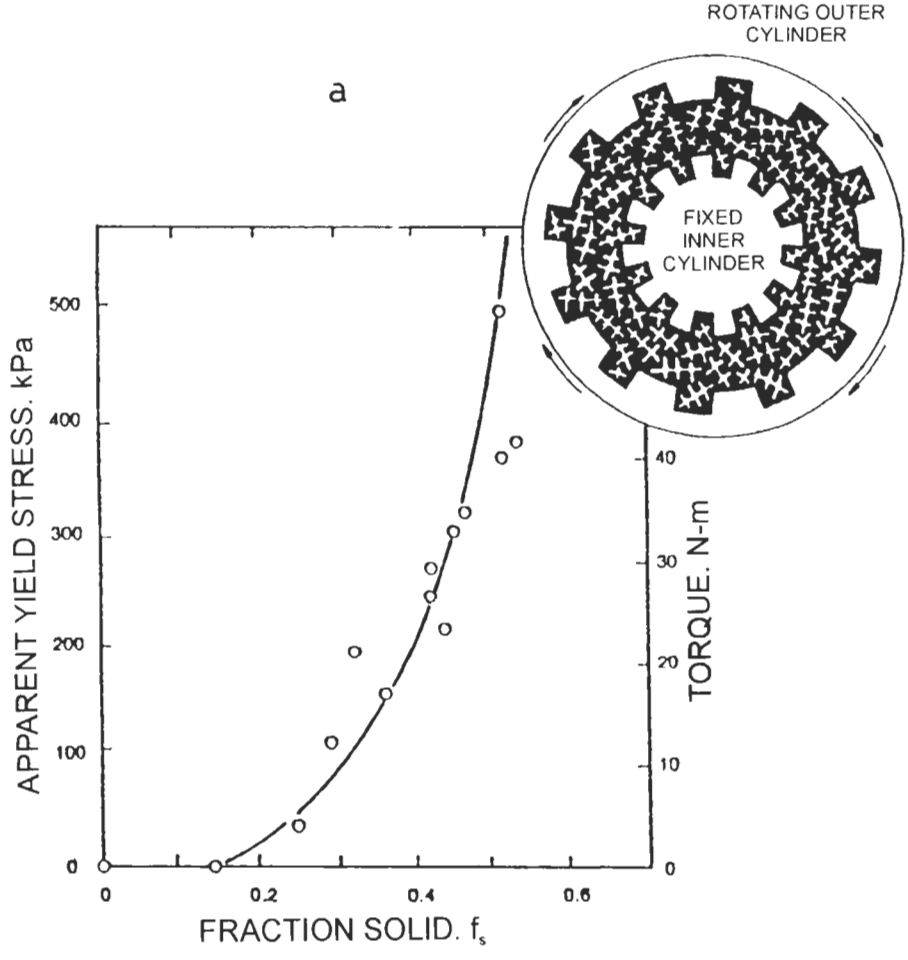

Fig. 79a

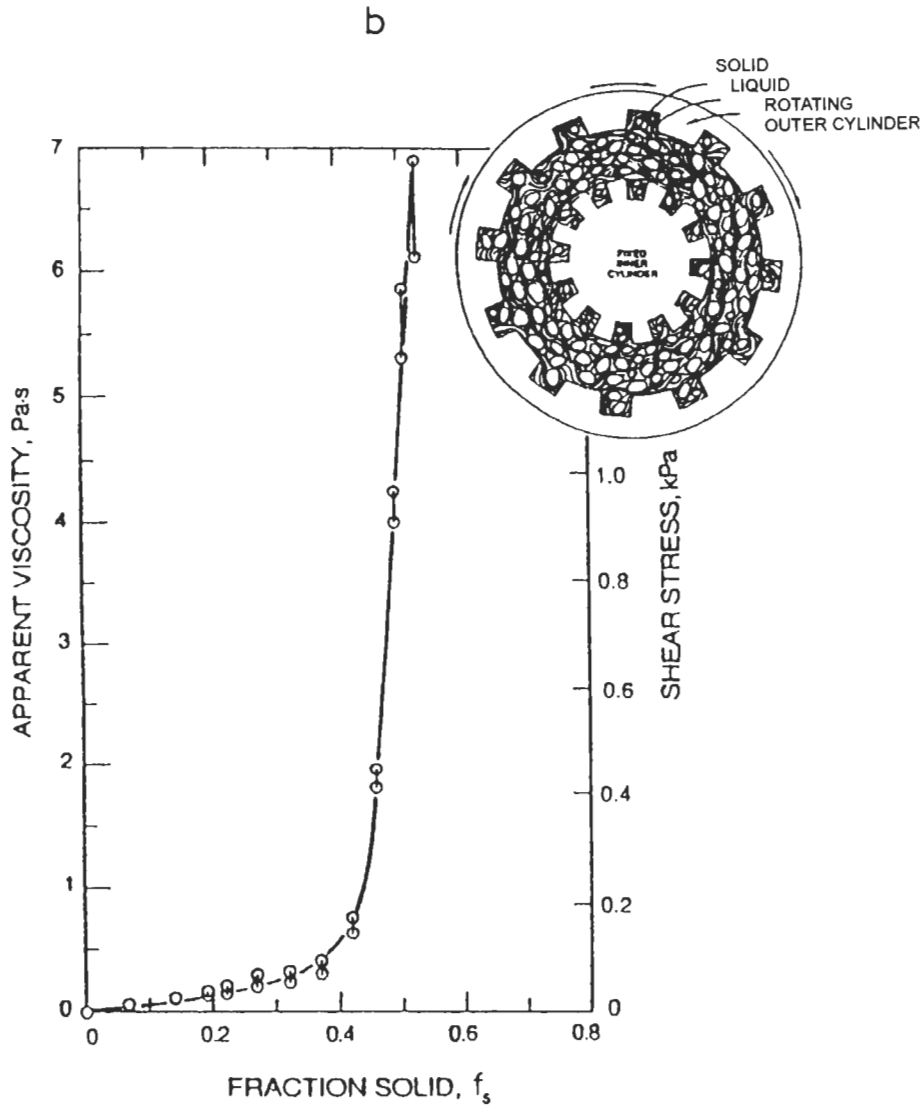

Fig. 79. (a) Maximum shear strength of semisolid dendritic Sn-15wt pct Pb alloy vs. fraction solid obtained in isothermal experiments. (at a shear rate of 0.16 s^{-1}). Schematic upper right shows test arrangement. (b) Viscosity and shear stress vs. fraction solid for Sn-15 wt pct Pb alloy cooled at 0.006 Ks^{-1} and sheared continuously at 200 s^{-1}. Schematic at upper right is an illustration of the test specimen. FLEMINGS [1991].

dendritic to non-dendritic structure; (ii) the shear stress is diminished for the dendritic structure compared to the nondendritic structure. For example, at $f_s = 0.4$ the shear stresses are 200 KPa and 0.2 KPa respectively. The material behaves as a liquid-like

slurry to which an apparent viscosity can be assigned, as has been done in fig. 79b). The fundamentals of the semi-solid metal (SSM) forming processes lie in these results. Recently FLEMINGS [1991] presented an extensive review of the development of this processes during the last 20 years as well as the current industrial applications. Also KENNEY *et al.* [1988] reviewed this area, especially from an applied and technological point of view.

Different names to characterize SSM forming processes exist in the literature. In *rheocasting* (from the Greek "rheo" to flow) strong shear forces break off dendrite fragments. If the alloy is poured when the viscosity is still low, it can be made to fill the mould. Each dendrite fragment becomes a separate crystal and a very fine grain size can be achieved without the disadvantages inherent in the use of grain-refining additions. The process also affects other casting features because the alloy is already partialy frozen when cast. Thus, shrinkage is reduced and economy in risers and gating may be substantial. Pouring temperature can also be much lower and as a consequence the amount of heat to be removed is lower and thermal stresses are reduced. Through this method all kinds of castings can be made including *continuous rheocasting* with or without electromagnetic stirring. The method can be used to prepare material to be utilised in subsequent casting processes. The prepared slugs are heatly rapidly to the partially molten state, dropped in the die-casting machine and forged under pressure into the mould. This method is named *thixocasting*. One important advantage is the dramatic improvement in die life due primarily to reduced metal temperature.

Compocasting corresponds to the development and production of metal-matrix composites containing nonmetallic particles, taking advantage of the rheological behaviour and structure of the partially solidified and agitated matrix. The particulate or fibrous nonmetals are added to the partially solid alloy slurry. The problems of wettability and their solutions are similar to those discussed in § 11.6. and the reader is referred to the MORTENSEN and JIN [1992] review of MMC processes. The high viscosity of the slurry and the presence of a high volume fraction of primary solid in the alloy slurry prevents the nonmetallic particles from floating, setting or aglomerating. With increasing mixing times, after addition, interaction between particles and the alloy matrix promotes bonding. The composites are subsequently reheated to the partially molten state in a second induction furnace and forged into shape with hydraulic presses. Very promising wear-resistant alloys have been obtained based on work by SATO and MEHRABIAN [1976] in Al alloys containing particulate additions of Al_2O_3 and SiC. MATSUMIYA and FLEMINGS [1981] extended the application of SMM to strip-casting and the basic technology of SMM provides a potential means of metal purification (MEHRABIAN *et al.* [1974]).

Acknowledgements

The authors wish to acknowledge the contributions of their various co-workers over the years and the financial support of many agencies. Special thanks are in order for S.R. Coriell and F. W. Gayle for criticisms of this manuscript, and to Miss Graciela Martínez for her effort and patience in the elaboration of the manuscript.

References: p. 830.

*References**

ADAM, C. M. and L. M. HOGAN, 1972, J. Australian Inst. of Metals, **17**, 81.

ADORNATO, M. and R. A. BROWN, 1987, J. Cryst. Growth **80**, 155.

AGUILAR RIVAS, R. A. and H. BILONI, 1980 a), Z. Metallk. **71**, 264.

AGUILAR RIVAS, R. A. and H. BILONI, 1980 b), Z. Metallk. **71**, 309.

ANDREWS, J. B., A. L. SCHMALE, and A. C. SANDLIN, 1992, J. Cryst. Growth **119**, 152.

ANNAVARAPU, S. and R. D. DOHERTY, 1993, Int. J. of Powder Metall. **29**, 331.

APELIAN, D., 1982, in: Aluminum Transformation Technology and Applications 1981, eds. C. A. Pampillo, H. Biloni, L. Mondolfo and F. Sacchi (ASM, Metals Park, OH) p. 423.

APTEKAR, J. L. and D. S. KAMENETSKAYA, 1962, Fiz Metal, Metalloved, **14**, 123.

ASHBY, M. F., 1993, Acta Metall Mater. **41**, 1313.

AUDERO, M. A. and H. BILONI, 1972, J. Cryst. Growth **12**, 297.

AUDERO, M. A. and H. BILONI, 1973, J. Cryst. Growth **18**, 257.

AZIZ, M. J., 1982, J. Appl Phys. **53**, 1158.

AZIZ, M. J. and T. KAPLAN, 1988, Acta Metall. **36**, 2335.

AZIZ, M. J. and W. J. BOETTINGER, 1994, Acta Metall. Mater. **42**, 527.

BACKERUD, L., K. NILSSON and H. STEEN, 1975, in: Metallurgy of Cast Iron (Georgy Pub. Co., St. Saphorin, Switzerland), p. 625.

*BAKER, J. C., 1970, Interfacial Partitioning During Solidification, Ph. D. Thesis, Massachusetts Institute of Technology, Chapter V, (see also CAHN *et al.* [1980]).

BAKER, J. C. and J. W. CAHN, 1971, in: Solidification (ASM, Metals Park, OH), p. 23.

BAKER, C. and V. SUBRAMANIAN, 1980, in: Aluminum Transformation Technology and Applications 1979, eds. C. A. Pampillo, H. Biloni and D. E. Embury (ASM, Metals Park, OH.) p. 335.

BANERJEE, D. K. and D. M. STEFANESCU, 1991, Trans. AFS, **99**, 747.

BASKARAN, V., W. R. WILCOX, 1984, J. Cryst. Growth **67**, 343.

BATTLE, T. P., 1992, Int. Mat. Rev. **37**, 249.

BATTLE, T. P., and R. D. PEHLKE, 1990, Metall. Trans. **21B**, 357.

BECKERMANN, C. and R. VISKANTA, 1988, Physicochem. Hydrodyn. **10**, 195.

BENNON, W. D. and F. P. INCROPERA, 1987 a), Int. J. Heat Mass Transfer **30**, 2161.

BENNON, W. D. and F. P. INCROPERA, 1987 b), Int. J. Heat Mass Transfer **30**, 2171.

BERRY, J. T. and R. D. PEHLKE, 1988, in: Metals Handbook, ninth ed., **15**: Casting (ASM, Metals Park, OH), 858.

BERTORELLO, H. R., and H. BILONI, 1969, Trans. Met. Soc. AIME **245**, 1375.

BILLIA, B. and R. TRIVEDI, 1993, in: Handbook of Crystal Growth 1B: Fundamentals, Transport and Stability, D. T. J. Hurle, ed., (North-Holland, Amsterdam) p. 899.

*BILONI, H., 1968, in: The Solidification and Casting of Metals (Iron and Steel Inst., London) Pub. 110, p. 74.

BILONI, H., 1970, Metallurgia ABM (Aso. Brasileira de Metais) **26**, 803.

BILONI, H., 1977, Ciencia Interamericana **18** (3–4), 3.

BILONI, H., 1980, in: Aluminum Transformation Technology and Applications 1979, eds. C. A. Pampillo, H. Biloni and D. E. Embury (ASM, Metals Park, OH) p. 1.

BILONI, H., 1983, Solidification, in: Physical Metallurgy, 3rd. ed, Ed. R. W. Cahn and P. Haasen (North Holland, Amsterdam), p. 478.

BILONI, H. and B. CHALMERS, 1965, Trans. Met. Soc. AIME, **233**, 373.

BILONI, H., G. F. BOLLING and H. A. DOMIAN, 1965 a), Trans. Met. Soc. AIME **233**, 1926.

BILONI, H., G. F. BOLLING and G. S. COLE, 1965 b), Trans. Met. Soc. AIME **233**, 251.

BILONI, H., G. F. BOLLING, and G. S. COLE, 1966, Trans. Met. Soc. AIME **236**, 930.

BILONI, H., R. DI BELLA and G. F. BOLLING, 1967, Trans. Met. Soc. AIME **239**, 2012.

BILONI, H. and B. CHALMERS, 1968, J. Mat. Sci. **3**, 139.

* References marked with an asterisk are suitable for Further Reading.

BILONI, H. and R. MORANDO, 1968, Trans. Met. Soc. AIME **242**, 1121.
BLODGETT, J. A., R. J. SCHAEFER, and M. E. GLICKSMAN, 1974, M. E., Metallography **7**, 453.
BOBADILLA, M., J. LACAZE, G. J. LESOULT, 1988, J. Cryst. Growth **89**, 531.
BOETTINGER, W. J., 1974, Metall. Trans. **5**, 2023.
BOETTINGER, W. J., 1981, in: Proc. Fourth Intl. Conf. on Rapidly Quenched Metals, edited by T. Masumoto and K. Suzuki, (The Japan Institute of Metals, Sendai, Japan), p. 99.
BOETTINGER, W. J., 1982, in: Rapidly Solidified Crystalline and Amorphous Alloys, B. H. Kear and B. C. Giessen, eds., (Elsevier North Holland, NY), p. 15.
BOETTINGER, 1988, unpublished research, NIST, Gaithersburg, MD, U.S.A.
BOETTINGER, W. J., D. SHECHTMAN, R. J. SCHAEFER, and F. S. BIANCANIELLO, 1984, Metall. Trans. **15A**, 55.
*BOETTINGER, W. J. and J. H. PEREPEZKO, 1985, in: Rapidly Solidified Crystalline Alloys, S. K. Das, B. H. Kear, C. M. Adam, eds., (TMS-AIME), p. 21.
BOETTINGER, W. J., L. A. BENDERSKY and J. G. EARLY, 1986, Metall. Trans. **17A**, 781.
BOETTINGER, W. J., and S. R. CORIELL, 1986, in: Science and Technology of the Supercooled Melt, P. R. Sahm, H. Jones and C. M. Adam, eds., (NATO ASI Series E-No. 114, Martinus Nijhoff, Dordrecht), p. 81.
BOETTINGER, W. J., L. A. BENDERSKY, S. R. CORIELL, R. J. SCHAEFER, and F. S. BIANCANIELLO, 1987, J. Cryst. Growth **80**, 17.
BOETTINGER, W. J., L. A. BENDERSKY, F. S. BIANCANIELLO and J. W. CAHN, 1988a), Mater. Sci. Eng. **98**, 273.
BOETTINGER, W. J., S. R. CORIELL, and R. TRIVEDI, 1988b), in: Rapid Solidification Processing: Principles and Technologies R. Mehrabian and P. A. Parrish, eds., (Claitor's Publishing, Baton Rouge), p. 13.
BOETTINGER, W. J., L. A. BENDERSKY, R. J. SCHAEFER and F. S. BIANCANIELLO, 1988c, Metall. Trans. **19A**, 1101.
BOETTINGER, W. J., and M. J. AZIZ, 1989, Acta Metall. **37**, 3379.
BOLLING, G. F., 1971, in: Solidification (ASM, Metals Park, Oh.), p. 341.
BOWER, T. F., H. D. BRODY, and M. C. FLEMINGS, 1966, Trans. Met. Soc. AIME **236**, 624.
BOWER, T. F. and M. C. FLEMINGS, 1967, Trans. Met. Soc. AIME **239**, 1620.
BOWER, T. F., D. A. GRANGER and J. KEVERIAN, 1971, in: Solidification (ASM Metals Park, OH), p. 385.
BRAUN, R. J., and S. H. DAVIS, 1991, J. Cryst. Growth **112**, 670.
BRICE, J. C., 1973, in: The Growth of Crystals from Liquids (North Holland, Amsterdam), p. 120
BRIMACOMBE, J. K., 1993, Metall. Trans., **24B**, 917.
BRIMACOMBE, J. K., and I. V. SAMARASEKERA, 1990, in: Principles of Solidification and Materials Processing, T. 1, (Trans. Tech. Publication), p. 179.
BRODY, H. D., 1974, in: Solidification Technology, eds. J. J. Burke, M. C. Flemings and A. E. Quorum (Brook Hill Pub., Chesnut Hills, MA) p. 53.
BRODY, H. D. and FLEMINGS, M. C., 1966, Trans. Met. Soc. AIME **236**, 615.
BRODY, H. D., and S. A. DAVID, 1979, in: Solidification and Casting of Metals (The Metals Society, London) p. 144.
BROUGHTON, J. Q., A. BONISSENT, and F. F. ABRAHAM, 1981, J. Chem Phys. **74**, 4029.
BROUGHTON, J. Q., G. H. GILMER, and K. A. JACKSON, 1982, Phys. Rev. Lett. **49**, 1496.
BROWN, R. A., 1988, J. AiChE J., **34**, 881.
BROWN, S. G. R. and J. A. SPITTLE, 1989, Mat. Sc. Tech. **5**, 362.
BURDEN, M. H., D. J. HEBDITCH and J. D. HUNT, 1973, J. Cryst. Growth **20**, 121.
BURDEN, M. H. and J. D. HUNT, 1974a), J. Cryst. Growth **22**, 99.
BURDEN, M. H., and J. D. HUNT, 1974b), J. Cryst. Growth **22**, 109.
BURDEN, M. H., and J. D. HUNT, 1974c), J. Cryst. Growth **22** 328.
BURTON, J. A., R. C. PRIM and W. P. SCHLICHTER, 1953, J. Chem. Phys. **21**, 1987.
CAGINALP, G., 1986, Arch. Rational Mech. Anal. **92**, 205.
CAHN, J. W., 1960, Acta Metall. **8**, 554.
CAHN, J. W., 1967, in: Crystal Growth, ed. H. S. Peiser (Pergamon Press, Oxford) p. 681.
CAHN, J. W., 1979, Metall. Trans. **10A**, 119.
CAHN, J. W., W. B. HILLIG, and G. W. SEARS, 1964, Acta Metall. **12**, 1421.
CAHN, J. W., S. R. CORIELL and W. J. BOETTINGER, 1980, in: Laser and Electron Beam Processing of Materials, C. W. White and P. S. Peercy eds. (Academic Press, NY), p. 89.

CAHN, R.W., 1983, in: Physical Metallurgy, Ch. 28, 3er. ed., eds. R.W. Cahn and P. Haasen (North Holland), p. 1709.
CALVO, C., and H. BILONI, 1971, Z. Metallk. **62**, 664.
CAMEL, D. and J.J. FAVIER, 1984 a), J. Cryst. Growth **67**, 42.
CAMEL, D. and J.J. FAVIER, 1984 b), J. Cryst. Growth **67**, 57.
CAMPBELL, 1981, Int. Met. Rev. **26**, 71.
CAMPBELL, J., 1991a), Castings (Butterworth–Heinemann, London).
CAMPBELL, J., 1991 b), Mat. Sc. and Tech. **7**, 885.
CAMPBELL, J., 1991 c), Cast Metals **4**, 101
CAMPBELL, J. and I.D. OLLIFF, 1971, AFS Cast Metals Research J. (ASM Metals Park, OH) **May**, 55.
CANTOR, B.and R. DOHERTY, 1979, Acta Metall. **27**, 33.
CAROLI, B., C. CAROLI and B. ROULET, 1982, J. Physique **43**, 1767.
CARRAD, M., M. GREMAUD, M. ZIMMERMANN, and W. KURZ, 1992, Acta Metall. Mater. **40**, 983.
CARRUTHERS, J.R., 1976, Thermal Convection Instabilities Relevant to Crystal Growth from Liquids in: Preparation and Properties of Solid State Materials, vol. 2 (Marcel Decker, N.Y.)
CECH, R.E., 1956, Trans. Met. Soc. AIME **206**, 585.
CHADWICK, G.A., 1963, in Progress in Materials Science, **12**, (Pergamon Press, Oxford) edited by B. Chalmers, p. 97.
CHADWICK, G.A., 1965, Brit. J. Appl. Phys. **16**, 1095.
CHALMERS, B., 1963, J. Aust. Inst. Metals **8**, 255.
*CHALMERS, B., 1964, Principles of Solidification (Wiley, N.Y.).
CHALMERS, B., 1971, in: Solidification (American Society for Metals, ASM, Metals Park, OH) p. 295.
CHANG, Ch. J. and R.A. BROWN, 1983, J. Cryst. Growth **63**, 343.
CHEN, C.H., C.P. JU and J.M. RIGSBEE, 1988a), Mat. Sci. and Tech. **4**, 161.
CHEN, C.H., C.P. JU and J.M. RIGSBEE, 1988b), Mat. Sci. and Tech. **4**, 167.
CHEN, S.W., and Y.A. CHANG, 1992, Metall. Trans. **23A**, 1038.
*CHERNOV, A.A., 1984, Modern Crystallography III: Crystal Growth, (Springer–Verlag, Berlin).
CHEVEIGNE de, S., C. GUTHMANN, P. KUROSKI, E. VICENTE and H. BILONI, 1988, J. Cryst. Growth **92**, 616.
CHOPRA, M.A., M.E. GLICKSMAN, and N.B. SINGH, N.B., 1988, Metall. Trans **19A**, 3087.
CLAPHAM, L. and R.W. SMITH, 1988, J. Cryst. Growth **92**, 263.
CLYNE, T.W. and A. GARCÍA, 1980, Int. J. Heat and Mass Transfer **23**, 773.
CLYNE, T.W., 1980 a), J. Cryst. Growth **50**, 684.
CLYNE, T.W., 1980 b), J. Cryst. Growth **50**, 691.
CLYNE, T.W., 1984, Metall. Trans. **15B**, 369.
CLYNE, T.W. and A. GARCIA, 1981, J. Mat. Sci. **16**, 1643.
COCHRANE, R.F., D.M. HERLACH and B. FEUERBACHER, 1991, Mat. Sci. Eng. **A133**, 706.
*COLE, G.S., 1971, in: Solidification (ASM Metals Park, OH), p. 201.
COLE, G.S. and G.F. BOLLING, 1968, Trans. Met. Soc. AIME **242**, 153.
COLE, G.S. and G.F. BOLLING, 1969, in: Proc.16th. Sagamore Army Materials Res. Conf. Conference quoted by BOLLING [1971].
COLLIGAN, G.A., V.A. SUPRENANT and F.D. LEMKEY, 1961, J. Metals **13**, 691.
CORIELL, S.R., D.T.J. HURLE and R.F. SEKERKA, 1976, J. Cryst. Growth **32**, 1.
CORIELL, S.R. and R.F. SEKERKA, 1979, J. Cryst. Growth **46**, 479.
CORIELL, S.R., R.F. BOISVERT, R.G. REHM and R.F. SEKERKA, 1981, J. Cryst. Growth **54**, 167.
CORIELL, S.R. and D. TURNBULL, 1982, Acta Metall. **30**, 2135.
CORIELL, S.R. and R.F. SEKERKA, 1983, J. Cryst. Growth **61**, 499.
CORIELL, S.R., G.B. MCFADDEN and R.F. SEKERKA, 1985, Ann Rev. Mat. Sci **15**, 119.
CORIELL, S.R., G.B. MCFADDEN, P.W. VOORHEES and R.F. SEKERKA, 1987, J. Cryst. Growth **82**, 295.
CORIELL, S.R., and G.B. MCFADDEN, 1989, J. Cryst. Growth **94**, 513.
CORIELL, S.R., and G.B. MCFADDEN, 1990, in: Low Gravity Fluid Dynamics and Transport Phenomena, eds. J.N. Koster and R.L. Sani, vol.130 of Progress in Astronautics and Aeronautics AIAA, Washington D.C., p. 369.
CORIELL, S.R., G.B. MCFADDEN, and R.F. SEKERKA, 1990, J. Cryst. Growth **100**, 459.

*CORIELL, S.R. and G.B. MCFADDEN, 1993, in: Handbook of Crystal Growth ed. D.T.J. Hurle (Elsevier Science Publishers, Amsterdam) vol. 1b, p. 785.
CORIELL, S.R. and W.J. BOETTINGER, 1994, NIST, unpublished research.
CRAIG, D.B., M.J. NORNUNG and T.K. CLUHAN, 1988, Metals Handbook, 9th.ed., (ASM, Metals Park, OH) **15 "Casting"**, 629.
CRATCHLEY, D., 1965, Metall. Rev. **10**, (37), 79.
CROKER, M.N., R.S. FIDLER, and R.W. SMITH, 1973, Proc. Roy. Soc. London **A335**, 15.
CROSSLEY, P.A. and L.F. MONDOLFO, 1966, Modern Casting **49**, 89.
CURRERI, P.A. and D.M. STEFANESCU, 1988, Metals Handbook, 9th.ed., (ASM, Metals Park, OH) **15 "Casting"**, 147.
DANTZIG, J.A. and S.C. LU, 1985, Metall. Trans. **16B**, 195.
DANTZIG, J.A. and J.W. WIESE, 1985, Metall. Trans. **16B**, 203.
DANTZIG, J.A. and J.W. WIESE, 1986, Advanced Manufacturing Processes **1**, 437.
DAS, S. and A.J. PAUL, 1993, Metall. Trans. **24B**, 1073.
DAVID, S.A. and J.M. VITEK, 1989, Int. Met. Rev. **34**, 213.
DAVID, S.A., J.M. VITEK, M. RAPPAZ and L.A. BOATNER, 1990, Metall. Trans. **21A**, 1753.
DAVID, S.A. and J.M. VITEK, 1992, in: The Metal Science of Joining, eds. A.J. Cieslak, J.H. Perepezko, S. Kang and M.E. Glicksman, (TMS Pub., Warrendale, PA) p. 101.
DAVID, S.A., T. DEBROY and J.M. VITEK, 1994, MRS Bull. **xix**, N° 1, 29.
DAVIES, G.J. and J.G. GARLAND, 1975, Int. Met. Rev. **20**, 83.
DAYTE, V., and J.S. LANGER, 1981, Phys. Rev. B **24**, 4155.
DAYTE, V., R. MATHUR and J.S. LANGER, 1982, J. Stat. Phys. **29**, 1.
DERBY, B., and J.J. FAVIER, 1983, Acta Metall. **31**, 1123.
DEVAU, G. and D. TURNBULL, 1987, Acta Metall. **35**, 765.
DRAPER, C.W. and J.M. POATE, 1985, Int. Met. Rev. **30**, n° 2, 85.
DUWEZ, P., R.H. WILLENS and W. KLEMENT, 1960, J. Apply Phys. **31**, 1136.
EASTERLING, K.E., 1984, Mat. Sci. and Eng. **65**, 191.
ECKLER, K., R.F. COCHRAN, D.M. HERLACH, B. FEUERBACHER, and M. JURISCH, 1992, Phys. Rev. B **45**, 5019.
ELMER, J.W., M.J. AZIZ, L.E. TANNER, P.M. SMITH, and M.A. WALL, 1994, Acta Metall. Mater. **42**, 1065.
ELLIOT, R., 1964, Br. Foundryman **9**, 389.
ELLIOT, R., 1988, in: Cast Iron Technology (Butterworths, London)
EMLEY, E.F., 1976, Int. Met. Rev. **21**, 175.
ESHELMAN, M.A., V. SEETHARAMAN and R. TRIVEDI, 1988, Acta Metall. **36**, 1165.
ESHELMAN, M.A., and R. TRIVEDI, 1988, Scripta Metall. **22**, 893.
FAINSTEIN–PEDRAZA, D. and G.F. BOLLING, 1975, J. Cryst. Growth **28**, 311.
FAVIER, J.J., 1981a), Acta Metall. **29**, 197.
FAVIER, J.J., 1981b), Acta Metall. **29**, 205.
FAVIER, J.J., 1990, J. Cryst. Growth **99**, 18.
FAVIER, J.J. and A. ROUZAUD, 1983, J. Cryst. Growth **64**, 367.
FAVIER, J.J. and D. CAMEL, 1986, J. Cryst. Growth **79**, 50.
FAVIER, J.J., and L.O. WILSON, 1982, J. Cryst. Growth **58**, 103.
FECHT, H.J., and J.H. PEREPEZKO, 1989, Metall. Trans. **20A**, 785.
FELICELLI, S.D., J.C. HEINRICH and D.R. POIRIER, 1991, Metall. Trans. **22B**, 847.
FELLIU, S., L. LUIS, D. SIGUIN and J. ALVAREZ, 1962, Trans. AFS **70**, 145.
FEURER, U., and R. WUNDERLIN, 1977, DGM Fachber. (Oberusel, FRG). See also KURZ and FISHER [1989]., p. 257.
FISHER, D.J. and W. KURZ, 1979, in: Solidification and Casting of Metals (The Metals Soc., London), p. 57.
FISHER, D.J., and W. KURZ, 1980, Acta Metall. **28**, 777.
*FLEMINGS, M.C., 1974, Solidification Processing (McGraw Hill, New York).
FLEMINGS, M.C., 1976, Scand. J. Metall. **5**, 1.
FLEMINGS, M.C., 1991, Metall. Trans. **22A**, 957.
FLEMINGS, M.C. and G.E. NEREO, 1967, Trans. Met. Soc. AIME **239**, 1449.

FLEMINGS, M.C., D.R. POIRIER, R.V. BARONE, and H.D. BRODY, 1970, J. Iron and Steel Inst. **208**, 371.
*FLEMINGS, M.C. and R. MEHRABIAN, 1971, in: Solidification (ASM, Metals Park, OH) p. 311.
FLEMINGS, M.C. and Y. SHIOHARA, 1984, Mat. Sci. and Eng. **65**, 157.
FLOOD, S.C. and J.D. HUNT, 1987a), J. Cryst. Growth **82**, 543.
FLOOD, S.C. and J.D. HUNT, 1987b), J. Cryst. Growth **82**, 552.
FLOOD, S.C. and J.D. HUNT, 1988, Metals Handbook 9th.ed., (ASM, Metals Park, OH) **15 "Casting"**, p. 130.
FRANK, F.C., 1949, Disc. Farad. Soc. **5**, 48.
FREDRIKSSON. H., and M. HILLERT, 1972, Scand. J. Metall. **2**, 125.
FREDRIKSSON, H., M. HILLERT and N. LANGE, 1973, J. Inst. Metals **101**, 285.
FREDRIKSSON, H., and T. NYLEN, 1982, Metall. Sci. **16**, 283.
FRENKEL, J., 1932, Phys. Z. Sowjetunion **1**, 498.
GANESAN, S. and D.R. POIRIER, 1989, J. Cryst. Growth **97**, 851.
GANESAN, S. and D.R. POIRIER, 1990, Metall. Trans. **21B**, 173.
GARBELLINI, O., H. PALACIO and H. BILONI, 1990, Cast Metals **3**, 82.
GARCIA, A. and M. PRATES, 1978, Metall. Trans. **9B**, 449.
GARCIA, A., T.W. CLYNE and M. PRATES, 1979, Metall. Trans. **10B**, 85.
GARCIA, A. and T.W. CLYNE, 1983, in: Solidification Technology in the Foundry and Casthouse, ed. J.A. Charles (The Metals Society, London), p. 33.
GETSELEV, Z.N., 1971, J. Metals **23**, 38.
GILL, S.C. and W. KURZ, 1993, Acta Metall. Mater. **41**, 3563.
GIOVANOLA, B., and W. KURZ., 1990, Metall. Trans. **21A**, 260.
GLASSON, E.L. and E.F. EMLEY, 1968, in: The Solidification of Metals (Iron and Steel Inst., London) Public. 110, p. 1.
GLICKSMAN, M.E., 1965, Acta Metall. **13**, 1231.
GLICKSMAN, M.E., 1981, in: Aluminum Transformation Technology and Applications 1981, eds. C.A. Pampillo, H. Biloni, L. Mondolfo and F. Sacchi (ASM, Metals Park, OH), p. 347.
GLICKSMAN, M.E., R.J. SCHAEFER, and J.D. AYERS, 1976, Metall. Trans. **7A**, 1747.
GLICKSMAN, M.E., S.R. CORIELL and G.S. MCFADDEN, 1986, Ann. Rev. Fluid Mech. **18**, 307.
*GLICKSMAN, M.E., and S.P. MARSH, 1993, in: Handbook of Crystal Growth 1B: Fundamentals, Transport and Stability, D.T.J. Hurle, ed., (North-Holland, Amsterdam) p. 1075.
GOSH, A.K., 1990, in: Principles of Solidification and Materials Processing (Oxford and IBH Publication Co.) p. 585.
GRANGER, D.A. and R. ELLIOT, 1988, Metals Handbook, 9th. ed., (ASM, Metals Park, OH) **15 "Casting"**, p. 159.
GRANT, N.J., 1992, Metall. Trans. **23A**, 1083.
GREMAUD, M., W. KURZ, and R. TRIVEDI, 1987, unpublished work. See TRIVEDI and KURZ [1988].
GREMAUD, M., M. CARRAD and W. KURZ, 1991, Acta Metall. Mater. **39**, 1431.
GRUGEL, R.N., A. HELLAWELL, 1981, Metall. Trans. **12A**, 669.
GRUGEL, R.N., T.A. LOGRASSO, A. HELLAWELL, 1984, Metall. Trans. **15A**, 1003.
GULLIVER, G.H., 1922, Metallic Alloys, ed. Charles Griffin (London) p. 397.
GUNDUZ, M., and J.D. HUNT, 1985, Acta Metall. **33**, 1651.
HANNA, M.D., SHU-ZU LU and A. HELLAWELL, 1984, Metall. Trans. **15A**, 459.
HAO, S.W., Z.Q. ZHANG, J.Y. CHEN and P.C. LIU, 1987, AFS. Trans. **95**, 601.
HARDY, S.C., G.B. MCFADDEN, S.R. CORIELL, P.W. VOORHEES, and R.F. SEKERKA, 1991, J. Cryst. Growth **114**, 467.
HAYES, A. and J. CHIPMAN, 1938, Trans. Met. Soc. AIME **135**, 85.
HEIPLE, C.R., P. BURGARDT and J.R. ROPER, 1984, in: Modeling of Casting and Welding Processes, III. The Met. Soc. of AIME, Warrendale. Ed. J.A. Dantzing and J.T. Berry, p. 193.
HELLAWELL, A., 1970, Prog. Mater. Sci. **15**, 3.
HELLAWELL, A., 1979, in: Solidification and Casting of Metals (The Metals So., London) p. 161.
HELLAWELL, A., 1990, in: F. Weinberg International Symp. on Solidification Processing, ed. V.E. Lait and I.V. Samarasekera (Pergamon Press), p. 395.
HENZEL, J.G. Jr. and J. KEVERIAN, 1965, J. Metals **17**, 561.

*HERLACH, D. M., R. F. COCHRANE, I. EGRY, H. J. FECHT and A. L. GREER, 1993, Internat. Mat. Reviews **38**, n° 6, 273.
HILLERT, M., 1953, Acta Metall. **1**, 764.
HILLERT, M., 1957, Jernkontorets Ann. **141**, 757.
HILLERT, M., 1979, in: Solidification and Casting of Metals, The Metals Society, London, p. 81.
HILLERT, M. and V. V. SUBBARAO, 1968, in: Solidification of Metals (Iron and Steel Inst., London), Publication n° 110, p. 204.
HILLIG, W. D. and D. TURNBULL, 1956, J. Chem. Phys. **24**, 219.
HILLIG, W. D., 1966, Acta Met. **14**, 1868.
HILLS, A. W. D., S. L. MALHOTRA and M. R. MOORE, 1975, Metall. Trans. **6B**, 131.
HO, K. and R. D. PEHLKE, 1984, AFS Trans. **92**, 587.
HO, K. and R. D. PEHLKE, 1985, Metall. Trans. **16B**, 585.
HOAGLUND, D. E., M. E. AZIZ, S. R. STIFFLER, M. O. THOMSON, J. Y. TSAO and P. S. PEERCY, 1991, J. Cryst. Growth **109**, 107.
HOFFMEYER, M. K. and J. H. PEREPEZKO, 1988, Scripta Metall. **22**, 1143.
HOFFMEYER, M. K. and J. H. PEREPEZKO, 1989a) in: Light Metals 1989, Ed. P. G. Campbell, (TMS, Warrendale, PA), p. 913.
HOFFMEYER, M. K. and J. H. PEREPEZKO, 1989b) Script. Metall. **23**, 315.
HOFFMEYER, M. K. and J. H. PEREPEZKO, 1991, in: Light Metals 1991, Ed. E. L. Roy, (TMS, Warrendale, PA), p. 1105.
*HOGAN, L. M., R. W. KRAFT, and F. D. LEMKEY, 1971, in: Advances in Materials Research, Vol. 5, (Wiley, New York), edited by H. Herman, p. 83.
HOLLOMON, J. H., and D. TURNBULL, 1953, Progress in Met. Phys., vol. 4, (Interscience, New York), p. 333.
HORVAY, G., 1965, Int. J. Heat Mass Transfer **8**, 195.
HUANG, S. C. and M. E. GLICKSMAN, 1981, Acta Metall. **29**, 717.
HUANG, S. C., E. L. HALL, K. M. CHANG, and R. P. LAFORCE, 1986, Metall. Trans. **17A**, 1685.
HUANG, S. C. and E. L. HALL, 1989, Mater. Res. Soc. Symp. Proc. **133**, 373.
HUGHES, I. R. and H. JONES, 1976, J. Mater. Sci. **11**, 1781.
HUGHES, I. C. H., 1988, Metals Handbook, 9th. ed., (ASM, Metals Park, OH) **15 "Casting"**, 647.
HUNT, J. D., 1979, in: Solidification and Casting of Metals (Metals Society, London), p. 3.
HUNT, J. D., 1984, Mat. Sci. and Eng. **65**, 75.
HUNT, J. D., 1990, Acta Metall. Mater. **38**, 411.
HUNT, J. D., and K. A. JACKSON, 1966, Trans. Met. Soc. AIME **236**, 843.
HUNT, J. D., and K. A. JACKSON, 1967, Trans. Met. Soc. AIME **239**, 864.
HURLE, D. T. J., 1969, J. Cryst. Growth **5**, 162.
HURLE, D. T. J., 1972, J. Cryst. Growth **13/14**, 39.
HURLE, D. T. J., 1987, J. Cryst. Growth **85**, 1.
HURLE, D. T. J., E. JAKEMAN, 1968, J. Cryst. Growth **3–4**, 574.
INOUE, A., T. MASUMOTO, H. TOMIOKA and N. YANO, 1984, Int. J. Rapid Solidification **1**, 115.
ISHIHARA, K. N., M. MAEDA and P. H. SHINGU, 1985, Acta Metall. **33**, 2113.
IVANTSOV, G. P., 1947, Dokl. Akad. Nauk S.S.S.R. **58**, 567.
JACKSON, K. A., 1958, in: Liquid Metals and Solidification (ASM, Metals Park, OH) p. 174.
JACKSON, K. A., 1968, Trans. Met. Soc. AIME **242**, 1275.
JACKSON, K. A., 1971, in: Solidification (ASM, Metals Park, OH) p. 121.
JACKSON, K. A., 1974, J. Cryst. Growth **24/25**, 130.
*JACKSON, K. A. and J. D. HUNT, 1966, Tran. Met. Soc. AIME **236**, 1129.
JACKSON, K. A., J. D. HUNT, D. R. UHLMANN and T. P. SEWARD, 1966, Trans. Met. Soc. AIME **236**, 149.
JACKSON, K. A., D. R. UHLMANN, and J. D. HUNT, 1967, J. Cryst. Growth **1**, 1.
JACKSON, K. A., 1975, in: Treatise on Solid State Chemistry, Vol. 5, edited by N. B. Hannay, (Plenum, NY), p. 233.
JACKSON, K. A., G. H. GILMER and H. J. LEAMY, 1980, in: Laser and Electron Beam Processing of Materials, edited by C. W. White and P. S. Peercy, (Academic Press, NY), p. 104.
JACOBI, H., and K. SCHWERDTFEGER, 1976, Metall. Trans. **7A**, 811.

JANSEN, R. and R.R. SAHM, 1984, Mat. Sci. and Eng. **65**, 199.
JOHNSSON, M., L. BACKERUD and G.K. SIGWORTH, 1993, Metall. Trans. **24A**, 481.
JONES, B.L. and G.M. WESTON, 1970 a) J. Aust. Inst. Met. **15**, 189.
JONES, B.L. and M. WESTON, 1970 b), J. Mat. Sci. **5**, 843.
JONES, H. and W. KURZ, 1980, Metall. Trans. **11A**, 1265.
JONES, H., 1982, Rapid Solidification of Metals and Alloys. Monograph, n° 8, (The Institute of Metals, London).
JORDAN, R.M. and J.D. HUNT, 1971, J. Cryst. Growth **11**, 141.
JORDAN, R.M. and J.D. HUNT, 1972, Metall. Trans. **3**, 1385.
JUNZE, J., K.F. KOBAYASHI and P.H. SHINGU, 1984, Metall. Trans. **15A**, 307.
KAMIO, A., S. KUMAI, and H. TEZUKA, 1991, Mat. Sci. and Eng. **A146**, 105.
KARMA, A., 1987, Phys. Rev. Let. **59**, 71.
KATO, H. and J.R. CAHOON, 1985, Metall. Trans. **16A**, 579.
KATTAMIS, T.Z., 1970, Z. Metallk. **61**, 856.
KATTAMIS, T.Z., 1976, J. Cryst. Growth **34**, 215.
KATTAMIS, T.Z., and M.C. FLEMINGS, 1965, Trans. Met. Soc. AIME **233**, 992.
KATTAMIS, T.Z. and M.C. FLEMINGS, 1966, Trans. Met. Soc. AIME **236**, 1523.
KATTAMIS, T.Z. and M.C. FLEMINGS, 1967, Mod. Cast. **52**, 97.
KATTAMIS, T.Z., J.C. COUGLIN, and M.C. FLEMINGS, 1967, M.C., Trans. Met. Soc. AIME **239**, 1504.
KELLY, A. and G.J. DAVIES, 1965, Metall. Rev. **10** (37), 1.
KELLY, T.F., and J.B. VANDERSANDE, 1987, Intl. J. of Rapid Solidification **3**, 51.
KENNEY, M.P., J.A. COURTOIS, R.D. EVANS, G.M. FARRIOR, C.P. KYONKA and A.A. KOCH, 1988, Metals Handbook, 9th.ed., (ASM, Metals Park, OH) **15**, **"Casting"** 327.
KERR, H.W., and W.C. WINEGARD, 1967, in: Crystal Growth (suppl. to the Physics and Chemistry of Solids), H.S. Peiser, ed., (Pergamon, Oxford), p. 179.
KERR, H.W., J. CISSE, and G.F. BOLLING, 1974, Acta Metall. **22**, 677.
KERR, H.W. and J.C. VILLAFUERTE, 1992, in: The Metal Science of Joining, eds. H.J. Cieslak, J.H. Perepezko, S. Kang and M.E. Glicksman, (TMS Pub., Warrendale, PA), p. 11.
KIM, Y.J. and S. KOU, 1988, Metall. Trans. **19A**, 1849.
KIM, Y.-W., H.-M. LIN, and T.F. KELLY, 1988 a), Acta Metall. **36**, 2525.
KIM, Y.-W., H.-M. LIN, and T.F. KELLY, 1988 b), Acta Metall. **36**, 2537.
KIM, W.T. and B. CANTOR, 1991, J. Mat. Sci. **26**, 2868.
KIRKALDY, J.S. and W.V. YOUDELIS, 1958, Trans. Met. Soc. AIME **212**, 833.
KIRKWOOD, D.H., 1985, Mat. Sci. and Eng. **73**, L1.
KITTL, J.A., M.J. AZIZ, D.P. BRUNCO, and M.O. THOMPSON, 1994, Apply. Phys. Lett. **64**, 2359.
KOBAYASHI, S., 1988, J. Cryst. Growth **88**, 87.
KOBAYASHI, R., 1991, J. Jpn. Assoc. Cryst. Growth **18(2)**, 209 in Japanese.
KOBAYASHI, R., 1992, in: Pattern Formation in Complex Dissipative Systems, S. Kai, ed., (World Science, Singapore) p. 121.
KOBAYASHI, K. and L.M. HOGAN, 1978, Met. Forum **1**, 165.
KOBAYASHI, K. and P.H. SHINGU, 1988, J. Mat. Science **23**, 2157.
KOCH, C.C., 1988, Int. Mat. Rev. **33**, 201.
KOFLER, A., 1950, Z. Metallk. **41**, 221.
KOU, S., S.C. HSU and R. MEHRABIAN, 1981, Metall. Trans. **12B**, 33.
KUBO, K. and R.D. PEHLKE, 1985, Metall. Trans. **16B**, 359.
*KURZ, W. and D.J. FISHER, 1979, Int. Met. Rev. **24**, 177.
KURZ, W. and T.W. CLYNE, 1981, Metall. Trans. **12A**, 965.
KURZ, W. and D.J. FISHER, 1981, Acta Metall. **29**, 11.
KURZ, W., B. GIOVANOLA, and R. TRIVEDI, 1986, Acta Metall. **34**, 823.
KURZ, W., B. GIOVANOLA, and R. TRIVEDI, 1988, J. Cryst. Growth. **91**, 123.
*KURZ, W. and D.J. FISHER, 1989, Fundamentals of Solidification, 3rd.ed. (Trans. Tech. Publication, Switzerland).

KURZ, W. and R. TRIVEDI, 1989, in: Series M.D., vol. 14, Microstructural Development and Control in Materials Processing, ed. D.R. Durham and A. Saigai (ASM, Metals Park, OH), p. 47.
LANGER, J.S., 1980, Phys. Rev. Lett. **44**, 1023.
LANGER, J.S., and H. MUELLER–KRUMBHAAR, 1978, Acta Metall. **26**, 1681.
LANGER, J.S., and H. MUELLER–KRUMBHAAR, 1981, Acta Metall. **29**, 145.
LARSON, M.A., and J. GARSIDE, 1986, J. Cryst. Growth **76**, 88.
LAVERNIA, E.J., J.D. AYERS and T.S. SRIVATSAN, 1992, Int. Mat. Rev. **37**, n° 1, 1.
LEAMY, H.J., and K.A. JACKSON, 1971, J. Appl. Phys. **42**, 2121.
LEAMY, H.J., and G.H. GILMER, 1974, J. Cryst. Growth **24/25**, 499.
LEE, J.T.C. and R.A. BROWN, 1993, Phys. Rev. **B 47**, 4937.
LEVI, C.G. and R. MEHRABIAN, 1982, Metall. Trans. **13A**, 221.
LIPTON, J., A. GARCIA and W. HEINEMANN, 1982, Archiv. für des Einsenhüttenwessen **53**, 469.
LIPTON, J., M.E. GLICKSMAN, and W. KURZ, W., 1984, Mat. Sci. and Eng. **65**, 57.
LIPTON, J., W. KURZ and R. TRIVEDI, 1987, Acta Metall. **35**, 957.
LIVINGSTON, J. and H. CLINE, 1969, Trans. Met. Soc. AIME **245**, 351.
LU, S.Z. and A. HELLAWELL, 1985, J. Cryst. Growth **73**, 316.
LU, S.Z. and A. HELLAWELL, 1987, Metall. Trans. **18A**, 1721.
LU, S.Z. and A. HELLAWELL, 1988, in: Proc. Solidification Processing 1987. The Institute of Metals (London), p. 44.
LU, S.Z., and J.D. HUNT, 1992, J. Cryst. Growth **123**, 17.
LU, S.Z., J.D. HUNT, P. GILGIEN, and W. KURZ, 1994, Acta Metall. Mater. **42**, 1653.
MCCARTNEY, D.G., J.D. HUNT, and R.M. JORDAN, 1980a, Metall. Trans. **11A**, 1243.
MCCARTNEY, D.G., J.D. HUNT, and R.M. JORDAN, 1980b, Metall. Trans. **11A**, 1251.
MCCARTNEY, D.G., 1989, Int. Mat. Rev. **34**, 247.
MCLEOD, A.J., 1971, J. Aust. Int. Metals **16**, 124.
MCLEOD, A.J. and L.M. HOGAN, 1978, Metall. Trans. **9A**, 987.
MCDONALD, C.A., A.M. MALVEZZI, F. SPAEPEN, 1989, J. Appl. Phys. **65**, 129.
MAGNIN P., and W. KURZ, 1987, Acta Metall. **35**, 1119.
MAGNIN, P., J.T. MASON and R. TRIVEDI, 1991, Acta Metall. Mater. **39**, 469.
MAGNIN, P., and R. TRIVEDI, 1991, Acta Metall. Mater. **39**, 453.
MAHAPATRA, R.B., J.K. BRIMACOMBE, I.V. SAMARASEKERA, N. WALKER, E.A. PATERSON and J.D. YOUNG, 1991 a), Metall. Trans. **22B**, 861.
MAHAPATRA, R.B., J.K. BRIMACOMBE and I.V. SAMARASEKERA, 1991 b), Metall. Trans. **22B**, 875.
MAJOR, J.F. and J.W. RUTTER, 1989, Mat. Sci. and Tech. **5**, 645.
MARCANTONIO, J.A. and L.F. MONDOLFO, 1974, Metall. Trans. **5**, 1325.
MASUR, L.J. and M.C. FLEMINGS, 1982, Proc.4th. Int. Conf. on Rapidly Quenched Metals, Sendai, Japan, edited by T. Masumoto and K. Suzuki (Jap. Inst. of Metals, Sendai), 1557.
MATSUMIYA, T. and M.C. FLEMINGS, 1981, Metall. Trans. **12B**, 17.
MAXWELL, I. and A. HELLAWELL, 1975, Acta Metall. **23**, 229.
*MEHRABIAN, R., 1982, Int. Met. Rev. **27**, 185.
MEHRABIAN, R., N. KEANE and M.C. FLEMINGS, 1970, Metall. Trans. **1**, 1209.
MEHRABIAN, R., D.R. GEIGER and M.C. FLEMINGS, 1974, Metall. Trans. **5**, 785.
MERCHANT, G.J., and S.H. DAVIS, 1990, Acta Metall. Mater. **38**, 2683.
METZ, S.A. and M.C. FLEMINGS, 1969a), Trans. AFS **77**, 329.
METZ, S.A. and M.C. FLEMINGS, 1969b), Trans. AFS **77**, 453.
MEYER, G.H., 1981, Int. J. Heat Mass Transfer **24**, 778.
MIKEEV, L.V., and A.A. CHERNOV, 1991, J. Cryst. Growth **112**, 591.
MINAKAWA, S., V. SAMARASEKERA and F. WEINBERG, 1985, Metall. Trans. **16B**, 595.
*MINKOFF, I., 1983, The Physical Metallurgy of Cast Iron (Wiley, N.Y.).
MINKOFF, I., 1986, Solidification and Cast Structure (John Wiley & Sons, N.Y.).
MINKOFF, I., 1990, in: F. Weinberg Int. Symposium on Solidification Processing, ed. J.E. Lait and L.V. Samarasekera (Pergamon Press, N.Y.) p. 255.
MOHANTY, P.S., F.H. SAMUEL and J.E. GRUZLESKI, 1993, Metall. Trans. **24A**, 1845.

MOLLARD F., and M.C. FLEMINGS, 1967, Trans. Met. Soc. AIME **239**, 1534.
MONDOLFO, L., 1965, J. Austr. Inst. Metals **10**, 169.
MOORE, K.I., D.L. ZHANG, and B. CANTOR, 1990, Acta Metall. Mater. **38**, 1327.
MORALES, A., J.J. FISSOLO and H. BILONI, 1977, Z. Metallk. **68**, 180.
MORALES, A., M.E. GLICKSMAN and H. BILONI, 1979, in: Solidification and Casting of Metals (The Metals Society, London) p. 184.
MORANDO, R., H. BILONI, G.S. COLE and G.F. BOLLING, 1970, Metall. Trans. **1**, 1407.
MORRIS, L.R. and W.C. WINEGARD, 1969, J. Cryst. Growth **5**, 361.
MORROG, H., 1968a), J. Iron Steel Inst. **206**, 1.
MORROG, H., 1968b), in: The Solidification of Metals (Iron and Steel Institute, London) Publication n° 110, p. 238.
MORTENSEN, A., 1991a), Metall. Trans. **22A**, 569.
MORTENSEN, A., 1991b), in: *Proceedings of the 12th. RISØ International Symposium on Materials Science: Metal matrix composites processing. Microstructures and Properties*, Ed. H. Hansen, D.J. Jensen, T. Leffers, H. Liholt, T. Lorentzen, A.S. Pedersen, O. Pedersen and B. Ralph. RISØ Nat. Lab. Rolskilde, Denmark, p. 101.
MORTENSEN, A. and I. JIN, 1992, Int. Mat. Rev. **37**, n° 3, 101.
MULLINS, W.W. and R.F. SEKERKA, 1963, J. Appl. Phys. **34**, 323.
MULLINS, W.W. and R.F. SEKERKA, 1964, J. Appl. Phys. **35**, 444.
MURRAY, J.L., 1983a, Mat. Res. Soc. Symp. Proc. **19**, 249.
MURRAY, J.L., 1983b, Bull. Alloy Phase Diagrams **4**, 271.
MURRAY, B.T., S.R. CORIELL and G.B. MCFADDEN, 1991, J. Cryst. Growth **110**, 713.
NAKAGAWA, H., H. KATO, F. MATSUDA and T. SENDA, 1970, J. Japan Weld. Soc. **39**, 94.
NANDAPURKAR, P. and D.R. POIRIER, 1988, J. Cryst. Growth **92**, 88.
NARASHIMAN, M.C., 1980, U.S. Patent 4221257.
NARAYAN, J.J., 1982, J. Cryst. Growth **59**, 583.
NI, J. and C. BECKERMANN, 1991, Metall. Trans. **22B**, 349.
NIYAMA, E., 1977, J. Japan Foundrymen Soc. **49**, 26.
O'HARA, and W.A. TILLER, 1967, Trans. Met. Soc. AIME **239**, 497.
OHNAKA, I., 1986, Trans. ISIJ **26**, 1045.
OHNAKA, I., 1988, Metals Handbook 9th. ed., (ASM, Metals Park, OH) **15 "Casting"**, p. 136.
OHNAKA, I., 1991, in: Freezing and Melting Heat Transfer in Engineering, eds. K.C. Ching and H. Seki, Chapter 21: Solidification Analysis of Casting (Hemispher Pub.), p. 1.
OHNO, H., 1986, J. of Metals **38**, 14.
OHNO, H., 1970, J. Japan Inst. Metals **34**, 244.
OHNO, H., T. MOTEGI and H. SODA, 1971, The Iron and Steel Inst.of Japan **11**, 18.
OKAMOTO, T.K., K. KISHITAKE, and I. BESSHO, 1975, J. Cryst. Growth **29**, 131.
OKAMOTO, T.K., and K. KISHITAKE, 1975, J. Cryst. Growth **29**, 137.
OLDFIELD, W., 1973, Mat. Sci. and Eng. **11**, 211.
OSTROWSKI, A. and E.W. LANGER, 1979, in: Solidification and Casting of Metals, (The Metals Society, London), p. 139.
OXTOBY, D.W., and A.D.J. HAYMET, 1982, J. Chem. Phys. **76**, 6262.
PALACIO, H., M. SOLARI and H. BILONI, 1985, J. Cryst. Growth **73**, 369. See also H. BILONI [1983].
PATON, B., 1959, Electroslag Welding (Foreing Language Publishing House, Moscow).
PAWLOWSKI, L. and P. FAUCHAIS, 1992, Int. Mat. Rev. **37**, 271.
PEHLKE, R.D., 1988, Metals Handbook, 9th. Ed., (ASM, Metals Park, OH) **15 – "Casting"**, p. 308.
PEREPEZKO, J.H., 1984, Mat. Sci. and Eng. **65**, 125.
PEREPEZKO, J.H., 1988, in: Metals Handbook, (ASM, Metals Park, OH) **15 – "Casting"**, p. 101.
PEREPEZKO, J.H., 1992, in: Thermal Analysis in Metallurgy, ed. by R.D. Shull and A. Joshi, (TMS, Warrendale, PA) p. 121.
*PEREPEZKO, J.H., 1994, Mat. Sci. and Eng. **A178**, 105. See also I.E. ANDERSON, Ph. D. Thesis, University of Wisconsin, Madison WI, 1983.

PEREPEZKO, J. H. and I. E. ANDERSON, 1980, in: Synthesis and Properties of Metastable Phases, edited by E. S. Machlin and T. S. Rowland, (TMS-AIME, Warrendale, PA), p. 31.
PEREPEZKO, J. H. and S. E. LEBEAU, 1982, in: Aluminum Transformation Technology and Applications 1981, eds. C. A. Pampillo, H. Biloni, L. Mondolfo and F. Sacchi (ASM, Metals Park, OH) p. 309.
PEREPEZKO, J. H. and W. J. BOETTINGER, 1983, Mat. Res. Soc. Symp. Proc. **19**, 223.
PEREZ, T., M. SOLARI and H. BILONI, 1981, Int. Inst. Weld. DOC11–541–81.
PETEVES, S. D. and G. J. ABBASCHIAN, 1986, J. Cryst. Growth **79**, 775.
PFANN, W. G., 1952, Trans. Met. Soc. AIME **194**, 747.
PFANN, W. G., 1966, Zone Melting, 2nd.ed. (Wiley, New York).
PIMPUTKAR, M. and S. OSTRACH, 1981, J. Cryst. Growth **55**, 614.
PIRES, O. S., M. PRATES and H. BILONI, 1974, Z. Metallk. **65**, 143.
PIWONKA, T. S. and M. C. FLEMINGS, 1966, Trans. TMS-AIME **236**, 1157.
PIWONKA, T. S., 1988, in: Metals Handbook, 9th. ed., (ASM, Metals Park, OH) **15 "Casting"**, p. 319.
PLASKETT, T. S. and W. C. WINEGARD, 1959, Trans. ASM **51**, 222.
POIRIER, D. R., 1987, Metall. Trans. **18B**, 245.
POIRIER, D. R., K. YEUM and A. L. MAPPLES, 1987, Metall. Trans. **18A**, 1979.
POND, R. B., 1958, U.S. Patent 2, 825, 198, Metallic Filaments and Method of Making Same.
POWELL, G. L. F., 1965, J. Aust. Inst. Met. **10**, 223.
POWELL, G. L. F., 1980, Metals Forum **3**, 37.
POWELL, G. L. F. and L. M. HOGAN, 1968, Trans. Met. Soc. AIME **242**, 2133.
POWELL, G. L. F. and L. M. HOGAN, 1969, Trans. Met. Soc. AIME **245**, 407.
PRATES, M. and H. BILONI, 1972, Metall. Trans. **3**, 1501.
PRESCOTT, P. J., F. P. INCROPERA and W. D. BENNON, 1991, Int. J. Heat Mass Transf. **34**, 2351.
QIYANG, L., L. QING CHUN and L. QIFU, 1991, Act. Metall. Mater. **39**, 2497.
*RAPPAZ, M., 1989, Int. Mat. Rev. **34**, 93.
RAPPAZ, M., and D. M. STEFANESCU, 1988, Metals Handbook, 9th.ed., (ASM, Metals Park, OH) **15 "Casting"**, p. 883.
RAPPAZ, M., S. A. DAVID, J. M. VITEK and L. A. BOATNER, 1989, Metall. Trans. **20A**, 1125.
RAPPAZ, M., S. A. DAVID., J. M. VITEK, L. A. BOATNER, 1990, Metall. Trans. **21A**, 1767.
RAPPAZ, M. and Ch. A. GANDIN, 1993, Acta Metall. Mater. **41**, 345.
RAPPAZ, M. and Ch. A. GANDIN, 1994, Mat. Research Bull. **xix**, n°1, 20.
RICHMOND, J. J., J. H. PEREPEZKO, S. E. LEBEAU and K. P. COOPER, 1983, in: Rapid Solidification Processing: Principles and Technologies III, edited by R. Mehrabian, (NBS, Washington, DC), p. 90.
RIDDER, S. D., S. KOU and R. MEHRABIAN, 1981, Metall. Trans. **12B**, 435.
RIPOSAN, T., M. CHISAMERA, L. SOFRONI and V. BRABIE, 1985, in: Physical Metallurgy of Cast Iron, ed. H. Fredricksson and M. Hillert (North Holland, N.Y.) p. 131.
RODWAY, G. H. and J. D. JUNT, 1989, J. Cryst. Growth **97**, 680.
RODWAY, G. H. and J. D. HUNT, 1991, J. Cryst. Growth **112**, 554.
ROHATGI, P., 1988, Metals Handbook, 9th. ed., (ASM, Metals Park, OH) **15 "Casting"**, p. 840.
ROSENTHAL, D., 1941, Welding J. **20**, 220-s.
ROSS, A. B. De and L. F. MONDOLFO, 1980, in: Aluminum Transformation Technology and Applications, eds. C. A. Pampillo, H. Biloni and D. E. Embury (ASM, Metals Park, OH) p. 81.
ROVIGLIONE, A. and H. D. HERMIDA, 1994, Materials Characterization **32**, 127.
ROVIGLIONE, A. and H. BILONI, 1994, Fifth International Symposium on the Physical Metallurgy of Cast Iron (SCI-S). To be published in Key Engineering Materials (Trans. Tech. Publications, London).
SADOCHA, J. P. and GRUZLESKI, 1975, in: Metallurgy of Cast Iron (Georgi Pub. Co, St. Saphorin, Switzerland) p. 443.
SATO, A. and R. MEHRABIAN, 1976, Metall. Trans. **7B**, 443.
SATO, T. and G. OHIRA, 1977, J. Cryst. Growth **40**, 78.
SATO, A., Y. OHSAWA and G. ARAGANE, 1989, Mat. Trans. JIM **30**, 55.
SATO, A., Y. OHSAWA and G. ARAGANE, 1991, Mat. Trans. JIM **32**, 77.
SATO, A., Y. OHSAWA and G. ARAGANE, 1992, Mat. Trans. JIM **33**, 66.
SAVAGE, W. F., C. D. LUNDIN and A. H. ARONSON, 1965, Welding J. **40**, 175-s.

SAVAGE, W.F. and E.S. SZEKERES, 1967, Welding J. **46**, 94-s.
SCHAEFER, R.J. and M.E. GLICKSMAN, 1970, Metall. Trans. **1**, 1973.
SCHAEFER, R.J. and S.R. CORIELL, 1984, Metall. Trans. **A15**, 2109.
SCHEIL, E., 1942, Z. Metallk. **34**, 70.
SCHWARZ, M., A. KARMA, K. ECKLER and D.M. HERLACH, 1994, Phys. Rev. Lett. **73**, 1380.
SEETHARAMAN, V., and R. TRIVEDI, 1988, Metall. Trans. **19A**, 2955.
SEKERKA, R.F., 1967, in: Crystal. Growth, ed. H.S. Peiser (Pergamon Press, Oxford) p. 691.
SEKERKA, R.F., 1986, Am. Assoc. Cryst. Growth Newslett. **16**, 2.
SHANGGUAN, D., S. AHUJA and D.M. STEFANESCU, 1992, Metall. Trans. **23A**, 669.
SHARMA, D.G.R. and KRISHMAN, 1991, AFS Trans. **99**, 429.
SHARP, R.M., and M.C. FLEMINGS, 1973, Metall. Trans. **4**, 997.
SHARP, R.M., and M.C. FLEMINGS, 1974, Metall. Trans. **4**, 823.
SHERCLIFF, H.R., O.R. NYHR and S.T.J. TOTTA, 1994, Mat. Research Bull **xix**, n°1, 25 .
SIKORA, J.A., G.L. RIVERA and H. BILONI, 1990, in: Proceedings of the F. Weinberg Symposium on Solidification Processing, eds. J.E. Lait and L.V. Samarasekera (Pergamon Press, N.Y.) p. 255.
SINGER, A.R.E., 1970, Met. Mater. **4**, 246.
SINGER, A.R.E., 1972, J. Inst. Metals **100**, 185.
SKALAND, T., O. GRONG and T. GRONG, 1993, Metall. Trans. **24A**, 2321.
SMITH, P.M. and M.J. AZIZ, 1994, Acta Metall. Mater. **42**, 3515.
SMITH, R.W., 1968, in: The Solidification of Metals (Iron and Steel Inst., London) Pub. 110, p. 224.
SOLARI, M., and H. BILONI, 1980, J. Cryst. Growth **49**, 451.
SOMBOONSUK, K., J.T. MASON, and R. TRIVEDI, 1984, Metall. Trans. **15A**, 967.
SOUTHIN, R.T., 1967, Trans. Met. Soc. AIME **236**, 220.
SOUTHIN, R.T. and G.M. WESTON, 1973, J. Aust. Inst. Met. **18**, 74.
SOUTHIN, R.T. and G.M. WESTON, 1974, J. Aust. Inst. Met. **19**, 93.
SOUTHIN, R.T. and G.A. CHADWICK, 1978, Acta Metall. **26**, 223.
SPAEPEN, F., 1975, Acta Metall. **23**, 729.
SPAEPEN, F., 1994, in: Solid State Physics, edited by H. Ehrenreich and D. Turnbull **47**, (Academic Press, San Diego) p. 1.
SPAEPEN, F. and R.B. MEYER, 1976, Scripta Metall. **10**, 257.
SPENCER, D.B. 1971, Ph. D. Thesis. Massachusetts Institute of Technology, Cambridge, MA. Quoted by M.C. Flemings 1991.
SPENCER D.B., R. MEHRABIAN and M.C. FLEMINGS, 1972, Metall. Trans. **3**, 1925.
STEEN, H.A.H., and A. HELLAWELL, 1975, Acta Metall. **23**, 529.
*STEFANESCU, D.M., 1988, Metals Handbook, 9th.ed., (ASM, Metals Park, OH) **15 "Casting"**, p. 168.
STEFANESCU, D.M., R. HUMMER and E. NECHTELBERGER, 1988, Metals Handbook, 9th. ed., (ASM, Metals Park, OH) **15 "Casting"**, p. 667.
STEFANESCU, D.M. and B.K. DHINDAW, 1988, Metals Handbook 9th.ed., (ASM, Metals Park, OH) **15 "Casting"**, p. 142.
STEFANESCU, D.M., G. UPADHYA and D. BANDYOPADHYAY, 1990, Metall. Trans. **21A**, 997.
STRANGE, E.H., 1911, U.S. Patent 993904.
SUBRAMANIAN, S.V., D.A.R. KAY and G.R. PURDY, 1985, in: Physical Metallurgy of Cast Irons, eds. H. Fredriksson and M. Hillert (North Holland, N.Y.), p. 47.
SUNDQUIST, B.E. and L.F. MONDOLFO, 1961, Trans. Met. Soc. AIME **221**, 157.
SURYANARAYANA, C., F.H. ROSS and R.G. ROWE, 1991, Int. Mat. Rev. **36**, n° 3, 85.
TADA, K. and H. OHNO, 1992, Keikinzoku **42**, 321. (In Japanese).
TAMMANN, G., and A.A. BOTSCHWAR, 1926, Z. Anorg. Chem. **157**, 27.
TARSHIS, C.A., J.L. WALKER and J.W. RUTTER, 1971, Met. Trans. **2**, 2589.
TASSA, M. and J.D. HUNT, 1976, J. Cryst. Growth **34**, 38.
TAYLOR, C.R., 1975, Metall. Trans. **6B**, 359.
TEMKIN, D.E., 1964, Crystallization Processes (Tranl. by Consultants Bureau, New York, 1966) p. 15.
TEMKIN, D.E., 1969, Sov. Phys. Crystallogr. **14**, 344.

THEVOS, Ph., J. L. DESBIOLLES, and M. RAPPAZ, 1989, Metall. Trans. **20A**, 311. See also M. RAPPAZ, 1989, Int. Mat. Rev. **34**, 93.
THOMPSON, C. V., A. L. GREER and F. SPAEPEN, 1983, Acta Metall. **31**, 1883.
THOMPSON, C. V. and F. SPAEPEN, 1983, Acta Metall. **31**, 2021.
THORTON, P. H., 1968, in: Techniques of Metals Research, Ed. R. F. Bunshah (Interscience, New York), vol.1, part 2, p. 1069.
TILLER, W. A., 1958, in: Liquid Metals and Solidification (ASM, Metals Park, OH) p. 276.
TILLER, W., 1970, Solidification, in: Physical Metallurgy, 2nd edition, ed. R. W. Cahn, (North-Holland, Amsterdam), p. 403.
TILLER, W. A., K. A. JACKSON, J. W. RUTTER and B. CHALMERS, 1953, Acta Metall. **1**, 453.
TILLER, W. A., and J. W. RUTTER, 1956, Can. J. Phys. **34**, 96.
TITCHENER, A. P. and J. A. SPITTLE, 1975, Acta Metall. **23**, 497.
TOLOUI, B. and A. HELLAWELL, 1976, Acta Metall. **24** 565.
TRAJAN, P. K., 1988, in: Metals Handbook, 9th. ed., (ASM, Metals Park, OH) **15 "Casting"**, p. 88.
TRIVEDI, R. and K. SOMBOONSUK, 1984, Mat. Sci. and Eng. **65**, 65.
TRIVEDI, R, P. MAGNIN, and W. KURZ, 1987, Acta Metall. **35**, 971.
TRIVEDI, R., and W. KURZ, 1988, in Solidification Processing of Eutectic Alloys, edited by D. M. Stefanescu, G. J. Abbaschian and R. J. Bayuzick, (The Metallurgical Society, Warrendale, PA), p. 3.
TRIVEDI R., and W. KURZ, 1994, Int. Mat. Rev. **39**, 49.
TRIVEDI, R., 1995, Met. Trans., **26A,** 1583.
TURNBULL, D., 1962, J. Phys. Chem. **66**, 609.
TURNBULL, D. and R. E. CECH, 1950, J. Appl. Phys. **21**, 804.
TURNBULL, D. and B. G. BAGLEY, 1975, in: Treatise on Solid State Chemistry, vol. 5, edited by N. B. Hannay, (Plenum, NY), p. 513.
UNGAR, L. H. and R. A. BROWN, 1985, Phys. Rev. B **31**, 5931.
VERHOEVEN, J. D., and E. D. GIBSON, 1978, J. Mat. Sci **13**, 1576.
VERHOEVEN, J. D., W. N. GILL, J. A. PUSZYNSKI and R. M. GINDE, 1988, J. Cryst. Growth **89**, 189.
VERHOEVEN, J. D., W. N. GILL, J. A. PUSZYNSKI and R. M. GINDE, 1989, J. Cryst. Growth **97**, 254.
VISKANTA, R., 1990, ISME Int. J. (Series II) **33**, 409.
VITEK, J. M. and S. A. DAVID, 1992, in: The Metal Science of Joining, eds. H. J. Cieslak, J. H. Perepezko, S. Kang and M. E. Glicksman (TMS Pub., Warrendale, PA) p. 115.
VIVES, Ch. and R. RICOU, 1985, Metall. Trans. **16B**, 377.
VOLLER, V. R., and S. SUNDARRAJ, 1993, in: Modeling of Casting, Welding and Advanced Solidification Processes V, T. S. Piwonka, V. Voller, and L. Katgerman eds., (TMS, Warrendale, PA), p. 251.
VOLMER, M. I., and M. MARDER, 1931, Z. Phys. Chem. **A154**, 97.
VOORHEES, P. W., 1990, Metall. Trans. **21A**, 27.
WALKER, J. L., 1959, in: The Physical Chemistry of Process Metallurgy, part 2, ed. G. S. St. Pierre (Interscience, New York), p. 845.
WALKER, J. L., 1964, cited in: Principles of Solidification, ed. B. Chalmers, Chap. 4, (Wiley, New York) p. 122.
WALTON, D. and B. CHALMERS, 1959, Trans. Met. Soc. AIME **188**, 136.
WANG, C. Y. and C. BECKERMANN, 1993, Mat. Sci. and Eng. **A171**, 199.
WANG, Y. H. and S. KOU, 1987, in: Advances in Welding Science and Technology, ed. S. A. David, (ASM, Metals Park, OH.), p. 65.
WANG, Y. H., Y. J. KIM and S. KOU, 1988, J. Cryst. Growth **91**, 50.
WARREN, J. A., and W. J. BOETTINGER, 1995, Acta Metall. et Mater. **43,** 689.
WEI, C. and J. T. BERRY, 1980, Int. J. Heat and Mass Transfer **25**, 590.
WEINBERG, F., 1975, Metall. Trans. **6A**, 1971.
WEINBERG, F., 1979 a), in: Solidification and Casting of Metals (The Metals Society, London) p. 235.
WEINBERG, F., 1979 b), Metals Technology **February**, 48.
WEINBERG, F. and E. TEGHTSOONIAN, 1972, Metall. Trans. **3**, 93.
WETTERFALL, S. E., H. FREDRICKSSON, H. and M. HILLERT, 1972, J. Iron Steel Inst. **210**, 323.
WHEELER, A. A., W. J. BOETTINGER, and G. B. MCFADDEN, 1992, Phys. Rev A **45**, 7424.

WHEELER, A. A., B. T. MURRAY, and R. J. SCHAEFER, 1993a, Physica D **66**, 243.
WHEELER, A. A., W. J. BOETTINGER, and G. B. MCFADDEN, 1993b, Phys. Rev E **47**, 1893.
WHITE, C. W., D. M. ZEHNER, S. U. CAMPISANO and A. G. CULLIS, 1983, in: Surface Modification and Alloying by Lasers, Ion, and Electron Beams, edited by J. M. Poate, G. Foti and D. C. Jacobson (Plenum Press, NY), p. 81.
WHITE, G. and D. W. OLSON, 1990, in: The New Materials Society. Challenges and Opportunities, (Bureau of Mines, U.S. Dept. of the Interior.) Quoted by MORTENSEN and JIM [1992].
WIESE, J. W. and J. A. DANTZIG, 1988, Applied Mathematical Modelling **12**, 213.
WILLNECKER, R., D. M. HERLACH and B. FEUERBACHER, 1989, in: Proc.7th. Europ. Symp. on "Materials and Fluid Sciences under Microgravity", Oxford, ESA SP-295, p. 193.
WILLNECKER, R., D. M. HERLACH, and R. FEUERBACHER, 1990, Apply Phys. Lett. **56**, 324.
WILSON, H. A., 1900, Phil Mag. **50**, 238.
WILSON, L. O., 1978, J. Cryst. Growth **44**, 371.
WILSON, L. O., 1980, J. Cryst.l Growth **48**, 363.
WINEGARD, W. and B. CHALMERS, 1954, Trans. Quart. ASM **46**, 1214.
WOLLKIND, D. and L. SEGAL, 1970, Phil. Trans. Roy. Soc. London **268**, 351.
WU, Y., T. J. PICONNE, Y. SHIOHARA, and M. C. FLEMINGS, 1987, Metall. Trans. **18A**, 915.
YOON, W., PAIK, J. S., LACOURT, D., and PEREPEZKO, 1986, J. H., J. Appl. Phys. **60**, 3489.
YOUNG, K. P., and D. H. KIRKWOOD, 1975, Metall. Trans. **6A**, 197.
ZACHARIA, T., A. H. ERASLA, and D. K. AIDUN, 1988, Weld. J. **67**, 18-s.
ZACHARIA, T., S. A. DAVID, J. M. VITEK, 1992, in: The Metal Science of Joining, eds. H. J. Cieslak, J. H. Perepezko, S. Kang and M. E. Glicksman, (TMS Pub., Warrendale, PA), p. 257.
ZENER, C., 1946, Trans Met. Soc. AIME **167**, 550.
ZHU, J. D. and I. OHNAKA, 1991, Modelling of Casting, Welding and Advanced Solidification Processes, eds. M. Rappaz, M. R. Ozgü and K. W. Mahin, (TMS Pub., Warrendale, PA), p. 435.
ZHU, P. and R. W. SMITH, 1992 a), Acta Metall. Mater. **40**, 683.
ZHU, P. and R. W. SMITH, 1992 b) Acta Metall. Mater. **40**, 3369.
ZIMMERMANN, M., A. KARMA, and M. CARRARD, 1990, Phys. Rev. B **42**, 833.
ZIV, I. and F. WEINBERG, 1989, Metall. Trans. **20B**, 731.

Further reading

The publications marked with an asterisk in the above list of references may be consulted.

CHAPTER 9

MICROSTRUCTURE

H. GLEITER

Forschungszentrum Karlsruhe, GmbH
D-76021 Karlsruhe, Germany

R. W. Cahn and P. Haasen†, eds.
Physical Metallurgy; fourth, revised and enhanced edition

1. Definition and outline

The *microstructure* of crystalline materials is defined by the type, structure, number, shape and topological arrangement of phases and/or lattice defects which are in most cases not part of the thermodynamic equilibrium structure.

In the first part (paragraph two) of this chapter, the different types of lattice defects involved in the formation of microstructure (elements of microstructure) will be discussed. As far as the arrangement, shape and crystal structure of phases are concerned, we refer to chs. 1, 4, 8, 15–17, and 28. The third and fourth paragraph of this chapter will be devoted to the characterization and to the present understanding of the development of microstructures.

2. Elements of microstructure

2.1. Point defects, dislocations and stacking faults

Point defects, point-defect clusters, dislocations and stacking faults are important elements of the microstructure of most materials. The atomistic structure and properties of these defects are discussed in chs. 18 and 20.

2.2. Grain boundaries

Control of the grain size is one of the most widely used means of influencing the properties of materials. Consequently, intense efforts have been directed in recent years towards a better understanding of grain boundaries. The progress achieved is documented in several comprehensive reviews (BALLUFFI [1980], AUST [1981], GLEITER [1982], SUTTON and BALLUFFI [1987], SUTTON [1990], FINNIS and RÜHLE [1991], WOLF and YIP [1992], SUTTON and BALLUFFI [1995]).

The complex nature of interatomic forces and relaxations at interfaces has motivated the development of simple, mostly crystallographic, criteria for predicting the structure, the energy and other physical properties of interfaces. Some of these criteria and the underlying physical concepts of the atomic structure of grain boundaries will be briefly discussed in the following sections.

2.2.1. Crystallography

2.2.1.1. Coincidence site lattice. The coincidence site lattice (CSL) has proved a useful concept in the crystallography of interfaces and in the description of dislocations in interfaces. It is defined as follows (fig. 1). Two crystal lattices A and B which meet at an interface are imagined to be extended through each other in both directions. Crystal A or B is then translated so that a lattice point in A coincides with one in B. This point which is labelled O is designated as the origin of coordinates. Now it is possible that no other lattice points of A and B coincide, in which case O is the only common lattice point. However, for many orientations of the two crystals there will be other coincidences. These coinciding lattice points form a regular lattice which is known as the

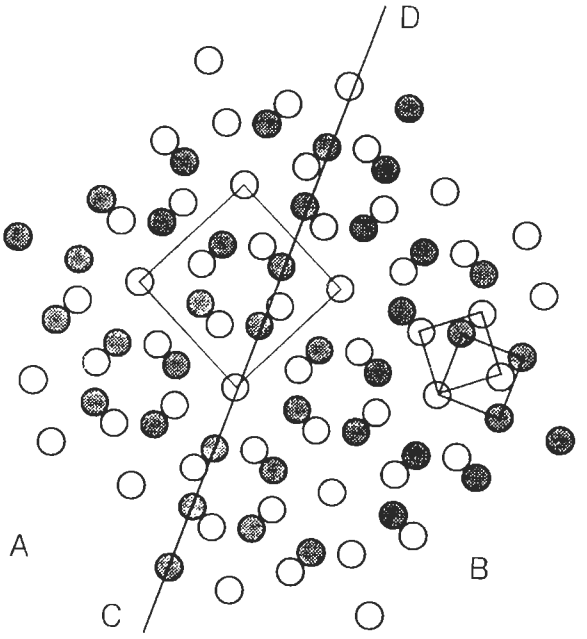

Fig. 1. Coincidence site lattice (Σ5) formed by interpenetration of two crystals. The unit cell of the CSL is outlined to the left, and the linear transformation relating the two lattices is shown on the right.

Coincidence Site Lattice, CSL.

Boundaries are classified according to the ratio of the volume of a unit cell of the CSL to the volume of a unit cell of A or B. This value is denoted by Σ. Thus a low value of Σ implies a high frequency of coincidences of the interpenetrating lattices, and at the other extreme, $\Sigma = \infty$ implies a completely incommensurate orientation. Boundaries with a relatively low (i.e., unambiguously measurable) value of Σ are referred to as *coincidence boundaries* and are sometimes associated with special properties. A boundary plane (e.g., CD in fig. 1) which is also a plane of the CSL has a certain planar density of coincidence sites Γ per unit area. The area $1/\Gamma$ is geometrically important. For CSL boundary planes, periodically repeating unit cells of the bicrystal can be defined (unit cells of the CSL) whose faces pave the boundary. An early idea was that boundaries with a high Γ would have a low free energy because the atoms occupying coincidence sites are in their bulk equilibrium positions relative to either crystal lattice.

2.2.1.2. O-lattice. A generalization of the CSL can be made and is called the *O-lattice*. Let us start with two ideal interpenetrating lattices A and B coinciding at one point which we take as the origin (fig. 2).

Consider a linear homogeneous mapping which brings A into complete coincidence with B at every site. In the simplest case, the mapping is a pure rotation or a shear. As all coincidence sites are completely equivalent, any one of them could be regarded as the origin of the transformation. In general, there are even more points which could be taken

as the origin of the mapping and all such points together form a set called the set of O-points (fig. 2, O stands for Origin) (BOLLMANN [1970]). A conceptual advantage of the O-lattice over the CSL is that the set of O-points moves continuously as crystal A is rotated or deformed with respect to crystal B, whereas CSL points disappear and appear abruptly. There are O-points even when there are no coincidences. Lines bisecting the array of Opoints in the boundary can be geometrically regarded as the cores of dislocations which accommodate the misfit. There is thus a close relationship between the O-lattice and the geometrical theory of interfacial dislocations (BOLLMANN [1974]) (fig. 2b). Such geometrical dislocations are a mathematical device, and do not necessarily correspond to physical dislocations, which are observable atomic structures. The principal utility of an O-lattice construction is that it enables the geometrical location and Burgers vectors of interfacial dislocations to be discussed. A weakness in the concept of an

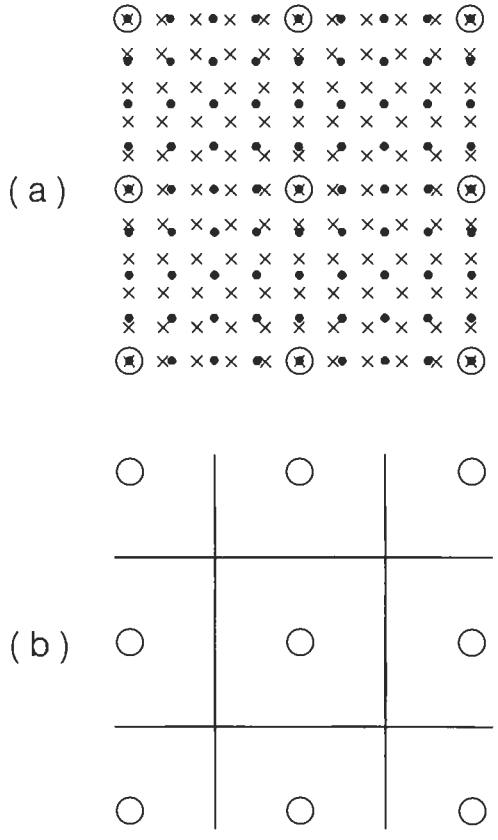

Fig. 2. An (001) projection of the O-lattice between two simple cubic lattices, called lattice A and B in the text, with different lattice parameters. (a) The atoms of each crystal are represented by dots and crosses and the O-points are circled. (b) Showing the lines midway between the O-points which can be geometrically regarded as the cores of dislocations. (After SMITH and POND [1976].)

O-lattice stems from the fact that for a given orientation of A and B, the transformation which brings A into coincidence with B is not representable by a unique matrix. This non-uniqueness is why one must be cautious about attaching any physical significance in terms of observable dislocations to the mathematical dislocations defined by means of the O-lattice.

2.2.1.3. DSC lattice. Another lattice which is of importance for the discussion of isolated dislocations and steps at boundaries is called the DSC lattice, sometimes referred to as *Displacement Shift Complete* (BOLLMANN [1970]) (fig. 3). This is defined as the coarsest lattice which includes the lattices of A and B (in an orientation for which there is some coincidence) as sublattices. Any vector joining a lattice point of crystal A to a lattice point of crystals A or B, and vice versa, is also a vector of the DSC lattice. Thus if either lattice is translated by a DSC vector, the complete pattern of the interpenetrating lattices and the CSL is either invariant or is simply displaced by the same vector. The DSC lattice is unique to the given orientations of A and B and is useful for predicting or explaining the observable (physical) dislocations in boundaries.

2.2.2. Coincidence models

The first attempt to correlate predictively the crystallographic parameters of a boundary (e.g., the lattice structure of the crystals forming the interface, the orientation relationship between the two crystals, the boundary inclination, etc.) with the actual atomic arrangement in the interface was made by KRONBERG and WILSON [1949] who

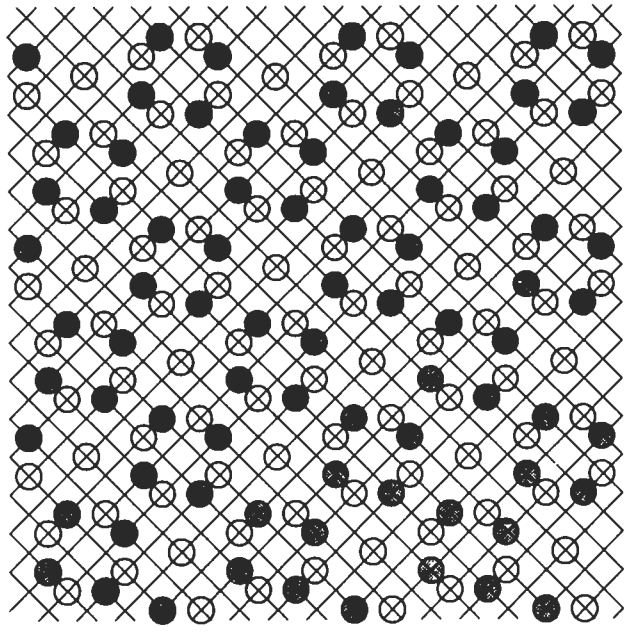

Fig. 3. The DSC lattice corresponding to the interpenetrating lattices illustrated in fig. 1. The DSC lattice points are the points of the fine grid.

applied the concept of lattice coincidence — which was developed independently by several crystallographers — to grain boundaries. An example of a coincidence lattice was shown in fig. 1.

It was also at this time that boundaries with "low" values of Σ were called "special" and all other boundaries were called "random" or "general". No limit on Σ for "special" boundaries was given. Hard-sphere models suggested that every atom at the boundary was at a site of one of the crystals or at a site common to both crystals. This led to the supposition that low-Σ boundaries had low energies because they contained high densities of atoms at shared sites. Such reasoning embodied the "coincidence model" of grain boundaries. BRANDON *et al.* [1964] subsequently pointed out that not all boundaries in a given coincidence system had the same density of coincidence sites. In fact, the density depends on the plane of the boundary. Indeed, one can always find boundaries in any coincidence system with extremely low densities of coincidence sites. They therefore proposed that the planar density, Γ, of coincidence sites in the plane of the boundary should be a more reliable indicator of low energy than Σ. This became known as the *planar coincidence site density*, or Γ *criterion*. Two arguments were given in support of this criterion: in a boundary with a high value of Γ there are more atoms at shared sites and hence the boundary "core" energy is lower. Secondly, by St. Venant's principle, the strain field of the boundary extends into the grains roughly as far as the period of the boundary structure: the higher Γ the smaller the period, and, hence, the lower the strain field energy. BRANDON *et al.* [1964] also extended the planar coincidence to non-coincidence boundaries by combining it with the dislocation model (§ 2.2.1.1).

Boundaries between crystals deviating from an ideal coincidence-orientation relationship were proposed to consist of areas with an array of coincidence atoms in the plane of the boundary (boundary coincidence) separated by (misfit) dislocations. The significance of boundary inclination was incorporated in the model by suggesting that the boundary follows the planes containing a high density of coincidence sites in order to minimize the misfit, as the boundary consists in these regions of atomic groups with little strain. Boundaries constrained to lie at an angle to the most densely packed coincidence-plane were visualized as taking a step structure.

2.2.3. Structural unit models

The concept of atoms occupying coincidence sites (in terms of boundary or lattice coincidences) had to be abandoned after it was discovered by means of computer simulations of the atomic structure of grain boundaries (WEINS *et al.* [1971]) that two crystals forming a coincidence boundary relax by a shear-type displacement (*rigid-body relaxation*) from the position required for the existence of coincidence-site atoms at the boundary (figs. 4a and b). This conclusion was confirmed in subsequent years by numerous more sophisticated computer simulations as well as by experimental observations.

The physical reason for the rigid-body relaxation may be seen from figs. 4 and 5. Figure 5 shows the boundary structure predicted by the lattice-coincidence model. Both closely and widely spaced pairs of atoms exist, resulting in a high-energy structure. The energy of the boundary may be lowered by translating the two crystals (without rotation) so that the "hills" on the "surface" of one crystal coincide with the "valleys" on the

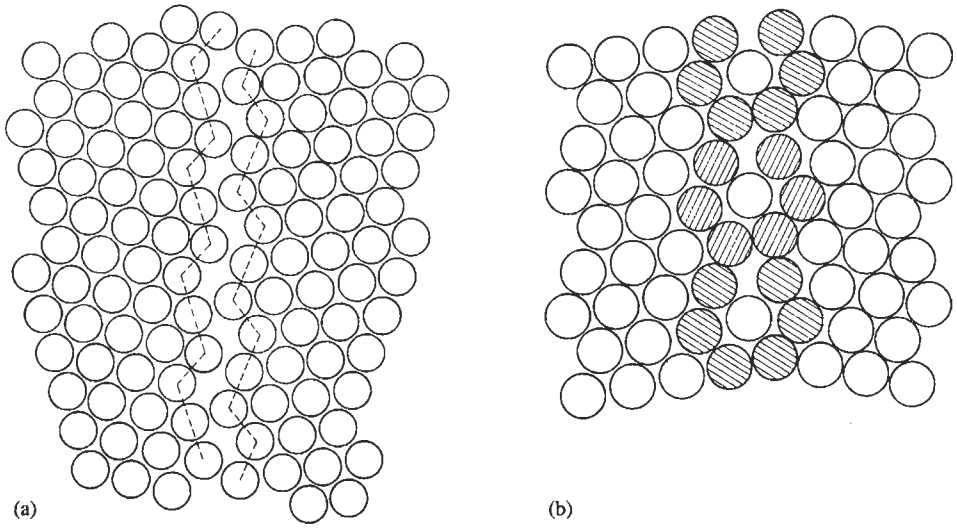

Fig. 4. Structure of the boundary shown in fig. 5 after a "rigid-body relaxation" of the two hexagonal arrays of atoms in order to remove large interatomic repulsion or attraction forces (a) and subsequent relaxation of individual atoms into positions of minimum energy (b). The interaction potential assumed between the atoms corresponds to gold. (From WEINS *et al.* [1971])

"surface" of the other crystal (fig. 4a) followed by the relaxation of individual atoms into minimum-energy positions (fig. 4b). The existence of rigid-body relaxations led CHALMERS and GLEITER [1971] to propose that the *boundary periodicity* rather than the existence of boundary coincidence per se is the physically meaningful parameter. In fact, the existence of small structural units with an atomic packing density comparable to that in a perfect lattice was hypothesized to result in low-energy boundaries (fig. 4b). By extending the structural unit concept originally proposed by BISHOP and CHALMERS [1968] for unrelaxed coincidence boundaries to boundaries with atomic relaxations, the following (relaxed) structural unit model of grain boundaries was put forward (CHALMERS and GLEITER [1971]): boundaries of low energy consist of only one type of (relaxed) structural units, whereas the structure of high-energy boundaries may be derived from a simple rule of mixing of the low-energy structural units of the nearest low-energy boundaries (GLEITER [1971]). This boundary model has been worked out in detail for different types of boundaries (POND and VITEK [1977]). One of the limitations of the model is its applicability to interpolate between two structures of short-periodic boundaries. When the misorientation between two crystals forming a boundary consisting of a mixture of different structural units is described in terms of an axis and an angle of rotation of one crystal relative to the other, and when the rotation axis is of high indices, the Burgers vector of secondary dislocations associated with the minority units may become unrealistically large. "Unrealistically large" means that the dislocation is unlikely to be localized within the minority unit unless the minority unit itself is large. If the dislocation is not localized then the assumption of the model, that local misorientation

References: p. 935.

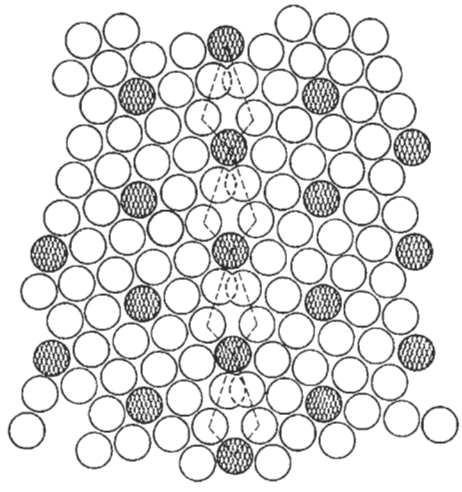

Fig. 5. Lattice-coincidence model of a 18° tilt-type grain boundary between two hexaqonal arrays of atoms. The atoms at coincidence sites are indicated by cross-hatching. The "surfaces" of the two crystals are marked by dashed lines.

changes occur so as to introduce structural units from other boundaries, breaks down. On the other hand, if large minority structural units are required then the misorientation range between the majority and minority structural unit boundaries is small and the predictive capacity of the model is limited. In practice this means that the model may usefully be applied pure tilt and pure twist boundaries with rotation axes of relatively low indices, i.e., <100>, <110>, <111> and possibly <112>.

A few years after the discovery of *quasiperiodicity* in crystals, the same concept was utilized to model grain and interphase boundaries (RIVIER [1986], GRATIAS and THALAL [1988], SUTTON [1989]) see ch. 4, Appendix). The simplest way to visualize quasiperiodicity at an irrational grain boundary is to apply the structural unit model to an irrational tilt boundary. Along the tilt axis (which is assumed to be rational) the structure of the boundary is periodic. However, perpendicular to the tilt axis in the boundary plane the boundary structure will be an aperiodic sequence of majority and minority structural units.

2.2.4. Broken bond model

While for free surfaces a broken-bond description of the structure-energy correlation has been commonly used for over half a century (HERRING [1953]), such an approach has only recently been adopted for grain boundaries, by WOLF and YIP [1992]. In an otherwise perfect crystal, thermal disorder is responsible for a broadening and shift of the interatomic spacings towards larger distances. Owing to the presence of planar defects, polycrystals are structurally disordered even at zero temperature, and their zero-temperature radial distribution function shows the same two effects. However, because of its localization near the interface, this type of disorder is *inhomogeneous,* by contrast with thermal disorder.

To illustrate this inhomogeneity in the direction of the interface normal, let us consider the radial distribution function (or the planar structure factor) for each of the atom planes near the interface. As seen from fig. 6 for the case of a symmetrical (100) twist boundary in the fcc lattice, the amount of structural disorder decreases rapidly from one (100) plane to another, indicating the existence of large gradients in structural disorder. Starting from the description of structural disorder in terms of the radial distribution function, $G(r)$, a broken-bond model seems to present a useful step towards simplification. By characterizing the atomic structure in terms of the number of broken nearest-neighbor (nn) bonds per unit area, essentially in a broken-bond model the detailed peak shapes in $G(r)$ are simply replaced by the areas under these peaks. Because all the

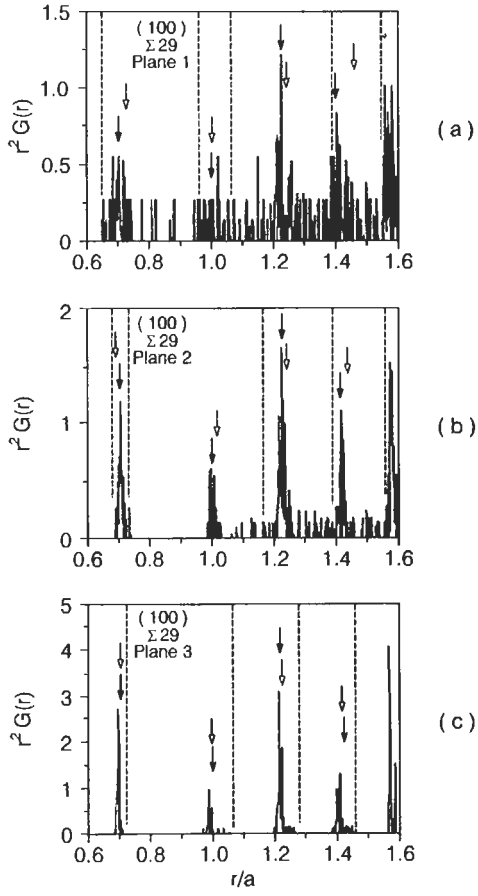

Fig. 6. Plane-by-plane zero-temperature radial distribution functions, $r^2G(r)$, on the three lattice planes closest to the (001) $\theta = 43.60°$ ($\Sigma 29$) symmetrical twist boundary simulated by means of an embedded atom potential for Cu. The full arrows indicate the corresponding perfect-crystal -δ-function peak positions; open arrows mark the average neighbor distance in each shell. The widths of these shells are indicated by dashed lines. (From WOLF and YIP [1992].)

References: p. 935.

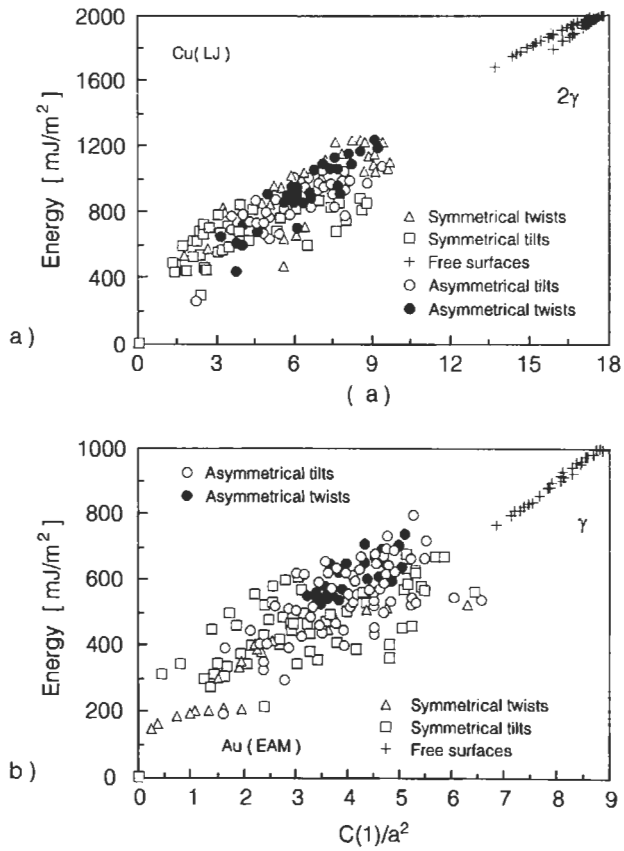

Fig. 7. Grain-boundary energy (mJ/m^2) versus number of nearest neighbor bonds per unit area, $C(1)$. The unit area is normalized by the lattice constant, a. The computations were performed for a Lennard–Johnes potential fitted to Cu (fig. 7a) and an embedded atom potential fitted to Au (fig. 7b). a is the lattice parameter. For comparison, the related free surface energies, γ, are also shown. (From WOLF and YIP [1992, p. 139].)

information contained in the detailed shapes of these peaks is thus lost, small long-range elastic strain-field effects associated, for example, with interface dislocations or surface steps are therefore not 'seen' in the coordination coefficient. This is an inherent limitation of a broken-bond model. Figure 7 indicates the correlation between the average number of broken nn bonds per unit grain boundary area, $C(1)$, and the grain boundary energy for the two fcc potentials (WOLF [1990]). While, in principle, more distant neighbors should also play a role, in fcc metals their contribution was found to be rather small (typically about 10–20% of the nn contribution). By contrast, in bcc metals the second-nearest neighbors were found to be practically as important as the nearest neighbors.

2.2.5. Dislocation models

The idea of modelling a high-angle grain boundary in terms of an array of closely spaced dislocations (fig. 8b, READ and SHOCKLEY [1950]) is an extension of the well established structure of small-angle boundaries (fig. 8a). If the dislocations are uniformly spaced in the plane of the boundary, a low-energy interface is formed because the strain fields of the dislocations extend into the lattices of both crystals over a distance comparable with the spacing of the dislocation array (St. Venant's principle), which is a relative minimum for periodic arrays. A uniform dislocation spacing can only result if the dislocation spacing is equal to an integral number of lattice planes terminating at the boundary. For all other tilt angles the boundary may be described as a boundary with a uniform dislocation spacing (e.g., a 53° tilt boundary, fig. 8b) and a superimposed small-angle tilt boundary that accounts for the deviation from the tilt angle required for uniformly spaced dislocations (fig. 8c). The idea of describing a boundary which deviates from a low-energy structure in terms of the superposition of a low-energy boundary and a small-angle boundary has been increasingly used in association with dislocation models as well as with boundary models that are not based on the dislocation concept.

The work of READ and SHOCKLEY, which is generally considered as a major achievement of the theory of interfacial structures, suffers from two inherent limitations. First, the singular behavior of the elastic strain fields near the dislocation centers was dealt with by removing the singularity mathematically with an inner "cut-off" radius. The second deficiency is the linear superposition of the strain fields of the individual dislocations, which results in complete neglect of the interactions among the dislocations in the array.

In order to ameliorate these deficiencies, the cores of dislocations in grain boundaries were modelled either by a hollow-core dislocation description (LI [1961]), by picturing the material in the core region as a second phase (MASAMURA and GLICKSMAN [1974]), or by assuming the dislocation cores to merge into a slab of core material. A special case of the latter group of boundary models is the "random grain boundary model" (WOLF [1991]). It applies to high-angle twist boundaries. From an investigation of the role of the plane of the boundary relative to the crystallographic orientation of both crystals it was concluded that two types of boundaries should be distinguished in metals with a bcc structure. If the boundary plane is parallel to a set of widely spaced lattice planes, the boundary behavior (energy, cleavage fracture energy, etc.) is governed by the interplanar lattice spacing only. In this case, the interaction of the atoms across the interface is independent of the relative orientation of the two crystals. This suggestion is based on the physical reasoning (WOLF and YIP [1992]) that atoms are shoved more closely together when creating a twist boundary on a plane with small rather than large interplanar spacings. As a consequence of the short-range repulsion between the atoms, the bicrystal then expands locally at the grain boundary, and this expansion is largest for the grain boundaries with the smaller interplanar spacings, resulting in boundaries with higher grain-boundary energy. More precisely, two criteria for low interfacial energy were suggested (WOLF [1985]). The first criterion applies to twist boundaries: On a given lattice plane local minima in the energy vs twist angle relationship are expected at twist angles corresponding to the "locally smallest" CSL unit-cell area. The second criterion

References: p. 935.

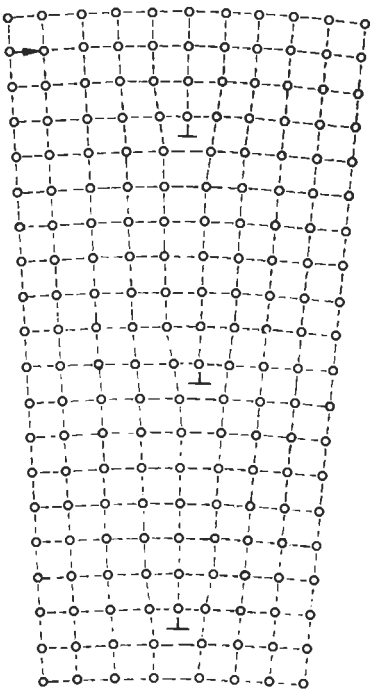

(a)

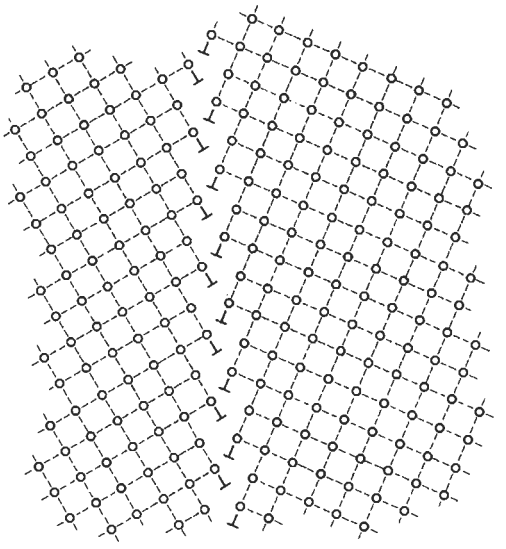

(b)

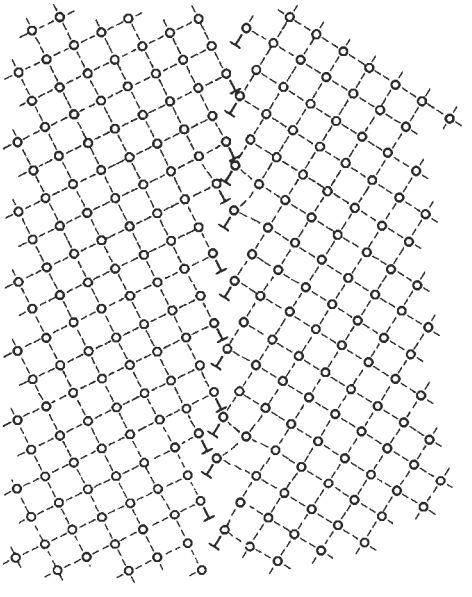

(c)

Fig. 8. Dislocation models of symmetrical tilt boundaries in a simple cubic structure: (a) small-angle boundary; (b) 53° (high-angle) boundary; (c) 60° boundary.

applies to tilt boundaries. This criterion states that local minima in the energy vs tilt angle relationship correspond to planes with "locally large" interplanar spacing. Thus, for symmetrical tilt boundaries high values of d(hkl) are suggested to correspond to local minima in the energy vs tilt angle relationship. In order to see that Wolf's criterion of the interplanar spacing is distinct from the criterion of a high density of coincidence sites (§ 2.1.1) in the boundary plane (Γ), let us consider non-periodic grain boundaries. There are no exactly periodic {111} {100} grain boundaries, for example. Thus, for all {111} {100} boundaries $\Gamma = 0$, whereas the interplanar spacing would attain a relatively high value.

The arguments discussed so far do not apply to grain boundaries on vicinal planes. Vicinal planes are planes that deviate little from the widely spaced ones. In this case, the "surfaces" of both crystals forming the boundary contain a pattern of ledges. In the case of boundaries of "vicinal" planes, the energy of the boundary will depend on the degree of matching between the two ledge patterns. The spacing of the lattice planes is of little relevance (see also ch. 20, § 6).

2.2.6. Polyhedral unit models

The concept of describing the atomic arrangements in grain boundaries in terms of densely packed atomic groups (e.g., the groups existing in amorphous structures) led to the development of the *polyhedral unit models.* Apparently, the idea of comparing the atomic arrangements in a grain boundary with the atomic arrangements existing in amorphous structures was first proposed by POTAPOV *et al.* [1971]. They analyzed the three-dimensional atomic structure of grain boundaries in tungsten by means of field-ion microscopy. Boundaries were found to consist of periodically arranged rings formed by five atoms with a central atom between the rings (fig. 9). On the basis of these observations it was concluded that a grain boundary may be represented in terms of the atomic configurations existing in amorphous metals. Some years later, a similar structural concept was worked out in detail by several other authors (ASHBY *et al.* [1978] and POND *et al.* [1978]). For example, fig. 10 shows the interpretation of the structure of a 36.9° [100] tilt boundary between fcc crystals in terms of the polyhedral unit model.

The comparison between grain-boundary structures and structural elements of amorphous materials is not without problems as the atoms in a boundary cannot relax to the same extent as in a glass. In an interface, the boundary conditions are given by the periodic structure of the two crystals on both sides, whereas an atomic group in a glass has no such periodic boundary conditions for its relaxation. This difference is borne out by several experiments. For example, positron annihilation measurements (CHEN and CHANG [1974]) and Mössbauer studies (OZAWA and ISHIDA [1977]) suggest that the atomic packing in grain boundaries is more "open" than in a glassy structure. This conclusion is supported by recent studies of the atomic arrangements in the interfaces of nanostructured materials (§ 5 of this chapter). Investigations of the atomic arrangements formed in the grain boundaries of nanostructured metals (e.g., by means of density measurements, X-ray diffraction, thermal expansion and various types of spectroscopies) suggest that the atomic structures of glasses differ from those of grain boundaries.

References: p. 935.

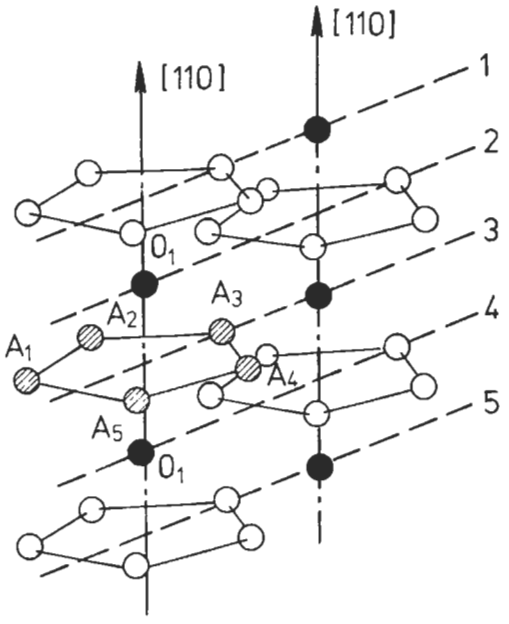

Fig. 9. Schematic diagram of the arrangement of the atoms in a 40° < 110> tilt boundary in tungsten, derived from a sequence of field-ion microscopy images. The position of the < 110 > common tilt axis in the two grains is indicated. Numbers 1–5 indicate subsequent layers of the boundary. Letters A_1–A_5 label one of the polyhedral rings proposed by POTAPOV *et al.* [1971].

2.2.7. Limitations of existing models

A detailed comparison of the experimental observations (SUTTON and BALLUFFI [1987]) indicates that none of the above models seems to predict the boundary energy reliably in all cases, i.e., for metal/metal, ionic/ionic and metal/ionic interfaces. Apparently, no geometric criterion can enshrine the universal answer to the question about the atomic structure of intercrystalline interfaces. This is not surprising since a severe shortcoming of all existing boundary models is the neglect of electronic effects. In fact, studies (HERRMANN *et al.* [1976] and MAURER *et al.* [1985]) of low-energy boundaries in metals with the same lattice structure but different electronic structure suggest a division of all low-energy boundaries into two groups: "electron-sensitive" and "electron-insensitive" boundaries. Physically, this different behavior was interpreted in terms of the different atomic arrangements in the boundaries. If the atomic arrangement is similar to the lattice structure (e.g., in a twin boundary), the boundary energy is low irrespective of the contribution of the conduction electrons to the boundary energy. However, for boundaries with complex atomic structures, the electronic contribution to the boundary energy is crucial so that any difference in the electronic structure (e.g., two materials with different Fermi energies) leads to different boundary behavior. In fact, free-electron calculations showed that the positive charge deficit associated with a grain boundary may

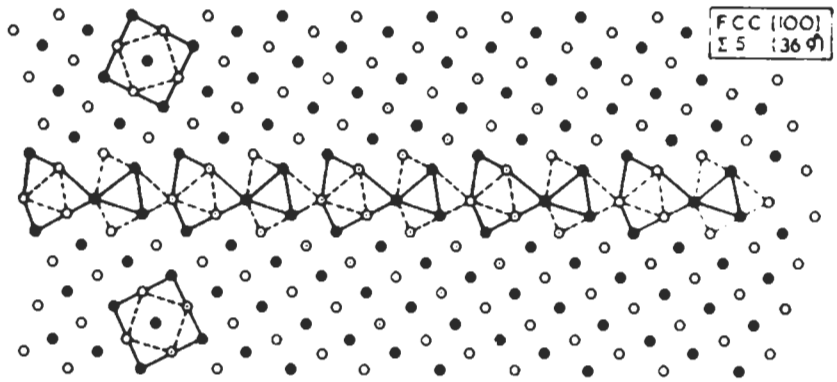

Fig. 10. Structure of a 36.9° < 100 > tilt boundary between fcc crystals, in terms of polyhedral units. The boundary is composed of stacks of capped trigonal prisms.

be the dominant part of the boundary energy (SEEGER and SCHOTTKY [1959]).

A first *ab initio* solution of the electronic and atomic structures of a $\Sigma = 5(001)$ twist grain boundary in Ge was performed recently by PAYNE *et al.* [1985] by means of the Car–Parrinello (CAR and PARINELLO [1985]) method. In this method one solves for both the electronic wave functions and the ion positions. The only approximations made in these computations were the use of a local pseudopotential for Ge, the local density approximation for the exchange–correlation potential, and a large but finite number of plane wave basis functions. By modern standards this is a first principles calculation. One of the interesting features reported was that a contraction could occur at the boundary and was associated with a relatively low energy. This is contrary to the common experience with grain boundaries in metals. As the boundary region becomes denser, five-fold coordinated atoms may arise, and this was indeed reported. With only 4 valence electrons per atom, the system cannot form the same type of bond to a fifth neighbor as it has already established to four neighbors. Instead, rehybridization must take place. We might expect a five-fold coordinated atom to cost less energy than a three-fold coordinated atom since the former represents a smaller perturbation to the tetrahedral bond order. These ideas have been developed further by SUTTON [1988], who proposed a bond-angle distribution function to characterize the boundary structure.

A further shortcoming of existing boundary models is their limited ability to account for temperature effects. The significance of temperature for the structure and properties of interfaces was demonstrated experimentally several years ago (e.g., ERB *et al.* [1982]). The *influence of temperature* on the stability and structures of interfaces has been modelled by a number of groups and was recently reviewed critically by PONTIKIS [1988]. Molecular dynamics and Monte Carlo techniques have been employed and attention has focussed on disordering of the boundary region through roughening or premelting. Such disordering processes are nucleated by thermal fluctuations. However, many thermal properties of a grain boundary like those of a perfect crystal do not depend on thermal fluctuations but on thermal vibrations averaged over a long period of time,

e.g., such as the thermal expansion coefficient, specific heat and elastic constants. As little is known about these boundary properties, it is difficult at present to evaluate the relevance of the above computations.

A great deal of information about the atomic structure of grain boundaries has been deduced by means of *computer simulations*. All simulations ultimately rest on the assumptions they make about *interatomic forces*. The majority of simulations assume some form of potential to describe atomic interactions. For simple s–p bonded metals, e.g., Li, Na, K, Mg, Al, such interatomic potentials can be derived rigorously from the electrostatics of interacting spherical screening clouds of electrons called pseudopotentials. The presence of d-electrons at or near the Fermi level spoils this simple linear screening picture. For substances of this kind pairwise potentials have been generated by fitting more or less arbitrary functions to bulk properties such as cohesive energy, lattice parameter, elastic constants and vacancy formation energy. A more realistic class of potentials for transition and noble metals goes beyond the purely pairwise description of the interaction. They are referred to as isotropic N-body potentials. They are derived from a simplified tight-binding description of electronic densities of states. The next step up the ladder of realism in metallic solids takes us to *3- and 4-body potentials* and to *tight-binding models* beyond the second-moment approximation. For insulators, simulations have used the Born model in which the cohesive part of the total energy is the pairwise summation of the Coulomb interaction of the ions. This is counterbalanced by a short-ranged repulsive energy which is either fitted to the lattice parameter and bulk modulus of the perfect crystal or determined by the *electron gas method*. In semiconductors, a number of empirical angular-dependent interatomic potentials have been developed, motivated by the stability of the fourfold coordination which results from sp^3-hybrid bonds. None can be regarded as completely reliable for structural predictions since they are fitted to bulk properties, and the energy associated with dangling bonds or rehybridization remains poorly represented. In semiconductors, ab initio pseudopotential methods have made rapid progress since 1985, when CAR and PARRINELLO [1985] showed how the Schrödinger equation could be solved for the wave functions with a simultaneous adjustment of the positions of the ions — either to solve their equation of motion or to minimize the total energy. (For further details see ch. 2).

On the experimental side, the most important sources of structural information about interfaces are *high-resolution electron microscopy* (HREM) and *X-ray diffraction* studies. A major experimental problem with X-ray diffraction studies is the fact that boundary scattering is relatively weak. For example, for a $\Sigma 5[001]$ twist boundary in Au the intensity of the weaker diffracted beams of the boundary region corresponds to about 4% of a monolayer of Au. In addition to the resulting poor signal-to-noise ratio, the presence of forbidden lattice reflections, double diffraction from the crystals adjoining the boundary, and scattering from free surfaces enhances the difficulties of obtaining reliable structural information (SASS [1980], SASS and BRISTOWE [1980], FITZSIMMONS and SASS [1988].

A promising new technique for studying interfaces by X-rays recently became important. This scattering of X-rays at grazing angles is called *grazing incidence X-ray scattering*, GIXS (MARRA *et al.* [1979] and EISENBERGER and MARRA [1981]). In this

technique, a grazing-incidence X-ray beam of high intensity is reflected not only by the bulk material, but also by the reflectivity of interfaces buried slightly underneath the surfaces. By fitting the computed and measured X-ray reflectivity curves, information about the density profile across an interface may be obtained. GIXS studies require relatively large sample areas (typically 0.2 cm × 1 cm) under which an interface is buried. The GIXS study averages over this area. In other words, films of extreme homogeneity are required. Those films can only be obtained so far for epitaxial layers of semiconductors or metals grown on rigid substrates such as semiconductors or ceramics.

Modern *high-resolution electron microscopes* have point-to-point resolutions of about 0.16 nm. In order to apply HREM to the problem of imagining the atomic structure of interfaces, only thin-film specimens (typical thicknesses 5 to 10 nm) and crystal orientations that result in close packed rows of atoms being parallel to the electron beam are suitable. In addition to these limitations, one has to keep in mind that the image of the boundary structure is a product of the wave field of the boundary in the objective plane and the contrast transfer function (CTF) of the microscope which depends on the lens errors and the focus conditions. In fact, the image of any object imagined in the electron microscope is severely modified by the CTF if electron scattering to large angle occurs since the influence of the spherical increases rapidly with the scattering angle. This effect is crucial for imagining the atomic structure of boundaries. Good imagining conditions are fulfilled for lattices with large lattice parameters. If, however, deviations in the periodicity exist, components of the diffraction pattern of such an object appear at large diffraction vectors (v_L). This applies, for example, most likely to the atomic arrangement in grain boundaries. Hence, the structure of grain boundaries can only be imagined reliably if the oscillating part of the CTF is outside of v_L. Naturally, all HREM studies imply that no structural changes occur during specimen preparation.

2.3. Interphase boundaries

2.3.1. Bonding at interphase boundaries

In comparison to the extensive body of work on grain boundaries, relatively few studies have been directed at the understanding of the structure and properties of interphase boundaries. The bonding between chemically different materials across an interface involves interactions with and without charge exchange. The interaction between induced dipoles (London), between neutral atoms polarized by a dipole (Debye) and dipole/dipole interactions (Keesom) constitute the first group and are summarized as *Van der Waals attractions.* Charge exchange results in the formation of ionic, covalent and metallic bonds. Among the numerous conceivable combinations of materials at interphase boundaries, interfaces between ceramics and transition and noble metals are of particular practical importance. Hence, it is of interest to understand the bonding between them. Most ceramics of technological use today are insulating metaoxides. They bind to a *free-electron-like* metal essentially owing to the Coulomb attraction between the ions of the ceramic and their screening charge density in the metal (STONEHAM and TASKER [1988], FINNIS [1992], FINNIS *et al.* [1990]). This image attraction is balanced mainly by the hard-core repulsion between the ceramic and metal ions and it seems

primarily (DUFFY *et al.* [1992]) the hard-core repulsion which determines the relative positions projected onto the plane of the interface of the ceramic and metal ions, i.e., the parallel rigid-body translation. The model of an electrostatic image interaction stems from the classical concept in the continuum electrostatics of point charges near a conducting surface, and makes no reference to discrete atoms. Hence, it usually has no place in simple models of adhesion based on chemical bonding. Nevertheless, its equivalent attractive force close to a real metal surface can be calculated quantum-mechanically for simple geometries. Fortunately, the results of these quantum-mechanical calculations can be simulated by a classical interatomic force model, suggesting a way to incorporate this effect in computations of the atomic structure of interphase boundaries (FINNIS [1992]).

The binding of a ceramic to a *transition* metal is less understood, since here, strong covalent *pd*-bonds may be formed across the interface between oxygen and the transition atoms (JOHNSON and PEPPER [1982]). The formation of such bonds is supported by the observation that the adhesion correlates with the free energy of oxide formation for the transition metal; both increase in the order Ag → Cu → Ni → Fe ... In this situation, it is remarkable that atomically sharp transition-metal/ceramic interfaces exist without inter-diffusion and formation of a transition-metal oxide layer. Whereas the hard-core repulsion favors translation states with the metal cores above the holes in the top layer of the ceramic, *pd*-bonding pulls the transition atoms on top of the oxygens.

Noble metals have filled, but polarizable *d*-shells so that their binding to a ceramic is presumably of intermediate nature. In this case, the question of the translation state is difficult and there could be several metastable states. Experimental results are lacking and, for the system (001) fcc Ag on (001) MgO, which has the rocksalt structure consisting of two interpenetrating fcc sublattices, the semi-empirical image-charge model predicts (DUFFY *et al.* [1992]) silver to be above the hole between two magnesiums and two oxygens, whereas ab initio electronic density-functional calculations (BLÖCHL *et al.* [1990], FREEMAN *et al.* [1990]) favor silver on top of oxygen.

However, no general prediction seems to be possible at this moment. For example, *ab initio* LDA calculations (SCHÖNBERGER *et al.* [1992]) indicate that the exact atomic positions and the type of bonds formed in interphase boundaries depend on the elements involved. Both Ti and Ag were found to bind on top of the O in Ti/MgO and Ag/MgO interfaces. However, the binding between Ti and O is predominantly covalent and weaker than in bulk TiO; it corresponds to a Ti oxidation state less than +1. The bonding between Ag and O is weak and predominantly ionic. The bond length and force constants resemble those in Ag_2O where the oxidation state of Ag is +1. Whether it is the polarization of the Ag *d*-shell which pulls Ag on top of O, or if this could also happen for an *sp*-metal is not yet known.

The understanding of the fundamental physics involved in the bonding between a metal and a ceramic requires quantum-mechanical models to be developed. The simplest approach involves cluster calculations (JOHNSON and PEPPER [1982]). Such calculations have established that the primary interactions at metal/oxide interfaces involve the metal (d) and oxygen (p) orbitals, to create both bonding and antibonding orbitals. For copper and silver in contact with Al_2O_3, both states are about equally occupied, resulting in zero net bonding. However, for nickel and iron, fewer antibonding states are occupied and net

bonding occurs. The calculations also reveal that a transfer of valence charge occurs, resulting in a contribution to the net ionic bonding which increases in strength as the metal becomes more noble. Consequently, in the case of metal-to-alumina bonding, strengths are predicted to increase in the order: Ag–Cu–Ni–Fe. This order is generally consistent with the measured trends in sliding resistance as well as with the energies of adhesion. However, it is emphasized that the calculations approximate the interface by an $(AlO_6)^{9-}$ cluster and one metal atom. The selection of the charge to be assigned to this cluster is non-trivial and the choice influences the predicted magnitudes of the energies (ANDERSON *et al.* [1985]). To further examine this issue, ANDERSON *et al.* [1987] performed calculations for the Al_2O_3/Pt couple that included more atoms: 31 close-packed platinum atoms and the corresponding numbers of aluminum and oxygen ions. Then, by applying a quantum-chemical superposition technique, including an electron delocalization molecular orbital method, bonding energies were calculated for different atomic configurations of the Pt/Al_2O_3 interface. These calculations confirmed that the bond was strongest when oxidized platinum atoms opposed close-packed oxygen ion planes.

Ab initio calculations seem to be essential for a full understanding of the bonding. LOUIE and coworkers (LOUIE and COHEN [1976], LOUIE *et al.* [1977]) have performed such calculations on metal-semiconductor interfaces. In these calculations, the metal was described by a *jellium*, so that insight emerged regarding the bonding mechanisms, but not on the atomistic structure. More recently, supercell calculations have been carried out that include an interface area and adjacent regions large enough to incorporate the distorted (relaxed) volumes of both crystals. With this approach, the electron distribution around all atoms has been calculated and the atomic potentials evaluated. In a next step, interatomic forces may be calculated and strains determined. Such calculations have been performed rather successfully for the interface between Ge–GaAs (KUNC and MARTIN [1981]) and Si–Ge (VAN DE WALLE and MARTIN [1985]). The crystals adjacent to those interfaces are isomorphous and very nearly commensurate, such that the misfit between lattice planes is very small. However, misfits between metals and ceramics are typically rather large so that extremely large supercells are required.

First attempts in this direction have been made. SCHÖNBERGER *et al.* [1992] performed *ab initio* local density-functional calculations of the equilibrium geometries, force constants, interface energies and works of adhesion for lattice-matched interfaces between rocksalt-structured MgO and a f.c.c. transition or noble metal. The interfaces had $(001)_M \| (001)_{MgO}$ and $[100]_M \| [100]_{MgO}$ (M = Ti or Ag). The full-potential LMTO method was used. Both Ti and Ag are found to bind on top of oxygen. The interface force constants are 3–4 times larger for Ti|MgO than for Ag|MgO. These, as well as the M–O distances, indicate that the Ti–O bonding is predominantly covalent and that the Ag-bonding is predominantly ionic. The calculated interface energies are both 0.8 eV/M|MgO and the interface adhesions are, respectively, 1.2 eV/Ti|MgO and 0.9 eV/Ag|MgO.

With the advent of a new calculational scheme (CAR and PARRINELLO [1985]), involving a combination of molecular dynamics (see, e.g., RAHMAN [1977]) and density-functional theory (KOHN and SHAM [1965]), it should be possible to conduct computa-

References: p. 935.

tions of *relaxed* interfaces much more efficiently. The scheme should also allow equilibrium computations of metal/ceramic interfaces at finite temperatures. The conduct of such analysis on model interfaces should greatly facilitate the basic understanding of the bonding phenomenon and allow judicious usage of both cluster calculations and continuum thermodynamic formulations.

For recent reviews of this area we refer to the articles by RÜHLE and EVANS [1989], FINNIS and RÜHLE [1991] and the Proceedings of an International Symposium on this subject edited by RÜHLE *et al.* [1992].

2.3.2. Chemistry of interphase boundaries

In multicomponent two-phase systems, non-planar interfaces or two-phase product regions can evolve from initially planar interfaces (BACKHAUS and SCHMALZRIED [1985]). The formalism previously developed for ternary systems can be adapted to metal/ceramic couples, with the three independent components being the two cations and the anion. In general, the problem is complicated by having several phase fields present, such that intermediate phases form: usually intermetallics with noble metals and spinels (or other oxides) with less noble metals. The actual phases depend on the geometry of the tie lines, as well as on the diffusion paths in the tenary phase field, and cannot be predicted *a priori*. In general, the following two cases can be distinguished:

2.3.2.1. Interfaces without reaction layers. Detailed scanning electron microscopy and TEM studies performed for Nb/Al_2O_3 (BURGER *et al.* [1987], RÜHLE *et al.* [1986], [1987]) have shown that no reaction layer forms. Concentration profiles revealed that, close to the interface, the concentration of aluminum is below the limit of detectability. However, with increasing distance from the interface, the concentration of aluminum, c_{Al}, increases to a saturation value. The corresponding oxygen content is below the limit of detectability. These measurements suggest that at the bonding temperature, c^*_{Al}, the local concentration of Al at the interface possesses a value governed by the solubility limit. Bonding between platinum and Al_2O_3 subject to an inert atmosphere also occurs without chemical reaction. However, for bonds formed subject to a hydrogen atmosphere containing about 100 ppm H_2O, aluminum is detected in the platinum, indicative of Al_2O_3 being dissolved by platinum (RÜHLE and EVANS [1989]).

2.3.2.2. Interfaces with reaction layers. For systems that form interphases, it is important to be able to predict those product phases created. However, even if all the thermodynamic data are known, so that the different phase fields and the connecting tie lines can be calculated, the preferred product phase still cannot be unambiguously determined. Sometimes, small changes in the initial conditions can influence the reaction path dramatically, as exemplified by the Ni–Al–O systems (WASYNCZUK and RÜHLE [1987]). Under high vacuum conditions (activity of oxygen $< 10^{-12}$) the diffusion path in the extended nickel phase field follows that side of the miscibility gap rich in aluminum and low in oxygen, (path I in fig. 11), caused by the more rapid diffusion of oxygen than aluminum in nickel. This interface composition is directly connected by a tie line to the Al_2O_3 phase field, such that no product phase forms. However, whenever nickel contains sufficient oxygen (about 500 ppm solubility), the Ni(O)/Al_2O_3 diffusion couple yields a spinel product layer. It is noted that the interface between spinel and nickel seems to be

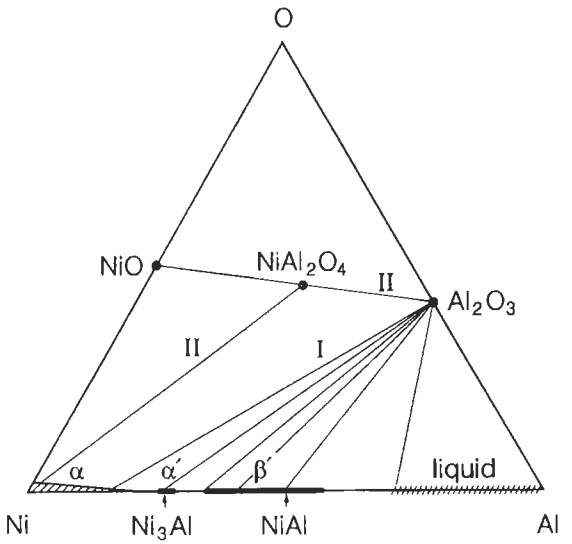

Fig. 11. Ni–Al–O phase diagrams (schematically for T = 1600 K). Two reaction paths are possible when nickel is bonded to Al_2O_3: (I) Low oxygen activity: no reaction product forms, (II) high oxygen activity: spinel forms. (From RUHLE and EVANS [1989].)

unstable, morphological instabilities becoming more apparent with increasing spinel layer thickness. Bonding of copper to Al_2O_3 seems to require a thin layer of oxygen on the surface of copper prior to bonding and $CuAl_2O_3$ or $CuAl_2O_4$ form (WITTMER [1985]). The spinel thickness can be reduced by annealing under extremely low oxygen activities, leading first to a "non-wetting" layer of Cu_2O and then to a direct Cu/Al_2O_3 bond. Bonding of titanium to Al_2O_3 results in the formation of the intermetallic phases TiAl or Ti_3Al, which probably also include oxygen. The thickness of the reactive layer increases with increasing bonding time, and morphologically unstable interfaces develop.

A recent study (JANG *et al.* [1993]) has demonstrated the capability of atom-probe field-ion microscopy to reveal the chemical composition profile across interphase boundaries on an atomic level. By applying this technique to Cu/MgO {111}-type heterophase boundaries along a common <111> direction it was demonstrated that these boundaries are formed by Cu|O|Mg bonds.

Experimental evidence for the formation of reaction layers at interphase boundaries has been obtained by studying nanostructured alloys (cf. § 5 of this chapter). These alloys were synthesized by consolidating nanometer-sized crystals with different chemical compositions, e.g., Ag–Fe, Cu–Bi, Fe–Cu, Cu–Ir, Sn–Ge. Although all systems exhibit little mutual solubility at ambient temperature in the crystalline state, it was found (by X-ray diffraction, EXAFS and spectroscopic methods) that solid solutions are formed at the interphase boundaries. In the case of Ag/Fe this result is particularly remarkable because Ag and Fe are immiscible even in the molten state.

Most structural ceramics are polyphase materials. They are either composites or

different crystalline phases or contain an intergranular vitreous phase in addition to a single crystalline phase. The vitreous intergranular phases can be caused (i) as a result of a liquid-phase sintering process (e.g., in Sialon ceramics, alumina, etc.), (ii) by an incomplete crystallization of a glass (glass ceramic), and (iii) by a condensation of impurities present in the single-phase component at the grain boundaries (e.g., silicates in zirconia).

In the materials noted above, most grain boundaries are covered with a glassy film and, in addition, glass is present at grain junctions. This observation may be explained by considering the energy of the grain boundary as a function of misorientation for crystalline and wetted boundaries. The curve of the interfacial energy vs. misorientation of a crystalline boundary exhibits cusps at the special misorientations. In contrast, the energy curve of the wetted grain boundary should be independent of orientation due to the isotropic nature of the glass. On the basis of such descriptions, low-angle grain boundaries will be free of glass, whereas all large-angle grain boundaries will contain an intergranular glass phase with the exception of "cusp" orientations (the "special" boundaries), as was observed.

2.3.3. Crystallographic structure: "lock-in" model

FECHT and GLEITER [1985] determined relatively low-energy interfaces between noble metal spheres and low-index ionic crystal substrates by the rotating crystallite method. They observed that in the resulting low-energy interfaces, some close-packed directions in the two phases are parallel and some sets of low-index planes are parallel, as well. On the basis of these observations it was concluded that no CSL orientation of low Σ exists in the vicinity of the observed relationships and, therefore, the applicability of the "CSL model" was ruled out for the systems studied. Instead, they proposed the following "lock-in" model: a) relatively low interfacial energy is achieved when a close-packed direction (<110>, <100>, <1100>, <1210>) in the crystal lattice of one phase is parallel to the interface and also parallel to a close-packed direction in the crystal lattice of the adjoining phase and if two sets of relatively low-index lattice planes are parallel to the interface. In this configuration, close-packed rows of atoms in the "surface" of the metal crystal can fit into the "valleys" between close-packed rows of atoms at the "surface" of the ionic crystal in "locked-in" configurations.

Generally, the two phases adjoining the boundary are incommensurate, and unless a small strain is allowed parallel to the interface, locked-in rows of atoms soon begin to ride up the valleys in the interface and cease to lock-in. The lock-in model is not entirely crystallographic in character. Certainly, the conditions for the existence of parallel close-packed directions in the interface and of the interface being parallel to low-index planes are geometrical. But the assumption that, when these conditions are fulfilled, the interface relaxes in such a way that rows of atoms along the close-packed directions form a "locked-in configuration" is equivalent to assuming a particular translation state of the interface is energetically favorable. On the other hand, the planar density of coincidence sites is unaffected by the translation state of the interface. Hence, there is an important distinction between the lock-in criterion and the Γ criterion (cf. paragraph 2.2.2). Discrepancies from the orientation relationships predicted by the "lock-in" model have

been found for interphase boundaries between Nb/Al_2O_3 and Cu/Al_2O_3. Relaxation effects are presumably responsible for these deviations.

3. *Characterization of microstructure*

The basic elements of microstructure are lattice defects and second-phase components. A complete description of the topology and crystallography of the microstructure of a crystalline material requires the following information:

(a) the spacial distribution of the orientation of all crystals;
(b) the characterization of the shape, type, size and spacial distribution of all the elements of the microstructure;
(c) the characterization of the orientation distribution of these elements in space (microstructural anisotropy).

Naturally, all of these parameters can be represented in terms of orientational and spacial correlation functions. Any special feature of a particular microstructure such as a special type of symmetry, self-similarity, order, etc., of all or of some of these elements are enshrined in the correlation functions. In reality, however, the correlation functions are frequently not known because they are difficult to measure. Hence, in most cases, the discussion of microstructural features had to be limited to a few, relatively simple microstructures (HORNBOGEN [1989]). However, in recent years modern on-line data evaluation procedures became available involving, for example, a combination of conventional microscopic methods with an on-line image processing attachment. By means of such systems the spacial orientation distributions of all crystals of a polycrystal can be measured (ADAMS [1993]). This procedure has been termed "orientation imaging microscopy". Similar systems have been developed to characterize the size distribution, shape distribution, etc., of crystallites and other elements of microstructure.

In the straightforward situation of randomly distributed defects and/or second phase particles, the microstructure may be characterized to a first approximation by an average density, ρ, of defects and/or second-phase particles. Depending on the type of microstructural element involved, ρ describes the number of O-dimensional defects (e.g., vacancies) per volume, the total length of one-dimensional defects (e.g., dislocations), the total area of two-dimensional defects (e.g., grain boundaries) per volume, or the total volume fraction of three-dimensional objects (e.g., pores, precipitates). However, even in the simple situation of uniformly distributed microstructural elements, the average defect spacing may not be the appropriate parameter to describe the microstructure. For example, in the case of a polycrystal with equiaxed grains of a narrow size distribution, the use of the average grain size as a length scale implies that all boundaries are the same. As this is mostly not so, a new length scale has to be introduced which accounts for the boundary to boundary variability. This new length scale is given by the clusters of grains linked by grain boundaries sharing misorientations in the same category. In fact, it has been shown that it is this length scale of the microstructure that controls crack propagation and failure of polycrystals (PALUMBO *et al.* [1991a], WATANABE [1984]). The

control of properties of materials by means of controlling the structure of interfaces seems to develop into a separate subdiscipline of materials science termed "interfacial engineering" or "grain boundary design" (WATANABE [1993], HONDROS [1993]). This new discipline is based on the structure-property relationship for individual boundaries and relates the boundary-induced heterogeneity of deformation and fracture of polycrystals to the topological arrangement and the spacial distribution of the character of grain boundaries in polycrystalline materials. It is these parameters that seem to be crucial in controlling the high-temperature plasticity, superplasticity and brittleness. (Ch. 28. § 3.7).

Frequently, the spacial arrangement of the microstructural elements is non-uniform. For example, a non-uniformity in the dislocation density may exist on different length scales; e.g., in heavily cold-worked materials, dislocation cell walls are formed on a nanometer scale whereas in irradiated specimens the formation of helical dislocations introduces roughness on a submicron scale. In some cases an isotropic or anisotropic length scale is required to characterize such microstructures. In other cases this is not so. For example, in some materials fractal microstructures have been reported (e.g., in polycrystalline alloys with localized slip). The significance of fractals in various types of microstructures in metals has been discussed recently by HORNBOGEN [1989].

In multiphase alloys different types of microstructures result depending on the volume fraction, shape and the distribution of the phases (HORNBOGEN [1986], [1989]). For the sake of simplicity let us limit the discussion first to two-phase systems (called α and β phases) with equiaxed grains or particles. In alloys of this type a variety of microstructures can be formed. A convenient parameter to characterize the various microstructures is the density (ρ) of grain and interphase boundaries. In a microstructure called an "ideal *dispersion*" of α particles in a β matrix no α/β interphase boundaries exist (fig. 12a). The other extreme results if the β particles cover all α/α grain boundaries completely. In other words, the α/α boundaries disappear and we are left with α/β interfaces and β/β boundaries the relative density of which depends on the β crystal size (fig. 12c). In both cases, two-phase microstructures (fig. 12b) exist that are characterized by different degrees of percolation of the α and β phases. One way to characterize this type of microstructure (called *duplex structure*) is to determine the relative densities of the α/β, β/β and α/β interfaces. In the ideal duplex structure the ratio between the total number of grain and interphase boundaries is 0.5. In the cases considered so far, the two phases were assumed to have no shape anisotropy. In reality, this is often not so. In order to exemplify the role of anisotropy, a few microstructures with different degrees of anisotropy are displayed in fig. 13 (HORNBOGEN [1984]). Depending on the aspect ratios of the second-phase crystals, a fibrous or lamellar structure may result. Obviously, other anisotropic microstructures are formed if the relative aspect ratios of a duplex or a skeleton-type microstructure are modified.

Microstructural transformations. The well-established scheme of phase transformations in condensed matter systems may be extended in a modified form to the transformation of one type of microstructure to another one. The following three cases have been discussed so far:

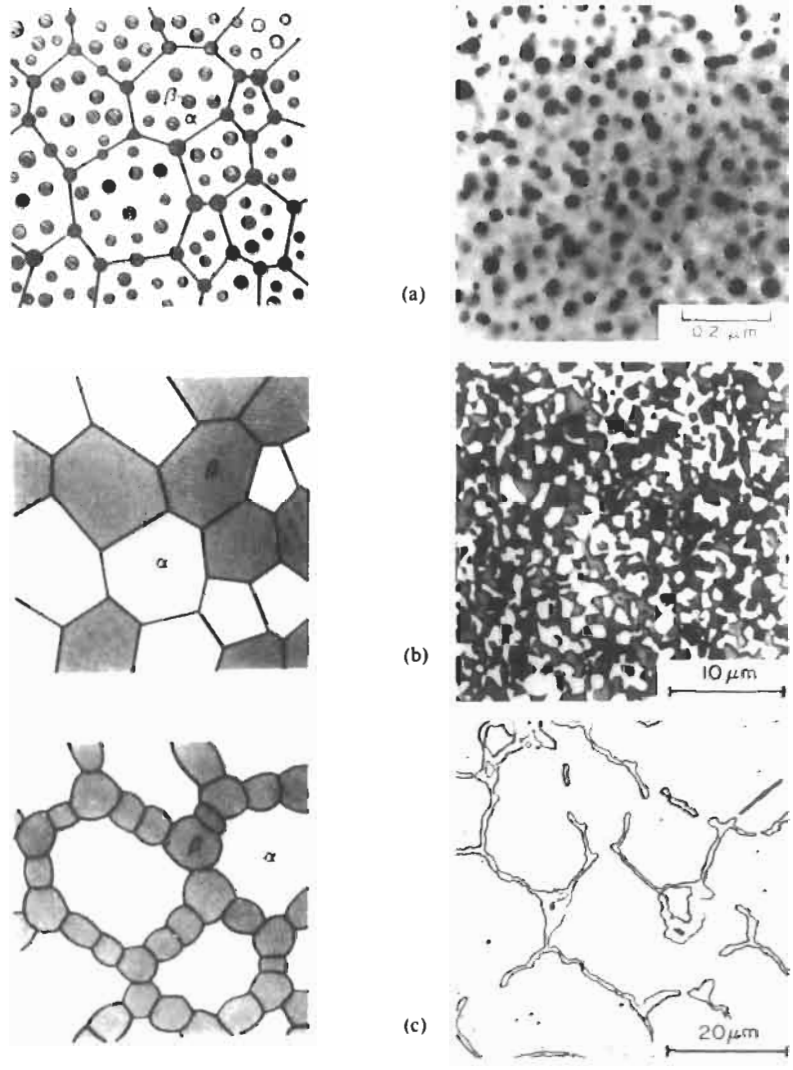

Fig. 12. Principal types of equi-axed two-phase microstructures. (a) Dispersion: Ni+ 18.2Cr+5.7Al, $\gamma+\gamma'$. (b) Duplex: Fe + 9wt%Ni, $\alpha+[\gamma+\alpha_M]$ (austenite transformed to martensite during cooling). (c) Net: Fe+0.6wt%C, $\alpha+Fe_3C$. (From HORNBOGEN [1984].)

a) *Transformation of microstructural elements.* Well known examples for this type of transformation of microstructural elements are as follows. The condensation of single vacancies into dislocation loops, the transformation of small-angle boundaries into high-angle grain boundaries by incorporation of additional dislocations, the incorporation of dislocations into high-angle grain boundaries which transforms them, for example, from a special (low-energy) boundary into a random (high-energy) one (cf.

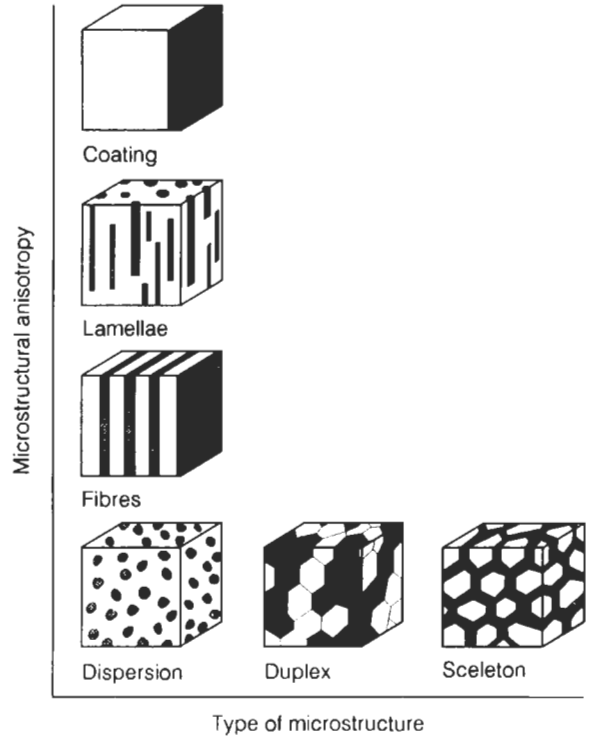

Fig. 13. Different two-phase microstructures depending on the topology of the two phases. (From HORNBOGEN [1984].)

§ 2 of this chapter), the change from coherent to incoherent interphase boundaries during the growth of precipitates are examples of this kind.

b) *Transformation of a crystalline material with a high defect density to a new phase*
Such a transformation may occur if the spacing between microstructural elements (e.g., dislocations, grain boundaries) in a crystal approaches atomic dimensions. If this is so, it may transform into an amorphous phase (OEHRING *et al.* [1992]). The same applies to the shock wave-induced transformation of a crystal into a glass or the dislocation model of melting. In the dislocation model of melting, melting is proposed to occur by the entropy-driven proliferation of dislocations in crystals (KUHLMANN–WILSDORF [1965], COTTERILL [1979], EDWARDS and WARNER [1979], HOLZ [1979]). The phase transition from α to β quartz has been shown to occur by the incorporation of a high density of regularly spaced Dauphiné twins.

c) *Transformations between different types of microstructures*
Transformations of this type are defined by the appearance of new microstructural elements. Two-phase microstructures shall serve as examples for such transformations. A transformation of one type of microstructure to another is associated with

the appearance or disappearance of a particular type of boundary which represents a characteristic topological feature. Transformations can take place as a function of volume fraction of the phases, and of their shape and orientation. For constant shape- and size-distribution, the transformation must take place at a critical volume fraction, f_r. This in turn leads to relations with alloy composition x and annealing temperature T and with the equilibrium phase diagram. Figure 14 shows two-dimensional representations of the following transformations: duplex ⇋ dispersion and net ⇋ dispersion.

Microstructural transformations are found not only under conditions of phase equilibrium, but also if the volume fractions change after nucleation and finally when an equilibrium value is approached. The first stage in formation of a duplex structure is usually the formation of randomly dispersed nuclei. In this case, the transformation, dispersion → duplex, takes place during isothermal annealing. Other examples for the occurrence of microstructural transformations in alloys are bulk concentration gradients as for example for decarburization or carburization of steels. Concentration gradients may cause microstructural gradients.

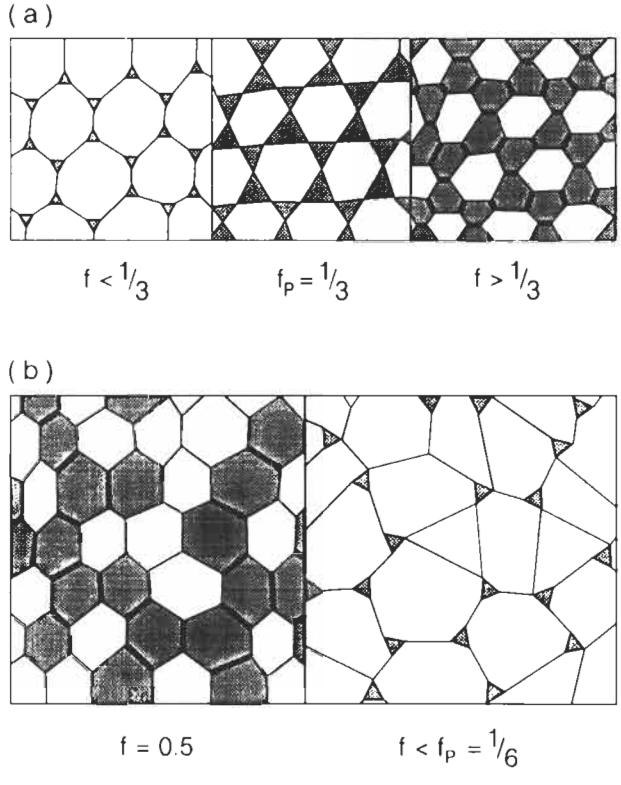

Fig. 14. Transformations of types of microstructure in planar sections (schematic). (a) Dispersion ⇋ net. (b) Duplex ⇋ dispersion. (From HORNBOGEN [1984].)

References: p. 935.

4. *Development of microstructure*

4.1. Basic aspects

The microstructure of a crystalline material may result from structural phase transformations and/or interaction processes between structural defects. In fact, a general and reciprocal relationship exists between microstructures and defect interactions. Any microstructure may be interpreted as the result of the interaction between structural defects and/or phase transformations. On the other hand, it should be possible to synthesize new microstructures (and, hence, materials with new properties) by utilizing this relationship, e.g., by means of more complex defect interactions (possibly combined with phase transformations). The thermomechanical treatment of materials represents an example of this kind. Microstructures generated by structural phase transformations are discussed in chs. 8, 15, 16, and 17. Microstructures resulting from the interaction between some specific types of lattice defects are treated in chs. 21–25 and 27. In this chapter, attention will be focused on those microstructures that are not the result of phase transformations. Despite the complexity of all conceivable processes for the development of microstructures, a guideline for a systematic understanding of the genesis of microstructures may be provided by considering some relatively simple and well studied types of interaction processes involving only one or two types of structural defects. This "model approach" will be used here.

4.2. Microstructural changes stimulated by interfacial-energy reduction

Three classes of microstructural changes driven by interfacial energy may be distinguished:

1. Microstructural changes in single-phase materials (without applied potential fields).
2. Microstructural changes in polyphase materials (without applied potential field) when the materials have: (a) a dispersion-type structure; (b) a duplex (or a network) structure.
3. Microstructural changes due to the effects of applied potential fields (e.g., temperature or electric field gradients).

An excellent review of these classes is the one by MARTIN and DOHERTY [1976].

4.2.1. Microstructural changes in single-phase materials, stimulated by interfacial energy: domain and grain growth

Internal interfaces in solids — such as grain boundaries or domain boundaries in ordered systems (atomic order, spin order, polarization order, etc.) — are associated with a positive excess energy resulting in grain or domain growth. Local atomic arrangements at or near moving interfaces can differ significantly from arrangements at or near stationary interfaces, giving rise, for example, to drag effects (solute or defect drag), structural changes of the interfaces due to defect production, etc. A complete theory of interfacial motion would have to account not only for these effects, but also for the topological changes of the array of interconnected interfaces during domain and grain

growth. For far no such theory is at hand. However, models treating various aspects of the problem separately have been put forward. The problems of the growth of grains or magnetic domains are treated in chs. 28 and 29, respectively. As many growth theories make no distinction between grain and domain growth, we refer to ch. 28 for all theories that apply to both processes.

Two approaches to describe the motion of a domain wall have been proposed. The earlier, widely used phenomenological approach states that the wall mobility is proportional to the thermodynamic driving force, the proportionality constant being a nositive quantity called the mobility. The driving force in this approach is the product of the mean of the local principal curvatures of the interface and the excess free energy per unit area (σ). This approach leads to a growth law of the type $\langle D \rangle^2 \alpha \sigma t$, where <D> is the average diameter of the domains in a polydomain structure and t is the time. This result has been experimentally confirmed for several ordered alloys (e.g., ARDELL *et al.* [1979] and ROGERS *et al.* 1975]) and can account for the broad distribution of domain sizes frequently observed experimentally.

The approach of ALLEN and CAHN [1979] models the motion of an interface by solving a diffusion equation that has been modified to account for the thermodynamics of non-uniform systems (LANGER and SEKERKA [1975]). Domain walls have a width in which there are compositional and order-parameter variations, i.e., a crystal containing a domain wall is a non-uniform system. The order-parameter variation is the basis of a diffusion potential whose gradient results in an atomic flux. This description leads to a time-independent Ginsburg–Landau equation for changes in the order parameter and hence for the wall motion. In the limit of large radii (r) of wall curvature, the propagation velocity (V) of the wall is found to be proportional to r, but independent of the excess energy (σ) of the wall. This does not imply that the energy dissipation during domain growth is independent of σ. In fact, the energy dissipation may be shown to be proportional to σ.

Experimental tests were carried out in which σ was varied by two orders of magnitude. Domain-coarsening kinetics and σ were found to scale differently with temperature as had been predicted theoretically. On the basis of the results discussed so far, we are led to conclude that cases exist where V is proportional to σ, and there are clearly other cases where V is independent or even nonlinearly dependent on σ (e.g., TURNBULL [1951] and LI [1969]). No general criterion seems apparent at present for relating V to σ and boundary curvature for different experimental conditions.

The development of our understanding of continuous ("normal") grain growth started when it was recognized that the driving force for grain growth is the decrease of grain boundary energy (SMITH [1952]). On the basis of this approach several simple and mostly qualitative interpretations of grain growth were given. The first quantitative model (BECK [1954]) predicted an increase of the average grain diameter with time as $t^{1/2}$ which, however, was rarely confirmed experimentally. Mostly, time exponents less than 0.5 were observed and attributed to the drag forces caused by inclusions or solute atoms. More insight into the processes involved in grain growth was obtained when more sophisticated theoretical approaches were used. HILLERT [1965] applied the statistical treatment of Ostwald ripening of precipitates to grain growth. Some of the foundations

References: p. 935.

of Hillert's analysis were reexamined by LOUAT [1974] who pointed out that in grain growth, as opposed to Ostwald ripening, "grain collisions" occur in which faces are gained and/or lost. In order to allow for these events, grain growth was considered as a particular case of random walk.

HUNDERI and RYUM [1979], [1981] applied a deterministic model considering individual boundaries and described the change of size of the individual grains by an extremely large set of differential equations (one for each grain), which they solved numericany. Very recently, ANDERSON *et al.* [1984] used the Monte Carlo method to simulate grain growth and included in this treatment also the case of Zener drag. Finally, ABBRUZZESE [1985] further developed the Hillert model by calculating the critical radius. He used discrete grain size classes which led to a reasonably small set of differential equations (only one for each class) and thus to the possibility to calculate numerically the evolution of the grain size distribution. This approach was extended further by including textural effects (ABBRUZZESE and LÜCKE [1986]) in the form of orientation-dependent grain-boundary energies and mobilities. The most important result of this extension was that, instead of the single critical radius found in the textureless case, now for each orientation a different critical radius is obtained but with a value depending on all orientations. It is shown that (very generally) grain growth leads to pronounced texture changes which are accompanied by characteristic changes of the scattering of the grain size distribution and by peculiarities of the grain growth kinetics, which then does not even approximately follow a $t^{1/2}$-law.

On the experimental side, the effect of particles has repeatedly been taken into account. The amount of work on the texture effects, however, is still small. For a long time, it was limited to measurements of the orientation of secondary grains. It was first shown for α-brass (BRICKENKAMP and LÜCKE [1983]) that also the apparently *continuous* grain growth leads to drastic texture changes and that these are connected with peculiarities in grain growth kinetics and grain size distribution. The authors were able to put forward some qualitative interpretations for these effects.

"Anomalous" grain growth (also termed secondary recrystallization) is characterized by an increase in size of a small fraction of the crystallites whereas the rest does not grow at all. Anomalous grain growth has been suggested to originate either from the fact that a few of the crystallites have higher grain-boundary energies and/or boundaries of higher mobilities than the majority of the grains.

In the experimental literature, anomalous grain growth was demonstrated to exist in pure polycrystals as well as multiphase alloys. MAY and TURNBULL [1958] demonstrated the significance of second phase particles for anomalous grain growth for the first time. In Fe–Si alloys, the occurance of anomalous grain growth was shown to depend on the presence of MnS particles which inhibited normal grain growth. In several high-purity materials (SIMPSON *et al.* [1971], ANTONIONE *et al.* [1980]) strain and texture inhibitation of normal grain growth was demonstrated. Texture inhibition is based on the following idea. If the grain structure is strongly textured, boundaries of low mobility result. The anomalous grains are assumed to have high mobility boundaries because their crystallographic orientations relative to their neighbouring grains deviate strongly from the texture. A firm link between texture and abnormal grain growth has been made by

HARASE *et al.* [1988]. In a $Fe_{50}Ni_{50}$ alloy they found that the largest grains after secondary recrystallization had a high frequency of coincidence boundaries such as $\Sigma 7$ or Σ 19b with the primary matrix grains.

4.2.2. Microstructural changes in polyphase materials with a dispersion structure, stimulated by interfacial energy: Ostwald ripening

If interfacial energy is the only driving force for an instability and if the rate of development of the instability is governed only by mass transport processes, the linear dimension, d, of any microstructural feature can be shown (HERRING [1950]) to scale with time by the expression:

$$d^n = d_0^n + \alpha G t \tag{1}$$

where d_0 is the value of d at time $t=0$, G is the parameter of the appropriate mass transport process and α is a dimensionless parameter which depends on the geometry. The scaling exponent, n, takes the values: $n=1$ for viscous flow, $n=2$ for interfacial control, $n=3$ for volume diffusion in all phases, $n=4$ for interfacial diffusion and $n=5$ for pipe diffusion. The growth laws discussed in the following paragraphs for specific processes extend eq. (1) by giving explicit expressions for α and G. Normally, microstructural changes in multiphase alloys involve changes of shape, size and/or position simultaneously. For convenience, these three aspects are discussed separately.

An array of inclusions or dislocation loops or pores of equilibrium shape, but different sizes, interact because the concentration of solute atoms (or the concentration of vacancies, or the vapor pressure in a gaseous system) in the vicinity of small (large) particles is higher (lower) than the average supersaturation. The solute, therefore, flows from the smaller to the larger particles. Hence, smaller particles shrink and larger particles grow by "devouring" the smaller ones, a process known as *Ostwald ripening*. For reviews of various aspects of the problem, we refer to the articles by JAIN and HUGHES [1978], KAHLWEIT [1975] and HENDERSON *et al.* [1978]. The phenomenon of Ostwald ripening was analyzed first for the solid state by GREENWOOD [1956], and then independently and simultaneously by WAGNER [1961] and by LIFSHITZ and SLYOZOV [1961], assuming the common case of spherical precipitates growing by volume diffusion. Analogous expressions have been developed for other types of coarsening. The corresponding constants (α, G, n) of eq. (1) are summarized in table 1. In the case of coarsening of spheres by volume diffusion, which is the most commonly observed case ($r^3 \propto t$), a steady-state distribution of sizes is predicted to be approached irrespective of the initial size distribution, with a maximum particle size of $1.5r$, where r is the mean particle radius (figs. 15a, b). (See also ch. 15, § 2.4.2)

A critical assumption in the Lifshitz–Slyozov–Wagner (LSW) theory is that the diffusion fields around each particle are spherically symmetrical. This is strictly valid for zero volume fraction of precipitates when the concentration gradients around adjacent particles do not interfere. If the LSW theory is extended (ARDELL [1972]) to account for finite volume fractions, the basic form of eq. (1) is retained but the proportionality constant α is increased and the particle size distribution is broadened. The LSW analysis cannot persist to very large times, because ultimately the system should ripen into one

large particle. In fact, it was shown (KAHLWEIT [1975]) that the coarsening rate of the largest particles initially increases rather rapidly, then passes through a maximum and slowly approaches zero for long periods of time. The value of the coarsening rate predicted by the LSW theory is reached shortly before reaching the maximum rate. The significance of coherency strains for Ostwald ripening effects will be discussed in the next sub-section on stability against coarsening. In the LSW treatment, solute transport is assumed to be the rate-controlling process. Hence, modifications are required if other processes play a role, for example, ternary additions, solvent transport effects or dissociation of solute and/or solvent molecules. The latter case has been discussed by WAGNER [1961]. The effect of solvent transport may be accounted for (ORIANI [1964]) by modifying the diffusion parameter D in the LSW equations, leaving the main result (growth law, size distribution) unaltered. The modification of D becomes important, however, if we use growth-law observations to derive σ, D, etc. The same applies to the effect of ternary additions on the ripening rate. Ternary additions alter the rate constants of coarsening by a factor $1/3(1-K)^{-2}c_0^{-1}$, leaving the scaling law unchanged (BJORKLUND *et al.* [1972]). c_0, is the ternary alloy content and K is the distribution coefficient. Ostwald ripening of semi-coherent plate-shaped precipitates (Widmanstätten plates) represents yet another case for which the LSW treatment cannot be applied without modifications. Ostwald ripening of Widmanstätten plates results in large aspect ratios, as the lengthening of these plates is diffusion-limited whereas the thickening is mobility-controlled by the good-fit (semi-coherent) interface (AARONSON *et al.* [1970] and FERRANTE and DOHERTY [1979]).

The experimental confirmations of the theoretical predictions on Ostwald ripening are still fragmentary (for a review see JAIN and HUGHES [1978]). Although numerous experiments confirming the scaling laws given in table 1 have been reported (for a review of the earlier data we refer to MARTIN and DOHERTY [1976]), the relatively small range of particle sizes that can be obtained experimentally is not sufficiently precise to allow unambiguous identification of the scaling exponent. In most cases, the observed

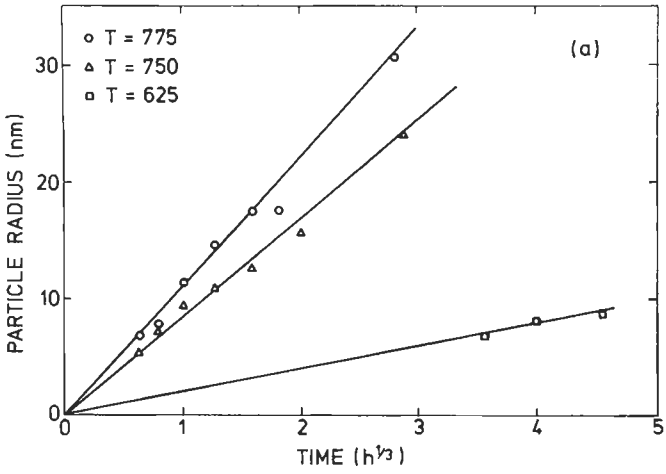

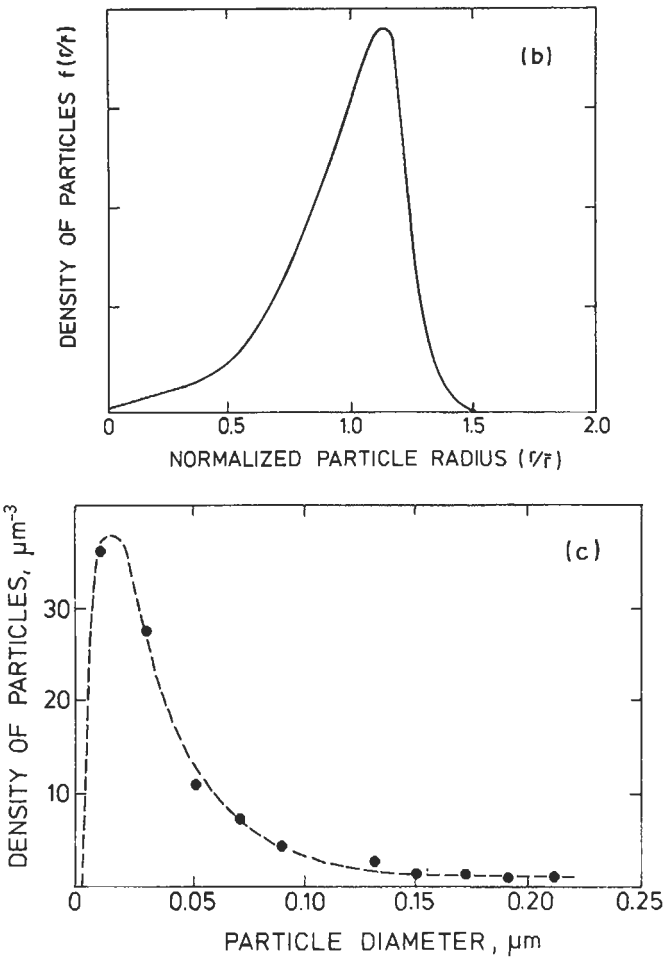

Fig. 15. (a) Plot of the particle radius against (time)$^{1/3}$ for a nickel–aluminium alloy annealed at three different temperatures (from ARDELL *et al.* [1966]). (b, c) Size distribution developed during Ostwald ripening: (b) theoretical prediction according to the Lifshitz–Slyozov–Wagner theory; (c) experimental observation on silica particles in copper annealed at 1173 K for 27 h. (From BHATTACHARYA and RUSSELL [1976].)

size distributions are wider than those predicted by the theory (figs. 15b and 15c). Frequently, also a few large particles are found which are not a part of the main system of particles. Furthermore, a tail on the large-size side of the size distribution is observed, in contradiction to the LSW theory (see also ch. 15, § 2.4.1).

The available experimental evidence on the effect of volume fraction on coarsening is conflicting. Studies on Cu–Co alloys showed clear dependence on volume fraction, whereas other work (Ni_3Al in Ni, NbC in Fe, Cu in α-Fe) failed to detect any effect. Recent experimental work has evidenced the possibility of contact between growing

References: p. 935.

Table 1
Ostwald ripening rates.

Rate-controlling process	Shape of particles	Expressions for constants[a]			Reference
		n	α	G	
Volume diffusion	Spheres	3	8/9	$D\sigma_b C_\alpha V_m/RT$	WAGNER [1961] LIFSHITZ and SLYOZOV [1961]
	Plates	3	$3A'(1+A'/A'_{eq})$	$Df\sigma_b V_m/2pRT$	DOHERTY [1982]
Grain-boundary diffusion	Spheres	4	9/32	$D_b\sigma C_\alpha V_m\delta/ABRT$	ARDELL [1972] KIRCHNER [1971]
Dislocation-pipe diffusion	Spheres	5	$(1.03)^5(3/4)^4 5/6\pi$	$D_d\sigma_b C_\alpha V_m qN\eta/RT$	ARDELL [1972]
Interface-limited growth		2	64/81	$\sigma_b\beta C_\alpha V_m/RT$	DOHERTY [1982]

[a] The symbols used are given below with their meaning or an expression.

A parameter, $A=2/3-\sigma_b/\sigma+(\sigma_b/\sigma)^2/24$.
B parameter, $B=\frac{1}{2}\ln 1/f$.
A', A'_{eq} average and equilibrium aspect ratios of precipitate, respectively.
C_α, C_β precipitate and matrix concentrations, respectively.
D, D_b, D_d general, boundary, and dislocation-pipe diffusion constants, respectively.
f function given by $f=C(1-C_\alpha)/(C_\beta-C_\alpha)^2$.
N number of dislocations intersecting one particle.
p parameter tending to π for large precipitates.
q diffusional cross-section of a dislocation.
R gas constant.
T temperature.
V_m molar volume.
β proportionality constant including the interface mobility.
δ boundary thickness.
η geometrical parameter.
$\sigma(\sigma_b)$ energy of grain boundary or interphase boundary.

precipitates. The theoretical discussion of this effect is based on independent growth of adjacent precipitates, the center-to-center distance between the particles remaining fixed (DAVIS *et al.* [1980a]). It is, however, difficult to see how the solute atoms are led into the narrowing gap between adjacent particles. An alternative hypothesis is that the particles will actually attract each other and move together in order to reduce the elastic strain energy. As similar effects have been seen in alloys with small lattice misfit (Ni–Cr–Al), this hypothesis seems not to provide a convincing explanation. In a number of alloys (e.g., carbides in steels, UAl_2 in α-U, θ in Al–Cu alloys) evidence has been presented suggesting substructure-enhanced diffusion, i.e., power laws during coarsening ($r^n \propto t$) where n is greater than 3. In none of these studies were attempts made to fit the results to one of the theoretically predicted relationships $r^n \propto t$ and no work seems to have been published which attempted to check if the details of the substructure-enhanced diffusion theories are correct. The general conclusion, though, is that the theories described seem successful in accounting qualitatively for the effect of lattice defects on coarsening.

4.2.2.1. Stability against coarsening. The general condition for Ostwald ripening to proceed is a decrease of the free energy. In the case of precipitates surrounded by an elastic strain field, the total energy (E) of an array of precipitates consists of the volume energy, the interfacial energy of the precipitates and the elastic energy of the strain fields. If the precipitate volume is constant, E depends only on the elastic energy and the interfacial energy. In the special case of two precipitates in a solid (volumes V_1 and V_2), the interfacial energy (S) and elastic energy (T) scale as $(V_1^{2/3} + V_2^{2/3})$ and $(V_1 + V_2) + V_1 V_2 f/a^3$, respectively, where a is the separation of the two precipitates and f is a function that is unity for distant precipitates. If $T \gg S$, the total energy (for $V_1 + V_2 = \text{const.}$) has a minimum if $V_1 = V_2$. In other words, the strain energy stabilizes the two particles of the same size against coarsening into one large particle. Basically, the same arguments hold for infinite arrays of particles as was apparently first recognized by KHATCHATURYAN and SHATALOV [1969]. The general conditions for stability of precipitate arrays against coarsening were recently worked out by PERKOVIC *et al.* [1979], LARCHE and CAHN [1973], [1978] and JOHNSON and ALEXANDER [1986]. Stability was found to be promoted by low interfacial energies, large elastic misfits and large volume fractions of precipitates. The phenomenon of elastic stabilization may be significant for the design of high-temperature alloys. In fact, the growth rates observed experimentally for θ' precipitates in Al–Cu alloys (BOYD and NICHOLSON [1971]) seem to support this view. AUBAUER [1972] has attempted to account for certain fine dispersions being stable against coarsening in terms of the diffuseness of the interface between a precipitate and the surrounding matrix, as described by CAHN and HILLIARD [1958]. If one assumes that the diffuse rim surrounding a precipitate is independent of precipitate size, it can readily be seen that the fraction of material that is in the precipitate and not in the rim will increase as the size increases. The bulk of the precipitate has a different structure and therefore a different atomic volume from the matrix while in the interface rim zone it is assumed that the structure changes steadily towards that of the matrix. Consequently, the precipitate and the rim zone are associated with an elastic distortion. The energy associated with this distortion increases as the particle grows, whereas the energy associated with the diffuse interfaces decreases as the total surface area is reduced during coarsening. If the surface energy is sufficiently small and if there is a finite rim thickness and appreciable strain energy, a minimum exists in the total energy, stabilizing the corresponding particle size. This conclusion was questioned because of the treatment of the strain energy used (DE FONTAINE [1973]) and because the precipitates, even if stabilized against growth, should be unstable against a change in shape, for example towards a disk (MORRALL and LOUAT [1974]). On the other hand, the Aubauer model seems to account successfully for several reported cases (GAUDIG and WARLIMONT [1969], WARLIMONT and THOMAS [1970]) where very fine dispersions of coherent ordered particles were seen to resist coarsening. The stability against coarsening ot two misfitting particles subjected to an applied tensile stress was examined by JOHNSON [1984] using a bifurcation approach. The stability of precipitates subjected to an applied stress may be enhanced or diminished depending on the relative orientation of the precipitates and the magnitude of the applied stress. The results obtained for cube-shaped particles are qualitatively different from those for spheres at short distances of separation.

References: p. 935.

The effects of the applied stress are manifested only in elastically inhomogeneous systems and are sensitive to the precipitate morphology. The theory predicts that precipitates may be stable up to a level of applied stress (threshold stress) sufficient to induce morphology changes.

4.2.2.2. Technological applications of coarsening theory. In all types of coarsening, the rate of the process is proportional to the interfacial energy (σ) driving the process and the solubility C_α of the solute atoms. Furthermore for all situations, except the relatively rare interface-controlled one, the coarsening rate also scales with the diffusion coefficient (D). Hence, alloys for high-temperature application, where low coarsening rates are desirable, may be obtained if σ, C_α or D are small. This expectation is borne out by various classes of high-temperature materials.

Nickel-based superalloys containin coherent ordered γ' precipitates (Ni_3Al structure) in a disordered γ-matrix (Ni–Al solid solution) have exceptionally *low interfacial energies* of the order of 10^{-2} J/m^2. In other words, the driving force for the coarsening of the γ' precipitates during creep is minimized. Alloys of this type retain their mircrostructure during creep. If the microstructure of such an alloy is tuned to a maximum creep lifetime, the microstructure changes little during creep loading. This is not so if the lattice misfit between γ and γ' is significant. The lattice misfit enhances the driving force for γ' coarsening, which changes the microstructure of the alloy in the coarse of a creep experiment. Hence, the microstructure tuned to maximimum creep life disappears during creep, and reduces the lifetime relative to an alloy with zero misfit. This difference is borne out by the observations. In fact, owing to the different solubilities of most elements in the γ and γ' phases, the γ/γ' misfit can be tailored to zero by the addition of solute elements to equalize the lattice constants of the two phases (e.g., Cr).

Low solubility can easily be achieved by using precipitate phases with high energies of formation and with a type of chemical bonding that differs from the surrounding matrix. The best-known examples are low-solubility oxide-dispersed phases, e.g., Al_2O_3 in Al. Except for very special cases, such phases cannot be precipitated from a supersaturated solid solution. Therefore, other techniques, such as powder metallurgy, internal oxidation or implantation are commonly applied. If the atomic radius of the solute atoms differs strongly from the atomic size of the matrix material, the two metals normally show negligible solubility in the solid state. Alloys of this type (e.g., W–Na, Al–Fe) have also been used to obtain coarsening-resisting materials.

Low diffusion coefficients have been applied in several ferrous alloys to resist coarsening. For example, the addition of a third component which segregates preferentially to the carbide phase (e.g., Cr, Mo, W) can slow down the coarsening of carbides considerably as it requires diffusion of both carbon and the third element and the latter, being substitutional, diffuses much more slowly than the carbon.

4.2.3. Microstructural changes in polyphase materials with a duplex structure, stimulated by interfacial energy

A *duplex structure* (SMITH [1954]) is an oriented crystallographic unit consisting of two phases with a definite orientation relationship to each other. Technologically and scientifically, the most important group of duplex structures are rod- or plate-shaped

duplex structures, such as directionally solidified eutectics (for a review, see LIVINGSTON [1971]). As the growth of large lamellae at the expense of smaller ones is associated with a decrease in the surface-to-volume ratio, lamellar structures are expected to coarsen. In the absence of substructural effects this process is expected to occur by motion of lamellar terminations.

Two mechanisms have been put forward for this process. CLINE [1971] and GRAHAM and KRAFT [1966] proposed the curvature at the lamellar termination (fault) to be associated with a flux of atoms from the α phase to the β phase (fig. 16). The second mechanism of lamellar coarsening involves the diffusion of solute atoms from the finely spaced (λ_1) lamellae along a migrating boundary to the widely spaced (λ_2) lamellae on the other side of the interface (fig. 17). The theoretical analysis of the process (LIVINGSTON and CAHN [1974]) relates the boundary migration rate (V) to the spacing λ_2 of the widely spaced lamellae. The coarsening rate increases with increasing temperature and decreasing spacing of the lamellae as both effects reduce the diffusion times required. As short-circuit diffusion along grain boundaries becomes dominant at lower temperatures, coarsening by boundary migration is expected to become more prominent than coarsening by fault migration with decreasing temperatures as was observed experimentally. In comparison to coarsening by fault recession (fig. 16), coarsening by boundary migration becomes more important at finer spacings of the lamellae. Rod-shaped microstructures

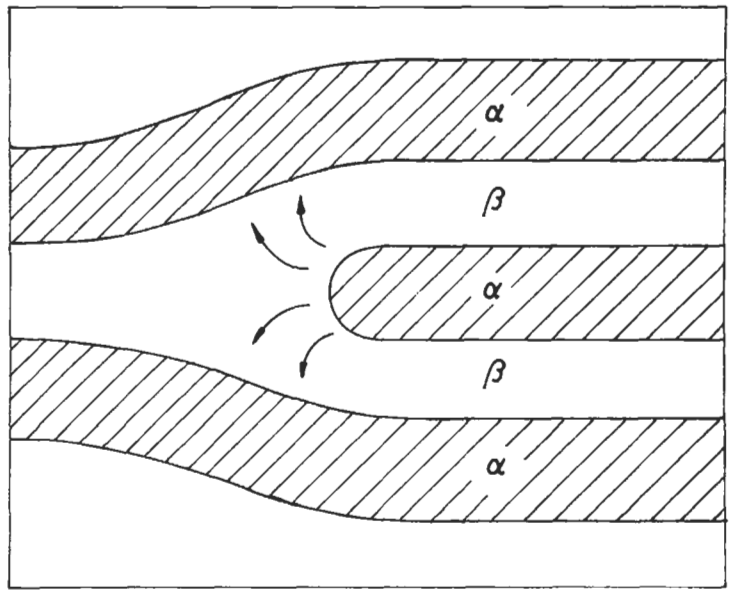

Fig. 16. Schematic of mass flux in the vicinity of a lamellar termination (fault). The curvature at the termination is proposed to induce mass flow of A atoms (from the α-phase) to the β matrix, leading to a recession of the termination with a corresponding increase in the thickness of the adjacent lamellae. (From CLINE [1971].)

References: p. 935.

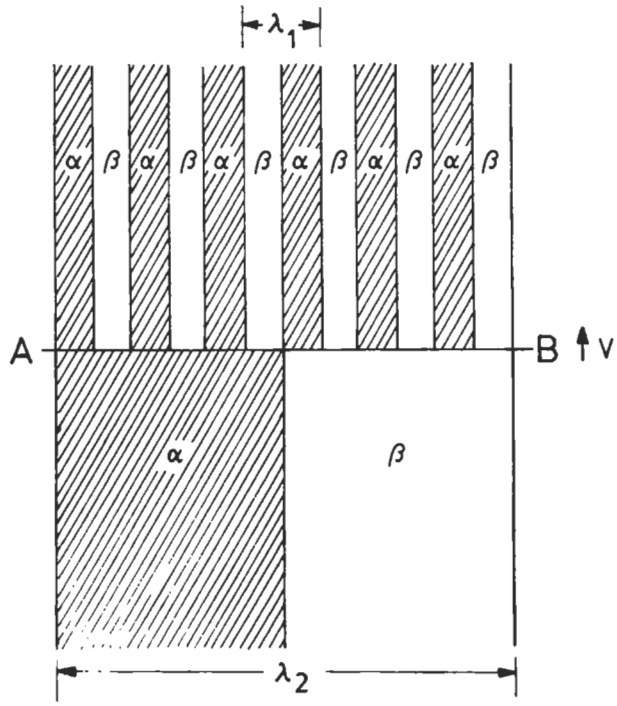

Fig. 17. Idealized model of discontinuous coarsening process. The grain boundary AB moves at a velocity V, consuming fine lamellae with spacing λ_1 and generating coarse lamellae with spacing λ_2. (From LIVINGSTON and CAHN [1974].)

are unstable with respect to shape and dimensional changes as they may decrease the surface-to-volume ratio by these processes. As was pointed out by CLINE [1971] and ARDELL [1972], the processes involved in dimensional changes are identical to Ostwald ripening (§ 4.2.2). In alloys produced by eutectic growth, the microstructure may be initially stabilized by the very uniform rod diameter. The time required for the steady state distribution of rod diameters to be built up during coarsening may be longer than for normal precipitate coarsening where a whole spectrum of particle sizes is present at the very beginning. In the present paragraph, attention will be focused on shape changes due to the coarsening of rod-shaped microstructures. The growth of a shape perturbation on a cylinder was already analyzed a century ago by RAYLEIGH [1878]. However, it is only relatively recently that quantitative models for the spheroidization of cylindrical precipitates have been put forward (CLINE [1971], HO and WEATHERLY [1975], NICHOLS [1976]). The theoretical treatments indicate (fig. 18) that a long fibre (length l) of radius d (with $l/d > 7.2$) is eventually replaced by a string of spheres (*Rayleigh instability*) where the sphere radii and spacing, λ, depend on the active kinetic processes. When the aspect ratio (l/d) is less than 7.2, shape relaxation to a single sphere is predicted. For infinite fibres, Rayleigh instabilities are predicted to dominate, whereas in the case of

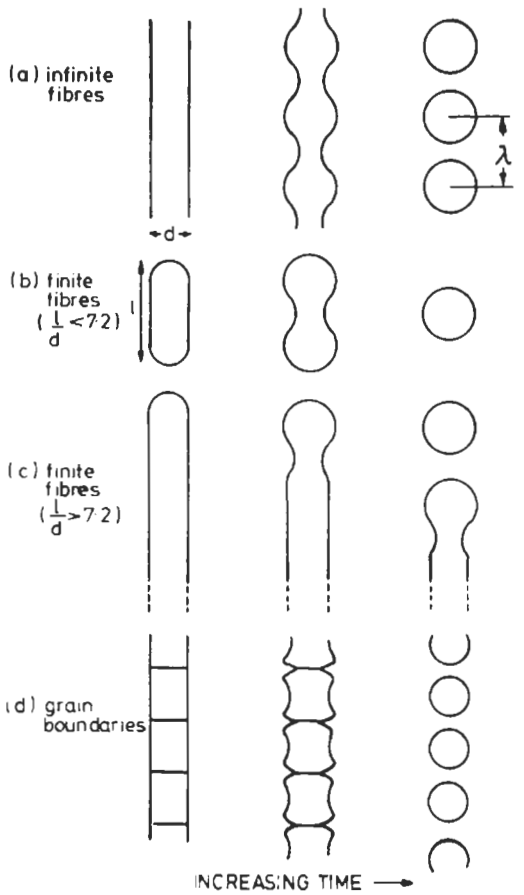

Fig. 18. Schematic representation of different modes of spheroidization of cylindrical inclusions. (From McLean [1978].)

fibres with finite length, drop detachment at the end of the fibres (fig. 18c) should be the faster process. Experimental observation for metallic (W–Na, Al–Pb, fig. 19) and nonmetallic systems ($NaNO_3$–H_2O, Ni–Al_2O_3) seem to support the view that progressive spheroidization from the ends of the fibres dominates. Yet another mechanism of spheroidization, which applies to both fibrous and lamellar inclusions, exists when grain boundaries in either phase intersect phase boundaries between the fibres and the matrix. At the points of intersection, grooves develop and progressively deepen with time to establish a local equilibrium configuration. Eventually, the grooves cause a division of one phase and result in spheroidization (fig. 18d). This process seems to be a serious limitation to many directionally solidified eutectic materials for high temperature operation. In addition to the instabilities mentioned so far, rod phases may also coarsen by *fault migration*. Faults are points of a rod at which additional rods form by branching

References: p. 935.

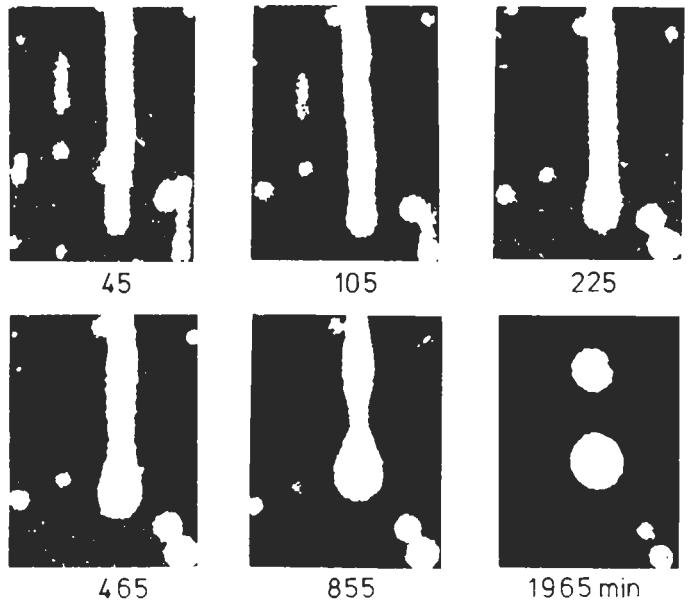

Fig. 19. Series of microradiographs showing the change in shape of Pb inclusions in Al as a function of annealing time at 620°C. (From McLean [1973].)

or at which a rod terminates. The termination of a rod is expected to shrink backward for the same reasons as apply to the shrinkage of a terminating lamella (cf. fig. 16). Because of the negative radius of curvature at the rod-matrix interface at a branching point, the branches are expected to fill in, i.e., to migrate in the growth direction, as was observed. Theories of the kinetics of fault migration have been presented by Cline [1971] and by Weatherly and Nakagawa [1971].

Instabilities were reported at the periphery of spherical cavities growing under stress along interfaces. If the stress was sufficiently large (Wingrove and Taplin [1969]), finger-shaped instabilities were seen to develop. The critical parameter for the development of these instabilities instead of spherical growth seems to be the ratio of the diffusion coefficients at the cavity surface and a boundary supplying the vacancies (Beeré [1978]). Instabilities cannot develop if this ratio is large (typically > 100). For materials with slower surface diffusion, cavities above a critical size become unstable. The critical size depends on the applied stress and the cavity spacing.

4.2.4. Coarsening by Brownian motion

The spontaneous random motion of gas-filled cavities, leading to a coarsening process by cavity coalescence when two cavities meet, has been deduced both by direct observation, and indirectly. The first observations were apparently made on UO_2 plates irradiated with neutrons to produce fission fraqments (krypton, xenon) which precipitated in the form of gas-filled cavities (Gulden [1969]). These cavities were seen in the

electron microscope to show Brownian motion, the rate of which was controlled by volume diffusion in the host crystal for cavities above 3.7 nm diameter. Similar observations were made for helium-filled cavities in gold and copper, krypton in platinum and xenon in aluminum (cf. GEGUZIN and KRIVOGLAZ [1973]) and helium bubbles in vanadium (TYLER and GOODHEW [1980]).

4.2.5. Microstructural changes stimulated by interfacial energy in the presence of external potential fields

The presence of a field of varying potential (e.g., due to a stress- or a temperature gradient, or due to electric or gravitational fields) modifies the driving forces for diffusion and, thus, may result in microstructural changes.

4.2.5.1. Temperature gradients. The theory of diffusional migration was first developed for volume diffusion in a temperature gradient. In the subsequent decade this work was extended by several authors to surface-diffusion controlled processes and other fields, such as electric, magnetic, stress or gravitational field gradients. For a review of this development, we refer to the book by GEGUZIN and KRIVOGLAZ [1973].

The dominant physical reason for an inclusion to migrate in a temperature gradient is the temperature-dependence of the solubility. For example, let us consider a liquid inclusion in a solid. We assume that at the "front" side of the inclusion (where the temperature is highest), the liquid in contact with the solid has a lower solute content than at the (colder) "rear" surface. The different solute content results in a concentration gradient and, hence, in a flux of solute atoms from the rear to the "front" surface, which causes the "front" surface to melt or dissolve and the "rear" surface to freeze or migrate by crystal growth from solution. In addition to the atom flux resulting from this process, causing the inclusion to migrate up the temperature gradient, there is also a drag exerted on the atoms by a directional flux of phonons (phonon wind) which results from the temperature gradient. Similarly, in metals with aspherical Fermi surfaces, the diffusing atoms are dragged by an electron wind which appears under these circumstances in a temperature gradient. In the simplest case of a spherical inclusion in a temperature gradient, the velocity (v) of the inclusion of size R is found to depend linearly on the temperature gradient (grad T). The velocity v is proportional to (grad T)$\cdot R^n$, with $n=0$, 1, -1 if the rate-controlling process is diffusion through the matrix, the particle-matrix boundary or the particle, respectively. As all parts of the inclusion move with the same velocity, there is no shape change during migration.

All of these results assume the matrix-particle interface to act as ideal sink and source for vacancies. If this is not so, the velocity is smaller or the inclusion is not mobile at all. The first experimental investigations on the motion of inclusions in a temperature gradient were apparently carried on the motion of aqueous solution droplets in sodium nitrate (LEMMLEIN [1952]), although the motion of brine inclusions in a temperature gradient was already invoked by WHITMAN [1926] to explain the fact that polar ice becomes purer at its cold upper surface. The motion of gaseous and liquid droplets in a solid in a temperature gradient has been studied in a variety of metallic and nonmetallic systems (e.g., He in Cu, Kr in UO_2, W in Cu, water in $NaNO_2$, water in KCL, water in NaCl, Li in LiF, NH_4Cl bubbles in NH_4Cl, gas-filled bubbles in KBr, NaCl, KCl, Pb in

References: p. 935.

Al; for a review we refer to the book by GEGUZIN and KRIVOGLAZ [1973]). The observed migration velocities as well as the correlation between the velocity and the inclusion size was in all cases well accounted for by the theoretical prediction.

Above a certain temperature gradient, the migrating droplets (e.g., voids or gas bubbles in nuclear fuel elements, metal droplets in semiconductors or water droplets in ionic crystals) start to break down by the growth of protrusions from the rear corner, releasing a thin trailing liquid veil. The physical reason for the breakdown is the difference between the thermal gradient at the edges and in the center of the droplets, resulting in different migration rates of the two regions. An additional factor comes in when the inclusion contains two phases, such as liquid and vapor. The additional factor is the change of the interfacial free energy with temperature, and it may cause the inclusion to migrate down the temperature gradient (ANTHONY and CLINE [1973]). Consider a spherical gas-filled inclusion in potassium chloride subjected to a temperature gradient. The wall of this gas-filled inclusion is assumed to be covered by a liquid film or brine. In addition to the normal diffusive flux from the hot to the cold surface, there is a flow of liquid in the liquid film caused by the fall in the liquid-vapor interfacial energy as the temperature falls. The interfacial-energy-induced flow in the liquid film is the essential step in the movement of the inclusion, as it carries potassium chloride that will be deposited at the hot side of the inclusion so that the inclusion moves to the cold end of the crystal. An analysis based on this model successfully predicted the observed velocities of two-phase inclusions in potassium chloride.

Probably the technologically most important observations are those of thermal migration of nuclear fuels through protective coatings in the temperature gradients associated with nuclear reactors (MCLEAN [1982]). In recent years, thermal migration effects led to some concern over the microstructural stability of high-temperature alloys; in particular, in-situ composite materials, exposed to high-temperature gradients, in turbine blades. Investigations on the thermal stability of eutectic composites (Ni-, Al-, Pb-base alloys) provide evidence for thermal instabilities under the conditions used in modern aircraft engines (HOUGHTON and JONES [1978]). The other problem of considerable practical relevance is the effect of temperature gradients on Ostwald ripening. The available evidence is controversial, indicating — often for the same system — that thermal gradients may increase, not affect or decrease the rate of Ostwald ripening (e.g., DAVIS *et al.* [1980b], and JONES and MAY [1975]). This controversy may be due to different rate-controlling processes in the various experiments. Ostwald ripening is enhanced if adjacent migrating particles collide and join up (JONES and MAY [1975]) or because the back and front of an inclusion migrate with different velocities owing to the different temperatures at those sites (MCLEAN [1978]). However, temperature gradients can also decrease Ostwald ripening owing to the generation of a shape instability, as was discussed previously (veil formation). (See als 'thermomigration', ch. 7, § 6).

4.2.5.2. Temperature cycling. This may affect the microstructure of alloys by three effects (MCLEAN [1982]):

(i) a variation of the solubility of the phases;
(ii) a differential thermal expansion leading to local strain gradients;
(iii) capillary terms arising from the Gibbs–Thompson effect.

In most alloys, the first effect seems to dominate and may result in accelerated Ostwald ripening or morphological changes, as was observed in composites that were remarkably stable under isothermal conditions (COOPER and BILLINGHAM [1980]).

4.2.5.3. Magnetic fields. The energy of a magnetic phase is altered by the presence of a magnetic field, and hence the microstructure of alloys that are magnetic will be changed by the application of a magnetic field. This subject has been extensively reviewed by CULLITY [1972]. Magnetic fields may affect both the atomic order in stable solid solutions and the precipitation from supersaturated solid solutions. In stable solid solutions, magnetic fields generate *directional order* by altering the proportion of like pairs that are aligned in the field direction. Such an alignment causes no change from the random situation in terms of the total fractions of like and unlike nearest-neighbor pairs.

During precipitation from solid solutions, magnetic fields favor the formation of those precipitates that are aligned with respect to the external field. The best known example is the preferred formation of magnetic rods aligned parallel to the magnetic field in Alnico alloys. A preferred orientation of precipitates may also be achieved during coarsening in the presence of a magnetic field. For example, if Fe_8N precipitates coarsened in a magnetic field, a complete orientation of the disc-shaped particles normal to the field direction was achieved (NEUHAUSER and PITSCH [1971]). Owing to the smaller demagnetization factor, the spins of the precipitates parallel to the magnetic field (H) become aligned so that a single-domain structure is formed. This domain structure increases the energy of the Fe_8N/Fe interphase boundary. Hence, precipitates oriented normal to H have the lowest free energy and, thus, grow at the expense of the other precipitates.

In materials of anisotropic magnetic susceptibility, external magnetic fields induce phase or grain-boundary migration. The first observation on this effect, was reported in the classical paper by MULLINS [1956] on boundary migration in diamagnetic bismuth. Magnetic annealing has recently been applied to ceramic superconductors (DE RANGO *et al.* [1991]). The objective was to align the crystallites in polycrystalline YBa_2Cu_3O8. Alignment of the crystallites (by other methods) has been shown previously to increase the maximum critical current density of these materials. In fact, magnetic annealing may prove to be applicable to all paramagnetic, diamagnetic or ferromagnetic materials provided the driving force due to the aligning field is large compared to the thermal fluctuation at the annealing temperature. Naturally, the same should apply to electrically polarizable materials (e.g., ferroelectrics) when annealed in an electric field.

4.2.5.4. Stress field. By analogy with magnetic fields, external stresses can modify the atomic order in stable solid solutions and the precipitate morphology in two-phase alloys. Directional atomic order has been induced in Fe–Al alloys by stress-annealing (BIRKENBEIL and CAHN [1962]).

In two-phase materials, external stresses may result in the alignment of precipitates and/or in shape changes. Several examples for the first effect have been reported: Fe_8N in FeN, Au in Fe–Mo–Au, θ and θ' in Al–Cu, $ZrH_{1.5}$ in Zr–H, Ti-hydride in Ti-H, γ' in Ni–Al alloys (MIGAZAKI *et al.* [1979]). Apparently, only a few observations of stress-induced shape changes have been published (MIGAZAKI *et al.* [1979], TIEN and COPLEY [1971]). Owing to the elastic anisotropy of the matrix and the precipitate, the free energy

References: p. 935.

of a precipitate depends on the precipitate orientation and shape. The theoretical treatment of both effects (GEGUZIN and KRIVOGLAZ [1973], SAUTHOFF [1976] and WERT [1976]) seem to be consistent with the experimental observations. Similar effects have been observed in alloys undergoing an order-disorder or a martensitic transformation. When a CuAu single crystal is ordered, it becomes subdivided into many domains, the tetragonal (c) axes of which are parallel to any of the three original cubic axes. In the bulk material and without an external stress field, the three possible cdirections are randomly distributed among the domains. The application of a compressive stress during ordering imposes a bias on the distribution of the c-axes such that the cube axis nearest to the compression axis becomes the preferred direction for the c-axes of ordered domains (HIRABAYASHI [1959] and ARUNACHALAM and CAHN [1970]).

The microstructure of materials undergoing martensitic transformations (cf. ch. 16) depends on external stress fields. The following two factors contributing to this effect are most important (DELAEY and WARLIMONT [1975]): (i) The orientation variant on whose macroscopic shear system the maximal resolved applied shear stress is acting will grow preferentially, (ii) near certain symmetric orientations, individual plates and self-accommodating groups will compete. Essentially, the same arguments apply to the microstructure of materials undergoing mechanical twinning. Effects of this type play an important role in shape-memory effects.

Gas bubbles situated at interfaces represent a special case of microstructural changes caused by stress fields. Owing to the compressibility of gas bubbles, the binding energy between a bubble and the interface depends on external stresses. Compression stresses lead to a decrease of the binding energy and, hence, may result in microstructural changes resulting from break-away effects of the boundaries from the bubbles (GREENWOOD *et al.* [1975]).

4.2.5.5. Electric fields. In bulk metals, strong electric fields may induce complex interactions between thermomigration and electromigration due to Joule heating (ch. 7). In thin films, efficient heat removal ensures reasonable isothermal conditions. Under these conditions, two effects resulting from the presence of electric fields were observed: (i) enhanced grain-boundary migration (LORMAND *et al.* [1974] and HAESSNER *et al.* [1974] and (ii) the growth of grain-boundary grooves which can eventually penetrate the film so that nucleation and growth of voids by grain-boundary diffusion occurs (HO and KIRKWOOD [1974]). The theoretical understanding of the processes involved is still poorly developed. In fact, the driving force exerted by a dc current on grain boundaries in gold was found to be several orders of magnitude larger than the theoretically estimated value (HAESSNER *et al.* [1974]). A similar result was also found from the motion of rod-shaped tungsten inclusions in Cu and from the displacement of deep scratches on the surface of Ag owing to the passage of a current along wire-shaped samples. (See also 'electromigration, ch. 7, § 6).

4.3. Deformation

All forms of plastic deformation may result in irnportant changes of the microstructure of materials with respect to the distribution and density of defects as well

as with regard to the morphology, volume fraction and sometimes also structure of second phases. They are discussed in chs. 19–26.

4.4. Multiphase microstructures generated by migrating lattice defects

4.4.1. Moving grain boundaries

If grain boundaries are forced (e.g., during recrystallization or grain growth) to sweep through a precipitate dispersion or a duplex structure, the following microstructures may result (DOHERTY [1982], HORNBOGEN and KÖSTER [1982]):

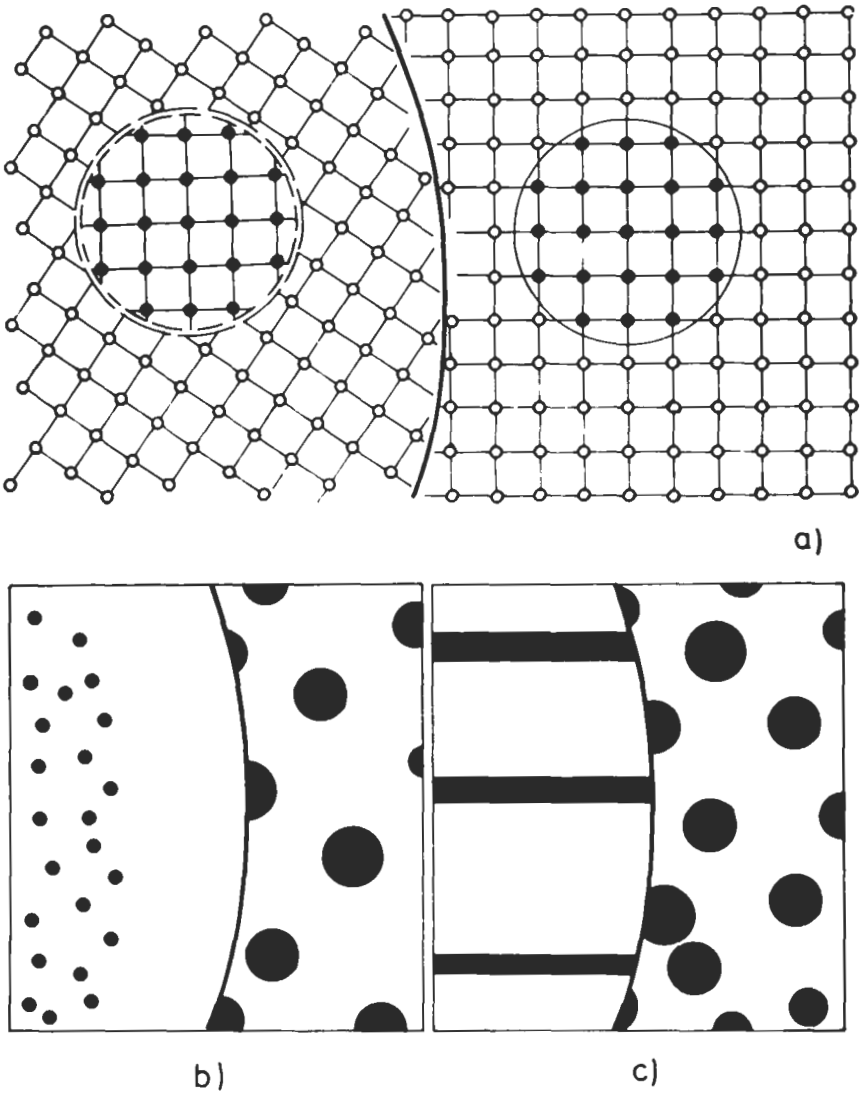

References: p. 935.

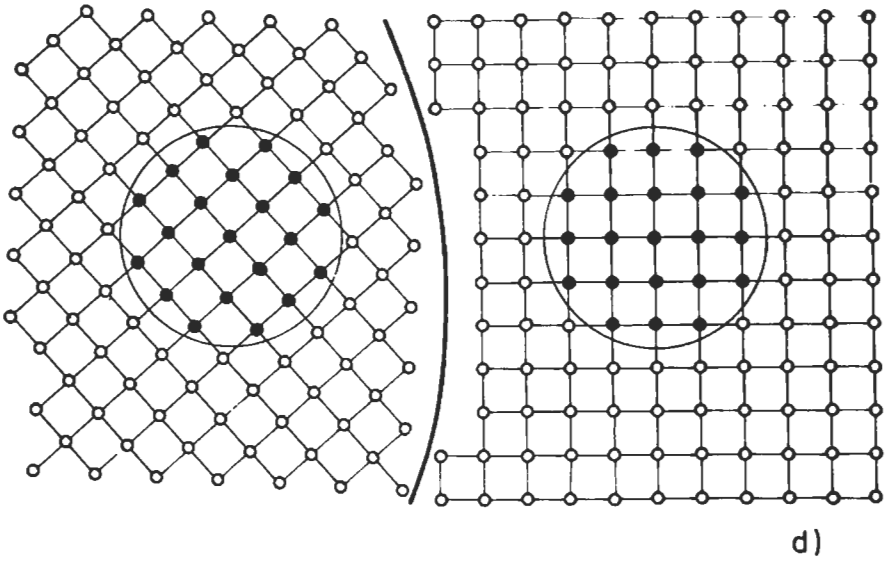

Fig. 20. Microstructural changes induced by a grain boundary migrating through a two-phase alloy containing dispersed precipitates: (a) transformation of coherent precipitates into incoherent ones as the boundary bypasses the precipitates; (b, c) dissolution of the precipitates, resulting a supersaturated solid solution, followed by continuous (b) and discontinuous (c) precipitation; (d) grain boundary passing through the precipitates without affecting the shape and size. The solid (open) circles in figs. 22a and 22d indicate solute (solvent) atoms.

(i) The boundary bypasses the precipitates which, therefore, retain their initial orientation and become incoherent (fig. 20a). Owing to the Gibbs–Thompson effect, the solubility of the precipitates rises so tfiat the smaller precipitates may dissolve, as was observed, for example, in the case of NbC in γ-Fe.

(ii) The coherent precipitates or the components of a duplex structure dissolve after contact with the moving grain boundary, so that a supersaturated solid solution is obtained. From this supersaturated solid solution, the solvent may reprecipitate either continuously (fig. 20b) or discontinuously (fig. 20c). Both cases have been observed experimentally. The dissolution as well as the precipitation processes seem to occur far more rapidly than anticipated, suggesting strongly enhanced diffusion in the migrating interfaces an in the lattice behind due to vacancy supersaturation (SMIDODA *et al.* [1978], GOTTSCHALK *et al.* [1980]).

(iii) The grain boundaries can pass through the coherent precipitates and, thereby, preserve the preexisting microstructure (fig. 20d). This precess seems rare as it requires the formation of new precipitates to match the rate of boundary migration.

(iv) The grain boundary is held by the coherent precipitates which then coarsen. This process occurs if the driving force for boundary migration is not sufficient to initiate one of the above processes.

(v) The moving grain boundary drags the precipitates (SMITH [1948]), as was reported for a variety of alloy systems containing gaseous particles as well as solid inclusions, for

example, for He in Cu, He in U, air in camphor, carbides in various metal transition alloys, GeO_2 in Cu, B_2O_3 in Cu, SiO_2 in Cu, Ag in W, Ag in Sn, Al_2O_3 in Ni, Al_2O_3 in Ag. The experimental results have been reviewed by GEGUZIN and KRIVOGLAZ [1973] and GLEITER and CHALMERS [1972]. *Particle drag* results from the directional movement of atoms from one ("front") side of the inclusion to the other ("rear") side. Hence, diffusional migration may occur by diffusion of atoms around or through the inclusion and diffusion of atoms along the particle-matrix interface. The kinetics of the particle drag may be controlled by the rate of one of these diffusion processes or by interfacial reaction at the boundary between the inclusion and the matrix. Examples of all cases mentioned have been reported and may be found in one of the reviews mentioned. Once particle drag starts, the boundary collects practically all particles in the volume which is swept. Particles collected in the boundary usually coarsen rapidly. Therefore, particle drag may result in the following changes of the properties of the boundary: (i) boundary brittleness and/or corrosivity due to a high density of undeformable particles, the electrochemical properties of which differ from the surrounding matrix; (ii) different mechanical and chemical properties in the particle-free zone and in the rest of the material. At high driving forces (e.g., during recrystallization) particle drag seems negligible as it is possible for the mobile boundary to migrate past the inclusions. (See also ch. 28, § 3.8).

4.4.2. Moving dislocations

The formation of colonies of precipitates in the vicinity of dislocations has been observed in a number of alloy systems, e.g., in iron, nickel, copper, aluminum and semiconductor materials.

In the initial model of this process (SILCOCK and TUNSTALL [1964]) and in the subsequent modification by NES [1974], a dislocation was proposed to climb so that precipitates can nucleate repeatedly in the moving stress field of the dislocation. During climb the dislocation emits vacancies. The incorporation of these emitted vacancies in the lattice of the precipitates is believed to reduce the precipitate-matrix mismatch energy if the precipitating phase has a larger atomic volume than the surrounding matrix. In the opposite case, a vacancy flux from the precipitate to the dislocation was also invoked (GUYOT and WINTENBERGER [1974]).

More recently, the experimentally observed coupling between dislocation climb and precipitate formation was re-interpreted by two other models. Dislocations were proposed to climb owing to the annihilation of quenched-in vacancies, while the precipitates form simultaneously by heterogeneous nucleation in the stress field of the moving dislocation. A study by transmission electron microscopy (WIRTH and GLEITER [1981a,b]) led to the conclusion that coherency strain relaxation by incorporation of vacancies in the precipitates may be only one of the processes involved. In fact, colony formation was found to occur (fig. 21a) by the climb of a prismatic dislocation loop which emits vacancies and, thus, generates a region of enhanced diffusivity. The excess solute atoms of this region of enhanced diffusivity migrate rapidly to the climbing dislocation and precipitate in the form of a chain of small particles (fig. 21b). Owing to their large surface-to-volume ratio, these fine particles rapidly coarsen by Ostwald ripening to form rows (colonies) of coarse precipitates behind the climbing dislocation loop. The spacing of the rows of coarse precipitates is

References: p. 935.

controlled by the balance between the interfacial energy and the diffusion path. Under steady-state conditions, such systems are known to approach a constant precipitate spacing. Hence, if the dislocation loop expands during growth, a constant precipitate spacing can only be maintained by increasing the number of precipitates as the loop radius increases. This condition results in a spoke-like precipitate arrangement, as was observed (fig. 21).

4.5. Periodic microstructures in open, dissipative systems ("self-organization")

Dissipative processes in open systems are frequently associated with pattern formation (NICOLIS and PRIGOGINE [1977], HAKEN [1978], MARTIN and KUBIN [1988]). The following microstructures seem to be the result of pattern formation in dissipative systems ("self-organization"):

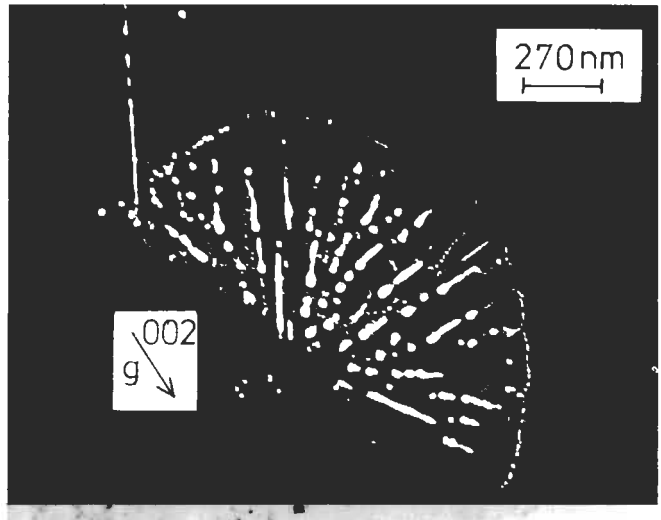

(a)

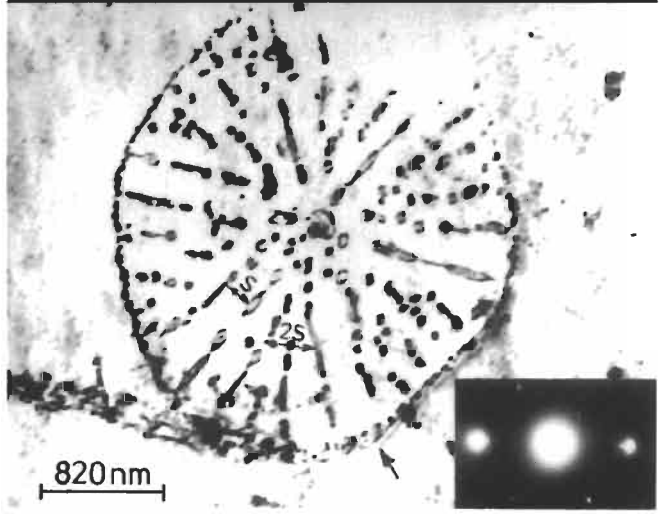

(b)

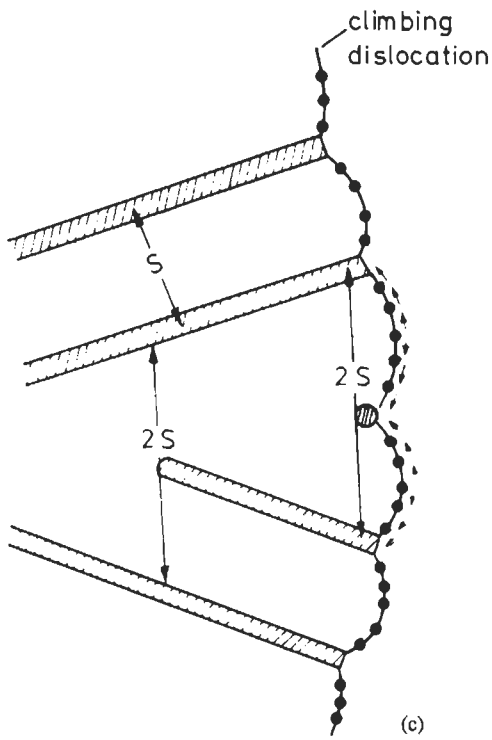

Fig. 21. (a) Bright-field and dark-field electron micrographs of colonies of silver precipitates in a Cu-5 wt% Ag alloy. The colonies formed behind the dislocation loops surrounding them. The loops expandes during colony growth. Two types of precipitates may be noticed. A chain of small precipitates along the dislocation loop, and large precipitates arranged radially in a spoke-like fashion. (b) Schematic model for colony formation by a two-step process involving the nucleation of a chain of small precipitates along the climbing dislocation followed by coarsening into large precipitates with a spacing S. (After WIRTH and GLEITER [1981a, b].)

a) precipitate lattices;
b) void lattices;
c) dislocation-loop lattices;
d) dislocation lattices*;
e) point-defect lattices, flux-line and magnetic-bubble lattices;
f) long-period antiphase boundary structures;
g) domain boundaries in ferromagnetic and ferroelectric materials**.

* For sub-boundaries see § 2.2.5, for periodic structures during fatigue see ch. 27.
** The arrangement of domain boundaries in ferromagnetic materials is discussed in ch. 29.

4.5.1. Periodic structures due to long-range interaction forces

4.5.1.1. Precipitate lattices. Several studies by means of X-ray diffraction and electron microscopy have revealed the existence of periodically arranged precipitates (fig. 22a) in alloys of Cu–Ni–Co, Cu–Ni–Fe, nickel-base alloys containing γ' (Ni_3X) precipitates, Cu–Ti, Au–Pt, Au–Ni, Co–Fe, Co–Nb, Co–Ti, Al–Zn, Fe–Bi, Fe–Be, as well as in Alnico-Ticonel alloys. The models first proposed (ARDELL *et al.* [1966] and KHACHATURYAN [1969]) to account for the formation of periodic precipitate arrays were based on (long-range) elastic interaction forces between the precipitates, due to coherency strain between the precipitates and the surrounding matrix. Both the precipitates and the matrix were assumed to be elastically isotropic. JOHNSON and LEE [1979] refined these approaches by including the strain fields induced by neighboring inclusions and by considering second-order terms. Elastically strained particles of arbitrary shape but identical moduli in an anisotropic medium were also shown (KHACHATURYAN [1969], JOHNSON and LEE [1979] and MORI *et al.* [1978]) to form periodic arrays. The arrays correspond to one of the 14 Bravais lattices.

In the particular case of spherical inclusions in a cubic matrix with a negative anisotropy parameter, a simple cubic lattice of precipitates was found to form the minimum-energy arrangement which is stable with respect to externally induced fluctuations. Precipitates positioned along <100> directions of the matrix turned out to exhibit attractive interaction forces with a maximum value at 2–3 precipitate radii. This result may provide an explanation for the frequently observed alignment of precipitates along <100> directions. For <110> and <111> alignments, the interaction forces depend on the anisotropy factor of the matrix. <111> alignment in Mo is found to result in attractive forces, whereas the precipitates in the same arrangement in Cu and Ni repel. By applying these results to inclusions associated with a dipole-type strain field embedded in an iron lattice, a precipitate lattice with bcc structure was found to be stable. This arrangement corresponds approximately to the arrangement of N atoms in $Fe_{16}N_2$. So far, the discussion of precipitate lattices has been limited to systems in which the precipitation process occurs by nucleation and growth. In systems decomposing by a spinodal process, periodic arrangements of precipitates result from the time-dependent growth of concentration fluctuations. The processes involved and the factors governing the periodicity are discussed in ch. 15.

4.5.1.2. Void lattices. EVANS' [1971] report on the creation of a stable bcc array (superlattice) of voids in irradiated Mo stimulated numerous studies on void lattices in other systems. Void lattices have been seen, for example, in Ni, Al, stainless steel, Mg, Mo, Mo–Ti, Nb, V, W and NbO, BaF_2, SrF_2, CaF_2 (fig. 22b). Two kinds of models have been advanced to explain the formation of void lattices.

The observed symmetry of the void lattices has originally initiated an interpretation in terms of equilibrium thermodynamics assuming elastic interaction forces between the voids (STONEHAM [1971], TEWARY [1973], WILLIS [1975]). As these theories do not include the radiation damage explicitly, they cannot explain the observed influence of temperature and damage type. Moreover, this approach would not predict void lattice formation in isotropic crystals such as tungsten in contrast to the experimental observation.

The second type of theoretical approach to explain void lattices, dislocation pattern-

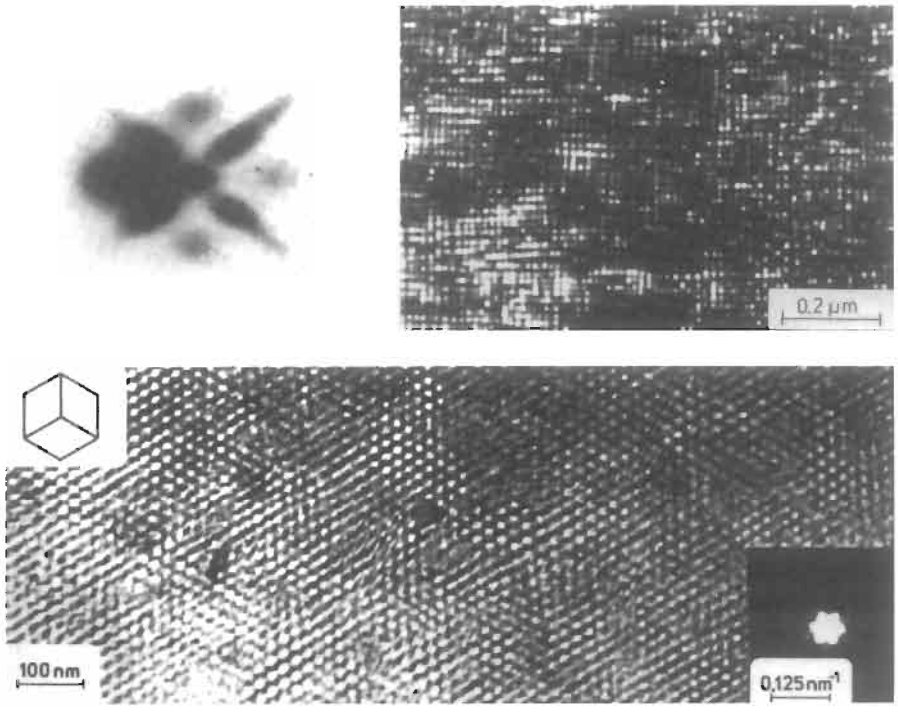

Fig. 22. (a) Dark-field electron microqraph and small-angle X-ray diffraction pattern of the precipitate lattice formed in an Fe–Be alloy (19.5 at% Be) after a 2 h anneal at 400°C. The specimen orientation is (100). (From TIAPKIN *et al.* [1976].) (b) Void lattice in < 111 > fluorite. The diffraction pattern shows superlattice reflections around the transmitted beam. The structure of the void lattice is indicated in the diagram. (From CHADDERTON *et al.* [1976].)

ing, etc., are based on the concept of synergetics. These models differ significantly concerning the basic processes involved. Some models consider only one type of point defects, e.g., vacancies (RYAZANOV and MAXIMOV [1981]). The experimental fact that the patterning saturates with increasing irradiation dose suggests, however, an additional destructive process to operate which removes point defects from the system. The most obvious destruction process is the point defect annihilation. For instance, self-interstitials may annihilate with vacancies in the materials forming vacancy type dislocation loops and voids. In the latter case, vacancy condensation and capture of vacancies and interstitials represent the constructive and destructive processes, respectively. The competition between such processes have been shown to induce pattern formation in irradiated systems (ABROMEIT [1989], TRINKHAUS *et al.* [1989], ABROMEIT and WOLLENBERGER [1988]). The void lattices are proposed to be the pattern formed in crystals during irradiation resulting in point-defect generation (cf. detailed account in ch. 18, § 4.6).

4.5.1.3. Dislocation-loop lattices. The first observation on the formation of dislocation loop lattices has apparently been made in neutron-irradiated copper. In

subsequent years, periodic arrays of dislocation loops have been detected in Al, Ni, U, BeO, Ti, Mg and Zr. In the case of Ni and Al, ordered clusters of loops were observed. Stereomicroscopy revealed that the clusters consisted of about six loops forming a fcc superlattice (STIEGLER and FARRELL [1974]). As the lattice regions between the clusters were found to be elastically strained, elastic interaction forces were proposed to be the dominant factor for the formation of the loop lattice.

Recent theoretical approaches to explain the formation of loop lattices are based on self organization principles. In fact, the dynamic models discussed in § 4.5.1.2 seem to apply to dislocation loop and void lattices as well.

4.5.1.4. Point-defect lattices. By analogy with the formation of void lattices, point defects may be expected to form ordered arrangements. This idea is indeed confirmed by recent studies on vacancy and interstitial lattices in certain alloys (cf. HIRAGA [1973] and JUNG and TRENZINGER [1974]). In alloy forming vacancy lattices, e.g., vanadium carbides of the V_6C_5 type, a variation in the alloy concentration between V_6C_5 and V_8C_7 did not result in an expansion (or contraction) of the spacing of the carbon vacancies, but rather caused the formation of a one-dimensional long-period superlattice structure consisting of enantiomorphic domains of the superstructure V_6C_5. For obvious reasons, the linear dimension of the enantiomorphic domains depends on the vacancy (carbon) content and increases with the increase in carbon vacancies. In vacancy lattices elastic interaction forces are believed to be the most important parameter. In pure metals, vacancy or interstitial lattices have not yet been revealed experimentally. However, calculations based on the vacancy–vacancy interaction potential showed that vacancy lattices may exist with a simple cubic structure aligned parallel to the identical axis of the host lattice (CHANG [1976]). The vacancy lattice constant was found to be about three times the lattice constant of the atomic lattice in the case of K and Na.

4.5.1.5. Long-period antiphase boundary structures. Ordered alloys, mostly of fcc structure in the disordered state, exhibit in the ordered state a regular three-dimensional array of antiphase boundary (APB) structures. Ordered structures of this type, which are called "long-period antiphase boundary structures", are treated in ch. 3, § 11.2. An excellent review dealing with various aspects of order/disorder phenomena in materials has been published recently (CAHN [1994]).

4.6. Microstructure in the vicinity of point defect sources and/or sinks

4.6.1. Enhanced precipitation and precipitate-free zones

The significance of point-defect sources/sinks for the precipitation of solute atoms from supersaturated solid solutions was first demonstrated by BARNES *et al.* [1958] for the *enhanced precipitation* of helium atoms in the vicinity of point-defect sources. Helium atoms were injected into metals (spectroscopically pure Cu and Be) by bombardment with alpha particles. On subsequent heating, the He atoms have a tendency to precipitate within the metal in the form of gas bubbles and, to acquire the extra space necessary for this, they capture vacancies. Thus a blanket of bubbles forms in the vicinity of a vacancy source. For low He contents and large grain sizes, grain boundaries as well as dislocations are the most important vacancy sources. For small grains, grain bound-

aries are the dominant suppliers. These results were confirmed later for a variety of other metals. *Precipitate-free zones* denuded of second-phase particles adjacent to grain boundaries in age-hardened alloys were originally attributed to the localized depletion of solute arising from preferential precipitation at the grain boundaries. However, it was soon recognized that local depletion of vacancies might be the more important factor, as a critical concentration of vacancies may be required for precipitate nucleation. In fact, this idea was discussed in terms of the thermodynamics of solute clustering (LORIMER and NICHOLSON [1969]) and in terms of the precipitation kinetics (PASHLEY *et al.* [1967]). Evidence for the local depletion of vacancies by annihilation at the boundaries was obtained from electron microprobe measurements and energy-analyzing electron microscopy for Al–Ag and Al–Zn–Mg alloys. The results of both investigations showed no solute depletion in the vicinity of the boundaries. In this simplified picture no coupling between vacancy flow and solid distribution is assumed. However, if a binding energy exists between solute atoms and vacancies, the vacancy flow from or to vacancy sources/sinks is necessarily coupled with a solute flow and thus produces a solute gradient in the vicinity of vacancy sources/sinks, such as grain boundaries, dislocations, pores, or free surfaces (JOHNSON and LAM [1976] and ANTHONY [1970]).

The solute segregation generated by vacancy flow involves two processes: the dragging of solute atoms by the moving vacancies and the reverse atom flow which is a consequence of vacancy flow. The first process dominates if the binding energy (E) between a vacancy and a solute atom is much greater than the thermal energy (kT). Under these circumstances, a solute atom is dragged to (from) the vacancy sink (source) so that solute enrichment (depletion) of the sink (source) regions will result. As a consequence, an enhanced density of precipitates forms in the vicinity of the sink. The opposite type of solute distribution may result in the second case ($E \ll kT$). For $E \ll kT$, solute atoms may be pumped in or out of the sink region depending on the relative diffusivity of solute and solvent atoms. When a vacancy flows into an enclosed sink region, an atom as a consequence must simultaneously flow out of this region. If the solute and solvent atoms in this region have identical mobilities, the ratio of solute to solvent atoms will remain the same as the original ratio. However, if the mobility of the solute atoms is greater than of the solvent atoms, proportionately more solute than solvent atoms will be moved out of the enclosed reqion by intruding vacancies, producing a solute-depleted sink zone. The solute depletion of the sink region will not continue indefinitely but will stop when the solute flow generated by the vacancy flux is balanced by the opposing solute flow produced by the solute gradient.

Two special *solute pumping* processes were proposed for *hydrogen* in stress gradients. The first mechanism (the Gorsky effect, for a review see VÖLKL [1972]) arises because hydrogen dissolved in a metal expands the crystal lattice for the host material. Hence, if a crystal contains a gradient in dilatation, the hydrogen concentration is enhanced in the dilatated region, e.g., in the vicinity of crack tips. The second effect (TILLER and SCHRIEFFER [1974]) is due to the redistribution of the free electrons in strain fields. Owing to this redistribution, dilatational centers (into which electrons flow) become cathodic. Hence, H^+ ions will migrate into the cathodic (dilatational) regions. Estimates for conditions typical for crack tips led to H^+ enhancements of up to ten orders of magnitude.

References: p. 935.

4.6.2. Irradiation-induced precipitation

In irradiated materials, a high supersaturation of vacancies and/or interstitials may be present. It follows from the previous section that the condensation of these point defects at suitable sinks (e.g., grain boundaries) may induce solute segregation in the vicinity of the sink. If this segregation is sufficiently strong, a local transgression of a phase boundary and, hence, irradiation-induced precipitation processes may be obtained, as has been reported for many alloy systems. For comprehensive reviews on this subject, we refer to conference proceedings (BLEIBERG and BENNET [1977] and POIRIER and DUPOUY [1979]), chs. 7 and 18.

4.6.3. Point-defect condensation

The significance of point-defect sources/sinks for the development of microstructures resulting from point-defect condensation was discovered by etch-pit studies. Etch pits were observed to form on electropolished surfaces of Al crystals during cooling from elevated temperatures. The formation of the pits was attributed to the condensation of vacancies at the surface. In polycrystalline specimens, pits were not observed in the vicinity of high-angle grain boundaries, suggesting that the vacancies in the pit-free region had been drained by the boundaries. In regions far away from the free surface, supersaturated point defects may condense in the form of dislocation loops, stacking-fault tetrahedra and/or voids which may be observed by transmission electron microscopy. The condensation process leads to a non-uniform microstructure in polycrystalline specimens in the sense that denuded zones exist near grain boundaries. As the condensation occurs by a nucleation and growth process, a certain supersaturation of point defects is required. Hence, the observation of *denuded zones* suggests a lower point-defect supersaturation in the vicinity of grain boundaries than in the perfect lattice, owing to the annihilation of point defects at the boundaries. With the exception of coherent twins and small-angle boundaries, the results suggest that high-angle grain boundaries are ideal vacancy sinks so that the width of the denuded zones is diffusion-controlled (for a review see GLEITER [1981a]).

4.7. Microstructure due to lattice defects formed by migrating grain boundaries

In recent years, it has become apparent that the microstructure of crystals growing by solid-state processes depends on the mode of crystal growth. The defect structures resulting from solid-state phase transformations and solid–liquid (glass) transformations, are discussed in chs. 15–19. In the present section, attention will be focussed on the microstructures developed due to the generation of vacancies, dislocations and twins by migrating grain boundaries. For a recent review of this field, we refer to the article by GLEITER [1981a].

Creation of vacancies. The creation of vacancies by migrating boundaries has been studied by means of the diffusion coefficient, the density, the electric resistivity and the morphology of the precipitates formed in the crystal region behind migrating boundaries (GORLIK *et al.* [1972] and GOTTSCHALK *et al.* [1980]). The observations reported suggest that behind a migrating grain boundary a high supersaturation of vacancies may exist. The high vacancy supersaturation observed was explained in terms of "growth accidents"

occurring during grain-boundary migration (GLEITER [1979]). A growth accident involves a jump of an atom of the growing crystal into the migrating boundary so that a vacant site is left behind in the lattice of the growing crystal. The excess vacancies retained in the lattice alter the properties of this crystal and exert a drag force on the migrating boundary ("vacancy drag", GLEITER [1979]) which may dominate impurity drag under certain conditions (ESTRIN and LÜCKE [1982]) (cf. also ch. 28, § 3.4.1).

Creation of dislocations. Indirect observations of dislocations created by migrating boundaries come from recrystallized materials. However, because of the high dislocation density ahead of the recrystallization front, the interpretation of these results is not unambiguous. A distinction between dislocations generated by the migrating interface and dislocations due to other processes is possible if the boundary migrates into a dislocation-free crystal or a crystal with low dislocation density. Studies of this type have been carried out in Cu, InP, InAs and Si (GLEITER *et al.* [1980]). The results obtained support the idea of dislocation generation by migrating boundaries. The generation process may be envisaged by growth accidents as well as the stress-induced dislocation emission (GASTALDI and JOURDAN [1979], GLEITER *et al.* [1980]).

Creation of two-dimensional lattice defects. The most prominent lattice defects generated during boundary migration (e.g., during grain growth) are *coherent twin boundaries* (cf. ch. 28, § 4.2). In order to explain the formation of twin boundaries during boundary migration, several models have been proposed. According to the *dissociation models* twins are formed by dissociating a grain boundary (A) into a twin boundary (T) and a new grain boundary (B). The *stimulation model* proposes that a twin boundary is created if a growing recrystallized grain meets a dislocation-bearing fragment which lies accurately in a twinned orientation to it. Since the fragment has discharged its dislocations, it is now stress-free and able to grow at the expense of the surrounding deformed matrix. The *coalescence model* proposes twin boundaries to be formed if the orientation relationship between the impinging grains corresponds exactly to a twin orientation. The *growth-accident hypothesis* of twin-boundary formations follows the concept that twins are formed and terminated by errors of the stacking of the <111> planes which happen in a random way. Studies by optical microscopy, thermo-ionic and photoemission microscopy, transmission electron microscopy, X-ray topography, grain-boundary migration experiments in bicrystals and polycrystals have been reported (for a review see GLEITER [1981a]). The results of these studies are inconsistent with the dissociation, the stimulation and the coalescence hypotheses. The observations so far available seem consistent only with the growth-accident hypothesis. In fact, in situ observations of twin formation in Al by X-ray topography agree with the evolution, shape and growth direction predicted by the growth-accident theory (GASTALDI and JOURDAN [1979]).

4.8. Microstructure of glasses

Historically, the observation and interpretation of microstructures have only dealt with crystalline materials. Indeed, until the late 1950s noncrystalline materials, e.g., oxide glasses, were regarded as free of all microstructure. This viewpoint was fostered in part by earlier triumphs of the random network theory of glass structure (ZACHARIASEN

[1932], WARREN [1937]) and was strengthened by the implicit glass engineering goal of this era: produce a homogeneous, single-phases product through fusion. As will be discussed below, this concept of a microstructure-free vitreous state has been seriously questioned in the last decade (ROY [1972]). This challenge has progressed sufficiently to occasion a rethinking of nearly all aspects of the fabrication and characterization of noncrystalline materials.

To a large extent this more modern concept of glass materials evolved from the discovery of the ability to induce, by appropriate thermal treatment, a clearly discernible and well-controlled microstructure in glasses. This microstructure is now recognized to be either crystalline or noncrystalline. Moreover, the occurrence of the noncrystalline variety is so ubiquitous that it has been suggested that its occurrence may be an intrinsic characteristic of all glass-forming melts (ROY [1972]).

4.8.1. Microstructure of amorphously phase-separated glasses

There are two ways of producing amorphously phase-separated glasses. First, one may simply prepare a glass-forming melt, quench it to room temperature and assess the extent to which the process has taken place.

A second and more controllable method involves the isothermal annealing of glass above its transformation temperature (ch. 7, § 9.1). One thus extends the amount of time available for the process to proceed. By intermittent examination of samples for telltale opalescence at various times and temperatures, it is possible to construct a time–temperature-transformation diagram. The microstructure developed in this process depends on the curvature of the free-energy vs. concentration curve. The loci of equilibrium compositions trace out the immiscibility gap. The loci of the inflection points delineate the region of spinodal decomposition. Between the equilibrium compositions and the inflection points, single, phase glasses transform into two-phase glasses by nucleation and growth. In this case, the microstructure is characterized by spherical glassy regions dispersed through a continuous glassy matrix of different chemical composition. If the decomposition is spinodal a microstructure characterized by a high interconnectivity of both glassy phases and irregularly shaped diffuse boundaries results.

Glass–glass phase transformations are, however, not limited to immiscibility effects. For example, it is known that the viscosity of liquid sulfur changes by a factor of two thousand when heated over the narrow temperature range 158–166°C (BACON and FANELLI [1943]). The low-temperature low-viscosity melt is thought to be constructed of 8-member rings, whereas the high-temperature high-viscosity melt is regarded as made up of long sulfur chains. Both liquids are in thermodynamic equilibrium (POWELL and EYRING [1943]). Evidence for a second-order phase transformation between the two liquid fields has been presented, leading to a microstructure of finely dispersed clusters with different molecular structure.

In addition to these considerations there is evidence for clustering effects in silicate glasses. Clusters have been defined as cooperative compositional fluctuations surrounded by melt of less organized structure (UBBELOHDE [1965]). These clusters are not necessarily equivalent to the crystalline nuclei. It has been suggested that such clusters could be "frozen in" during quenching of a glass-forming melt (MAURER [1956]).

4.8.2. Microstructure of partially crystallized glasses

Figure 23 summarizes the major reaction paths for crystallization of glasses and the resulting microstructures. Path (1) represents the direct transformation of a pure single-phase glass into a more stable crystalline phase. This transformation involves both the creation of stable nuclei and the subsequent growth of the crystalline phase.

In contrast to path (1), the development of an intermediate amorphous phase as in path (2, 3) and also for path (2, 4, 5) is well documented for a number of glassforming systems. A good representative of the former is the crystallization of Al_2O_3-SiO_2 glasses (MACDOWELL and BEALL [1969]). The latter path has been observed in classical glass ceramic compositions, e.g., Li_2O-SiO_2-Al_2O_3-TiO_2 (DOHERTY *et al.* [1967]). On cooling, glasses in this system show amorphous phase separation on a scale of about 5 nm. On reheating, this microstructure promotes formation of a nucleant phase, $Al_2Ti_2O_7$, which in turn crystallizes a major crystalline phase of this system, β-eucryptite.

Path (6, 5) represents the case where small amounts of metals such as Ag, Au, Pt, Cu, Rh, Pd, etc. are incorporated into a glassy matrix and by suitable control of initial concentration, melting conditions, thermal history, and in some cases (Au, Ag) exposure to actinic radiation, nanometer-sized particles of these metals are precipitated in the glass. Since the process involves both a reduction to a metallic state and diffusiPon of the reduced species to form a particle, their mean size may vary over a wide range depending on the interplay of the above factors. MAURER [1959] has shown that the minimum size of a gold particle capable of catalyzing lithium metasilicate is about 8 nm (10,000 atoms). This is in contrast to the smallest, stable gold particle which may contain only three or four atoms. Thus, the need for microstructure control to achieve catalyzed crystallization is apparent. It has been recognized for some time that the presence of these metal particles induces a characteristic color in the bulk glass. Thus, gold and copper particles give rise to a magneta color, silver to a yellow cast, and platinum to a somewhat dull grey appearance. Similarly, selenium gives a characteristic pink color in soda-lime silica glasses (average particle size 5–20 nm). Since this pink color is complementary to the bluish green arising from ionic iron in these same glasses, this element is used extensively in the glass container industry as a decolorizer. It is here that the control of microstructure in glass is crucial because the precise shade of pink required to achieve decolorization depends on composition, furnace atmosphere, and thermal history (PAUL [1975]). The need to understand the origin and significance of microstructure in glass to render a product commercially acceptable is evident.

Still another group of technologically important glasses which are partially crystalline is the photochromic glasses (ARANJO and STOOKEY [1967]). Their photochromic behavior arises from minute silver halide crystals which may be regarded as being suspended in an inert glass. Satisfactory photochromic properties are obtained when the average particle size is about 5–10 nm at a concentration of $\sim 10^{15}$ particles/cm^3. This corresponds to an average particle separation distance of about 60 nm. This separation distance is crucial since the inert glass host prevents diffusion of the halogens freed by absorption of light by the halide crystal. Thus, recombination with free silver within the halide crystal is enhanced. It is this alternate decomposition and recombination that gives rise to the variable optical transmission of these glasses.

References: p. 935.

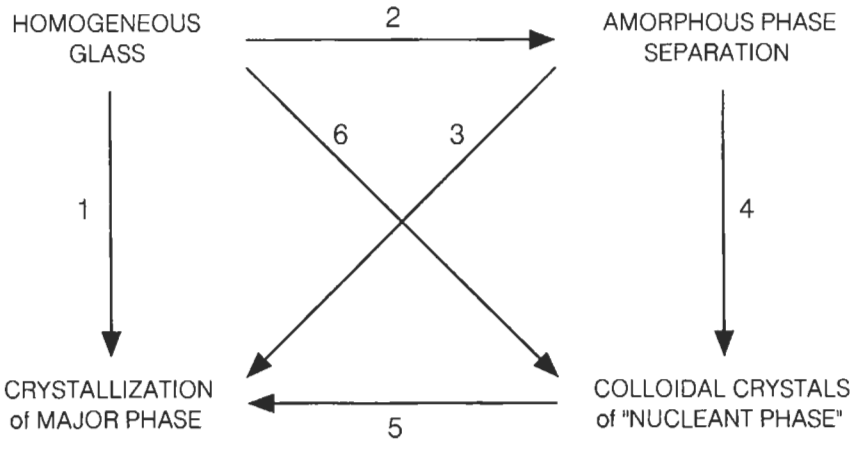

Fig. 23. Various paths associated with potential crystallization of glass forming melts. (From STEWART [1972].)

5. *Nanostructured materials*

5.1. Materials with reduced dimensionality, reduced dimensions and/or high densities of defect cores

The perfect single crystal of infinite size has been the model system of solid state physics for several decades. Remarkable progress was achieved in the physical understanding of solids by means of this idealized approach. However, about 40 years ago, scientists started to realize that the disorder present in most real materials cannot be treated as a weak perturbation of the corresponding ideally ordered crystals. In fact, a variety of new physical effects (e.g., new types of phase transitions, quantum size effects, new transport phenomena, etc.) were discovered which existed only in imperfectly ordered solids. In fact, if the characteristic dimensions (e.g., the diameters of small spheres or the thickness of a thin film) of the crystalline regions of a polycrystal approach certain characteristic lengths such as an electron wavelength, a mean free path, a coherency length, a screening length, a correlation length, etc. one obtains materials the properties of which are controlled by their reduced dimensionality or their reduced dimensions and/or their high density of defect cores (e.g., grain boundary cores). As a kind of introduction, let us consider two specific examples. The first example is shown in fig. 24 in the form of a compositional superlattice characterized by a length scale, d, which characterizes the thickness of the layers. If d is equal or less than the mean free path of the conduction electrons, the electronic band structure and, hence the electric properties of this materials differ significantly from the ones of a superlattice with the same chemical composition but with a modulation length, d, that is much larger than the electronic mean free path (cf. section 5.2). The second example to be considered here is a crystalline solid with a high density of grain boundary (i.e., defect) cores (fig. 36, below). About 50% of the atoms are located in the cores of these grain boundaries. In

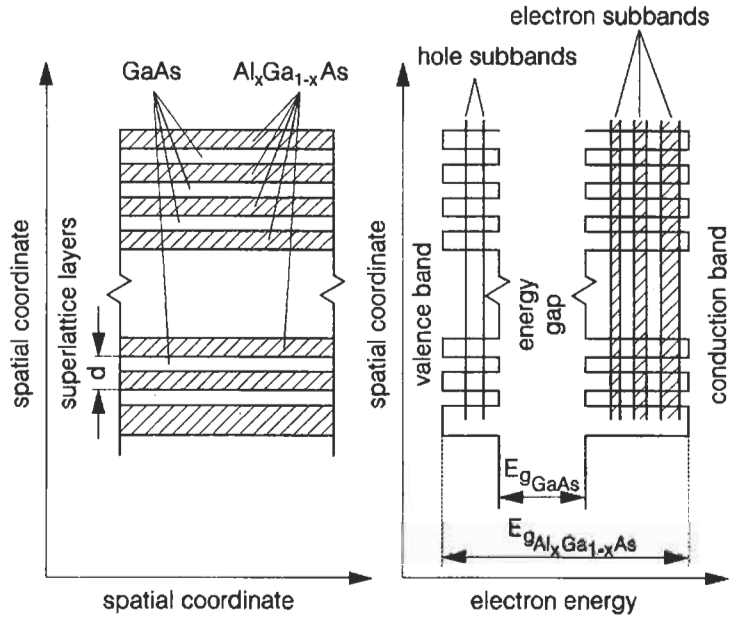

Fig. 24. Schematic illustration of the layer sequence (left side) and of real-space energy-band profile (right side) of a GaAs/Al_xGa_{1-x} as superlattice. Both, the GaAs and the Al_xGa_{1-x} as layers are assumed to be equally thick. E_g is the energy of the band gap edge.

grain-boundary cores, the atomic structure (e.g., the density and the nearest neighbor coordination) differs from that of a perfect crystal with the same chemical composition. Hence the atomic structure and the properties of a material with a structure as shown in fig. 36 may deviate (in some cases by many orders of magnitude) from those of the corresponding single crystal (cf. sections 5.4, 5.5 and 5.6). Materials exhibiting reduced dimensionalities, reduced dimensions and/or high densities of defect cores are termed nanostructured materials, because the typical size of the crystalline regions or of another characteristic length scale in such materials are in the order of a few nanometers. In recent years, the following five types of nanostructured materials have attracted widespread scientific attention:

1) Thin metallic, semiconducting or polymeric films with clean or coated surfaces.
2) Man-made superlattices and quantum well structures.
3) Semicrystalline polymers and polymer blends.
4) Nanocrystalline and nanoglassy materials.
5) Nanocomposites made up of metallic, covalent, ionic and/or molecular components.

This paragraph will be limited to the materials mentioned in 2, 3, 4 and 5. Concerning thin films and free surfaces we refer to chapters 28 and the numerous reviews in the literature and textbooks on surface science as well as thin solid films.

References: p. 935.

5.2. Man-made superlattices and quantum-well structures

In 1969 research on man-made superlattices was initiated by the proposal of Esaki and Tsu to engineer the electronic structure and properties of semiconductors by generating superlattices with a periodicity shorter than the electronic mean free path either by alternating the chemical composition (compositional superlattice) or the doping (doping superlattice) of consecutive layers in a multilayer structure.

The first *compositional superlattice* was grown from the material system $GaAs/Al_xGa_{1-x}As$. The layer sequence (chemical composition) and the real-space energy band structure of the electrons in such a superlattice are illustrated in fig. 24. The different energy levels of the bands of the two components at the heterointerfaces determine the potential barriers for the electrons and holes in the vertical direction (fig. 24), and thus define the periodic superlattice potential in the conduction and in the valence bands. The characteristic feature of this superlattice is that layers of a narrow-gap semiconductor are sandwiched between layers of a wide-gap semiconductor. This structure results in two square quantum wells: one for the electrons and one for the holes. Figure 25 displays the corresponding density of states in such a two-dimensional system in comparison to the parabolic curve of the classical (three-dimensional) free electron gas. If the electron mean free path exceeds the superlattice periodicity, resonant tunneling between adjacent subbands occurs. Technological applications of such superlattice structures lie primarily in the optoelectronic regime, comprising injection lasers, light emitting diodes, avalanche photo diodes and photoconducting detectors.

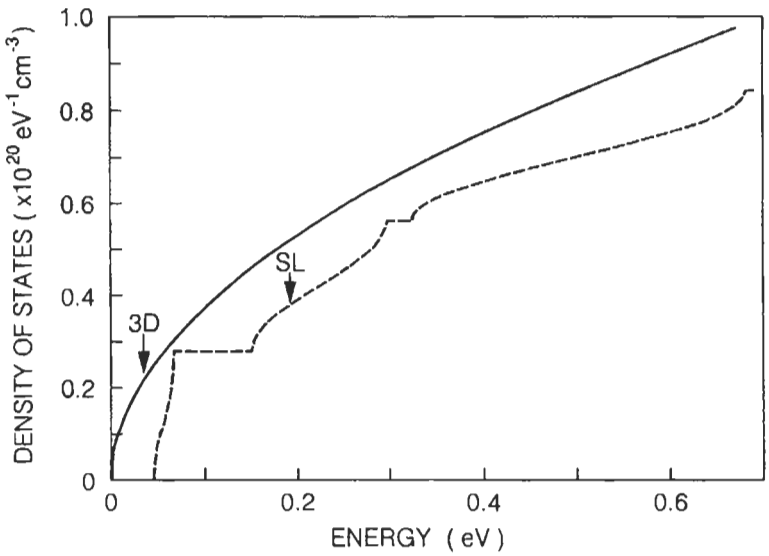

Fig. 25. Comparison of density of states in the three-dimensional (3D) electron system with those of a superlattice (SL) assuming a quantum well and barrier width of 10 nm, and an effective electron mass 0.067 m_0 in the SL. The first three subbands are indicated (MENDEZ and VON KLITZING [1989]. m_0 is the mass of the free electron).

The term *doping superlattices* refers to periodic arrays consisting of layers of the same semiconductor doped in two different ways e.g., n- and p-doped layers. The unusual electronic properties of doping superlattices derive from the specific nature of the superlattice potential which, in this case, is the space charge potential of ionized impurities in the doping layers. This is in contrast to the compositional superlattices (fig. 24), in which the superlattice potential originates from the different band gaps of the constituents. The space charge potential in the doping superlattices modulates the band edges of the host material in such a way that electrons and holes become spatially separated (fig. 26). This separation can be made nearly perfect by the appropriate choice of the doping concentrations and the layer thicknesses. One of the attractive features of doping superlattices is that any semiconductor that can be doped in both n- and p-type in well controlled ways can be used as the host material. Another advantage of doping superlattices originates from their structural perfection. The relatively small concentrations of impurities used in doping superlattices (typically 10^{17}–$10^{19}/cm^{-3}$), induce only minor distortions of the lattice of the host material. Thus, doping superlattices do not contain interphase boundaries as does compositional superlattice. The absence of any significant disorder or misfit strains leads to unprecedented electron and hole mobilities. Doping supperlattices have had profound impact on not only the progress made in recent years in the physics of two-dimensional electronic systems (quantum Hall effect, Shubnikov–de Haas oscillations) but also on device applications such as high-speed MODFETS. For further details we refer to some of the excellent reviews in this rapidly growing area of research (MENDEZ and VON KLITZING [1989], FERRY *et al.* [1990], KIRK and REED [1992]).

5.3. Semicrystalline polymers

Semicrystalline polymers constitute a separate class of nanostructured materials. The remarkable feature of this class of polymers is that the nanostructured morphology is always formed if the polymers are crystallized from the melt or from solution unless crystallization occurs at high pressure or if high pressure annealing is applied subsequent to crystallization. If a polymer is crystallized from a dilute solution, isolated single polymer crystals or multilayer structures consisting of stacks of polymer single crystals result (fig. 27). Inside the crystals, the atoms forming the polymer chains arrange in a periodic three-dimensional fashion. The interfaces between neighboring crystals consist of both macromolecules folding back into the same crystal and tie molecules that meander between neighboring crystals. The typical thicknesses of the crystal lamellae are in the order of 10 to 20 nm. These relatively small crystals thicknesses have been interpreted in terms of one of the following models. The first model hypothesizes the formation of the thin crystallites to result from nucleation kinetics. If the height of the energy barrier for the formation of a critical nucleus of a chain-folded polymer crystal formed in a supersaturated solution is computed by means of homogeneous nucleation theory, it is found that the energy barrier of a critical nucleus consisting of extended chain molecules is larger than the barrier height for a nucleus of folded chains. The physical reason for this energy difference is as follows. Extended chain crystallization

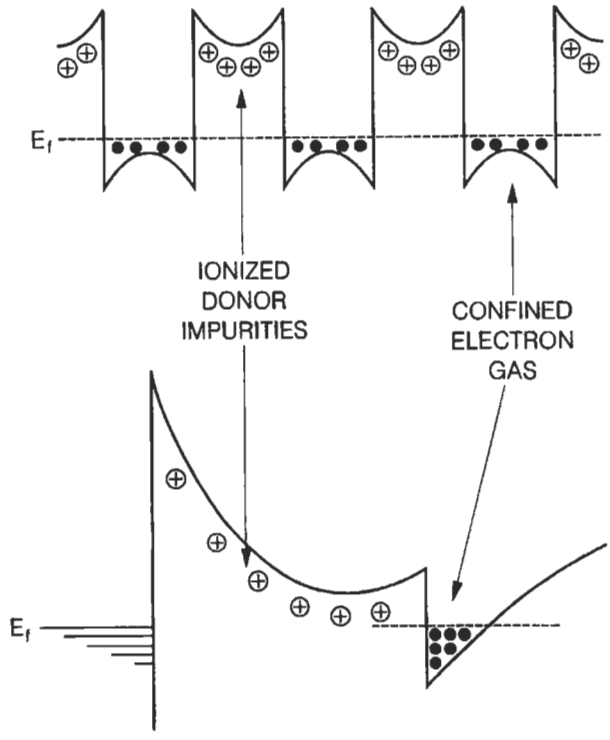

Fig. 26. Modulation doping for a superlattice and a heterojunction with a Schottky junction. E_f indicates the position of the Fermi energy (MENDEZ and VON KLITZING [1989]).

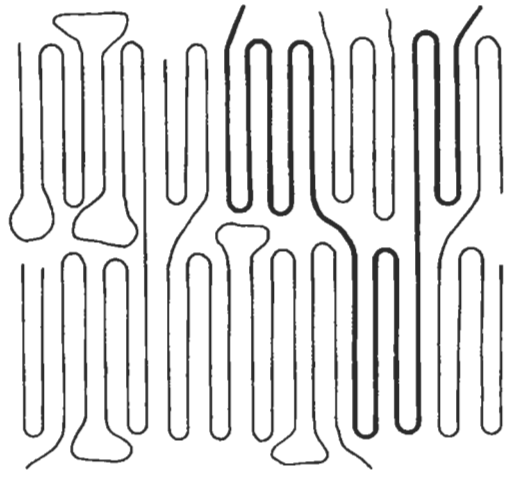

Fig. 27. Schematic representation of the conformation of chain-folded polymer molecules in a semicrystalline polymer. One molecule belonging to adjacent crystals is indicated as a heavy line.

results in a needle-shaped critical nucleus, the length of which is equal to the length of the molecular chains. Hence the system is left with only one degree of freedom to reduce the energy barrier for the critical nucleus. This reduction occurs by adjusting the diameter of the needle. However, if chain folding occurs, the energy barrier associated with the critical nucleus can be minimized by adjusting the size of the nucleus in all three dimension. Detailed computations reveal that the energy barrier for chain folded nuclei is in general significantly lower than for extended chain crystallization. The second group of models for chain-folding is based on the excess entropy associated with the folds relative to an extended-chain crystals. If the Gibbs free energies of an extended chain crystal and of a chain-folded crystal are compared, the chain folds are found to increase the internal energy of the system. However, the chain folds also contribute to the entropy of the system. Hence, at finite temperatures, a structure of lowest Gibbs free energy is obtained, if a certain concentration of chain folds is present in the crystal. In other words, chain-folded crystals have a lower Gibbs free energy at finite temperatures than extended chain crystals (cf. also ch. 32, § 2.2–2.6).

Polymers crystallizing from the molten state form more complex morphologies. However, the basic building blocks of these morphologies remain thin lamellar crystals. Figure 28 shows spherulitic crystallization of thin molten polymer film. The spherulites consist of twisted lamellae which exhibit radiating growth. If the molten thin film is strained during solidification, different morphologies may result, depending on the strain rate. However, all of these morphologies have in common that the macromolecules are

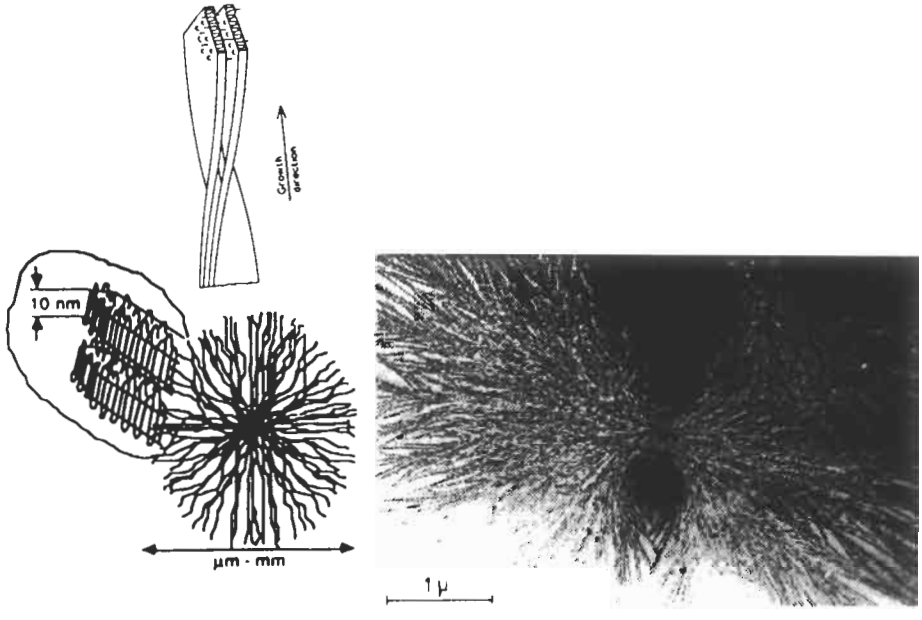

Fig. 28. Bright field transmission electron micrograph (defocus contrast) of a two-dimensional spherulite in isotactic polystyrene. The spatial arrangement of the lamellae formed by the folded macromolecules is indicated on the left side (PETERMANN [1991]).

References: p. 935.

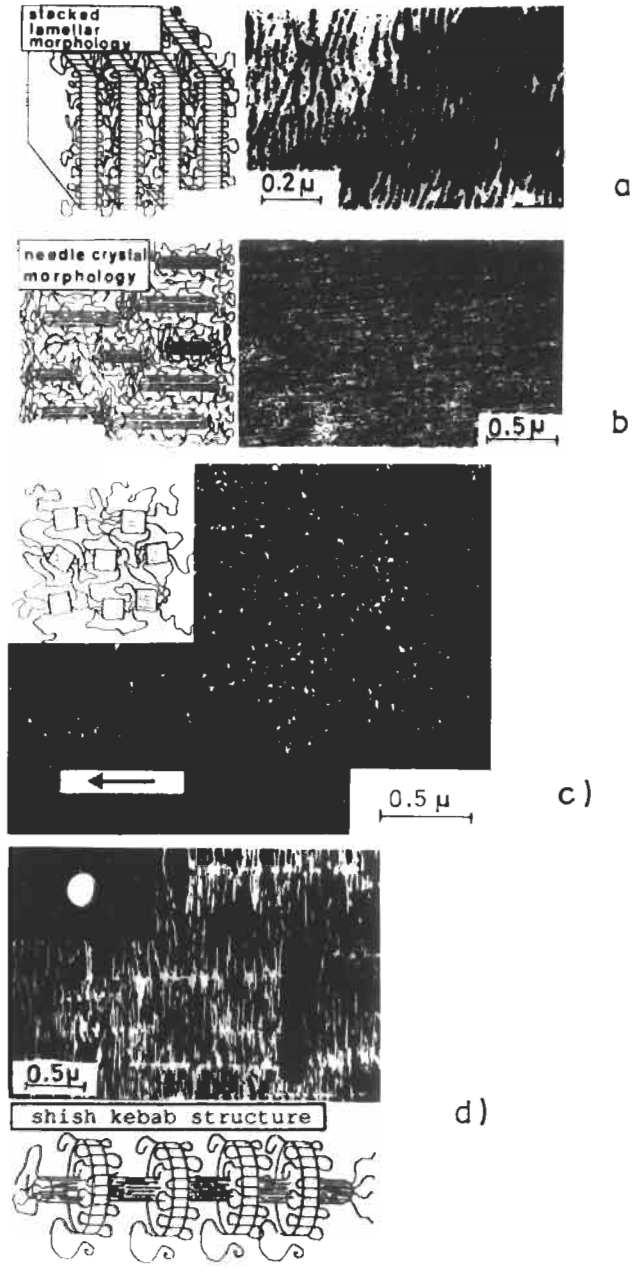

Fig. 29. (a) Stacked lamellar morphology in polyethylene (TEM bright field). (b) Needle-like morphology in polybutene-1 (TEM bright field). (c) Oriented micellar morphology in polyethylene terephthalate (TEM dark field micrograph). (d) Shish-kebab morphology in isotactic polystyrene (TEM dark field micrograph) (PETERMANN [1991]).

more or less aligned in the straining direction. High temperatures and small strain rates favour a stacked lamellar morphology (fig. 29a), high temperatures combined with high strain rates result in needle-like arrangements (fig. 29b). Low temperatures and high strain rates lead to oriented micellar structures (fig. 29c). The transition between these morphologies is continuous and mixtures of them may also be obtained under suitable conditions (fig. 29d). The way to an additional variety of nanostructured morphologies was opened when multicomponent polymer systems, so-called polymer blends, were prepared. For thermodynamic reasons, polymer blends usually do not form homogeneous mixtures but separate on length scales ranging from a few nanometers to many microns depending on the thermomechanical conditions of crystallization and the molecular structure of the costituents involved. So far the following types of nanostructured morphologies of polymer blends have been reported for blends made up by one crystallizable and one amorphous (non-crystallizable) component: Type I morphology: The spherulites of the crystallizable component grow in a matrix mainly consisting of the noncrystallizable polymer. Type II morphology: The non-crystallizable component may be incorporated into the interlamellar regions of the spherulites of the crystallizable polymer. The spherulites are spacefilling. Type III morphology: The non-crystallizable component may be included within the spherulites of the crystallizable polymer forming domains having dimensions larger than the interlamellar spacing. For blends of two crystallizable components, the four most frequently reported morphologies are: Type I morphology: Crystals of the two components are dispersed in an amorphous matrix. Type II morphology: One component crystallizes in a spherulitic morphology while the other crystallizes in a simpler mode e.g., in the form of stacked crystals. Type III morphology: Both components exhibit a separate spherulitic structure. Type IV morphology: The two components crystallize simultaneously resulting in so-called mixed spherulites, which contain lamellae of both polymers.

Morphologies of lower complexity than spherulites, such as sheaves or hydrides may also be encountered. In these cases, the amorphous phase, may be arranged homogeneously or heterogeneously depending on the compatibility of the two components. The morphology of blends with one crystallizable component has been studied for a variety of macromolecular substances e.g., poly(ε-caprolactrone)/poly(vinylchloride), poly(2,6dimethyl-phenylene oxide)/isotactic polystyrene, atactic polystyrene/isotactic polystyrene blends.

Block copolymers constitute a third class of nanostructured polymers. All macromolecules of a block copolymers consist of two or more, chemically different sections which may be periodically or randomly arranged along the central backbone of the macromolecules and/or in the form of side branches. An example of a block copolymer are atactic polytyrene blocks alternating with blocks of polybutadiene or polyisoprene. The blocks are usually non-compatible and aggregate in separate phases on a nanometer scale. As an example for the various nanostructured morphologies possible in such systems, fig. 30 displays the morphologies formed in the system polystyrene/polybutadiene as a function of the relative polystyrene fraction. The large variety of nanostructured morphologies that may be obtained in polymers depending on the crystallization conditions and the chemical structure of the macromolecules causes the

References: p. 935.

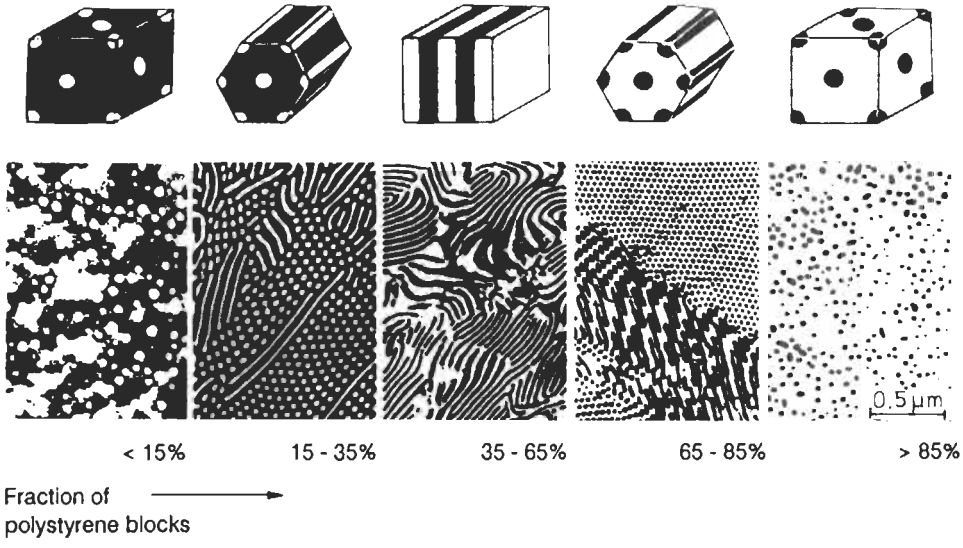

Fig. 30. Electron micrographs of the morphologies of a co-polymer consisting of polystyrene and polybutadiene blocks, as a function of the fraction of polystyrene blocks. The spacial arrangements of the polystyrene and polybutadiene in the solidified polymer are indicated in the drawings above the micrographs (PETERMANN [1991]).

properties of polymers to vary dramatically depending on the processing conditions. An example of a polymeric material with novel properties originating from a special nanoscale microstructure is shown in figs. 31 and 32. Polyethylene with a nanostructured morphology consisting of stacked crystalline lamellae (fig. 31a) exhibits remarkable elastic properties (fig. 32) if strained in tension in the direction perpendicular to the plane of the lamellae. The strain causes the lamellae to separate so that fibres of extended tie molecules form between them (fig. 31b). Upon unloading, the surface-energy of these molecular fibres causes them to shrink and thus pull the lamellar crystals together again. In other words, one obtains a material that can be strained reversibly by more than 100%. The restoring force (contraction) of the material is driven by surface energy and hence the material may be termed surface-energy pseudoelastic. If the stacked morphology is replaced by, e.g., a spherulitic microstructure, no such effects are noticed. In recent years, the large variety of nanostructured morphologies that may be generated for example in polymer blends or block copolymers has caused a rapidly expanding research activity in this type of materials (MARTUSCELLI *et al.* [1980], PETERMANN [1991]). For further details, see ch. 32.

5.4. Nanocrystalline and nanoglassy materials

5.4.1. Basic concepts

The difference between the atomic structure of nanocrystalline materials and other states of condensed matter (e.g., single crystals, glasses, quasicrystals) may be understood by considering the following two facts:

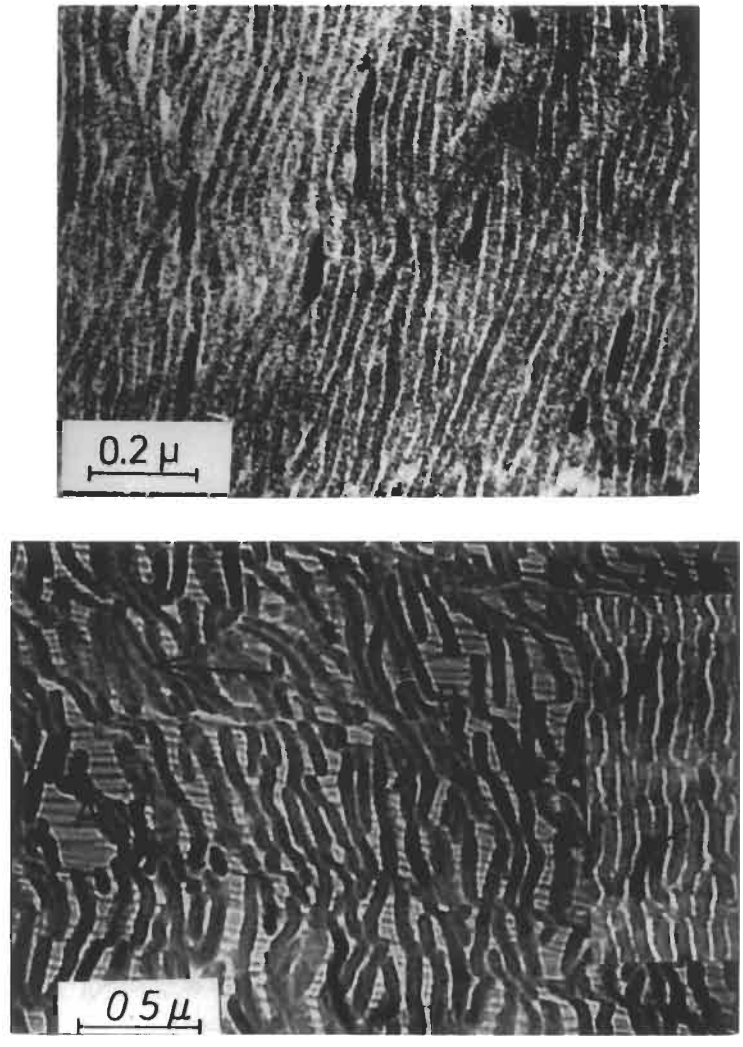

Fig. 31. (a) Defocus electron micrograph showing the stacked-lamellae structure of a polyethylene fiber. The dark regions are the crystallites. The pattern of bright lines indicates the positions of the chain folds between the lamellae (cf. fig. 27). (b) Electron micrograph of a strained polyethylene fiber (cf. fig. 31a) showing complete separation of the lamellae interconnected by fibrils. The horizontal arrow indicates the straining direction (the strain is approximately 100%).

(i) The properties of a solid depend (in addition to its dimensions and its dimensionality) primarily on its density and the coordination of nearest neighbors. The physical reason is that interatomic forces are of short-range character and hence the interaction between nearest neighbors is the most dominant factor. The total interaction energy between nearest neighbors depends on the number (coordination) of nearest neighbors and their

References: p. 935.

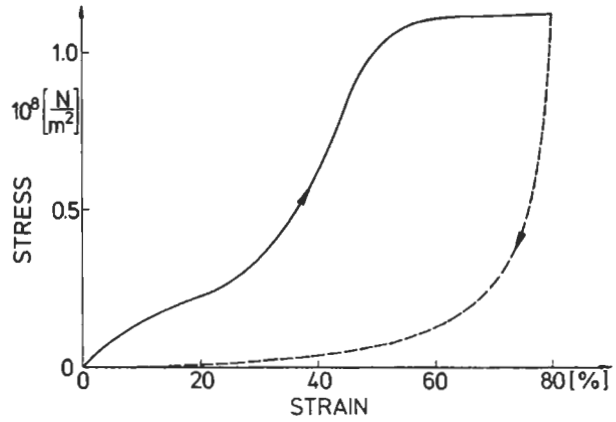

Fig. 32. Stress-strain curve for straining and destraining (in air) of a stacked-lamellae structure of polyethylene (cf. fig. 31) at 22° C at a strain rate of 0.0005/s. In the plateau region, the deformation occurs primarily by the separation of the lamellae and the formation of the fibrils between them (cf. fig. 31b).

interatomic spacing (i.e., the density). Perhaps, the best-known example demonstrating the significance of the density and the coordination of nearest neighbors is the phase transformation between diamond and graphite (fig. 33). During this phase transformation, the density and coordination number change by about 30 to 40%. The resulting variation of the properties is well known: A hard, brittle, insulating material (diamond) transforms into a soft, ductile and electrically conducting substance (graphite).

(ii) In the cores of incoherent interfaces (grain boundaries, interphase boundaries) and other lattices defects, the density and nearest-neighbor coordination deviates significantly from the surrounding perfect crystal lattice. For example, fig. 34 displays the computed

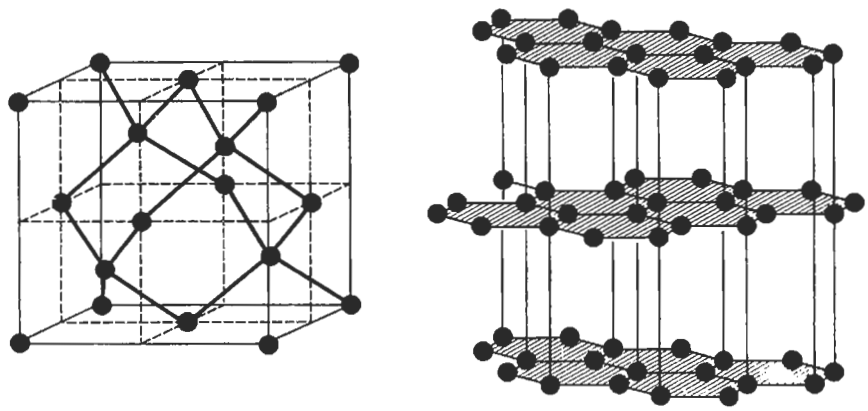

Fig. 33. Atomic structure of diamond (left side) and graphite. The carbon atoms are represented as closed circles.

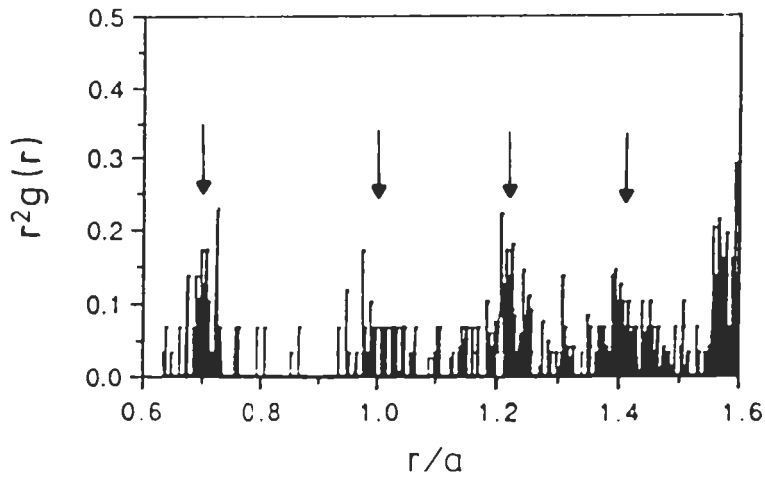

Fig. 34. Computed radial distribution function, $r^2g(r)$, for the atoms in the core of a 43.60° [100] (Σ29) grain boundary in Au (cf. fig. 35). Arrows indicate the corresponding perfect crystal peak positions. The interatomic spacings between the atoms in the boundary core are strongly affected by the presence of the interface. In the computations, the interatomic forces were represented by an embedded atom potential corresponding to Au (PHILLPOT *et al.* [1990]).

radial distribution function in a Σ29 (100) grain boundary in Au. The positions of the delta-function-like distribution peaks of the Au crystal lattice are indicated by arrows. Obviously, the boundary core structure is characterized by a broad distribution of interatomic spacings. In fact, the width of this distribution is also much larger than the one in glassy solids. Concerning the density reduction in the boundary core regions, the situation appears similar. For instance, in the case of the grain boundary shown in fig. 35 (deduced from a high resolution electron micrograph of this boundary between two misoriented NiO crystals) the density is about 80% of the cubic crystal far away from the boundary.

With these facts in mind, it was proposed (MARQUARDT and GLEITER [1980], GLEITER [1981b]) that if one generates a material that consists primarily of incoherent interfaces (i.e., a material that consists for example of 50 vol% incoherent grain boundaries and 50 vol% crystals), the structure (and properties) of such a material will deviate significantly from those of a crystal and/or glass with the same chemical composition. Materials with such a high density of interfaces were called *nanocrystalline materials**. In order to specify this idea further, let us consider a hard-sphere model of a nanostructured material which may be generated in the following way: We start off with isolated nanometer-sized

* Other terms used in the literature in the subsequent years were nanophase materials, nanometer-sized materials, nanostructured materials or materials with ultra-fine microstructures.

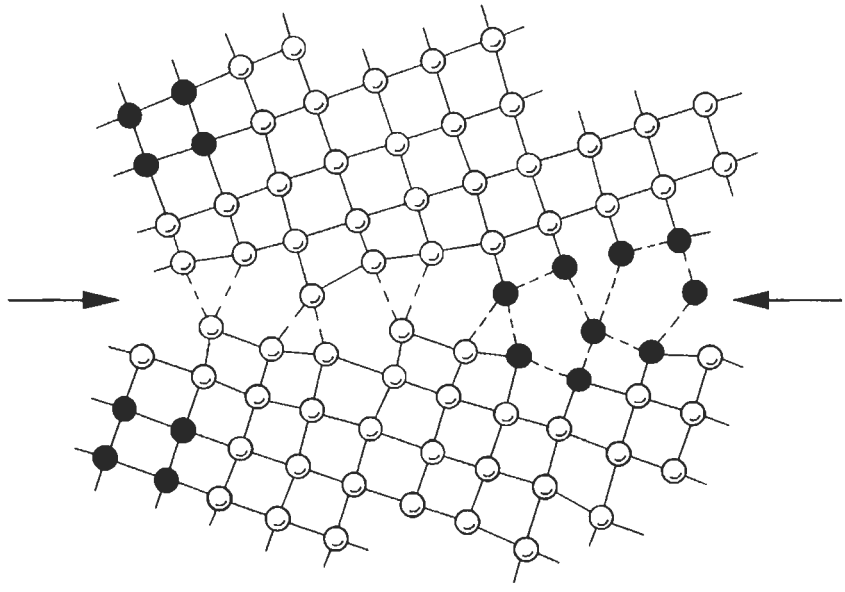

Fig. 35. Atomic structure of the core of a grain boundary between two NiO crystals that are tilted relative to one another by 36,9° about a common [100] direction normal to the plane of the figure. The structure was deduced from the high resolution electron micrograph of 36,9° [100] tilt boundary in NiO (MERKLE *et al.* [1987]). The boundary core structure may be described as a two-dimensional periodic array comprising two different pentagonal polyhedra (indicated on the right side of the boundary by broken lines). The two NiO crystals forming the boundary have cubic structure.

crystals with uncontaminated surfaces and consolidate them at high pressure. If this is done, one obtains a structure that is represented (for the sake of simplicity) in the form of a two-dimensional hard-sphere model in fig. 36. The open and full circles represent atoms all of which are assumed to be chemically identical. Different symbols (open/full circles) are used to emphasize the heterogeneity of the structure of nanostructured materials. Obviously, the structure consists of the following two components: (i) The crystallites which have all the same atomic arrangement. The only difference between the crystallites is their crystallographic orientation. The atoms in the interior of the crystallites are represented in fig. 36 as full circles. (ii) The second component of the nanocrystalline structure is formed by the interfaces (grain boundaries) between the crystallites. At the interfaces, two crystallites are joined together. Due to the different crystallographic orientations between adjacent crystallites, a region of misfit (called a grain boundary) results. In these grain boundaries, the atoms (indicated as open circles) are packed less densly than in the interior of the crystallites and the arrangement of nearest neighbors is changed relative to the crystal interior. The fraction of atoms situated in interfaces increases if the crystallites are made smaller. In fact, a straightforward estimate shows that (in the three-dimensional case) about 50% of the atoms are located in interfaces (open circles) if the crystal size is in the order of 5 to 10 nm. A crystal size

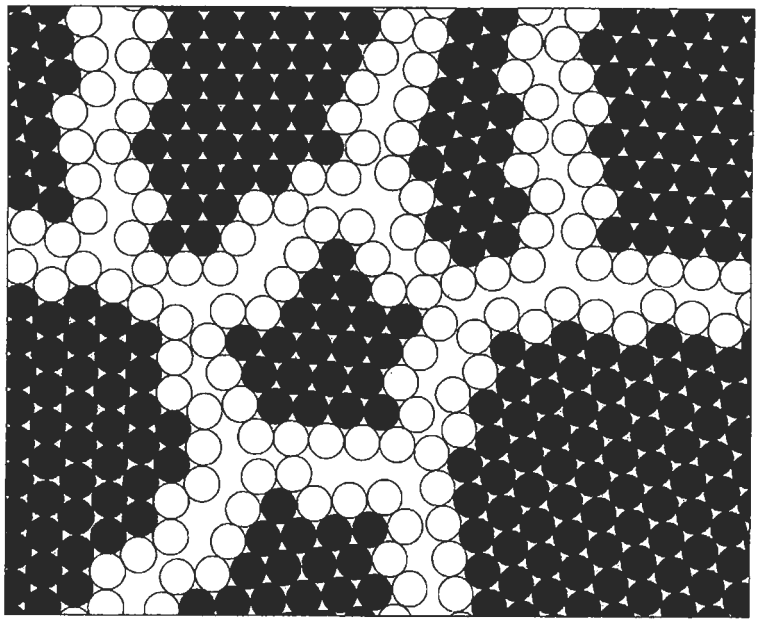

Fig. 36. Two-dimensional hard sphere model of the atomic structure of a nanocrystalline material. For the sake of clarity the atoms in the centers of the "crystals" are indicated in black. The ones in the boundary core regions are represented by open circles. Both types of atoms are assumed to be chemically identical.

in the order of a few nanometers has been the reason for calling materials that consist primarily of interfaces "nanocrystalline materials". Obviously, the structure and properties of nanocrystalline materials depend on the large fraction of interfaces with densities and nearest neighbor coordination numbers that deviate from the ones of crystalline and the glassy state and on the reduced size of the crystallites.

In order to achieve a high density of interfaces, the size of the crystals forming a nanocrystalline material has to be reduced to a few nanometers. If the size of the crystalline regions approaches a few nanometers, size effects as well as reduced dimensionality effects may become important as well. In other words, in addition to the *effects* resulting from the *variation of the density* and the *nearest neighbor coordination* in the *interfacial region*, nanocrystalline materials are also expected to exhibit *size* and *reduced dimensionality* effects.

The structural difference between a nanocrystalline and a glassy material (with the same chemical composition) may be seen by considering the physical origin of both structures. In a glass generated by quenching the molten state, the spacial density and coordination variations are controlled by the frozen-in thermal fluctuations. This is not so in nanocrystalline materials. The density and coordination numbers in the boundaries are controlled by the misfit between adjacent crystallites (fig. 36) with different crystallographic orientations. In other words, the density and the coordination are controlled by geometry (or crystallography) rather than by thermal fluctuations.

References: p. 935.

In the following section an attempt will be made to summarize our present knowledge about nanocrystalline materials. This section will be subdivided into the following five paragraphs: (a) The generation of nanocrystalline materials. (b) The atomic structure of nanocrystalline materials. (c) Nanoglasses. (d) Nanocomposites. (e) Technological applications. For obvious reasons, the summary given in this section is not intended to be encyclopaedic. In discussing the atomic structure and properties of nanocrystalline materials, we draw attention to those aspects of the experimental evidence that must be examined the most critically. The discussion of the properties will be limited to properties that appear relevant to technological application. For further details, the reader is referred to one of the recent review articles (e.g., GLEITER [1989], BIRRINGER [1989], SURYANARAYANA and FROES [1992], SIEGEL [1993], SHULL [1993]), GLEITER [1995].

5.4.2. Generation of nanocrystalline materials

In principle the following three routes have been used so far to generate nanocrystalline materials. The first one starts from a noncrystalline structure, e.g., a glass. The nanocrystalline materials are obtained by nucleating numerous crystallites in the glass e.g., by annealing. These nuclei subsequently grow together and result in a nanocrystalline material. The various modifications of this approach differ primarily in the starting material used. So far metallic glasses (e.g., produced by melt spinning, LU *et al.* [1991]) and the sol-gel technique (CHAKRAVORTY [1992]) have been successfully applied. The most important advantages of this approach are as follows. Low-cost mass production is possible and the material obtained exhibits little or no porosity. Obviously this approach is limited to chemical compositions which permit the generation of glasses or sols.

The second route is based on increasing the free energy of a (initially coarse-grained) polycrystal. The various modifications differ by the procedures that are applied to increase the free energy. Ball-milling, high-strain-rate deformation, sliding wear, irradiation with high-energy particles, spark erosion and detonation of solid explosives have been used so far. All of these techniques are based on introducing a high density of lattice defects by means of plastic deformations or local atomic displacements. The crystal size of the final product can be varied by controlling the milling, the deformation, the irradiation or the wear conditions (e.g., the milling speed, temperature, type of mill used, etc.). This group of methods have been scaled up successfully. For example, cryomilling has been applied to produce commercial quantities of nanocrystalline Al/Al_2O_3 alloys.

The third route of production processes for nanocrystalline materials involves a two-step procedure. In the first step, isolated nanometer-sized crystallites are generated which are subsequently consolidated into solid materials. PVD, CVD, electrochemical, hydrothermal, thermolytic, pyrolytic decomposition and precipitation from solution have been used so far. The most widely applied PVD method involves inert gas condensation (fig. 37). Here, the material is evaporated in an inert gas atmosphere (most frequently He at a pressure of about 1 kPa). The evaporated atoms transfer their thermal energy to the (cold) He and hence, condense in the form of small crystals in the region above the vapor source. These crystals are transported by thermal convection to the surface of a cold finger. In addition to thermal evaporation, dc or ac sputtering as well as laser

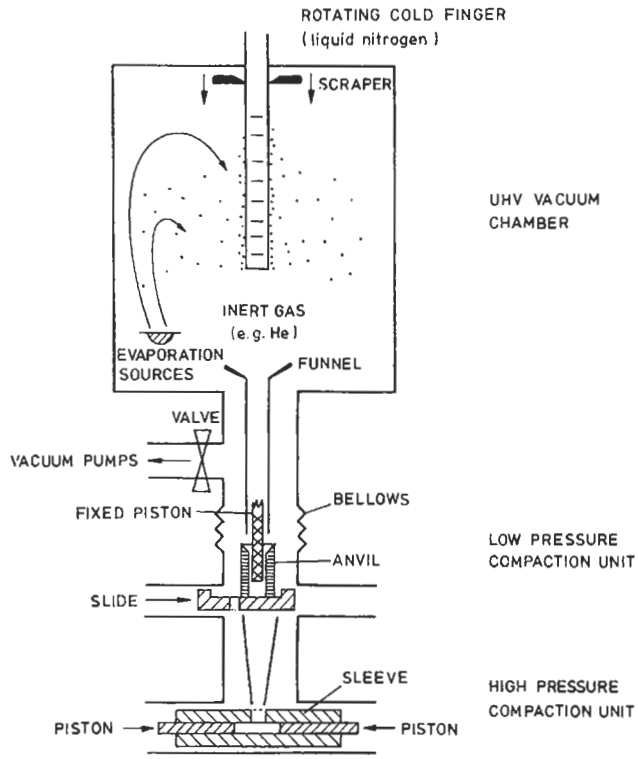

Fig. 37. Schematic drawing of gas-condensation chamber for the synthesis of nano-crystalline materials. The material evaporated condenses in the inert gas in the form of small crystallites which are subsequently transported via convection (arrows) to the liquid-nitroqen-filled cold finger. The powder of crystallites is finally scraped from the cold finger, collected via the funnel and consolidated first in the low-pressure compaction device and then in the high-pressure compaction unit. Both compaction units are kept under UHV conditions (GLEITER [1989]). Instead of an evaporation device, a sputtering source has been utilized as well.

evaporation or laser ablation have been used. Instead of evaporating the material into an inert gas atmosphere, bulk nanocrystalline materials may also be obtained by depositing the material in the form of a nanometer-sized polycrystalline layer onto a suitable substrate. PVD, CVD and electrochemical deposition has been applied successfully (CHATTERJEE and CHAKRAVORTY [1989], OSMOLA *et al.* [1992], VEITH *et al.* [1991, 1992], HASEEB *et al.* [1993]). In the special case of nanocrystalline Si, plasma-enhanced CVD using an rf or dc plasma source turned out to be a versatile method that permits one to generate thin Si films. Depending on the deposition parameters, any microstructure may be obtained between amorphous Si and coarse-grained crystalline Si (VEPREK and SAROTT [1987]). The methods for generating small crystallites by precipitation reactions may be divided into processes involving precipitation in nanoporous host materials and host-free precipitation. In both cases a wide range of solvents (e.g., water, alcohol, etc.) as well as different reactions (e.g., addition of complex forming ions,

photochemical processes, hydrolytic reaction, etc.) have been utilized. A widely applied method for generating nanometer-sized composits is based on the sol-gel process. An interesting subgroup of sol-gel generated nanocomposits are organic-inorganic nanoscale ceramics, so called *ceramers, polycerms* or *ormocers* (SCHMIDT [1992]). Following the ideas of Mark and Wilkes, (GARRIDO *et al.* [1990]), these materials are prepared by dissolving preformed polymers in sol-gel precursor solutions, and then allowing the tetraalkyl orthosilicates to hydrolyze and condense to form glassy SiO_2 phases of different morphological structures. Alternatively, both the organic and inorganic phases can be simultaneously generated through the synchronous polymerization of the organic monomer and the sol-gel precursors. Depending upon such factors as the structures of the organic and inorganic components, the phase morphologies, the degree of interpenetration, and the presence of covalent bonds between the phases, the properties of these composites can vary greatly and range from elastomeric rubbers to high-modulus materials.

Precipitation in nanoporous materials involves a large spectrum of host substances. Hosts providing a three-dimensional framework containing nanometer-sized pores include zeolites, microemulsions, organogels (microemulsions containing gelatin), porous glasses, protein cages, micelles, capped materials. Graphite tubes, urea channels, phosphazene tunnel, lipid bilayer vesicles are examples of one-dimensional tunnel hosts. Layered (two-dimensional) hosts are provided by clays, graphite, halide layers and self-assembled mono- or multilayers. For a recent review of the fascinating developments in these areas we refer to the paper by OZIN [1992]. One of the attractive features of such nanosized *confined precipitates* is that they allow one to produce bulk quantities of unagglomerated nanoparticles.

During the second step of the third production method, the loose powder of nanometer-sized crystals is consolidated into a bulk material. Consolidation of the small crystals has been performed at low as well as elevated temperatures under static (e.g., uniaxial pressure, hydrostatic pressure, laser-sintering, laser reactive sintering) or dynamic conditions (e.g., sinter-forging, shear, explosive consolidation). Laser reactive sintering is applicable preferentially to nanocomposits. The strategy of this method is to select mixtures (e.g., a nanocrystalline ceramic and a metal) so that one component has a significantly lower melting point than the other(s). The objective is to achieve enhanced sintering from the low-melting component during pulse heating by a laser beam that is scanned over the pre-consolidated material (MANTHIRAM *et al.* [1993]). In consolidating/sintering nanocrystalline powders it is noticed that the nanometer-sized powders densify at much lower temperatures (lower pressures) than coarse grained powders with the same chemical composition.

In comparison to the first two methods described at the beginning of section 5.4.2, the main advantages of producing nanocrystalline materials by a two-step procedure (involving the generation of isolated nanometer-sized crystals followed by a consolidation process) are as follows: (i) Crystals with different chemical compositions can be co-generated, leading to "alloying" on a nanometer-scale. (ii) The free surfaces of the small crystals may be coated prior to the compaction process by evaporation, sputtering, chemical reaction (e.g., surface oxidation) or in suspension. (iii) The interior of the crystallites may be modified by ion implantation before consolidation. Due to the small

crystal size, the implantation results in materials that have the same chemical composition throughout the volume. In bulk materials, ion implantation is limited to surface regions.

Due to the high density of interfaces, single-component nanostructured materials frequently exhibit crystal growth during sintering. One approach to minimise crystal growth is to limit the time spent at the consolidation temperature. This may be achieved by sinter-forging or explosive consolidation. Another approach is to use grain growth inhibitors such as pores, second phase particles, etc. (MAYO and HAGUE [1993]). The latter method has been utilized, for instance, to sinter nanostructured WC alloys (cf. § 5.7.1). Grain growth was inhibited by transition metal carbides.

5.4.3. Atomic structure

The hypothesized reduced density in the cores of the grain boundaries in nanocrystalline materials (cf. fig. 36) agrees with the following observations. In comparison to a single crystal of the same chemical composition, nanocrystalline materials exhibit: (i) A reduced bulk density and a reduced Debye temperature; (ii) a positron lifetime spectrum that indicates the presence of interfacial free volume which varies locally in size from a single vacancy to about eight vacancies (WÜRSCHUM *et al.* [1993]); (iii) an enhanced small-angle X-ray and/or neutron diffraction cross-section; (iv) an enhanced specific heat; (v) a modified isomer shift in the Mössbauer spectrum; (vi) a hyperfine field distribution that differs from that of the crystalline state; (vii) an enhanced solute diffusivity and substitutional solute solubility; (viii) an enhanced compressibility of the boundary regions and (ix) the observation of quantum size-effects in nanocrystalline semiconductors (e.g., in nanocrystalline ZnO) which indicates that the boundary regions act as barriers for electron propagation.

In addition to these findings, high-resolution electron microscopy, wide-angle X-ray or neutron diffraction measurements and computer simulations of the structure of individual grain boundaries (in bicrystals) indicate a boundary core density that is in the order of 75% to 90% of the corresponding crystal density (cf. fig. 35). Depending on the method used to study the grain-boundary structure, core widths between about 0.5 and several nanometers were measured. The boundary core densities and widths in bicrystals seem comparable with the boundary-core densities in nanocrystalline materials deduced from the data of the various measurements listed above. However, at this point it should be noted that the structure of the grain boundaries in nanocrystalline materials may be expected to differ from the one in bicrystals if the crystal size is reduced to a few nanometers. If the crystal size approaches a few nanometers, the lengths of the boundary segments between adjacent triple junctions are just a few interatomic spacings. In other words, the boundary lengths are shorter than the boundary periodicity. This is not the case for boundaries in macroscopic bicrystals. Moreover, the elastic interaction between neighboring boundaries (spaced a few nanometers only) may result in significant structural changes of the atomic arrangements in the boundary cores. The significance of both effects has been demonstrated recently by means of computations based on elasticity theory and computer simulations (KING [1993], HAHN [1994]). Computer simulations of the boundary structure indicate that the atomic arrangements in the boundary cores

References: p. 935.

change significantly, if the boundary lengths and spacings between adjacent boundaries approach the periodicity of the atomic structure of the boundaries. In fact, experimental evidence suggesting a different boundary structure in bicrystals and nanocrystalline materials has been reported. For example, the grain-boundary free volume (measured by positron lifetime spectroscopy, fig. 38a) and the specific electric resistivity per unit area of the boundaries of nanocrystalline materials was noticed to vary as a function of the crystal size (TONG *et al.* [1992]). The crystal size dependence suggest that the atomic structure of the grain boundaries depends on the lateral dimensions of the grain boundaries and on the spacings between neighbouring boundaries. This result agrees with recent theoretical studies of grain boundaries of finite extent (GERTSMAN *et al.* [1989]). These studies suggest that boundaries of finite extent differ from infinite boundaries primarily due to the disclinations formed at the triple junction between these boundaries. As the crystal size decreases, these disclinations become more and more important for the boundary structure. Another explanation for the experimentally observed grain size dependence has been proposed by PALUMBO *et al.* [1991b]. They pointed out that the volume fraction of the triple junctions between three boundaries in a nanocrystalline material becomes equal or larger, than the volume fraction of the planar boundary segments, if the crystal size is reduced below about 5 nm. If the atomic structure of the triple junctions differs from that of the boundaries, a grain size dependence will be noticed. Experimental evidence supporting this view by means of hydrogen diffusion in nanocrystalline Ni has been presented (PALUMBO *et al.* [1991b]). A correlation between the atomic structure of the boundaries and the preparation procedure has been evidenced by positron lifetime as well as Mössbauer spectroscopy. Nanocrystalline iron was produced by ball-milling and inert-gas condensation. Although both materials had the same chemical composition and comparable crystal size, they exhibited different hyperfine parameters i.e., different atomic structures. Similar results were obtained by means of positron annihilation measurements for nanocrystalline Cu or Ni in comparison to nanocrystalline metals produced by crystallizing metallic glasses.

The expected modified *number of nearest neighbor atoms* and the *broad distribution of interatomic spacings in the boundary cores* agree with computer simulations of the structure of grain boundaries, with the results of measurements by means of wide angle X-ray diffraction, EXAFS and the enhanced width of the distribution of the quadruple splitting in the Mössbauer spectrum of a nanocrystalline material in comparison to single crystals with the same chemical composition (LOEFFLER *et al.* [1995]). A discussion of the various measurements mentioned in this paragraph and the relevant original publications may be found in recent review articles listed at the end of § 5.4.1.

Ample evidence for *size effects and effects resulting from a reduced dimensionality* has been reported for nanocomposits and will, hence, be discussed in paragraph 5.6. In single component nanocrystalline materials only rather few observations of this kind seems to be available up to now. Figure 38b shows the blue shift of nanocrystalline (consolidated) ZnO resulting from quantum size effects. Apparently the grain boundaries act as potential barriers separating the individual crystals electronically. Size and/or dimensionality effects have been noticed by positron lifetime measurements as a function of the grain size. With decreasing grain size, the free volume in the interfaces becomes larger (fig. 38a) (TONG *et al.* [1992]).

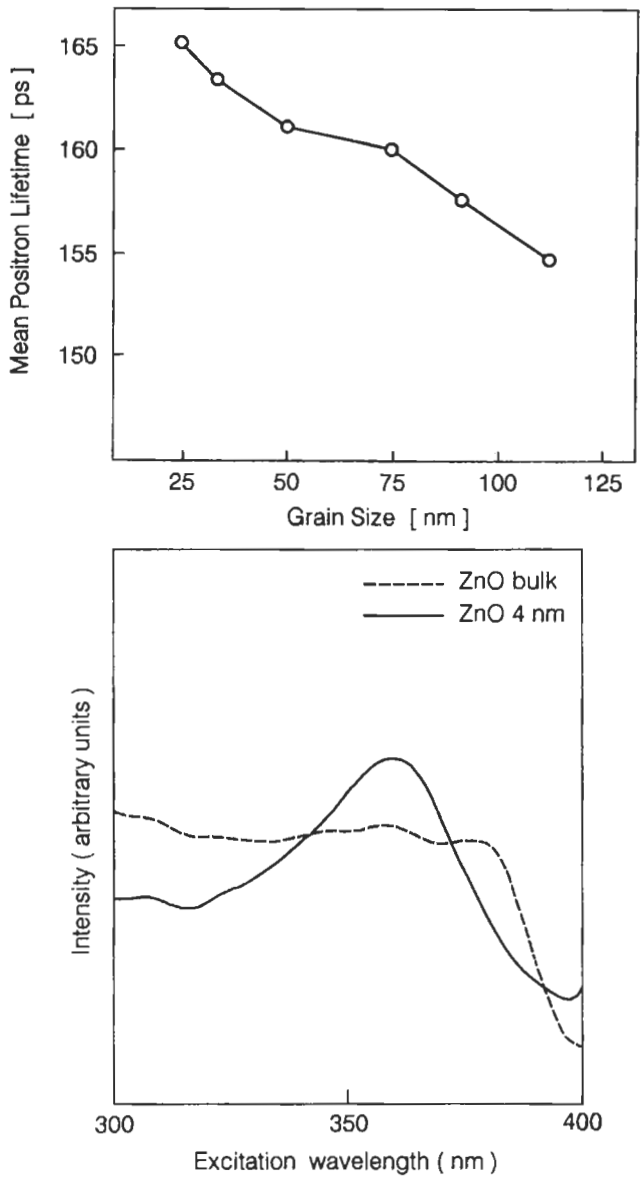

Fig. 38. (a) Variation of the mean positron lifetime as a function of the grain size in nanocrystalline $Fe_{78}B_{13}Si_9$ (TONG *et al.* [1992]). With decreasing grain size (at constanct chemical composition) the lifetime increases, indicating that the size of the sites of enhanced free volume in the grain boundaries changes as a function of grain size. (b) Photoluminescence spectrum of bulk (crystalline) ZnO in comparison to the (blue-shifted) spectrum of nanocrystalline ZnO (crystal size 4 nm). The detection wavelength used was 550 nm. The nanocrystalline ZnO was generated by inert-gas sublimation. The resulting crystallites were consolidated at 0.9 GPa pressure (MCMAHON [1994]).

References: p. 935.

The presently available experimental observations indicate that the structural model outlined so far (cf. fig. 36) is oversimplified in several ways. The atomic structure in the boundary cores (e.g., the average density, coordination number, etc.) depends not only on the crystal size and chemical composition. It also depends on the type of chemical bonding, the presence of impurities, the preparation mode and the time–temperature history of the specimens. For example, Mössbauer spectroscopy reveals that nanocrystalline Fe specimens prepared by ball milling or inert gas condensation exhibit different atomic structures in the boundary regions although the grain sizes and chemical compositions are comparable. The same applies to the structure of the boundary regions with and without impurity atoms. For instance, nanocrystalline Fe containing about 1% oxygen in the boundaries was noticed (by X-ray diffraction) to exhibit a different grain-boundary structure from the same material without or with less oxygen. The effect of the production procedure on the structure and properties of nanocrystalline materials, generated by electroplating and other techniques, has been discussed by ERB *et al.* [1993]. Some of the differences revealed were attributed to the residual porosity. However also pore-free, high-purity nanocrystalline materials (e.g., prepared by rapid shear and electroplating) exhibit properties that differ significantly from those of bulk materials. The deviations were found to depend primarily on the grain size and the preparation procedure (BAKONYI *et al.* [1993]). This result agrees with the basic concepts of nanocrystalline materials discussed in section 5.4.1 and suggests that the details of the atomic arrangement in the boundaries depend (for a given chemical composition) primarily on the grain size, the preparation procedure and the time–temperature history of the material. The significance of the type of chemical bonding for the structure of nanocrystalline materials was recently demonstrated for nanocrystalline diamond. Studies by means of Raman spectroscopy revealed a mixture of sp^2 and sp^3 bonds in nanocrystalline diamond. The sp^2 (graphite like) bonds seem to be associated with the boundary regions. The crystalline regions exhibited pure (diamond-like) sp^3 bonds. A change of the type of chemical bonding does not seem to occur in systems with non-directional bonds such as in metals. In all metallic systems studied so far, the chemical bonding in single-crystalline and nanocrystalline materials seems to remain metallic. Nevertheless, the reduced atomic density, electron density and the modified nearest-neighbor structure in the boundary regions seem to change the interatomic interaction. This is evidenced by the variation of the ferromagnetic properties of the boundary regions in comparisons to the interior of the crystallites (e.g., in Fe, Ni and Gd). Several other measurements (e.g., by X-ray diffraction, positron lifetime spectroscopy, EPR-spectroscopy, Raman spectroscopy, IR-spectroscopy, the diffusivity, the thermal expansion or the the excess energy stored in nanocrystalline materials), support the results discussed so far. In other words, nanocrystalline materials are not fully characterized in terms of their chemical composition and grain size. Depending on the preparation procedure or the time–temperature history, the atomic arrangements in the interfaces, and hence the properties of nanocrystalline materials vary significantly even if the chemical composition and grain size are identical. In certain nanocrystalline ionic materials (e.g., AgCl, AgBr, TlCl, LiI, β-AgI) space charge effects (MAIER *et al.* [1988]) are expected to play an important role in addition to the grain-boundary core effects discussed so far.

If the crystal size becomes comparable to the Debye length of the space charge region at the boundaries, the electric conductance was observed to be dominated by the electric conductivity of space charge region.

5.5. Nanoglasses

The considerations so far were limited to arrays of nanometer-sized crystallites (fig. 36). However, arguments similar to the ones advanced in § 5.4.1, apply to so-called *nanoglasses* as well. Nanoglasses are solids that are generated by consolidating nanometer-sized glassy spheres (JING *et al.* [1989]). A two-dimensional model of the resulting structure is displayed in fig. 39. The similarity between a nanostructured material composed of nanometer-sized crystallites and nanometer-sized glassy spheres may be apparent. In fact, the nanoglass may be considered as consisting of glassy regions (represented by full circles in fig. 39) joined together by a network of "interfaces" that are represented by open circles. The interfaces are created when the originally free surfaces of the glassy spheres are "welded" together during consolidation. Just as in the case when two crystals of different crystallographic orientations are joined together during consolidation, a region of reduced density and modified nearest-neighbor coordination may be expected to result in the regions where the glassy spheres are joined together. If this is so, a close analogy may be expected to exist between the microstructure of nanocrystalline materials and of nanoglasses. As a matter of fact, such an analogy has been suggested on the basis of studies by Mössbauer spectroscopy

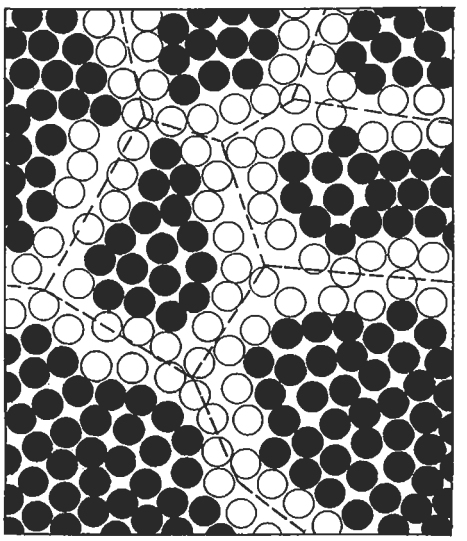

Fig. 39. Schematic (hard-sphere) model of the atomic structure of a nanoglass. The nanoglass is assumed to be generated by consolidating nanometer-sized glassy spheres. The atoms in the interior of the glassy spheres are represented by full circles. The atoms in the interfacial regions between adjacent spheres are drawn as open circles. Both types of atoms are assumed to be chemically identical (GLEITER [1992]).

References: p. 935.

(fig. 40). The quadrupole splitting distribution* of nanocrystalline materials indicates that these materials consist of two components (fig. 40b): The crystalline component and the interfacial one. The crystalline component is characterized by a narrow quadrupole splitting distribution (fig. 40a), whereas the distribution of the interfacial component (fig. 40b) extends over a wide range along the horizontal (QS) axis. By analogy to the

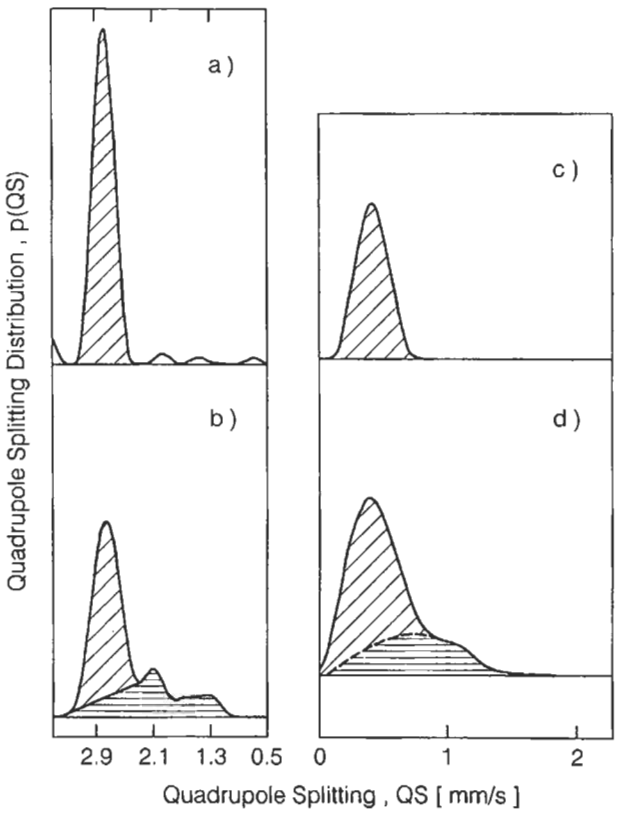

Fig. 40. Comparison of the quadrupole splitting distribution of a single crystal FeF_2 (fig. 40a) and of nanocrystalline FeF_2 (fig. 40b). Right side: Comparison of the quadrupole splitting distribution of a $Pd_{70}Si_{27}Fe_3$ metallic glass produced by melt-spinning (fig. 40c) and in the form of a nanoglass (fig. 40d) produced by consolidating 4 nm-sized glassy spheres. Both glasses had the same chemical composition. The interfacial components in the Mössbauer spectra of the nanocrystalline and nanoglassy materials are the areas hatched horizontally (JING *et al.* [1989]).

* The quadrupole splitting distributions shown in fig. 40 are essentially plots that display the probability, p(QS), that a particular atom is surrounded by nearest neighbors forming arrangements of different degrees of asymmetry. Atoms surrounded by symmetrically arranged nearest neighbors appear on the left side of the QS axis (horizontal axis in fig. 40). The Mössbauer signals of atoms in asymmetric environments appear on the right side of the QS axis.

spectrum of the nanocrystalline material, tbe quadrupole splitting distribution of a nanoglass was found to exhibit the same features (fig. 40d): It consists of a (narrow) glassy (fig. 40c) and an (wide) interfacial component (fig. 40d) as might be expected on the basis of the model suggested (fig. 39).

5.6. Nanocomposites

Nanocomposites are compositionally modulated nanostructured materials. Basically the following three types of microstructures have been revealed experimentally in the case of cluster-assembled materials. (Compositionally modulated layer structures have been treated in section 5.2).

5.6.1. Nanocomposites made up of crystallites with different chemical compositions

Figure 41a displays schematically the expected atomic structure of this kind of a nanocomposite. Examples of real nanocomposites of this type are Fe–Ag nanometer-sized alloys. Although Fe and Ag are immiscible in the crystalline and liquid state, the formation of solid solutions (probably in the interphase boundary regions) was noticed in Fe–Ag nanocomposites. The proposed structure of nanocrystalline Fe–Ag nanocomposites deduced from Mössbauer spectroscopy and X-ray diffraction is shown in fig. 41b. Similar alloying effects were reported for many other nanometer-sized composites produced by one of the methods discussed in section 5.4.2 (cf. SHINGU *et al.* [1989], RADLINSKI and CALKA [1991], OEHRING and BORMANN [1991], MURTY *et al.* [1993]). The formation of metastable nanocrystalline solid solutions and/or amorphous phases during the production process, e.g., by ball-milling seem to depend primarily on the free energy of the phases. A large free energy difference relative to the amorphous phase favors the nanocrystalline structure. Nanocrystalline metastable solid solutions seem to result if these phases have a higher stability than the amorphous phase, as was demonstrated for Nb–Al (OEHRING and BORMANN [1991]). The significance of the interfacial structure between chemically dissimilar and immiscible materials was also emphasized by the results of thermodynamic studies (TURNBULL *et al.* [1990]). A reduction of the melting point and the melting enthalpy of finely dispersed Ge particles in a Sn or Pb matrix was interpreted in terms of a disordered interphase boundary structure between both materials. Remarkable reductions or exchange reactions in the solid state at the interfaces between chemically dissimilar components in nanometer sized materials, e.g., metals and sulfides or oxides have been reported during ball-milling or heavy mechanical deformation (*mechanochemical reactions*). The existing evidence indicates that the newly formed interfaces during milling play a crucial role. The reactivity of newly formed solid/solid interfaces has been demonstrated about two decades ago by co-extruding different materials, e.g., mixtures of metallic and ceramic powders or mixtures of metallic and polymer powders (e.g., Al/Al_2O_3, Al/NaCl or Al/Teflon) (FROMMEYER and WASSERMANN [1976]). In all cases studied, the adhesion between the highly extruded components at the newly formed interphase boundaries was much stronger than the cohesion at interphase boundaries formed during conventional sintering. In order to explain the reactions and/or adhesion, the formation of free radicals,

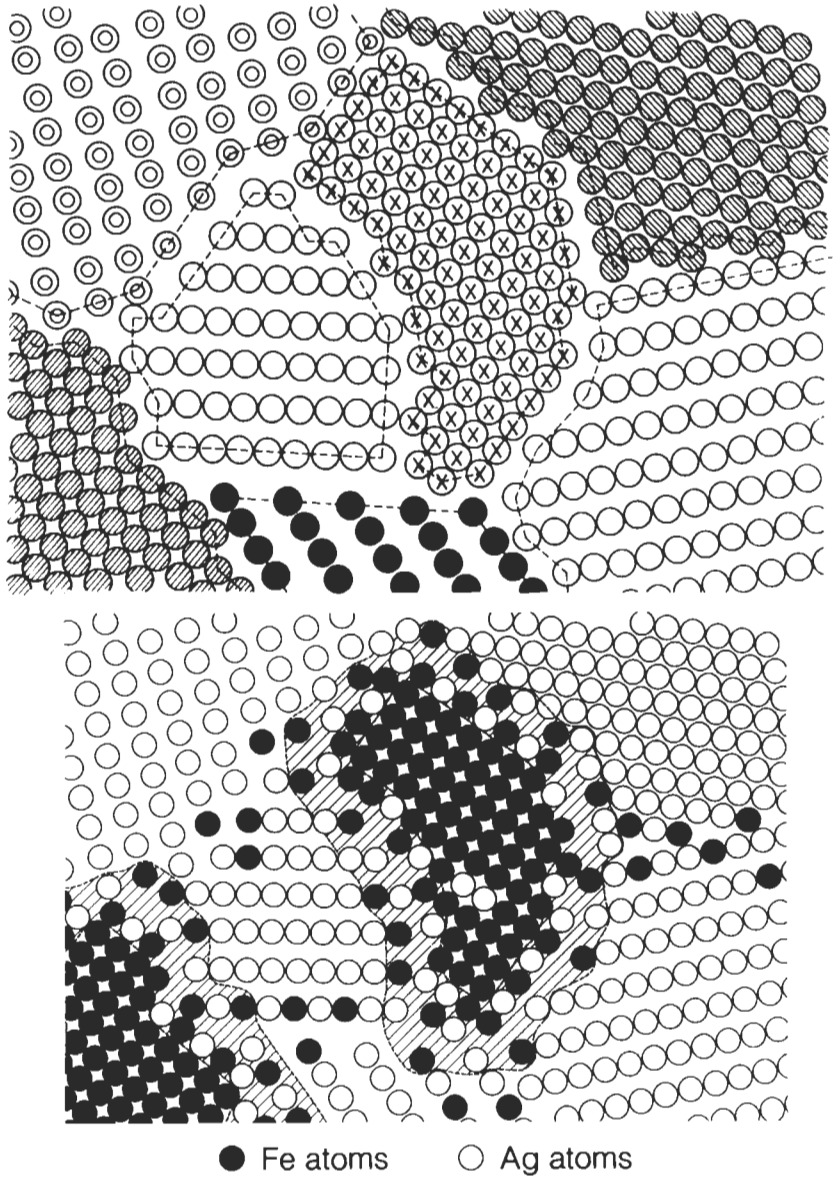

Fig. 41. (a) Schematic (hard sphere) model of a nanocomposite consisting of crystals with different chemical compositions. The chemically different atoms are represented by different symbols (open, closed etc. circles). (b) Schematic model of a nanocrystalline Ag–Fe alloy deduced from Mössbauer spectroscopy. The alloy consisting of a mixture of nanometer-sized Ag and Fe crystals. In the (strained) interfacial regions between Ag and Fe crystals, solid solutions of Fe atoms in Ag, and Ag atoms in Fe are formed although both components are insoluble in the liquid as well as in the solid state. Similar effects may occur in grain boundaries between adjacent Fe and Ag crystals (HERR *et al.* [1990]).

deformed chemical bonds, ions and free electrons at the interfaces has been suggested. Reactions having positive enthalpies or even positive free energies are shown to occur. In fact, mechanochemical reactions seem to open new ways for processing, mining or generating materials avoiding high temperature reactions (CALKA [1993]). Nanocomposites consisting of metallic crystallites embedded in an insulating matrix exhibit interesting electrical properties such as quantum size effects (HENGLEIN [1988], HALPERIN [1986]), large dielectric permittivities as well as ac and dc resistivities. For example, the conductivity of the metallic particles embedded in an insulating matrix has been reported to decrease by several orders of magnitude if the particle size is reduced into the nanometer regime (Size Induced Metal Insulator Transition, MARQUARDT *et al.* [1988]). The physical interpretations of this "SIMIT" effect is still a matter of controversy. Quantum size effects as well as a statistical approach of free electrons in small metallic particles based on a modified Drude model have been proposed.

5.6.2. Nanocomposites made up of crystallites and glassy components with different chemical compositions

An interesting example of this type of nanocomposites are nanometer-sized metallic or semiconductor particles (e.g., Ag, CdS or CdSe) embedded in an amorphous dielectric matrix (e.g., SiO_2) (fig. 42). If the embedded particles are metallic, the plasmon resonance of the particles is broadened (relative to the bulk material) by more than a factor 3. According to Mie's theory, this broadening results from chemical interfacial effects between the metallic clusters and the (dielectric) matrix. Electron mean free path and quantum size effects seem to be of limited significance in the metallic systems studied so far (HÖVEL *et al.* [1993]. This is not so for semiconductor particles. They are found to exhibit quantum size effects (blue-shifted band gap, discrete molecule-like excited electronic states, appearance of interface states in the band gap causing fast non-radiative recombinations, or luminescence with a large Stokes shift). If one encapsulates the embedded nanocrystals in a high-band-gap insulator, then resonances occur at very high energies. The nanocrystalline HOMO and LUMO states remain as confined bulk eigenstates inside the insulator shell. This is the ideal quantum dot case, where surface states are not important in luminescence. For example, CdS has been encapsulated inside a monolayer of $Cd(OH)_2$, CdSe inside ZnS, Si inside SiO_2, etc. More complex structures have recently been made: a three layer "quantum dot quantum well" involving a monolayer of HgS grown on a CdS core and capped with four monolayers of CdS, shows luminescence from the HgS shell monolayer. The conceivable possibilities for generating new optical materials in this way are vast: experimental progress depends critically upon the development of advanced synthetis methods for high-quality materials with closely specified dimensional tolerances.

5.6.3. Nanocomposites with intercalated (doped) grain boundaries

The thickness of the intercalate layers in the cores of the boundaries may vary from less than a monolayer to multilayers. In the case of thin intercalates (less than a monolayer), the atoms of the intercalate seem to enter specific, low energy sites. For example Bi atoms that are incorporated in the boundaries of nanocrystalline Cu, were

References: p. 935.

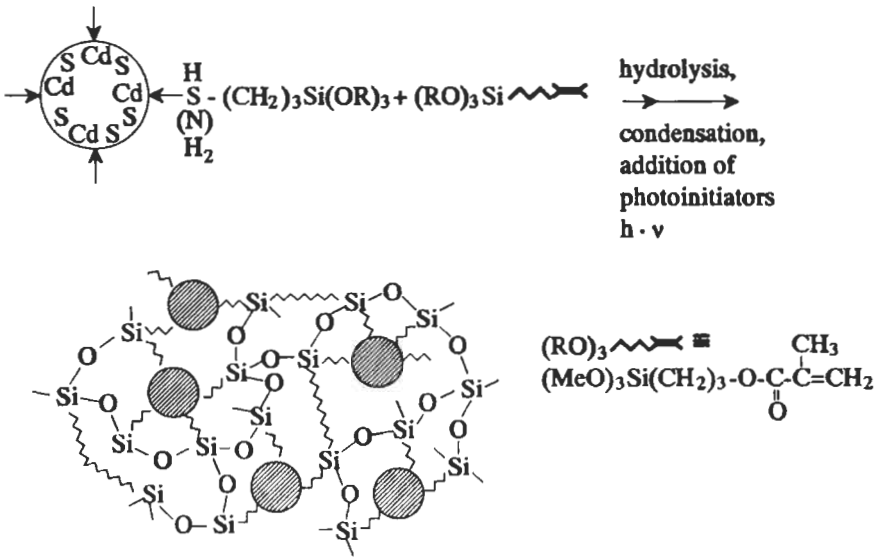

Fig. 42. Reaction and structural model of the incorporation of ligand stabilized CdS quantum dots into ormocer matrices (SCHMIDT [1992]).

found by EXAFS studies (HAUBOLD [1993]) to enter sites that are characterized by three Cu atoms surrounding every Bi atom (fig. 43a). Multilayer intercalate boundary structures (fig. 43b) are apparently less well ordered. For example the structure of Ga in nanocomposites consisting of nanometer-sized W crystals separated by several layers of Ga was found (by PAC measurements) to exhibit a disordered structure. A special case of this type of nanocomposite structures are soft ferromagnetic nanostructured materials generated by partial crystallization of certain metallic glasses (cf. section 5.7.3). Another way in which nanocomposites with doped grain boundaries may be formed has been discussed by TANAKOV *et al.* [1991]. The energy stored in the stress field in the vicinity of grain boundaries may be reduced by a spacial redistribution of the solute atoms. This effect was proposed first by Cottrell for the redistribution of solute atoms in the stress field of a dislocation (Cottrell cloud). Under suitable conditions, the stress-induced solute redistribution in the vicinity of grain boundaries may lead to nanocomposites with solute-enhanced boundary regions. Stress-induced solute segregation to the boundaries may be important for the stability of nanostructured materials against grain growth. Stability against grain growth may be expected if the reduction of the strain energy by removing a solute atom from the lattice of the crystallites is equal or larger than the energy required to bring the solute atom into the boundary core. A potential model system of this kind are nanocrystalline Y-Fe solid solutions. Indeed, little grain growth was noticed in Fe-rich nanocrystalline Y-Fe alloys (WEISMÜLLER *et al.* [1992]). (See also ch. 28, § 4.3).

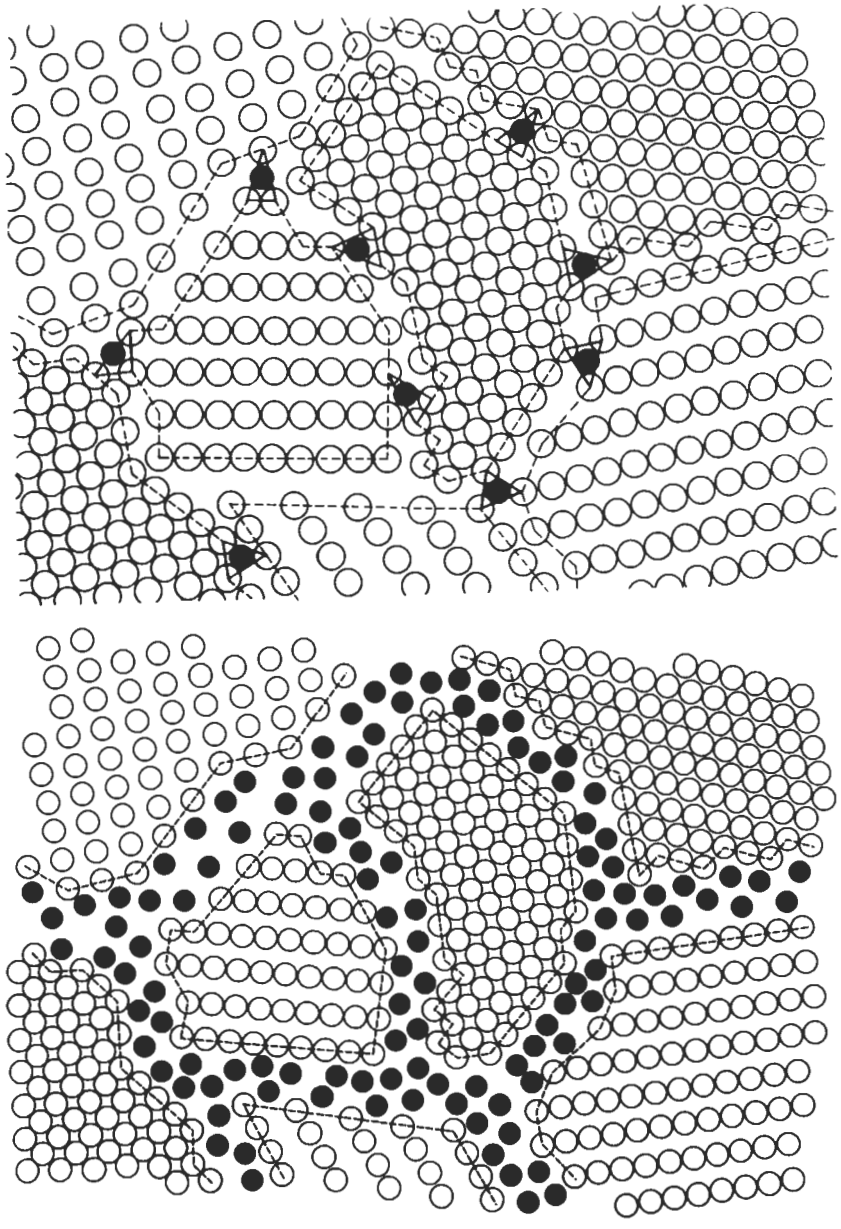

Fig. 43. Two-dimensional model of the atomic structure of a (doped) grain-boundary alloy. The doping atoms (full circles) are confined to the boundary core regions between the nanometer-sized crystals (open circles). In the case of grain boundaries with less than a monolayer of doping atoms (fig. 43a, e.g., Bi in nanocrystalline Cu) the doping atoms occupy specific sites of low energy. If the doping concentration is increased, intercalate structures may result that are more than one monolayer thick, (fig. 43b, e.g., Ga in nanocrystalline W).

References: p. 935.

5.7. Technological applications

Although nanocrystalline materials were proposed just about 15 years ago (MARQUARDT and GLEITER [1980], GLEITER [1981b]), a few technological applications have already emerged.

5.7.1. Hard, wear-resistant nanocrystalline WC–Co materials

Nanostructured WC–Co materials have been commercially generated and are presently applied as protective coatings and cutting tools. Both applications utilize the enhanced hardness, wear resistance and toughness of the nanostructured WC–Co in comparison to the conventional, coarser-grained materials of this kind. As may be seen from figs. 44 and 45, the replacement of coarse-grained WC–Co by nanostructured WC–Co alloys improves the mechanical properties by up to one order of magnitude. This improvement does not seem to be the upper conceivable limit because these new materials are not yet optimized in any way. The nanostructured WC–Co was produced on an industrial scale either by high energy milling (SCHLUMP and WILLBRAND [1992]) or by chemical processing (MCCANDLISH *et al.* [1990]). Chemical processing involves three coordinated steps: preparation and mixing of starting solutions; spray-drying to form chemically homogeneous precursor powders; and, finally, fluid-bed thermochemical conversion of the precursor powders to nanocrystalline WC–Co powders. Both spray-drying and fluid-bed conversion are proven scalable technologies that have been used for producing bulk quantities of cemented carbide powders (KEAR and MCCANDLISH [1993]).

5.7.2. Near net shape forming of nanocrystalline ceramics/intermetallics

The small crystal size of nanocrystalline ceramics suggests that superplastic deformation can occur in these materials at temperatures as low as ambient. This idea (KARCH and BIRRINGER [1990]) has been recently tested for various ceramics as well as metallic nanometer-sized materials. In some of the fine-grained materials, large deformations (100% to > 1000%) were obtained at strain rates in the order of 1/s (e.g., HIGASHI [1993]). Failure occured in ceramic nanocrystalline material preferentially by nucleation, growth and interlinkage of cavities if the specimens were deformed in tension. Superplastic deformation of nanocrystalline materials may be utilized for near net shape forming of brittle materials such as ceramics or intermetallics. Figure 46 reveals the replication of a surface step by low temperature plastic deformation of nanostructured TiO_2. A control experiment was performed with polycrystalline TiO_2 (50 pm grain size) under the same conditions (KARCH and BIRRINGER [1990]). The polycrystalline TiO_2 showed no measurable plastic deformation. The plasticity of nanostructured materials has also been suggested to improve the mechanical properties of non-oxide ceramics such as Si_3N_4 or SiC. These materials exhibit poor high-temperature mechanical properties owing to crack growth and boundary embrittlement which prevent their application in gas-turbines and aerospace technology. Many attempts have been made to solve this problem e.g., by incorporating second-phase particles, platelets or whiskers. The success achieved has been very limited. Hence, it attracted attention when striking improvements were recently reported upon preparing these ceramics in the form of nanocomposites (NIIHARA [1991]).

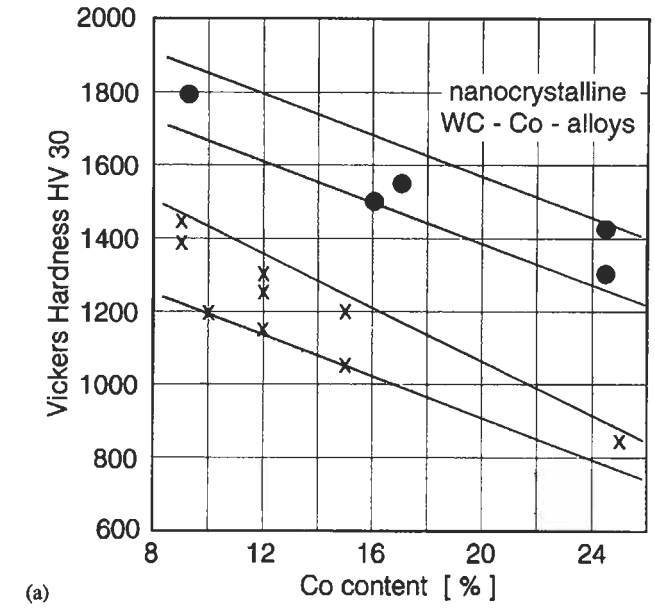

(a)

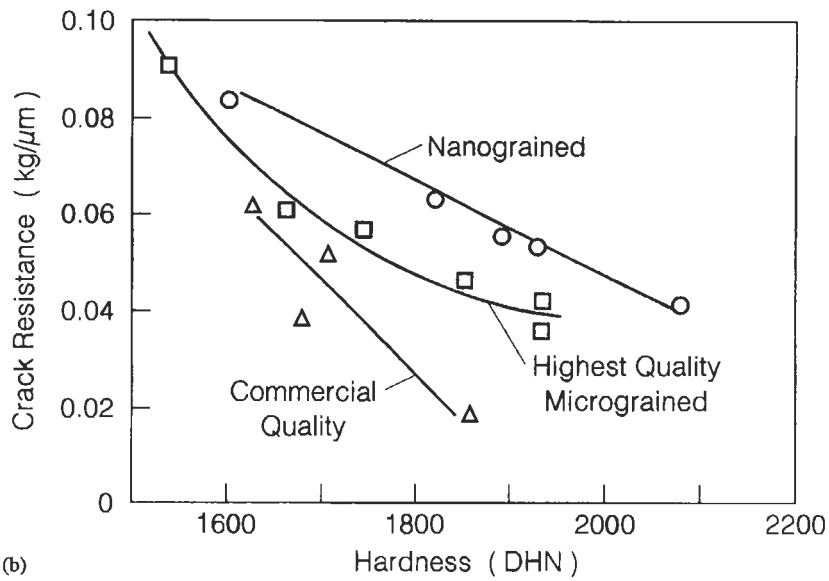

(b)

Fig. 44. (a) Comparison of the Vickers hardness of commercial (crossed lower lines) and nano-crystalline WC–Co alloys (circles, upper lines) as a function of the Co content (SCHLUMP and WILLBRANDT [1992]). (b) Comparison of the crack resistance of nanocrystalline and commercial grades of fully sintered WC–Co materials (KEAR and MCCANDLISH [1993]). In physical terms, the crack resistance measures the mechanical energy required to displace the crack tip by one μm. In other words, the tougher the material the higher is its crack resistance.

References: p. 935.

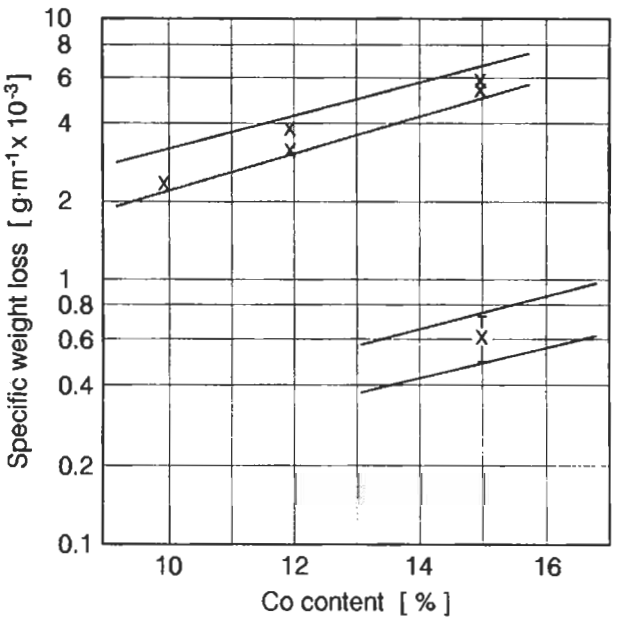

Fig. 45. Comparisons of the measured wear rate (under identical wear conditions) of conventional (upper lines) and nanocrystalline WC–Co alloys as function of the Co content (SCHLUMP and WILLBRAND [1992]). The wear rate was measured by means of the rate of weight loss of the specimens during the wear experiment.

5.7.3. Soft ferromagnetic nanostructured materials ("Finemet")

Partial crystallization of certain metallic glasses with the composition $Fe_{73.5}Si_{13.5}B_9Cu_1Nb_3$ leads to nanometer-sized Fe–Si (B) crystallites (5 to 20 nm diameter) embedded in a residual glassy matrix (YOSHIZAWA *et al.* [1988]). The dopants (Cu, Nb) are found to be accumulated in the non-crystalline regions left between crystallites. The small crystal size is achieved by enhancing the nucleation rate of the crystallites dramatically. In fact, the numerous clusters of Cu atoms formed in the glassy matrix act as nucleation sites. Studies of the magnetic properties of these materials revealed high ($\sim 10^5$) initial permeabilities, low ($\sim 10^{-2}$ A/cm) coercitivities, high saturation induction (up to 1.7 T) combined with a low mean magnetostriction ($\sim 10^{-6}$). These properties are comparable or better than the best values achieved with (the more expensive) permalloys and cobalt-based amorphous magnetic alloys. The attractive magnetic properties of these "Finemet" materials are believed to result from a small mean anisotropy together with a drastically reduced mean magnetostriction and an enhanced saturation magnetization of the crystallites. The small anisotropy is explained in terms of the fact that the magnetic exchange length is larger than the grain size. Therefore, the domain wall width exceeds the size of the grains.

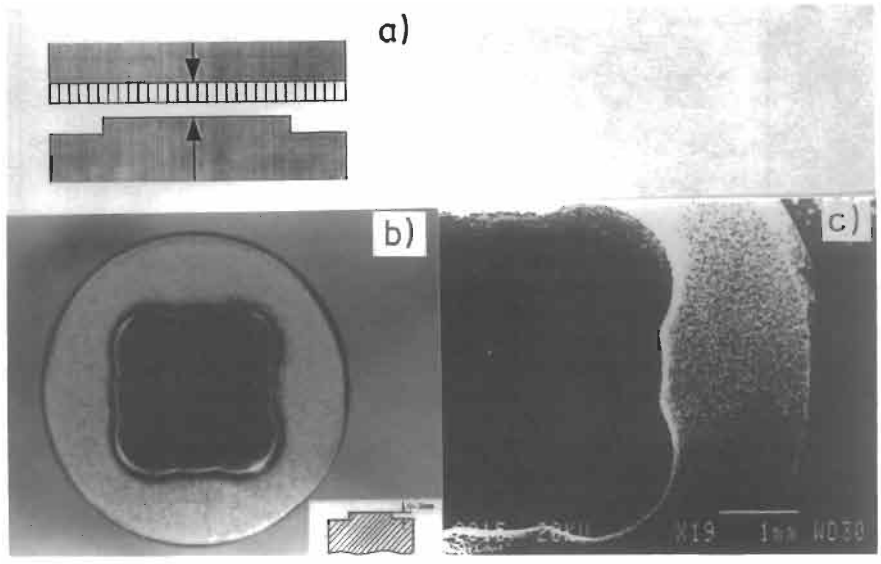

Fig. 46. Replication of a surface step by nanocrystalline TiO2. The experimental arrangement used is drawn in fig. 46a. A nanocrystalline TiO2 pellet is compressed between two WC pistons. The free surface of the lower piston contains a surface step (height 0,3 mm). Fig. 46b shows a top view of the piston with the surface step. Fig. 46c displays the TiO2 pellet which replicated the surface step. The deformation was performed at 800° C over 10 min at a pressure of 1 GPA. (KARCH and BIRRINGER [1990])

5.7.4. Magneto-caloric cooling with nanostructured materials

The magnetic properties of nanostructured materials containing nanometer-sized magnetic particles dispersed in a nonmagnetic matrix differ from those of the corresponding bulk magnetic material. These differences affect the magnetocaloric properties of such materials. Upon the application of an external magnetic field, the magnetic spins in a nanostructured material of this kind tend to align with the field, thereby reducing the entropy of the spin system. If this process is performed adiabatically, the specimen's temperature will rise. This effect is called *magneto-caloric heating.* The incremental temperature rise during magneto-caloric heating, dT, is related to the degree of spin alignment and the magnitude of the magnetic spin moment of the individual particles. Creation of a nanostructured material with many small ferromagnetic regions provides an effectively enhanced magnetic moment which can result (in certain temperature and magnetic field ranges) in an increased dT over that provided by either paramagnetic or ferromagnetic materials, with potential application to magnetic refrigeration. It was shown that efficient magnetic refrigerators may then be operated at hiqher temperatures (above 20 K) and require relatively low magnetic fields (< 5 T) in comparison to magneto-caloric cooling with paramagnetic materials. Figure 47 shows an example for the temperature variation (magneto-caloric cooling and heating) of a nanostructured material due to a varying external magnetic field. The details of how the altered magneto-caloric effect is governed by composition and processing has recently been studied in detail by MCMICHAEL *et al.* [1993].

References: p. 935.

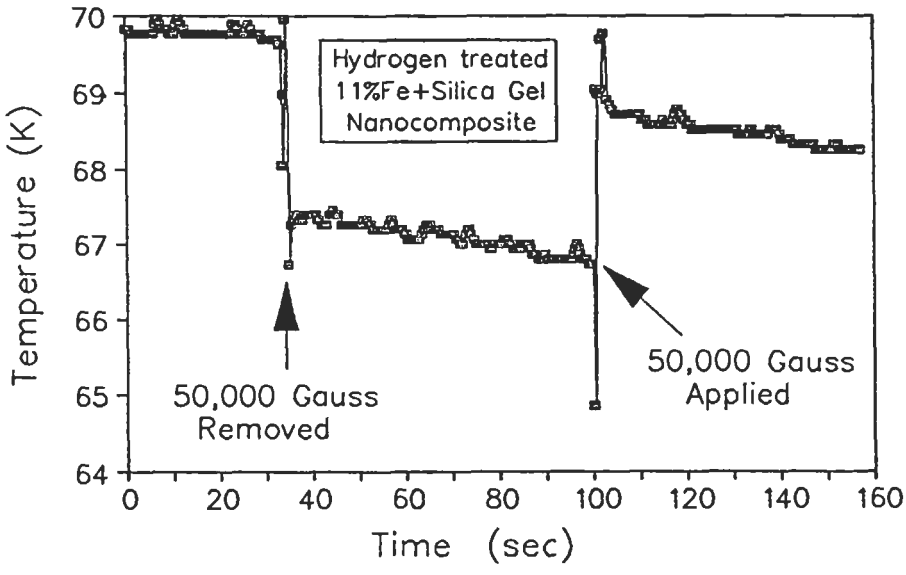

Fig. 47. Temperature vs. time data for a superparamagnetic H_2-treated 11% Fe+silica gel nanocomposite in a 5 Tesla magnetic field. The magnetic field was first removed and then applied to the sample (McMichael *et al.* [1993]).

5.7.5. Nanocrystalline magnetic recording materials

In most video recorders used today, the magnetic material of the record/playback head is usually a crystalline ferrite. These materials are, however, not suitable, when substantially finer details on the magnetic tape are required, e.g., for high-definition television (HDTV) recording. The search for an alternative has resulted in a new type of nanometer-sized magnetic materials: multilayers in which crystalline iron layers of about 10 nm thickness are alternated with even thinner amorphous iron-alloy layers. The chemical composition of the layers used are Fe/FeCrB, NiFe/FeC, FeAl/SiN and FeNbSiB/FeNbSiBN. These nanocrystalline materials combine high saturation magnetization with a high permeability in the MHz frequency range, allowing video recording at much increased information densities (De Wit *et al.* [1991]).

5.7.6. Giant magnetoresistance in nanostructured materials

The recent reports of *giant magnetoresistance* (GMR) in a number of antiferromagnetically coupled multnayer systems have stimulated widespread research activity because the effect is of interest for basic research as well as for technological applications in the area of recording and data storage. Modeling of the GMR has emphasized spin-dependent scattering both within the ferromagnetic layers and at the interfacial regions between the ferromagnetic and non-ferromagnetic layers. The GMR phenomenon is different from the conventional magnetoresistance which is due to the effect of magnetic fields acting directly on the conduction electrons or on the scattering impurities. The GMR in multilayered structures comes from the reorientation of the single-domain

magnetic layers. This is the reason why GMR is not usually seen in conventional bulk magnetic materials. GMR was observed first in both antiferromagnetically coupled and uncoupled layer structures, as a consequence of the fact that the relative orientation of the magnetization of successive ferromagnetic layers changes from antiparallel to parallel in an applied external magnetic field. The change in the magnetization of the layers by the external field reduces the scattering of the conduction electrons travelling through these layers and hence leads to a remarkable change of the dc resistivity of the material. This resistivity change is called GMR (BAIBICH *et al.* [1988]). For systems with uncoupled magnetic layers, the orientation of the magnetization is random at the coercive magnetic field (H_c) and there are many magnetic layers which are statistically arranged antiparallel. If these uncoupled layers are replaced by nanometer-sized particles in a non-magnetic matrix, one may also expect GMR as well. This is indeed the case (fig. 48). The data indicate that a GMR effect in annealed Cu–Co samples is associated with the presence of appropriately sized and spaced Co precipitates in the Cu matrix (BERKOWITZ *et al.* [1992].

5.7.7. Luminescence from porous Si

The recent discovery of visible photoluminescence from porous Si has captured considerable attention (CANHAM [1990], LEHMANN and GÖSELE [1991]). Prepared by electrochemical and chemical etching of single-crystal Si wafers in hydrofluoric acid solutions, porous Si consists of a network of pores that can range in size from micrometers down to a few nanometers. The origin of visible luminescence in porous Si is still controversial. Bulk Si, with a bandgap at 1.12 eV, is weakly luminescent in the near-infrared region of the optical spectrum. For porous Si, the luminescence peak energy can range from 1.12 (infrared) to about 2.3 eV (green light), depending on parameters such as dopant concentration and type, current density during etch, duration of etch, and

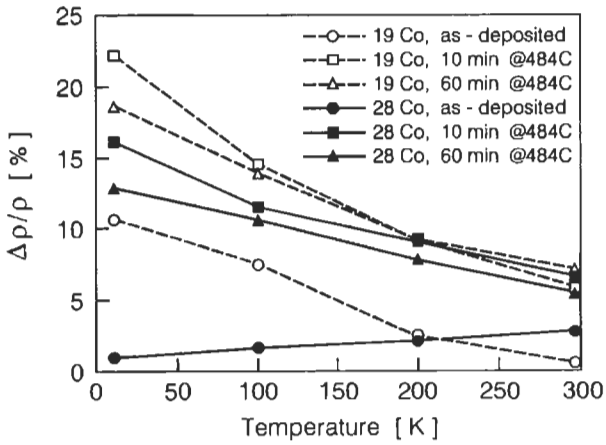

Fig. 48. Temperature dependence of the magnetoresistance ($\Delta\rho/\rho$) for Cu-19 at% and Cu-28 at% Co samples, treated as indicated (BERKOWITZ *et al.* [1992]).

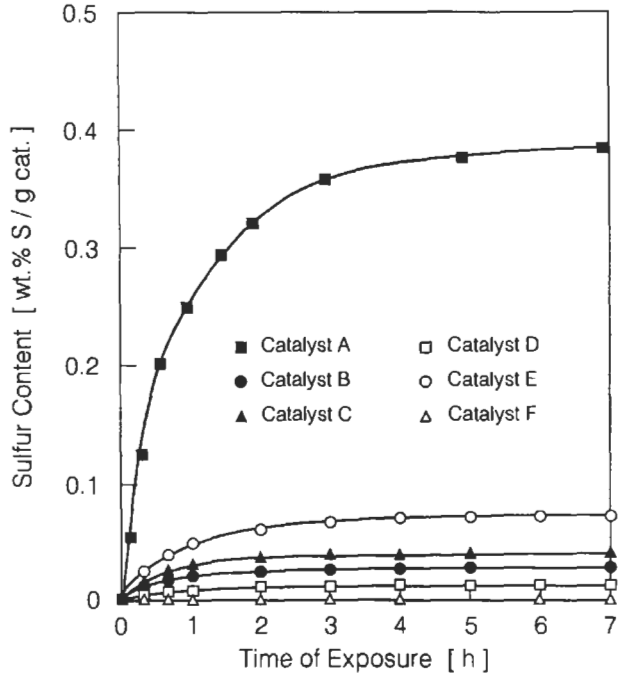

Fig. 49. Activity of nanocrystalline TiO_2 (curve A) for H_2S decomposition as a function of exposure time at 500°C compared with that from several commercial TiO_2 materials and a reference (A: 76 m^2/g nanocrystalline rutile; B: 61 m^2/g anatase; C: 2,4 m^2/g rutile; D: 30 m^2/g anatase; E: 20 m^2/g rutile: F: reference alumina) (BECK and SIEGEL [1992]).

subsequent chemical treatments. These results have been qualitatively explained by invoking size-dependent quantum confinement effects. In fact, transmission electron microscopy (TEM) data support the existence of crystalline Si domains with dimensions small enough (~5 nm) to expect such phenomena. Indeed, recent studies on size-selected, surface-oxidized Si nanocrystals agree well with this idea (WILSON *et al.* [1993]). Another proposed explanation for the luminescence of porous Si is that the electrochemical etch generates surface or bulk chemical species: for example, polysilanes or polysilylenes. Polymers containing only Si and hydrogen are well known as chemicals that can photoluminesce at visible wavelengths. Moreover, siloxene, a chemical which contains Si, oxygen and hydrogen, has emissive properties that are very similar to those of the luminescence of porous Si. Although the current emphasis for utilization of the unique properties of luminescent porous Si is in electroluminescence, other potential applications are beginning to emerge. The high sensitivity of the luminescence to chemical adsorbates, mentioned above, has been found to be readily reversible for a variety of molecules (BAWENDI *et al.* [1992]). This observation may lead to chemical microsensors that are easily incorporated into hybrid Si chips. In addition, photoelectrochemical and ion-irradiation techniques have been developed to allow the resistless

patterning of luminescent porous Si directly onto Si substrates, which may lead to a range of optical display or storage applications (DOAN and SAILOR [1992]).

5.7.8. Catalytic materials

Nanocrystalline cerium oxide, iron carbides and titaniumdioxide have been studied for catalytic applications. The cerium oxide catalysts were generated by inert gas condensation (cf. section 5.4.2), the iron carbides by high-energy milling. Selective catalytic reduction of sulfur dioxide by carbon monoxide on nanocrystalline cerium oxide was investigated in a microreactor, and compared to that of conventional cerium dioxide synthesized by the decomposition of cerium acetate. The nanocrystalline cerium oxide catalyst enabled 100% conversion at 500°C, about 100°C lower than the temperature needed in conventional cerium dioxide catalysts (TSCHOEPE and YING [1994]). The higher activity seems to be related to the oxygen deficiency of the nanocrystalline cerium oxide due to imcomplete oxidation. The nonstoichiometry of the nanocrystalline cerium oxide was confirmed by thermogravimetric analysis and X-ray photoelectron spectroscopy. The iron carbides are found to be active and stable catalysts for CO_2 hydrogenation. The catalytic properties for this reaction appear to be comparable or superior to those of more expensive catalytic materials, such as noble metals dispersed on porous supports. Figure 49 shows the enhanced catalytic activity of nanocrystallite TiO_2 for S removal from H_2S via decomposition compared with commercial (coarser-grained) TiO_2. Obviously, the nanocrystalline sample with a rutile structure was far more reactive than the other ones. Similarly to the enhanced reactivity of nanocrystalline cerium oxide, it was found that the activity of the nanocrystalline TiO_2 results from a combination of features: the high surface area combined with its oxygen deficiency and its rutile structure (BECK and SIEGEL [1992]).

References

AARONSON, H.I., C. LAIRD and K.R. KINSMAN, 1970, Phase Transformations (ASM, Metals Park, Ohio) p. 313.

ABBRUZZESE, G., 1985, Acta Metall. Mater. **33,** 1329.

ABBRUZZESE, G. and K. LÜCKE, 1986, Acta Metall. Mater. **34,** 905.

ABROMEIT, C. and H. WOLLENBERGER, 1988, J. Mat. Res. **3,** 640.

ABROMEIT, C., 1989, J. Modern Phys. **B3,** 1301.

ADAMS, B.L., 1993, Mat. Sci. and Eng. **A166,** 59.

ALLEN, S.M. and J.W. CAHN, 1979, Acta Metall. **27,** 1085.

ANDERSON, A.B., S.P. MEHANDRU and J.L. SMIALEK, 1985, J. Electrochem. Soc. **132,** 1695.

ANDERSON, A.B., C. RAVIMOHAN and S.P. MEHANDRU, 1987, J. Electrochem. Soc. **134,** 1789.

ANDERSON, M.P., D.J. SROLOVITZ, G.S. GREST and P.S. SAHNIG, 1984, Acta Metall. Mater. **32,** 783.

ANTHONY, T.R., 1970, Acta Metall. **18,** 307.

ANTHONY, T.R. and H.E. CLINE, 1973, Acta Metall. **21,** 117.

ANTONIONE, L. BATTEZZATI, A. LUCCI, G. RIONTI and M.C. TABASSO, 1980, J. Mat. Sci. **15,** 1730.

ARANJO, R.D. and S.D. STOOKEY, 1967, Glass Ind. **48,** 687.

ARDELL, A., 1972, Acta Metall. **20,** 601.

ARDELL, A., R.B. NICHOLSON and J.D. ESHELBY, 1966, Acta Metall. **14,** 1295.

ARDELL, A., N. MARDESICH and C. WAGNER, 1979, Acta Metall. **27,** 1261.

ARUNACHALAM, V. S. and R. W. CAHN, 1970, In: Proc. 3rd Bolton Landing Conf., eds. B. Kear, C. Sims and N. S. Stoloff (Claitor's Publ. Div., Baton Rouge, LA) p. 215.
ASHBY, M. F., F. SPAEPEN and S. WILLIAMS, 1978, Acta Metall. **26,** 1647.
AUBAUER, H. P., 1972, Acta Metall. **20,** 165.
AUST, K. T., 1981, Structure and Properties of Grain Boundaries, in: Chalmers Anniversary Volume, Prog. Mater. Sci., eds. J. W. Christian, P. Haasen and T. B. Massalski (Pergamon Press, Oxford) p. 27.
BACKHAUS-RICOULT, M. and H. SCHMALZRIED, 1985, Ber. Bunsengesellsch. Phys. Chem. **89,** 1323.
BACON, R. and FANELLI, 1943, J. Am. Chem. Soc. **65,** 639.
BAIBICH, M. N, J. M. BROTO, A. FERT, F. NGUYEN VAN DAU, F. PETROFF, P. ETIENNE, G. CREUZET, A. FRIEDRICH and J. CHAZELAS, 1988, Phys. Rev. Lett. **61,** 2472.
BAKONYI, I., E. TOTH-KADAR, T. TARNOCI, L. K. VARGA, A. CZIRAKI, I. GEROECS and B. FOGARASSY, 1993, Nanostructured Materials **3,** 155.
BALLUFFI, R. W., 1980, Grain Boundary Structure and Kinetics (ASM, Metals Park, OH).
BARNES, R. S., G. B. REDDINS and A. H. COTTRELL, 1958, Phil. Mag. **3,** 97.
BAWENDI, M. G., P. J. CAROLL, W. L. WILSON and L. E. BRUS, 1992, J. Chem. Phys. **96,** 946.
BECK, D. D. and R. W. SIEGEL, 1992, J. Mat. Res. **7,** 2840.
BECK, P. A., 1954, Phil. Mag. **3,** 245.
BEERÉ, W., 1978, Phil. Mag. **A38,** 691.
BERKOWITZ, A. E., J. R. MITCHELL, M. J. CAREY, A. P. YOUNG, S. ZHANG, F. E. SPADA, F. T, . PARKER, A. HUTTEN and G. THOMAS, 1992, Phys. Rev. Letters **68,** 3745.
BHATTACHARYA, S. K. and K. C. RUSSELL, 1976, Metallurg. Trans **7A,** 453.
BIRKENBEIL, H. J. and R. W. CAHN, 1962, Proc. Phys. Soc. **79,** 831.
BIRRINGER, R., 1989, Mater. Sci and Eng. **A117,** 33.
BISHOP, G. H. and B. CHALMERS, 1968, Scripta Metall. **2,** 133.
BJORKLUND, S., L. DONASHEY and M. HILLERT, 1972, Acta Metall. **20,** 867.
BLEIBERG, M. L. and J. W. BENNET, 1977, in: Radiation Effects in Breeder Reactor Structural Materials (Met. Soc. AIME, Warrendale, PA) p. 211.
BLOECHL, P., G. P. DAS, H. F. FISCHMEISTER and U. SCHOENBERGER, 1990: Metal-Ceramic Interfaces, eds. M. Rühle, A. G. Evans, M. F. Ashby and J. P. Hirth (Pergamon Press, Oxford) p. 2.
BOLLMANN, W., 1970, Crystal Defects and Crystal Interfaces (Springer, Berlin).
BOLLMANN, W., 1974, Phys. Stat. Solidi **21,** 543.
BOYD, A. and R. B. NICHOLSON, 1971, Acta Metall. **19,** 1370.
BRANDON, D. G., B. RALPH, S. RANGANATHAN and M. S. WALD, 1964, Acta Metall. **12,** 813.
BRICKENKAMP, W. and K. LÜCKE, 1983, Ph. D. Thesis RWTH Aachen.
BURGER, M., W. MADER and M. RÜHLE, 1987, Ultramicroscopy **12,** 1.
CAHN, J. W. and J. E. HILLIARD, 1958, J. Chem. Phys. **28,** 258.
CAHN, R. W., 1994, Springer Series in Materials Science **27,** 179, Springer Verlag Berlin.
CALKA, A., 1993, Proceedings of the 122 TMS Annual Meeting and Exhibition, Denver Col., USA, 21-25 February 1993, TMS Commonwealth Drive Warrandale, PA 15086 USA, p. B 63.
CANHAM, L. T., 1990, Appl. Phys. Lett. **57,** 1046.
CAR, R. and M. PARINELLO, 1985, Phys. Rev. Letters **55,** 2471.
CHADDERTON, L. T., E. JOHNSON and T. WOHLENBERG, 1976, Comm. Solid State Phys. **VII, 5,** 105.
CHAKRAVORTY, D., 1992, New Materials, eds. J. K. Joshi, T. Tsuruta, C. N. R. Rao and S. Nagakura, Narosa Publishing House, New Dehli, India, p. 170.
CHALMERS, B. and H. GLEITER, 1971, Phil. Mag. **23,** 1541.
CHATTERJEE, A. and D. CHAKRAVORTY, 1989, J. Phys. D: Appl. Phys. **22,** 1386.
CHANG, R., 1976, Scripta Metall. **10,** 861.
CHEN, H. S. and S. Y. CHANG, 1974, Phys. Stat. Sol. **25,** 581.
CLINE, H., 1971, Acta Metall. **19,** 481.
COOPER, S. P. and J. BILLINGHAM, 1980, Met. Sci. J. **14,** 225.
COTTERILL, R. M. J ., 1979, Phys. Rev. Lett. **42,** 1541.
CULLITY, B. D., 1972, Introduction to Magnetic Materials (Addison-Wesley, London) p. 357 and 565.
DAVIS, C. K., P. NASH and R. STEVENS, 1980a, Acta Metall. **28,** 179.

DAVIS, J.R., T.A. COURTNEY and M.A. PRZYSTUPA, 1980b, Metallurg. Trans. **11A,** 323.
DE FONTAINE, D., 1973, Scripta Metall. **7,** 463.
DELAEY, L. and H. WARLIMONT, 1975, in: Shape Memory Effects in Alloys, ed. J. Perkins, Plenum, New York, p. 89.
DE RANGO, P., M. LEES, P. LEJAY, A. SULPICE, R. TOURNIER, M. INGOLD, P. GERNIE and M. PERNET, 1991, Nature **349,** 770.
DE WIT, H. J, C.H. M WITTMER and F.W.A. DIRNE, 1991, Advanced Materials **3,** 356.
DOAN, V.V. and M.J. SAILOR, 1992, J. Appl. Phys. **60,** 619.
DOHERTY, P.E., D.W. LEE and R.S. DAVIS, 1967, J. Am. Ceram. Soc. **50,** 77.
DOHERTY, R.D., 1982, Met. Sci. J. **16,** 1.
DUFFY, D.M., J.H. HARDING and A.M. STONEHAM, 1992, Acta Metal. Mater. **40,** 11.
EDWARDS, S.F. and M. WARNER, 1979, Phil. Mag. **40,** 257.
EISENBERGER, P. and W.C. MARRA, 1981, Phys. Rev. Lett. **46,** 1081.
ERB, U., W. ABEL and H. GLEITER, 1982, Scripta Metall. **16,** 1317.
ERB, U., A.M. EL-SHERIK, G. PALUMBO and K.T. AUST, 1993, Nanostructured Materials **2,** 383.
ESTRIN, Y. and K. LÜCKE, 1982, Acta Metall. **30,** 983.
EVANS, J.H., 1971, Nature **229,** 403.
FECHT, H.J. and H. GLEITER, 1985, Acta Metall. Mater. **33,** 557.
FERRANTE, M. and R.D. DOHERTY, 1979, Acta Metall. **27,** 1979.
FERRY, D.K., J.R. BAKER and C. JACOBINI, 1990, Granular Nanoelectronics NATO Advanced Study Series, Series B: Physics, Vol. **251.**
FINNIS, M., A.M. STONEHAM and P.W. TASKER, 1990, Metal-Ceramic Interfaces, eds. M. Ruhle, A.G. Evans, M.F. Ashby and J.P. Hirth, Pergamon Press Oxford, p. 35.
FINNIS, M.W. and M. RÜHLE, 1991, Structure of Interfaces in Crystalline Solids, in: Structure of Solids, ed. V. Gerold, Vol. 1 of Materials Science and Technology, eds. R.W. Cahn, P. Haasen and E.J. Kramer (VCH, Weinheim), p. 553.
FINNIS, M., 1992, Acta Metall. Mater. **40,** 25.
FITZSIMMONS, M.R. and S.L. SASS, 1988, Acta Metall. **36,** 3103.
FREEMAN, A.J., C. LI and C.L. FU, 1990, Metal-Ceramic Interfaces, eds. M. Rühle, A.G. Evans, M.F. Ashby and J.P. Hirth, Pergamon Press Oxford, p. 2.
FROMMEYER, G. and G. WASSERMANN, 1976, Zeitschrift für Werkstofftechnik **7,** 129, 136 and 154.
GASTALDI, J. and J. JOURDAN, 1979, Phys. Stat. Sol. (a) **52,** 139.
GAUDIG, W. and H. WARLIMONT, 1969, Z. Metallk. **60,** 488.
GARRIDO, L., J.L. ACKERMANN and J.E. MARK, 1990, Mat. Res. Soc. Sympos. Proceedings **171,** 65.
GEGUZIN, Ya.E. and M.A. KRIVOGLAZ, 1973, Migration of Microscopic Inclusions in Solids (Consultants' Bureau, NewYork) p. 157.
GERTSMAN, V., A.A. NAZAROV, A.E. ROMANOV, R.Z. VALIEV and V.I. VLADIMIROV, 1989, Phil. Mag. **A59,** 1113.
GLEITER, H., 1971, Phys. Stat. Sol. (b) **45,** 9.
GLEITER, H., 1979, Acta Metall. **27,** 1754.
GLEITER, H., 1981a, Chalmers Anniversary Volume, Prog. Mater. Sci., eds. J.W. Christian, P. Haasen and T. B. Massalski (Pergamon Press, Oxford).
GLEITER, H., 1981b, Proceedings Second Risø International Symposium on Metallurgy and Materials Science, eds. N. Hansen, T. Leffers and H. Lilholt, Røskilde, Denmark, p. 15.
GLEITER, H., 1982, Mater. Sci. Eng. **52,** 91.
GLEITER, H., 1989, Progress Materials Science, eds. J.W. Christian, P. Haasen and T.P. Massalski, Vol. **33** (4), 223.
GLEITER, H., 1992, Nanostructured Materials **1,** 1.
GLEITER, H., 1995, Nanostructured Materials **6,** 3.
GLEITER, H. and B. CHALMERS, 1972, Prog. Mater. Sci. **16,** 145.
GLEITER, H., S. MAHAJAN and K.J. BACHMANN, 1980, Acta Metall. **28,** 1603.
GORLIK, S.S., L. KOVALEVA and M. BLAUTER, 1972, Fiz. Met. Metalloved. **33(3),** 658.
GOTTSCHALK, C., K. SMIDODA and H. GLEITER, 1980, Acta Metall. **28,** 1653.

GRAHAM, L. D. and R. W. KRAFT, 1966, Metallurg. Trans. **236,** 94.
GRATIAS, D. and A. THALAL, 1988, Phil. Mag. Letters **57,** 63.
GREENWOOD, G. W., 1956, Acta Metall. **4,** 243.
GREENWOOD, G. W., H. JONES and J. H. WESTBROOK, 1975, Phil. Mag. **31,** 39.
GULDEN, M. E., 1969, J. Nucl. Mater. **30,** 30.
GUYOT, C. and M. WINTENBERGER, 1974, J. Mater. Sci. **9,** 614.
HAESSNER, F., S. HOFFMANN and H. SEKEL, 1974, Scripta Metall. **8,** 299.
HAHN, W., 1994, private communication.
HAKEN, H., 1978, Synergetics, (Springer Verlag), Berlin.
HALPERIN, W. P., 1986, Rev. Mod. Phys. **58,** 566.
HARASE, J., R. SHIMIZU and T. WATANABE, 1988, Eighth Int. Conf. on Textures in Metals, eds.: J. S. Kallend and G. Gottstein, The Metallurgical Society, Warrendale, PA, p. 723.
HASEEB, A., B. BLANPAIN, G. WONTERS, J. P. CELIS and J. R. Roos, 1993, Mater. Sci. and Eng. **A168,** 137.
HAUBOLD, T., 1993, Acta Metall. et Mater. **41,** 1769.
HENDERSON, D., W. JOST and M. MCLEAN, 1978, Met. Sci. J. **12,** 113.
HENGLEIN, A., 1988, Topics in Current Chemistry, (Springer Verlag, Berlin), Vol. **143,** p. 113.
HERR, U., J. JING, U. GONSER and H. GLEITER, 1990, Solid State Comm. **76,** 197.
HERRING, C., 1950, J. Appl. Phys. **21,** 301.
HERRING, C., 1953, Structure and Properties of Solid Surfaces, eds. R. Gomer and C. S. Smith, (University of Chicago Press), Chicago, p. 4.
HERRMANN, G., H. GLEITER and G. BAERO, 1976, Acta Metall. **24,** 353.
HIGASHI, K., 1993, Mater. Sci. and Eng. **A166,** 109.
HILLERT, M., 1965, Acta Metall. **13,** 227.
HIRABAYASHI, M., 1959, J. Phys. Soc. Jap. **14,** 149.
HIRAGA, K., 1973, Phil. Mag. **27,** 1301.
HO, P. and C. G. WEATHERLY, 1975, Acta Metall. **23,** 1451.
HO, P. S. and J. K. KIRKWOOD, 1974, J. Appl. Phys. **45,** 3229.
HOEVEL, H., S. FRITZ, A. HILGER, U. KREIBIG and M. VOLLMER, 1993, Phys. Rev. **B48,** 18178.
HOLZ, A., 1979, Physica 97, **A75.**
HONDROS, E. D., 1993, Mater. Sci. and Eng. **A166,** 1.
HORNBOGEN, E. and U. KÖSTER, 1982, Recrystallization of Metallic Materials, ed. F. Haessner (Riederer Verlag, Stuttgart) p. 159.
HORNBOGEN, E., 1984, Acta metall. mater. **32,** 615.
HORNBOGEN, E., 1986, J. Mater. Sci. **21,** 3737.
HORNBOGEN, E., 1989, Internat. Materials Rev. **34,** 277.
HOUGHTON, D. C. and D. JONES, 1978, Acta Metall. **26,** 695.
HUNDERI, O. and N. RYUM, 1979, Acta Metall. Mater. **27,** 161.
HUNDERI, O. and N. RYUM, 1981, Acta Metall. Mater. **29,** 1737.
JAIN, S. C. and A. E. HUGHES, 1978, J. Mater. Sci. **13,** 1611.
JANG, H., D. N. SEIDMAN and K. L. MERKLE, 1993, Interface Science, **1,** 61.
JING, J., A. KRAEMER, R. BIRRINGER, H. GLEITER and U. GONSER, 1989, J. Non-Cryst. Solids, **113,** 167.
JOHNSON, K. H. and S. V. PEPPER, 1982, J. Appl. Phys. **53,** 6634.
JOHNSON, R. A. and M. G. LAM, 1976, Phys. Rev. **B13,** 434.
JOHNSON, W. C. and J. K. LEE, 1979, Metallurg. Trans. **10A,** 1141.
JOHNSON, W. C., 1984, Acta Metall. Mater. **32,** 465.
JOHNSON, W. C. and J. I. D. ALEXANDER, 1986, J. Appl. Phys. **59,** 2735.
JONES, D. R. and G. J. MAY, 1975, Acta Metall. **23,** 29.
JUNG, P. and K. TRENZINGER, 1974, Acta Metall. **22,** 123.
KAHLWEIT, H., 1975, Adv. Colloid and Interface Sci. **5,** 1.
KARCH, J. and R. BIRRINGER, 1990, Ceramics International **16,** 291.
KEAR, B. H. and L. E. MCCANDLISH, 1993, Nanostructured Materials **3,** 19.
KHATCHATURYAN, A. G., 1969, Phys. Stat. Sol. **35,** 119.
KHATCHATURYAN, A. and G. SHATALOV, 1969, Sov. Phys. Solid State JETP **11,** 118.

KING, A. H., 1993, Materials Science Forum **126–128,** 221.
KIRCHNER, H., 1971, Metallurg. Trans. **3,** 2861.
KIRK, W. P. and M. A. REED, 1992, Nanostructures and Mesoscopic Systems, Proceedings of an International Symposium held at Santa Fe, New Mexico 20–24 May 1991, (Academic Press, Boston, San Diego, New York), p. 1.
KOHN, W. and L. J. SHAM, 1965, Phys. Rev. **140,** A1133.
KRONBERG, M. L. and F. H. WILSON, 1949, Trans. AIME **185,** 501.
KUHLMANN-WILSDORF, D., 1965, Phys. Rev. **140,** A1599.
KUNC, M. and R. M. MARTIN, 1981, Phys. Rev. **B24,** 3445.
LANGER, J. S. and R. SEKERKA, 1975, Acta Metall. **23,** 1225.
LARCHE, F. C. and J. W. CAHN, 1973, Acta Metall. Mater. **21,** 1051.
LARCHE, F. C. and J. W. CAHN, 1978, Acta Metall. Mater. **26,** 1579.
LEHMANN, V. and U. GÖSELE, 1991, Appl. Phys. Lett. **58,** 856.
LEMMLEIN, G. G., 1952, Dokl. Adad. Neuk SSSR **85,** 325.
LI, J. C. M., 1961, J. Appl. Phys. **32,** 525.
LI, J . C. M ., 1969, Trans. Met. Soc. AIME **245,** 1591.
LIFSHITZ, I. M. and V. V. SLYOZOV, 1961, J. Phys. Chem. Solids **19,** 35.
LIVINGSTON, J. D., 1971, J. Mater. Sci. **7,** 61.
LIVINGSTON, J. D. and J. W. CAHN, 1974, Acta Metall. **22,** 495.
LOEFFLER, J., J. WEISMUELLER and H. GLEITER, 1995, Nanostructured Materials **6,** 567.
LORIMER, G. W. and R. B. NICHOLSON, 1969, Acta Metall. **13,** 109.
LORMAND, G., J. ROUAIS and C. EYRAND, 1974, Acta Metall. **22,** 793.
LOUAT, N. P., 1974, Acta Metall. **22,** 721.
LOUIE, S. G. and M. L. COHEN, 1976, Phys. Rev. **B13,** 2461.
LOUIE, S. G., J. G. CHELIKOWSKY and M. L. COHEN, 1977, Phys. Rev. **B15,** 2154.
LU, K., J. T. WANG and W. D. WEI, 1991, J. Appl. Phys. **69,** 522.
MAC DOWELL, J. F. and G. H. BEALL, 1969, J. Am. Ceram. Soc. **52,** 117.
MAIER, J., S. PRILL and B. REICHERT, 1988, Solid State Ionics **28–30,** 1465.
MANTHIRAM, A., D. L. BOURELL and H. L. MARCUS, 1993, Journal of Metals **11,** November 1993, 67.
MARQUARDT, P., G. NIMTZ and B. MUEHLSCHLEGEL, 1988, Solid State Comm. **65,** 539.
MARQUARDT, P. and H. GLEITER, 1980, Verhandlungen der Deutsch. Physikal. Gesellsch. **15,** 328.
MARRA, W. C., P. EISENBERGER and A. Y. CHO, 1979, J. Appl. Phys. **50,** 6927.
MARTIN, G. and L. P. KUBIN, 1988, editors, Nonlinear Phenomena in Materials Science, Vols. 3 and 4 of Solid State Phenomena (Trans. Tech. Aedermannsdorf, Switzerland).
MARTIN, J. W. and R. D. DOHERTY, 1976, Stability of Microstructure in Metallic Systems (Cambridge University Press) p. 154. (Second edition, 1996, in press).
MARTUSCELLI, E., R. PALUMBO and M. KRYSZEWSKI, 1980, Polymer Blends, Plenum Press, NewYork, p. 1.
MASAMURA, R. A. and M. E. GLICKSMAN, 1974, Can. Met. Quest. **13,** 43.
MAURER, R. and H. GLEITER, 1985, Scripta Metall. **19,** 1009.
MAURER, R. D., 1956, J. Chem. Phys. **25,** 1206.
MAURER, R. D., 1959, J. Chem. Phys. **31,** 244.
MAY, J. E. and D. TURNBULL, 1958, Trans. Metall. Soc. AIMF **212,** 769.
MAYO, M. J. and D. C. HAGUE, 1993, Nanostructured Materials **3,** 43.
MCCANDLISH, L. E., B. H. KEAR and B. K. KIM, 1990, Materials Science and Technology, **6,** 953.
MCLEAN, M., 1973, Phil. Mag. **27,** 1235.
MCLEAN, M ., 1978, Met. Sci. J. **12,** 113.
MCLEAN, M., 1982, Met. Sci. J. **16,** 31.
MCMAHON G., 1994, Ph. D. Thesis Universität des Saarlandes, FB 15, 66041 Saarbruecken, Germany.
MCMICHAEL, R. D., R. D. SHULL, L. H. BENNETT, C. D. FUERST and J. F. HERBST, 1993, Nanostructured Materials **2,** 277.
MENDEZ, E. E. and K. VON KLITZING, 1989, Physics and Applications of Quantum Wells and Superlattices, NATO Advanced Studies Series, Series B: Physics, Vol. **170.**
MERKLE, K. L., J. F. REDDY, C. L. WILEY and D. J. SMITH, 1987, Phys. Rev. Letters **59,** 2887.

MIGAZAKI, T., K. NAKAMURA and H. MORI, 1979, J. Mater. Sci. **14,** 1827.
MORI, T., P. CHENG, M. KATO and T. MURA, 1978, Acta Metall. **26,** 1435.
MORRALL, J. E. and N. P. LOUAT, 1974, Scripta Metall. **8,** 91.
MULLINS, W. W., 1956, Acta Metall. **4,** 421.
MURTY, B. S., M. M. RAO and S. RANGANATHAN, 1993, Nanostructured Materials **3,** 459.
NES, E., 1974, Acta Metall. **22,** 81.
NEUHAEUSER, H. J. and W. PITSCH, 1971, Z. Metalik. **62,** 792.
NICHOLS, F. A., 1976, J. Mater. Sci. **11,** 1077.
NICOLIS, G. and I. PRIGOGINE, 1977, Self Organization in Non-Equilibrium Systems, Wiley-Interscience New York.
NIIHARA, K., 1991, J. Ceram. Soc. Japan, **99,** 974.
OEHRING, M., Z. H. YAN, T. KLASSEN and R. BORMANN, 1992, phys. stat. solidi **(a)131,** 671.
OEHRING, M. and R. BORMANN, 1991, Mater. Sci. and Eng. **A134,** 1330.
ORIANI, R. A., 1964, Acta Metall. **12,** 1399.
OSMOLA, D., P. NOLAN, U. ERB, G. PALUMBO and K. T. AUST, 1992, phys. stat. sol. **(a)131,** 569.
OZAWA, T. and Y. ISHIDA, 1977, Scripta Metall. **11,** 835.
OZIN, G. A., 1992, Advanced Materials **4,** 612.
PALUMBO, G., P. J. KING, K. T. AUST, U. ERB and P. C. LICHTENBERGER, 1991a, Scripta Metall. **25,** 1775.
PALUMBO, G., D. M. DOYLE, A. M. EL-SHERIK, U. ERB and K. T. AUST, 1991b, Scripta Metall. et Mater. **25,** 679.
PASHLEY, D. W., M. H. JAKOBS and J. T. VIETZ, 1967, Phil. Mag. **16,** 51.
PAUL, A., 1975, J. Mat. Sci. **10,** 415.
PAYNE, M. C., P. D. BRISTOWE and J. D. JOANNOPOULOS, 1985, Phys. Rev. Lett. **58,** 1348.
PERKOVIC, V., C. R. PURDY and L. M. BROWN, 1979, Acta Metall. **27,** 1075.
PETERMANN, J., 1991, Bulletin of the Institute of Chemical Research, Kyoto University **69,** 84.
PHILLPOT, S. R., D. WOLF and S. YIP, 1990, MRS Bulletin **11,** 38.
POIRIER, J. and J. M. DUPOUY, 1979, Proc. Int. Conf. on Irradiation Behaviour of Metallic Materials for Reactor Core Compounds, Ajaccio, Corsica (publ. by CEA-DMCEN, 91190, Gif-sur-Yvette, France).
POND, R. C. and V. VITEK, 1977, Proc. Roy. Soc. **A357,** 453.
POND, R. C., D. SMITH and V. VITEK, 1978, Scripta Metall. **12,** 699.
PONTIKIS, V., 1988, J. Physique **49,** C5–327.
POTAPOV, L. P., B. F. GLOWIN and P. H. SHIRYAEV, 1971, Fiz. Met. Metalloved. **32,** 227.
POWELL, R. E. and H. EYRING, 1943, J. Am. Ceram. Soc. **65,** 648.
RADLINSKI, A. P. and A. CALKA, 1991, Mater. Sci. and Eng. **A134,** 1376.
RAHMAN, A., 1977, Correlation Functions and Quasiparticle Interactions in Condensed Matter, NATO Adv. Stud. Ser. **35,** Plenum Press, New York, p. 37.
RAYLEIGH, LORD, 1878, Proc. Lond. Math. Soc. **10,** 4.
READ, W. T. and W. SHOCKLEY, 1950, Phys. Rev. **78,** 275.
RIVIER, N., 1986, J. Physique **47,** C3–299.
ROGERS, J. T., H. M. FLOWERS and R. RAWLINGS, 1975, Met. Sci. **9,** 32.
ROY, R., 1972, Advances in Nucleation and Crystallization in Glasses, eds. L. L. Heck and S. Freiman, Am. Cer. Soc., Columbus, Ohio, USA, p. 57.
RÜHLE, M., K. BURGER and W. MADER, 1986, J. Microsc. Spectr. Electron. **11,** 163.
RÜHLE, M., M. BACKHAUS-RICOULT, K. BURGER and W. MADER, 1987, Ceramic Microstructure, Plenum Press New York, p. 295.
RÜHLE, M. and A. G. EVANS, 1989, Mater. Sci. and Eng. **A107,** 187.
RÜHLE, M., A. H. HEUER, A. G. EVANS and M. F. ASHBY, 1992, Proc. Internat. Symp. on Metal-Ceram. Interfaces, Acta metall. mater. **40,** 1.
RYAZANOV, A. I. and L. A. MAXIMOV, 1981, Rad. Effects **55,** 165.
SASS, S. L., 1980, J. Appl. Cryst. **13,** 109.
SASS, S. L. and P. D. BRISTOWE, 1980, Grain Boundary Structure and Kinetics, eds. R. W. Balluffi, Metals Park Ohio, American Metals Soc., p. 71.
SAUTHOFF, G., 1976, Scripta Metall. **10,** 557.

SCHLUMP, W. and J. WILLBRAND, 1992, VDI Nachrichten **917,** 23.
SCHMIDT, G., 1992, Mat. Res. Soc. Sympos. Proceedings **274,** 121.
SCHONBERGER, U., O. K. ANDERSON and M. METHFESSEL, 1992, Acta Metall. Mater. **40,** 1.
SEEGER, A. and G. SCHOTTKY, 1959, Acta Metall. **7,** 495.
SHINGU, P. H, B. HUANG, J. KUYAMA, K. N. ISHIHARA and S. NASU, 1989, in New Materials by Mechanical Alloying, eds. E. Arzt and L. Schultz (DGM Verlag Oberursel), p. 319.
SHULL, R. D., 1993, Nanostructured Materials **2,** 213.
SIEGEL, R. W., 1993, Mater. Sci. and Eng. **A168,** 189.
SILCOCK, J. M. and W. T. TUNSTALL, 1964, Phil. Mag. **10,** 361.
SIMPSON, C. J., K. T. AUST and C. WINEGARD, 1971, Metall. Trans. **2,** 987.
SMIDODA, K., CH. GOTTSCHALK and H. GLEITER, 1978, Acta Metall. **26,** 1833.
SMITH, C. S., 1948, Trans. AIME **175,** 15.
SMITH, C. S., 1952, Metal Interfaces, Amer. Soc. for Metals, Cleveland, Ohio, USA, p. 65.
SMITH, C. S., 1954, Met. Rev. **9,** 1.
SMITH, D. A. and R. C. Pond, 1976, Internat. Met. Rev. **205,** 61.
STEWART, 1972, Introduction to Glass Science, eds. L. D. Pye, H. J. Stevens, W. C. LaCourse (Plenum Press New York, USA), p. 237.
STIEGLER, J. O. and K. FARRELL, 1974, Scripta Metall. **8,** 651.
STONEHAM, A. M., 1971, J. Phys. **F1,** 118.
STONEHAM, A. M. and P. W. TASKER, 1988, Surface and Near Surface Chemistry of Oxide Materials, eds. J. Nowotny and L. C. Dufour (Elsevier Publ., Amsterdam), p. 1.
SURYANARAYANA, C. and F. H. FROES, 1992, Met. Trans **A23,** 1071.
SUTTON, A. P. and R. W. BALLUFFI, 1987, Acta Metall. **35,** 2177.
SUTTON, A. P., 1988, Interfacial Structure, Properties and Design, in: Mat. Res. Soc. Symp. Proc. **122,** 43 (see also *Further reading*).
SUTTON, A. P., 1989, Phase Transitions **16/17,** 563.
SUTTON, A. P., 1990, J. de Physique suppl no 1 **51,** C1–35.
SUTTON, A. P. and R. W. BALLUFFI, 1995, Interfaces in Crystalline Materials. Oxford University Press.
TANAKOV, M. YU., L. I. TRUSUV and B. YA. LJUBOV, 1991, Scripta Metall. et Mater. **25,** 413.
TEWARY, V. K., 1973, J. Phys. **F3,** 1275.
TIAPKIN, YU. D., N. T. TRAVINA and T. V. YEVTSUSHENKO, 1976, Scripta Metall. **10,** 375.
TIEN, J. and S. COPLEY, 1971, Metallurg. Trans. **2,** 215.
TILLER, W. A. and R. SCHRIEFFER, 1974, Scripta Metall. **8,** 487.
TONG, H. Y., B. Z. DING, J. T. WANG, K. LU, J. JIANG and J. ZHU, 1992, J. Appl. Phys. **72,** 5124.
TRINKHAUS, H., C. ABROMEIT and J. VILLAIN, 1989, Phys. Rev. **B40,** 12531.
TSCHOEPE, A. and J. YING, 1995, Nanostructured Materials, **6,** 1005.
TURNBULL, D., 1951, Trans. AIME **191,** 661.
TURNBULL, D., J. S. C. JANG and C. C. KOCH, 1990, J. Mat. Res. **5,** 1731.
TYLER, S. K. and P. J. GOODHEW, 1980, J. Nucl. Mater. **92,** 201.
UBBELOHDE, A. R., 1965, Melting and Crystal Structure (Oxford Univ. Press).
VAN DER WALLE, C. G. and R. M. MARTIN, 1985, J. Vac. Sci. Techn. **B3,** 1256.
VEITH, M. and K. KUNZE, 1991, Angew. Chem. **103,** 845.
VEITH, M., D. KAEFER, J. KOCH, P. MAY, L. STAHL, V. HUCH, 1992, Chem. Ber. **125,** 1033.
VEPREK, S. and F. A. SAROTT, 1987, Phys. Rev. **B36,** 3344.
VOLKL, J., 1972, Ber. Bunsen Gesell. **76,** 797.
WAGNER, C., 1961, Z. Elektrochem. **65,** 581.
WARLIMONT, H. and G. THOMAS, 1970, Met. Sci. J. **4,** 47.
WARREN, B. E., 1937, J. Appl. Phys. **8,** 645.
WASYNCZUK, J. A. and M. RÜHLE, 1987, Ceramic Microstructure '86: Role of Interfaces, eds.: J. A. Pask and A. G. Evans (Plenum Press, New York), p. 87.
WATANABE, T., 1984, Res. Mechanica **2,** 47.
WATANABE, T., 1993, Mater. Sci. and Eng. **A166,** 11.
WEATHERLY, G. C. and Y. G. NAKAGAWA, 1971, Scripta Metall. **5,** 777.

WEISSMUELLER, J., W. KRAUSS, T. HAUBOLD, R. BIRRINGER and H. GLEITER, 1992, Nanostructured Materials **1,** 439 and ibid **3,** 261.
WEINS, M., H. GLEITER and B. CHALMERS, 1971, J. Appl. Phys. **42,** 2639.
WERT, J., 1976, Acta Metall. **24,** 65.
WHITMAN, W. D ., 1926, Amer. J. Sci., Ser. 5, **11,** 126.
WILLIS, J. R., 1975, Mech. Phys. Sol. **23,** 129.
WILSON, W. L., P. F. SZAJOWSKI and L. E. BRUS, 1993, Science **262,** 1242.
WINGROVE, M. and D. M. TAPLIN, 1969, J. Mater. Sci. **4,** 789.
WIRTH, R. and H. GLEITER, 1981a, Acta Metall. **29,** 1825.
WIRTH, R. and H. GLEITER, 1981b, J. Mater. Sci. **16,** 557.
WITTMER, M., 1985, Mat. Res. Soc. Symp. Proc. **40,** 393.
WOLF, D., 1985, J. Physique **46,** C4–197.
WOLF, D., 1990, J. Appl. Phys. **68,** 3221.
WOLF, D., 1991, Philos. Mag. **A63,** 1117.
WOLF, D. and S. YIP, eds. 1992, Materials Interfaces, Chapman and Hall, London, p. 1 and 139.
WUERSCHUM, R., W. GREINER and H.-E. SCHAEFER, 1993, Nanostructured Materials **2,** 55.
YOSHIZAWA, Y., S. OGUMA and K. YAMAUCHI, 1988, J. Appl. Phys. **64,** 6044.
ZACHARIASEN, W. H., 1932, J. Am. Chem. Soc. **54,** 3841.

Further reading

For further reading we refer to the review articles mentioned in the various sections.

Since this chapter was written, a major text has been published: A. P. Sutton and R. W. Balluffi: "Interfaces in Crystalline Materials". (Oxford University Press, 1995).

– SUBJECT INDEX –

1st Volume: Pages 1–942
2nd Volume: Pages 943–1830
3rd Volume: Pages 1831–2740

"page number ff" signifies that treatment of the topic continues on the following page(s).

The late Prof. Peter Haasen

Colour picture on front cover:

Simulation of an alloy dendrite growing into a supercooled liquid using the phase-field method. The colours show variation of composition (atomic fraction Cu) in the liquid and solid for parameters approximating a Ni-Cu alloy with 0.41 atomic fraction Cu. See ch. 8, par. 7.5 (Courtesy of William J. Boettinger and James A. Warren).

ISBN 0 444 89875 1